HANDBOOK OF Reflector Antennas and Feed Systems

VOLUME II

Feed Systems

Lotfollah Shafai
Satish K. Sharma
Sudhakar Rao
editors

Handbook of Reflector Antennas and Feed Systems

Volume II

Feed Systems

For a listing of recent titles in the
Artech House Antennas and Propagation Series,
turn to the back of this book.

Handbook of Reflector Antennas and Feed Systems

Volume II

Feed Systems

Sudhakar Rao
Satish K. Sharma
Lotfollah Shafai

ARTECH
HOUSE

BOSTON | LONDON
artechhouse.com

Library of Congress Cataloging-in-Publication Data
A catalog record for this book is available from the U.S. Library of Congress

British Library Cataloguing in Publication Data
A catalog record for this book is available from the British Library.

ISBN-13: 978-1-60807-517-1

Cover design by Vicki Kane

© 2013 Artech House

All rights reserved. Printed and bound in the United States of America. No part of this book may be reproduced or utilized in any form or by any means, electronic or mechanical, including photocopying, recording, or by any information storage and retrieval system, without permission in writing from the publisher.

All terms mentioned in this book that are known to be trademarks or service marks have been appropriately capitalized. Artech House cannot attest to the accuracy of this information. Use of a term in this book should not be regarded as affecting the validity of any trademark or service mark.

10 9 8 7 6 5 4 3 2 1

Contents

Preface xi

CHAPTER 1
Introduction 1

1.1 Introduction 1
1.2 The Feed System 3
1.3 Phase Center Determination 6
1.4 Feed Efficiency 7
1.5 Organization of the Book 9
References 11

CHAPTER 2
Numerical Methods 13

2.1 Introduction 13
2.2 Maxwell's Equations: Foundations of Electromagnetic Analysis 14
  2.2.1 Green's Functions and Integral Representations 16
2.3 Method of Moments (MoM) 17
  2.3.1 Integral Equation Formulation 18
  2.3.2 Geometry Representations and Meshing 19
  2.3.3 Basis Functions 22
  2.3.4 Construction of the Impedance Matrix Equation 22
  2.3.5 Direct and Iterative Solution Methods 23
  2.3.6 Examples 24
2.4 Finite-Element Method (FEM) 28
  2.4.1 Functional Formalism and Discrete Formulation 30
  2.4.2 Material Modeling, Boundary Conditions, and Feed Modeling 31
  2.4.3 Discretization and Basis Functions 31
  2.4.4 Example 34
2.5 Hybrid FE-BI and Domain Decomposition Techniques 35
  2.5.1 Hybrid Finite-Element-Boundary Integral (FE-BI) Formulation 35
  2.5.2 Example 36
2.6 Fast Methods for Integral Equations 36
  2.6.1 Fast Multipole Method (FMM) 38
  2.6.2 Examples 40

- 2.6.3 Model Order Reduction for Fast Frequency Sweep 41
- 2.6.4 Example 43
- 2.7 High-Frequency Techniques 43
  - 2.7.1 Physical Optics (PO) and Geometrical Optics (GO) 43
  - 2.7.2 Example 46
  - 2.7.3 Geometrical Theory of Diffraction and Uniform Theory of Diffraction 46
- Acknowledgments 49
- References 49

CHAPTER 3
Electrically Small Feeds 51

- 3.1 Introduction 51
- 3.2 Design Requirements 53
- 3.3 Waveguide Feeds 56
  - 3.3.1 Small Waveguide Feeds 57
  - 3.3.2 Small Coaxial Feeds 64
  - 3.3.3 Small Wide Angle Feeds 67
  - 3.3.4 Small Backfire Feeds 70
- 3.4 Microstrip Feeds 74
  - 3.4.1 Single Patch Antenna as the Reflector Feed 74
  - 3.4.2 Planar Antenna Array Feeds 81
- 3.5 Backfire Printed Dipole Feeds 83
  - 3.5.1 Design Approach 83
  - 3.5.2 Performance Results 84
  - 3.5.3 Printed Dipole Performance with a Reflector 89
- 3.6 Asymmetric Feeds 90
- 3.7 Feed Pattern Shaping by Superstrate Loading 92
- References 93

CHAPTER 4
Smooth Wall Multimode Horns for High Aperture Efficiency—Theory, Design, and Applications 97

- 4.1 Introduction 97
- 4.2 Theory for High Aperture Efficiency 99
- 4.3 Circular Aperture 102
  - 4.3.1 Realization of the Modes 103
  - 4.3.2 Circular Horn Design 105
  - 4.3.3 Three-Step Horn 110
- 4.4 Square High-Efficiency Horn 111
- 4.5 Multiflared High-Efficiency Horns 113
- 4.6 Other High-Efficiency Horn Structures 115
- 4.7 Applications 115
  - 4.7.1 In Direct Radiating Arrays 115
  - 4.7.2 In Multiple-Beam Reflectors 117
- 4.8 Conclusions 119
- References 119

CHAPTER 5

Profiled Horns and Feeds 123

5.1 Introduction 123
5.2 Basis of Optimum Horns 124
    5.2.1 Pattern Constraints 125
    5.2.2 Input Mismatch 126
    5.2.3 Aperture Efficiency 126
    5.2.4 Phase Center Stability 129
    5.2.5 Compactness and/or Physical Constraint Due to Existing Environment 131
5.3 Choice of Horn Profiles 133
5.4 Optimization of Horn Profile 134
    5.4.1 Possible Approaches 134
    5.4.2 Optimization Methods 137
5.5 Examples of Horn Designs 139
    5.5.1 Corrugated Horn 140
    5.5.2 Smooth-Walled Circular and Coaxial Horns 140
    5.5.3 Rectangular Horn 143
    5.5.4 Dielectric Rod and Horn 145
    5.5.5 Arrays of Profiled Horns 148
5.6 Conclusion 151
References 151

CHAPTER 6

Soft and Hard Horn Antennas 157

6.1 Introduction to Hybrid Mode Horn Antennas 157
6.2 Definition of Soft and Hard Surfaces 158
6.3 Soft and Hard Horn Designs and Implementations 160
    6.3.1 Soft Corrugated Horns 160
    6.3.2 Horns with a Dielectric Core (Dielcore Horns) 162
    6.3.3 Soft Strip-Loaded Horns 171
    6.3.4 Hard Strip-Loaded and Corrugated Horns 172
    6.3.5 Metamaterial Horns (Meta-horns) 173
6.4 Hard Horns as Feeds for Array Antennas 183
6.5 Conclusions 186
References 188

CHAPTER 7

Circularly Polarized Feed Antennas 193

7.1 Introduction 193
7.2 Analysis Methods for CP Feed Antenna Design 195
    7.2.1 Method of Moments (MoM) 195
    7.2.2 Finite-Difference Time-Domain Method (FDTDM) 199
7.3 Polarizer and Two-Point Excitation Patch 202
7.4 One-Point Excitation CP Patch Feed Antenna 205
7.5 End-Fire Helical CP Feed Antenna 207

7.5.1 Effects of a Cavity 208
7.5.2 Frequency Response 210
7.6 CP Feed Array Antenna Composed of End-Fire Helical Elements 215
7.7 Conical Helical CP Feed Antennas 219
7.8 Back-Fire-Mode CP Helical Feed Antenna 227
7.8.1 Back-Fire Radiation 227
7.8.2 Frequency Response of the Current 230
7.8.3 Effects of Pitch Angle on the Frequency Response of the Antenna Characteristics 231
7.9 Spiral CP Feed Antenna 237
7.10 Curl CP Feed Antenna 245
7.10.1 CP Radiation 245
7.10.2 Beamwidth 247
7.10.3 Frequency Response 249
Acknowledgments 253
References 253

CHAPTER 8
Generalized Asymmetric Reflector Antenna Feeds for Polarization Control and Adaptive Virtual Array Design 257

8.1 Introduction 257
8.2 Applications of Asymmetric Feeds 260
8.2.1 Cross Polarization Reduction in Offset Reflector Antennas 261
8.3 Asymmetric Feed Designs for Cross Polarization Reduction 273
8.3.1 Feed 1: Ring Choke Excited Circular Waveguide with Slot 273
8.3.2 Feed 2: Stepped Circular Waveguide with Tuning Blocks 278
8.4 Multiphase Center Reflector Antennas and Virtual Array Formation 282
8.4.1 The Concept Theory 283
8.4.2 Symmetrical-Cut Paraboloids 284
8.4.3 Adaptive Asymmetric Feed Designs for Multiphase Center Applications 286
8.4.4 Feed 3: Adaptive Dual-mode TE_{11} and TE_{21} Feed 287
8.4.5 Feed 4: Adaptive Dual-mode TE_{11} and TM_{01} Feed 290
8.4.6 Feed 5: Adaptive Triple-Mode $TE_{11} + TM_{01} + TE_{21}$ Feed 295
8.5 Concluding Remarks 297
References 297

CHAPTER 9
Array Antennas and Low-Gain TT&C Antennas 299

9.1 Introduction 299
9.2 Array Antennas 300
9.2.1 Array Design 301
9.2.2 Radiating Elements 310
9.2.3 Array Radiation Patterns 315
9.3 Low Gain TT&C Antennas 320

9.3.1 TT&C Subsystem and Antenna Applications 322
9.3.2 TT&C Antennas Introduction 324
9.3.3 TT&C RF Block Diagram and Link Budgets 327
9.3.4 Low-Gain TT&C Antennas 328
References

About the Editors 351

Index 355

Preface

L. Shafai, University of Manitoba

Reflector antennas are extraordinary devices that combine high gain with geometrical simplicity and can operate in broad frequency bands. However, their performance depends on the electrical characteristics of the feed antennas that they operate with. The feed design is therefore the most important aspect of the reflector antenna design, and this volume is devoted to its theory, design, and analysis. From a practical point of view, the reflector feeds can be electrically small when used with single reflectors and large in dual reflectors. The mathematical approach and methodology for their design and analysis will also be different. In addition, the intended applications of reflector antennas will influence their characteristics and thus the feed properties and design.

To provide a comprehensive treatment of the topic, different chapters of this volume are devoted to different feed types, and experts in the area have authored each chapter. Following the introductory chapter, the mathematical techniques, in the form of efficient numerical methods for the feed design and analysis, are presented in Chapter 2. Chapter 3 addresses electrically small feeds, and both waveguide and printed planar types are discussed. Chapter 4 concentrates on the theory and design techniques for maximizing the feed efficiency, from the point of view of reflector antenna gain. Chapters 5 and 6 deal with the feed geometry and boundary conditions on its walls. Profiled geometries are considered to reduce the size and optimize the efficiency, while soft and hard boundary conditions are used to generalize the feed design and introduce metamaterials to improve the performance and physical characteristics. Chapter 7 addresses the circularly polarized feeds, which are important in mobile and satellite communications. Chapter 8 presents a special class of multimode horns in the form of asymmetric feeds for polarization control and adaptive virtual arrays in parabolic reflector antennas. The mathematical treatment of the concept, along with practical equivalent hardware for both areas of interest, is discussed. The applications of the feed antennas are not limited to the reflector antennas. They are equally important in reflectarrays, lenses, and large direct radiating antenna arrays. They can be used in reflectarrays and lenses, as in reflector antennas, with similar performance and design criteria, as presented in these chapters. However, antenna arrays must take into account the array design rules and performance characteristics. For this reason, Chapter 9 is devoted to antenna arrays. It also covers the telemetry, tracking, and command antennas, which are important in satellite communications but not discussed adequately in open literature.

While the book is intended to address the fundamental aspects of the feed theory and design, ample examples are also provided to help with the practical aspects of the feed design. In most cases, the material in various chapters is based on the published work of the authors. However, other pertinent works are also included to explain the underlying principles and to help with improving the practical designs. It is hoped that the materials in different chapters of the book will provide comprehensive insights into the critical aspects of reflector antenna feeds and impart useful design rules to readers.

Many people have contributed to the preparation and completion of this volume, and I would like to extend my sincere appreciation for their interest, dedication, contributions, and hard work. Special thanks are due to sixteen authors who volunteered to write their respective chapters and share their knowledge and visions with the antenna community. Thanks are also due to Shelly Girardin for patiently reviewing the manuscripts, unifying the text formats and writing styles, and working with Artech House staff. I would also like to thank Artech House staff for their support and help throughout the preparation of this volume. Special thanks are due to Samantha Ronan, the Development Editor, for handling the project and helping with intermediate planning and completion of the work. Thanks are due also to Mark Walsh, Senior Acquisition Editor, and other Artech House staff in the production department for working on this project and the completion of this volume.

Personally, I would like to thank my students and colleagues, whom I have had the privilege to work with throughout my professional career, for their scientific and technical contributions. I would also like to thank Mr. Brad Tabachnick, the antenna technologist, for fabrication and test of the feed prototypes and his valuable advice throughout the design stage. Special thanks are due to Dr. Ahmed Kishk for developing the first-ever feed design software and accurate analysis of many novel feed designs. Special thanks are due also to Dr. Z. A. Pour for developing asymmetric feeds and for her extensive contributions to chapters of this volume and related technical reviews.

I would also like to thank my coeditors, Drs. Sudhakar Rao and Satish Sharma, for their contributions, help, and encouragement throughout this project.

Last, but not least, I would like to thank my family for their support and encouragement, Joanne for her invaluable help with publication and copyright issues, and Cyrus and Leili for their engineering and other technical contributions.

L. Shafai
May 2013

CHAPTER 1

Introduction

L. Shafai, University of Manitoba
S. K. Sharma, San Diego State University
Z. A. Pour, University of Manitoba

1.1 Introduction

Reflector antennas have a variety of configurations that have been tailored for different applications. There are three main configurations that can be symmetric or offset. The symmetric geometries, shown in Figure 1.1, consist of a single reflector system, in Figure 1.1(a), normally known as the prime focus system; the Cassegrainian dual reflector system, in Figure 1.1(b); and the Gregorian dual reflector system, in Figure 1.1(c). Most of these reflector antennas deal with communications and remote sensing applications that operate within the far field range and require high gains and narrow beamwidths. Important near field applications also exist. One such case is in antenna testing, where the spherical wave of the transmit antenna is converted to quasi-uniform field distribution in front of the reflector aperture, where the test antenna is located. The system, known as the compact range, eliminates the need for large outdoor test ranges for testing large antennas. Figures 1.2(a) and (b) show representative cases: symmetric and offset prime focus reflector systems being tested in a compact range. Figure 1.3 shows the compact range system, which is based on a large, serrated-edge offset reflector while being used for testing another smaller reflector antenna.

In nearly all reflector antenna applications, the reflector dimensions are large in terms of the wavelength. Their analysis can be simplified using asymptotic techniques, such as the physical optics approximation or methods based on the diffraction theory. Analyses based on more exact numerical techniques, however, become time consuming. This is more important in dual reflector systems, especially the offset systems, where more than one reflection must be considered, and simplifications based on geometrical symmetry cannot be used. For this reason, equivalent parabolas are defined to convert a dual reflector system into a single one and are used to simplify the analysis [1]. This chapter deals with the feed systems only, and so the details of the reflector analysis techniques are omitted here for brevity. They are discussed in Volumes I and III of this series.

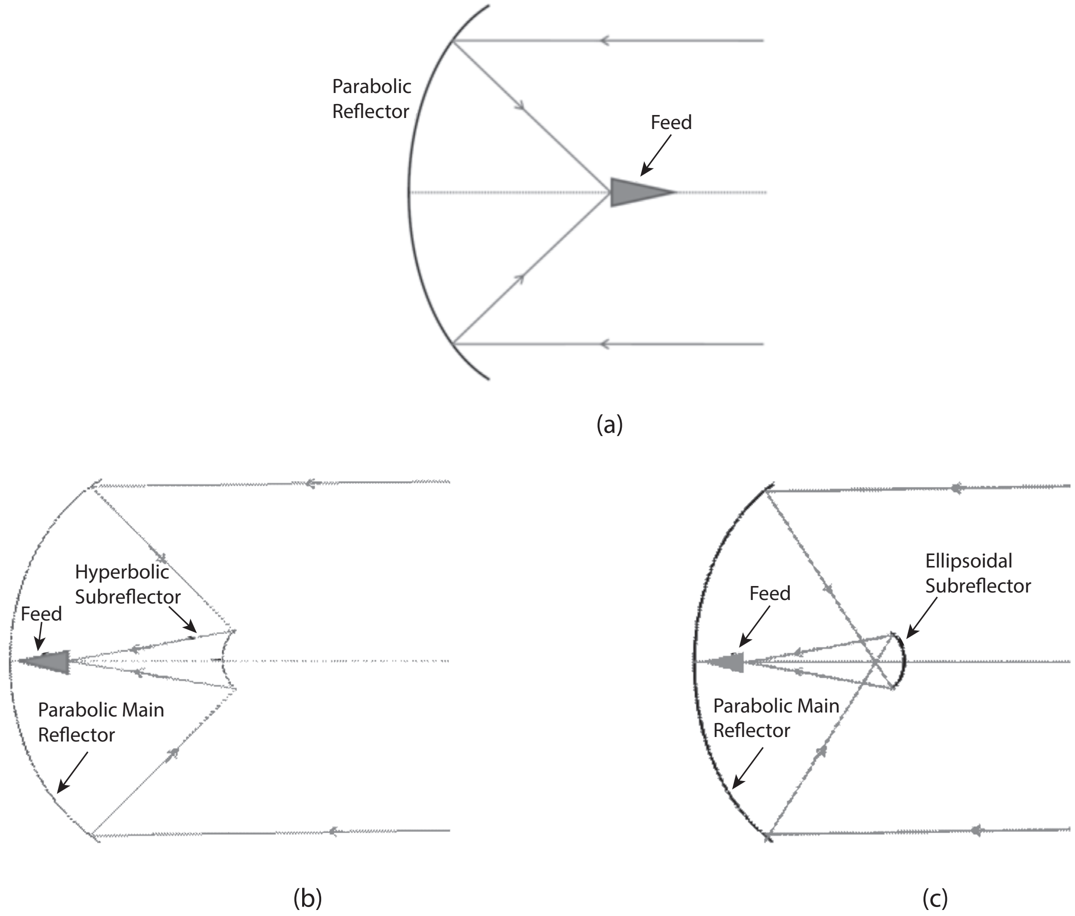
Parabolic Reflector
Feed
Hyperbolic Subreflector
Feed
Parabolic Main Reflector
Ellipsoidal Subreflector
Feed
Parabolic Main Reflector

(a)

(b)

(c)

Figure 1.1 Geometries of three main symmetric reflector antennas. (a) Prime focus system, (b) Cassegrainian system, and (c) Gregorian system.

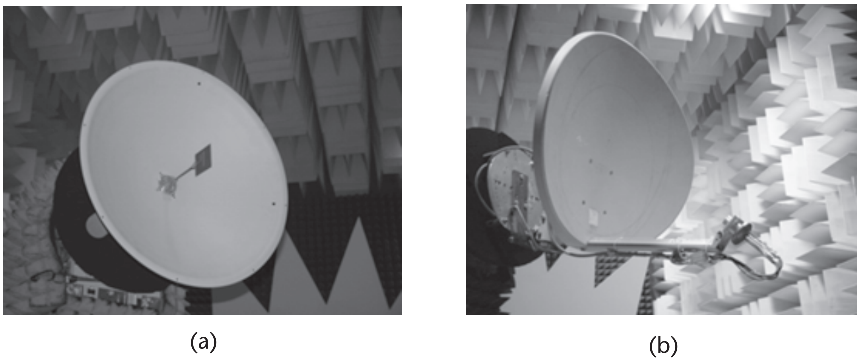

(a)

(b)

Figure 1.2 Typical prime focus reflector antennas with the feed at their focal points. (a) Symmetric reflector with a low cross-section printed dipole feed. (b) Offset prime focus reflector with a multimode feed; both antennas shown while being tested in the compact range of the University of Manitoba.

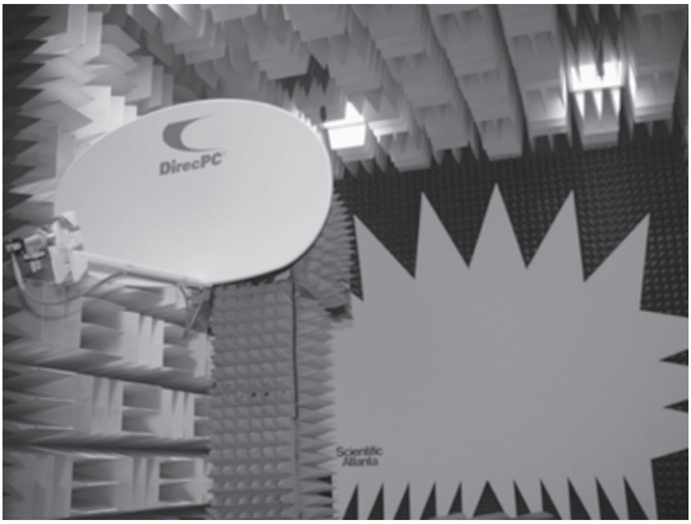

Figure 1.3 Compact range reflector of the University of Manitoba, while testing another reflector.

1.2 The Feed System

In reflector antennas, the feed is the primary source of illumination and as such it influences the performance of the system. Its importance, however, is dependent on the reflector focusing system. In dual reflectors, the shaping of one or both reflector profiles can partly overcome the deficiency of the feed. However, in single prime focus reflectors, the feed controls the system performance. Thus, its design is the most critical challenge. Even in offset systems, where the reflector asymmetry causes undesired cross polarization, a proper feed design can significantly reduce the cross polarization of the reflected field.

The aperture size of the feed is strongly dependent on the reflector configuration as well as the directivity and sidelobe levels of the secondary reflector patterns. In dual reflector antennas, the subtended angle of the reflector, facing the feed, is small. Thus, the feed aperture size tends to be large to generate far field radiation patterns with narrow beamwidths. Although the large feed size complicates the fabrication, the narrow beamwidth simplifies the design rules for analytic solutions. Consequently, accurate formulations are developed and used for excellent feed designs. In prime focus reflectors, the reflector-subtended angles are normally large, which require small feed aperture sizes. Thus, asymptotic or other approximations cannot be made for their accurate analysis. Efficient numerical techniques are required, or the use of experimental techniques, which were used in the early feed designs. Such experimental techniques are efficient for an experienced designer, but difficulties arise in the optimization stage. Additional help from the electromagnetic properties of the feeds and the secondary patterns of the reflector are needed to simplify the design. Fortunately, such information has been found through the radiation patterns and the cross polarization.

In small feeds, the aperture field distribution can be approximated by electric and magnetic dipoles [2]. The equivalence principle can be used to compute the radiated field, which can be in terms of the aperture electric field, the aperture magnetic field, or both [3]. In the latter case, the dipole field equivalence is used to simplify the formulation and find the relationship between the electric and magnetic dipoles to minimize the cross polarization and control the radiation patterns. For example, for an electric dipole, oriented along the x-axis, the radiated far field will be [1, 4]:

$$E_\theta^e = c^e \cos\theta \cos\phi \frac{e^{-jkr}}{r} \tag{1.1}$$

$$E_\phi^e = -c^e \sin\phi \frac{e^{-jkr}}{r} \tag{1.2}$$

where c^e is a complex constant dependent on the strength of the electric dipole.

Then, from Ludwig's third definition [5] of cross polarization the co-polarized and cross-polarized components of the radiated field become

$$E_{\text{co}}^e = \frac{1}{2}\left[(1+\cos\theta) - (1-\cos\theta)\cos 2\phi\right] c^e \frac{e^{-jkr}}{r} \tag{1.3}$$

$$E_{\text{cross}}^e = -\frac{1}{2}\left[(1-\cos\theta)\sin 2\phi\right] c^e \frac{e^{-jkr}}{r} \tag{1.4}$$

Similarly, for a magnetic dipole oriented along the y-axis the corresponding radiation field components become

$$E_\theta^m = c^m \cos\phi \frac{e^{-jkr}}{r} \tag{1.5}$$

$$E_\varphi^m = -c^m \cos\theta \ \sin\phi \frac{e^{-jkr}}{r} \tag{1.6}$$

which give the co-polarized and cross-polarized components as

$$E_{co}^m = \frac{1}{2}\left[(1+\cos\theta) + (1-\cos\theta)\cos 2\phi\right] c^m \frac{e^{-jkr}}{r} \tag{1.7}$$

$$E_{cross}^m = \frac{1}{2}\left[(1-\cos\theta)\sin 2\phi\right] c^m \frac{e^{-jkr}}{r} \tag{1.8}$$

Adding the contribution of the two orthogonal dipoles, and for $c^e = c^m$ one gets

$$E_{\text{co}} = \left(1 + \cos\theta\right) c^{e} \frac{e^{-jkr}}{r} \tag{1.9}$$

$$E_{\text{cross}} = 0 \tag{1.10}$$

Thus, the resulting radiated field of the combined orthogonal electric and magnetic dipoles is a perfectly linearly polarized field, with zero cross polarization. This provides a simple rule for designing small feeds for symmetric prime focus reflectors, which is equalizing the contribution of the electric and magnetic fields of the aperture to the far field radiations to provide zero cross polarization. For instance, in an open-ended waveguide the radiation is mostly due to the aperture field and the ring current on the waveguide end. Thus, by increasing the waveguide diameter, from its size at cut-off, the cross polarization of the radiated field decreases until it reaches a minimum before the excitation of the second mode. Similarly, in a circular microstrip antenna, the patch radiation is due to the electric dipole, and that of the substrate beyond the patch is due to both electric and magnetic fields. By increasing

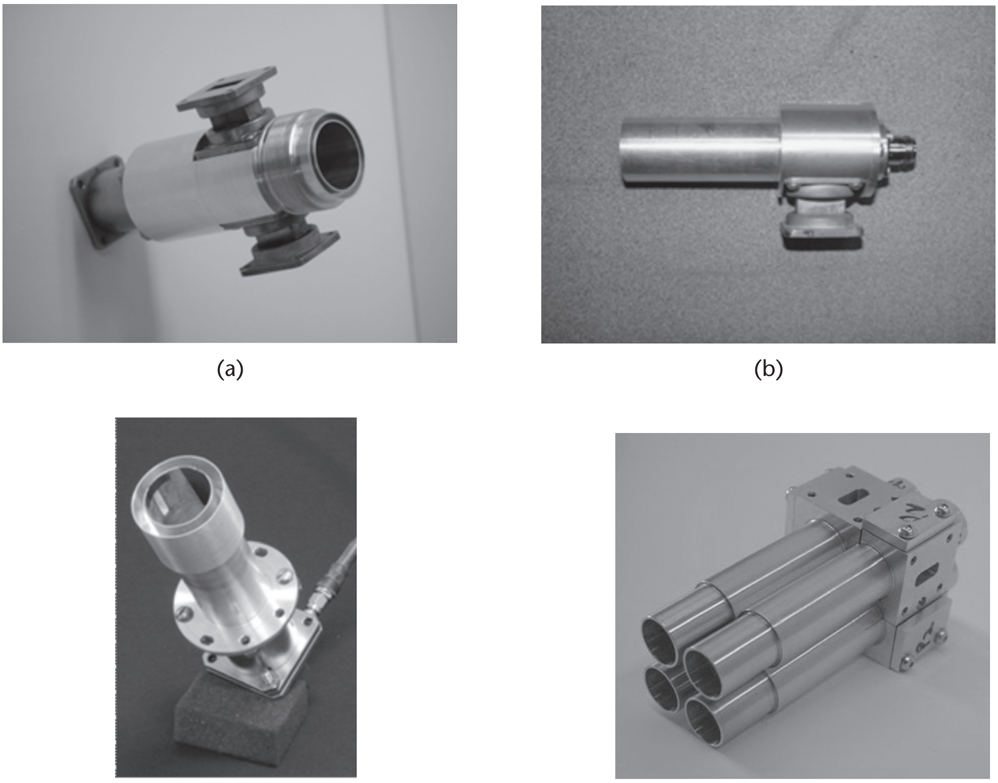

(a) (b)

(c) (d)

Figure 1.4 Family of special application feeds designed by the authors for reflector antennas. (a) $TE_{11} + TE_{21}$ and (b) $TE_{11} + TM_{01}$ adaptive feeds for adaptive aperture reflector antennas, (c) $TE_{11} + TE_{21}$ asymmetric feed for polarization control in offset reflectors, and (d) four-element TE_{11} monopulse feed for tracking and communication.

the ground plane diameter, from the patch size, the cross polarization decreases initially and reaches a minimum before starting to increase again. This property is used in Chapter 3 to design circular microstrip patch feeds with low cross polarization. Note that in the latter case, the cross polarization cannot be reduced significantly, unless the higher order modes of the patch can be cancelled by its feed or by other means. For other feed types, similar techniques can be developed to design feeds with low cross polarization, which are discussed in the upcoming chapters.

Aside from providing efficient reflector illumination for high gains, the reflector feed can also be used to perform other functions, such as the polarization control in dual-polarized reflectors, reduction of cross polarization in offset reflectors, and signal processing. To improve the feed performance in such cases, normally an array of feeds or feeds with multimode operation are used. Representative cases of such sophisticated feeds are shown in Figure 1.4. Two examples of adaptive dual-mode feeds are shown in Figure 1.4(a) and (b), which will be detailed in Chapter 8 of this volume for multiphase center virtual antenna applications. A simple dual-mode matched feed is depicted in Figure 1.4(c) for cross polarization reduction in offset reflectors, which will be fully explained in Chapter 3 of this volume. Finally, a four-element array feed is shown in Figure 1.4(d) for monopulse tracking systems.

1.3 Phase Center Determination

In the preceding dipole equivalence case, both electric and magnetic dipoles shared a common coordinate origin, that is, the feed had a unique phase center location. In practical feeds, on the other hand, this is no longer the case, and the phase center locations differ in the orthogonal planes. However, for low cross polarization they must be either coincident or very close to each other. In the design of the feeds for low cross polarization, the two phase centers must be as close to each other as possible. To accomplish this, the phase center location must be determined from the radiation patterns. For symmetric configurations the phase center is located on the axis of symmetry, which can be assumed to be along the z-axis. The feed radiation function can therefore be expressed as

$$E(r,\theta,\phi) = \left[A(\theta)\sin\phi\, \boldsymbol{u}_\theta + C(\theta)\cos\phi\, \boldsymbol{u}_\phi\right]\frac{e^{-jkr}}{r} \tag{1.11}$$

The diagonal component of the co-polarized term of (1.11) can be written as

$$A(\theta) + C(\theta) = \left|A(\theta) + C(\theta)\right| \exp\left[j\Phi(\theta)\right] \tag{1.12}$$

where $\Phi(\theta)$ represents the phase of the co-polarized term at the diagonal plane, measured from the coordinate origin, which may not be the phase center location. The actual phase center will be on the z-axis, but at a distance d_c from the origin. Thus, transforming (1.12) to the feed phase center location gives

$$A(\theta) + C(\theta) = \left|A(\theta) + C(\theta)\right| \exp\left[j\Phi_{d_c}(\theta)\right] \tag{1.13}$$

with

$$\Phi_{d_c}(\theta) = \Phi(\theta) - kd_c \cos\theta \tag{1.14}$$

where d_c is the distance of the phase center from the coordinate origin. The steps for determining the distance d_c (i.e., the location of the phase center) depend on the design requirements. In practice, the feed is required to illuminate the reflector over a certain angular range. However, within any angular range the E-plane and H-plane patterns (i.e., $A(\theta)$ and $C(\theta)$) will not have the same behavior and the computed value of d_c is θ dependent. For this reason, its value over a given angular range must be found as the most desirable value. That is, the phase center location over a given angular range must be determined by optimizing a certain required function, such as the least variation of the feed phase pattern over the reflector aperture or maximization of the reflector gain factor, and so on. In the former case, the phase of the feed radiation pattern is computed in principal planes and determines d_c to minimize its variation. In general, d_c will not be the same in both principal planes, and the average value may be selected. Alternatively, if the objective of the feed design is to maximize the reflector gain, one must determine d_c to maximize the feed efficiency, defined in the next section, for the reflector.

1.4 Feed Efficiency

The feed efficiency η_f is the measure of its ability in illuminating the reflector to provide high gain. As such, it is defined as the ratio of the reflector gain over the gain of the uniformly illuminated aperture [6]. For a parabolic reflector having a subtended half-angle of ψ_0 and excluding the aperture blockage, the feed efficiency using (1.11) through (1.14) becomes

$$\eta_\mathrm{f} = \cot^2\left(\frac{\psi_0}{2}\right) \times \frac{\left[\int_0^{\psi_0} \left|A(\theta) + C(\theta)\right| \exp\left\{j\Phi_{d_c c}(\theta)\right\} \tan(\theta/2)\, d\theta\right]^2}{\int_0^{\pi} \left[\left|A(\theta)\right|^2 + \left|C(\theta)\right|^2\right] \sin\theta\, d\theta} \tag{1.15}$$

Because the feed is not ideal, a number of factors contribute to its efficiency:

- The power lost beyond the reflector edge, which does not illuminate the reflector (i.e., the spillover efficiency η_sp);
- The cross polarization of the feed that channels the feed power to unwanted polarization (i.e., the polarization efficiency η_p);
- The nonuniformity of the aperture field illumination that contributes to the illumination efficiency η_I;
- The phase error of the aperture field that contributes to the phase efficiency η_ϕ.

The overall feed efficiency is the product of these four subefficiencies and can be written as

$$\eta_{\mathrm{f}} = \eta_{\mathrm{sp}}\, \eta_{\mathrm{p}}\, \eta_{\mathrm{I}}\, \eta_{\phi} \tag{1.16}$$

The expression for these subefficiencies can be written from their definitions, and in terms of the co- and cross-polarized components of the fourfold symmetric field, as provided in [8], which are listed below for convenience.

$$\eta_{\mathrm{f}} = 2\cot^2\left(\frac{\psi_0}{2}\right)\frac{\left|\int_0^{\psi_o}\mathrm{CO}(\theta)\tan(\theta/2)\,d\theta\right|^2}{\int_0^{\pi}\left[|\mathrm{CO}(\theta)|^2+|\mathrm{XP}(\theta)|^2\right]\sin\theta\,d\theta} \tag{1.17}$$

$$\eta_{\mathrm{sp}} = \frac{\int_0^{\psi_0}\left[|\mathrm{CO}(\theta)|^2+|\mathrm{XP}(\theta)|^2\right]\sin\theta\,d\theta}{\int_0^{\pi}\left[|\mathrm{CO}(\theta)|^2+|\mathrm{XP}(\theta)|^2\right]\sin\theta\,d\theta} \tag{1.18}$$

$$\eta_{\mathrm{p}} = \frac{\int_0^{\psi_0}|\mathrm{CO}(\theta)|^2\sin\theta\,d\theta}{\int_0^{\psi_0}\left[|\mathrm{CO}(\theta)|^2+|\mathrm{XP}(\theta)|^2\right]\sin\theta\,d\theta} \tag{1.19}$$

$$\eta_{\mathrm{I}} = 2\cot^2\left(\frac{\psi_0}{2}\right)\frac{\left[\int_0^{\psi_0}|\mathrm{CO}(\theta)|\tan(\theta/2)\,d\theta\right]^2}{\int_0^{\psi_0}|\mathrm{CO}(\theta)|^2\sin\theta\,d\theta} \tag{1.20}$$

$$\eta_{\phi} = \frac{\left|\int_0^{\psi_0}\mathrm{CO}(\theta)\tan(\theta/2)d\theta\right|^2}{\left[\int_0^{\psi_0}|\mathrm{CO}(\theta)|\tan(\theta/2)\,d\theta\right]^2} \tag{1.21}$$

where

$$\mathrm{CO}(\theta) = \left[A(\theta)+C(\theta)\right]/2 \tag{1.22}$$

$$\mathrm{XP}(\theta) = \left[A(\theta)-C(\theta)\right]/2 \tag{1.23}$$

The preceding feed efficiencies are defined in the feed coordinate system and are valid with the assumption that the feed radiation patterns are symmetric. As such, they are valid for both symmetric and offset reflectors. However, all blockage effects are neglected.

1.5 Organization of the Book

This volume is organized into nine chapters:

Chapter 1: Introduction
Chapter 2: Computational EM Methods
Chapter 3: Electrically Small Feeds
Chapter 4: Smooth Wall Multimode Horns for High Aperture Efficiency—Theory, Design, and Applications
Chapter 5: Profiled Horns and Feeds
Chapter 6: Soft and Hard Horn Antennas
Chapter 7: Circularly Polarized Feed Antennas
Chapter 8: Generalized Asymmetric Reflector Antenna Feeds for Polarization Control and Adaptive Virtual Array Design
Chapter 9: Array Antennas and Low-Gain TT&C Antennas

Chapter 1 provides a general description of reflector antenna feeds and introduces their important electrical characteristics. The phase center concept is introduced and methods for its determination are provided. Feed efficiencies are also defined.

Chapter 2 deals with the mathematical techniques for feed design and analysis. Modern computational electromagnetics (CEM) methods have matured tremendously over the past decade, with several commercial software alternatives currently available (such as FEKO, HFSS, and so on). This chapter provides a brief summary of some of the most popular computer modeling techniques for the analysis and design of reflector antennas, their feeds, and other radiating structures in general. Starting from the first-principle of mathematical theory of electromagnetism, it introduces the method of moments (MoM) and the finite-element method (FEM) for the solution of integral and differential forms of Maxwell's equations, respectively. Crucial implementation details of MoM and FEM are summarized, along with representative examples to illustrate these methods. Hybrid formulations of MoM and FEM are also introduced as a generalization for modeling fidelity and efficiency. The chapter concludes with fast methods and high-frequency approximations (physical optics and geometrical theory of diffraction) for solving electrically large problems. This introductory chapter with the most recent developments in the field of CEM is by no means complete. Key references are provided for the interested readers to guide them into the "enchanted" realm of CEM.

Chapter 3 deals with electrically small feeds, an important class of feeds used in prime focus reflectors for both symmetric and offset types. The design rules are presented first, and their applications are discussed. The feed types are divided into two main categories of waveguide type feeds and the planar microstrip type feeds. In the former case, the design procedures are followed stepwise, from simple open-ended waveguides to more complex structures involving corrugated horns. For each case, the feed performance in efficiency, phase center, cross polarization, and back lobe levels is determined and discussed. The influence of different feed parameters is also studied and discussed. The advantages of coaxial waveguide feeds for dual-band applications are presented and used in practical feed designs. Beam shaping to tailor the feed radiation pattern to the available reflector is also studied and useful designs are provided. In the case of planar microstrip feeds, both microstrip patch and printed dipole feeds are considered and studied. The design rules are presented and practical designed feeds are provided. As a whole, the chapter provides comprehensive families of useful and practical feeds and methods for their designs and improvements.

Chapter 4 presents the design and analysis of high-efficiency, smooth wall horn structures. It begins with a discussion on the general principle of high aperture efficiency radiation. It is shown analytically that for achieving high aperture efficiency from a horn radiator, only the transverse electric (TE) types of waveguide modes should be excited. Also, for a given aperture shape, the relative amplitude and phase distributions of the modes are independent of the aperture size. It is then demonstrated that the required amplitude and phase distributions of the desired modes can be realized by using multiple steps and flared sections. It then presents the characteristics of circular and square high efficiency horn structures followed by their design procedures. The multiflared high-efficiency horns without steps are also considered, and their performances are compared with that of "step-and-flared" horns. Characteristic features of other types of high-efficiency horn structures are also discussed. Potential applications of high-efficiency horns in arrays and multibeam reflectors are shown and the advantages are discussed.

Chapter 5 outlines the historical development of employing the horn profile in designs to achieve a suitable radiation performance of an antenna feed for a reflector or lens. In particular, we show that by the use of modern computational methods for both representing the horn structure and automatic design through optimization, nonintuitive horn structures can be created that meet specified performance specifications. Representative examples are given that demonstrate the power of this design approach for general horn types that are metallic, smooth-walled or corrugated or for open structures such as dielectric rods, as well as for arrays of these horns. It is anticipated that profiled horns will be employed more frequently in the future to develop designs that are fit to meet ever-demanding requirements, whether for communications, radar, or security.

Chapter 6 deals with soft and hard horns and their implementation using metamaterials. Soft and hard horn antennas belong to a class of antennas called hybrid mode horns. These horns produce low cross polarization over a wide bandwidth, which makes them ideal for satellite communications, where frequency reuse is a requirement. Soft horns produce low sidelobes, making them ideal as feeds for reflector antennas. Hard horns can be used in array antennas to generate high aperture efficiency. Various soft and hard horns are introduced and compared, including metamaterial-based horn antennas.

In communication systems that use circularly polarized (CP) transmitting and receiving reflector antennas, there is no need to adjust the orientation of the antenna polarization. Chapter 7 presents feed antennas for CP reflector antennas and discusses their characteristics, including the radiation pattern, beamwidth, axial ratio, gain, and input performance. Ten sections constitute this chapter. Section 7.2 briefly describes two analysis methods for CP feed antenna design: the method of moments (MoM), and finite-difference time-domain method (FDTDM). Sections 7.3 and 7.4 discuss generation of CP radiation, referring to a parallel plate polarizer, a conducting fin in a circular waveguide, and the two-point excitation of a patch. The technique in these two sections is called the synthesized CP radiation technique. The remaining sections, Sections 7.5 to 7.10, are devoted to presentation and discussion for CP feed antennas based on a traveling wave current distribution. These CP feed antennas are end-fire helical, end-fire helical array, back-fire helical, conical-helical, spiral, and curl feed antennas. The CP waves from these antennas are designed by the loop-based circularly-polarized radiation technique and have wideband characteristics.

Chapter 8 is devoted to asymmetric multimode horns for polarization control and a new class of multimode horns for adaptive reflector aperture distributions. The principle of multimode horn excitation is introduced mathematically, and the equivalent hardware using multimode antennas (such as waveguides, horns, and microstrip patches) is identified, which formalizes the design process. Two separate application areas are also discussed. In one, the asymmetric feeds for polarization control in offset reflector are introduced, and sample designs with excellent terminal isolation are presented and studied. In the second class of the feeds, adaptive multimode feeds are introduced and shown how they can be used with reflector antennas to design and implement adaptive virtual arrays with adaptive electrical characteristics.

Finally, Chapter 9 covers array antennas and TT&C (telemetry, tracking, and command) antennas that are widely used in satellite communications. Although the array antennas are used by themselves or as feed arrays for reflector antennas, the low-gain TT&C antennas are critical components of the antenna payloads and are part of any communication satellite, together with reflector antennas. Practical design aspects of array antennas and design equations are presented. TT&C antennas are not covered in detail in textbooks and are included in this volume for the first time. Design, radio frequency (RF) performance, and hardware pictures are provided for these low-gain antennas.

The feed antennas presented and discussed in the volume have been identified with conventional reflector antennas. However, lens and reflectarrays share similar optical principles with the reflectors. Thus, the feeds presented in this volume are equally useful for lens and reflectarray antennas. Modifying their design parameters meets the needs of the latter two antennas.

References

[1] Balanis, C. A., *Antenna Theory: Analysis and Design*, Hoboken, NJ: Wiley Interscience, Third Edition, 2005.

[2] Koffman, I., "Feed Polarization for Parallel Currents in Reflectors Generated by Conic Sections," *IEEE Trans. on Antennas and Propagation*, Vol. AP-14, No. 1, 1966, pp. 37–40.

[3] Collin, R. E., and F. J. Zucker, "Antenna Theory," *Part 1*, New York: McGraw-Hill, 1969.

[4] Rudge, A. W., K. Milne, A. D. Olver, and P. Knight, "The Handbook of Antenna Design," *Vol. 1, IEE Electromagnetic Waves Series 15*, London: Peter Peregrinus, 1982.

[5] Ludwig, A. C., "The Definition of Cross Polarization," *IEEE Trans. on Antennas and Propagation*, AP-21, No. 1, 1973, pp. 116–119.

[6] Silver, S. "Microwave Antenna Theory and Design," *IEE Electromagnetic Waves Series 19*, London: Peter Peregrinus, 1984.

[7] Olver, A. D., P. J. B. Clarricoats, A. A. Kishk, and L. Shafai, "Microwave Horns and Feeds," *Chapter 7, IEE Electromagnetic Waves Series 39*, London: Peter Peregrinus, 1994.

[8] Kildal, P.-S. "Factorization of the Feed Efficiency of Paraboloids and Cassegrain Antennas," *IEEE Trans. on Antennas and Propagation*, AP-33, No. 8, 1985, pp. 903–908.

CHAPTER 2

Numerical Methods

Kubilay Sertel, Ohio State University
C. J. Reddy, EM Software & Systems (EMSS) USA Inc.

2.1 Introduction

Modern computers make it possible to analyze and design reflector antennas and arrays using first principle mathematical theory of electromagnetic fields. This chapter is intended to introduce the reader to some of the most popular numerical methods that are in use today. With increasing computer speeds and the introduction of multicore parallel computing, the past decade has witnessed an unprecedented proliferation of commercial simulation packages as the main tool in analyzing and designing antennas, RF components, and integrated systems. However, one should not overlook the fact that the popularity of these numerical algorithms is primarily due to theoretical breakthroughs that ensure solution accuracy as well as reliability and efficiency.

In this chapter, we first summarize two of the most popular numerical analysis methods, the moment of method (MoM) and the finite-element method (FEM). We start from the basic principles described by Maxwell's equations given in Section 2.2 and develop integral representations suitable for MoM implementation in Section 2.3. Perhaps the most profound leap that introduces discrete representations, and thus the use of computers for solving arbitrary real-life problems, is the mathematical foundations of finite elements. We introduce finite elements first in the context of MoM discretizations as surface triangulations, and subsequently more generally in the context of the FEM in Section 2.4.

Hybrid algorithms combining MoM for the exact truncation of the FEM domain are discussed in Section 2.5. Another efficient method to reduce the computational cost of MoM is the fast multipole method (FMM) and its multilevel implementations (MLFMM). We provide the essential theory that allows for compression of the MoM matrix and the main equations behind FMM in Section 2.6. We also touch upon the fast frequency sweep algorithms utilizing Pade expansions in this section.

The MoM and the FEM are so-called full-wave methods that model the exact electromagnetic behavior of the problem. As such, the size of the discrete problem generated by either method is proportional to the wavelength (in linear dimension), generating larger size matrix equations as the frequency of interest increases. This frequency scaling often limits the applicability of full-wave methods to problems of several hundred wavelengths in size. For even larger geometries, high-frequency approximations are employed. Approximations based on physical optics and ray-tracing are among the most popular and are discussed in Section 2.7.

These numerical solution methodologies are illustrated with suitable examples that can be utilized in reflector feed antennas as well as reflector antenna analysis.

2.2 Maxwell's Equations: Foundations of Electromagnetic Analysis

All computational electromagnetics (CEM) methods are formulated to solve Maxwell's equations in one fashion or the other to obtain electric and magnetic fields or electric and magnetic currents. Electromagnetic properties of antennas such as return loss, radiation patterns, and so on can be obtained using these quantities.

We shall start by introducing Maxwell's theory of electromagnetic fields, neatly summarized in the following four equations that relate various source, field, and flux quantities.

$$\nabla \times \boldsymbol{H}(\boldsymbol{r},t) = \boldsymbol{J}(\boldsymbol{r},t) + \frac{\partial \boldsymbol{D}(\boldsymbol{r},t)}{\partial t} \quad \text{(Ampere-Maxwell Law)} \tag{2.1}$$

$$\nabla \times \boldsymbol{E}(\boldsymbol{r},t) = -\boldsymbol{M}(\boldsymbol{r},t) - \frac{\partial \boldsymbol{B}(\boldsymbol{r},t)}{\partial t} \quad \text{(Faraday's Law)} \tag{2.2}$$

$$\nabla \cdot \boldsymbol{D}(\boldsymbol{r},t) = \rho(\boldsymbol{r},t) \quad \text{(Gauss' Law)} \tag{2.3}$$

$$\nabla \cdot \boldsymbol{B}(\boldsymbol{r},t) = \rho_m(\boldsymbol{r},t) \quad \text{(Gauss' Law for Magnetics)} \tag{2.4}$$

Here $\boldsymbol{H}(\boldsymbol{r},t)$ and $\boldsymbol{E}(\boldsymbol{r},t)$ are the magnetic and electric field intensities, respectively. $\boldsymbol{B}(\boldsymbol{r},t)$ and $\boldsymbol{D}(\boldsymbol{r},t)$ are the magnetic and electric flux densities; $\boldsymbol{M}(\boldsymbol{r},t)$ and $\boldsymbol{J}(\boldsymbol{r},t)$ are the magnetic and electric current densities, $\rho_m(\boldsymbol{r},t)$ and $\rho(\boldsymbol{r},t)$ are the magnetic and electric charge densities, respectively. The relationship between the field intensities and the flux densities in (2.1–2.4) are given by the material properties via the constitutive relations $\boldsymbol{D}(\boldsymbol{r},t) = \bar{\bar{\varepsilon}} \cdot \boldsymbol{E}(\boldsymbol{r},t)$ and $\boldsymbol{B}(\boldsymbol{r},t) = \bar{\bar{\mu}} \cdot \boldsymbol{H}(\boldsymbol{r},t)$ where $\bar{\bar{\varepsilon}}$ and $\bar{\bar{\mu}}$ are the permittivity and permeability dyadics. For linear isotropic media, the permittivity and permeability are simple scalars and are often represented in their relative forms, $\varepsilon = \varepsilon_r\varepsilon_0$ and $\mu = \mu_r\mu_0$, in which $\varepsilon_0 = 8.854 \times 10^{-12}$ F/m is the permittivity of the vacuum, and $\mu_0 = 4\pi \times 10^{-7}$ H/m is the permeability. For conducive media, the following additional relations hold: $\boldsymbol{J}(\boldsymbol{r},t) = \sigma \boldsymbol{E}(\boldsymbol{r},t)$ and $\boldsymbol{M}(\boldsymbol{r},t) = \sigma_m \boldsymbol{H}(\boldsymbol{r},t)$, where σ and σ_m and the electric and magnetic conductivities in S/m and Ω/m, respectively.

Taking the divergence of (2.1) and substituting (2.3), we arrive at the continuity equation:

$$\nabla \cdot \boldsymbol{J}(\boldsymbol{r},t) + \frac{\partial \rho(\boldsymbol{r},t)}{\partial t} = 0 \tag{2.5}$$

The dual of (2.5) corresponds to the continuity condition for the magnetic currents, given as

$$\nabla \cdot \boldsymbol{M}(\boldsymbol{r},t) + \frac{\partial \rho_m(\boldsymbol{r},t)}{\partial t} = 0 \tag{2.6}$$

The preceding are simply the mathematical statements of conservation of charge.

For time-harmonic excitations, Maxwell's equations are recast in the simpler phasor form as

$$\nabla \times \boldsymbol{H}(\boldsymbol{r}) = \boldsymbol{J}(\boldsymbol{r}) + j\omega\varepsilon \boldsymbol{E}(\boldsymbol{r}) \tag{2.7}$$

$$\nabla \times \boldsymbol{E}(\boldsymbol{r}) = -\boldsymbol{M}(\boldsymbol{r}) - j\omega\mu \boldsymbol{H}(\boldsymbol{r}) \tag{2.8}$$

$$\nabla \cdot \boldsymbol{D}(\boldsymbol{r}) = \rho(\boldsymbol{r}) \tag{2.9}$$

$$\nabla \cdot \boldsymbol{B}(\boldsymbol{r}) = \rho_m(\boldsymbol{r}) \tag{2.10}$$

where the time derivative is replaced by $\partial/\partial t \leftarrow j\omega$, assuming a $e^{j\omega t}$ time convention. Also, $\nabla \cdot \boldsymbol{J}(\boldsymbol{r}) = -j\omega\rho(\boldsymbol{r})$ and $\nabla \cdot \boldsymbol{M}(\boldsymbol{r}) = -j\omega\rho_m(\boldsymbol{r})$. A solution of the preceding coupled differential equation system exists (and is unique) once the necessary boundary conditions are also specified. In real-life problems, these boundary conditions are determined by the geometry of the problem using the following natural boundary conditions constructed using Figure 2.1. They are

$$\hat{n} \times (\boldsymbol{H}_1 - \boldsymbol{H}_2) = \boldsymbol{J}_s \tag{2.11}$$

$$\hat{n} \times (\boldsymbol{E}_1 - \boldsymbol{E}_2) = -\boldsymbol{M}_s \tag{2.12}$$

$$\hat{n} \cdot (\mu_1 \boldsymbol{H}_1 - \mu_2 \boldsymbol{H}_2) = \rho_{ms} \tag{2.13}$$

$$\hat{n} \cdot (\varepsilon_1 \boldsymbol{E}_1 - \varepsilon_2 \boldsymbol{E}_2) = \rho_s \tag{2.14}$$

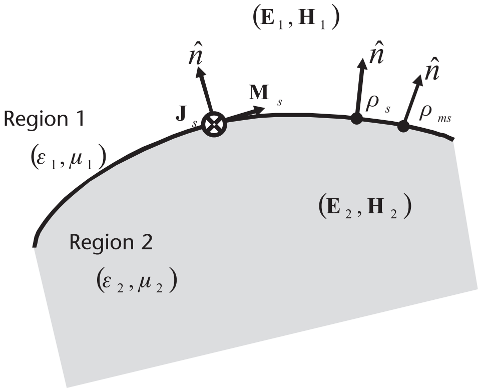

Figure 2.1 Illustration of the interface between two dissimilar media to construct the natural electromagnetic boundary conditions.

where J_s, M_s, ρ_{ms}, and ρ_s are the magnetic and electric surface current and charge densities, respectively.

It is also customary to generate a second order differential equation from the coupled first-order differential equations of Maxwell. This is accomplished by taking the curl of (2.8), giving

$$\nabla \times \left(\frac{1}{\mu_r} \nabla \times \boldsymbol{E} \right) - k_0^2 \varepsilon_r \boldsymbol{E} = -j\omega\mu_0 \boldsymbol{J} - \nabla \times \left(\frac{1}{\mu_r} \boldsymbol{M} \right) \tag{2.15}$$

where $k_0 = \omega\sqrt{\varepsilon_0\mu_0}$ is the free-space wave number. In case of homogeneous media, $\nabla\left(\frac{1}{\mu_r}\right) = 0$ and (2.15) can be written as

$$\nabla \times \nabla \times \boldsymbol{E} - k_0^2 \boldsymbol{E} = -j\omega\mu \boldsymbol{J} - \nabla \times \boldsymbol{M} \tag{2.16}$$

which can be further simplified using the vector identity $\nabla \times \nabla \times \boldsymbol{A} = \nabla\nabla \cdot \boldsymbol{A} - \nabla^2 \boldsymbol{A}$ and Gauss' law (2.9) to obtain

$$\nabla^2 \boldsymbol{E} + k_0^2 \boldsymbol{E} = j\omega\mu \boldsymbol{J} - \frac{\nabla\nabla \cdot \boldsymbol{J}}{j\omega\varepsilon} + \nabla \times \boldsymbol{M} \tag{2.17}$$

and by duality

$$\nabla^2 \boldsymbol{H} + k_0^2 \boldsymbol{H} = j\omega\varepsilon \boldsymbol{M} - \frac{\nabla\nabla \cdot \boldsymbol{M}}{j\omega\mu} - \nabla \times \boldsymbol{J} \tag{2.18}$$

CEM is the branch of science that deals with the approximate numerical solutions of (2.17) and (2.18). A natural step in formulating the solution is to make use of linearity of Maxwell's equations and formulate closed-form solutions of elemental delta function sources, as introduced next.

2.2.1 Green's Functions and Integral Representations

The solution of the electric field Helmholtz equation (2.17) in free-space is concisely given in terms of the dyadic Green's function and the convolution

$$\boldsymbol{E}(\boldsymbol{r}) = \iiint_v \left\{ \left[\nabla \times \bar{\Gamma}(\boldsymbol{r}, \boldsymbol{r}') \right] \cdot \boldsymbol{M}(\boldsymbol{r}') + jk_0 Z_0 \bar{\Gamma}(\boldsymbol{r}, \boldsymbol{r}') \cdot \boldsymbol{J}(\boldsymbol{r}') \right\} dv \tag{2.19}$$

where $Z_0 = \sqrt{\mu_0 / \varepsilon_0} = 377\Omega$ and $\bar{\Gamma}(\boldsymbol{r}, \boldsymbol{r}')$ is the dyadic Green's function given by the solution of $\nabla \times \nabla \times \bar{\Gamma}(\boldsymbol{r}, \boldsymbol{r}') - k_0^2 \bar{\Gamma}(\boldsymbol{r}, \boldsymbol{r}') = -\delta(\boldsymbol{r}, \boldsymbol{r}')$.

$$\bar{\Gamma}(\boldsymbol{r}, \boldsymbol{r}') = -\left[\bar{I} + \frac{\nabla\nabla}{k_0^2} \right] g(\boldsymbol{r}, \boldsymbol{r}') \tag{2.20}$$

in which

$$g(\boldsymbol{r},\boldsymbol{r}') = \frac{e^{-jk_0|\boldsymbol{r}-\boldsymbol{r}'|}}{4\pi|\boldsymbol{r}-\boldsymbol{r}'|} \tag{2.21}$$

is the scalar Green's function. Likewise, the magnetic field generated by a given source distribution in free-space is given as

$$\boldsymbol{H}(\boldsymbol{r}) = \iiint_v \left\{ -\left[\nabla \times \bar{\Gamma}(\boldsymbol{r},\boldsymbol{r}')\right] \cdot \boldsymbol{J}(\boldsymbol{r}') + \frac{jk_0}{Y_0}\bar{\Gamma}(\boldsymbol{r},\boldsymbol{r}') \cdot \boldsymbol{M}(\boldsymbol{r}') \right\} dv \tag{2.22}$$

Explicit representations of the dyadic Green's function and its curl can be also found using

$$\bar{\Gamma}(R) = \left(\frac{j}{k_0 R} + \frac{1}{(k_0 R)^2} - 1 \right) g(\mathrm{R}) + \left(1 - \frac{3j}{k_0 R} + \frac{3}{(k_0 R)^2} \right) g(\mathrm{R}) \hat{R}\hat{R} \tag{2.23}$$

$$\nabla \times \bar{\Gamma}(\mathrm{R}) = \left(jk_0 + \frac{1}{R} \right) g(\mathrm{R}) \hat{R} \times \tag{2.24}$$

where $R = |\boldsymbol{r}-\boldsymbol{r}'|$ and $\hat{R} = (\boldsymbol{r}-\boldsymbol{r}')\,/\,|\boldsymbol{r}-\boldsymbol{r}'|$.

The integral representations of the field radiated by sources $\boldsymbol{M}$ and $\boldsymbol{J}$ in (2.19) and (2.22) will be used below to construct integral equations for a given problem geometry. In the resulting integral equation, the known field quantities are given in terms of incident fields and/or port voltages/currents. As such, the quantity of interest is the induced electric and/or magnetic current densities in the solution domain. These quantities appear under the integral operator in (2.19) and (2.22) and the properties of the Green's function (2.23) as well as the continuity conditions must be respected in the solution of such integral equations. In the next section, we introduce the MoM procedure using a simple electric field integral equation for a scattering target made of perfectly conducting surface(s).

2.3 Method of Moments (MoM)

The MoM is the workhorse method for solving scattering and radiation problems. The procedure starts with an integral equation that describes the problem in terms of known incident field and unknown induced current quantities. The boundary conditions are determined by the specific geometry as well as the material distribution in the solution domain [1]. A typical problem setup is shown in Figure 2.2, where an incident field is impinging upon a conducting antenna with open-circuited terminals. Here, the antenna is a simple bow-tie dipole and its open circuited port is simply represented by a gap in the two dipole arms.

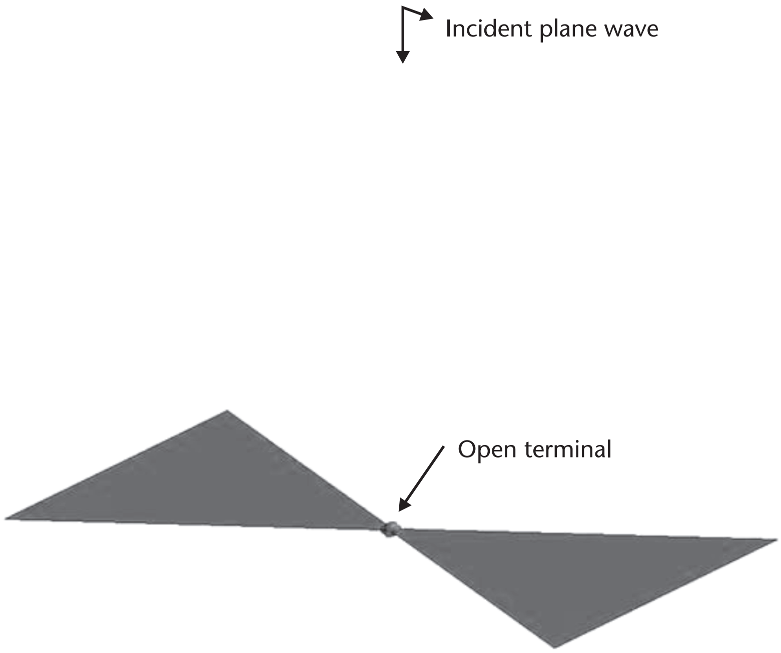

Figure 2.2 Antenna problem example (bowtie antenna).

Once the suitable integral equation is constructed, it is discretized to convert the continuous problem into a discrete one that can be solved using a digital computer. This is accomplished using a discrete approximation of the unknown quantity (such as current density) using a set of *known* basis functions with *unknown* coefficients. To represent the unknown currents in discrete form, first the geometry of the problem is approximated using simple element shapes, such as triangular elements. This step is called the *mesh generation*, or simply *meshing*. Next, basis functions are defined on these simple elements and the mesh connectivity and continuity conditions are enforced. Through a relatively straightforward enforcement of the *approximated* integral equation via the *testing* process, the point-wise continuous integral equation is transformed into a system of linear equations of dimension N proportional to the number of finite elements used in the discretization. These steps are illustrated below using an antenna scattering problem, as depicted in Figure 2.2.

2.3.1 Integral Equation Formulation

The natural boundary condition for the total tangential electric field over a perfectly electrically conducting (PEC) surface can be used to formulate an integral equation for most scattering and radiation problems that do not involve any materials. It is known that an incident field induces surface currents on the antenna (or the scatterer) surface that give rise to scattered fields formulated as:

$$E_{scat}(\boldsymbol{r}) = jk_0 Z_0 \iint_{s'} \bar{\Gamma}(\boldsymbol{r}, \boldsymbol{r}') \cdot J_s(\boldsymbol{r}') ds' \tag{2.25}$$

where s is the PEC surface of the antenna and $\boldsymbol{J}_s(\boldsymbol{r})$ is the induced currents on the surface. We note that we used (2.19) and reduced the integration domain to the antenna surface in (2.25).

The total tangential electric field on the PEC parts of the antenna must be equal to zero on s,

$$\hat{t} \cdot \boldsymbol{E}_{total}(\boldsymbol{r}) = \hat{t} \cdot \left(\boldsymbol{E}_{inc}(\boldsymbol{r}) + \boldsymbol{E}_{scat}(\boldsymbol{r})\right) = 0 \tag{2.26}$$

where $\hat{t}$ is any vector tangential to the antenna surface s. The electric field integral equation (EFIE) can thus be formulated as

$$\hat{t} \cdot \boldsymbol{E}_{inc}(\boldsymbol{r}) = -jk_0 Z_0 \hat{t} \cdot \iint_{s'} \overline{\Gamma}(\boldsymbol{r}, \boldsymbol{r}') \cdot \boldsymbol{J}_s(\boldsymbol{r}')\, ds' \tag{2.27}$$

Typically, the incident field is provided in terms of a plane wave propagating along the $\hat{k}$ direction and having a specific polarization as $\boldsymbol{E}_{inc}(\boldsymbol{r}) = \boldsymbol{E}_0 \boldsymbol{e}^{j\boldsymbol{k}\cdot\boldsymbol{r}}$ where $\boldsymbol{k} = k_0\hat{k}$ and E_0 is the electric field polarization.

Now we are ready to formulate a solution to (2.27) for the unknown induced surface current density $\boldsymbol{J}_s(\boldsymbol{r})$ on the antenna surfaces. To do so, we first express $\boldsymbol{J}_s(\boldsymbol{r})$ in terms of known basis functions as

$$\boldsymbol{J}_s(\boldsymbol{r}) \approx \sum_{n=1}^{N} a_n \boldsymbol{b}_n(\boldsymbol{r}) \tag{2.28}$$

and convert (2.27) into

$$\hat{t} \cdot \boldsymbol{E}_{inc}(\boldsymbol{r}) \approx -jk_0 Z_0 \sum_{n=1}^{N} a_n \hat{t} \cdot \iint_{s'} \overline{\Gamma}(\boldsymbol{r}, \boldsymbol{r}') \cdot \boldsymbol{b}_n(\boldsymbol{r}')\, ds' \tag{2.29}$$

where $\boldsymbol{b}_n(\boldsymbol{r})$ are the known basis functions.

In order to mathematically represent these basis functions as surface vector fields flowing conformally on the antenna geometry, a mathematical representation of the antenna surfaces themselves is needed. For arbitrary geometries encountered in real-life situations, a closed form representation of the problem geometry is almost never available. As such, the geometry is approximately represented in terms of a connected mesh of simplex shapes, called finite elements or mesh elements. Although general multilateral and curvilinear element representations have been developed, simple flat triangulations are among the most widely used meshing methods.

2.3.2 Geometry Representations and Meshing

Mathematical representation of the problem geometry is a first step in the MoM solution of scattering and radiation problems. As mentioned previously, it is necessary in order to define the basis functions used in the expansion (2.28) for discretizing

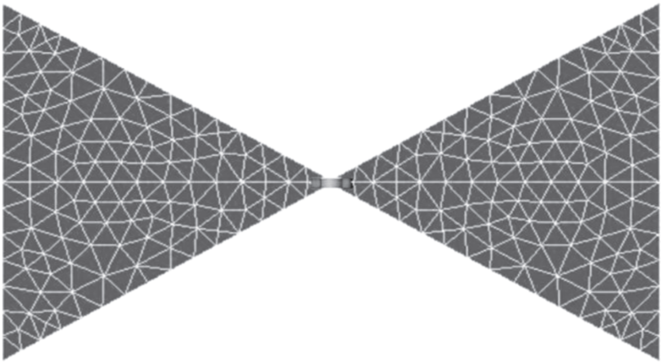

Figure 2.3 Flat triangular element discretization of the bowtie antenna geometry (from FEKO's graphical user interface).

the unknown currents. Perhaps the simplest way of describing an arbitrarily shaped 3-D surface of a typical antenna is to use flat triangular elements, as shown in Figure 2.3. Here, the surface of the bowtie dipole is meshed uniformly using the commercial software FEKO (http://www.feko.info/). Since this particular antenna does not involve any curved surfaces and/or edges, the geometry representation using flat triangular mesh is excellent. For geometries with curved boundaries and/or surfaces, curvilinear elements may be employed for better fidelity. However, a dense flat triangulation can resolve and represent curved surfaces quite effectively as well. As such, the simplicity of flat triangulations is often advantageous in the implementation of the MoM procedure for general shapes.

A flat triangular element is uniquely represented by the three ordered vertices in space ($\boldsymbol{r}_1,\boldsymbol{r}_2,\boldsymbol{r}_3$), as shown in Figure 2.4. Any point $\boldsymbol{r}$ within the triangle is given by its barycentric (area) coordinates (ξ_1,ξ_2,ξ_3),

$$\boldsymbol{r}\left(\xi_1,\xi_2,\xi_3\right) = \xi_1\boldsymbol{r}_1 + \xi_2\boldsymbol{r}_2 + \xi_3\boldsymbol{r}_3 \tag{2.30}$$

The order of the list of corner nodes ($\boldsymbol{r}_1,\boldsymbol{r}_2,\boldsymbol{r}_3$) also determines a unique surface normal, which must be respected throughout the complete geometry mesh. This is

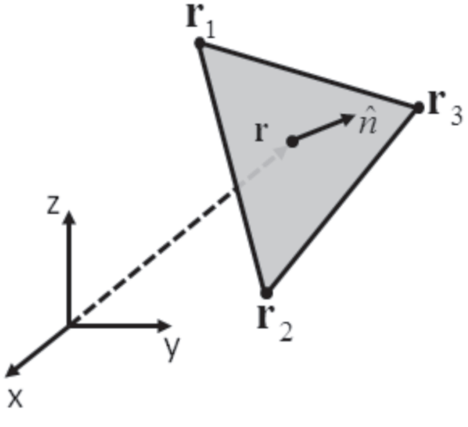

Figure 2.4 Representation of the flat-triangular surface elements in 3-D.

Table 2.1 Simplex Triangular Mesh

List 1		*List 2*	
Node Number	*Node Coordinates*	*Element Number*	*Element Nodes*
1	(x_1, y_1, z_1)	1	(1, 2, 3)
2	(x_2, y_2, z_2)	2	(2, 3, 4)
3	(x_3, y_3, z_3)		
…	…	…	…
n	(x_n, y_n, z_n)	t	(n_t, p_t, q_t)
…	…	…	…
N_{nodes}	(x_N, y_N, z_N)	N_{tri}	(N_T, P_T, Q_T)

particularly important for the accurate implementation of integral equation formulations that involve surface normals, such as the magnetic field integral equation (MFIE).

The simplex triangular mesh can be easily represented on the computer using two lists. The first list has the coordinates of all nodes in the mesh and the second list defines each triangular element in terms of the three node numbers, as illustrated in Table 2.1.

The connectivity information can be deduced from these lists by searching the nodes that are shared between multiple triangles. For example, in the list in Table 2.1, Element 1 and Element 2 share the Nodes 2 and 3 and are thus connected, sharing an edge. Mesh connectivity is necessary for enforcing continuity conditions on the basis functions representing current densities. Such continuity conditions are essential in the physical world and must also be respected when defining the basis functions used in the MoM procedure properly.

Other multilateral mesh elements are also common in MoM implementations. In addition to flat triangulations, bi-linear quadrilateral elements, curvilinear triangular, and quadrilateral elements are also used in Figure 2.5. In particular, for problem geometries involving curved surfaces, curvilinear meshes can provide much improved accuracy by minimizing the geometry modeling error introduced in the MoM discretization [2]. However, it must be noted that the MoM implementation, including the conformal basis functions, the evaluation of the derivatives and the singular integrals in the self terms ($m = n$) of (2.34) become considerably involved and care must be exercised in the implementation.

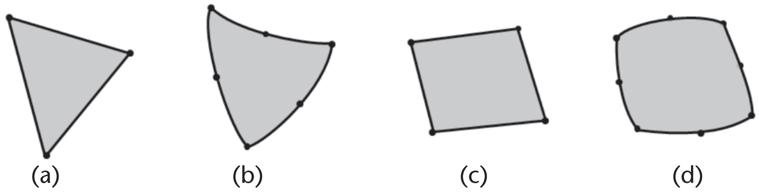

Figure 2.5 Surface mesh elements used in MoM implementations: (a) flat triangle, (b) curvilinear triangle, (c) flat quadrilateral, and (d) curvilinear quadrilateral.

2.3.3 Basis Functions

It is relatively straightforward to formulate tangential vector fields representing the surface current basis functions on the triangular elements described. However, care must be taken to enforce the continuity of the normal current component across the neighboring triangular elements. The simplest basis function that respects normal current continuity is the well-known Rao-Wilton-Glisson (RWG) basis function [3] defined over two neighboring elements (see Figure 2.6). The basis function flowing from triangle s^+ to triangle s^- is defined as

$$\boldsymbol{b}_n(\boldsymbol{r}) = \begin{cases} \dfrac{l_c}{2A^+}\boldsymbol{r}^+ & \boldsymbol{r} \in s^+ \\ \dfrac{l_c}{2A^-}\boldsymbol{r}^- & \boldsymbol{r} \in s^- \\ 0 & \text{otherwise} \end{cases} \tag{2.31}$$

Here, l_c is the length of the common edge between the two triangles, A^+ and A^- are the areas of s^+ and s^-, respectively. Also, the vectors $\boldsymbol{r}^+$ and $\boldsymbol{r}^-$are defined with respect to the free nodes of each triangle as $\boldsymbol{r}^+ = \boldsymbol{r} - \boldsymbol{r}_p^+$ and $\boldsymbol{r}^- = \boldsymbol{r} - \boldsymbol{r}_p^-$.

It can be shown that with the definition in (2.31), the normal component of the two vector field defined over s^+ and s^- are continuous across the common edge, which is a physical necessity for the surface currents.

Several other element types and basis functions can be found in the literature. See Volakis and Sertel [4] for an in-depth discussion on the subject.

2.3.4 Construction of the Impedance Matrix Equation

To arrive at the solution of (2.27), we are looking for the unknown coefficients in the basis function expansion (2.28) that best satisfies (2.29). By describing the problem geometry with discrete elements and the unknown function $\boldsymbol{J}_s(\boldsymbol{r})$ using basis functions defined over the elements, we have reduced the point-wise continuous problem of finding $\boldsymbol{J}_s(\boldsymbol{r})$ at every location on s to finding a set of N coefficients that best satisfy (2.29). This can be accomplished by weakly enforcing (2.29) at a set of

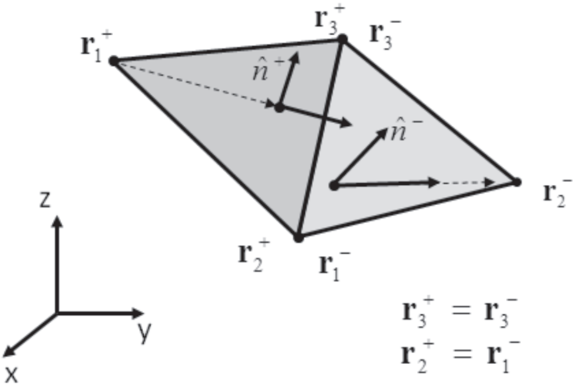

Figure 2.6 Rao-Wilton-Glisson (RWG) basis function defined on a pair of neighboring flat-triangular elements.

N points on the problem geometry s. This is called point matching (or collocation) and it results in an $N \times N$ system of linear equations in a_n. However, the locations of the N points are not unique and thus affect that overall accuracy of the resulting solution. Typically, the collocation points must be chosen as uniformly as possible over the antenna surface.

Alternatively, instead of enforcing (2.29) at a specific set of points on the antenna surface, one can use a weighted sum to test it over subdomains. In particular, we may use the same basis functions as weights to enforce (2.29). This is called Galerkin's testing, and the idea will be made clear in the following. Using N weighting functions $\boldsymbol{w}_m(\boldsymbol{r})$, $m = 1,\ldots,N$; we enforce the original equation in a weak sense

$$\iint_{s'} \boldsymbol{w}_m(\boldsymbol{r}) \cdot \boldsymbol{E}_{inc}(\boldsymbol{r}) ds \approx -jk_0 Z_0 \sum_{n=1}^{N} a_n \iint_{s'} \boldsymbol{w}_m(\boldsymbol{r}) \cdot \iint_{s'} \bar{\Gamma}(\boldsymbol{r},\boldsymbol{r}') \cdot \boldsymbol{b}_n(\boldsymbol{r}') ds' ds \qquad \text{for } m = 1,\ldots,N \tag{2.32}$$

over each testing domain. The surface integrals are evaluated over the domains of the basis and testing functions, respectively, using numerical quadrature. Equation (2.32) simply represents a linear system of equations $\{\boldsymbol{V}\} = [\boldsymbol{Z}]\{\boldsymbol{I}\}$ where $\{\boldsymbol{I}\} = [a_1 a_2 a_3 \ldots a_N]^T$ is the unknown current coefficients,

$$v_m = \iint_{s'} \boldsymbol{w}_m(\boldsymbol{r}) \cdot \boldsymbol{E}_{inc}(\boldsymbol{r}) ds \tag{2.33}$$

is the known incident field vector and

$$Z_{mn} = \iint_{s'} \boldsymbol{w}_m(\boldsymbol{r}) \cdot \iint_{s'} \bar{\Gamma}(\boldsymbol{r},\boldsymbol{r}') \cdot \boldsymbol{b}_n(\boldsymbol{r}') ds' ds \tag{2.34}$$

is the impedance matrix. Evaluation of (2.34) using numerical quadrature is relatively simple for plane wave excitations. However, extreme care must be taken in evaluating (2.34) since the dyadic Green's function involves singularities that must be accurately treated (see [4] for more details). From (2.34), it is clear that the $[\boldsymbol{Z}]$ matrix is of full rank and the storage and solution of large size matrix equations can be computationally very demanding. For instance, for $N = 1{,}000{,}000$ double precision complex storage cost of the $[\boldsymbol{Z}]$ matrix is $10^{12} \times 16/10^9 = 16{,}000$ GB. Obviously, such a large size matrix cannot be stored on the computer random access memory (RAM) and is typically stored on the hard disk. For more manageable sizes, direct solution is preferred when possible. For larger size problems, iterative solvers can be very effective.

2.3.5 Direct and Iterative Solution Methods

We next proceed to solve the linear system of equations in (2.32) to determine the unknown coefficients of the induced surface current expansion (2.28). For smaller problems where the system size N is less than a few thousands, direct solution of the impedance matrix equation is most effective. For this, the LU decomposition with pivoting provides the most cost-effective method with a computational complexity of $O(N^3)$. Once the impedance matrix is decomposed into $[\boldsymbol{Z}] = [\boldsymbol{L}][\boldsymbol{U}]$, multiple incidence angles and excitations can be solved easily in $O(N^2)$ operations using back-substitution. For large problems, pivoting must be employed to make sure that the *LU* decomposition does not suffer from round-off errors.

However, in order to ensure accuracy, one often uses a finer mesh discretization and ends up with very large MoM systems in the order of millions of unknowns. This is a situation also encountered when high-frequency solutions are required for electrically large structures. For such large systems, direct solvers can take a prohibitively long time to compute the solution due to the very high $O(N^3)$ computational complexity. Alternatively, iterative solvers are employed for large linear systems.

For a given excitation vector and an initial guess for $\{\boldsymbol{I}\} = \{\boldsymbol{I}_0\}$, iterative solvers aim to arrive at the solution through successively updating the initial guess. Several matrix-vector products are executed at each iteration and updates to the initial guess are computed using different algorithms. Among these, the most popular ones, conjugate gradient (CG), conjugate gradient squared (CGS), bi-conjugate gradient (BiCG), and stabilized bi-conjugate gradient (BiCGStab), are the mostly used, gradient-based algorithms. In addition, Krylov subspace methods such as generalized minimal residual (GMRES) and quasi-minimal residual (QMR) are also quite effective for ill-conditioned problems.

Typically, the computational cost for iterative solvers is $O(N^2)$ per iteration due to the matrix-vector products involved. So, if the impedance matrix is well conditioned such that the iterative solver converges quickly in a few iterations, then the overall solution cost can be kept reasonable. However, we must remember that for each new excitation, a new iterative solution is needed. This may increase the simulation time significantly if many different excitations must be considered, such as incident fields from different directions. Moreover, if the impedance matrix condition number is high, the iterative solution may take a large number of iterations to reach a prespecified error tolerance or even fail to converge due to numerical round-off errors. Thus, extreme care must be exercised while using iterative solvers. In most instances, iterative solvers are used in conjunction with effective preconditioners that significantly improve iterative convergence. The catch here is that the construction and storage cost of the preconditioner should also be low, to justify its benefits. This is a current research area, and new numerical and analytical preconditioners are becoming available.

Solution of the matrix (2.32) results in current distribution on the surface, which can be used to compute near and far fields as well as input impedance and other antenna characteristics. An example of current distribution on the bowtie antenna is shown in Figure 2.7.

The outline of the MoM was based on purely conducting surfaces. When only homogeneous material regions are present within the problem geometry, it is also possible to use a surface integral representation and apply the MoM procedure [5]. For more general geometries, volume integral equation representations can be used, as discussed in Volakis, Sertel, and Usner [6] and Sancer, Sertel, and Volakis [7].

2.3.6 Examples

To illustrate the MoM procedure, we next present a simple example using the commercial FEKO code. The bowtie dipole antenna example is excited by a plane wave, and the induced open circuit voltage is presented in Figure 2.8.

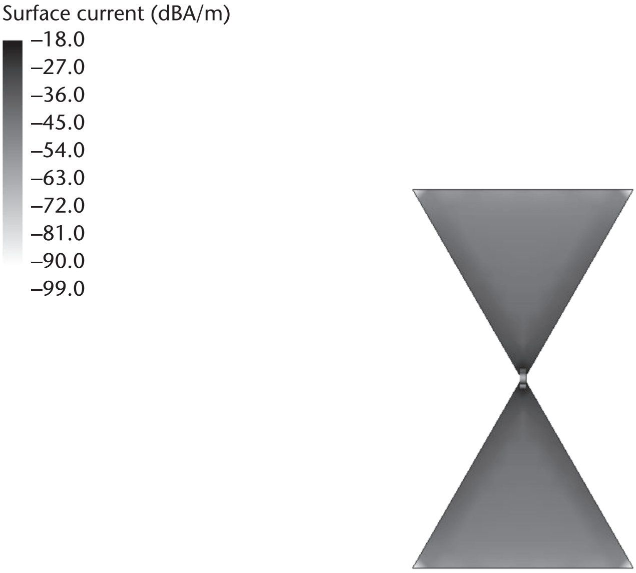

Figure 2.7 Surface electric currents on bowtie antenna after solving MoM matrix equation at 3.95 GHz (from FEKO).

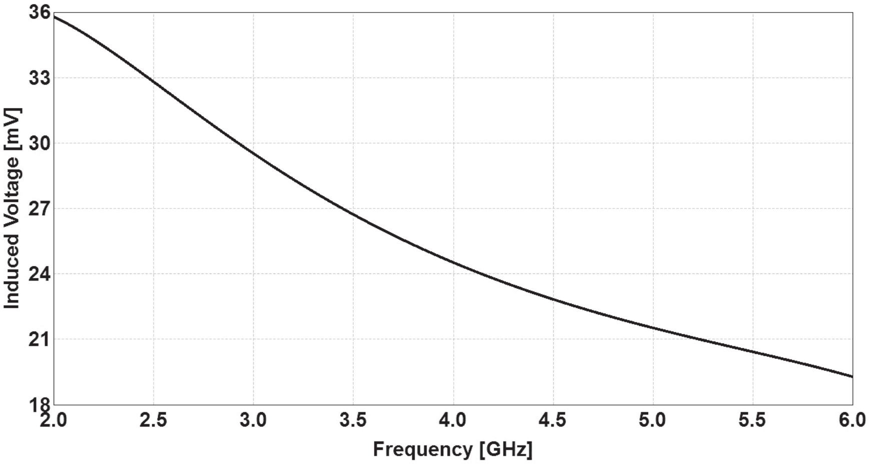

Figure 2.8 Open circuit voltage induced by a broad side plane wave incident on bowtie antenna. Induced currents are shown in the inset.

Next, we present a few examples of reflector feed antennas that are analyzed using MoM. Following antennas are analyzed using the commercial software FEKO.

- Pyramidal horn;
- Corrugated conical horn;
- Axial choke corrugated horn.

Table 2.2 shows the memory and central processing unit (CPU) time requirements to analyze these antennas using the MoM approach.

Table 2.2 Memory and CPU Time Requirements

Antenna	*Unknowns*	*Memory*	*CPU time*
Pyramidal horn (Figure 2.9)	3,132	27.4 Mbytes	37 seconds
Corrugated conical horn (Figure 2.10)	16,404	707.104 Mbytes	666.439 seconds
Axial choke corrugated horn (Figure 2.11)	19,640	831.192 MBytes	704.545 seconds

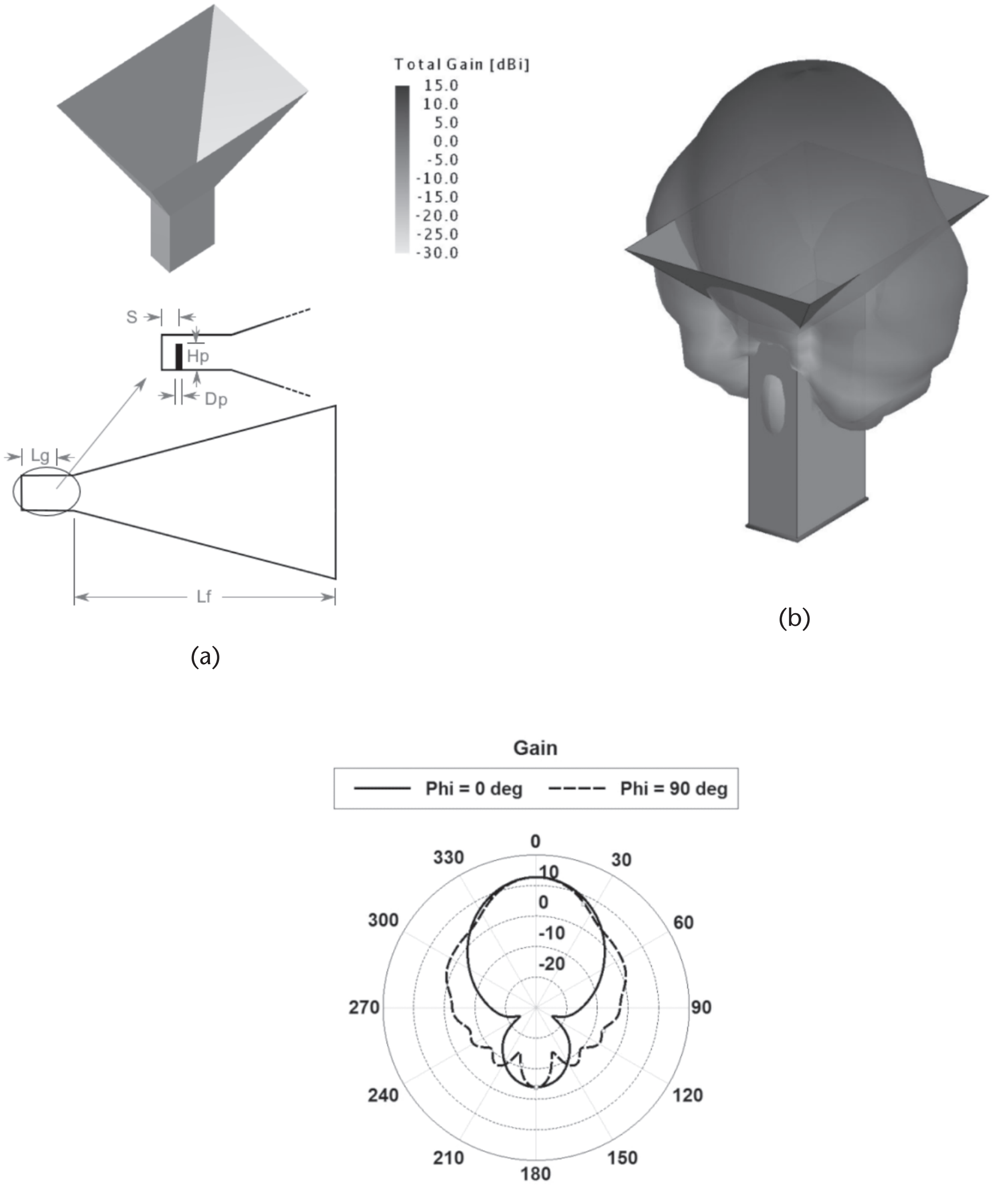
S
Hp
Dp
Lg
Lf
Total Gain [dBi]
15.0
10.0
5.0
0.0
-5.0
-10.0
-15.0
-20.0
-25.0
-30.0
Gain
Phi = 0 deg
Phi = 90 deg
0
30
60
90
120
150
180
210
240
270
300
330
10
0
-10
-20

(a)

(b)

(c)

Figure 2.9 Radiation characteristics of pyramidal horn at 5.4 GHz. (a) 3-D computer-aided design (CAD) drawing of pyramidal horn antenna, (b) 3-D radiation pattern, and (c) realized gain of the horn antenna in principal planes.

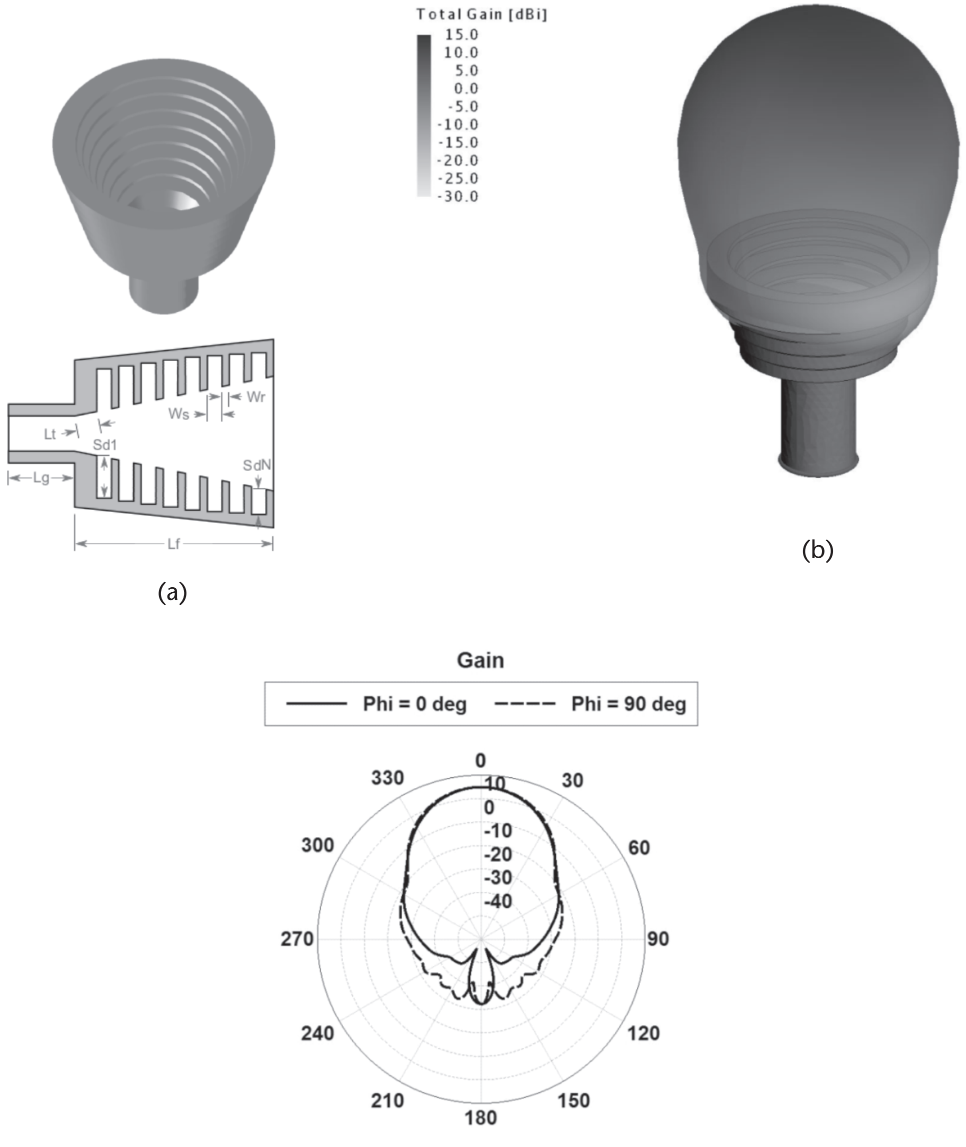

(a)

(b)

(c)

Figure 2.10 Radiation characteristics of corrugated conical horn. (a) Corrugated conical horn, (b) 3-D pattern at 5.4 GHz, and (c) realized gain in principal planes at 5.4 GHz.

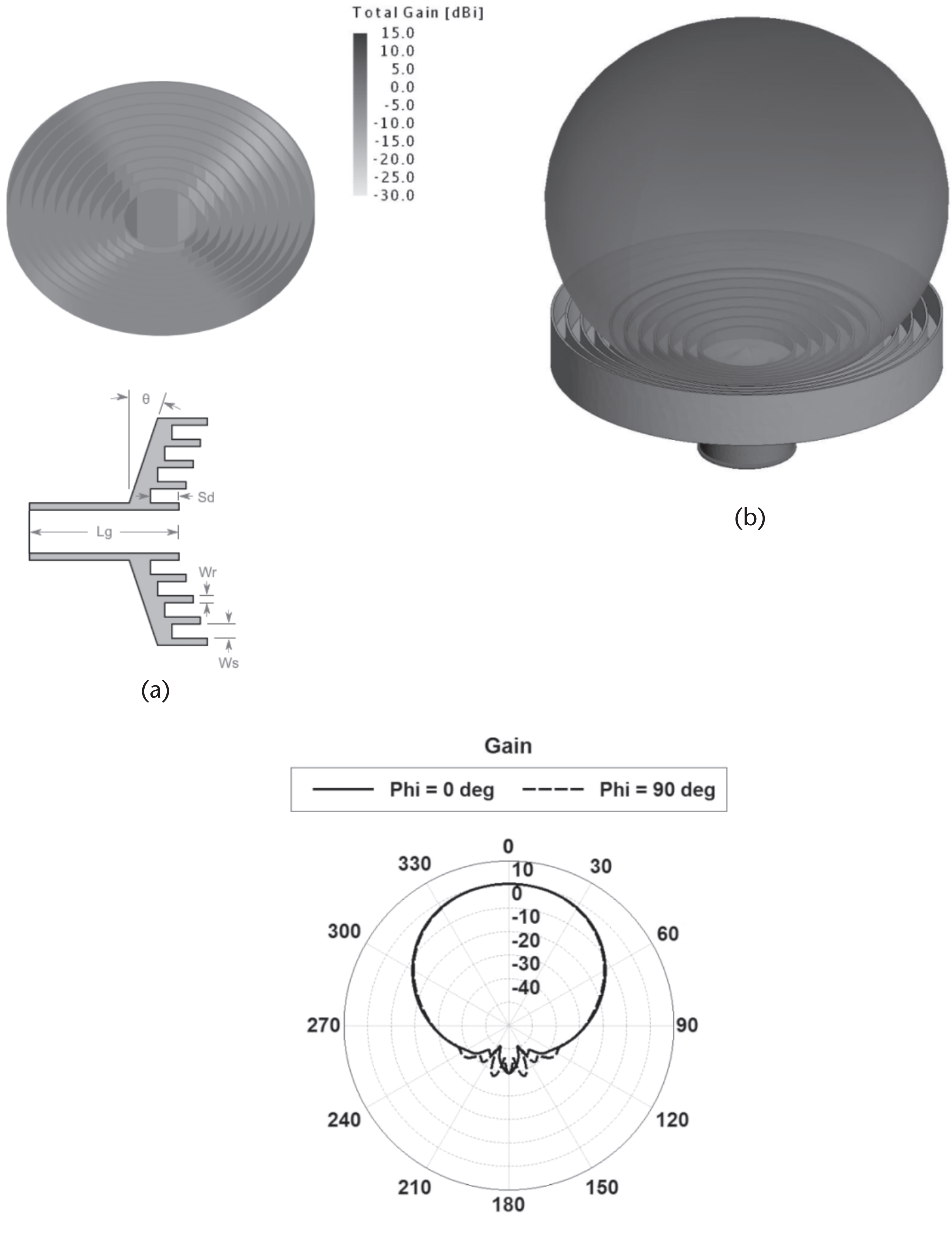

(a)

(b)

(c)

Figure 2.11 Radiation characteristics of axial choke corrugated horn: (a) axial choke corrugated horn, (b) 3-D radiation pattern at 5.4 GHz, and (c) realized gain in principal planes at 5.4 GHz.

2.4 Finite-Element Method (FEM)

Maxwell's equations given in (2.7–2.10) can be directly solved in differential form using the FEM, in much the same manner as the MoM is used for solving integral equations. Starting with the wave equation

$$\nabla \times \left(\frac{1}{\mu_r} \nabla \times \boldsymbol{E} \right) - k_0^2 \varepsilon_r \boldsymbol{E} = -j\omega\mu_0 \boldsymbol{J} - \nabla \times \left(\frac{1}{\mu_r} \boldsymbol{M} \right) \tag{2.35}$$

for a given distribution of electric and magnetic current densities as the excitations of the problem domain, we may proceed to approximate the unknown electric field intensity using known basis functions and unknown coefficients,

$$\boldsymbol{E}(\boldsymbol{r}) \approx \sum_{n=1}^{N} a_n \boldsymbol{e}_n(\boldsymbol{r}) \tag{2.36}$$

where $\boldsymbol{e}_n(\boldsymbol{r})$ are the volumetric basis functions defined over 3-D finite elements. Substituting (2.36) into (2.35) we get

$$\sum_{n=1}^{N} a_n \left[\nabla \times \left(\frac{1}{\mu_r} \nabla \times \boldsymbol{e}_n(\boldsymbol{r}) \right) - k_0^2 \varepsilon_r \boldsymbol{e}_n(\boldsymbol{r}) \right] = -j\omega\mu_0 \boldsymbol{J} - \nabla \times \left(\frac{1}{\mu_r} \boldsymbol{M} \right) \tag{2.37}$$

Using Galerkin's testing, with testing functions $\boldsymbol{e}_m(\boldsymbol{r})$ for $m = 1,\ldots,N$ enforcing (2.37) in a weak sense, we arrive at

$$\begin{aligned} &\sum_{n=1}^{N} a_n \iiint_v \boldsymbol{e}_m(\boldsymbol{r}) \cdot \left[\nabla \times \left(\frac{1}{\mu_r} \nabla \times \boldsymbol{e}_n(\boldsymbol{r}) \right) - k_0^2 \varepsilon_r \boldsymbol{e}_n(\boldsymbol{r}) \right] dv \\ &= -j\omega\mu_0 \iiint_v \boldsymbol{e}_m(\boldsymbol{r}) \cdot \boldsymbol{J} dv - \iiint_v \boldsymbol{e}_m(\boldsymbol{r}) \cdot \nabla \times \left(\frac{1}{\mu_r} \boldsymbol{M} \right) dv \end{aligned} \tag{2.38}$$

The next step is to reduce the double curl operation in the first term on the right-hand side using the vector identity $\nabla \cdot (\boldsymbol{A} \times \boldsymbol{B}) = \boldsymbol{B}(\nabla \times \boldsymbol{A}) - \boldsymbol{A}(\nabla \times \boldsymbol{B})$. We can write

$$\boldsymbol{e}_m(\boldsymbol{r}) \cdot \left[\nabla \times \left(\frac{1}{\mu_r} \nabla \times \boldsymbol{e}_n(\boldsymbol{r}) \right) \right] = \left(\nabla \times \boldsymbol{e}_m(\boldsymbol{r}) \right) \cdot \frac{1}{\mu_r} \left(\nabla \times \boldsymbol{e}_n(\boldsymbol{r}) \right) - \nabla \cdot \left(\boldsymbol{e}_m(\boldsymbol{r}) \times \left[\left(\frac{1}{\mu_r} \right) \nabla \times \boldsymbol{e}_n(\boldsymbol{r}) \right] \right) \tag{2.39}$$

The last term in (2.39) is further simplified using Gauss' theorem

$$\iiint_v \nabla \cdot \left(\boldsymbol{e}_m(\boldsymbol{r}) \times \left[\left(\frac{1}{\mu_r} \right) \nabla \times \boldsymbol{e}_n(\boldsymbol{r}) \right] \right) dv = \oiint_s \left(\boldsymbol{e}_m(\boldsymbol{r}) \times \left[\left(\frac{1}{\mu_r} \right) \nabla \times \boldsymbol{e}_n(\boldsymbol{r}) \right] \right) \cdot \mathrm{ds} \tag{2.40}$$

Note that the right-hand side of (2.40) represents the coupling of electromagnetic energy into the solution domain via the boundary surface and must be treated with care, using the appropriate boundary condition. In fact, since $\nabla \times \boldsymbol{e}_n(\boldsymbol{r})$ cannot be readily evaluated on the boundary surface, it must be treated separately. Often, an extra unknown is assigned on the boundary surface using Maxwell's equations $\nabla \times \boldsymbol{e}_n(\boldsymbol{r}) = -jk_0 Z_0 \hat{n} \times \boldsymbol{h}_{sn}(\boldsymbol{r})$.

The resulting FEM system can then be written as

$$\sum_{n=1}^{N} a_n \iiint_v \left(\nabla \times \boldsymbol{e}_m(\boldsymbol{r})\right) \cdot \left(\frac{1}{\mu_r} \nabla \times \boldsymbol{e}_n(\boldsymbol{r})\right) dv - k_0^2 \varepsilon_r \iiint_v \boldsymbol{e}_m(\boldsymbol{r}) \cdot \boldsymbol{e}_n(\boldsymbol{r}) dv$$
$$-\oiint_s \left(\boldsymbol{e}_m(\boldsymbol{r}) \times \left[\left(\frac{1}{\mu_r}\right) \nabla \times \boldsymbol{e}_n(\boldsymbol{r})\right]\right) \cdot \mathrm{ds} = -j\omega\mu_0 \iiint_v \boldsymbol{e}_m(\boldsymbol{r}) \cdot \boldsymbol{J} dv - \iiint_v \boldsymbol{e}_m(\boldsymbol{r}) \cdot \nabla \times \left(\frac{1}{\mu_r} \boldsymbol{M}\right) dv \tag{2.41}$$

which again results in a matrix equation in the form $\{\boldsymbol{I}\} = [\boldsymbol{Y}]\{\boldsymbol{V}\}$ where

$$Y_{mn} = \iiint_v \left(\nabla \times \boldsymbol{e}_m(\boldsymbol{r})\right) \cdot \left(\frac{1}{\mu_r} \nabla \times \boldsymbol{e}_n(\boldsymbol{r})\right) dv - k_0^2 \varepsilon_r \iiint_v \boldsymbol{e}_m(\boldsymbol{r}) \cdot \boldsymbol{e}_n(\boldsymbol{r}) dv \tag{2.42}$$
$$-\oiint_s \left(\boldsymbol{e}_m(\boldsymbol{r}) \times \left[\left(\frac{1}{\mu_r}\right) \nabla \times \boldsymbol{e}_n(\boldsymbol{r})\right]\right) \cdot \mathrm{ds}$$

and

$$I_m = -j\omega\mu_0 \iiint_v \boldsymbol{e}_m(\boldsymbol{r}) \cdot \boldsymbol{J} dv - \iiint_v \boldsymbol{e}_m(\boldsymbol{r}) \cdot \nabla \times \left(\frac{1}{\mu_r} \boldsymbol{M}\right) dv \tag{2.43}$$

As noted, the surface integral term in (2.42) requires special attention. Unlike the MoM where the unknown quantity of interest lives on a bounded domain (such as the induced electric currents on the conducting surfaces of the antenna), the FEM unknown (the electric field intensity) is nonzero everywhere in space. That is, the solution domain is unbounded. However, in practice the solution domain must be truncated and the truncation boundary must be handled with care. The simplest domain truncation approach is to use the radiation boundary condition,

$$\hat{n} \times \left(\nabla \times \boldsymbol{e}_n(\boldsymbol{r})\right) = jk_0 \hat{n} \times \left(\hat{n} \times \boldsymbol{e}_n(\boldsymbol{r})\right) \tag{2.44}$$

Note that the above radiation boundary condition is only valid when the domain truncation boundary is sufficiently far away from the scatterings centers in the solution domain such that the total field behaves as an outgoing plane wave. With the proper domain truncation such as (2.44), $[\boldsymbol{Y}]\{\boldsymbol{V}\} = \{\boldsymbol{I}\}$ can be solved to determine unknown coefficients $\{\boldsymbol{V}\} = [a_1 a_2 a_3 \ldots a_N]^T$ in (2.36). Incident fields are also incorporated into the boundary truncation and can be easily handled.

2.4.1 Functional Formalism and Discrete Formulation

A more formal derivation of the FEM is formulated using the electric field functional in a source-free region [8–10]:

$$F(\boldsymbol{E}) = \frac{1}{2}\iiint_v \left[(\nabla\times\boldsymbol{E})\cdot\mu_r^{-1}\cdot(\nabla\times\boldsymbol{E}) - k_0^2\boldsymbol{E}\cdot\varepsilon_r\cdot\boldsymbol{E}\right]dv - jk_0Z_0\oiint_s(\boldsymbol{E}\times\boldsymbol{H})\cdot \mathrm{ds} \tag{2.45}$$

where we seek the solution $\boldsymbol{E}$ that satisfies

$$\frac{\partial F(\boldsymbol{E})}{\partial \boldsymbol{E}} = 0 \tag{2.46}$$

with the given boundary conditions ($\partial\boldsymbol{E} = 0$ on s). Here, the same basis function expansion in (2.36) is used to express $\boldsymbol{E}$ in (2.45) and the stationary condition (2.46) results in the same matrix equation $[\boldsymbol{Y}]\{\boldsymbol{V}\} = \{\boldsymbol{I}\}$ where the matrix elements are given by (2.42) and (2.43). We note here that the resulting $[\boldsymbol{Y}]$ matrix is highly sparse due to the local nature of the electric field basis functions. This is one of the main advantages of FEM as it is much easier to store and solve sparse matrices. However, since the domain truncation must be chosen sufficiently away from the problem geometry, it is necessary to discretize the free-space region around the problem, thus leading to large matrix size.

2.4.2 Material Modeling, Boundary Conditions, and Feed Modeling

The other advantage of FEM is its ability to easily model materials in the solution domain. Nonuniform material regions can be easily incorporated into the FEM matrix by defining the dielectric permittivity $\varepsilon_r(\boldsymbol{r})$ and the magnetic permeability $\mu_r(\boldsymbol{r})$ in (2.42). Moreover, PEC surface and volumes within the solution domain are modeled by simply zeroing out the tangential electric field unknowns. As such, simply removing the PEC finite elements from the mesh results in an accurate representation.

Moreover, the modeling of excitation ports within the finite-element (FE) domain is relatively straightforward. Voltage sources can be modeled as impressed, localized electric fields. Current sources are simply incorporated into (2.41). Waveguide ports can be represented in terms of the electromagnetic distribution of the waveguide modes, where a modal expansion is utilized to account for near-zone field distribution around the feed.

2.4.3 Discretization and Basis Functions

The basis function expansion in (2.36), representing the unknown electric field intensity, must be expressed on a discrete volumetric mesh in order to solve for the unknown coefficients in (2.41). Much like the MoM discretization, finite elements are first employed to express the problem geometry.

Perhaps the most commonly used volumetric discretization is the tetrahedral finite elements, depicted in Figure 2.12. Following a similar approach as in the case of flat triangular elements, any point inside the tetrahedral element is represented using the normalized volume coordinates,

$$\boldsymbol{r}(\xi_1,\xi_2,\xi_3,\xi_4) = \xi_1\boldsymbol{r}_1 + \xi_2\boldsymbol{r}_2 + \xi_3\boldsymbol{r}_3 + \xi_4\boldsymbol{r}_4 \tag{2.47}$$

where $r_1,\ldots,r_4$ are the coordinates of the four nodes defining the element.

Vector fields representing the electric field basis functions are concisely defined using the normalized coordinates $(\xi_1,\xi_2,\xi_3,\xi_4)$. Due to the vector nature of these basis functions and their commonplace use in FEM, they are often referred to as vector finite elements. For instance, the vector basis function associated with the tetrahedral edge joining r_4 to r_2 is defined as

$$\boldsymbol{e}_{42}(\boldsymbol{r}) = \xi_4 \nabla \xi_2 - \xi_2 \nabla \xi_4 \tag{2.48}$$

The vector functions associated with the remaining three edges can be similarly defined. It is important to note that (2.48) defines a vector field that flows along the edge joining r_4 to r_2 and linearly decreases to zero as the observation point moves away from the edge. Moreover, the tangential component of (2.48) on edge joining r_4 to r_2 is independent of the rest of the geometry. This property is an essential condition in order to enforce tangential electric field continuity across all elements that share a common edge. The spurious resonance problem plagued FEM analysis before the advent of vector finite elements and explicitly enforcing tangential continuity is of paramount importance for avoiding these spurious resonances in FEM solution and is readily resolved using vector finite elements.

Various other types of finite elements are also employed in FEM analysis, some of which are depicted in Figure 2.13. As seen, higher-order curvilinear elements can also be used along with higher-order vector basis function expansions [11].

In order to properly enforce the tangential continuity and construct the FEM matrix equation, all common edges in the FEM mesh must be identified prior to analysis. Usually, (2.42) is evaluated for each tetrahedral element and this 4 × 4 matrix is called *the element matrix*. The entries of the element matrix are then used to assemble the global FEM matrix using the mesh connectivity information. As such, if a common edge is shared by six finite elements, then six contributions are added into the global matrix. This process is called the *FEM system assembly* and care must be exercised during this apparently simple procedure. Particularly, the vector

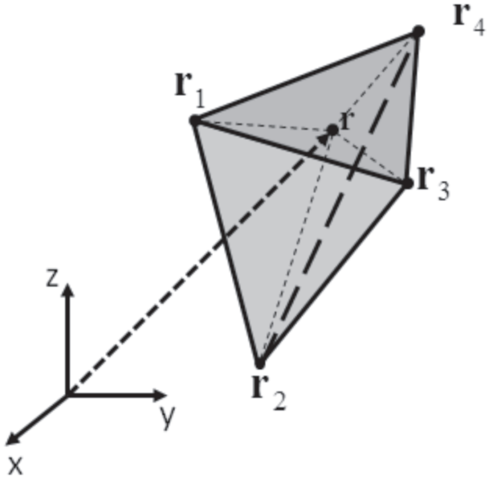

Figure 2.12 Tetrahedral finite elements in 3-D.

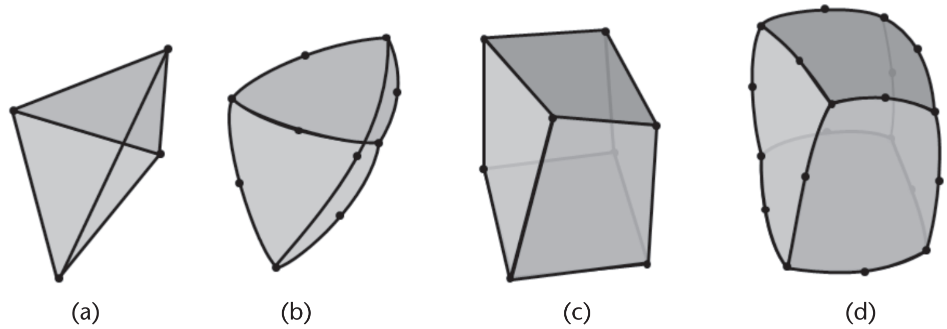

Figure 2.13 Tetrahedral and hexahedral higher-order finite elements. (a) Flat tetrahedron, (b) quadratic tetrahedron, (c) bi-linear hexahedron, and (d) bi-quadratic hexahedron.

directions of the individual basis functions residing in each finite element must be respected during the assembly.

2.4.3.1 h- and p- Refinement FEM

Once the matrix is fully populated, direct and iterative matrix solvers are used to arrive at the FEM solution. We note here that the overall solution accuracy depend on the FEM mesh density, as well as basis function order. Thus, finer FEM meshes and/or higher-order basis functions are needed to further improve solution accuracy. Moreover, the overall accuracy of the FEM solution usually varies from point-to-point in the problem domain. Thus, localized re-meshing (termed as *h-refinement*) and/or localized use of higher-order basis functions (termed as *p-refinement*) is applied in modern FEM software. The approach is implemented in an iterative refinement fashion, such that a user-defined error criterion is achieved via successive *h*- and *p*-refinement of a coarse-mesh solution.

2.4.3.2 Higher-Order Absorbing Boundary Conditions and Perfectly Matched Layers

Since the FEM matrix is highly sparse due to (2.42) being nonzero only over the same finite element, iterative solvers are typically employed. Nonetheless, for very large problems, the sparse FEM matrix still poses a formidable computational bottleneck. Moreover, error propagation (due to the discrete nature of the FEM wave equation) may prevent an accurate solution for very large FE domains. In order to keep the FEM mesh as small as possible, the mesh truncation boundary must be as close to the geometry of interest as possible.

First order radiation condition in (2.44) is not valid when the truncation is close to the scattering centers in the problem domain. Higher-order representation of the radiation condition is one possibility to improve its accuracy. In addition, fictitious absorber layers can be used prevent outgoing waves from returning into the solution domain. Perhaps the most widely used artificial absorber is the perfectly matched layers (PMLs). These are implemented as fictitious, nonphysical, anisotropic layers on the truncation boundary and designed to absorb all outgoing wave. With a proper implementation, PMLs can significantly reduce the FEM domain by allowing the truncation boundary to be placed very close to the problem geometry. However, caution must be exercised since PMLs have their own limitations for extremely oblique incidences [8, 9].

2.4.4 Example

Here, we repeat the horn antenna example given in Section 2.3.6. The computational cost of the FEM solution using the commercial tool HFSS is summarized in Table 2.3. The solution was carried out on an Intel Core i5 CPU@3.20 GHz.

Table 2.3 Computational Cost of the FEM Solution Using HFSS

Antenna	*Number of Mesh Elements*	*Memory*	*CPU time*
Pyramidal horn (Figure 2.14)	3182	42.1 MB	48 seconds

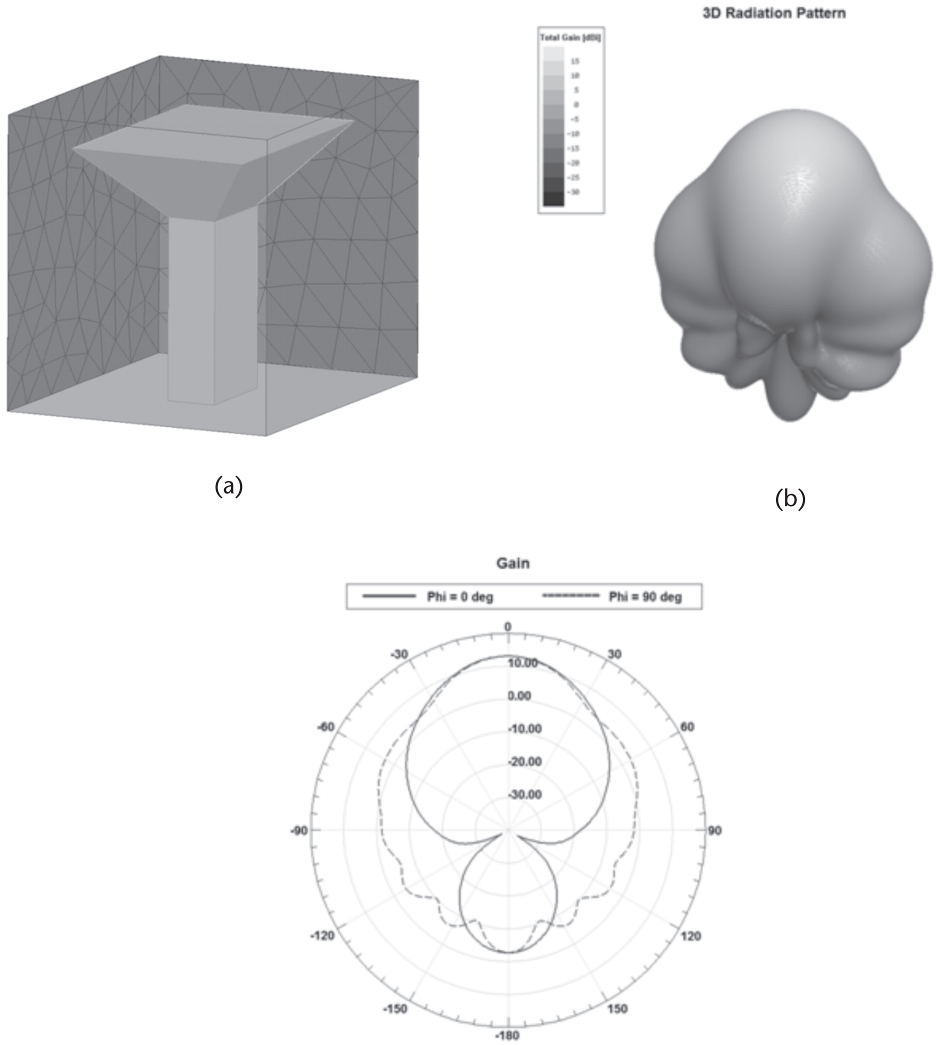

(a)

(b)

(c)

Figure 2.14 Radiation characteristics of a pyramidal horn antenna given in Figure 2.9 at 5.4 GHz computed using the commercial FEM solver HFSS. (a) 3-D HFSS drawing of the pyramidal horn antenna shown in Figure 2.9, illustrating the FEM mesh of the radiation boundary, (b) 3-D radiation pattern of the horn antenna, and (c) realized gain in the two principal planes.

2.5 Hybrid FE-BI and Domain Decomposition Techniques

It is also possible to combine integral equation solvers, such as the MoM, with differential equation solvers such as FEM into a hybrid method. Doing so, one can take advantage of the strengths of both methods and address solutions of extremely complex real-life problems. In essence, highly efficient and accurate analysis tools can be developed by combining multiple methods under a hybrid framework. Since both the MoM and the FEM are based on similar geometry representations and meshes, it is natural to first introduce the hybrid finite-element boundary integral method.

2.5.1 Hybrid Finite-Element-Boundary Integral (FE-BI) Formulation

As noted above, one of the main challenges in FEM is the accurate truncation of the solution domain. The radiation condition (2.44) provides a first-order approximation and needs to be applied away from the geometry. Higher-order absorbing boundary conditions and PMLs may reduce the computational domain to some extent. An alternative and exact way of truncating the FE domain is to use the exact boundary conditions given by integral representations [4, 6]. The electric field integral equation (EFIE) and magnetic field integral equations are given by
EFIE:

$$Z_0\Theta\{\hat{n}\times \boldsymbol{H}\} - \Omega\{\boldsymbol{E}\times\hat{n}\} = \boldsymbol{E}^{inc} \tag{2.49}$$

MFIE:

$$Z_0\Omega\{\hat{n}\times \boldsymbol{H}\} + \Theta\{\boldsymbol{E}\times\hat{n}\} = \boldsymbol{H}^{inc} \tag{2.50}$$

where the integral operators are defined as

$$\Theta\{\boldsymbol{X}\} = -jk\iint_{s'}\overline{\Gamma}(\boldsymbol{r},\boldsymbol{r}')\cdot\boldsymbol{X}(\boldsymbol{r}')\,ds' \tag{2.51}$$

and

$$\Omega\{\boldsymbol{X}\} = -\frac{1}{2}\hat{n}\times\boldsymbol{X}(\boldsymbol{r}) + \iint_{s'}\boldsymbol{X}(\boldsymbol{r}')\times\nabla g(\boldsymbol{r},\boldsymbol{r}')\,ds' \tag{2.52}$$

A combined field integral equation can be simply obtained by a weighted sum of (2.51) and (2.52).

In the hybrid FE-BI approach, the surface magnetic field intensity $\boldsymbol{H}$ in (2.45) is treated as an unknown and expressed in terms of a basis expansion as in (2.28). As such, three sets of unknowns are identified after the FEM assembly:

- Volumetric electric field intensity $\boldsymbol{E}_v$;
- Surface electric field intensity $\boldsymbol{E}_s$;
- Surface electric field intensity $\boldsymbol{H}_s$.

In order to solve all three uniquely, an additional equation is needed, relating $\boldsymbol{E}_s$ and $\boldsymbol{H}_s$, much the same way the radiation condition is used in (2.44). This equation is provided by either of the integral representations (2.49) and (2.50). In particular, when the CFIE is used, the hybrid FE-BI system takes the form [6] and [12]

$$\begin{bmatrix} \boldsymbol{E}^{vv} & \boldsymbol{E}^{vs} & 0 \\ \boldsymbol{E}^{sv} & \boldsymbol{E}^{ss} & \boldsymbol{B} \\ 0 & \boldsymbol{P} & \boldsymbol{Q} \end{bmatrix} \begin{bmatrix} \boldsymbol{E}_v \\ \boldsymbol{E}_s \\ \boldsymbol{H}_s \end{bmatrix} = \begin{bmatrix} 0 \\ 0 \\ \boldsymbol{b} \end{bmatrix} \tag{2.53}$$

where $\boldsymbol{E}^{vv}$, $\boldsymbol{E}^{vs}$, $\boldsymbol{E}^{sv}$, $\boldsymbol{E}^{ss}$, $\boldsymbol{B}$, $\boldsymbol{P}$, and $\boldsymbol{Q}$ represent submatrices whose entries are given by

$$E_{mn} = \iiint_v \left(\nabla \times \boldsymbol{e}_m(\boldsymbol{r})\right) \cdot \left(\frac{1}{\mu_r} \nabla \times \boldsymbol{e}_n(\boldsymbol{r})\right) dv - k_0^2 \varepsilon_r \iiint_v \boldsymbol{e}_m(\boldsymbol{r}) \cdot \boldsymbol{e}_n(\boldsymbol{r}) dv \tag{2.54}$$

$$B_{mn} = jkZ_0 \iint_{s'} \boldsymbol{e}_m(\boldsymbol{r}) \cdot \left(\hat{n} \times \boldsymbol{h}_{sn}(\boldsymbol{r})\right) ds \tag{2.55}$$

$$P_{mn} = \iint_{s'} \left(\hat{n} \times \boldsymbol{h}_{sm}(\boldsymbol{r})\right) \cdot \left[-\alpha \Omega\left\{\boldsymbol{e}_n(\boldsymbol{r}) \times \hat{n}\right\} + (1-\alpha)\Theta\left\{\boldsymbol{e}_n(\boldsymbol{r}) \times \hat{n}\right\}\right] ds \tag{2.56}$$

$$Q_{mn} = Z_0 \iint_{s'} \left(\hat{n} \times \boldsymbol{h}_{sm}(\boldsymbol{r})\right) \cdot \left[\alpha \Theta\left\{\hat{n} \times \boldsymbol{h}_{sn}(\boldsymbol{r})\right\} + (1-\alpha)\Omega\left\{\hat{n} \times \boldsymbol{h}_{sn}(\boldsymbol{r})\right\}\right] ds \tag{2.57}$$

$$b_m = \alpha \iint_{s'} \left(\hat{n} \times \boldsymbol{h}_{sm}(\boldsymbol{r})\right) \cdot \boldsymbol{E}^{inc}\, ds + (1-\alpha) Z_0 \iint_{s'} \left(\hat{n} \times \boldsymbol{h}_{sm}(\boldsymbol{r})\right) \cdot \boldsymbol{H}^{inc}\, ds \tag{2.58}$$

where α is an arbitrary CFIE combination parameter. The submatrices in [$\boldsymbol{P}$] and [$\boldsymbol{Q}$] (2.53) are fully populated matrices coming from the MoM implementation of the BI relation. The remaining submatrices are sparse FEM matrices and can be easily compressed for storage. Iterative solution of (2.53) is also typically well behaved owing to the CFIE used in the BI representation. Other FE-BI hybridizations, starting from variational representations can also be found in the literature [13].

2.5.2 Example

To illustrate the use of the hybrid FEM-BI method, we considered dielectric loaded helix antenna (Figure 2.15). Dielectric material is analyzed using FEM, whereas the boundary of FEM and the metallic parts are analyzed using BI. Discretization of the FEM region resulted in 32,218 tetrahedrals and BI portion results in 3,292 triangles. Analysis required 457.232 MB memory and 190.634 seconds.

2.6 Fast Methods for Integral Equations

The large computational cost of the MoM and BI implementations quickly become a bottleneck electrically for larger problems, such as reflector antennas. Storage of

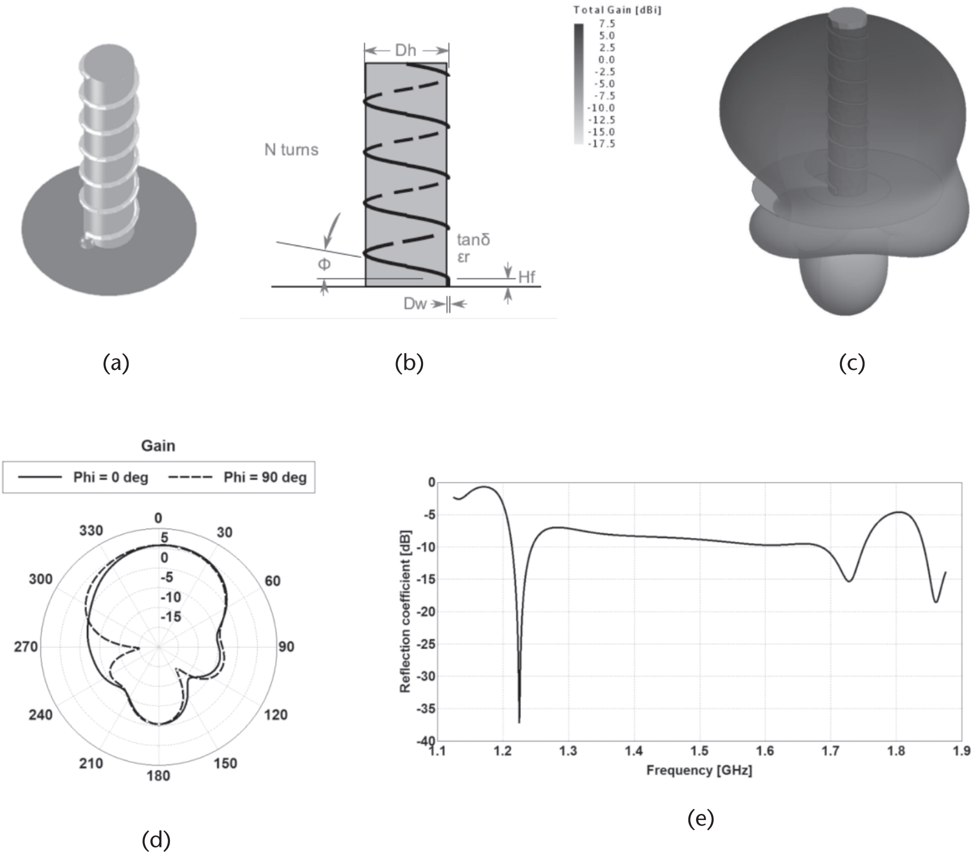

(a) (b) (c)

(d) (e)

Figure 2.15 Radiation characteristics of dielectric loaded helix antenna. (a) CAD drawing of dielectric loaded helix antenna, (b) schematic drawing, (c) 3-D radiation pattern at 1.125 GHz, (d) realized gain in principal planes at 1.125 GHz, and (e) broadband performance of the dielectric loaded helix antenna.

the fully populated MoM matrix grows as $O(N^2)$ and iterative solvers require $O(N^2)$ floating-point operations per iteration. Fast methods improve both of these costs by making clever use of the properties of the Green's function. In particular, the free-space Green's function is often encountered in antenna analysis. As outlined, the MoM matrix elements are formulated as

$$Z_{mn} = \iint_{s'} \boldsymbol{w}_m(\boldsymbol{r}) \cdot \iint_{s'} \overline{\Gamma}(\boldsymbol{r},\boldsymbol{r}') \cdot \boldsymbol{b}_n(\boldsymbol{r}')\, ds'\, ds \tag{2.59}$$

where the dyadic Green's function $\overline{\Gamma}(\boldsymbol{r},\boldsymbol{r}')$ is given by (2.23). In practice, (2.59) is further simplified using the continuity properties of the basis functions, resulting in the more common form

$$Z_{mn} = \iint_{s'} \boldsymbol{w}_m(\boldsymbol{r}) \cdot \iint_{s'} g(\boldsymbol{r},\boldsymbol{r}') \cdot \boldsymbol{b}_n(\boldsymbol{r}')\, ds'\, ds + \iint_{s'} \nabla \cdot \boldsymbol{w}_m(\boldsymbol{r}) \iint_{s'} g(\boldsymbol{r},\boldsymbol{r}')\, \nabla \cdot \boldsymbol{b}_n(\boldsymbol{r}')\, ds'\, ds \tag{2.60}$$

in which the scalar Green's function $g(\boldsymbol{r},\boldsymbol{r}')$ is given by (2.21). As noted in Section 2.3, the MoM impedance matrix is full and its storage and solution is computationally very expensive. However, it is important to note that off-diagonal blocks of the [*Z*] matrix, which represent the interactions between two well-separated groups of basis and testing functions, are rank deficient. That is, off-diagonal blocks of the [*Z*] matrix can be further compressed to reduce storage and solution complexity. Standard singular value decomposition (SDV)–based compression approaches can be applied algebraically, such as the adaptive cross approximation (ACA) method to speed-up the MoM solution. However, the fast multipole method (FMM) relies on the properties of the Green's function and allows for an analytic compression of the solution process. Next, we describe the key equations leading FMM compression of the MoM matrix.

2.6.1 Fast Multipole Method (FMM)

The FMM is based on the expression of the Green's function in terms of the multipole expansions. Using the vector construct shown in Figure 2.16, we can express the scalar Green's function as

$$g(\boldsymbol{r}_p,\boldsymbol{r}_q) = \frac{\boldsymbol{e}^{jkr_{qp}}}{\boldsymbol{r}_{qp}} = \frac{jk}{4\pi}\oiint \boldsymbol{e}^{j\boldsymbol{k}\cdot\boldsymbol{r}_{qm}} T_L\left(kr_{mm'},\hat{k}\cdot\hat{r}_{mm'}\right) e^{-j\boldsymbol{k}\cdot\boldsymbol{r}_{pm'}}\, d^2\hat{k} \tag{2.61}$$

where $r_{\zeta\xi} = \left|\boldsymbol{r}_\xi - \boldsymbol{r}_\zeta\right|$, and

$$T_L\left(kr_{mm'},\hat{k}\cdot\hat{r}_{mm'}\right) = \sum_{l=0}^{L} j^l(2l+1)h_l^{(1)}\left(kr_{mm'}\right)P_l(\hat{k}\cdot\hat{r}_{mm'}) \tag{2.62}$$

in which $h_l^{(1)}(\cdot)$ is the Hankel function of the first kind and of order *l*, and $P_l(\cdot)$ is the Legendre Polynomial of order *l*. In (2.62), *L* is the truncation parameter for the multipole expansion and is chosen to achieve a desired level of accuracy in the approximation. Moreover, a suitable numerical quadrature is chosen to evaluate the $\hat{k}$-space integral in (2.61).

Inserting (2.61) into (2.60), we can rewrite the impedance matrix element for well-separated basis and testing functions as

$$Z_{mn} = \frac{jk}{4\pi}\oiint \boldsymbol{V}_{qm}(\hat{k})\cdot T_L\left(kr_{mm'},\hat{k}\cdot\hat{r}_{mm'}\right)\boldsymbol{V}^*_{pm'}(\hat{k})d^2\hat{k} \tag{2.63}$$

where

$$V_{pm'}(\hat{k}) = \iint_{s'} \boldsymbol{e}^{j\boldsymbol{k}\cdot\boldsymbol{r}_{pm'}}[\bar{\boldsymbol{I}} - \hat{k}\hat{k}]\cdot\boldsymbol{b}_p(\boldsymbol{r})ds \tag{2.64}$$

and

$$V_{qm}(\hat{k}) = \iint_{s'} \boldsymbol{e}^{j\boldsymbol{k}\cdot\boldsymbol{r}_{qm}}[\bar{\boldsymbol{I}} - \hat{k}\hat{k}]\cdot\boldsymbol{t}_q(\boldsymbol{r})ds \tag{2.65}$$

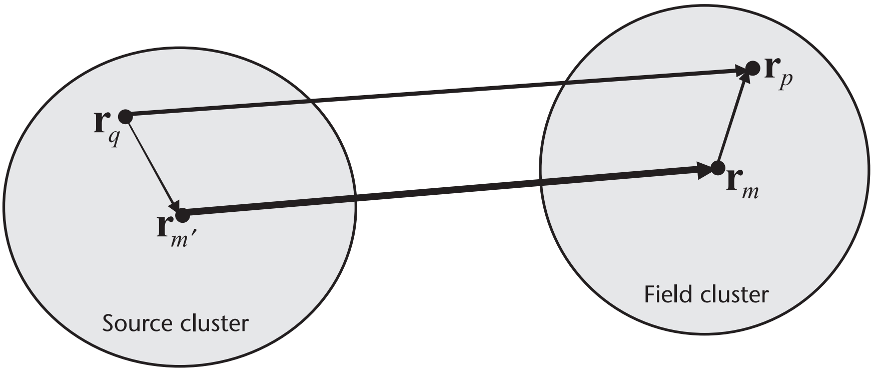

Figure 2.16 Vector construct illustrating the FMM expansion (2.61).

Note that in converting (2.60) into (2.63), we also used the identity $[\bar{I} - \hat{k}\hat{k}] \cdot [\bar{I} - \hat{k}\hat{k}] = \bar{I} - \hat{k}\hat{k}]$.

To proceed with the FMM, first all N basis functions are grouped into M groups, with respect to their geometrical proximity. Groups that are touching each other are considered near-zone, and those that are well separated are considered as far-zone. Since (2.63) is only valid for well-separated basis and testing functions, the impedance matrix is partitioned into a sparse near-zone matrix and a far-zone matrix as $[\mathbf{Z}] = [\mathbf{Z}_{\text{near}}] + [\mathbf{Z}_{\text{far}}]$ using the above grouping. The far-zone interactions are never computed, only the near field matrix $[\mathbf{Z}_{\text{near}}]$ is computed and stored in sparse form using the standard MoM implementation (2.60).

In order to compress far-zone matrix $[\mathbf{Z}_{\text{far}}]$, the far field signatures of the basis and testing functions are also computed and stored using (2.64) and (2.65) for each $\hat{k}$ sample of the chosen numerical quadrature. The translation operator (2.62) is also precomputed and stored.

The FMM-compressed matrix-vector product of $[\mathbf{Z}_{\text{far}}]$ proceeds in three steps:

- *Aggregation:* In this step, all signatures of the basis functions are summed-up to form the group signature, as outgoing plane wave at prespecified $\hat{k}$ quadrature samples.
- *Translation:* Outgoing group signatures are converted into incoming group signatures for each testing function group.
- *Disaggregation:* Incoming group signatures are distributed onto each testing function and the entries of the multiplication vector are computed.

With N basis function and M groups, the computational complexities of the aggregation and disaggregation steps are $O(N^2/M)$ whereas that of the translation stage is $O(NM)$. Also, the near-field matrix vector product cost is $O(N^2/M)$. The overall cost of the matrix-vector product can thus be minimized by choosing $N = \sqrt{M}$, which results in a much reduced $O(N^{1.5})$ complexity. Compared to the $O(N^2)$ complexity of the standard MoM matrix-vector product, this may not seem like a significant reduction; however, as N increases beyond several tens of thousands, this small difference makes a huge impact. Thus, with FMM, much larger MoM problems can be solved using less computer resources.

It is also possible to apply the three-step FMM process in a multilevel fashion, resulting in the multilevel FMM (MLFMM) by Chew, Jin, and Michielssen [14]. The overall complexity of MLFMM further reduces down to $O(N \log N)$ for both storage and execution. MLFMM has been the workhorse for large-scale MoM modeling and full-rank systems of several hundred million unknowns have been solved recently. Combination of single-level FMM with fast Fourier transform (FFT) has been shown to be highly parallelizable [15], leading to the largest problem size ever solved [16].

2.6.2 Examples

To illustrate use of MLFMM, a horn-fed Gregorian axis-symmetrical dual reflector is analyzed using commercial software FEKO, as depicted in Figure 2.17. Number of unknowns for this problem is 102,332. The problem was solved with a memory of 1.886GB and took a time of 3133.439 seconds. MoM would have required 80.7GB of memory as opposed to 1.886GB required for MLFMM.

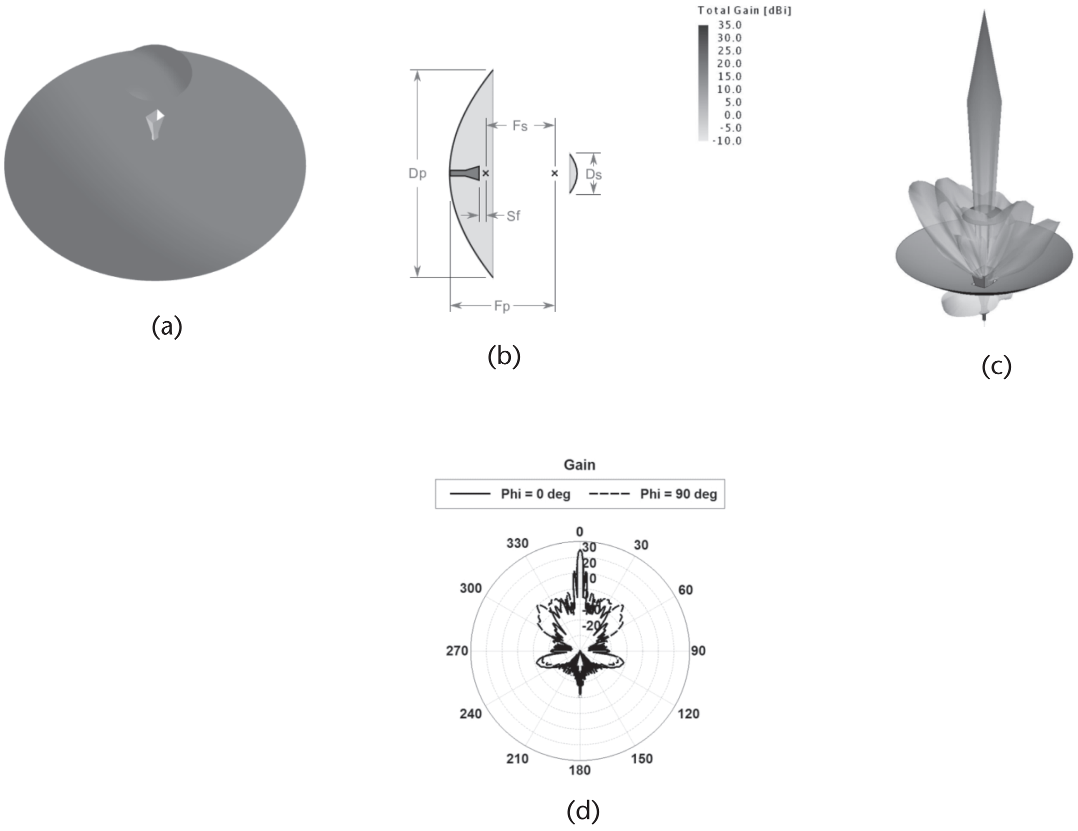

Figure 2.17 Radiation characteristics of horn-fed Gregorian axis-symmetrical dual reflector. (a) 3-D CAD drawing of horn-fed Gregorian axis-symmetrical dual reflector, (b) schematic drawing, (c) 3-D radiation pattern at 9.37 GHz, and (d) realized gain in principal planes at 9.37 GHz.

2.6.3 Model Order Reduction for Fast Frequency Sweep

Numerical methods described above often result in a system matrix equation such as

$$A(k)x(k) = v(k) \tag{2.66}$$

where $A(k)$ is the system matrix, $x(k)$ is the solution vector, and $v(k)$ is the excitation vector due to the plane wave incident.

Solution of (2.66) at any frequency f_0 gives the solution vector $x(k_0)$, where k_0 is the free-space wavenumber at f_0. Instead of directly solving for $x(k_0)$, it can be written as a rational function,

$$x(k) = \frac{P_L(k)}{Q_M(k)} \tag{2.67}$$

where

$$P_L(k) = a_0 + a_1 k + a_2 k^2 + a_3 k^3 + \cdots + a_L k^L \tag{2.68}$$

$$Q_M(k) = b_0 + b_1 k + b_2 k^2 + b_3 k^3 + \cdots + b_M k^M \tag{2.69}$$

b_0 is set to $b_0 = 1$ as the rational function can be divided by an arbitrary constant. The coefficients of the rational function are obtained by matching the frequency derivatives of $x(k)$. If (2.69) is differentiated t times with respect to k, the resulting equation can be written as [17]

$$\begin{gathered}
xQ_M = P_L \\
x'Q_M + xQ'_M = P'_L \\
x''Q_M + 2x'Q'_M + xQ''_M = P''_L \\
x'''Q_M + 3x''Q'_M + 3x'Q''_M + xQ'''_M = P'''_L \\
\vdots \\
x^{(t)}Q_M + tx^{(t-1)}Q_M^{(1)} + \cdots + C_{t,t-m}x^{(m)}Q_M^{(t-m)} + \cdots + xQ_M^{(t)} = P_L^{(t)}
\end{gathered} \tag{2.70}$$

where $C_{r,s} = \dfrac{r!}{s!(r-s)!}$ is the binomial coefficient. The system of $(t + 1)$ equations provides the information from which the rational function coefficients can be found if $t \geq L + M + 1$. If the frequency derivatives are available at only one frequency f_0, the variable in the rational function can be replaced with $(k - k_0)$,

$$x(k) = \frac{P_L(k - k_0)}{Q_L(k - k_0)} \tag{2.71}$$

The derivatives are evaluated at $k = k_0$. The coefficients of the rational function can be obtained from the following equations:

$$a_0 = x(k_0) \tag{2.72}$$

$$\begin{bmatrix} 1 & \cdots & -x_0 & 0 & \cdots & 0 \\ 0 & \cdots & -x_1 & -x_0 & \cdots & 0 \\ 0 & \cdots & -x_2 & -x_1 & \cdots & 0 \\ 0 & \cdots & -x_3 & -x_2 & \cdots & 0 \\ \vdots & \cdots & \vdots & \vdots & \cdots & \vdots \\ 0 & \cdots & -x_{L+M-1} & -x_{L+M-2} & \cdots & -x_L \end{bmatrix} \begin{bmatrix} a_1 \\ a_2 \\ \vdots \\ a_L \\ \vdots \\ b_M \end{bmatrix} = \begin{bmatrix} x_1 \\ x_2 \\ \vdots \\ x_L \\ \vdots \\ x_{L+M} \end{bmatrix} \tag{2.73}$$

where $x_m = \dfrac{x^{(m)}}{m!}$.

If the frequency derivatives are known at more than one frequency, then the expansion about $k = k_0$ cannot be used and the system matrix to solve the rational function coefficients takes a general form [17]. For the sake of simplicity, let us examine a two-frequency model. Assume that at two frequencies, f_1 (with free-space wavenumber k_1) and f_2 (with free-space wave number k_2), four derivatives are evaluated at each frequency. Hence ten samples of data are needed (two frequency samples and a total of eight derivative samples) to form a rational function with $L = 5$ and $M = 4$.

$$x(k) = \frac{a_0 + a_1 k + a_2 k^2 + a_3 k^3 + a_4 k^4 + a_5 k^5}{1 + b_1 k + b_2 k^2 + b_3 k^3 + b_4 k^4} \tag{2.74}$$

Equation (2.74) can be written as

$$\left(1 + b_1 k + b_2 k^2 + b_3 k^3 + b_4 k^4\right) x(k) = \left(a_0 + a_1 k + a_2 k^2 + a_3 k^3 + a_4 k^4 + a_5 k^5\right) \tag{2.75}$$

Differentiating (2.75) four times at each frequency, the matrix equation for the solution of the coefficients of the rational function (2.74) can be written as

$$\begin{bmatrix} M_{11} & M_{12} & \cdots & \cdots & M_{19} & M_{110} \\ M_{21} & M_{22} & \cdots & \cdots & M_{29} & M_{210} \\ M_{31} & M_{32} & \cdots & \cdots & M_{39} & M_{310} \\ \vdots & \vdots & \cdots & \cdots & \vdots & \vdots \\ \vdots & \vdots & \cdots & \cdots & \vdots & \vdots \\ M_{101} & M_{102} & \cdots & \cdots & M_{109} & M_{110} \end{bmatrix} \begin{bmatrix} a_0 \\ a_1 \\ a_2 \\ \vdots \\ b_3 \\ b_4 \end{bmatrix} = \begin{bmatrix} x_1^{(0)} \\ x_1^{(1)} \\ x_1^{(2)} \\ \vdots \\ x_2^{(3)} \\ x_2^{(4)} \end{bmatrix} \tag{2.76}$$

where $x_1^{(m)} = \frac{d^m}{dk^m} x(k)\big|_{k=k_1}$, $x_2^{(m)} = \frac{d^m}{dk^m} x(k)\big|_{k=k_2}$.
The matrix elements (M_{11}, M_{12}, and so on) are given in [18].

In the above equations, $x^{(t)}$, the t^{th} derivative is obtained using the recursive relationship

$$x^{(t)} = A^{-1}(k)\left[v^{(t)}(k) - \sum_{q=0}^{t}\left(1-\delta_{q0}\right)C_{t,q}A^{(q)}(k)x^{(t-q)}(k)\right] \tag{2.77}$$

where $A^{(q)}(k)$ is the q^{th} derivative with respect to k of $A(k)$ and $v^{(t)}(k)$ is the t^{th} derivative with respect to k of $v(k)$. The Kronecker delta δ_{q0} is defined as

$$\delta_{q0} = \begin{cases} 1 & q = 0 \\ 0 & q \neq 0 \end{cases} \tag{2.78}$$

The above procedure can be generalized for multiple frequencies with frequency-derivatives evaluated at each frequency to increase the accuracy of the rational function. Alternatively, the two-frequency-four-derivative model can be used with multiple frequency windows. In practical applications, one can solve for $x(k)$ in (2.74) by simply solving (2.66) at various frequencies.

2.6.4 Example

To illustrate the use of fast-frequency sweep, consider the broadband frequency response of bowtie antenna Figure 2.18. Solid trace in Figure 2.18 represents calculations using discrete frequency calculations, whereas the dashed trace represents calculations using continuous frequency calculations.

2.7 High-Frequency Techniques

Full-wave solutions, such as MoM and MLFMM, offer accuracy and flexibly. With advances in computer technology, now we have desktop computers that offer 8–16GB of memory and 4–16 cores at an affordable price. Despite these advances in computer technology, solving electrically large problems such as very high gain reflector antenna with a complex feed may be beyond commonly available resources. To solve such problems, one will have to use asymptotic methods such as physical optics (PO), geometrical optics (GO), geometrical theory of diffraction (GTD), and uniform theory of diffraction (UTD). As these techniques are applicable only at high frequencies where geometries are electrically large, they are commonly referred to as high- frequency techniques [19–21]. In the next section we introduce some of these high-frequency techniques along with some examples.

2.7.1 Physical Optics (PO) and Geometrical Optics (GO)

For electrically large scatterers, where the primary scattering contribution is coming from specular reflections (such as large reflector antennas), PO approximation yields

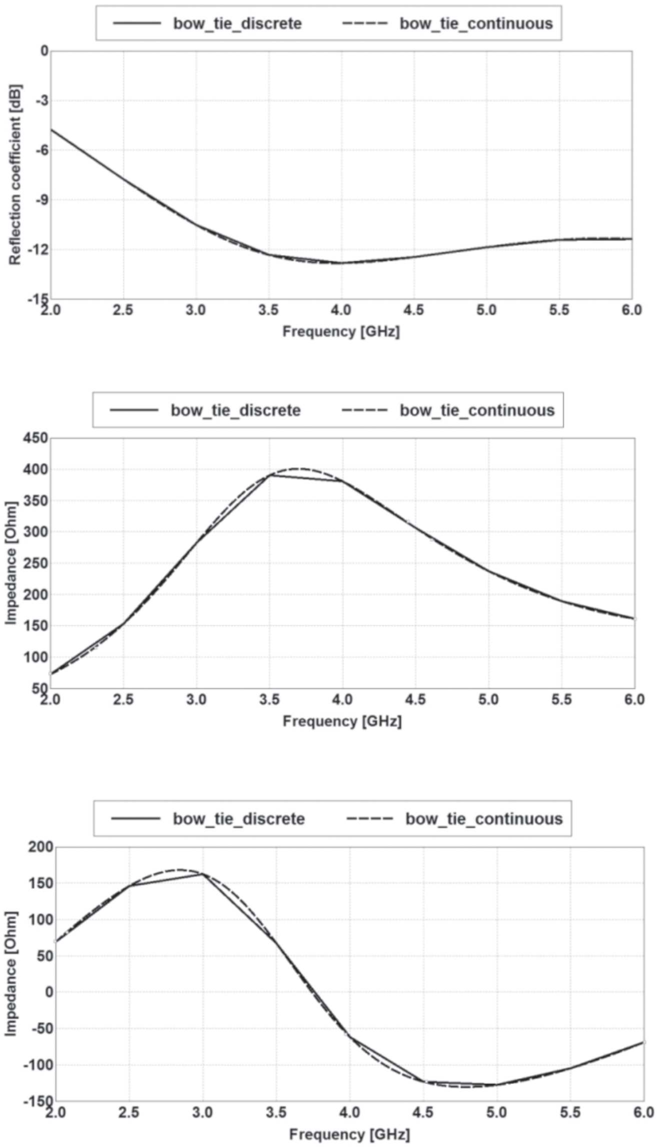

Figure 2.18 Input impedance of bowtie antenna over the frequency range using discrete points and using continuous frequency sweep.

quite accurate answers in the primary radiation direction. Owing to its simplicity, it is one of the most widely used techniques for electromagnetic scattering analysis in general and in reflector design in particular. The PO approximation is based on surface equivalence and locally flat approximation of the reflector surface. Under these assumptions, the induced surface current on the antenna is approximated in terms of the incident magnetic field intensity as

$$J_{PO} = \begin{cases} 2\hat{n} \times \boldsymbol{H}^{inc} & \text{in lit region} \\ 0 & \text{in shadow region} \end{cases} \tag{2.79}$$

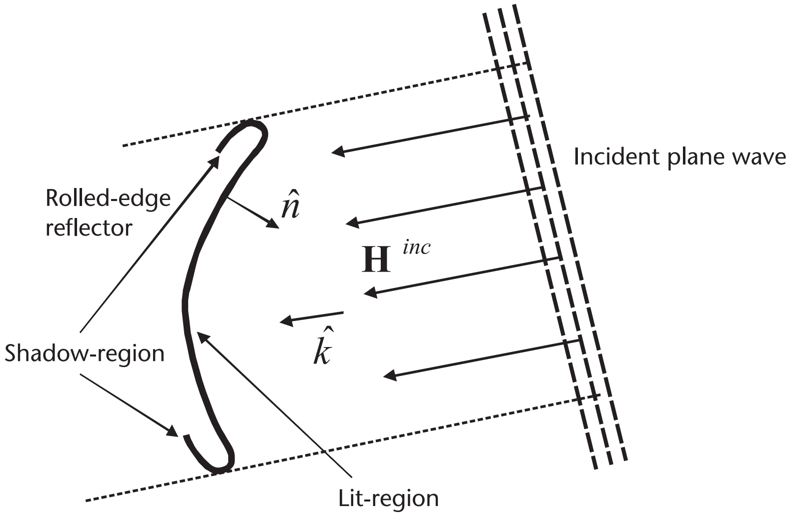

Figure 2.19 Illustration of the lit- and shadow-regions of the PO and GO approximations.

where J_{PO} is the PO current induced on the lit side of the geometry.

The scattered fields can in turn be computed using the far-field integrals

$$\boldsymbol{E}_{ff} = -jkZ_0 \frac{e^{jkr}}{4\pi r} \iint_{s'} \hat{r} \times \hat{r} \times \boldsymbol{J}_{PO} e^{-jk \cdot r} \, ds \tag{2.80}$$

$$\boldsymbol{H}_{ff} = jk \frac{e^{jkr}}{4\pi r} \iint_{s'} \hat{r} \times \boldsymbol{J}_{PO} e^{-jk \cdot r} \, ds \tag{2.81}$$

As seen, only the knowledge of the incident magnetic field and the lit parts of the problem geometry is needed to apply PO. The simplicity of the PO implementation and the accuracy of the solutions for highly directive antennas make PO the first choice for approximate analysis of large reflector antennas. The incident field H^{inc} is typically computed from a full-wave analysis. To a first-order approximation, the main reflector is illuminated by the computed fields of the feed. Subsequently, the radiation in the main beam of the reflector is computed using (2.80) with the PO currents from (2.79).

We note that the geometry mesh and MoM basis functions can be incorporated into (2.79) such that the mesh of the problem geometry can be used to compute J_{PO} via a simply projection similar to (2.33). This mesh-based PO also allows for a much more general geometry representation capability. More importantly, hybridization of MoM and PO becomes more organic since the same basis functions are used on both methods.

However, a critical drawback of the PO method is the identification of the lit and shadow regions in the problem geometry see Figure 2.19 and 2.20. *Ray-tracing* or *Z-buffer* based methods are typically applied. Also, since the boundary between the lit and shadow regions is abrupt, unwanted diffraction effects are introduced in the radiated fields computed via (2.80) and (2.81). This can be alleviated through a

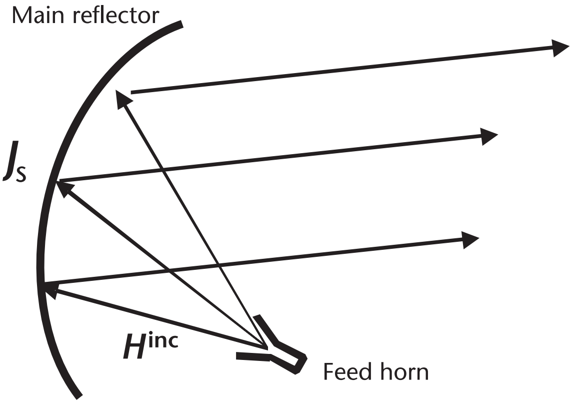

Figure 2.20 PO approximation for modeling reflector antennas.

more sophisticated treatment of the shadow boundaries using the physical theory of diffraction (PTD) [22].

On the contrary, in GO the wavefronts of the incident field are associated with rays, representing the energy flow direction normal to the wavefronts. Subsequently, each ray is traced through the problem domain and the usual ray-matter interactions, such as reflections from conducting surfaces and refractions at material boundaries, are accounted for. The scattered or reflected fields are computed from the collection of rays that arrive at the observation point. GO is highly utilized in optics where the optical components such as lenses, reflectors, diffraction gratings, beam-splitters, and so on closely obey the ray-tracing rules and the diffraction effects are minimal due to the extremely large sizes. A detailed discussion on this subject can be found in introductory level optics texts [23].

2.7.2 Example

Figure 2.21 shows helix-fed reflector antenna analyzed using ray-launching GO and PO in FEKO at 9.37 GHz.

2.7.3 Geometrical Theory of Diffraction and Uniform Theory of Diffraction

As noted above, the GO approximation makes use of a ray-based description of electromagnetic energy propagation. For example, for the simple half-plane problem illustrated in Figure 2.22, the total GO electric field is written as a sum of incident and reflected fields with associated regions of validity as

$$\mathbf{E}^{GO} = \mathbf{E}^{inc} u_i + \mathbf{E}^{ref} u_r \tag{2.82}$$

where u_i and u_r are unit step functions defined as

$$u_i = \begin{cases} 1 & \text{in regions 1 and 2} \\ 0 & \text{otherwise} \end{cases} \tag{2.83}$$

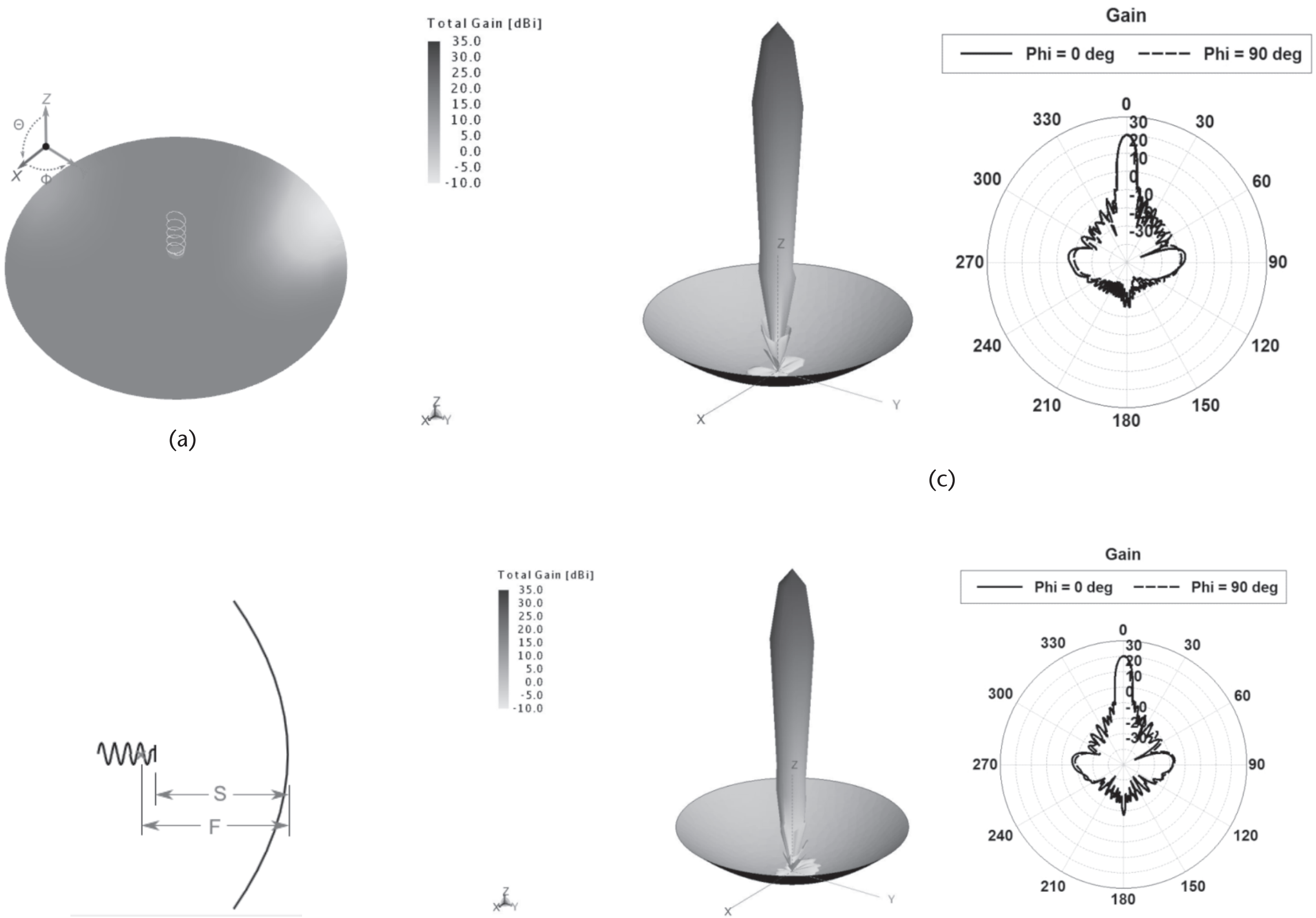

(a)

(b)

(c)

(d)

Figure 2.21 Radiation characteristics of helix-fed reflector antenna using GO and PO. (a) 3-D CAD model of helix-fed reflector, (b) schematic drawing, (c) radiation characteristics using geometrical optics (GO) at 9.37 GHz, and (d) radiation characteristics using physical optics (PO) at 9.37 GHz.

and

$$u_i = \begin{cases} 1 & \text{in region 1} \\ 0 & \text{otherwise} \end{cases} \tag{2.84}$$

Obviously, (2.82) introduces abrupt, nonphysical transitions across the incident-shadow boundary (ISB) and the reflection-shadow boundary (RSB). An additional field contribution is needed to incorporate the effects of diffraction coming from the finite edge. This is incorporated in (2.82) as the diffracted field component

$$\boldsymbol{E}^{GO} = \boldsymbol{E}^{inc}\, u_i + \boldsymbol{E}^{ref} u_r + \boldsymbol{E}^d \tag{2.85}$$

where $\boldsymbol{E}^d$ is given for the two-dimensional problem in Figure 2.22 as

$$\boldsymbol{E}^d = \boldsymbol{E}^{inc}(\boldsymbol{r}_E)\;\; D_{\substack{s\\h}}(\phi,\phi')\,\frac{\boldsymbol{e}^{jk\rho}}{\sqrt{\rho}} \tag{2.86}$$

In (2.86), ρ is the usual cylindrical coordinate of the receiver location and $D_{\substack{s\\h}}(\phi,\phi')$ is Keller's diffraction coefficient for parallel and perpendicular polarizations give by

$$D_{\substack{s\\h}}(\phi,\phi') = \frac{\boldsymbol{e}^{j\frac{\pi}{2}}}{2\sqrt{2\pi k}}\left[\frac{1}{\cos\left(\dfrac{\phi-\phi'}{2}\right)} \mp \frac{1}{\cos\left(\dfrac{\phi+\phi'}{2}\right)}\right] \tag{2.87}$$

For more general cases, such as diffraction by a wedge, a curved edge, or a curved wedge, $D_{\substack{s\\h}}(\phi,\phi')$ must be replaced by the appropriate diffraction coefficient to compute $\boldsymbol{E}^d$ via (2.86). We note here that by definition the diffraction coefficient is only a function of local geometry of the discontinuity in the problem geometry. As such, the geometrical theory of diffraction (GTD) provides a powerful approach to analyzing electrically large structures from a purely geometrical perspective, bypassing Maxwell's equation completely.

Unfortunately, diffraction coefficient given in (2.87) is not uniform, that it, at the ISB and RSB (2.87), has a singularity due to $\phi - \phi' = \pi$ and $+\phi' = \pi$. Resolution of this problem is achieved in the uniform theory of diffraction (UTD) (Kouyoumjian R., 1975). In UTD, a new diffraction coefficient is developed using asymptotic approximations of the half-space problem solution, and the resulting UTD diffraction coefficients are well behaved across ISB and RSB.

The diffraction effects include not only the edge and wedge diffractions but also diffraction from curved edges and wedges, creeping waves, as well as slope diffraction. In general, when the geometry has diffraction centers in close proximity of each other, multiple diffraction effects must also be accounted for, for an accurate analysis. UTD is perhaps one of the most widely utilized tools for reflector antenna

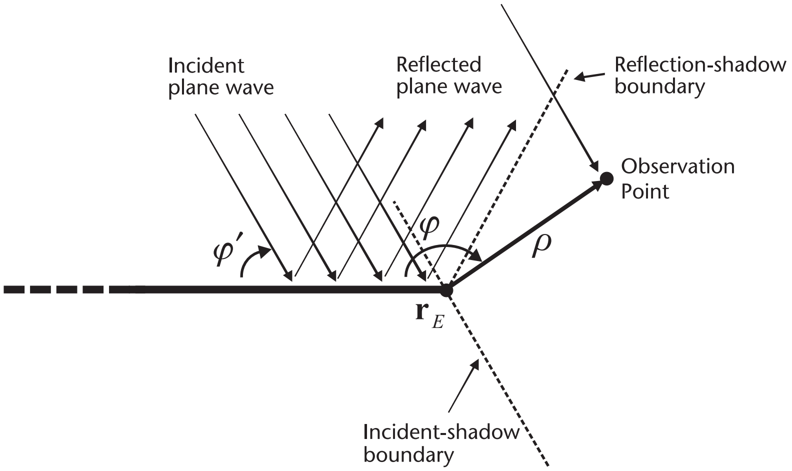

Figure 2.22 Illustration of incident-shadow boundary (ISB) and reflection-shadow boundary (RSB) of the half-plane problem.

analysis and design. Several legacy computer codes are in use today, such as NEC-BSC and NEC-REF (http://electroscience.osu.edu/9263.cfm) and TICRA (http://www.ticra.com/).

Acknowledgments

Example antenna designs in this chapter are designed using commercial antenna design software, Antenna Magus (www.antennamagus.com). Authors acknowledge support from Magus (Pty) Ltd for providing Antenna Magus and EM Software& Systems-S.A. (Pty) Ltd. for providing FEKO.

References

[1] Harrington, R. F., *Field Computation by Moment Methods*, Hoboken, NJ: Wiley-IEEE Press, 1993.

[2] Graglia, R., "The use of Parametric Elements in the Moment Method Solution of Static and Dynamic Integral Equations," *IEEE Transactions on Antennas and Propagation*, Vol. 36, No. 5, 1988, pp. 636–646.

[3] Rao, S. M., D. R. Wilton, and A. W. Glisson, "Electromagnetic Scattering by Surfaces of Arbitrary Shape," *IEEE Transactions on Antennas and Propagation*, Vol. 30, No. 3, 1982, pp. 409–418.

[4] Volakis, J. L., and K. Sertel, *Integral Equation Methods for Electromagnetics*, Raleigh, NC: SciTech Pub. Inc., 2012.

[5] Medgyesi-Mitschang, L., J. Putnam, and M. Gedera, "Generalized Method of Moments for Three-Dimensional Penetrable Scatterers," *Journal of Optical Society of America A*, Vol. 11, No. 4, April 1994, pp. 1383–1398.

[6] Volakis, J. L., K. Sertel, and B. C. Usner, "Frequency Domain Hybrid Finite Element Methods in Electromagnetics." In *Synthesis Lectures on Computational Electromagnetics*, C. A. Balanis, (ed.), USA: Morgan & Claypool Publishers, 2006.

[7] Sancer, M., K. Sertel, and J. L. Volakis, et al., "On Volume Integral Equations," *IEEE Transactions on Antennas and Propagation*, Vol. 54, No. 5, May 2006, pp. 1488–1495.

[8] Volakis, J. L., A. Chatterjee, and L. C. Kempel, *Finite Element Method for Electromagnetics*, Hoboken, NJ: Wiley-IEEE Press, 1998.

[9] Jin, J., *The Finite Element Method in Electromagnetics*, 2nd ed., New York: John Wiley & Sons, Inc., 2002.

[10] Monk, P., *Finite Element Methods for Maxwell's Equations*, UK: Oxford University Press, 2003.

[11] Nedelec, J., "Mixed Finite Elements in R3," *Numerische Mathematik*, Vol. 35, No. 3, 1980, pp. 315–341.

[12] Antilla, G., and N. Alexopoulos, "Scattering from Complex Three-dimensional Geometries by a Curvilinear Hybrid Finite-element-integral-equation Approach," *Journal of Optical Society of America A*, Vol. 11, No. 4, April 1994, pp. 1445–1457.

[13] Vouvakis, M. N., S.-C. Lee, and K. Zhao, et al., "A Symmetric FEM-IE Formulation with Single-Level IE-QR Algorithm for Soling Electromagnetic Radiation and Scattering Problems," *IEEE Transactions on Antennas and Propagation*, Vol. 52, No. 11, 2004, pp. 3060–3070.

[14] Chew, W. C., J. Jin, and E. Michielssen, (eds.), *Fast and Efficient Algorithms in Computational Electromagnetics*, Norwood, MA; Artech House Publishers, 2001.

[15] Waltz, C., K. Sertel, and M. A. Carr, et al., "Massively Parallel Fast Multipole Method Solutions of Large Electromagnetic Scattering Problems," *IEEE Transactions on Antennas and Propagation*, Vol. 55, June 2007, pp. 1810–1816.

[16] Taboada, J., M. G. Araujo, and J. M. Bertolo, et al., "MLFMA-FFT Parallel Algorithm for the Solution of Large-scale Problems in Electromagnetics," *Progress In Electromagnetics Research*, Vol. 105, 2010, pp. 15–30.

[17] Miller, E., and G. Burke, "Using Model-based Parameter Estimation to Increase the Physical Interpretability and Numerical Efficiency of Computational Electromagnetics," *Computer Physics Communications*, Vol. 68, 1991, pp. 43–75.

[18] Reddy, C. J., "Application of Model Based Parameter Estimation for Fast Frequency Response Calculations of Input Characteristics of Cavity-backed Aperture Antennas Using Hybrid FEM/MoM Technique," *NASA Contractor Report*-1998-206950, 1998.

[19] Deschamps, G., "Ray Techniques in Electromagnetics," *Proc. IEEE*, Vol. 60, No. 9, 1972, pp. 1022–1035.

[20] Kouyoumjian, R. G., "Asymptotic High-frequency Methods," *Proc. IEEE*, Vol. 53, 1965, pp. 864–876.

[21] Kouyoumjian, R. G., and P. H. Pathak, "A Uniform Geometrical Theory of Diffraction for an Edge in a Perfectly Conducting Surface," *Proc. IEEE*, Vol. 62, Nov. 1974, pp. 1448–1461.

[22] Ufimtsev, P. Y., *Fundamentals of the Physical Theory of Diffraction*, Hoboken, NJ: Wiley-IEEE Press, 2007.

[23] Saleh, B. E., and M. C. Teich, *Fundamentals of Photonics*, New York: John Wiley & Sons, 1991.

[24] Kouyoumjian, R. G., *The Geometrical Theory of Diffraction and Its Applications*, R. Mittra (ed.), New York: Springer-Verlag, 1975.

[25] Garbacz, R., and R. Turpin, "A Generalized Expansion for Radiated and Scattered Fields," *IEEE Transactions on Antennas and Propagation*, Vol. 19, No. 3, 1971, pp. 348–358.

[26] Harrington, R., and J. Mautz, "Theory of Characteristic Modes for Conducting Bodies," *IEEE Transactions on Antennas and Propagation*, Vol. 19, No. 5, 1971, pp. 622–628.

[27] Gross, F. B., *Frontiers in Antennas: Next Generation Design and Engineering*, New York: McGraw Hill, 2011.

[28] Bleszynski, E., M. Bleszynski, and T. Jaroszewicz, "AIM: Adaptive Integral Method for Solving Large-scale Electromagnetic Scattering and Radiation Problems," *Radio Science*, Vol. 31, No. 5, 1996, pp. 1225–1251.

[29] Mautz, J., and R. F. Harrington, "Radiation and Scattering from Bodies of Revolution," *Applied Scientific Research*, Vol. 20, No. 1, 1969, pp. 405–435.

[30] Munk, B. A., *Frequency Selective Surfaces: Theory and Design*, New York: Wiley-InterScience, 2000.

CHAPTER 3

Electrically Small Feeds

L. Shafai, University of Manitoba
Z. A. Pour, University of Manitoba
S. Latif, University of Manitoba

3.1 Introduction

This chapter deals with small feeds, which are mainly developed for prime focus reflectors. They have been mostly waveguide based, but planar configurations, using microstrip patch or dipole antennas, have also been investigated. In this form, they are small, with respect to the wavelength, and relatively easy to fabricate by the printed circuit technology. However, they can also be used in array forms, which allow radiation pattern shaping, but at the expense of increasing the feed size. In the following sections, initially, a brief background is provided, which is followed by the waveguide-based designs and then by the planar configurations. For completeness, a case of asymmetric feeds for offset prime focus reflectors is also discussed at the end of the chapter. More detailed coverage of asymmetric feeds is provided later in Chapter 8.

The early feeds were based on simple antenna configurations to facilitate their design. They were also designed mostly for radar applications and required high-power capability. Thus, open-ended waveguides and dipoles were selected for such applications. In the former case, small flare angles were used to control the waveguide radiation patterns and match the aperture impedance to that of free space. In the latter case, planar disks were utilized to direct the dipole radiation field toward the reflector [1]. However, they performed poorly as feeds for reflector antennas, which resulted in low aperture efficiencies, and high cross polarizations. Further improvements in the performance of these feeds were achieved by altering the configurations and combining their unique design features, which resulted in smaller, simpler, and more efficient feeds such as the Cutler feed [2] and Calvin feed [3]. These feeds performed better, but they were not optimum. Additional improvements were achieved by inclusion of higher order modes in the waveguides, such as the Potter horns [4, 5] or the excitation of hybrid modes [5, 6]. The latter designs were achieved by investigation of the focal plane field of reflector antennas, and enforcing the reciprocity principle, to identify the feed aperture field, by matching the aperture field of the feed to that of the reflector focal plane field.

Another important factor in the design of early feeds was the limitations in availability of efficient computation tools, which influenced the solutions and favored the analytic and asymptotic techniques. In turn, they helped in understanding the physical principles behind the operation of reflector antennas and the importance of various feed parameters. However, analytic formulations and most simplifying approximations are valid in the asymptotic sense, and in the case of reflector feeds, they have helped in accurate design of large aperture feeds. Such feeds are normally used in dual reflector antennas, which require narrow angle illumination for their subreflectors.

The prime focus reflectors, on the other hand, must support the feed and the receiver assembly at their focal point, which will cause aperture blockage and performance degradation. In such cases, deeper reflector geometries are favored to reduce the blockage, which in turn require small-size feeds in terms of the wavelength. The aperture dimensions of most feeds in this category fall around one to two wavelengths, where asymptotic approximations are invalid or inaccurate. Experimental or numerical methods must be used. They require anechoic chambers, which are costly to install, or accurate numerical codes, which were not available to antenna engineers until quite recently. The development of efficient small feeds for prime focus reflectors, therefore, had to wait until numerical techniques, based on moment and finite-element methods or the finite-difference time-domain method became available to the antenna engineering community. Their small sizes make them ideal candidates for design and optimizations by such numerical codes.

The conceptual design of small feeds for prime focus reflectors was helped by the analysis of focal plane fields of parabolic reflectors [7], which showed that they can be expressed in terms of hybrid modes. This led to the development of several feeds that could support hybrid modes, such as the corrugated horns, dielectric loaded horns, and, recently, metamaterial horns. The corrugated horns were the most successful designs and found applications in both large and small aperture horns. Until recently they were unchallenged in terms of performance. The latter metamaterial horns are still in their infancy and have not been studied extensively yet, but they show advantages in cost, weight, and performance over corrugated horns and promises for large-scale applications. Their design and performance are investigated in Chapter 6.

The excitation and investigation of hybrid modes using corrugated horns have been reported by Clarricoats and Olver [8] and Minnett and Thomas [9]. Experimentally, they were designed and studied by Kay [10] and Koch [11]. The former used passive corrugations on the inside wall of a conical horn to influence the wall surface impedance and consequently the horn aperture field distribution. The latter used active corrugations, excited through slots and probes on the wall of the feeding waveguide, to control the aperture field distribution over the surface of the waveguide flange. A similar design, but with considerably simpler configuration, was developed by Wohlleben [12] and James [13], in which the corrugations were excited directly through aperture coupling. The advantage of the latter two feeds is in the independence of the corrugated flange surface from the waveguide that can be moved axially, with respect to each other, to control the feed radiation patterns.

The real breakthrough in design of small prime focus reflector feeds happened with realization of the fact that the dominant mode in circular waveguides can be excited by a transverse dipole source on their axis, and that the azimuth dependence of the radiated fields is separated from the other coordinates and governed by simple sine or cosine functions. The former reduced the computation time for electromagnetic analysis of the feeds, and the latter allowed altering the radiated field simply by shaping the transverse cross section of the feed. Consequently, numerical analysis and optimization of the feeds became reality even with small computers, and efficient feeds with low cross polarization were investigated and designed. For a good summary of such studies and design of various efficient feeds, see Olver, Clarricoats, Kishk, and Shafai [14] for a dedicated manuscript on microwave horns and feeds. The development of more-efficient numerical methods and advancements in the computer technology further facilitated the feed design and investigation, but the fundamental principles have remained the same; only techniques for achieving these goals are different, which are discussed separately in the following chapters.

3.2 Design Requirements

Fundamentally, there are three main requirements for the design of high-performance feeds for symmetric reflector antennas:

1. Low cross polarization;
2. Phase center uniqueness;
3. High antenna gain factor.

Low cross polarization: The condition of low cross polarization can be met by balancing the radiation from electric and magnetic currents. Since this chapter deals with small feeds, their aperture fields can be approximated by electric and magnetic dipoles, having the following co-polar and cross-polar radiations.

For the x-polarized electric dipole,

$$E_{co}^{e} = \frac{1}{2}[(1+\cos\theta) - (1-\cos\theta)\cos 2\phi]\, c^{e}\, \frac{e^{-jkr}}{r} \tag{3.1}$$

$$E_{cross}^{e} = -\frac{1}{2}[(1-\cos\theta)\sin 2\phi]\, c^{e}\, \frac{e^{-jkr}}{r} \tag{3.2}$$

And for the y-polarized magnetic dipole,

$$E_{co}^{m} = \frac{1}{2}[(1+\cos\theta) + (1-\cos\theta)\cos 2\phi]\, c^{m}\, \frac{e^{-jkr}}{r} \tag{3.3}$$

$$E_{cross}^{m} = \frac{1}{2}[(1-\cos\theta)\sin 2\phi]\, c^{m}\, \frac{e^{-jkr}}{r} \tag{3.4}$$

From these equations, for the balance condition of $c^e = c^m$, the cross polarization cancels exactly, and the radiation is perfectly linearly polarized, which for $c^e = c^m = 1$ becomes

$$E^T_{co} = (1 + \cos\theta)\frac{e^{-jkr}}{r} \tag{3.5}$$

$$E^T_{cross} = 0 \tag{3.6}$$

As shown in Chapter 1, the cross polarization will cancel when the radiation from the electric and magnetic dipoles equalizes. For example, in an open-ended waveguide, the cross polarization decreases by increasing its radius, due to a reduction in the wall current, until the radius approaches 0.6λ, where λ is the wavelength in the medium [14]. At this point, provided higher order modes are not excited, the waveguide is equivalent to a quasi-Huygen source. This implies that the back radiation is also minimized [14]. The same is true for a microstrip patch antenna. As it will be shown later in this chapter, the cross polarization will decrease as the ground plane size increases from the patch size until the magnetic dipole radiation from the substrate balances the electric dipole radiation of the patch. This means that regardless of the patch size, which depends on the substrate permittivity, the cross polarization will decrease initially until it minimizes at a ground plane size near one wavelength, the exact size being dependent on the substrate permittivity.

The preceding rule of balancing the electric and magnetic dipoles also applies to other and more complex configurations, such as corrugated walls and flanges. In the absence of an optimization code, this information helps in rapid design of low cross polarization feeds.

Phase center uniqueness: The phase center uniqueness is an important feed design parameter but is often neglected. Equalizing the principal plane amplitude patterns guarantees neither low cross polarization nor high gain factor, unless the phase patterns are also equalized to unify the feed phase centers in the principal planes.

High antenna gain factor: An elegant way of determining a feed design for insuring high antenna gain factor is to match the aperture field of the feed to the focal plane field of the reflector, when illuminated by a plane wave [7]. For an aperture antenna, this is in the form of $J(x)/x$, which is also the focal plane field of a parabolic reflector with a small subtended angle. The actual focal plane field, however, is somewhat different (shown in Figure 3.1), for different reflector subtended angles. In circular reflector apertures, these field intensities correspond to Airy disks, with alternating positive and negative intensities, which continue to infinity. However, because of the diminishing intensities, the first few peaks (normally less than three) are used to design practical feeds. This focal plane field truncation influences the design and reduces the achievable reflector gain factors. Nevertheless, this is the most practical design approach to maximize the reflector gain factor while minimizing the feed size and its aperture blockage.

In a vectorial representation, the field distribution, corresponding to three Airy disks, or the main lobe and two sidelobes of the focal plane field, up to the third null, resembles the plot shown in Figure 3.2. It is evident that the field cross polarization

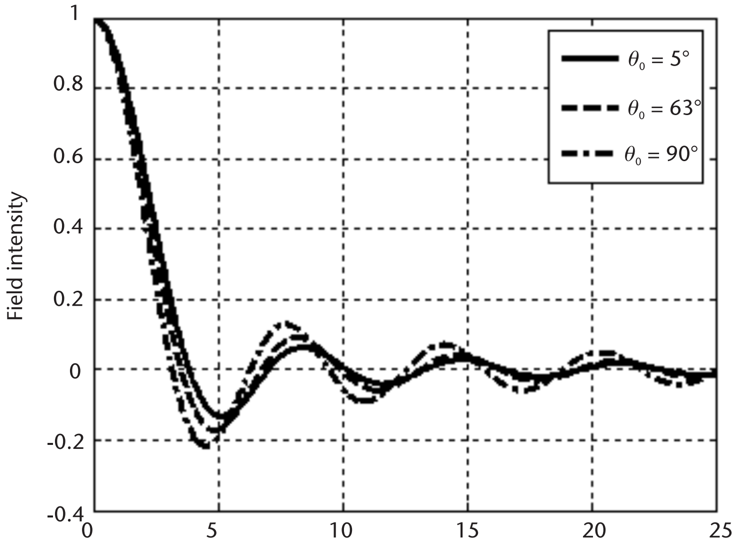

Figure 3.1 Focal plane field of a paraboloid reflector, for different subtended angle θ_o, with $U = k\rho \sin\theta_o$, ρ being the radial distance in the focal plane.

is zero. Such a field distribution can be provided by hybrid modes in a corrugated waveguide [7], or a combination of the dominant and higher order modes in a smooth wall waveguide [11].

Using the preceding methods, Koch [11] has systematically synthesized feeds with properly excited waveguides and rings. To eliminate the higher order modes, as many as 12 longitudinal slots around the waveguide have been used to excite

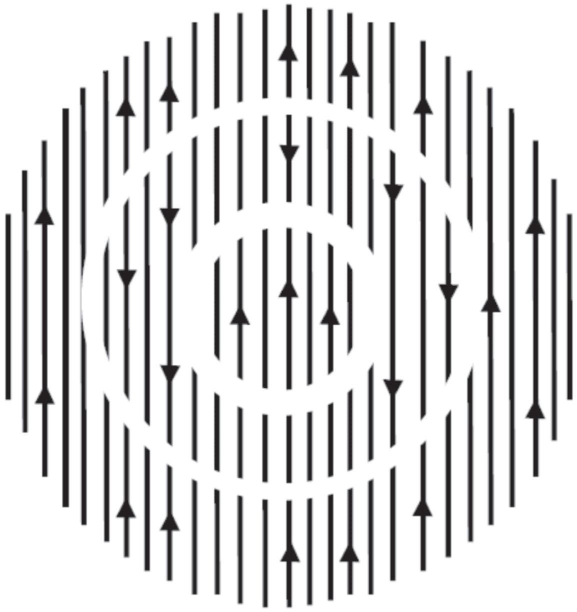

Figure 3.2 Vectorial representation of a paraboloid focal plane field, corresponding to Figure 3.1, including up to three nulls.

the required TM_{11} and TE_{12} modes. This is an excellent example of science-based antenna design. However, the designs are complex and costly to fabricate.

In waveguides with shorted rings (such as chokes), the coupling between the waveguide and rings is strong and can be controlled by their dimensional parameters. Analytic solutions are normally beyond the reach, but the problem can be handled numerically with available software packages. Since passive chokes are considerably easier to fabricate, they have been used in most practical small feed designs. In the following sections, a summary is provided (though by no means complete) that includes the most successful designs so far used in practice.

3.3 Waveguide Feeds

Antennas are generally easier to design for forward radiation, and the reflector feeds are no exception. For this reason, most reflector feeds, especially the high-performance ones, are designed for forward radiation. However, in prime focus reflectors the feed must be at the focal point, which is in front of the reflector and causes aperture blockage. In addition, the feed needs supporting struts that contribute to more blockage. Fortunately, with small feeds this is not a major issue, but nevertheless it limits the reflector performance. For these reasons, offset reflector geometries are considered to eliminate the blockage and improve the reflector performance. While this solution eliminates the blockage and improves the reflector gain and sidelobe performance, the asymmetry of the reflector geometry contributes to cross polarization. Thus, there is a merit for designing backward-radiating feeds that can be installed from the reflector center, to eliminate the supporting struts and their blockage. However, as indicated, the design of such backward-radiating feeds is more complex and influences their performance. In this section, we will discuss both feed types, but more attention will be focused on forward radiating feeds and their design optimization. A representative backward-radiating feed will also be presented and discussed.

Because of geometrical simplicity, and high power handling capability, most forward-radiating feeds are waveguide based. Circular waveguides are preferred, as their hybrid modes can generate efficient reflector illumination with low cross polarization [7]. Also, as shown in the previous section, the combination of the first two modes in smooth wall waveguides can provide excellent reflector illuminations with low cross polarization. These properties favor the use of circular waveguides as preferred reflector feeds. However, circular waveguides have one important property, not present in other waveguides, which is the separation of the radial and azimuth wave functions. This means that their aperture field and wall currents will also depend on separate azimuth and transverse wave functions. The significance of this property is in the fact that their outside wall can be shaped, in the form of corrugated flanges, or other profiles, to shape their radiated field, minimize the cross polarization, and unify their phase centers in various planes. In other words, small feeds are designed with excellent radiation properties.

A similar principle can also be used in microstrip antennas, where shaping of the ground plane can be used to improve the radiation patterns. This can also be explained in terms of Huygen source equivalence, as discussed earlier. The shaping of the waveguide outside wall provides an opportunity for balancing the electric and magnetic dipole radiations to improve the feed characteristics. Because this form of radiated field optimization is based on the aperture field coupling, the resulting geometry is normally simpler in shape and easier to fabricate. Small physical size of the feed also simplifies the design optimization. Consequently, nearly all small reflector feeds are based on circular waveguides with corrugated or shaped flanges. Their design and performance are discussed next.

3.3.1 Small Waveguide Feeds

Even though a waveguide is not an ideal feed for reflector antennas, it is discussed here to show the steps involved in the design process. Figure 3.3(a) shows the geometry of an open-ended waveguide, excited by the dominant TE_{11} mode. Adding a choke on the outside wall, Figure 3.3(b), brings the contribution of the second ring of the focal plane field (shown in Figure 3.1), and a quarter wavelength choke also increases the surface impedance near the wall edge that considerably reduces the edge diffraction and its subsequent side and back lobe levels in the radiation patterns. Figure 3.4 shows the resulting 10 dB beamwidths of the radiation patterns in the two principal planes. It is evident that the pattern symmetry of the waveguide without the choke improves as its radius increases, which is as a result of balancing the contribution of aperture electric and magnetic dipole fields. The corresponding cross polarizations in the 45° plane are shown in Figure 3.5, which for a waveguide without the choke decreases continuously until the waveguide radius of $a = 0.6\lambda$, where the next higher order mode TM_{01} becomes excited. A sample of the principal plane radiation patterns, along with the cross polarization in the 45° plane, are shown in Figure 3.6, for a waveguide with a half wavelength radius of $a = 0.5\lambda$. The excellent symmetry of the patterns is evident, which provides a low cross polarization level of below −30 dB.

As Figure 3.4 shows, the 10 dB beamwidths for a waveguide with a choke are narrower than those of the waveguide without a choke and equalize earlier in the principal planes around the radius of $a = 0.4\lambda$. Similarly, the peak cross polarization also minimizes earlier at about the same waveguide radius of $a = 0.4\lambda$, with significantly lower values of around −36 dB. Figure 3.7 shows its principal plane radiation patterns, with the cross polarization in the diagonal plane and the back lobe levels decreased significantly. To understand the influence of the choke on the back lobe level, they are compared for a waveguide with and without a choke in Figure 3.8.

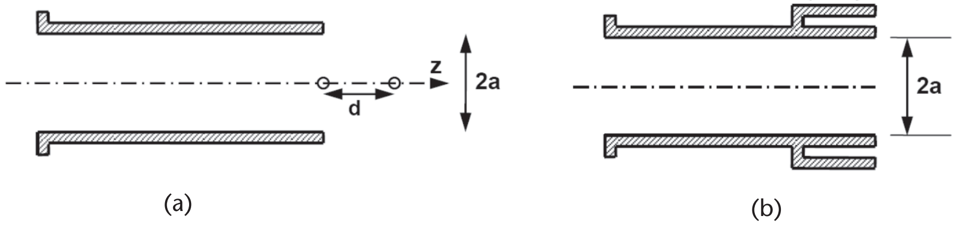

(a) (b)

Figure 3.3 Geometry of circular waveguide (a) without a choke and (b) with a quarter wavelength choke, TE_{11} excitation.

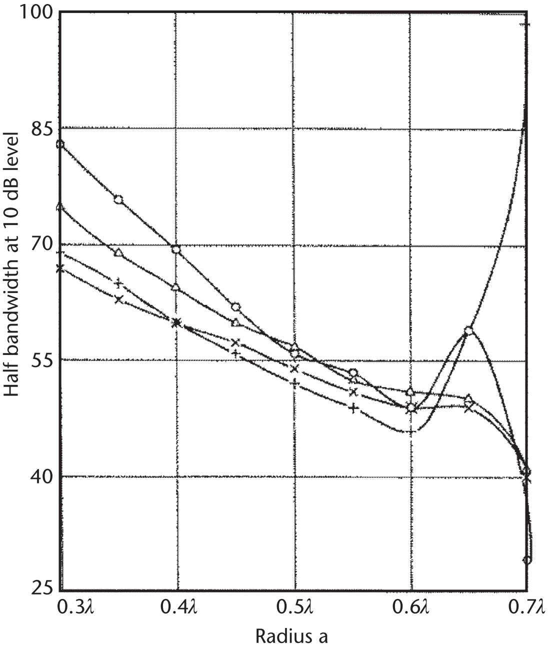

Figure 3.4 10 dB beamwidths of the radiation patterns of circular waveguides with TE_{11} excitation. Δ H-plane without a choke, ○ E-plane without a choke, + H-plane with a choke, × E-plane with a choke. (©1985 AEÜ [15].)

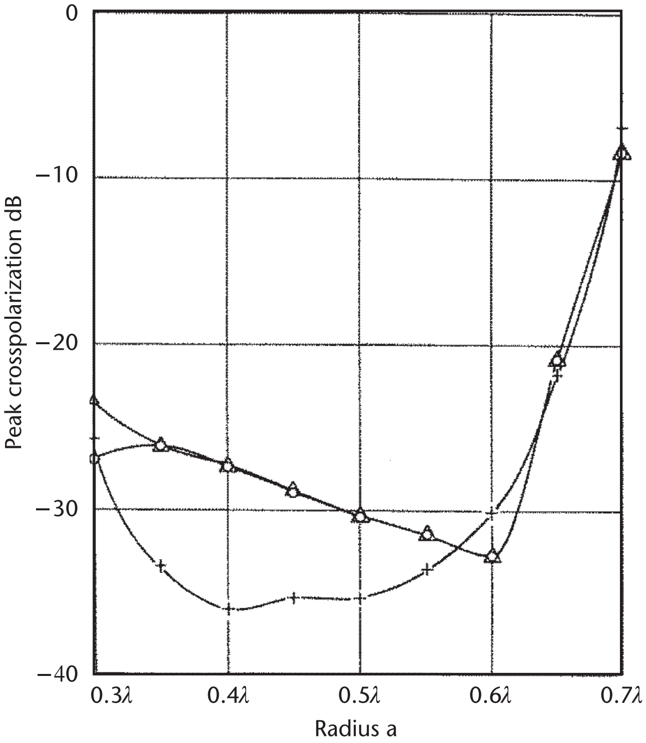

Figure 3.5 Peak cross polarization of circular waveguides with TE_{11} excitation. ○ without a choke $0 \leq \theta \leq 70°$, Δ without a choke $0 \leq \theta \leq 90°$, + with a choke $0 \leq \theta \leq 90°$. (©1985 AEÜ [15].)

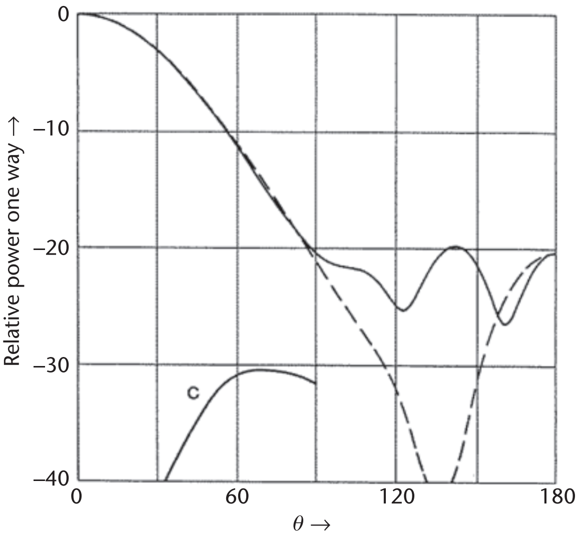

Figure 3.6 Principal plane radiation patterns and cross polarization in the diagonal plane, of circular waveguide without a choke, $a = 0.5\lambda$, TE_{11} excitation. — E-plane, ---- H-plane, $\overset{c}{\text{——}}$ cross polarization at $\phi = 45°$. (©1985 AEÜ [15].)

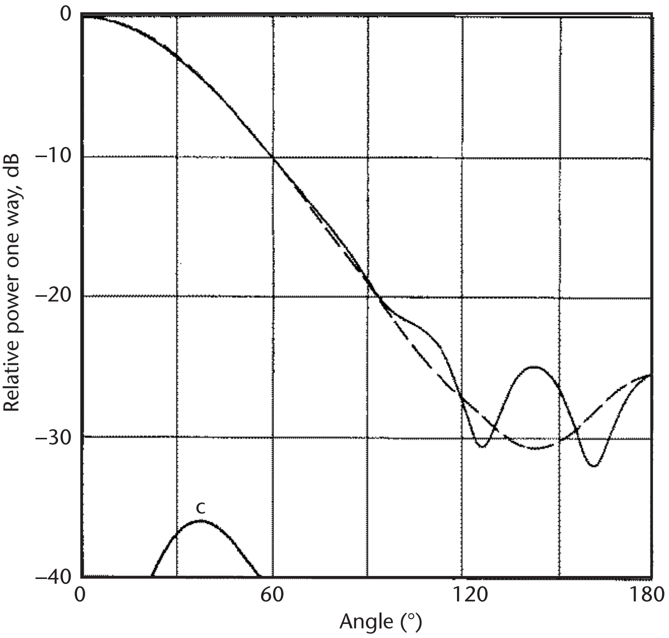

Figure 3.7 Principal plane radiation patterns and cross polarization in the diagonal plane of circular waveguide with a choke, $a = 0.4\lambda$, TE_{11} excitation. — E-plane, ---- H-plane, $\overset{c}{\text{——}}$ cross polarization at $\phi = 45°$. (©1985 AEÜ [15].)

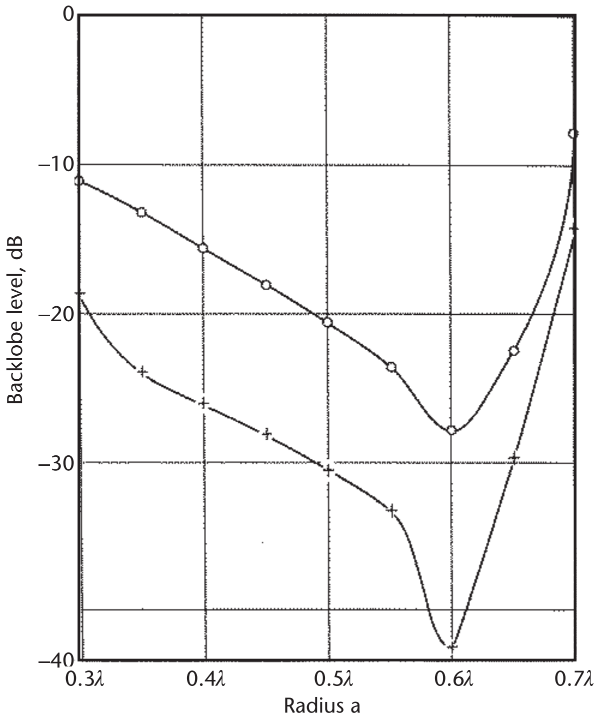

Figure 3.8 Back lobe levels of a circular waveguide with TE_{11} mode excitation, ○ without a choke, + with a choke. (©1985 AEÜ [15].)

It is clear that the introduction of a single choke decreases the back lobe level by about 10 dB. In addition, in both cases the back lobe level decreases continuously by increasing the waveguide radius, until the excitation of the TM_{01} mode at $a = 0.6\lambda$.

The phase center locations for the waveguides with and without a choke are shown in Figure 3.9 [16]. Here, d_c in the vertical axis is the distance of the waveguide aperture from the phase center location. Thus, from the geometry of Figure 3.3, when the phase center is in front of the aperture, that is, outside of the waveguide, d_c becomes negative, and when it is inside the waveguide it is positive. The case of the waveguide without the choke, in Figure 3.9(a), is quite interesting. Here, the

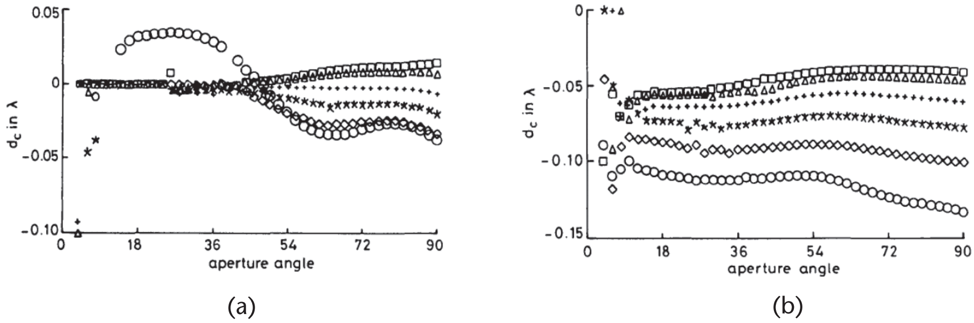

(a) (b)

Figure 3.9 Distance d_c of the waveguide aperture from the phase center (a) waveguide without a choke, and (b) waveguide with a choke, TE_{11} excitation. ○ $a = 0.3\lambda$, ◊ $a = 0.35\lambda$, * $a = 0.4\lambda$, + $a = 0.45\lambda$, Δ $a = 0.5\lambda$, □ $a = 0.55\lambda$. (©1985 IEE [16].)

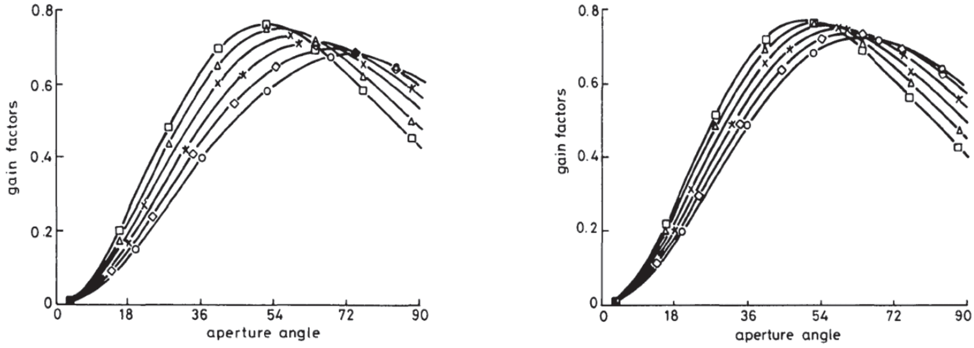

(a)

(b)

Figure 3.10 Gain factors of the waveguide feed on parabolic reflector antennas (a) without a choke, (b) with $\lambda/4$ choke, TE_{11} excitation. ○ $a = 0.3\lambda$, ◊ $a = 0.35\lambda$, * $a = 0.4\lambda$, × $a = 0.45\lambda$, Δ $a = 0.5\lambda$, □ $a = 0.55\lambda$. (©1985 IEE [16].)

currents on the outside of the waveguide wall are strong, especially when the waveguide radius approaches its cut-off value, which runs backward. The phase center location is therefore influenced strongly by this current and changes its location with the aperture angle. However, as the waveguide diameter increases, the percentage of its aperture radiation increases, and the phase center location moves to the waveguide aperture, where its location becomes independent of the direction. This uniqueness of the phase center location is manifested in the cross polarization reduction, as shown in Figure 3.5. The phase center location of the choked waveguide, shown in Figure 3.9(b), on the other hand, is more stable with the aperture angle and is generally outside the waveguide aperture. This is a clear indication that the quarter wavelength choke pushes the aperture field away from the waveguide wall.

The gain factor (the feed efficiency) performances of these simple feeds are shown in Figure 3.10(a) and (b), for the waveguide without and with a quarter wavelength choke. They are almost the same, being slightly higher for the waveguide with a choke, as shown numerically in Table 3.1.

The preceding results for the open-ended waveguide without and with a choke demonstrated two important facts. One, the performance of the feed in pattern uniformity, low cross polarization, and consequently the uniqueness of the phase center

Table 3.1 Gain Factor and Spill-Over Efficiencies of the Waveguide Feeds for Different Reflector *F*/*D*

	Gain factor (%)		*Spill-over (%)*		*F/D*	
a/λ	*without choke*	*with choke*	*without choke*	*with choke*	*without choke*	*with choke*
0.30	68.72	72.78	81.95	85.10	0.33	0.40
0.35	70.07	74.12	82.42	86.42	0.37	0.42
0.40	71.78	75.04	84.47	86.97	0.40	0.45
0.45	73.54	75.84	84.80	88.47	0.45	0.47
0.50	75.15	76.65	86.07	88.17	0.49	0.51
0.55	76.58	77.35	88.48	89.15	0.51	0.54

location improves by increasing the waveguide diameter, until the next higher order mode becomes excited, after $a = 0.6\lambda$. Second, using even a single quarter wavelength choke reduces the waveguide edge diffraction and waveguide outside wall currents sufficiently, to further lower the cross polarization and especially the back radiation. In practice, the choke height, depth, and location from the waveguide edge can be used as additional design parameters to modify the beamwidth or other feed parameters. In particular, recessing the choke, that is, moving it behind the waveguide aperture, will broaden the beamwidth, which can be used as a parameter to match the feed performance to a chosen reflector.

Adding more chokes will further enhance their influence on the radiation patterns and the feed performance. For instance, more chokes will capture more powers from the sidelobes of the focal plane field in Figure 3.1, to increase the gain factor. Similarly, more chokes further diminish the waveguide wall currents and reduce the back radiation. However, the most important factor in using additional chokes is in providing additional parameters to the feed design, to allow further feed performance optimizations. For instance, recessing the chokes progressively broadens the feed radiation patterns. Conversely, moving the chokes to the front of waveguide aperture, to form a corrugated conical horn, will reduce its beamwidth. Obviously, one needs not to move the chokes linearly to form forward or backward corrugated horn. The corrugation chokes can be moved in a nonlinear fashion to generate undulated corrugated waveguide flanges and thus provide additional parameters for optimization. Similarly, the choke shape need not be only rectangular; other shapes, such as trapezoidal, sinusoidal, or even arbitrary shapes, can also be selected. By optimizing their dimensions, feeds with high performance can be easily designed. We provide the parameters for the two special cases of waveguides with three rectangular or trapezoidal chokes. Their geometries are shown in Figure 3.11. Their radiation patterns, phase center locations, and gain factors are shown in Figures 3.12–3.14. The beamwidths are somewhat smaller than those of the waveguide with a single choke and have lower back lobe levels. The gain factors of the trapezoidal choke feed are slightly higher than those of the rectangular one. The gain factors are quite stable as L increases, where L is the distance between the apertures of the waveguide and the chokes. By adding more chokes, the relative size increases, resulting in further aperture blockage. Thus, it may not be suitable for applications in small reflectors.

An example of shaping the radiation patterns by moving multiple chokes with respect to each other is shown in Figure 3.15(a) and (b), which is designed for operation in the X-band, from 8 to 12.4 GHz. The second choke is moved slightly forward to reduce its −10 dB beamwidth to about 90°, resulting in a waveguide with a corrugated cone. At the upper end of the band, the radiation patterns and cross polarization are shown in Figure 3.16, and its performance improves as the frequency decreases. The beamwidth is decreased considerably from the case of a waveguide with a single choke. The back lobe level could be decreased further by embedding a narrow choke on the upper wall. Further reduction of the beamwidth can be accomplished by adding more chokes and moving the chokes farther ahead, resulting in a corrugated cone, and shown in Figure 3.15(c), where six corrugations are used and its −10 dB beamwidth is reduced to 50°. Since both feeds cover a full waveguide band, they can be scaled to other frequencies, such as the 20–30 GHz satellite band.

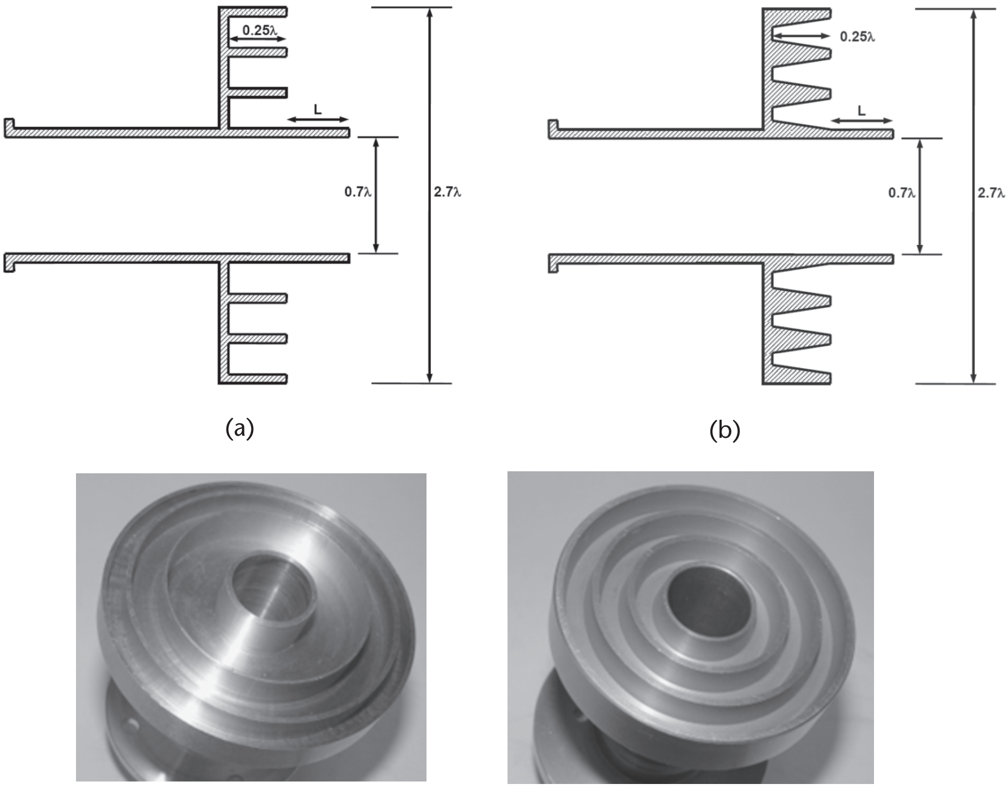

(a) (b)

(c) (d)

Figure 3.11 Geometries of circular waveguide with three rectangular and trapezoidal chokes, TE_{11} excitation. (a) Feed with rectangular chokes, (b) Feed with trapezoidal chokes, (c) picture of the feed with rectangular corrugations, and (d) picture of the feed with trapezoidal corrugations.

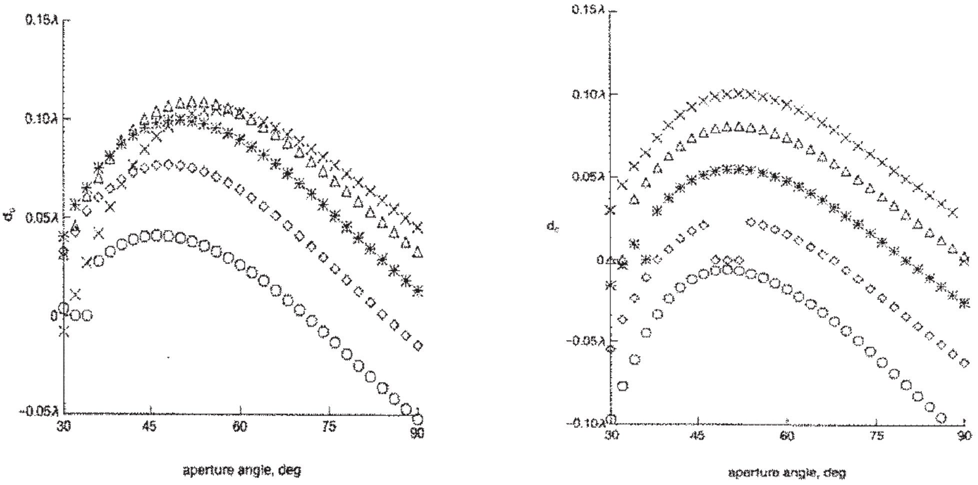

(a) (b)

Figure 3.12 Distance d_c of the waveguide aperture from the phase centers of the feeds shown in Figure 3.11. (a) Feed with rectangular chokes, and (b) feed with trapezoidal chokes. ○ $L = 0.0$, ◊ $L = 0.05\lambda$, * $L = 0.1\lambda$, Δ $L = 0.15\lambda$, × $L = 0.2\lambda$. (©1985 IEE [16].)

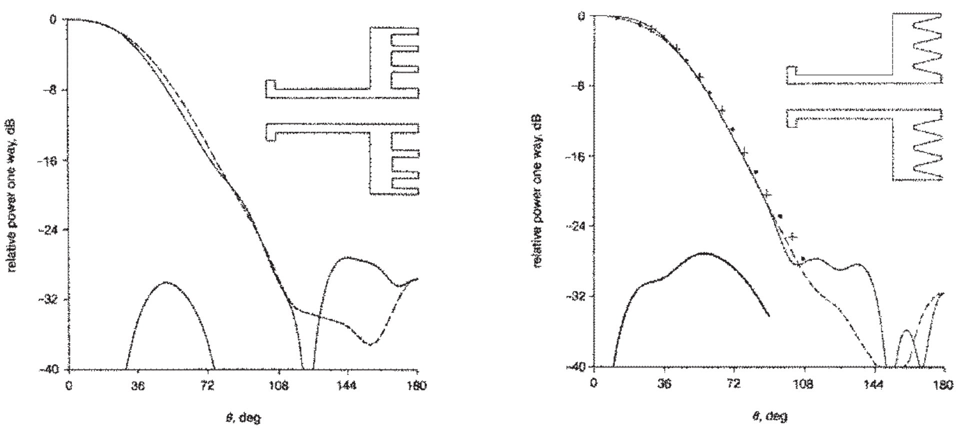

(a) (b)

Figure 3.13 Principal radiation patterns of the feeds in Figure 3.11. (a) Feed with rectangular chokes, and (b) feed with trapezoidal chokes. — E-plane, ---- H-plane, + measured E-plane, • measured H-plane. (©1994 IEE [14].)

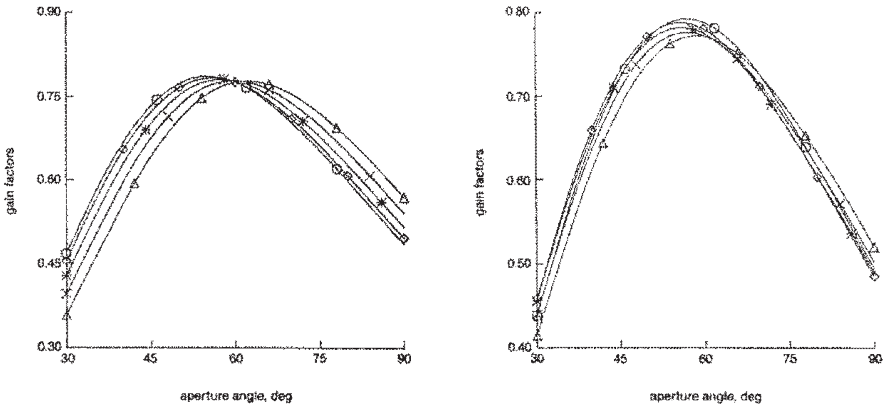

(a) (b)

Figure 3.14 Gain factors of the feeds in Figure 3.11 (a) with rectangular chokes, and (b) with trapezoidal chokes. ○ $L = 0.0$, ◊ $L = 0.05\lambda$, * $L = 0.1\lambda$, × $L = 0.15\lambda$, Δ $L = 0.2\lambda$. (©1985 IEE [16].)

3.3.2 Small Coaxial Feeds

Coaxial waveguides offer additional parameters for optimization. The mode structures are more complex, and the desired TE_{11} mode must be excited by an appropriate feed transition, such as a rectangular waveguide or multiple probes, to eliminate the dominant coaxial mode. However, they offer a unique advantage in the possibility of using the central conductor as another feed. Depending on the proximity of the two bands, the central conductor can be used with air or a dielectric loaded circular waveguide. In the latter case, the loading dielectric can be shaped to improve the

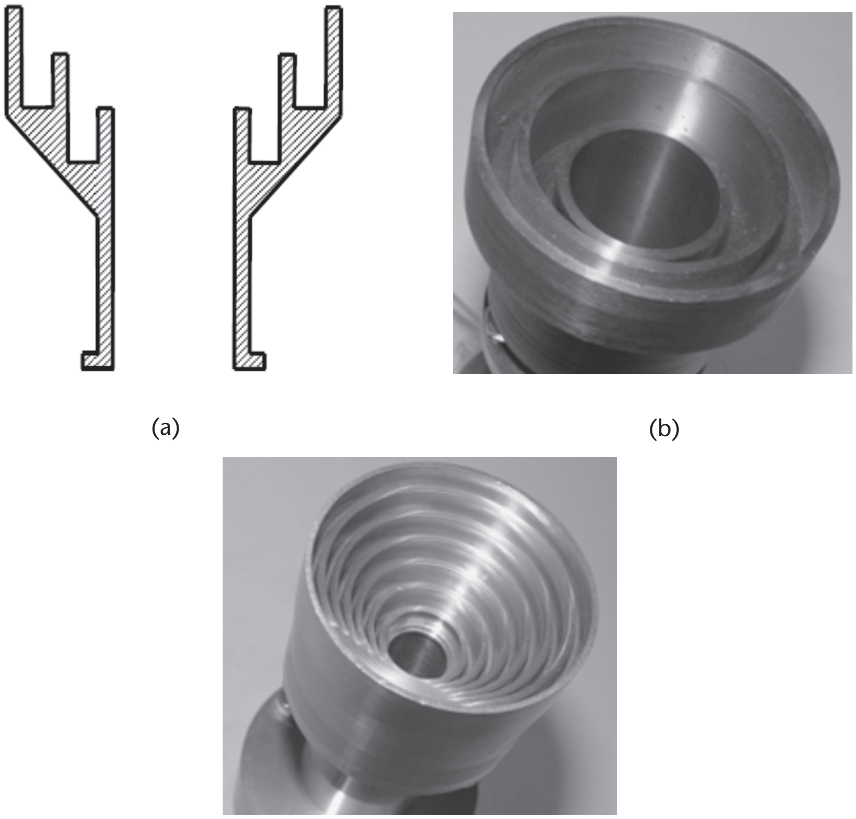

(a)

(b)

(c)

Figure 3.15 (a) Geometry of a circular waveguide with two corrugations, when the second choke is moved forward resulting in waveguide-cone feed, TE_{11} excitation, (b) its picture, and (c) corresponding waveguide-cone feed with six corrugations.

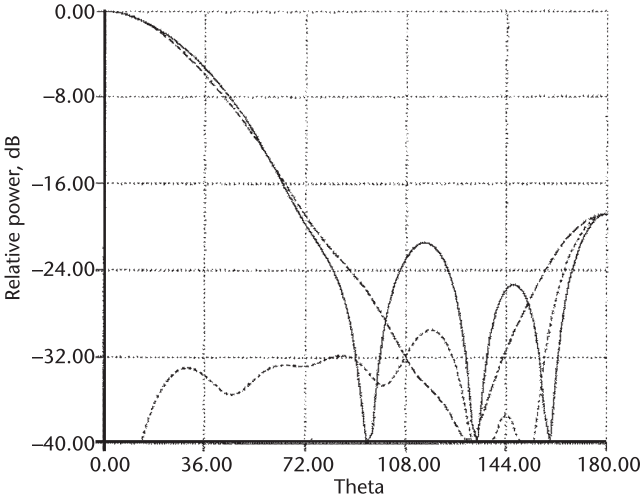

Figure 3.16 Radiation patterns and cross polarization of the feed shown in Figure 3.15(a). — E-plane, — — — H-plane, ----- cross polarization. (©1994 IEE [14].)

feed radiation characteristics [17]. Using such an approach, a dual band feed has been designed for operation in the two adjacent 4 and 6 GHz bands. Its geometry is shown in Figure 3.17, and its radiation patterns and the gain factors are depicted in Figures 3.18 and 3.19, respectively. The coaxial region operates in the lower 4 GHz band, and the dielectric loaded central region operates in the upper 6 GHz band. The dielectric extension is used to equalize the principal plane patterns and move the phase center of the upper band to the location of the lower band, which is in front of the waveguide aperture. On the outer wall, a quarter wavelength choke is used to improve the radiation characteristics of the coaxial feed, and an iris is incorporated to improve both the radiation patterns and the impedance bandwidth. It is clear from Figure 3.18 that the feed performs well in both bands, and good pattern symmetry is established in both bands. The gain factors in Figure 3.19 show slight advantage of the lower 4 GHz band. But this was done intentionally to maximize its gain. At the higher band, the reflector is larger and gives sufficient gains. This design demonstrates the challenges one must consider in designing dual- or multi-band feeds. The phase centers must be coincident, and the feed performance must be satisfactory in both bands, including the required isolation of the two bands and the input

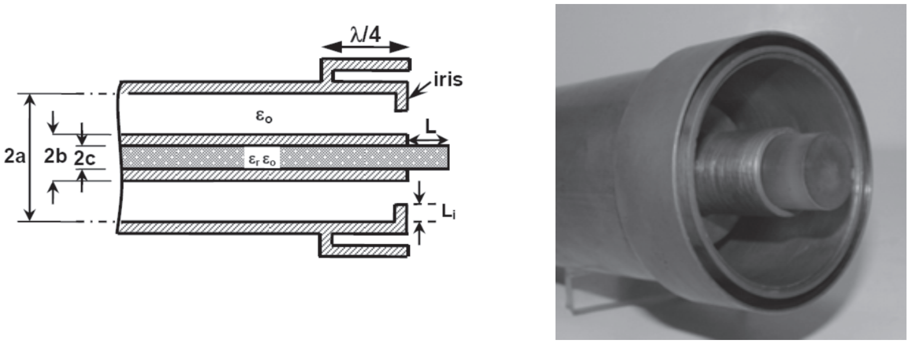

(a) (b)

Figure 3.17 (a) Geometry of a dual-band coaxial feed, and (b) the fabricated unit.

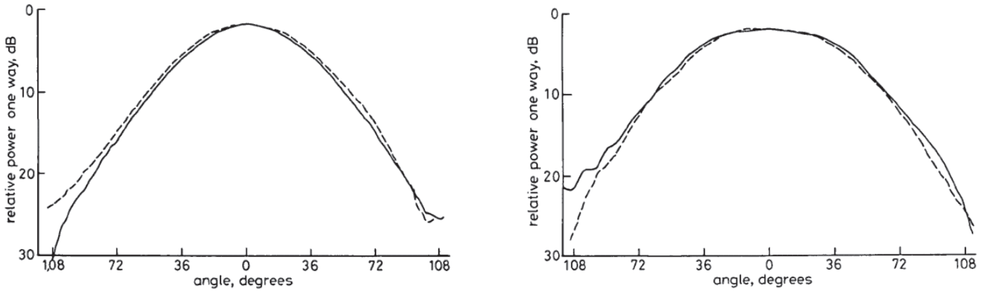

(a) (b)

Figure 3.18 Radiation patterns of the coaxial dual-band feed of Figure 3.17 at the frequency of (a) 4 GHz, and (b) 6.175 GHz. — E-plane; ----- H-plane. (©1984 IEE [17].)

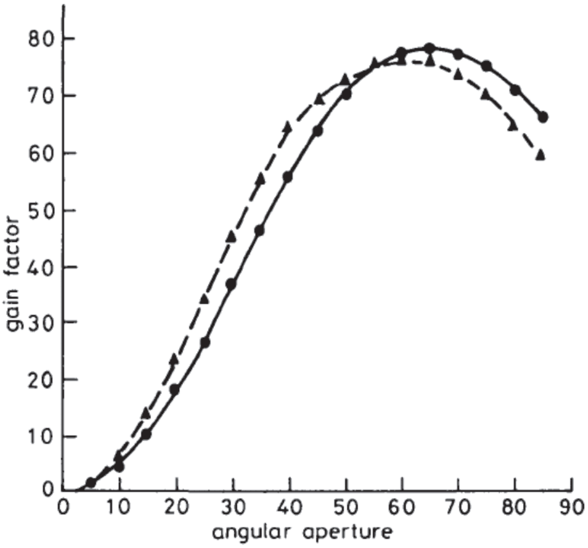

Figure 3.19 Gain factors of the dual-band coaxial feed of Figure 3.17. ▲ 6 GHz, ● 4 GHz. (©1984 IEE [17].)

impedance match. The latter has been simplified in the shown coaxial design, where the input ports for the two bands are geometrically separated.

3.3.3 Small Wide Angle Feeds

Designing feeds for deep reflectors, especially when *F*/*D* is at or near 0.25, corresponding to a reflector half-subtended angle of 90°, is challenging. Pattern symmetry, low cross polarization, and the phase center uniqueness must be maintained over the entire range of this large aperture angle. In addition, the edge distance from the focus is twice the focal length and gives 6 dB spherical wave attenuation. This results in poor aperture illuminations and low gain factors. The latter can be remedied to some degree by placing a shallow axial null in the radiation patterns of the feed. While this is feasible by creating an array factor between the waveguide aperture radiation and the choke-radiated field, it often creates a phase center problem and an increased cross polarization [14]. Thus, the design must be handled with care. In using circular waveguide as a feed, the easiest way of placing an axial null in the radiation patterns is to increase the choke width to form a coaxial cavity around the waveguide. Then, by a dimensional optimization, one can cause a phase reversal between the waveguide and cavity radiations while maintaining satisfactory phase center location and minimizing the cross polarization. A representative design is shown in Figure 3.20, with its radiation patterns and cross polarization in Figure 3.21. There is an axial null of 6 dB and good pattern symmetry until beyond 90° aperture angle, over which the cross polarization is maintained below –30 dB. The back lobe level can similarly be lowered by an incorporation of a quarter wavelength choke on the outer wall, as shown in Figure 3.22.

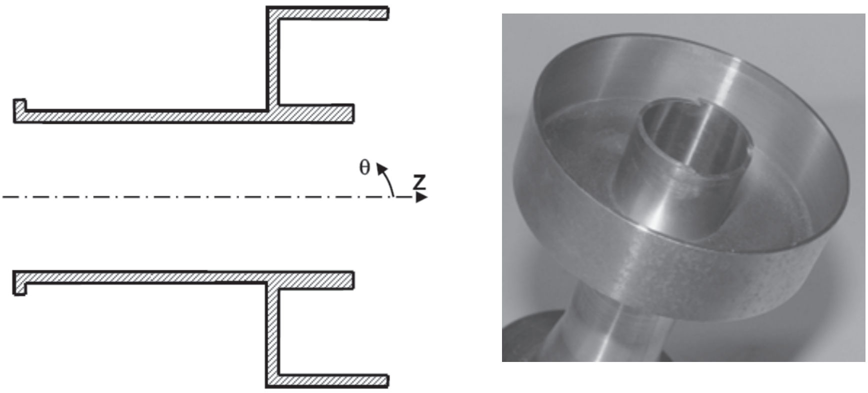

(a)

(b)

Figure 3.20 (a) Geometry of a cavity loaded circular waveguide for use in a deep reflector, having a large subtended angle, TE_{11} excitation, and (b) the fabricated unit.

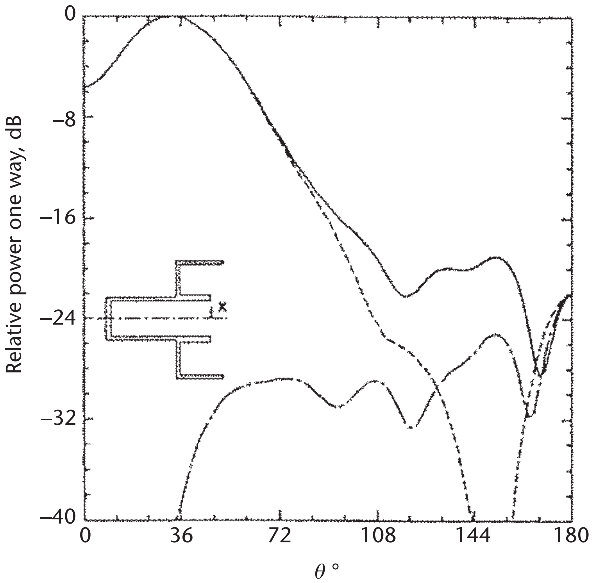

Figure 3.21 Radiation patterns of the feed of Figure 3.20. — E-plane, ----- H-plane, – – – - cross polarization. (©1994 IEE [14].)

Table 3.2 Performance Parameters of the Feed in Figure 3.20

	$0.95\ f_0$	$0.975\ f_0$	f_0	$1.025\ f_0$	$1.05\ f_0$
ψ_0	68	66	64	62	60
η_g	82.23	81.52	81.47	81.57	80.77
η_s	89.13	88.99	88.89	88.90	88.49
η_i	92.28	91.61	91.68	91.77	91.29
χ_p	–20.41	–30.87	–28.77	–25.93	–23.94
d_c			–0.04		

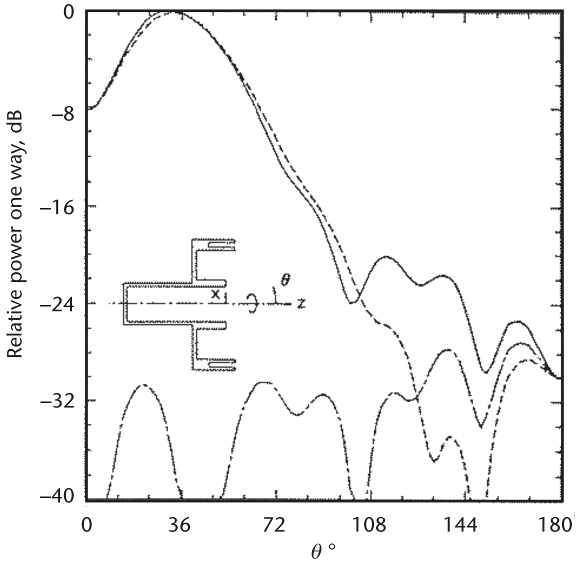

Figure 3.22 Radiation patterns of the feed in Figure 3.20 with a quarter wavelength choke on its outer wall. — E-plane, ----- H-plane, – – – - cross polarization. (©1994 IEE [14].)

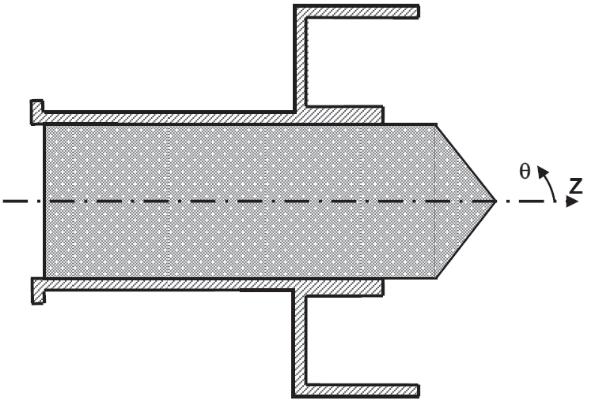

Figure 3.23 Geometry of a dielectric loaded cavity back feed, TE_{11} excitation.

To further broaden the radiation patterns, the waveguide diameter needs to be reduced, which can be done by a dielectric loading, as shown in Figure 3.23. The radiation patterns of this feed, without and with an outside wall choke, are shown in Figure 3.24. The gain factor performance of these feeds is compared in Figure 3.25, where Feeds 2 and 3 are the designs in Figures 3.20 and 3.23. As observed, the aperture angle of Feed 3, at which the peak gain factor occurs, increases to 74° from 64°, corresponding to that of Feed 2.

It should be noted that for these feeds, as shown in Figure 3.25, the gain factors do not drop rapidly beyond the aperture angle for the peak gain factor, which is due to the small size of these feeds. Since the antenna noise temperature decreases by increasing the reflector aperture angle, the performance of reflectors with these feeds will in fact improve by selecting reflectors with larger aperture angles, especially for the dielectric loaded feed of Figure 3.23.

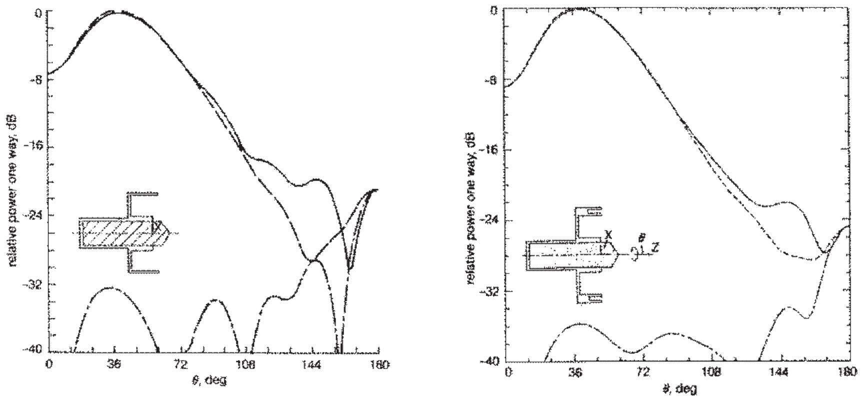

(a) (b)

Figure 3.24 Radiation patterns of the dielectric loaded cavity back feed of Figure 3.23 (a) Without a choke, and (b) with a choke. — E-plane, ----- H-plane, – – – - cross polarization. (©1994 IEE [14].)

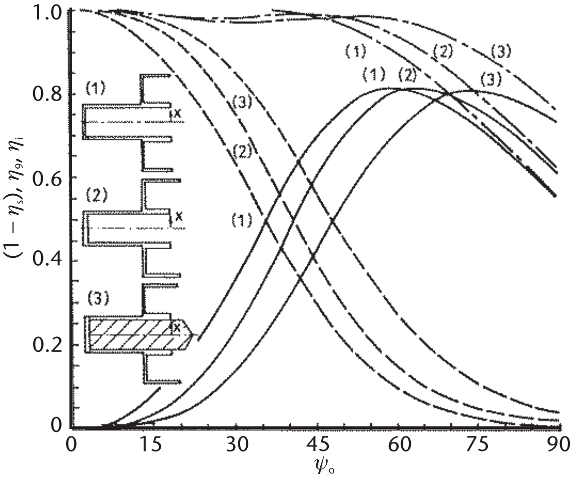

Figure 3.25 The gain factors, spill-over losses, and illumination efficiencies of the deep reflector feeds, (1) feed with flush choke, (2) feed in Figure 3.20, and (3) feed in Figure 3.23. — η_g, – – – $(1 - \eta_s)$, – – – - η_i. (©1994 IEE [14].)

3.3.4 Small Backfire Feeds

A second class of feeds that are especially useful with small reflector antennas are back radiating feeds that can be mounted directly on the reflector from a hole on its apex. Consequently, they do not need special strut supports, which eliminate their aperture blockage. The early design of such feeds were introduced by Silver [1], known as dipole-disk antennas. The disk was used to eliminate the back radiation. An improvement on this feed was made by feeding the dipole by a reduced height waveguide and replacing the disk by a cylindrical cavity, known as the Calvin feed [3]. For circular polarization the dipole was replaced by two orthogonal dipoles [18, 19] and modest performance was obtained. Later, numerical computations were used to optimize the dipole-disk performance. Kildal [20] introduced a beamforming ring, in front of the dipole-disk assembly, to equalize its principal plane patterns. Shafai [21] equalized the principal plane patterns by replacing the disk by a conical reflector. The cone parameters were then used to shape the radiation patterns, for improving the reflector gain factor, and reduction of the cross polarization. The back lobe level was reduced by incorporating a choke on the cone wall. The geometry of the dipole feed and its radiation patterns are shown in Figure 3.26. Other backward-radiating feeds have also been investigated, which include the cup feeds [22, 23], hat feed [24], and splash plate feeds [25, 26]. The circularly polarized versions are discussed later in Chapter 7. As a representative example of these feeds, in the following section a modified version of the cup feed is presented and discussed. It was designed by Kishk and Shafai [27] for low sidelobe applications with small reflector antennas in the frequency range of 5.725–5.875 GHz.

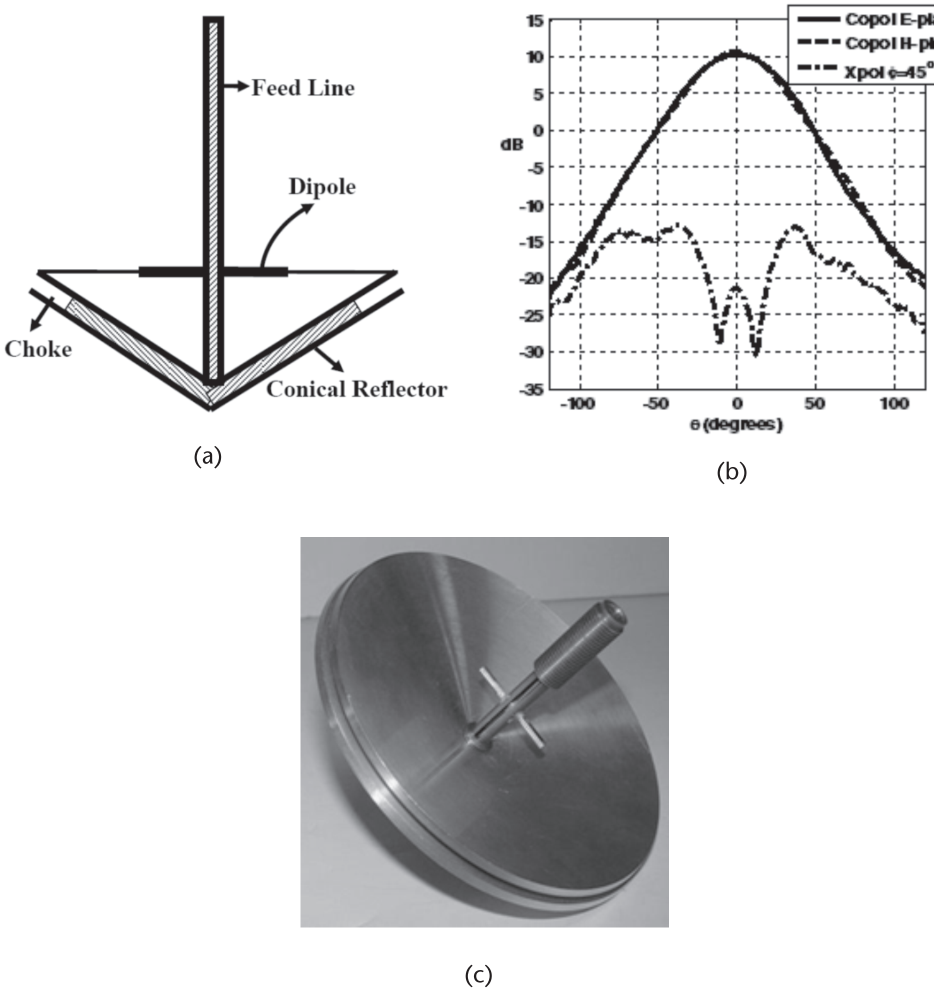

(a)

(b)

(c)

Figure 3.26 (a) Geometry of the dipole feed with a conical reflector, (b) the fabricated unit, (c) its measured principal radiation patterns and the cross polarization at $\phi = 45°$ plane at $f = 4.14$ GHz.

3.3.4.1 Modified Cup Feed

The photographs of the feed itself and assembled reflector and the feed are shown in Figure 3.27. The feed is assembled on a 45 cm reflector by its feeding circular waveguide, without additional struts, thus reducing the blockage. In addition, to obtain low sidelobe levels, the waveguide is loaded with a dielectric material of $\varepsilon_r = 2.5$ to reduce its subreflector size. As a result, the subreflector is accommodated in front of the waveguide aperture, which is tapered, as shown in Figure 3.27(a). To mechanically support the subreflector, the dielectric material, which had a cylindrical shape, is extended by about one wavelength beyond the waveguide aperture. The subreflector shape itself has a small inner conducting cone to improve the return loss of the feed. The loading dielectric is also tapered inside the waveguide to improve the return loss when excited by the TE_{11} mode.

The primary radiation patterns of the feed, computed by the method of moment surface integral equations [14], are shown in Figure 3.28. The small undulations of the

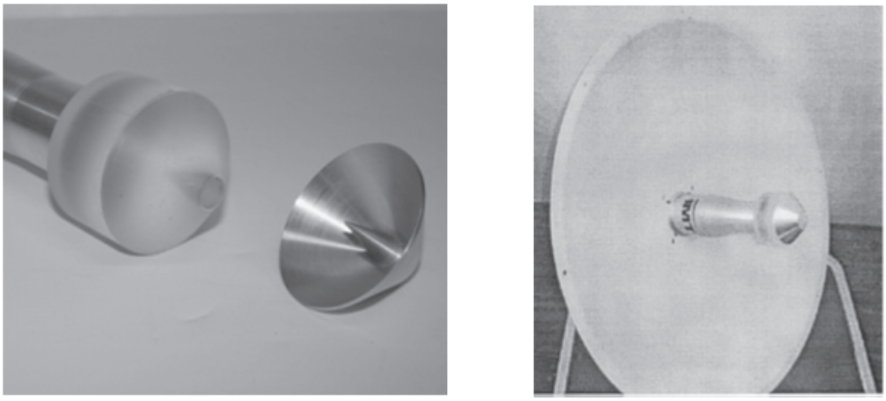

(a) (b)

Figure 3.27 (a) Photo of the modified cup feed with the supporting subreflector, and (b) photo of the assembled reflector and the feed. (©2003 IEEE [27].)

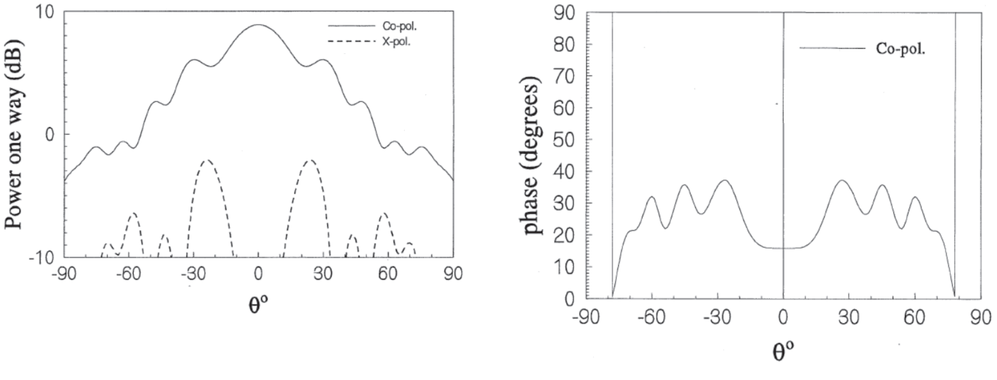

(a) (b)

Figure 3.28 Computed far-field radiation patterns of the feed shown in Figure 3.27(a). (a) Amplitude, and (b) phase patterns. (©2003 IEEE [27].)

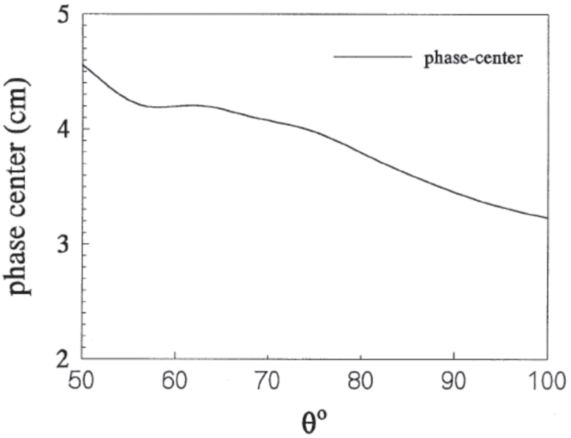

Figure 3.29 Phase center location of the feed shown in Figure 3.27(a) versus reflector half-subtended angles. (©2003 IEEE [27].)

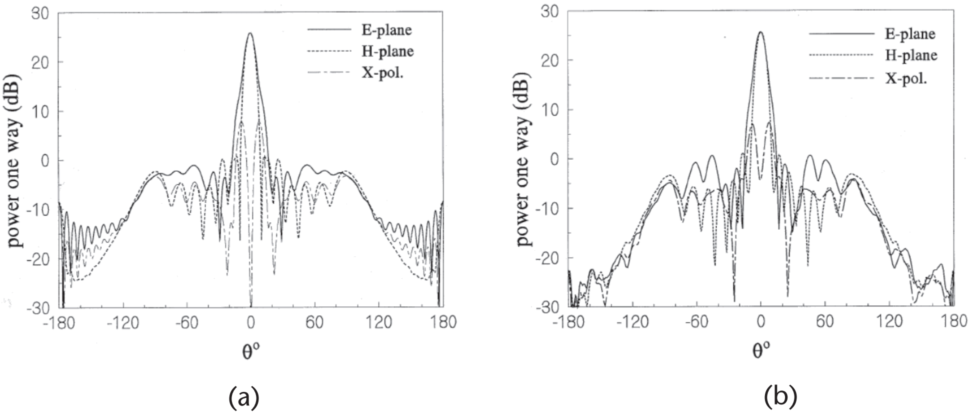

(a) (b)

Figure 3.30 (a) Computed, and (b) measured secondary radiation patterns of the feed on a 45 cm reflector, with $F/D = 0.375$ at $f = 5.75$ GHz. (©2003 IEEE [27].)

amplitude pattern of the feed are due to the waveguide tapering. Also, the observed phase variation within the reflector angular range is about 23°, which results in a gain loss of 0.1 dB. The optimum phase center location of the feed is plotted in Figure 3.29, against the reflector half-subtended angle. It is evident that the phase center location of the feed is nearly invariant, for the half-subtended angle range of 60–80°.

The computed and measured radiation patterns of the feed-reflector assembly, on a 45 cm reflector with an $F/D = 0.375$, are illustrated in Figure 3.30, at the operating frequency of 5.75 GHz. The measurement was done in the Compact Antenna Test Range at the University of Manitoba. Good agreement between the results is observed. However, nonzero axial cross polarization seen in the measurement, Figure 3.30(b), is due to the cross polarization of the compact range and not the feed-reflector assembly. Also, the near-in sidelobe levels are less than –20 dB, while the far-out sidelobes diminish monotonically.

Summarizing the results, the optimized rear-radiating feeds, using dipoles and cup feeds, are good alternatives to forward radiating waveguide feeds. Although their performances do not match those of the latter, their low profile and simpler assembly on the reflector compensate for their deficiencies. Consequently, they are preferred in small reflectors.

3.4 Microstrip Feeds

Microstrip antennas are low profile, lightweight, and easy to fabricate. They also have potential to be low cost. However, they have not found widespread applications as reflector feeds, because of difficulty in shaping their radiation patterns, without altering their low profile, or using arrays. With a single feed, they also excite higher order modes that contribute to cross polarization. In spite of these limitations, simple primary feeds, using microstrip patch antennas, have been designed and studied [28], and good performance obtained. On the other hand, they can also offer advantages. Microstrip antennas can be designed to operate wideband, multiband, and form small arrays for shaping the beam or generating multiple beams. What is important, therefore, is to understand their radiation properties and find simple methods to achieve good feed performance. Parameters that are available to the designer are the substrate permittivity and the ground plane size and shape, and their modifications have been used, recently, to develop efficient designs [29–31].

3.4.1 Single Patch Antenna as the Reflector Feed

As a small feed, a single circular patch antenna operating at its dominant TM_{11} mode is a natural choice. However, other patch shapes can equally be used. Normally, the operating frequency is determined by the patch size and substrate permittivity, but the radiation pattern shape is controlled by the ground plane. With a common substrate permittivity such as $\varepsilon_r = 2.5$, large ground planes give asymmetric principal plane patterns, and small ones cause large back radiations. Somewhere in between, a suitable ground plane size can be determined, satisfactory for both. However, even with large ground planes, reducing the substrate permittivity gradually equalizes the principal plane patterns [14, 29, 32, 33]. Thus, for a given substrate permittivity there can be an optimum ground plane size for symmetric radiation patterns and low back lobe level. Symmetric radiation patterns can also be obtained by shaping the ground plane, but it will affect its low-profile characteristic [31–33].

3.4.1.1 Pattern Optimization by Substrate Material and Ground Plane Size

The geometry of a typical circular patch antenna is shown in Figure 3.31, where R is the radius of the patch and R_{Gr} is the radius of the ground plane. A circular microstrip patch usually operates in one of the TM_{mn} modes, and the TM_{11} mode is the most practical one. This mode radiates in the broadside direction with a good gain and small patch size. At this mode, the antenna generates the field patterns that

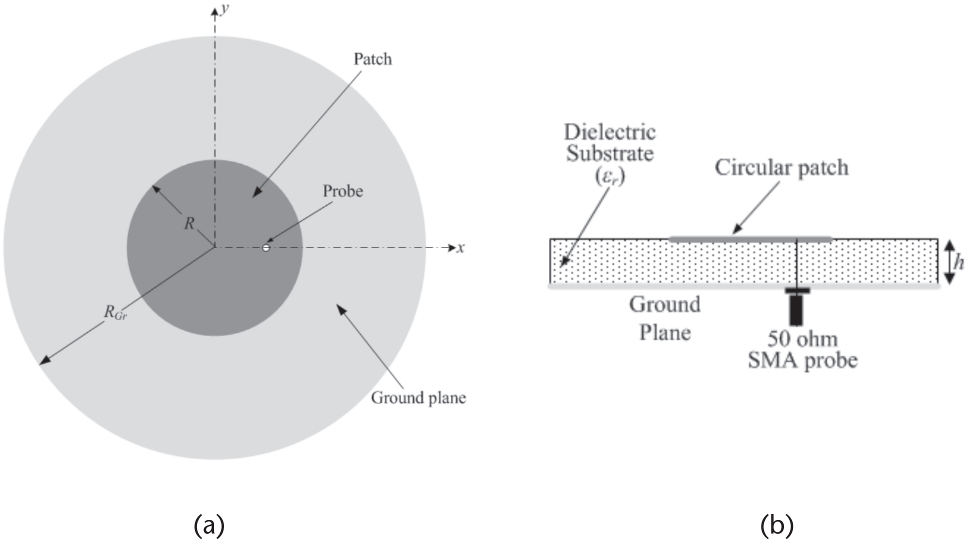

Figure 3.31 Geometry of the circular patch antenna. (a) Top view, and (b) side view.

are considerably different in the principal E- and H-planes. For $\varepsilon_r = 1$, pattern equalization is difficult to achieve and is omitted here. For $\varepsilon_r = 1.5$, when $R_{Gr} \approx 0.7\lambda_o$, circular symmetric patterns are achieved with reasonably low cross polarization. The phase variation between two principal plane patterns is also small for this ground plane size, as can be noticed in Figure 3.32. For larger R_{Gr}, $|E_\theta| > |E_\phi|$, and for smaller R_{Gr}, $|E_\theta| < |E_\phi|$.

In the case of $\varepsilon_r = 2.5$, one can notice in Figure 3.33 that when $R_{Gr} = 0.3\lambda_o$, the phase variation is minimum with unequal $|E_\theta|$ and $|E_\phi|$ beyond $\theta = \pm 30°$. $R_{Gr} = 0.35\lambda_o$ provides almost equal principal plane patterns with reasonably small phase variations up to 60°. For larger ε_r, smaller ground plane size is required to obtain pattern symmetry. However, the back radiation increases, as can be noticed in Figure 3.34, which can be minimized by using a choke on the ground plane. This suggests that for a given substrate permittivity, a particular ground plane size gives nearly circular symmetric patterns with low cross polarization and phase variations. Figure 3.35 shows the best ground plane size to obtain symmetric feed patterns, for up to at least 70°, from a circular patch antenna operating at the TM_{11} mode and different ε_r.

The circular patch antenna on a substrate having $\varepsilon_r = 2.5$ and $h = 1.59$ mm with the optimized ground plane size ($R_{Gr} = 0.35\lambda_o$) is used as the feed to calculate spillover, illumination efficiencies, and the overall gain factor, for different F/D ratios of the reflector antenna, and tabulated in Table 3.3. The gain factor increases as F/D increases, reaches its peak when $F/D = 0.375$, and then decreases. The variations in gain factor with aperture angle for different ε_r are shown in Figure 3.36(a). For $\varepsilon_r = 2.5$, the peak gain factor is achieved at an aperture angle of 67.5°, and for $\varepsilon_r = 10$, it peaks at 80°, which is suitable for deep reflectors. The variation of the phase center with aperture angle is plotted in Figure 3.36(b) for different ε_r. The phase center is located just above the patch for all cases.

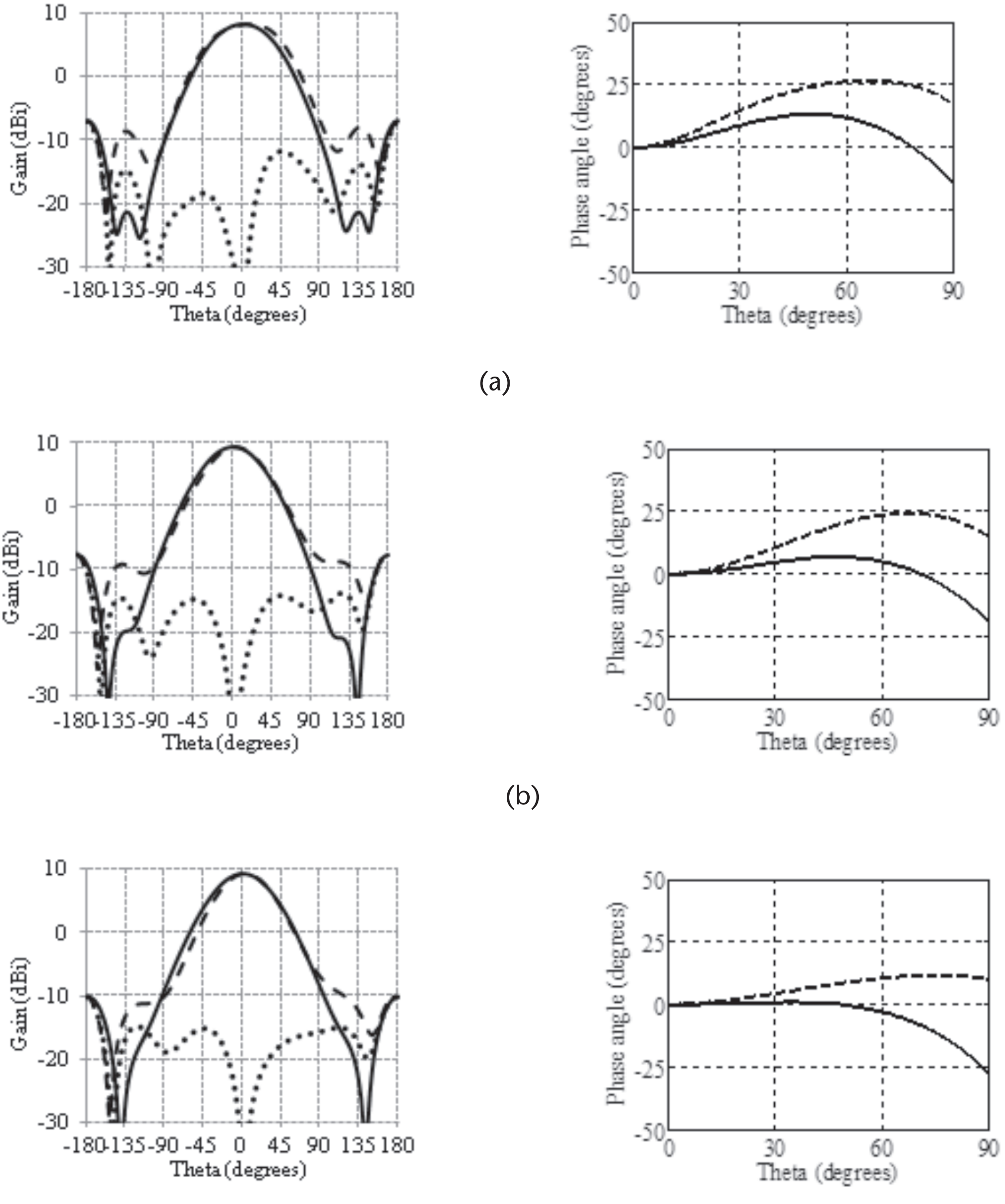

(a)

(b)

(c)

Figure 3.32 Co- and cross-polarization patterns and phase distributions at the TM_{11} mode of a circular patch antenna for different ground plane sizes with substrate parameters: $\varepsilon_r = 1.5$ and $h = 1.59$ mm. (a) $R_{Gr} = 0.8\lambda_o$, (b) $R_{Gr} = 0.7\lambda_o$, and (c) $R_{Gr} = 0.6\lambda_o$. — E_ϕ ($\phi = 90°$), — — — E_θ ($\phi = 0°$), ······ cross-pol ($\phi = 45°$).

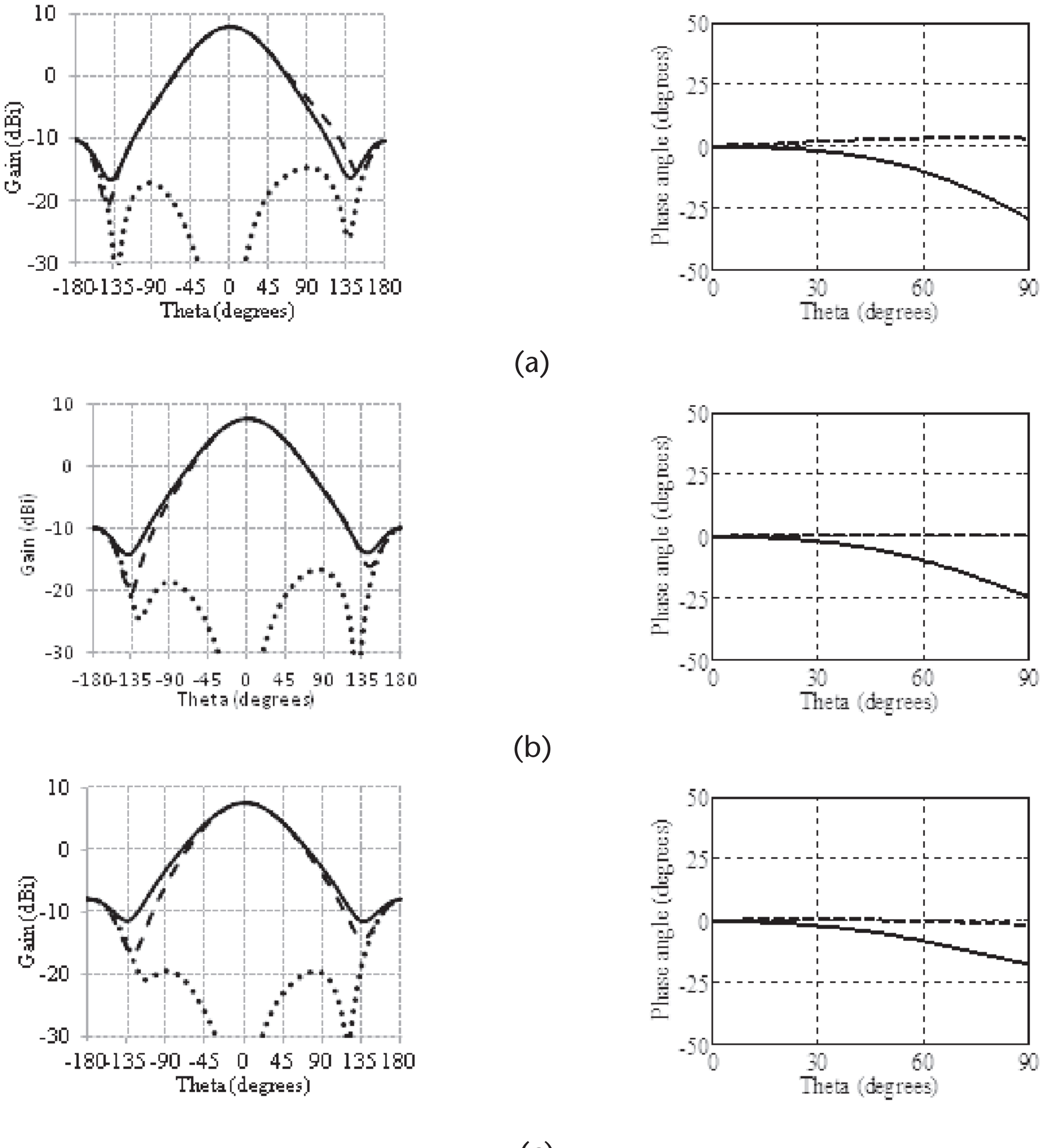

Figure 3.33 Co- and cross-polarization patterns and phase distributions at the TM_{11} mode of a circular patch antenna for different ground plane sizes with substrate parameters: $\varepsilon_r = 2.5$ and $h = 1.59$ mm. (a) $R_{Gr} = 0.4\lambda_o$, (b) $R_{Gr} = 0.35\lambda_o$, and (c) $R_{Gr} = 0.3\lambda_o$. — E_ϕ ($\phi = 90°$), — — — E_θ ($\phi = 0°$), ······ cross-pol ($\phi = 45°$).

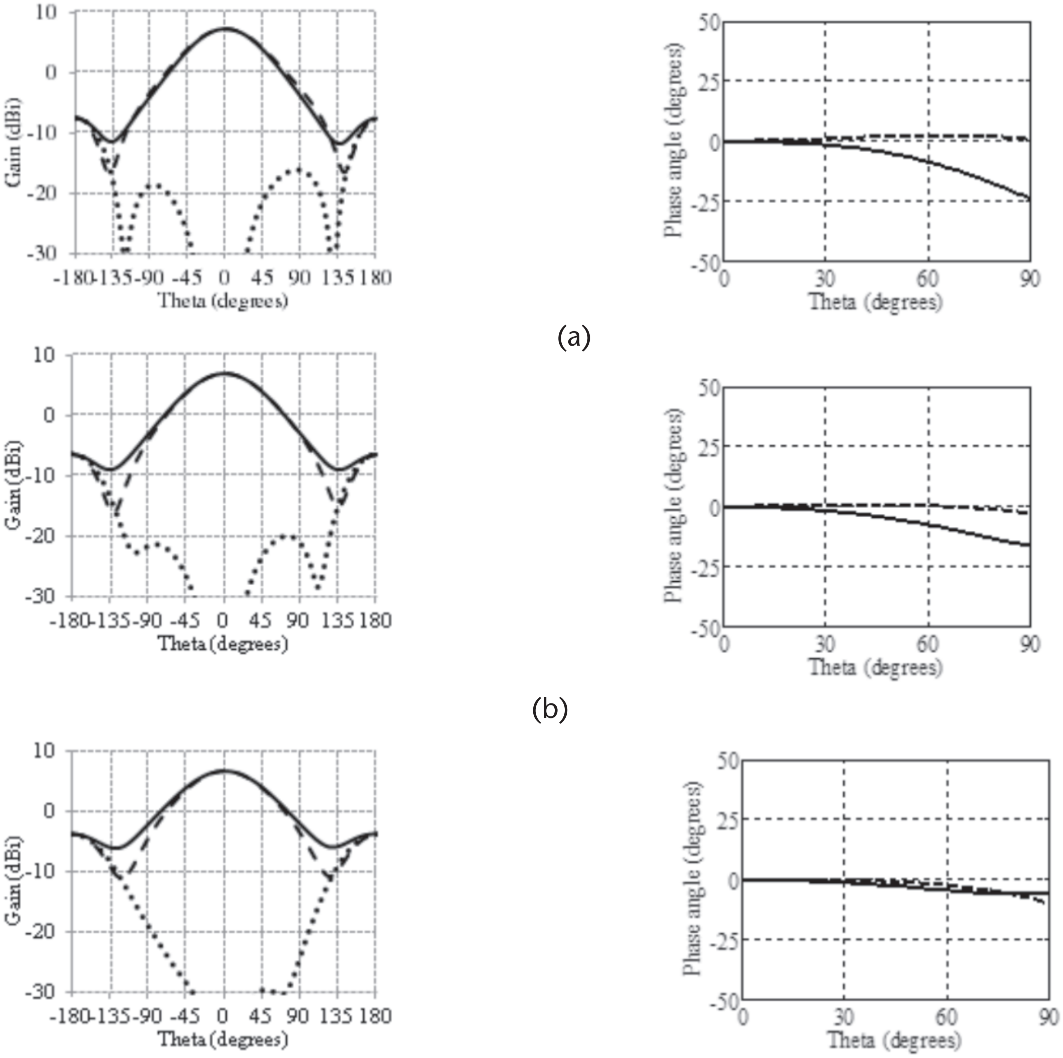

(a)

(b)

(c)

Figure 3.34 Co- and cross-polarization patterns and phase distributions at the TM_{11} mode of a circular patch antenna for different ground plane sizes with substrate parameters: $\varepsilon_r = 4$ and $h = 1.59$ mm. (a) $R_{Gr} = 0.35\lambda_o$, (b) $R_{Gr} = 0.3\lambda_o$, and (c) $R_{Gr} = 0.25\lambda_o$. — E_ϕ ($\phi = 90°$), — — — E_θ ($\phi = 0°$), ⋯⋯ cross-pol ($\phi = 45°$).

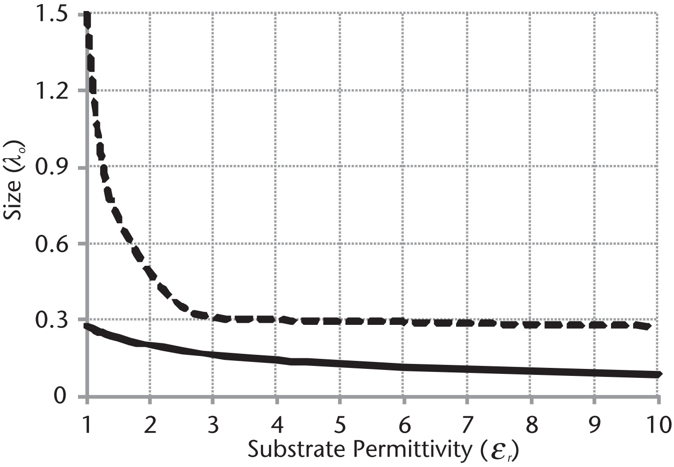

Figure 3.35 Patch size and optimized ground plane size for obtaining circular symmetric patterns with low cross polarization from a circular patch antenna operating at the TM$_{11}$ mode for different substrate permittivities. — R, — — — R_{Gr}.

Table 3.3 Variations in Reflector Spill-Over, Illumination, Cross-Polarization and Phase Efficiencies, and Overall Gain Factor for Different F/D for the Circular Patch Antenna at the TM$_{11}$ Mode. The Ground Plane Size is $R_{Gr} = 0.35\lambda_o$. The Substrate Parameters are $\varepsilon_r = 2.5$, $h = 1.59$ mm.

F/D	*Spill-over efficiency*	*Illumination efficiency*	*Cross-pol efficiency*	*Phase efficiency*	*Gain factor*
0.25	0.9345	0.7202	0.9964	0.9883	0.67
0.30	0.8929	0.8021	0.9972	0.9925	0.71
0.375	0.8072	0.8881	0.9982	0.9963	0.72
0.45	0.7205	0.9321	0.9987	0.9979	0.67
0.50	0.6613	0.9509	0.9990	0.9985	0.63

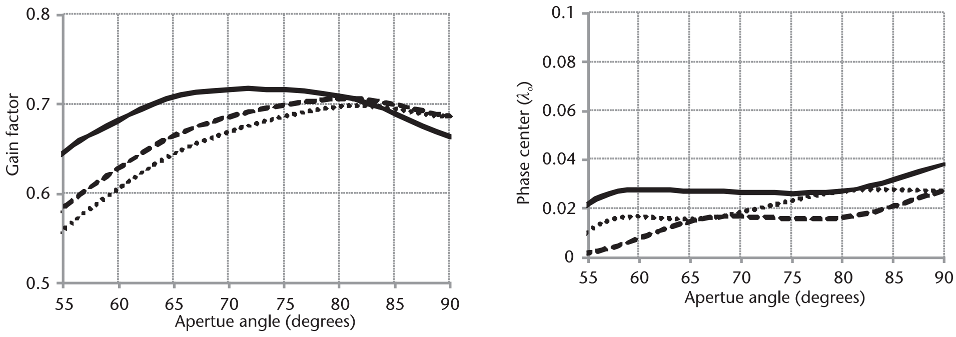

(a) (b)

Figure 3.36 Variations in (a) the reflector gain factor and (b) the phase center location of the circular patch antenna operating at the TM$_{11}$ mode for different substrate permittivities with optimized ground plane size to achieve circular symmetric patterns, low cross polarization, and small phase variations in principal planes. — $\varepsilon_r = 2.5$, $R_{Gr} = 0.35\lambda_o$, — — — $\varepsilon_r = 6.0$, $R_{Gr} = 0.3\lambda_o$, ⋯⋯ $\varepsilon_r = 10$, $R_{Gr} = 0.275\lambda_o$.

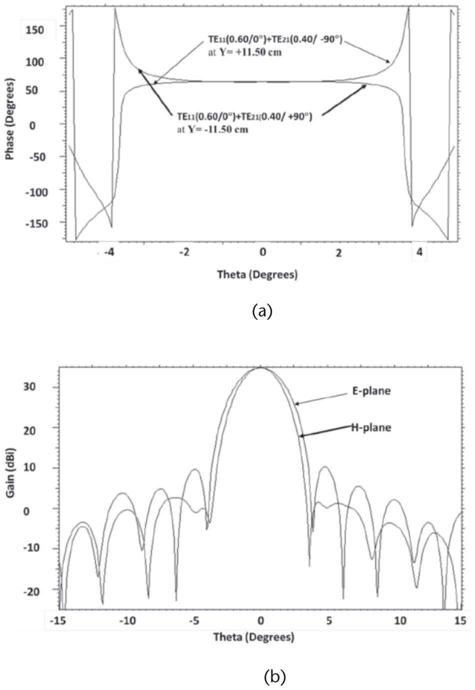

(a)

(b)

Figure 3.37 (a) Geometry of the circular patch antenna with shaped ground plane, and (b) its co-polarization patterns in principal planes ($\phi = 0°$ and $\phi = 90°$ planes) and axial ratio plot. ⚹ E-plane, ···⊙···H-plane, ……AR.

3.4.1.2 Pattern Control by Ground Plane Shape

The change in ground plane shape also provides symmetric radiation patterns and reduces the back radiation [31]. A simple example is a circular patch antenna with the rim around the ground plane edge, which creates a cavity structure, as shown in Figure 3.37(a). The rim around the ground plane limits the amount of radiation to the sides and back. Here, the rim has a height $r = 0.4\lambda_o$ and wall thickness $d = 0.1\lambda_o$. The radiation pattern of this structure is shown in Figure 3.37(b), which shows excellent pattern symmetry, over the entire upper hemisphere. In lieu of the cross polarization, the axial ratio for circular polarization is provided, which over the same range is below 2 dB, indicating that the feed can also be used for circular polarization. For further reduction of back radiation, a quarter wavelength choke can be employed at the rim wall. With a single choke, the back radiation can be lowered by as much as 10 dB, as shown in Figure 3.8.

3.4.1.3 Bandwidth Control of Microstrip Feeds

A single patch antenna has only a few percent bandwidth, which is useful as feeds for narrowband system. If larger bandwidths are required, coupled patches, or patch-slot combinations, may be used. If the resonant frequencies of two coupled patches

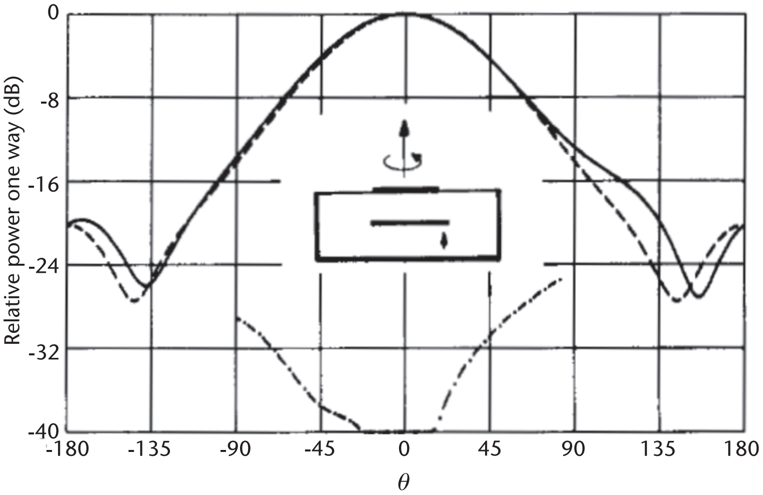

Figure 3.38 Geometry of the two-layer stacked circular patch antenna with finite ground plane and surrounding metallic collar, and its co-polarization in principal planes ($\phi = 0°$ and $\phi = 90°$ planes) and cross polarization patterns in the $\phi = 45°$ plane. — E-plane, ----- H-plane, – – – - cross polarization. (©1989 IEEE [29].) Diameters: 0.34λ (bottom), 0.32λ (top), separation = 0.05λ. Ground plane radius: 0.4λ, $\varepsilon_r = 2.32$, thickness = 0.1λ.

are nearly the same, a wide impedance bandwidth can be achieved by adjusting their coupling. The coupled patches can be considered as a single wideband microstrip antenna, which can be used alone or in an array. However, to be used as a reflector feed, symmetric patterns with low cross polarization must be achieved, which can be obtained by choosing an appropriate substrate permittivity and ground plane size, as discussed in previous sections.

An example is shown in Figure 3.38. The antenna has low cross polarization below –25 dB. An optimized feed with stacked circular patch antenna on a finite ground with a choke was fabricated and measured by Kishk and Shafai [29]. The calculated results with the feed geometry are shown in Figure 3.39(a), and the measured patterns are shown in Figure 3.39(b). It provides equal E-plane and H-plane co-polar patterns and low cross polarization in the $\phi = 45°$ plane.

3.4.2 Planar Antenna Array Feeds

Planar antennas simplify the array formation, which may be required for radiation pattern shaping or for improving the reflector performance. The simplification may be in the feed structure at high frequencies, in geometrical simplicity, in beamforming networks, or reduction in size and weight [34–37]. The advantages, however, must be significant to necessitate their use. The reason is that the material properties for fabricating planar antennas are seldom repeatable, and fabrication tolerances, especially using the conventional etching or metallization, are normally poor. As a result, the performance of planar arrays seldom matches those of conventional feeds. Nevertheless, applications may arise that favor their use [38–42]. Here an example is provided, at millimeter wave frequencies, where waveguide or microstrip patch feeds are impractical.

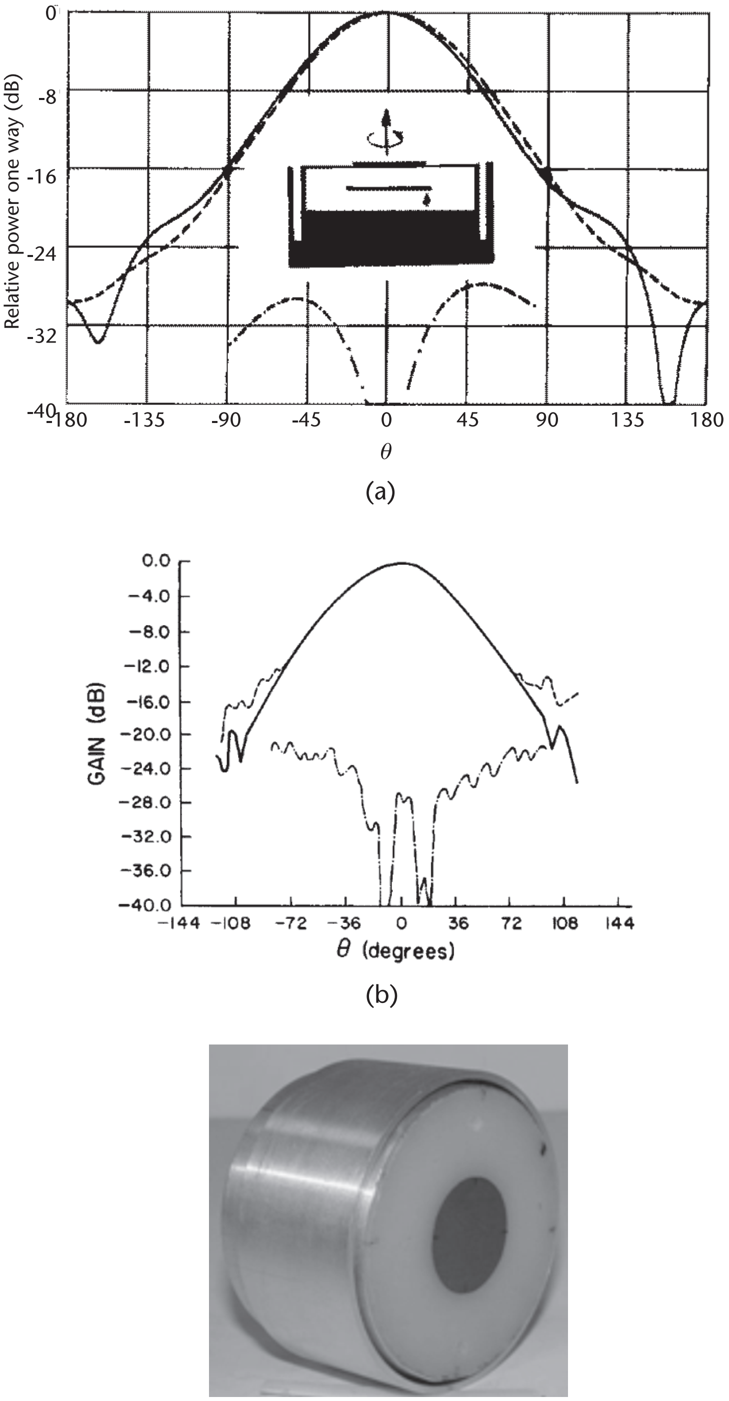

(a)

(b)

(c)

Figure 3.39 (a) Simulated and (b) measured co–polarization patterns in principal planes ($\phi = 0°$ and $\phi = 90°$ planes) and cross polarization pattern in the $\phi = 45°$ plane of the stacked circular patch antenna with a $\lambda/4$ choke, and (c) the fabricated stacked circular patch antenna with choke. (©1989 IEEE [29].) — E-plane, ----- H-plane, – – – - cross polarization. Diameters: 0.34λ (bottom), 0.32λ (top), separation = 0.05λ. Ground plane radius: 0.4λ, $\varepsilon_r = 2.32$, thickness = 0.1λ.

An array feed of printed dipoles consisting of two dipoles integrated on a dielectric membrane and backed by a ground plane was presented in Flilipovic, Ali-Ahmad, and Rebeiz [43]. The design frequency of the feed was 246 GHz. The radiation patterns of the array feed were made circularly symmetric by appropriately choosing the antenna lengths, the antenna spacing, and the ground plane distance from the membrane. Two dipoles were integrated at the center of a coplanar stripline with an impedance of 300Ω. The feed had a 10% bandwidth, with 10 dB beamwidth of 78°, and a directivity of 11.7 dBi. Its measured cross polarization was less than –22 dB at 30–35°. The test dipole array antenna, designed for a wavelength of 119μm to feed a 30λ parabolic reflector, provided a gain of 37 dBi. This corresponds to an overall gain factor of 55%, a significant achievement at this frequency.

3.5 Backfire Printed Dipole Feeds

The planar feeds so far presented were forward-radiating antennas, requiring a supporting arm. In this section, we present the design of a printed dipole feed with a dipole-reflector, to act as a backward-radiating antenna. The antenna design follows those in Zheng et al. and Eldek, Eisherbeni, and Smith [44–46], except that the antenna main beam is directed backward, toward the feed transmission line, for backward radiation. Therefore, it can be mounted on a parabolic reflector, directly from its apex, using a simple support, thereby eliminating the need for strut supports and their blockage. Hence, the overall reflector-feed mounting system is simple and low cost to implement.

The simulation and analysis for the presented feed antennas were performed using a finite element three-dimensional (3-D) full wave simulator. To confirm the simulation results, prototype feeds were fabricated and tested on a parabolic reflector. The available reflector was a deep dish with $F/D = 0.25$, and a small diameter of $D = 45$cm. This feed has a wider H-plane pattern than the E-plane and thus is suitable for reflectors with an elliptic aperture. However, as it will be shown later, it provided a respectable performance even on a symmetric reflector.

3.5.1 Design Approach

The geometry and coordinate system of the proposed feed antenna are shown in Figure 3.40. The antenna is designed for operation at 3 GHz and is printed on a substrate with metallization on both sides. The two arms of the dipole antenna act as a driver element, which is fed from a microstrip line through a two-parallel strip transmission line. The arms of the dipole are located at the end of this transmission line, placed on either face of the substrate in a mirror image configuration, which creates 180° phase difference between the arms, providing the correct feed to the antenna. The length of the printed dipole, that is, the driver length L_{DRI}, which is basically half wavelength, is chosen through numerical simulation. It is found numerically to be about $0.4\lambda_o$, indicating that the substrate effective permittivity is about 1.56. The width of the dipole arm, W_{DRI}, is chosen approximately to be one-tenth of a wavelength based on an iteration process to achieve good radiation patterns

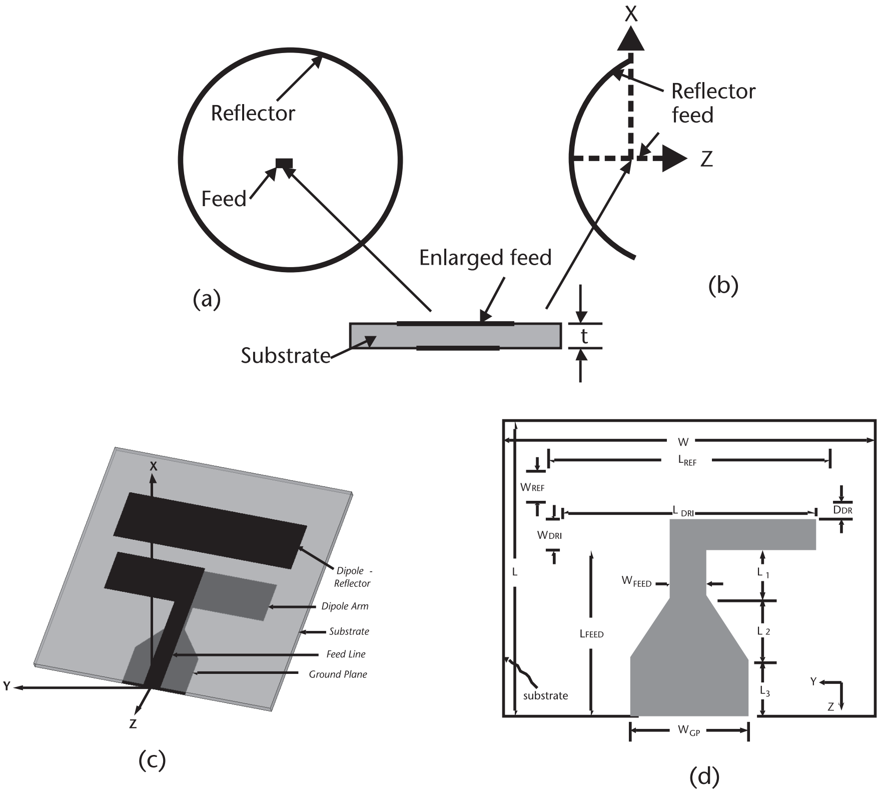
X
Reflector
Reflector
feed
Z
Feed
Enlarged feed
(a)
(b)
Substrate
t
X
Dipole - Reflector
Dipole Arm
Substrate
Feed Line
Ground Plane
Y
Z
(c)
W
L_{REF}
W_{REF}
L_{DRI}
D_{DR}
W_{DRI}
L
W_{FEED}
L_1
L_{FEED}
L_2
L_3
substrate
Y
Z
W_{GP}
(d)

Figure 3.40 Geometry and coordinate system of a microstrip-fed printed dipole antenna (feed) with a reflector. (a) Reflector and feed front view with enlarged feed cross section, (b) reflector and feed side view, (c) feed 3-D view, and (d) feed bottom view.

and impedance bandwidth. The metallization on the bottom plane is a truncated ground plane and behaves like a director element for the antenna.

The dipole-reflector is placed parasitically on the upper face of the substrate opposite to the ground plane. The main function of the dipole-reflector is to direct the radiation backward, toward the microstrip feed line. Its length L_{REF} is set slightly larger than the driver length, L_{DRI}, similar to Yagi antennas. Its width W_{REF} is the same as that of the dipole arm, about one-tenth of the wavelength. The separation between the driver and dipole-reflector is set approximately one-twentieth of the wavelength. This selection is based on the coupling between the dipole-reflector and driver element. The feeding structure consists of a microstrip line on one side of the substrate and truncated ground plane on the other side, both connecting to two arms of a parallel strip transmission line L_1 that feeds the dipole, as shown in Figure 3.40. The length of the transmission line affects the radiation patterns and should be carefully selected, but must be small, as it increases the cross polarization.

3.5.2 Performance Results

The parameters of the feed, for operation at 3 GHz, were selected after several simulations and iterations. It was fabricated in the antenna laboratory of the University

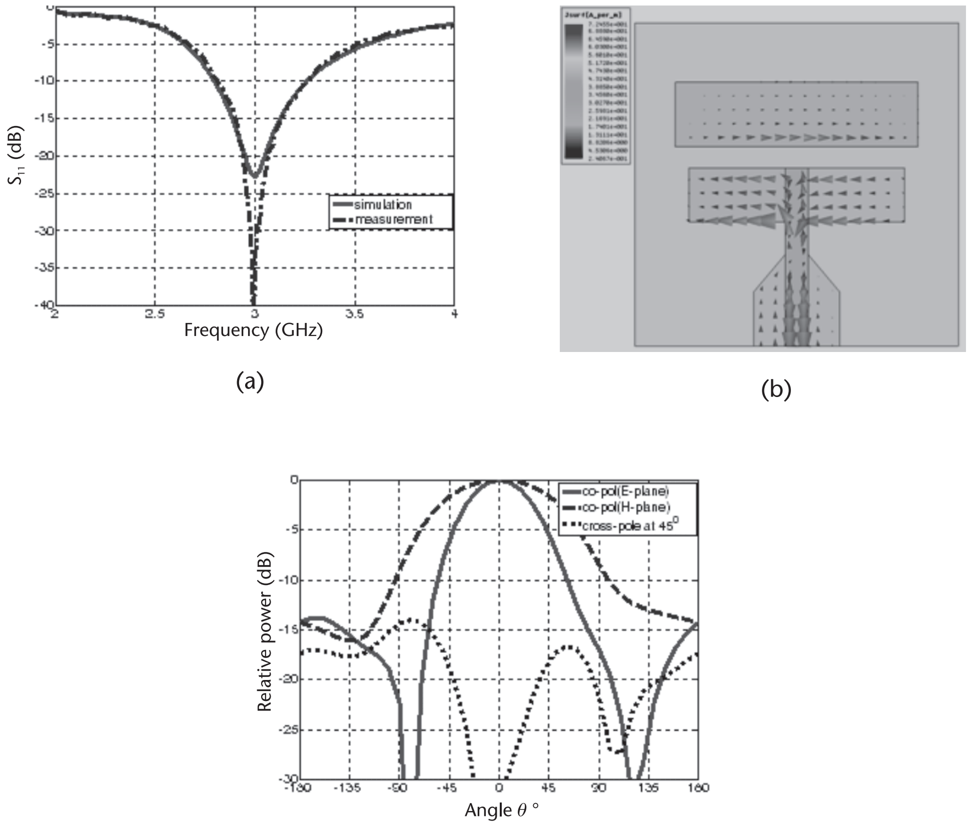

(a)

(b)

(c)

Figure 3.41 Performance of the feed antenna. (a) S_{11}, (b) current distribution, and (c) simulated radiation patterns at 3 GHz. With $L_{REF} = 45$ mm, $W_{REF} = 12$ mm, $D_{DR} = 4$ mm, $W_{DRI} = 10$ mm, $L_{DRI} = 40$ mm, $W_{FEED} = 4.2$ mm, $L_{FEED} = 23$mm, $W_{GP} = 16$ mm, $L_1 = 10$mm, $L_2 = 7$ mm, and $L_3 = 7$ mm.

of Manitoba, on an Arlon Diclad substrate with a thickness of 1.58 mm, dielectric constant of $\varepsilon_r = 2.5$, a loss tangent of $\tan(\delta) = 0.0022$, and an area of 60×60 mm^2.

Figure 3.41(a) shows the simulated and measured S_{11} of the antenna. The simulated –10 dB S_{11} bandwidth is from 2.78–3.28 GHz (16.5%), and the corresponding measured one is from 2.81–3.28 GHz, (15.4%). The surface currents are shown in Figure 3.41(b), and the simulated radiation patterns at the center frequency of 3 GHz are shown in Figure 3.41(c). As expected, the H-plane radiation pattern has a wider beamwidth than the E-plane one. In addition, Figure 3.41(c) shows that the main beam is not fully symmetric about the axis, although the antenna geometry is. This implies that the microstrip feed line also radiates. It should be mentioned that the effect of the supporting rod, which was a semiflexible cable with an SMA connector, was also studied. It had a negligible effect on the feed patterns.

3.5.2.1 Broadening Impedance Bandwidth

An advantage of this antenna is in its printed configuration that allows simple modifications to improve its impedance bandwidth. The preceding antenna had an

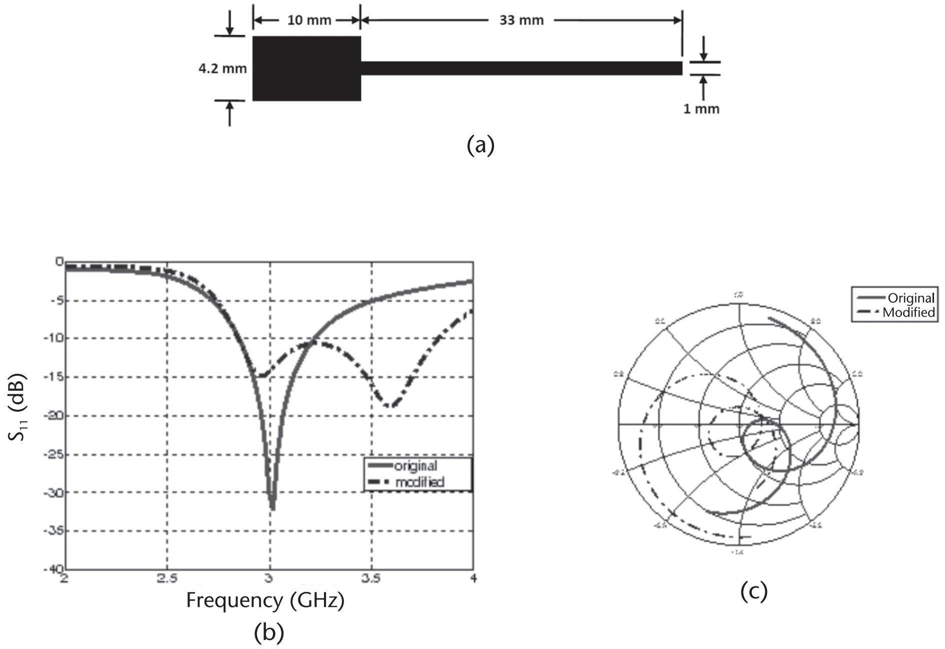

Figure 3.42 Modified microstrip feed line case. (a) Geometry, (b) S_{11}, and (c) Smith Chart.

impedance bandwidth of 16.5%. The feed line geometry was modified as shown in Figure 3.42(a) to improve its impedance bandwidth. The new S_{11} and its Smith Chart plot are shown in Figure 3.42(b) and (c). The impedance bandwidth has now increased to 29%, from 2.85–3.82 GHz. The radiating parts of the antenna have remained the same as in Figure 3.41.

3.5.2.2 Improving Pattern Symmetry

The original antenna was symmetric about the x-z plane but had asymmetric E-plane radiation patterns, which was caused by the feed line radiation. To improve the E-plane pattern symmetry for co-polarization, the lengths of the dipole arms were made unequal, but keeping the total dipole length the same. Using this technique, a good symmetry was found for co-polarization patterns. Figure 3.43(a) shows the left and right dipole arms, with unequal lengths, connected through the microstrip line. The width of the dipole arms is the same as the original case. With the change of the dipole arms lengths, the pattern symmetry about the x-z plane is improved and the back lobe level is reduced, as shown in Figure 3.43(b).

3.5.2.3 Miniaturizing Printed Dipole Feed

The printed dipole antenna of Figure 3.40(d) is miniaturized by introducing a pair of slits in the dipole arms, as shown in Figure 3.44(a) [47]. The width and length of the slits are 1 mm and 8 mm, respectively. The position of the slits in the dipole arms is important because it changes the characteristics of the input impedance and also the radiation patterns of the antenna. When they are located 4 mm and

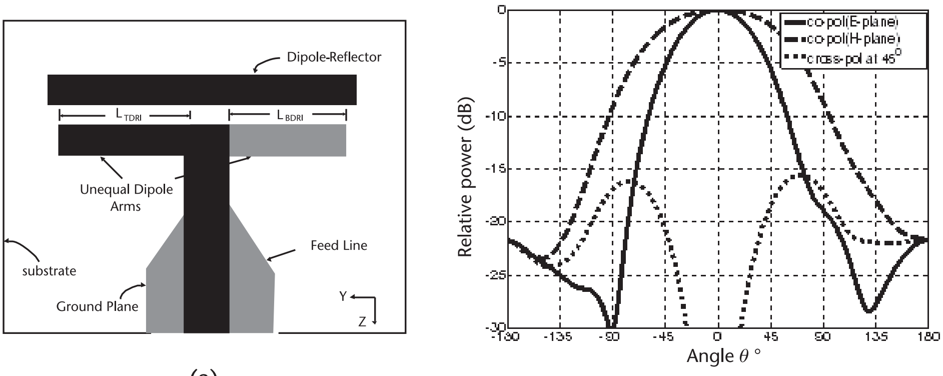

(a)

(b)

Figure 3.43 Feed antenna with unequal dipole arms. Antenna parameters are the same as given in Figure 3.41, except L_{TDRI} = 20.4 mm and L_{BDRI} = 15.4 mm. (a) Geometry, and (b) radiation patterns at 3 GHz.

9 mm from the feed line, the impedance bandwidth remains high and about 29%. The slits in the dipole arms change the current distribution on the surface and force the current to follow a meander route. Thus, the electrical length of the antenna is increased while its physical length is decreased. With two slits the dipole and its reflector lengths become 26 mm and 36 mm, respectively, which is a 20% reduction in the dipole feed size. For further miniaturization, the shape of the dipole arms is changed to H-shape so that current distribution is increased further. More slits can be introduced to further miniaturize; however, it degrades the radiation efficiency of the feed. To further improve the E-plane pattern symmetry, the dipole-reflector was also shaped by extending the end edges toward the dipole arms, as depicted in Figure 3.44(a). The simulated feed patterns of the proposed antenna at 3 GHz are illustrated in Figure 3.44(b).

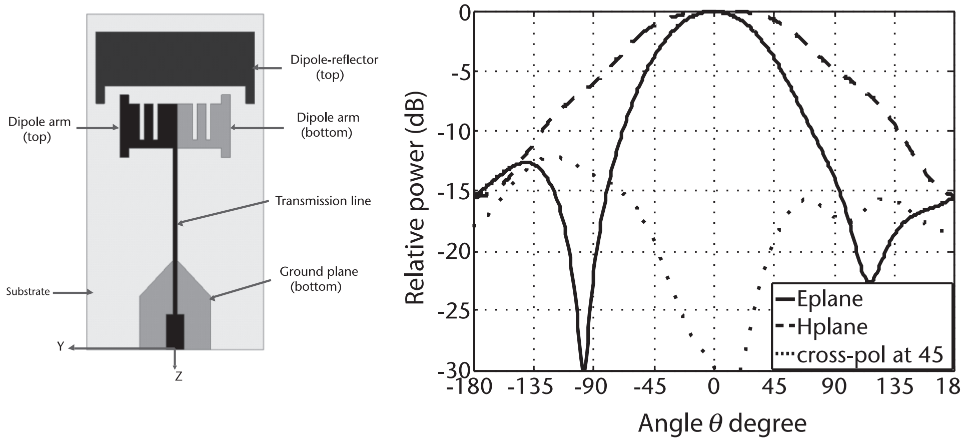

(a)

(b)

Figure 3.44 (a) Miniaturized microstrip-fed printed dipole antenna feed for reflectors, and (b) its radiation patterns at 3 GHz.

3.5.2.4 Printed Dipole Pattern Equalization

The preceding dipole feeds did not address the asymmetric beamwidths of the dipole. In using the feed with reflectors, having circular aperture shapes, it is desirable to have symmetric radiation patterns, with equal beamwidths in its principal planes. This can be achieved using different approaches. Here, it is accomplished by loading the dipole arms by vertical stubs, which is a variation of the previous slotted dipole case. The selected geometry and its performance are shown in Figure 3.45, which resembles a corrugated dipole [48]. Its parameters are optimized to equalize the principal plane beamwidths while keeping the impedance bandwidth above 24%. The stub length is the most important parameter, and its influence on the beamwidth and other feed parameters is shown in Table 3.4. The stub length of 12 mm provides symmetric radiation patterns, with nearly equal –10 dB beamwidths. The lengths and widths of the dipole and its reflector are the same as the previous case of the miniaturized feed. The cross polarization is high, but as in previous cases, it is primarily due to the radiation from the transmission line. As Figure 3.45(d) shows, the E- and H-plane radiation patterns are almost identical. Table 3.5 shows

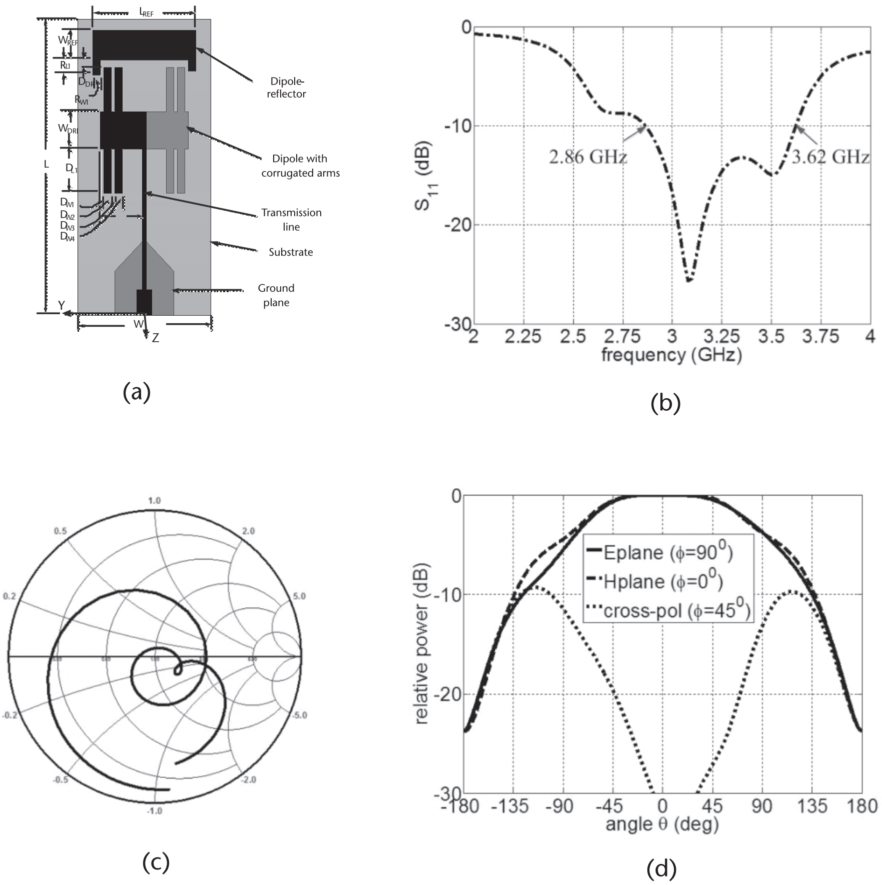

(a) (b)

(c) (d)

Figure 3.45 The geometry and simulated parameters of the corrugated dipole feed, designed for symmetric radiation patterns with equal beamwidths. (a) The geometry, (b)S_{11}, (c) the Smith Chart, and (d) the E- and H-plane radiation patterns at 3 GHz.

Table 3.4 Radiation and Impedance Characteristics of the Corrugated Microstrip Dipole Antenna by Varying Length of the Vertical Stub D_{L1}, Operating at 3 GHz

	$D_{L1} = 10$ mm	$D_{L1} = 11$ mm	$D_{L1} = 12$ mm	$D_{L1} = 13$ mm
–10 dB beamwidth (E-plane)	186°	214°	265°	260°
–10 dB beamwidths (H-plane)	220°	248°	270°	272°
Cross-pol at 45° ($0° < \theta \leq 90°$)	–15.4 dB	–13.2 dB	–12.9 dB	–11.4 dB
Front to back ratio	–15.8 dB	–28.6 dB	–23.8 dB	–24.6 dB
–10 dB bandwidth	22%	20%	24%	24%

Table 3.5 Simulated Performance of the Corrugated Microstrip Dipole Feed for Three Different Frequencies, within its Impedance Bandwidth

Parameter	*2.9 GHz*	*3.0 GHz*	*3.1 GHz*
θ_0	92°	92°	94°
η_s	83.2%	81.6%	80.2%
η_i	85.1%	86.8%	86.8%
η_g	70%	70%	69%
d_c	56 mm	57 mm	59 mm

the performance of this feed within a 0.2 GHz bandwidth, centered at 3 GHz. The simulated efficiencies are almost constant.

3.5.3 Printed Dipole Performance with a Reflector

The performance of the above feeds on a parabolic reflector antenna was investigated following established procedures. The reflector has a diameter of 45 cm with a focal length of 11.25 cm. The feed is connected to a semirigid coaxial cable RG 402 and is mounted centrally on the reflector, using a foam support. The coaxial cable had an insertion loss of 0.2 dB at 3 GHz. The measured principal plane radiation patterns of the reflector with the corrugated printed dipole feed are shown in Figure 3.46(a). At 3 GHz, the measured reflector gain is 21.2 dBi, which includes the feed cable loss. This corresponds to an overall gain factor of 66%, slightly lower than the simulated value of 70%. Considering the simplicity of the feed, the measured gain and its efficiency are respectable. Figure 3.46(b) also shows the measured S_{11} of the feed when mounted on the reflector. Its –10 dB bandwidth is about 29%, which is slightly higher than its bandwidth of 24% without the reflector.

The measured radiation patterns show excellent symmetry of the main beam, which is an indication of the symmetric feed radiation patterns. The sidelobe levels are below –20 dB in both principal planes and slightly lower in the E-plane. Their level can be adjusted, to some degree, by adjusting the feed distance from the reflector. This is due to the fact that in such a small reflector there is a strong interaction between the feed and reflector. This allows the control of both S_{11} and sidelobe level by the feed distance from the reflector. Such an adjustment also affects the reflector gain, and in practice, a compromise has to be made.

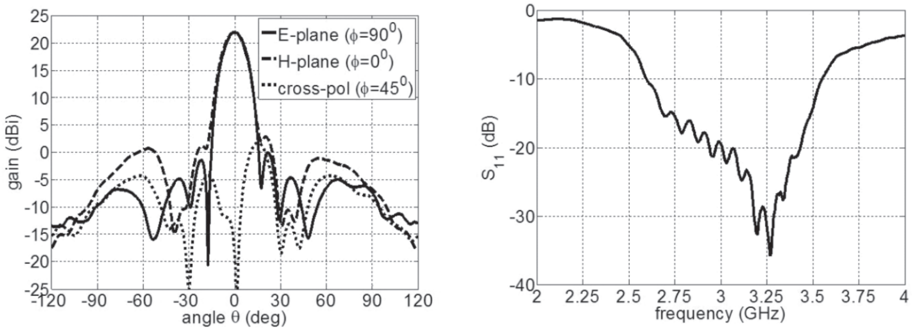

(a) (b)

Figure 3.46 (a) Measured radiation patterns of the reflector-feed antenna at $f = 3.0$ GHz, and (b) measured S_{11} of the corrugated feed when mounted on the reflector. Reflector diameter and focal length are 45 mm, and 11.25 cm. The feed is the corrugated printed dipole of Figure 3.45(a).

3.6 Asymmetric Feeds

The primary feeds discussed in the preceding sections were designed for symmetrically cut parabolic reflector antennas. In most applications, the symmetrical geometry of the reflecting surface naturally enforces the use of feeds with symmetric radiation patterns. However, in asymmetrical focusing surfaces, such as offset parabolic reflectors, this is not necessarily the case. The use of such structures is desirable in most modern applications due to their distinct features over the parent parabolas. For instance, with a proper offset geometry, the blockage due to the feeds and supporting struts will be cancelled or reduced, whereas in symmetric parabolas this shadowing effect becomes troublesome for large aperture feeds and their support structure, resulting in higher sidelobes and cross polarizations. In addition, offset reflectors provide excellent isolation between the feed and the reflector and have reasonable structure rigidity, even with large *F*/*D* ratios [1, 6, 49]. Despite their profound advantages over symmetrical parabolas, the offset reflectors generate high cross polarization in the plane of asymmetry when illuminated by conventional symmetric feeds. To alleviate the stated problem, the concept of matched primary feeds may be used. In Rudge and Adatia [50], it was shown that the over-mode waveguides are good candidates to conjugately match the focal plane electric fields in the offset reflectors. The distinguishing characteristic of such matched feeds is their asymmetrical radiation patterns. This will, in turn, result in high cross polarization component in the feed radiation patterns, which will eliminate the inherent cross polarization of the offset geometry. Therefore, the secondary patterns will have low cross polarizations.

In this section, an example of such asymmetric feeds is provided, which can be used in low cross-talk offset reflector antennas. More detail on the concept and these asymmetric feeds are found in Chapter 8. The geometry of proposed asymmetric feed [51] is shown in Figure 3.47. It consists of only two waveguide sections. It generates both TE_{11} and TE_{21} modes with a –90° phase difference between them, with the proper selection of the larger waveguide. The excitation sources of the TE_{21} mode are two radial blocks/screws, which can be placed at any arbitrary axial position. In the present design, they are placed on the feed aperture, to be far from the

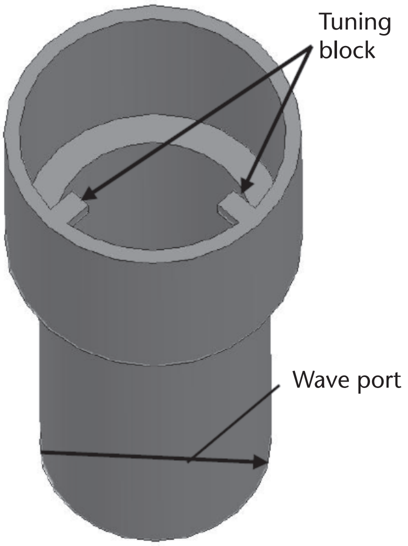

Figure 3.47 The geometry of the proposed dual-mode circular waveguide horn with tuning blocks/screws to use as an asymmetric primary feed in offset reflector antennas. (©2011 IEEE [51].)

waveguide discontinuity, to cause maximum attenuation of the higher order modes at the junction. In this manner, the input waveguide port is not influenced by their detrimental effects, and the feed can be designed easily to be broadband. The inner and outer radii are 13.0 and 17.3 mm, respectively. The length of the larger waveguide is 24 mm, and the total antenna length and waveguide wall thickness are 77.5 and 2 mm, respectively. This structure can now operate as a dual-mode feed with adjustable mode content ratios using the tuning screws.

The simulated and measured co-polar and cross-polar far-field radiation patterns of the dual-mode asymmetric feed are plotted in Figure 3.48 at the frequencies of 8.0 and 9.0 GHz, when the length of the blocks is 4 mm. The measurement and simulated results agree well at both frequencies. It is evident that the primary

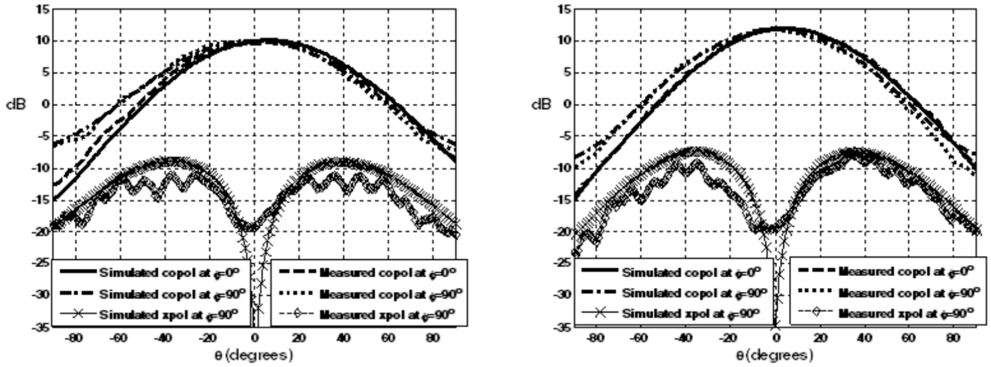

(a) (b)

Figure 3.48 Measured and simulated co-polar and cross-polar radiation patterns at the principal planes for the feed shown in Figure 3.47 with the block length of 4mm. (a) $f = 8.0$ GHz, and (b) $f = 9.0$ GHz.

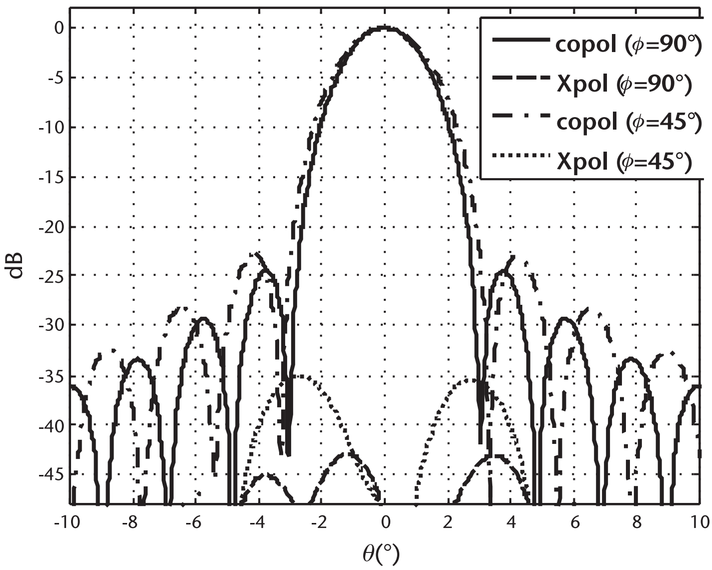

Figure 3.49 Normalized co-polar and cross-polar radiation patterns of the elliptical-rim offset reflector antenna fed by simulated feed shown in Figure 3.47 at both $\phi = 90°$ and 45° planes at $f = 8.3$ GHz.

co-polar patterns are not symmetric at the principal planes, as the peaks of the main beams are not coincident. Moreover, the cross polarization component is quite high, which is necessary in order to reduce the unwanted cross polarization of offset reflector antennas. To show this, the secondary radiation patterns of an elliptical offset reflector illuminated by the proposed feed are shown in Figure 3.49 [52] at both $\phi = 90°$ and 45° planes at 8.3 GHz. The reflector has an *F*/*D* of 0.6. The major and minor axes of the projected ellipse are 91 and 68 cm, respectively. As observed, the cross polarization level is below –35 dB at both asymmetry and diagonal planes.

3.7 Feed Pattern Shaping by Superstrate Loading

The feeds discussed so far dealt with small antennas, having dimensions in order of one wavelength or less. With such a small dimension, it is difficult to cause excessive pattern shaping to continue improving the reflector secondary patterns. However, in spite of these difficulties, excellent feeds suitable for both shallow and deep reflectors were presented. One area that these small feeds suffer is the pattern roll-off beyond the reflector edge, which causes the spill-over power. For additional pattern shaping or reduction of the spill-over power, consider enlarged feed dimensions, discussed in upcoming chapters, or load the feed with reflectors or lenses. All these solutions increase the feed cross section and consequently the reflector aperture blockage. Thus, they may only be considered with large reflector antennas or offset configurations. Since the chapter is dedicated to small feeds, covering such large aperture feeds is out of the scope of this chapter. Instead, a few examples of such feeds, especially those with superstrate and engineered structures, are briefly introduced for the interested readers.

Considerable work has been done recently on planar cavity type antennas to improve their gain or shape their radiation patterns [53–55]. The excitation can be due to either waveguide or planar microstrip type feeds, as discussed earlier. The beam shaping, or gain enhancement, is done normally by either stacking dielectric sheets in the form of superstrate [53] or using a single partially reflective surface in the forms of artificial surfaces and frequency selective superstrates [54–55]. For parabolic reflector antennas, the ideal aperture illumination is given by a $f(\theta) = (\sec\theta)^2$, which requires a shallow axial null on the feed radiation patterns, similar to those in Figures 3.21, 3.22, and 3.24. Using cavity antennas, radiation patterns with axial nulls have been generated to design feeds for offset reflector antennas. A large cavity antenna loaded with a planar lens in the form of an electromagnetic bad gap (EBG) superstrate was also reported [56]. The antenna was fed by a standard WR90 *X*-band waveguide. Two commercially available dielectric slabs with $\varepsilon_r = 2.2$ were used as superstrate layers, separated from one another and from the ground plane by foam slabs. The superstrate layer size was $16\lambda_o \times 16\lambda_o$, where λ_o is the free space wavelength at the frequency of 10.67 GHz [56]. The pattern roll-off of such a large antenna, beyond the peak around 36°, is about 1 dB/degree, which is four times higher than that of small feeds in Figures 3.21, 3.22, and 3.24. The price paid for this rapid roll-off is the increased size of the feed, which is impractical with small reflectors but may be accommodated in large or offset reflectors.

References

[1] Silver, S., *Microwave Antenna Theory and Design*, Peter Peregrinus, London, 1984, IEE Electromagnetic Waves Series 19.

[2] Cutler, C. C., "Parabolic-Antenna Design for Microwaves," *Proceedings of IRE.*, Vol. 35, 1947, pp. 1284–1294.

[3] Calvin, A., "A New Antenna Having Equal E- and H-Plane Patterns," *IRE Trans. on Antennas and Propagation*, Vol. 2, 1954, pp. 113–119.

[4] Potter, P. D., "A New Horn Antenna with Suppressed Sidelobes and Equal Beamwidths," *Microwave Journal*, Vol. 6, 1963, pp. 71–76.

[5] Love, A. W., *Electromagnetic Horn Antennas*, Selected Report Series, IEEE Press, 1976.

[6] Rudge, A. W., K., Milne, A. D. Olver, and P. Knight, *The Handbook of Antenna Design*, Peter Peregrinus, London, 1982, IEE Electromagnetic Waves Series 15.

[7] Minnett, H. C., and B. MacA.Thomas, "Fields in Image Space of Symmetric Focusing Reflectors," *Proceedings of IEE*, Vol. 115, No. 10, 1968, pp. 1419–1430.

[8] Minnett, H. C., and B. MacA. Thomas, "A Method for Synthesizing Radiation Patterns with Axial Symmetry," *IEEE Trans. on Antennas and Propagation*, Vol. 14, 1966, pp. 654–656.

[9] Clarricoats, P. J. B., and A. D. Olver, *Corrugated Horns for Microwave Antennas*, Peter Peregrinus, London, UK, 1984, IEE Electromagnetic Waves Series 18.

[10] Kay, A. F., "The Scalar Feed," *AFCRL*, Report 64–347, AD601609, March 1964.

[11] Koch, F. G., "Coaxial Feeds for High Aperture Efficiency and Low Spill-over of Paraboloid Reflector Antennas," *IEEE Trans. on Antennas and Propagation*, Vol. 21, 1973, pp. 164–169.

[12] Wohlleben, R., H. Mattes, and O. Lochner, "Simple Small Primary Feed for Large Angles and High Aperture Efficiency," *Electronics Letters*, Vol. 8, No. 19, 1972, pp. 474–476.

[13] James, G. L., "Primary Feeds with Wide Beamwidths," *Electronics Letters*, Vol. 14, No. 14, 1973, pp. 447–448.

[14] Olver, A. D., P. J. B. Clarricoats, A. A. Kishk, and L. Shafai, *Microwave Horns and Feeds*, Peter Peregrinus, London, UK, IEE Electromagnetic Waves Series 39, 1994.

[15] Shafai, L., and A. A. Kishk, "Coaxial Waveguides as Primary Feeds for Reflector Antennas and their Comparison with Circular Waveguides," *AEÜ*, Vol. 39, No. 1, 1985, pp. 8–14.

[16] Shafai, L., and A. A. Kishk, "Phase Centre of Small Primary Feeds and Its Effects on the Feed Performance," *IEE Proceedings*, Vol. 132, Pt. H, No. 3, 1985, pp.207–214.

[17] Shafai, L., A. Ittipiboon, E. Bridges, and F. Hyjazie, "Dualband Horn with Inherent Isolation between Its Transmit and Receive Ports," *IEE Proceedings*, Vol. 131, Pt. H, No. 3, 1984, pp.143–146.

[18] Bolster, M. F., "A New Type of Circular Polarizer Using Crossed Dipoles," *IRE Trans. on Microwave Theory Technique*, Vol. 9, September 1961, pp. 385–388.

[19] Silberberg, R. W., "The 'Paradisc' Antenna-A Novel Technique to Improve the Axial Ratio of a Circularly Polarized High Gain Antenna System," *IEEE Trans. on Antennas and Propagation*, Vol. 21, No. 1, 1973, pp. 108–110.

[20] Kildal, P.-S., and S. A. Skyttemyr, "Dipole-Disk Antenna with Beam-Forming Ring," *IEEE Trans. on Antennas and Propagation*, Vol. 30, No. 4, 1982, pp. 529–534.

[21] Shafai, L., and P. Bhartia, "High Performance Dipole Feed for Reflector Antennas," United States Patent, Patent number: 4982198, January 1, 1991.

[22] Poulton, G. T., and T. S. Bird, "Improved Rear-Radiating Waveguide Cup Feeds," *Proc. IEEE Antennas and Propagation Society Int. Symposium*, Vol. 1, 1986, pp. 79–82.

[23] Bird, T. S., "TE_{11} Mode Excitation of Flanged Circular Coaxial Waveguides with an Extended Center Conductor," *IEEE Trans. on Antennas and Propagation*, Vol. 35, No. 12, 1987, pp. 1358–1366.

[24] Kildal, P.-S., "The Hat Feed: A Dual-Mode Rear-Radiating Waveguide Antenna Having Low Cross Polarization," *IEEE Trans. on Antennas and Propagation*, Vol. 35, No. 9, 1987, pp. 1010–1016.

[25] James, G. L., and D. P. S. Malik, "Towards the Theoretical Design of Splash-plate Feeds," *Electronics Letters*, Vol. 11, No. 24, 1975, pp. 593–594.

[26] Newham, P., "A High efficiency Splash Plate Feed for Small Reflector Antennas," *Proc. Fourth Int. Conference on Antennas and Propagation*, Coventry, UK, April 16–19, 1985, pp. 420–423.

[27] Kishk, A. A., and L. Shafai, "Small Reflector Antenna with Low Sidelobes," *IEEE Trans. on Antennas and Propagation*, Vol. 51, No. 10, 2003, pp. 2907–2912.

[28] Kishk, A. A., and L. Shafai, "The Effect of Various Parameters of Circular Microstrip Antennas on Their Radiation Efficiency and the Mode Excitation," *IEEE Trans. on Antennas and Propagation*, Vol. 34, No. 8, 1986, pp. 969–976.

[29] Kishk, A. A., and L. Shafai, "Optimization of Microstrip Feed Geometry for Prime Focus Reflector Antennas," *IEEE Trans. on Antennas and Propagation*, Vol. 37, No. 4, 1989, pp. 445–451.

[30] Bhattacharya, A. K., "Effects of Finite Ground Plane on the Radiation Characteristics of a Circular Patch Antenna," *IEEE Trans. on Antennas and Propagation*, Vol. 38, No. 2, 1990, pp. 152–159.

[31] Noghanian, S., and L. Shafai, "Control of Microstrip Antenna Radiation Characteristics by Ground Plane Size and Shape," *IEE Proceedings on Microwaves, Antennas and Propagation*, Vol. 145, No. 3, 1998, pp. 207–212.

[32] James, J. R., and P. S. Hall, (eds.) *Handbook of Microstrip Antennas*, London, UK: Peter Peregrinus, 1989.

[33] Latif, S. I., and L. Shafai, "Pattern Equalization of Circular Patch Antennas Using Different Substrate Permittivities and Ground Plane Sizes," *IEEE Trans. on Antennas and Propagation*, Vol. 59, No. 10, 2011, pp. 3502–3511.

[34] Yang, S., S. Lee, and A. E. Fathy, "Patch Antennas: An Alternative Feed to Reflectors," *Proc. IEEE Int. Symposium on Antennas and Propagation*, Washington, DC, July 2005.

[35] Mishra, A. R., K. K. Sood, and A. Kumar, "Cavity Backed Microstrip Patch Array Feed for Multiple Beam Applications," *Electronics Letters*, Vol. 34, No. 1, 1998, pp. 4–6.

[36] Luk, K. M., and L. Yonglun, "Radiation Analysis of Parabolic Cylindrical Reflector Antenna with a Rectangular Microstrip Patch Array as Feed," *Proc. IEEE Int. Symposium on Antennas and Propagation*, Seattle, WA, Vol. 2, June 20–24, 1994, pp. 974–977.

[37] Rahmat-Samii, Y., J. Huang, B. Lopez, M. Lou, E. Im, S. Durden, S., and K. Bahadori, "Advanced Precipitation Radar Antenna: Array-Fed Offset Membrane Cylindrical Reflector Antenna," *IEEE Trans. on Antennas and Propagation*, Vol. 53, No. 8, August 2005, pp. 2503–2515.

[38] Kira, F., N. Honma, K. Cho, and H. Mizuno, "Modified Multi-Focal Paraboloid Design for High Aperture Efficiency Multibeam Reflector Antenna," *Proc. IEEE Int. Symposium on Antennas and Propagation*, San Antonio, TX, Vol. 1, June 16–21, 2002, pp. 662–665.

[39] Wight, J., and D. J. Roscoe, "Array Feed for Axially Symmetric and Offset Reflectors," U.S. Patent 5 912 645, June 1999.

[40] Hall, P. S., and P. J. Prior, "Microstrip Feeds for Prime Focus Fed Reflector Antennas," *IEE Proceedings, Pt. H.*, Vol. 134, No. 2, 1987, pp. 185–193.

[41] Brown, K. W., "Efficient Array-Fed Reflector Antenna," *Proc. IEEE Int. Symposium on Antennas and Propagation*, Vol. 2, July 16–21, 2000, pp. 822–825.

[42] Huang, J., and Y. Rahmat-Samii, "Fan Beam Generated by a Linear-Array Fed Parabolic Reflector," *IEEE Trans. on Antennas and Propagation*, Vol. 38, No. 7, 1990, pp. 1046–1053.

[43] Flilipovic, D. F., W. Y. Ali-Ahmad, and G. M. Rebeiz, "Millimeter-Wave Double Dipole Antennas for High-Gain Integrated Reflector Illumination," *IEEE Trans.on Microwave Theory and Techniques*, Vol. 40, No. 5, 1992, pp. 962–967

[44] Zheng, G., A. A. Kishk, A. W. Glisson, and A. B. Yakovlev, "Simplified Feed for Modified Printed Yagi Antenna," *Electronics Letters*, Vol. 40, No. 8, 2004, pp. 464–466.

[45] Zheng, G., A. A. Kishk, A. B. Yakovlev, and A. W. Glisson, "A Broad Band Printed Bow-Tie Antenna with a Simplified Feed," *Proc. IEEE Int. Symposium on Antennas and Propagation*, Monterey, CA, June 20–25, 2004, Vol. 4, pp. 4024–4027.

[46] Eldek, A. A., A. Z. Elsherbeni, and C. E. Smith, "Wideband Modified Printed Bow-Tie antenna with Single and Dual Polarization for C and X-Band Applications," *IEEE Trans. on Antennas and Propagation*, Vol. 53, No. 9, 2005, pp. 3067–3072.

[47] Maula, M. Q., and L. Shafai, "Size Reduction of a Rear Radiating Microstrip Fed Printed Dipole Antenna," *Proc. IEEE Int. Symposium on Antennas and Propagation*, July 8–14, 2012.

[48] Maula, M. Q., "Design and Performance Improvement of Electrically Small Feeds for Prime Focus Reflectors," Ph.D. dissertation, University of Manitoba, 2013.

[49] Jacobson, J., "On the cross polarization of asymmetric reflector antennas for satellite applications," *IEEE Trans. on Antennas and Propagation*, Vol. AP-25, March 1977, pp. 276–283.

[50] Rudge, A. W., and N. A. Adatia, "New Class of Primary-feed Antennas for Use with Offset Parabolic-reflector Antennas," *Electronics Letters*, Vol. 11, November 1975, pp. 597–599.

[51] Allahgholi Pour, Z., and L. Shafai, "A Novel Impedance Matched Mode Generator for Excitation of the TE_{21} Mode in Compact Dual-mode Circular Waveguide Feeds," *IEEE Antennas and Wireless Propagation Letters*, Vol. 10, May 2011, pp. 427–430.

[52] Allahgholi Pour, Z., and L. Shafai, "A Simplified Feed Model for Investigating the Cross Polarization Reduction in Circular- and Elliptical-Rim Offset Reflector Antennas," *IEEE Trans. on Antennas and Propagation*, Vol. 60, No. 3, March 2012, pp. 1261–1268.

[53] Kaymaram, F., and L. Shafai, "Enhancement of Microstrip Antenna Directivity Using Double-superstrate Configurations," *Canadian Journal of Electrical & Computer Engineering*, Vol. 32, No.2, Spring 2007, pp. 77–82.

[54] Foroozesh, A., and L. Shafai, "Investigation into the Application of Artificial Magnetic Conductors to Bandwidth Broadening, Gain Enhancement and Beam Shaping of Low Profile

and Conventional Monopole Antennas," *IEEE Trans. on Antennas and Propagation*, Vol. 59, No. 1, January 2011, pp. 4–20.

[55] Foroozesh, A., and L. Shafai, "Investigation into the Effects of the Patch-Type FSS Superstrate on the High-Gain Cavity Resonance Antenna Design," *IEEE Trans. on Antennas and Propagation*, Vol. 58, No. 2, February 2010, pp. 258–270.

[56] Neto, A., N. Llombart, G. Gerini, M. Bonnedal, and P. De Maagt, "EBG Enhanced Feeds for the Improvement of the Aperture Efficiency of Reflector Antennas," *IEEE Trans. on Antennas and Propagation*, Vol. 55, No. 8, August 2007, pp. 2185–2193.

CHAPTER 4

Smooth Wall Multimode Horns for High Aperture Efficiency—Theory, Design, and Applications

Arun K. Bhattacharyya, Northrop Grumman Corporation
Guy Goyette, The Boeing Company

4.1 Introduction

The horn radiators are commonly used in the space and ground-based antenna systems for their inherent advantages of manufacturing simplicity and low RF loss even at millimeter and submillimeter frequency ranges [1–5]. In a direct radiating array smooth wall horn elements are preferable due to lower weights as compared with corrugated and dielectric loaded horn elements. In addition, with respect to a desired array-gain, a smooth wall horn array utilizes lower aperture area compared to other types of horn arrays. This is primarily due to the thin walls that allow the elements to be closely spaced. Horn radiators are also useful as feeds for reflector antennas generating shaped-beam or multiple pencil beams [6]. As a phased array element, it is desirable that a horn has high aperture efficiency in order to achieve a high array-gain. The array-gain could also be improved by increasing the aperture size of the elements; but for many applications that may not be a viable option due to the grating lobe problems. Furthermore, for a desired array-gain the high element-aperture-efficiency reduces the number of elements. For a scanned beam array, a small number of elements implies a small number of array modules. Consequently, the beam forming network design becomes less complex, reducing the implementation cost of the array antenna.

In a multiple-beam reflector antenna, the physical aperture size of a feed horn is restricted by the presence of the neighboring horns. In that situation, high aperture efficiency of the feed horns is desirable to maintain the necessary edge-taper of the reflector. The reflector edge-taper is dictated by the edge of the coverage gain of the spot beams and the beam-to-beam isolation. A Potter horn [7], typically designed for low cross-polarization level, has low aperture efficiency. Intrinsic to the low aperture efficiency, such a horn may not satisfy the edge-taper requirement due to small pattern roll-off. Linearly flared conical horns have somewhat larger aperture efficiency compared to a Potter horn but suffer from bad cross-polarization performance [2].

The latter is due to the difference in the E- and H-plane patterns, which plays an important role in deciding the cross-polarization level of a circular aperture.

Implementing identical aperture distributions along the E- and H-planes can minimize the cross-polarization of a circular horn. The Potter type of design essentially utilizes this concept by adding the TM_{11} mode with the fundamental TE_{11} mode in the right amplitude and phase [7]. However, such a modal combination results in a highly tapered aperture distribution in both planes, lowering the aperture efficiency of the horn. For achieving high aperture efficiency, a rectangular horn with symmetrical steps in E-plane walls is employed [8]. However, this design is limited to single linear polarization radiation only. A multimode rectangular horn with elliptical beam is reported in [9]. This horn is the rectangular equivalent of the "Potter horn"; therefore it also has low aperture efficiency. Tsandoulas and Fitzgerald [10] and Baldwin and McInnes [11], used dielectric loading to enhance aperture efficiency of a rectangular horn. Such horns are heavy, have fabrication complexity, and may have surface charge accumulation on the dielectric surface leading to electrostatic discharge. In [12] the efficiency of a square or rectangular horn is increased by dividing the entire radiating aperture into a number of small apertures by inserting a cross-shaped taper septum. Gain enhancement was also demonstrated by introducing a symmetrical metal plate inside a conical horn [13]. Hard wall horns using photonic-band-gap structure walls and strip-loaded walls were proposed for gain enhancement purpose [14–18].

In this chapter, we present a simple step-horn that has almost uniform field distributions along the E- and H-planes of the aperture [19]. As a result, the aperture efficiency becomes very high, about 90%, which is about 30% more than that of a Potter horn of comparable aperture size. In addition, because of identical distributions along the E- and H-planes, the E- and H-plane patterns are very close to each other, resulting in a low cross-polar level in the main lobe region. It is found that for obtaining such high aperture efficiency, only the TE_z types of modes should exist on the horn aperture with proper amplitudes and phases [20, 21], where z is the propagation direction. For a given aperture shape, the relative amplitude and phase distributions for various TE_z modes are independent of the aperture size. The amplitudes and the phases of the desired modes are realized using multiple step discontinuities and flared sections with various slopes [21]. A typical horn has four linearly flared sections and two steps as shown in Figure 4.1. These steps not only generate the desired TE_z modes but also generate the undesired TM_z modes. The distances between the steps are critical in order to suppress the undesired TM_z modes by "out-of-phase" cancellation method. This chapter presents operation principle, detailed analysis, and design guidelines of such horn structures.

The remaining part of the chapter is organized in the following way. In Section 4.2 we discuss the general principle of high aperture efficiency radiation. In Section 4.3 we present the characteristics of a circular high-efficiency horn, and in Section 4.4 we discuss the square aperture version. Section 4.5 presents the performance of a flared high-efficiency horn without the steps. In Section 4.6 we discuss the thin wall high-efficiency horns proposed by others. Potential applications and advantages of these horns are presented in Section 4.7 and concluding remarks are presented in Section 4.8.

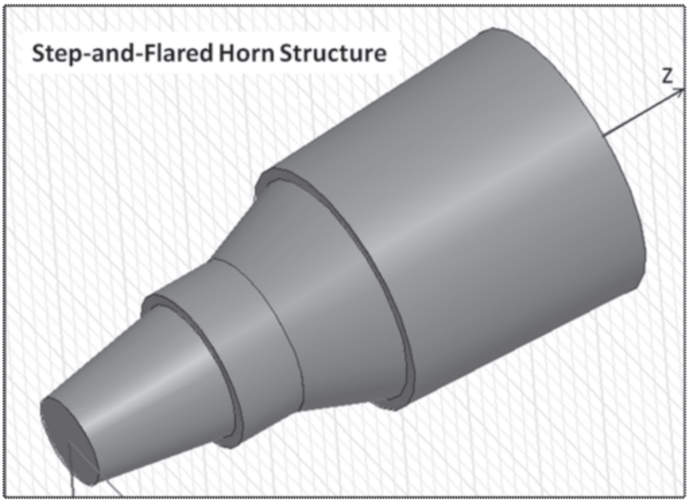

Figure 4.1 A high-efficiency step horn structure.

4.2 Theory for High Aperture Efficiency

Consider a horn radiator with arbitrary-shaped aperture as shown in Figure 4.2. The aperture field can be described as a superposition of the $\mathrm{TE_z}$ and $\mathrm{TM_z}$ orthogonal modes, where the z-axis is perpendicular to the aperture plane. Each mode satisfies the conductive boundary condition at horn's wall; consequently, the modes are mutually orthogonal [22]. The transverse components of the horn-aperture electric field can be expressed as:

$$\vec{E}_t^{ap} = \sum_m V_m^{\mathrm{TE}} \vec{e}_m^{\,\mathrm{TE}} + V_m^{\mathrm{TM}} \vec{e}_m^{\,\mathrm{TM}} \tag{4.1}$$

where V^{TE} and V^{TM} are the modal voltages of the TE_z and TM_z modes and $\vec{e}^{\,\mathrm{TE}}$ and $\vec{e}^{\,\mathrm{TM}}$ are the corresponding normalized modal vectors with the z-components suppressed. The normalization condition is given by:

$$\begin{aligned} \iint_A \vec{e}_i^{\,\mathrm{TE}} \cdot \vec{e}_j^{\,\mathrm{TE}*}\, dS &= 0 \text{ for } i \neq j \\ &= 1 \text{ for}\,\mathrm{i} = j \end{aligned} \tag{4.2}$$

In (4.2), A represents the aperture area and the asterisk indicates the complex conjugate. A similar relation holds for the TM_z modes. In addition, the TE_z and TM_z modes are mutually orthogonal irrespective of the modal indices. Using the orthogonality given in (4.2) we can determine the modal voltages for each mode as

$$V_m^{\mathrm{TE}} = \iint_A \vec{E}_t^{ap} \cdot \vec{e}_m^{\,\mathrm{TE}*}\, dS \tag{4.3a}$$

$$V_m^{\mathrm{TM}} = \iint\limits_A \vec{E}_t^{ap} \cdot \vec{e}_m^{\,\mathrm{TM}*}\, dS \tag{4.3b}$$

The transverse magnetic field on the horn aperture can also be expressed in a similar fashion. However, for obtaining the aperture efficiency using the E-field model one does not need to know the aperture magnetic field explicitly. We define the aperture efficiency (AE) as

$$AE = \frac{G}{G_{\max}} = \frac{G\lambda^2}{4\pi A} \tag{4.4a}$$

where G is the realized gain, $G_{\max}$ is the maximum achievable gain from an aperture area A, and λ is the wavelength in free space. The expression for $G_{\max}$ is used as $4\pi A/\lambda^2$, which is asymptotically true for electrically large apertures.[1] Using the definition of the antenna gain (assuming that the gain and directivity are identical), we can express (4.4a) as

$$AE = \frac{120\pi\lambda^2 P(\theta,\phi)}{A\iint\limits_A \left|\vec{E}_t^{ap}\right|^2 dS} \tag{4.4b}$$

where P represents the radiated power per unit solid angle. Using the equivalence principle and the image theory [23] the far-field radiated power per unit solid angle can be expressed as

$$P(\theta,\phi) = \frac{1}{480\pi\lambda^2}\left|\hat{r} \times \iint\limits_A \vec{M}\exp(j\vec{k}.\,\vec{\rho})\,dS\right|^2. \tag{4.5}$$

In (4.5), $\vec{M} = 2\vec{E}_t^{ap} \times \hat{z}$ is the equivalent magnetic current, $\hat{r}$ is the unit vector along the far-field point (θ,ϕ), $\vec{k}$ is the corresponding wave number vector, and $\vec{\rho}$ is the position vector on the aperture plane. For a fixed amount of total radiated power, the denominator of (4.4b) is a constant.[2] Thus, the aperture efficiency will have its maximum value at a desired far-field point (θ,ϕ), if $P(\theta,\phi)$ is maximized. Using triangle inequality and Schwartz's inequality [24], it can be shown that the right-hand side of (4.5) will exhibit its upper bound (maximum) if $\vec{M}$ is unidirectional and the components of $\vec{M}$ are proportional to the complex conjugate of the companion exponential function of the integrand in (4.5). Symbolically, $\vec{M}$ should be expressed as $\vec{M} = \vec{C}\exp\left(-j\vec{k}.\vec{\rho}\right)$, where $\vec{C}$ is a constant vector. At the bore-sight direction $\vec{k}.\hat{\rho} = 0$, implying that $\vec{M}$ must be independent of $\vec{\rho}$ (uniform distribution).

---

[1] For electrically small apertures, the achievable gain is greater than $4\pi A/\lambda^2$; but (4.4a) is typically used to define aperture efficiency.

[2] Under the assumption that the integral in the denominator is proportional to the total radiated power.

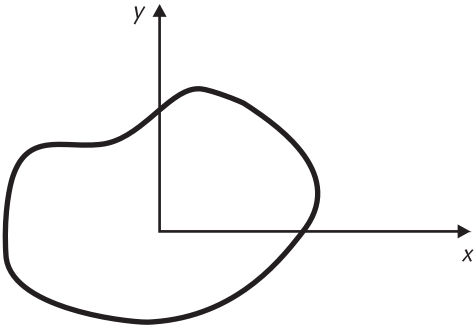

Figure 4.2 A horn aperture with arbitrary cross-sectional geometry.

This follows that for attaining the maximum aperture efficiency along the bore-sight direction, $\vec{E}_t^{ap}$ should be uniform and unidirectional as follows:

$$\vec{E}_t^{ap} = \hat{c}E_0 \tag{4.6}$$

In (4.6) $\hat{c}$ is a unidirectional unit vector.

The next step is to determine the modal voltages associated with the aperture electric field given in (4.6). Let us consider the TM_z modes first. We know that the TM_z field can be constructed from the z-directed magnetic vector potential, $\hat{z}A_z$ [23], therefore the transverse components of the TM_z modal vector can be expressed as

$$\vec{e}_m^{\,\mathrm{TM}} = \frac{1}{j\omega\varepsilon}\nabla_t\left[\frac{\partial A_z}{\partial z}\right], \tag{4.7}$$

where ω is the angular frequency, ε is the permittivity of free space and ∇_t is the transverse gradient operator with the z-component suppressed. Using (4.6) and (4.7) in (4.3b) we obtain the TM_z modal voltage as

$$V_m^{\mathrm{TM}} = \frac{E_0}{j\omega\varepsilon}\iint_A \hat{c}\cdot\nabla_t\left[\frac{\partial A_z}{\partial z}\right]^* dS \tag{4.8}$$

Since $\hat{c}$ is a constant vector, without a loss of generality, we can assume $\hat{c} = \hat{x}$ and then write (4.8) as

$$V_m^{\mathrm{TM}} = \frac{E_0}{j\omega\varepsilon}\iint_A \nabla_t\cdot\left[\hat{x}\frac{\partial A_z}{\partial z}\right]^* dS = \frac{E_0}{j\omega\varepsilon}\oint_\Omega\left[\frac{\partial A_z}{\partial z}\right]^*(\hat{y}.\hat{\tau})\,dl \tag{4.9}$$

In (4.9) Green's theorem [25] is applied to convert the double integral to the contour integral. In (4.9) Ω is the closed boundary-contour of A and $\hat{\tau}$ is a unit vector tangential to the contour. The differentiation with respect to z can be taken outside the integral sign. For the TM$_z$ mode, A_z is zero at the boundary (because A_z is proportional to E_z and E_z vanishes on the conducting wall); therefore, $V_m^{\mathrm{TM}} = 0$ identically. We thus prove that for obtaining the maximum aperture efficiency the TM$_z$ mode should not exist on the horn aperture.

A similar development for the TE$_z$ modal voltages gives a contour integral in the z-component of the electric vector potential [23], instead of A_z. The electric vector potential does not vanish everywhere on the horn's walls; therefore the TE$_z$ modal voltages are not identically zero.

4.3 Circular Aperture

We have shown that for the maximum aperture efficiency only the TE$_z$ types of modes should exist on the horn's aperture. The amplitudes of the TE$_z$ modes must be in appropriate proportions in order to produce a uniform and unidirectional aperture field. We will consider a circular aperture and determine the modal amplitudes. For a circular horn, the TE$_z$ modal vector can be represented as [26],

$$\vec{e}_{mn}^{\,\mathrm{TE}}(\rho,\phi) = C_{mn}\left\{-\hat{\rho}\, n \cos n\phi \frac{1}{\rho} J_n\left(k_{mn}\,\rho/a\right) + \hat{\phi} \sin n\phi \frac{k_{mn}}{a} J_n'\left(k_{mn}\,\rho/a\right)\right\}, \tag{4.10}$$

where a is the radius of the aperture, $J_n(x)$ represents the Bessel function of order n, and the prime indicates its derivative with respect to the argument x. The term C_{mn} is the normalization factor to satisfy (4.2) and k_{mn} represents the mth zero of $J_1'(x)$. The expression for C_{mn} is given by

$$C_{mn} = \frac{1}{J_n(k_{mn})}\sqrt{\frac{\varepsilon_n}{\pi(k_{mn}^2 - n^2)}} \tag{4.11}$$

with $\varepsilon_0 = 1$ and $\varepsilon_n = 2$ for $n \neq 0$. For most of the antenna applications, the incident mode at the horn input is the TE$_{11}$ mode; therefore, $n = 1$ for all the modes on the aperture unless the rotational symmetry of the circular horn is perturbed. Therefore, the aperture field of a high-efficiency circular horn with the TE$_{11}$ incident mode at the horn input can be represented as

$$\vec{E}^{ap}(\rho,\phi) = \sum_{m=1}^{\infty} V_{m1}^{\mathrm{TE}}\, \vec{e}_{m1}^{\,\mathrm{TE}}(\rho,\phi) \tag{4.12}$$

Assuming the principal polarization along the x-direction, the aperture electric field corresponding to the maximum aperture efficiency is given by

$$\vec{E}^{ap}(\rho,\phi) = \hat{x}E_0 \tag{4.13}$$

Substituting (4.13) in (4.12) and using orthogonality we obtain

$$V_{m1}^{\mathrm{TE}} = E_0 \int_0^{2\pi}\int_0^{a} \hat{x} \cdot \vec{e}_{m1}^{\,\mathrm{TE}*}(\rho,\phi)\rho\, d\rho\, d\phi \tag{4.14}$$

After performing the integration we get a closed form expression for V_{m1}^{TE} as

$$V_{m1}^{\mathrm{TE}} = -E_0 a\sqrt{\frac{2\pi}{k_{m1}^2 - 1}} \tag{4.15}$$

The first three roots of $J_1'(x)$ are $k_{11} = 1.841$, $k_{21} = 5.331$, $k_{31} = 8.536$; therefore the ratio of the modal voltages for the first three TE$_z$ modes calculated using (4.15) are

$$\left|V_{11}^{\mathrm{TE}}\right| : \left|V_{21}^{\mathrm{TE}}\right| : \left|V_{31}^{\mathrm{TE}}\right| : .... = 1.0 : 0.295 : 0.182 : .... \tag{4.16}$$

The phases of the propagating modes are identical.[3] For evanescent modes, the phase angles are ±90°; the positive or negative sign depends on the sign used for the normalization factor in (4.11). In practice, only the propagating modes arrive at the aperture plane, so the radiated fields are contributed by propagating modes only.[4] Therefore an ideal aperture field distribution can never be realized in practice. In the following section we discuss the method used to realize the necessary modal distribution.

4.3.1 Realization of the Modes

The desired modes with appropriate amplitudes and phases can be realized with multiple steps and flared sections in a smooth wall horn as shown in Figure 4.3(a) and (b). The location of the steps should be such that after the generation, the desired modes can propagate toward the aperture. For example, if the horn aperture size is such that it can support three TE$_z$ modes, then two steps on the horn's wall may be used. The first step nearest to the input section should create the TE$_{21}$ mode and the second step should create the TE$_{31}$ mode. Accordingly, the horn dimension after the first step should be above the cut-off dimension of the TE$_{21}$ mode. Similarly, the dimension after the second step should be above the cut-off dimension of the TE$_{31}$ mode. Linearly (or profile) flared section between the discontinuities may be used. The relative amplitudes of the desired higher order modes determine the step heights, slopes, and the section lengths. It should be mentioned that the step discontinuities also produce the undesired TM$_z$ modes. The distance between the step discontinuities and the flared angles between the steps can be adjusted to minimize the amplitudes of the undesired TM$_z$ modes. For instance, the TM$_{11}$ mode generated at the first

---

[3] It should be mentioned that the phase of a mode is determined with respect to the modal vector defined in (4.10). The phase of the modal voltages will differ if a different definition is used.

[4] Evanescent modes may be produced on the aperture due to the discontinuity of guided modes at the aperture-air interface, but those evanescent modes generally have insignificant contributions to the far field.

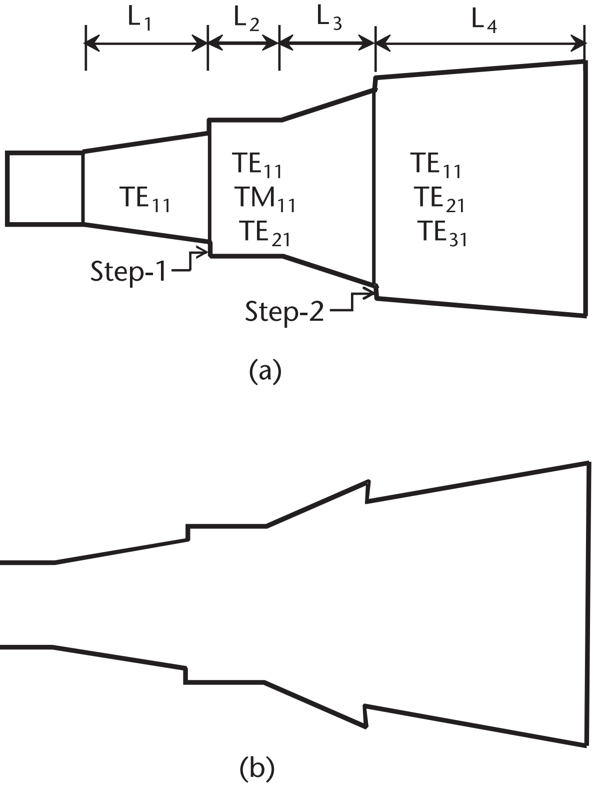

Figure 4.3 Two-step high-efficiency horn geometry. (a) with two outward steps. (b) with inward and outward steps.

step is cancelled by the “out of phase” TM_{11} mode generated at the second step. The distance between the two steps is critical for this effect.

Both inward and outward steps may be used as shown in Figure 4.3(a) and (b). For an outward step, the incident TE_{11} mode produces TM_{11} mode in phase. However, for an inward step, the incident TE_{11} mode produces the TM_{11} mode about 180° out of phase. The distance between the two steps should be such that the TM_{11} mode produced at the first step is cancelled by the second step. Therefore, if both steps are in outward directions as in Figure 4.2(a), the following condition should be satisfied:

$$\frac{1}{2} \approx \left(L_2 + L_3\right)\left[\frac{1}{\lambda_{11}^{\mathrm{TE}}} - \frac{1}{\lambda_{11}^{\mathrm{TM}}}\right] \tag{4.17}$$

where λ_{11} represents the average guide wavelength in the section between the two steps. It should be mentioned that the left-hand side could be any odd multiple of one-half, but we consider the smallest possible number to minimize the length of the horn. Equation (4.17) is not rigorous because the horn flare modifies the relative amplitude and phase of the mode. Also, the multiple reflections between the two discontinuities modify the relative phase and amplitude. Furthermore, the flare at the input section creates some amount of the TM_{11} mode, which differs in phase from the incident TE_{11} mode. In practice, the actual value of $L_2 + L_3$ is smaller than that obtained using (4.17). Nevertheless, (4.17) gives an idea about the approximate distance between the steps, but in a real design this distance must be obtained by numerical optimization. The left-hand side would be different if one of the steps is in the inward direction as depicted in Figure 4.3(b).

4.3.2 Circular Horn Design

To illustrate the design procedure, we consider a horn of 4λ aperture diameter, where λ represents the wavelength at the center frequency of the band of interest. The input diameter of the horn is 0.72λ. The first step is placed at a location where the diameter is about 1.7λ (the cut-off dimension for the TE_{21} mode). Similarly for the TE_{31} mode, the second step is at 2.7λ diameter location. A third step near 3.7λ diameter location could have been placed to produce the TE_{41} mode, but that would require an extra horn-length for phase adjustment on the aperture (the aperture being near cut-off for the TE_{41} mode, the guide wavelength becomes large, resulting in a long, flared section to achieve a desired phase for that mode). The actual dimensions are obtained by optimizing the structure to achieve high efficiency and good cross-polarization. A gradient search-based algorithm is employed toward that end. The axial length of the horn is obtained as 8.25λ. For the horn analysis, software based on multimode moment method [27] is used. For the two-step horn, the normalized modal voltages at the aperture are shown in Table 4.1.

From the numerical data we notice that the achieved modal voltage for the TE_{21} mode is fairly close to the desired amount. For the higher order modes, however, the deviation increases primarily due to the limited number of adjustable parameters (degrees of freedom). For the same reason, the TM_z modes are not completely suppressed as observed in Table 4.1.

It is instructive to examine the aperture field distribution of the horn with respect to the achieved modal voltage distribution. Figure 4.4 shows the magnitude of the transverse electric field along the E-, H-, and diagonal-planes. The field is fairly uniform in the major portion of the aperture as desired. On the E-plane, the aperture field is nonzero near the boundary wall. This is not so for the H-plane because of the boundary condition of the modal fields. As a result, the field distributions are somewhat different on the two orthogonal planes, particularly near the boundary wall. This difference improves with the increasing number of modes. However, for a finite aperture size the modes beyond certain order are evanescent; consequently such evanescent modes cannot be realized on the aperture.

Table 4.1 Normalized Modal Voltages on the Aperture of a Two-Step, High-Efficiency Circular Horn (Aperture Diameter = 4λ, Horn Length = 8.25λ, Realized Aperture Efficiency = 91.4%)

Mode	*Ideal Modal Voltage*	*Achieved Modal Voltage*
TE_{11}	$1.0\angle 0$	$1.0\angle 0$
TM_{11}	0.0	$0.110\angle 5.5$
TE_{21}	$0.295\angle 0$	$0.263\angle 15.4$
TM_{21}	0.0	$0.059\angle 3.8$
TE_{31}	$0.182\angle 0$	$0.109\angle -39.5$
TM_{31}	0.0	$0.029\angle 68.0$

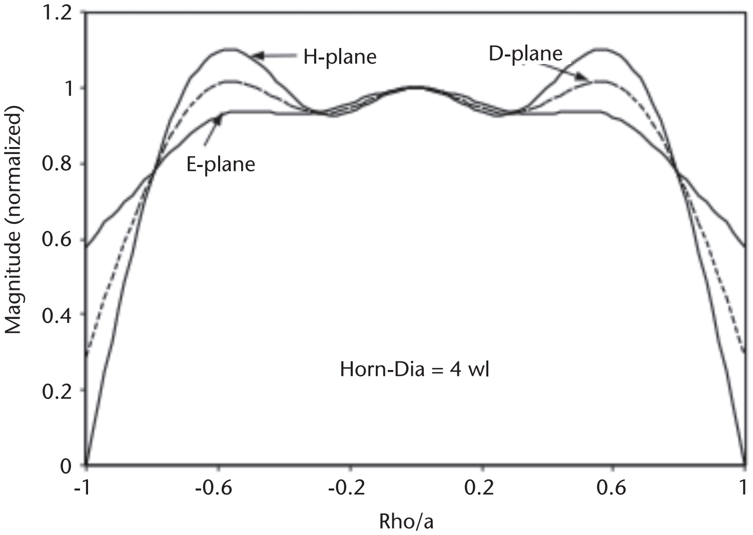

Figure 4.4 Magnitude (normalized with respect to the intensity at the aperture center) of the *x*-component of the electric field on the aperture of a two-step high-efficiency horn. Horn length = 8.25λ, aperture diameter = 4λ. (©2004 IEEE [21].)

Figure 4.5 shows the electric field lines on the aperture plane. Since the realized phase angles are non-zero for the higher order modes (see Table 4.1), the field lines should not be time invariant. In the present plot we ignore the phase difference between the two orthogonal polarizations. The field lines are fairly unidirectional across the aperture, indicating low cross-polarization level in the far-field pattern. The small deflection from being unidirectional is partly due to the small number of propagating modes and partly due to the nonideal modal amplitudes.

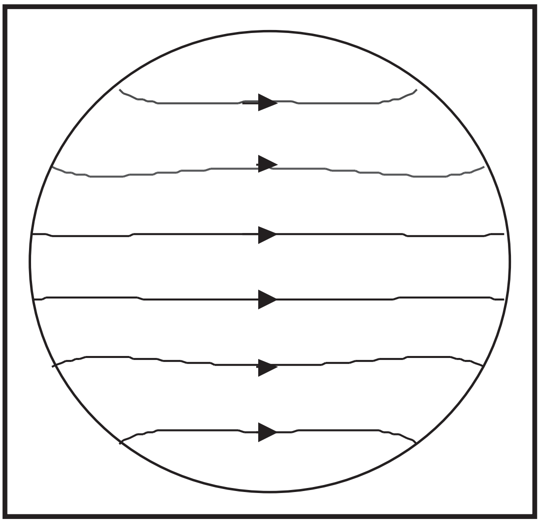

Figure 4.5 Electric field lines on the aperture plane of the horn described in Figure 4.4. (©2004 IEEE [1].)

Figure 4.6 shows the 3-D linear co-polarization pattern of the 4λ-horn. The realized gain is 21.6 dBi, which corresponds to 91.4% aperture efficiency. Such aperture efficiency is significantly higher than that of a Potter horn of identical aperture size (the Potter horn efficiency is estimated as about 68%). The pattern appears to be rotationally symmetrical. The sidelobe level is about 19 dB below the beam peak, which is expected from a uniformly illuminated circular aperture (ideally the sidelobe should be 17.6 dB). Figure 4.7 shows the co- and cross-polarization pattern-cuts at 45° plane (diagonal plane). The cross-polarization level is below −34 dB within

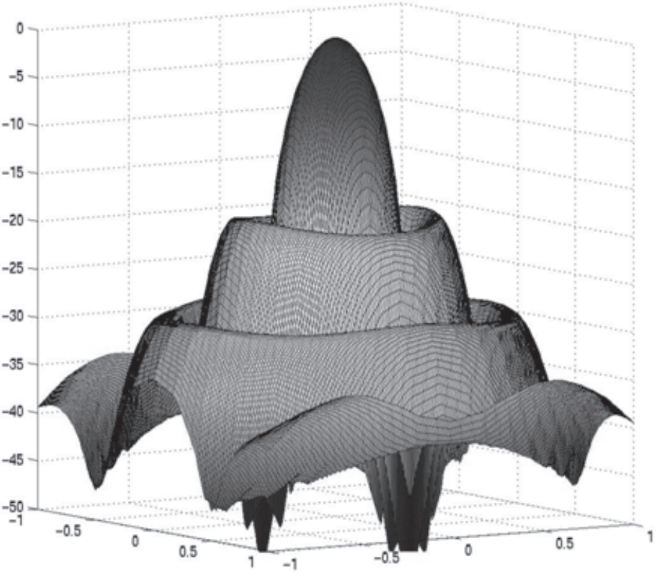

Figure 4.6 Three-dimensional co-polar pattern (linear polarization) of the two-step horn described in Figure 4.4. Horn aperture diameter = 4λ, aperture efficiency = 91.4%. (©2004 IEEE [21].)

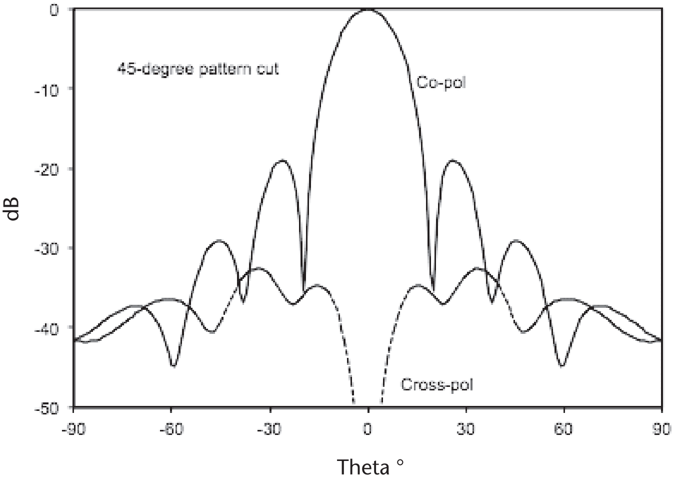

Figure 4.7 Co-polar and cross-polar pattern-cuts of the horn described in Figure 4.4. (©2004 IEEE [21].)

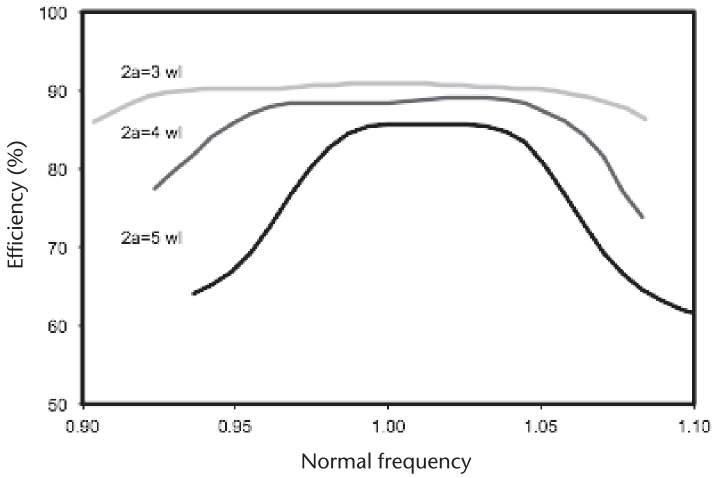

Figure 4.8 Aperture efficiency versus normalized frequency of two-step circular high-efficiency horns of diameters 3λ, 4λ, and 5λ. (©2004 IEEE [21].)

the main lobe of the co-polar beam. This cross-polar level is much better than that of a conical horn and is very comparable with that of a Potter horn of the same aperture size.

To evaluate the bandwidth performance of two-step high-efficiency horns, we designed three horns of aperture diameters 3λ, 4λ, and 5λ, respectively. The design objective was to obtain a good cross-polarization and return loss performance while maintaining aperture efficiency above 85%. Figure 4.8 shows the variation of the aperture efficiency with normalized frequency. For the 3λ aperture (diameter), 15% bandwidth is achievable with respect to a minimum aperture-efficiency of 90%. The bandwidth increases to about 20% with respect to a minimum aperture efficiency of 85%. The peak efficiency and the bandwidth both decrease with the aperture size. For 5λ-aperture the bandwidth reduces to 5% with respect to 85% aperture efficiency. It is worth mentioning that the bandwidth increases significantly if the return loss and cross-polarization constraints are relaxed or withdrawn from the objective function.

Figure 4.9 shows the variations of input return loss and cross-polarization[5] with the normalized frequency. The –30 dB cross-polarization bandwidth is larger for smaller aperture. The input match is better than –25 dB within the band.

Figure 4.10 compares the performances of conical, Potter, and high-efficiency circular horns of similar aperture sizes and axial lengths. Expectedly, the high-efficiency horns have significantly larger aperture efficiency compared to the other horns. The aperture efficiency of the high-efficiency horn varies from 95–90% when the diameter increases from $3–5\lambda$. The aperture efficiencies vary from 71–64% and 81–66% in the case of Potter and conical horns, respectively. The cross-polarization level of the high-efficiency horn is comparable with that of the Potter horn and much better than that of a conical horn.

---

[5] Unless otherwise mentioned, the cross-polarization of a horn is referred to as the worst-case cross-polarization level within the –10 dB co-polarization taper.

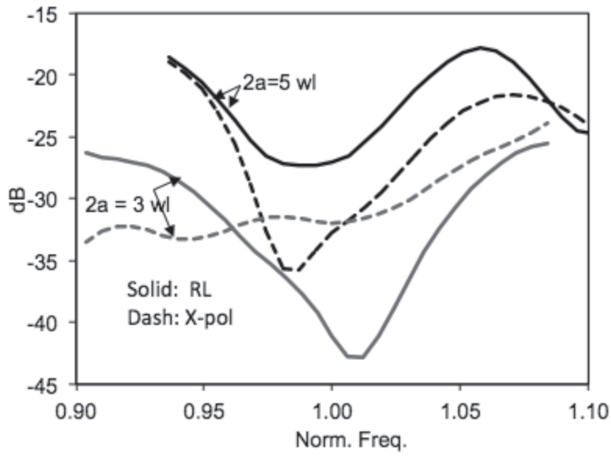

Figure 4.9 Input return loss and worst-case cross-polarization level (within 10 dB below co-polarization peak) of two-step circular high-efficiency horns of diameters 3λ and 5λ. (©2004 IEEE [21].)

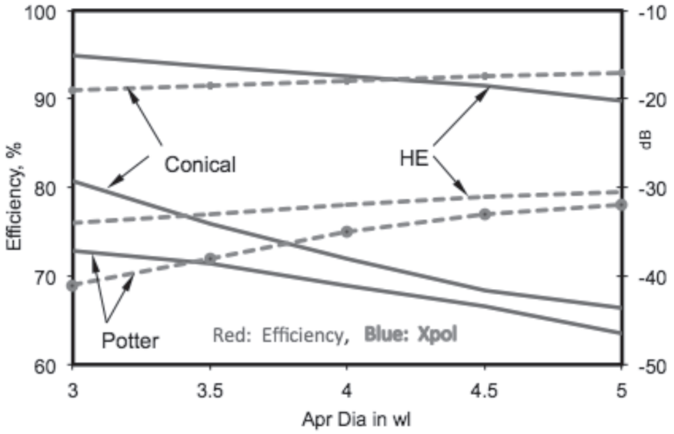

Figure 4.10 A comparison of the aperture efficiency and cross-polarization level between conical, Potter, and high-efficiency horns with circular apertures. (©2004 IEEE [21].)

It is possible to design two-step high-efficiency horns of various aperture diameters only by adjusting the axial length of the aperture section while keeping the first three sections unchanged. This is particularly true for the aperture efficiency performance. With reference to Figure 4.11, the horn-dimensions are given in Table 4.2 in terms of free-space wavelength, λ, at the center frequency of the band. The input waveguide diameter is assumed as 0.73λ. For other input waveguide diameter, the dimensions change slightly, particularly the input section length L_1.

The preceding dimensions yield an aperture efficiency ranging from 86–90% if the aperture diameter D_a lies between 3λ and 5λ. The efficiency can be improved further with fine-tuning the dimensions. The cross-polarization and return loss can also be improved. For that matter, the dimensions can be used as a starting solution in an optimization routine. It should be mentioned that several other designs are

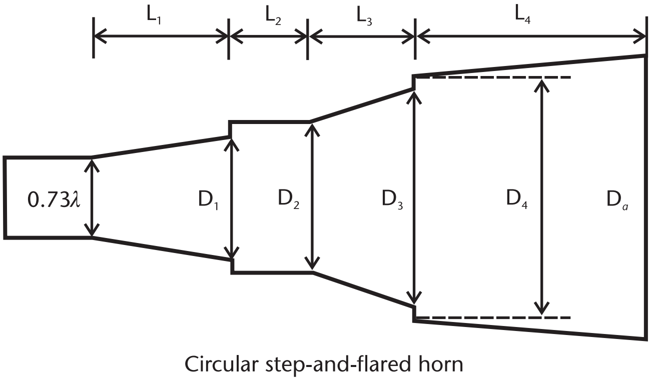

Figure 4.11 A two-step circular high-efficiency horn. Table 4.2 yields the design dimensions in wavelengths.

Table 4.2 Initial Design Dimensions of Circular High-Efficiency Horns. The Input Waveguide Diameter = 0.73λ, Aperture Diameter = D_a. The Reference Horn is Shown in Figure 4.11.

$L_1/\lambda = 1.72$	$L_2/\lambda = 0.86$	$L_3/\lambda = 1.46$	$L_4/\lambda = 2.895 + 1.497(D_a/\lambda - 3)$
$D_1/\lambda = 1.58$	$D_2/\lambda = 1.88$	$D_3/\lambda = 2.58$	$D_4/\lambda = 2.92$

also possible. Note that the axial length for the design in Table 4.2 is about twice the aperture diameter.

4.3.3 Three-Step Horn

For aperture diameter less than 4.5λ, the two-step design provides good aperture efficiency with reasonable cross-polarization performance. The performance deteriorates if the aperture size increases beyond 4.5λ. It is found that an additional step improves the performance significantly. A three-step horn with aperture dimension of 5λ is designed to achieve about 88% aperture efficiency with –30 dB cross-polarization level. Figure 4.12 shows efficiency, return loss, and the worst-case cross-polarization

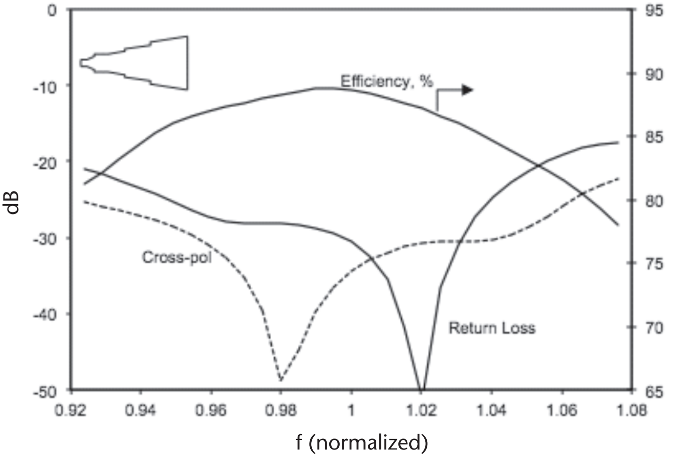

Figure 4.12 Aperture efficiency, return loss, and cross-polarization versus normalized frequency of a three-step, circular high-efficiency horn of diameter 5λ. (©2004 IEEE [21].)

level versus normalized frequency. The cross-polarization level is better than –30 dB within 10% bandwidth. As noted, the aperture efficiency is better than 86% within the band, and the return loss is better than 25 dB.

The multistep horn design is extended for dual band operation. A dual band horn is successfully designed to operate at 11.7–12.2 GHz and 14.0–14.5 GHz bands [28]. Over 85% aperture efficiency is achieved for both bands. The return loss was better than 25 dB in both bands. The cross-polarization levels are –32 and –27 dB, respectively, for the bands. The aperture diameter was 3.8 inches, and the horn length was about 7.5 inches.

4.4 Square High-Efficiency Horn

A similar design procedure can be invoked for square high-efficiency horns. It is found that in a square (also in rectangular) aperture, the modal voltages should be in the following ratio.

$$\left|V_{10}^{\mathrm{TE}}\right| : \left|V_{30}^{\mathrm{TE}}\right| : \left|V_{50}^{\mathrm{TE}}\right| : \ldots. = 1.00 : 0.333 : 0.200 : \ldots$$

The phase of the modes should be identical for the propagating modes. The modal voltage corresponds to the modal vector as defined in Marcuvitz [26]. As for the circular geometry, the TM_z modes should not exist on the horn's aperture. Also, the TE_{m0} even order modes (i.e., with $m = 2, 4, 6, \ldots$) should not exist on the aperture. For the TE_{10} incident mode at the horn's input, the undesired TE_z modes are not produced unless the horn has nonsymmetrical discontinuities.

For a linearly polarized (LP) radiated field the desired TE_z modes can be produced with steps on the H-plane of the horn [8, 29]. Interestingly, symmetrical H-plane steps do not produce the TM_z modes, which is a desirable feature in a high-efficiency rectangular horn. However, for dual *LP* radiation or for circular polarization (CP) radiation, the incident modes being TE_{10} and TE_{01}, steps in both E- and H-planes are required to produce necessary modes for both polarizations. As in the case of a circular horn, the steps must be placed where the cross sections allow propagation of the intended higher order modes. For instance, to produce the TE_{30} and TE_{03} modes effectively in a square horn, the step must be placed near the waveguide region that has $1.5\lambda \times 1.5\lambda$ cross-sectional area. However, this step will also produce the undesired TE_{12}, TE_{21}, TM_{12}, and TM_{21} modes that have lower cut-off frequency than the TE_{30} and TE_{03} modes. The second step helps cancel out these undesired modes by generating these modes again with 180° out of phase. Another purpose of the second step is generating the desired TE_{50} and TE_{05} modes. The optimum dimensions are given in Table 4.3 that can be used to design a two-step high-efficiency square horn as depicted in Figure 4.13 for aperture dimensions ranging from 3–4.5λ.

The design yields an aperture efficiency varying from 85–90% when a varies from 4.5–3λ. The aperture efficiency and other characteristics can be improved by fine-tuning these dimensions using an optimizer routine.

Figure 4.14 shows the radiation patterns of a two-step square high-efficiency horn with aperture size of 3.54λ. The aperture efficiency was 90.8%. Notice that the

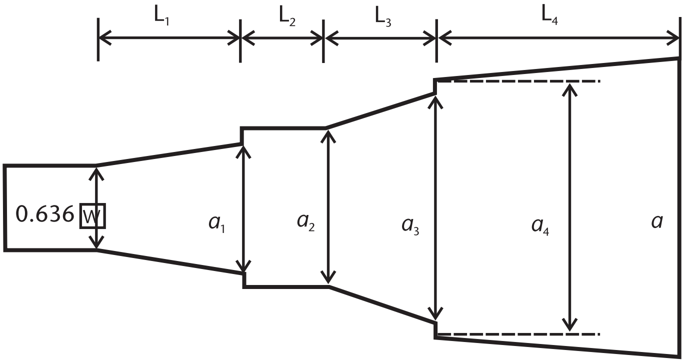

Square step-and-flared horn

Figure 4.13 Two-step square horn. Table 4.3 yields the design dimensions.

Table 4.3 Initial Design Dimensions of Square Horns Shown in Figure 4.13. The Input Waveguide Size is 0.636λ. The Aperture Size, a, Should be Within $3–4.5\lambda$.

$a_1 = 1.46\lambda$	$a_2 = 1.771\lambda$	$a_3 = 2.44\lambda$	$a_4 = 2.656\lambda$
$L_1 = 1.686\lambda$	$L_2 = 1.223\lambda$	$L_3 = 1.177\lambda$	$L_4 = [3.356 + 2.119(a/\lambda - 3)]\lambda$

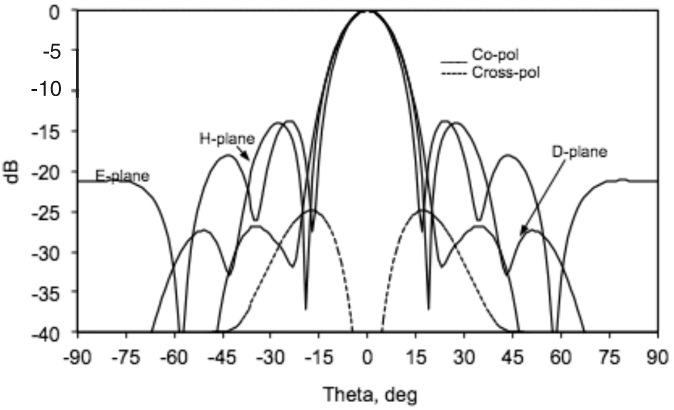

Figure 4.14 Three principal radiation pattern-cuts of a high-efficiency square horn of aperture length 3.54λ. (©2004 IEEE [21].)

sidelobes in the E- and H-planes are about 14 dB below the main lobe peak, which corresponds to a uniform aperture distribution of a square aperture. The worst-case cross-polarization level is 25 dB below the co-polarization peak. It is generally observed that the circular high-efficiency horns have better cross-polar performance than that of a high-efficiency square horn. This may not be a problem in reality, because high-efficiency square horns are generally used as array elements, and the cross-polarization level within the scanning range (usually 3–5 dB below the co-polarization peak) is better than –30 dB, which is acceptable in most applications.

To examine the characteristics of high-efficiency square horns we plot the efficiency and return loss of two optimized horns in Figure 4.15. The efficiency for a

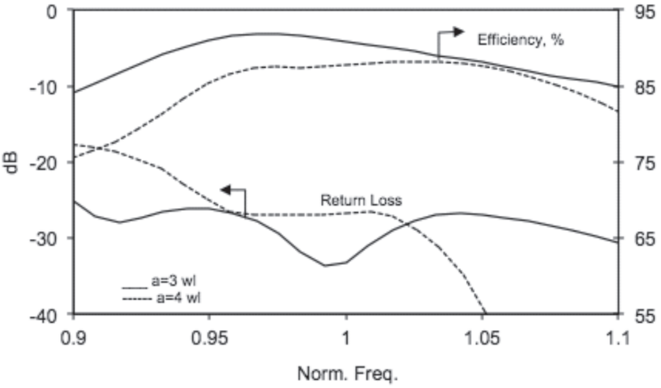

Figure 4.15 Aperture efficiency and return loss performances of two-step high-efficiency square horns of aperture lengths 3λ and 4λ. (©2004 IEEE [21].)

3λ square aperture is about 90% within 10% bandwidth. As in the case of circular high-efficiency horns, the bandwidth decreases with the increase in aperture size. The return loss is better than 25 dB over the band. For larger aperture dimensions (over 4.5λ) more than two steps may be needed to achieve maximum aperture efficiency and good return loss performance.

4.5 Multiflared High-Efficiency Horns

The steps of a "step-and-flared" structure in Figure 4.2 are removed and then reoptimized to examine the aperture efficiency performance of the modified structure. It is found that a good efficiency performance can be achieved from such a "multiflared" structure [30]. The general profile of the modified horn remains very similar to that of a step-and-flared horn (see Figure 4.16). The slopes become different, however, in order to compensate the effects of the steps. With respect to the aperture efficiency, the performance of a step-horn and a flared-horn are very much comparable. Figure 4.17 shows the aperture efficiency comparison of 4λ-circular horns. The parameters for optimization are section lengths, slopes, and step sizes, and the goal is to achieve a minimum of 88% aperture efficiency within 15% bandwidth. Both horns generally satisfy the requirements. The step-and-flared horn, however, shows somewhat larger bandwidth than the multiflared horn primarily because the steps provide additional degrees of freedom to the optimization process. It is generally observed that for moderate aperture efficiency requirements in wide band, the step sizes of a step-horn become small. However, this may not be the case if high aperture efficiency in a smaller band is desired. Figure 4.18 shows the performances of 4λ horns with and without steps. In this case, the requirement is to achieve maximum possible aperture efficiency within 5% bandwidth. The horn with steps performs better than the horn without steps. The step sizes are substantial (about 0.1λ) in this case. For a given aperture size, a step-and-flared horn has smaller axial length than that of a multiflared horn. With respect to the 4λ horns associated with Figure 4.18, the step-horn is about 0.5λ shorter than the flared-horn.

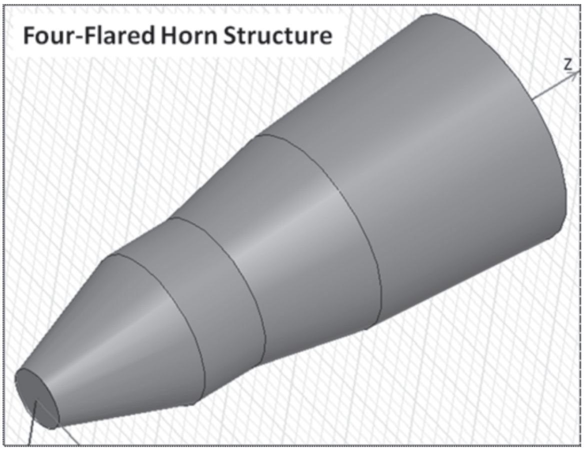

Figure 4.16 Three-dimensional view of a four-flared horn structure.

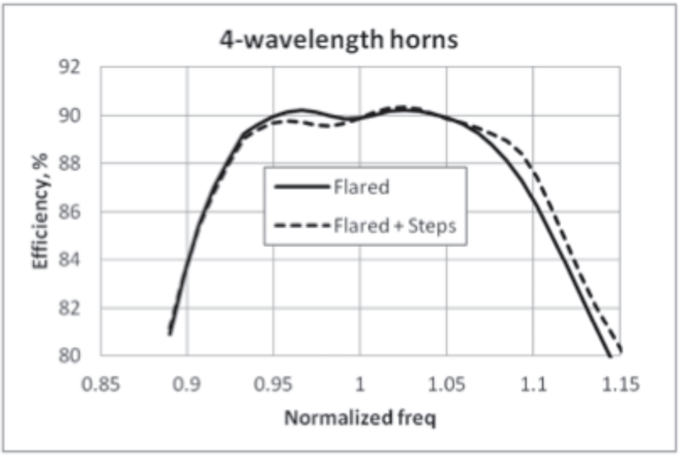

Figure 4.17 Aperture efficiency versus frequency for step-and-flared horns. The aperture diameter is 4λ for both horns.

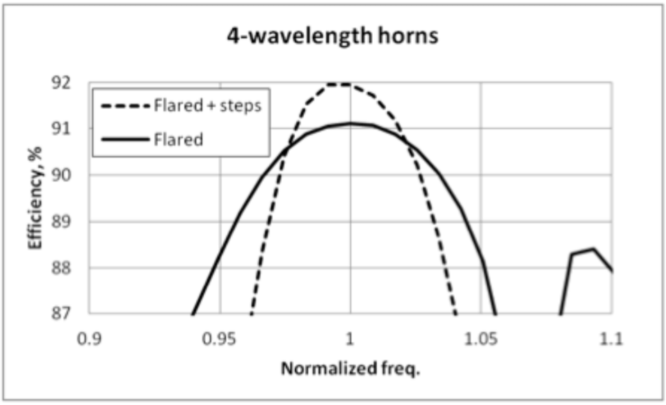

Figure 4.18 A comparison of aperture efficiency performances between step-and-flared horns within a small bandwidth.

4.6 Other High-Efficiency Horn Structures

Several high-efficiency thin-wall horn structures are proposed in the literature. Bird and Granet [31] present “spline-profile” rectangular horn designs for high-aperture efficiency. The size and the performance of the horns are comparable with that of a rectangular step-and-flared horn considered in Section 4.4. Chan and Rao [32] present multiflared (five-flared sections) circular horn designs for single and dual band operations. For a single band horn, the reported performance is very similar to that of a four-flared horn, presented before. The axial length of the dual band design [32] is over three times the aperture diameter, which is significantly longer than the dual band design presented [28], however. Ruggerini [33] presents very compact designs with axial lengths about 1.2 times of the aperture diameter. Reduction of axial length was accomplished with wave-shaped horn walls. Such compact horns have narrower bandwidth than that of step-and-flared horns.

4.7 Applications

4.7.1 In Direct Radiating Arrays

Horn elements are very suitable for direct radiating arrays [5] for small scan angles. High-efficiency horn elements would be very attractive because they yield enhanced array gain due to their high-aperture efficiency. For a given element size and for a desired array gain, the high-efficiency horns significantly reduce the number of elements in the array. For a given element size, there is a maximum limit for the scan angle where the high-efficiency horn is advantageous over other horns of identical aperture size. To illustrate this, consider an array of square horn elements where the element aperture size is $3\lambda \times 3\lambda$. The limiting scan angle can be estimated by comparing the gain pattern of a high-efficiency horn with that of a pyramidal horn of the same size, because the scan gain is directly proportional to the element gain [5] if the mutual coupling is ignored. Figure 4.19 shows the gain pattern of such horns of the

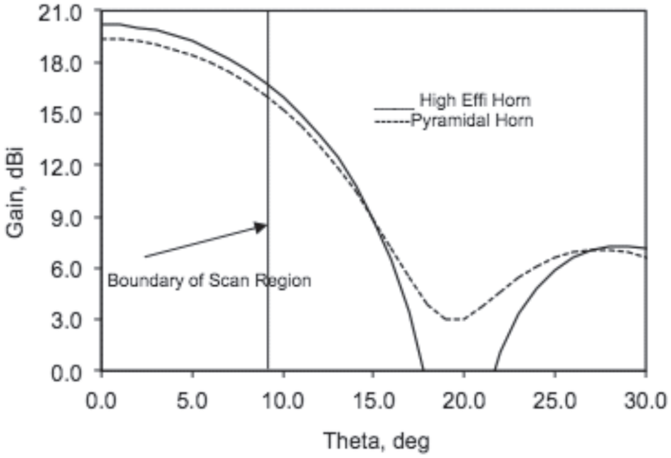

Figure 4.19 Gain patterns of a square high-efficiency step horn and a square pyramidal horn of identical length and aperture size. Aperture size = 3λ, —— high-efficiency step horn, ---- pyramidal horn. (©2004 IEEE [21].)

same aperture dimensions of $3\lambda \times 3\lambda$. The crossover point is at $\theta = 15°$. Therefore, if the scanning range is ±15°, an array with a high-efficiency horn will have higher gain than that with a pyramidal horn for all scanned beams. However, if the array scans beyond ±15º, pyramidal horns will yield a higher gain. Such a situation generally does not arise in practice, because for a given element size, the grating lobe positions limit the maximum scan angle. In the present case, for instance, the scan angle should not exceed 9.6° (for a rectangular lattice) in order to keep the grating lobes outside the scanning region. Within 9.6° scan angle, the high-efficiency horn array shows about 0.8 dB more gain than a pyramidal horn array of equal number of elements. To compensate the gain difference, either 20% more pyramidal horn elements or bigger horn-apertures are required. This increases cost and complexity of the array.

For spot beams, the high-efficiency horn array shows better edge-of-coverage gain than the pyramidal horns. For a desired array gain, the aperture area of the array made with pyramidal horns will be bigger than the array made with high-efficiency square horns. As a result, the beam of the pyramidal horn array becomes sharper than that of the high-efficiency horn array. This causes lower edge of the coverage gain for the pyramidal horn array. To illustrate this effect, we plot the radiation patterns of two arrays of identical gain at the beam peak (40.2 dBi). The high-efficiency square horn array is a 10 × 10 element-array with an element size of 3λ. The pyramidal horn array is an 11 × 11 element-array with an element size of 3λ. The gain patterns are plotted in Figure 4.20. The high-efficiency horn array has a bigger beam size (defined by the –3 dB relative gain contour) than that of the pyramidal horn array. Equivalently, for a given coverage area (1.5° beam diameter, for example) the high-efficiency horn array shows 0.6 dB more edge of the coverage gain than that of the pyramidal horn array.

It should be pointed out that the above array analysis is conducted ignoring mutual coupling effects. In order to examine the mutual coupling effects, we computed the horn aperture efficiency in an infinite array environment using a Floquet

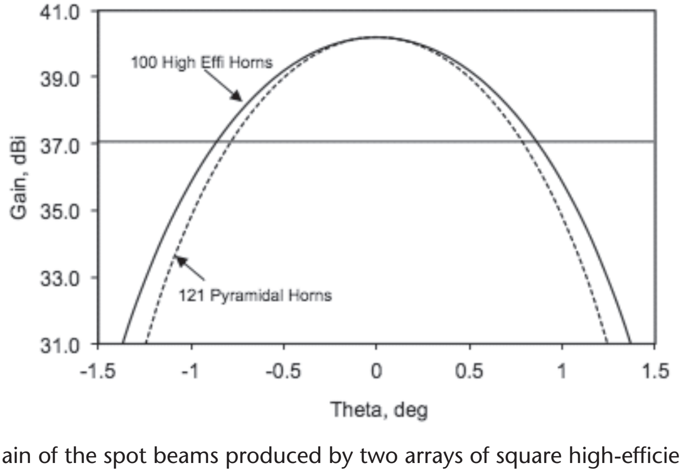

Figure 4.20 Gain of the spot beams produced by two arrays of square high-efficiency step horns and square pyramidal horns. Peak gain = 40.2 dBi for both arrays. Number of elements in the high-efficiency horn array = 100; number of elements for the pyramidal horn array is 121. Aperture size of each element is 3λ, —— 100 high-efficiency step horn array, ----121 pyramidal horn array. (©2004 IEEE [21].)

modal-based analysis [34]. The numerical results reveal that the aperture efficiency of an isolated high-efficiency horn of aperture size greater than 3λ does not differ significantly from that in an infinite array environment. The difference was within 1.5% only for horns with 3–4.5λ aperture dimensions. Furthermore, using the methodology presented by Bird [29], the embedded element gain for the center element of a 3 × 3 element array differs by 0.1 dB only from an isolated element gain. Thus, two independent approaches confirm that the mutual coupling can be ignored for those cases considered.

4.7.2 In Multiple-Beam Reflectors

A second important application of the high-efficiency horn lies in satellite multiple-beam reflector antennas. A typical example is shown in Figure 4.21. The continental United States is divided in a number of hexagonal cells that share the total available frequency spectrum. The azimuth-elevation angular view shown in the figure is from the satellite geo-stationary orbital location. The antenna produces multiple beams to cover these cells. Following a four-cell reuse scheme, one of the frequency channels (A, B, C, or D in Figure 4.21) is assigned to each beam in an arrangement that maintains a minimum spacing between two cells of identical frequency and polarization. This arrangement reduces the RF interference between users located in different cells of the same channel frequency.

The antenna system consists of four-reflector apertures with a single feed per beam [35]. The four-aperture design allows increasing the feed aperture size by a factor of 2 compared to a single reflector design, improving significantly the spill-over efficiency of the reflector antenna. In this example, the beams carrying channel A are produced by the reflector a fed by 12 feeds.

To show the advantage of the high-efficiency horn, the co-polar gain and the co-polar isolation of the beams were computed using Potter horn feeds and

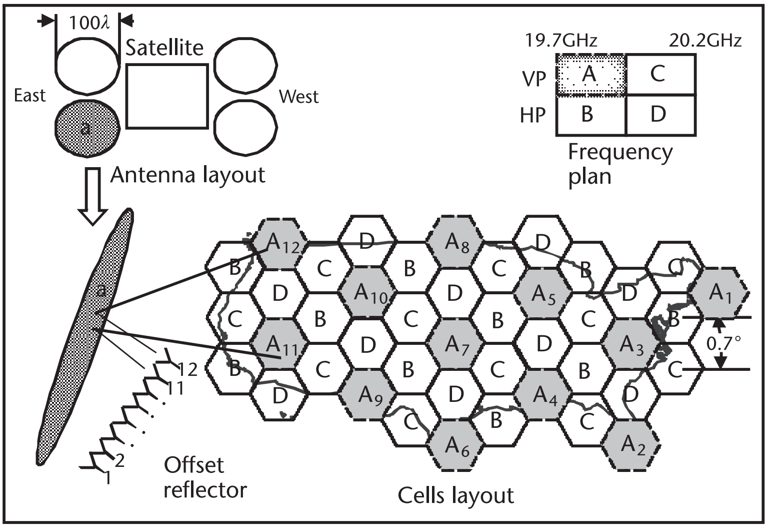

Figure 4.21 Hexagonal beam layout for a four-cell frequency reuse scheme implemented on a four-reflector multiple-beam antenna system.

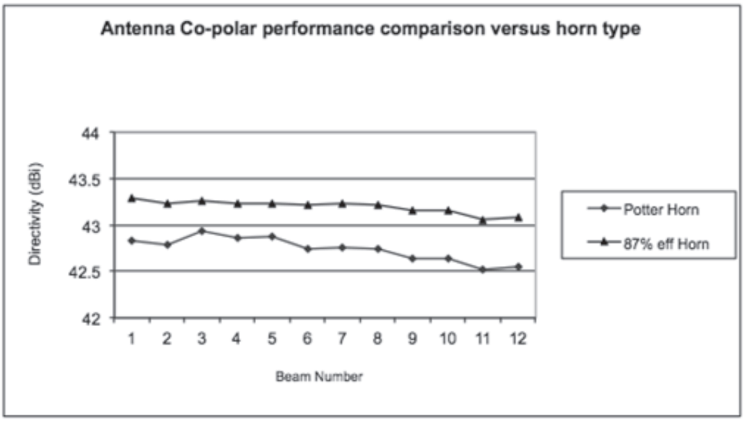

Figure 4.22 Minimum directivity performance comparison between horn types for channel-A beams. (©2004 IEEE [21].)

high-efficiency horn feeds with 87% aperture efficiency. The antenna performance was computed using physical optics reflector analysis software. The primary feed patterns were computed using the moment method analysis [27] and were fed to the antenna analysis software through a numerical data file.

The co-polar performance of the beams using channel-A is shown in Figure 4.22. The plot shows the minimum directivity over each cell. The result shows that the high-efficiency horn feeds improve the directivity of about 0.5 dB over Potter horn feeds. This improvement is primarily due to the larger edge taper of the reflector caused by the high-efficiency feed patterns. A large edge taper of the reflector results in a flat top type of beam, improving the directivity in the edge-of-coverage region.

Using the definition of co-polar isolation [35], the worst case co-polar isolation for each antenna beam was plotted in Figure 4.23. A high-efficiency horn feed improves the isolation by 2.5 dB compared with a Potter horn feed. In the interference calculation, contributions from the A-beams were considered only. In this case also, the increased edge taper of the reflector created by the high-efficiency horn feed

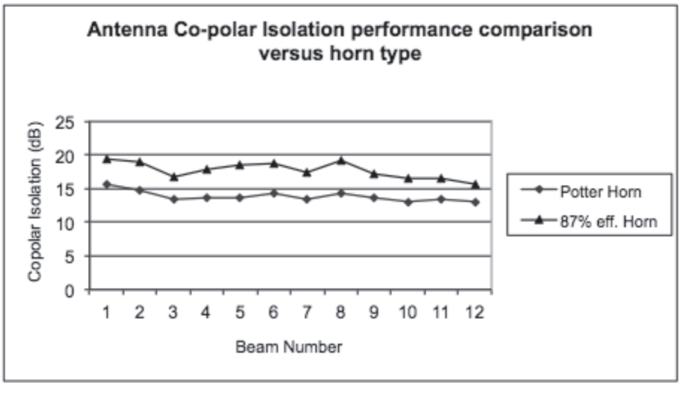

Figure 4.23 Minimum co-polar isolation performance comparison between horn types for channel-A beams. (©2004 IEEE [21].)

resulted in low sidelobes in the secondary pattern; hence the beam-to-beam co-polar isolation improved significantly.

It is worth mentioning that the horn efficiency value needed to optimize a multibeam antenna performance generally depends on many parameters, including the antenna geometry, the beam layout, and the frequency reuse scheme. In some cases, the highest horn efficiency does not produce the optimum antenna performance, and an intermediary horn efficiency value may be preferred. The modal contents at the aperture of the high-efficiency horn can be slightly perturbed to generate the desired aperture efficiency value while maintaining a good cross-polar performance.

4.8 Conclusions

We presented multimode high-efficiency horn antenna structures for aperture efficiency over 90%. The principle of operation of such a horn radiator was presented, and the design procedures of circular and square horns were outlined. The return loss, aperture efficiency, cross-polarization, and bandwidth characteristics were studied with respect to the horn aperture dimension. It was found that a circular high-efficiency horn has a better cross-polar performance than that of a square high-efficiency horn. Between step-and-flared and multiflared structures, the former showed somewhat wider bandwidth with respect to a moderate efficiency requirement. For narrow band operation, step-and-flared structure showed enhanced efficiency performance. Since the steps provide additional flexibilities to a multiflared structure, a step-horn will always show improved performance compared to that of a flared-horn. For some scenarios, this improvement could be substantial. The proposed high-efficiency horns have potential applications in phased arrays and multiple-beam reflectors. It was found that in phased arrays, high-efficiency horn elements reduce the element counts as much as 30% for a desired array gain. In the multiple-beam reflector under consideration, a high-efficiency horn feed showed 0.5 dB more gain and 2.5 dB beam isolation improvement as compared with a Potter horn feed.

References

[1] Love, A.W., *Electromagnetic Horn Antennas*, New York: IEEE Press, 1976.

[2] Olver, A. D., P. J. B. Clarricoats, and A. A. Kishk, et al., “Microwave Horns and Feeds,” *IEE Electromagnetic Wave Series* 39, 1994.

[3] Silver, S. (ed.), *Microwave Antenna Theory and Design*, New York: McGraw Hill, 1949.

[4] Balanis, C. A., *Antenna Theory Analysis and Design*, New York: John Wiley & Sons, 1982.

[5] Mailloux, R. J., *Phased Array Antenna Handbook*, Norwood, MA: Artech House, 1994.

[6] Love, A. W., *Reflector Antennas* (edited book), New York: IEEE Press, 1978.

[7] Potter, P. D., “A New Horn Antenna with Suppressed Sidelobes and Equal Beamwidths,” *Microwave Journal*, Vol. VI, June 1963, pp. 71–78.

[8] Jakes, W. C., “Horn Antennas.” In *Antenna Engineering Handbook*, H. Jasik (ed.), New York: McGraw Hill, 1961.

[9] Han, C. C., and A. N. Wickert, “A New Multimode Rectangular Horn Antenna Generating a Circularly Polarized Elliptical Beam,” *IEEE Trans. on Antennas and Propagation*, Vol. AP-22, Nov. 1974, pp. 746–751.

[10] Tsandoulas, G. N., and W. D. Fitzgerald, "Aperture Efficiency Enhancement in Dielectrically Loaded Horns," *IEEE Trans. on Antennas and Propagation*, Vol. AP-20, Jan. 1972, pp. 69–74.

[11] Baldwin, R., and P. A. McInnes, "Radiation Patterns of Dielectric Loaded Rectangular Horns," *IEEE Trans. on Antennas and Propagation*, Vol. AP-21, May 1973, pp. 375–376.

[12] Cherrette, A., R. Parrikar, and T. Smith, "High Efficiency Dual Polarized Horn Antenna," U.S. Patent Number 6,211,838, February 2000.

[13] Clénet, M., and L. Shafai, "Gain Enhancement of Conical Horn by Introducing Bodies of Revolution Inside the Horn," *Proc. IEEE APS International Symposium*, 1998, pp. 1718–1721.

[14] Lier, E., "Hard Waveguide Feeds with Circular Symmetry for Aperture Efficiency Enhancement," *Electronic Letters*, Vol. 24, No. 3, Feb. 4, 1988 pp. 166–167.

[15] Skoblev, S. P., and P.-S. Kildal, "Design of a Dual-Polarized Horn Antenna with Very High Aperture Efficiency by Using PBG Hard Surface Walls," *ESTEC Antenna Workshop*, May 2001.

[16] Kishk, A. A., and M. Morgan, "Analysis of Circular Waveguides with Soft and Hard Surfaces Realized by Strips Loaded Walls Using Asymptotic Boundary Conditions," *Microwave and Optical Technology Letters*, Vol. 29, No. 6, June 2001, pp. 433–436.

[17] Skobelev, S., and P.-S. Kildal, "Influence of Hard Corrugated PBG Wall Design on Performance of Conical Horn Antenna," *Microwave and Optical Technology Letters*, Vol. 32, No. 5, February 2002.

[18] Skobelev, S., and P.-S. Kildal, "Some features of hard strip loaded conical horn antenna," *Proc. of IEE, MAP*, Vol. 150, No. 3, June 2003, pp. 171–176.

[19] Bhattacharyya, A. K., and G. Goyette, "Multi-step Circular Horn Systems," U.S. Patent 6,384,795, May 7, 2002.

[20] Bhattacharyya, A. K., and G. Goyette, "Step-Horn Antenna with High Aperture Efficiency and Low Cross-polarization," *Electronics Letters*, Vol. 38, No. 24, Nov. 21, 2002, pp. 1495–1496.

[21] Bhattacharyya, A. K., and G. Goyette, "A Novel Horn Radiator with High Aperture Efficiency and Low Cross-polarization and Applications in Arrays and Multibeam Reflector Antennas," *IEEE Trans. on Antennas and Propagation*, Vol. AP-52, No. 11, Nov. 2004, pp. 2850–2859.

[22] Collin, R. E., *Field Theory of Guided Waves*, New York: IEEE Press, 1990.

[23] Harrington, R. F., *Time-Harmonic Electromagnetic Fields*, Chap. 3, New York: McGraw Hill, 1961.

[24] Abramowitz, M., and I. A. Stegun (ed.), *Handbook of Mathematical Functions*, National Bureau of Standards, Applied Math. Series 55, Dec. 1972.

[25] Spiegel, M. R., *Vector Analysis*, Schaum's Outline Series, New York: McGraw-Hill, 1959.

[26] Marcuvitz, N., *Waveguide Handbook*, New York: Dover Publications, 1965.

[27] Bhattacharyya, A. K., "Multimode Moment Method Formulation for Waveguide Discontinuities," *IEEE Trans. on Antennas and Propagation*, Vol. AP-42, No. 9, Aug. 1994, pp. 1567–1571.

[28] Bhattacharyya, A. K., and D. H. Roper, "High Radiation Efficient Dual Band Feed Horn," U.S. Patent 6,642,900, Nov. 4, 2003.

[29] Bird, T. S., "Mode Matching Analysis of Stepped Rectangular Horns and Application to Satellite Antenna Design," *Proc. IEE Conference, Antennas and Propagation, ICAP*, April 1991, pp. 849–852.

[30] Bhattacharyya, A. K., and J. Sor, "Multiple Flared Horn Antenna with Enhanced Aperture Efficiency," U.S. Patent 7,183,991, Feb. 27, 2007.

[31] Bird, T. S., and C. Granet, "Optimization of Profiles of Rectangular Horns for High Efficiency," *IEEE Trans. on Antennas and Propagation*, Vol. AP-55, No. 9, Sept. 2007, pp. 2480–2488.

[32] Chan, K. K., and S. K. Rao, "Design of High Efficiency Circular Horn Feeds for Multibeam Reflector Applications," *IEEE Trans. on Antennas and Propagation*, Vol. AP-56, No. 1, Jan. 2008, pp. 253–258.

[33] Ruggerini, G., "A Compact Circular Horn with High Efficiency," *Proc. Fourth European Conference, EuCAP* 2010.

[34] Bhattacharyya, A. K., *Phased Array Antennas: Floquet Analysis, Synthesis, BFNs and Active Array Systems*, New York: John Wiley & Sons, 2006.

[35] Rao, S. K., "Design and Analysis of Multiple-Beam Reflector Antennas," *IEEE Antennas and Propagation Magazine*, Vol. 41, No.4, August 1999.

CHAPTER 5

Profiled Horns and Feeds

Trevor S. Bird, Principal Antengenuity, & CSIRO Fellow
Christophe Granet, BAE Systems Australia

5.1 Introduction

Horns are required to give the desired illumination and to minimize extraneous reflections and sidelobes [1–5] when used as feeds for classical unshaped or shaped reflector systems, or as direct radiators. These horn properties are especially desirable in some applications such as for shaped beams from satellites that require the edge-of-coverage gain maximized or in radio astronomy and satellite ground terminals where spurious sidelobes result in increased noise and interference. In addition, frequently, high aperture efficiency is desirable for individual feeds as well as for the reflector itself. In array feeds, for instance, the aperture sizes of the horns are usually small enough to ensure array grating lobes are not a problem, to satisfy beam spacing needs and to meet edge illumination requirements as well as to fit within the limited space in the focal region of the reflector, and often meet demands of a high efficiency over the operating frequency band. In some applications, such as on-board satellites, the array elements should also be as short as possible to minimize ohmic loss and weight. To meet these and other performance objectives, the walls of the horn and its lengthwise profile have been modified from a simple linear taper. Some common examples of horn profiles are illustrated in Figure 5.1. Conventional changes to the profile include steps and dielectric inserts and more recently profiled smooth-wall and corrugated circular horns [5–8] have been used. Other horns include multimode horns [9], partially dielectric-loaded horns [3, 10, 11], and high-efficiency horns, such as the scrimphorn [12].

With the advent of high-speed computer processing and accurate general analysis methods, it has become feasible to meet specific performance objectives in design. The most common types of horn in use today have circular and rectangular cross-section geometries, but these are not the only types available for high performance. Other cross sections employed include elliptical and polygonal shapes. Typical performance objectives for horn design include input reflection coefficient and aperture efficiency as well as sidelobe levels, maximum cross-polarization, and reflector edge illumination. The intention of profiling is to excite modes in the aperture with amplitudes and phases that meet the performance objectives. Profiling can be undertaken manually, as it has in the past, or automatically, as it is possible today. In this chapter, we outline ways of carrying out the latter approach and give some examples.

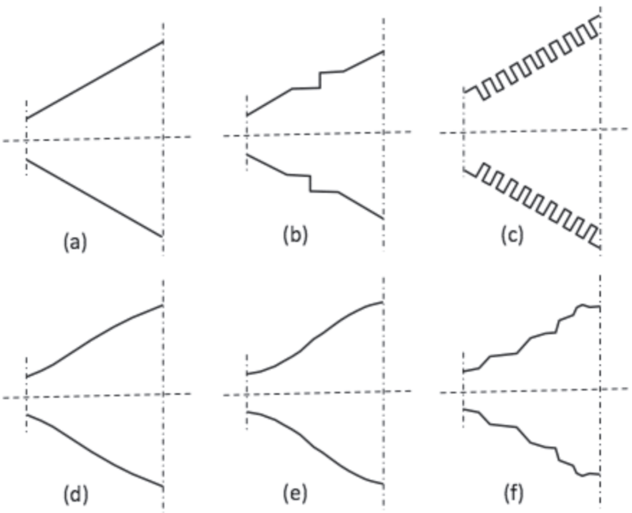

Figure 5.1 Examples of horn profiles: (a) linear, (b) stepped, (c) corrugated, (d) sine-squared, (e) Gaussian, and (f) general.

Several methods have been adopted in the past to create a feed horn that meets all specifications. The most common approach, and historically the first one, was to vary the linear taper angle of the horn from the input exciter, usually a waveguide section where only a few modes can propagate, to a larger diameter where many modes contribute to the radiation pattern. A variation of this approach was to adopt several different tapers along the path [13] (see Figure 5.1). Apart from linear tapers, several alternative empirical profiles have been employed successfully such as sine-squared [13,14] and Gaussian [15] that give relatively broadband performance and a bowl-shaped profile [16] that provides low sidelobes over a narrow 5% bandwidth. Another approach is to introduce steps along the inside of the horn, where the steps and lengths between sections are chosen so that the modes arrive in the desired amplitude and phase relationship. As well as steps, uniform and linearly tapered sections have been used [9] to produce horns with high efficiency.

With automatic computer-based methods, it has now become feasible to design horns of general cross section with a nonintuitive profile that allows specific system objectives to be achieved on efficiency, directivity, radiation pattern shape, reflector edge illumination, or sidelobe levels. The 3 dB beamwidth of an individual aperture is usually constrained within certain limits by the physical dimensions of the aperture as well as the mode content, but in an array configuration further variations are possible due to the excitation strategy and mutual coupling. This chapter describes some possible approaches in an array and some results achieved so far. Before doing this, we will discuss the physical limits that bound the possibilities provided by optimization of the profile and of profiled horns in general.

5.2 Basis of Optimum Horns

The design of horns to achieve optimum performance has been attempted in many different ways. The horn profile is only one option. Other options include the linear flare [17], aperture shape [18], and flange additions from chokes [3] to curved or nonplanar surfaces [19]. While selecting these options, there are system performance measures that need to be addressed. These include factors such as directivity (and aperture efficiency), input return loss, beamwidth, sidelobes, phase center and environmental factors such as operation in a vacuum, or physical limitations imposed by the application. Each of these aspects will now be considered.

5.2.1 Pattern Constraints

The field radiated by a horn of arbitrary cross section has a general distribution on a hypothetical surrounding spherical surface that has no planes of symmetry. The resulting radiation power pattern can be represented diagrammatically by a three-dimensional plot or by several planar cuts. Fortunately, most horns in common use are either axisymmetric or have only two planes of symmetry. In both instances, pattern cuts in three planes are usually sufficient to fully describe the radiation pattern. With these planar cuts, as well as orthogonal pattern cuts for the dual polarizations, the radiated field can be fully represented. Taking into consideration the co-polar and cross-polar patterns, it is possible to apply constraints on the radiation pattern of the horn during the design process. This is similar to the implementation of constraints such as for the design of shaped beam patterns with reflectors using an array feed [20]. It is usual to implement these feed pattern constraints in the three planes in both co-polar and cross-polar directions. Figure 5.2 shows typical constraints on the co-polar and cross-polar pattern cuts. Upper and lower bounds are often applied on the co-polar pattern. On the cross-polar pattern, there is usually only an upper

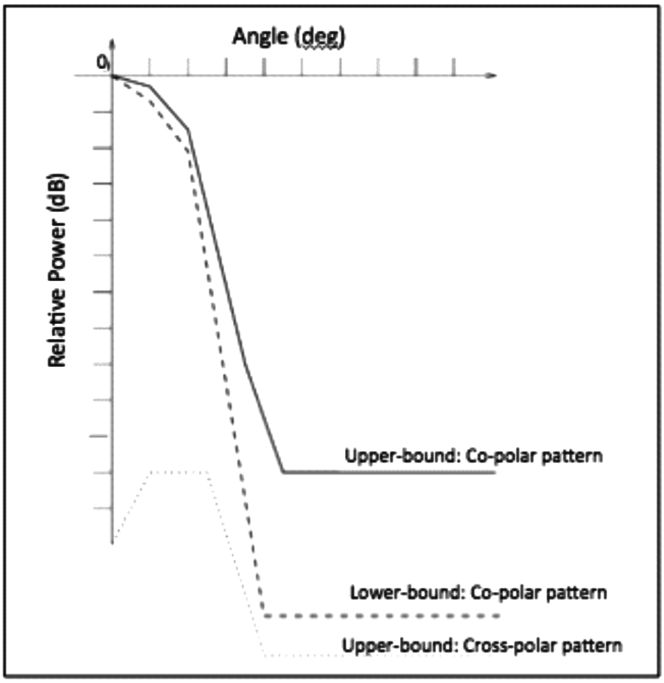

Figure 5.2 Radiation pattern envelope constraints.

bound as shown. For a reflector application, the level of the bounds on the primary feed pattern is usually determined from the secondary pattern requirements of the reflector such as the edge illumination, spill-over, or peak cross-polarization. Each type of reflector system has its own physical limitations and requirements that need to be included in the specifications. For example, concerning cross-polarization in an axisymmetric parabolic reflector, the peak level, for linear polarization applications, is given in the 45° plane, and the corresponding peak for the horn feed is typically +4 dB above that of the requirement of the overall secondary pattern.

5.2.2 Input Mismatch

The input reflection is determined by discontinuities along the length of the horn in combination with reflection from the aperture. Additionally it will be impacted by any reflection from the nearby secondary system, such as a reflector or lens. Frequently, the horn return loss is measured in isolation in an anechoic environment so that its performance is known independently before installation as a feed. The bandwidth of the horn is usually given by the input reflection coefficient. Whether the horn is simple linear, profiled, or corrugated, any perturbations on the walls or the interior due to imperfect manufacturing or extraneous objects contribute further to the return loss. In some environments, if the performance allows, a radome is placed over the aperture to ensure dry surfaces, and any oxidation does not increase the reflection level over time. The base level of reflection can be controlled by the design of the horn profile, and this is included in the automatic procedure described in Section 5.4. The reflection coefficient is usually specified and constrained by an upper bound only in the same way as for the cross-polar pattern in Figure 5.2.

5.2.3 Aperture Efficiency

In some applications a feed with high aperture efficiency is desired. The aperture efficiency of a horn antenna is defined as the ratio of the effective aperture area and the physical area and is equivalent to the ratio of the horn gain to that of a uniformly illuminated aperture, which is $4\pi A/\lambda^2$, where A is the aperture area and λ is the wavelength at the operating frequency. It was shown by Silver [1] that close to maximum gain is produced with a uniform aperture field. This led to an approach of exciting the modes in the aperture of a horn with amplitudes that approximated a uniform aperture distribution. However, as pointed out by Silver [1], the assumption of a high efficiency with a uniform aperture distribution is strictly true only for a constant phase distribution as well. The study of high efficiency horns commenced in the 1940s with aspects of this work reported by Silver [1] and Jakes [2], where the TE_{10} and TE_{30} modes are used in the aperture of a box horn. An increased efficiency over a single mode was reported with high-order mode amplitude of about 35%. A rectangular horn operating in only the TE_{10} mode has a maximum aperture efficiency of 81%, but with several high-order modes, higher efficiency can be obtained. In general, uniform aperture amplitude is obtained with TE_{n0} modes of amplitude $1/n$, where n is odd [21]. In addition, the present authors [22] achieved high efficiency with rectangular horns by profiling. Other examples, with square waveguide sections, for dual polarization, are shown [23–25]. Multiple mode circular horns have also been developed by Love [26], Potter [27], and Koch [28]. More recently Bhattacharyya and Goyette [9] and also Ruggerini [29] obtained circular horns with higher aperture efficiency.

Maximum aperture efficiency is found by maximizing the gain relative to the physical area of the aperture. Bouwkamp and de Bruijn [30] and later Riblet [31] showed that there is no theoretical limit to the related quantity, directivity, for a linear antenna of any given size, if the current distribution is unconstrained. This could lead to efficiencies close to and in excess of 100%. Such high efficiencies for horns imply no infringement of physical limits as it indicates only that the effective radiating aperture is greater than the physical area. A gain greater than that produced by a uniform aperture distribution is called a supergain. This topic has been discussed in the past by many workers [4, 32], usually in connection with two-dimensional arrays. For a horn, an aperture distribution can be synthesized by exciting and phasing the modes between the input and the aperture, although there is less flexibility in aperture synthesis for horns than for arrays, because individual modes have to be excited with correct amplitude and phase. Nonetheless, it is useful to consider what aperture efficiency might be achievable under certain practical constraints. In the design of individual horns, there are some other basic physical limits that cannot be exceeded through design variations. These are related to the size of the aperture and the aperture configuration and are limited by physical diffraction and the currents on the aperture walls and the aperture flange. For arrays there is the added complication of mutual coupling between modes at the aperture and in adjacent apertures. However, there are means of including this in an analysis. We will assume that the horn is excited by an input probe or a waveguide section where several modes can propagate. The horn aperture efficiency in the direction (θ_{m}, ϕ_{m}) is defined as [1]

$$\eta_a = \frac{\lambda^2}{4\pi A} G(\theta_m, \phi_m) \tag{5.1}$$

where G is the gain function given by

$$G(\theta, \phi) = \frac{4\pi r^2 \, P(\theta, \phi)}{P_T} \tag{5.2}$$

$P(\theta,\phi) = \frac{1}{2}\Re e\left\{(\mathbf{E}_f \times \mathbf{H}_f^*) \cdot \hat{r}\right\}$ is the radial Poynting vector in the direction (θ,ϕ) and $P_T = \frac{1}{2}\Re e\left\{\iint_A (\mathbf{E}_a \times \mathbf{H}_a^*) \cdot \hat{z}\, dS'\right\}$ is the total radiated power. $\mathbf{E}_f$ and $\mathbf{H}_f = Y_o\, \hat{r} \times \mathbf{E}_f$ are the electric and magnetic far fields of the horn, $\hat{r}$ is the unit vector along the radial direction, $\Re e\{x\}$ refers to the real part of x, and Y_o is the wave admittance of free space while $\mathbf{E}_a$ and $\mathbf{H}_a$ are the aperture fields of the horn. When all field quantities are expressed in terms of the fundamental modes, the expression for aperture efficiency takes the form [22]:

$$\eta_a = \frac{(\underline{\mathbf{x}}^\dagger \, \underline{\mathbf{c}}^\dagger)(\underline{\mathbf{c}}\, \underline{\mathbf{x}})}{\underline{\mathbf{x}}^\dagger \, \underline{\mathbf{x}}} \tag{5.3}$$

where $\underline{\boldsymbol{x}}$ is related to the unknown input mode excitation coefficients, $\underline{\mathbf{c}} = \underline{\mathbf{t}}^{T}\left(\underline{\underline{\mathbf{U}}} + \underline{\underline{\mathbf{S}}}^{(0)}\right)\underline{\underline{\mathbf{D}}}^{-1/2}$ wherein $\underline{\underline{\mathbf{D}}} = \left(\underline{\underline{\mathbf{I}}} - \underline{\underline{\mathbf{S}}}^{(0)\,\dagger}\,\underline{\underline{\mathbf{S}}}^{(0)}\right)$, $\underline{\underline{\mathbf{S}}}^{(0)}$ is the scattering matrix of the aperture, and the elements of the vector $\underline{\mathbf{t}}$ are:

$$t_p = \sqrt{\tfrac{Y_o}{2}}\, Y_p^{-1/2} \sqrt{\left|F_{xp}(0,0)\right|^2 + \left|F_{yp}(0,0)\right|^2} \tag{5.4}$$

where $F_{xp}(u,v) = \dfrac{1}{\sqrt{A}} \iint_{\Sigma} e_{xp}(x',y') \exp\left(j2\pi(ux'+vy')\right) dx'dy'$ is the Fourier transform of the electric field component x or y of mode p in the aperture field. The functions $u = \sin\theta \cos\phi/\lambda$ and $v = \sin\theta \sin\phi/\lambda$ are the variables of u–v space and Σ is the cross section of the array element in the aperture supporting the modes. The superscripts T and † indicate the matrix transpose and conjugate transpose operations, $\underline{\underline{\mathbf{I}}}$ is the unit matrix, and Y_{p} is the mode admittance and equals γ_{p}/k for TE modes and $\varepsilon_{\mathrm{r}}k/\gamma_{\mathrm{p}}$ for TM modes where γ_{p} is the propagation constant of mode p and $k = 2\pi/\lambda$.

The solution for the maximum of (5.3) is well known and is $\eta_{a\max} = \underline{\mathbf{c}}\,\underline{\mathbf{c}}^{\dagger}$, when $\underline{\mathbf{x}}_{\max} = \underline{\mathbf{c}}^{\dagger}$. That is, the general expression for maximum aperture efficiency is given by [22]:

$$\eta_{a\max} = \underline{\mathbf{t}}^{T}\left(\underline{\underline{\mathbf{I}}} + \underline{\underline{\mathbf{S}}}^{(0)}\right)\underline{\underline{\mathbf{D}}}^{-1}\left(\underline{\underline{\mathbf{I}}} + \underline{\underline{\mathbf{S}}}^{(0)}\right)^{\dagger} \underline{\mathbf{t}}^{\dagger} \tag{5.5}$$

Without loss of generality, it is assumed here that the maximum radiated field occurs on axis; that is, when $u = 0 = v$. The scattering matrix of the aperture $\underline{\underline{\mathbf{S}}}^{(0)}$ may include one or more subapertures as well as a number of modes. In the ideal case of no reflection from the aperture or there is no coupling between modes in adjacent apertures, then $\underline{\underline{\mathbf{S}}}^{(0)} = 0$ and as a result (5.5) simplifies to $\eta_{a\max} = \underline{\mathbf{t}}^{T}\,\underline{\mathbf{t}}^{\dagger}$ with $\underline{\mathbf{x}}_{\max} = \underline{\mathbf{t}}^{\dagger}$ where $\underline{\mathbf{t}}^{\dagger}$ is defined by (5.4). In this simplified case, as indicated by (5.4), the maximum aperture efficiency depends only on the geometry of the aperture and the modes that have been excited. The maximum aperture efficiency in the ideal case has been evaluated for circular, rectangular, coaxial, and elliptical aperture shapes for incident fundamental modes, and the asymptotic results for the first three cross sections are listed in Table 5.1 [22, 33].

In Table 5.1, N is the largest integer satisfying $\alpha_{\mathrm{mN}} < ka$, and the indices n or p run over the N modes above cut-off. Note that the summation for each efficiency in Table 5.1 is only over the TE modes. This demonstrates that TM modes do not contribute to the efficiency, as pointed out originally by Bhattacharyya and Goyette [9].

It is emphasised that the expressions in Table 5.1 are asymptotic expressions for large N and have been simplified by the omission of the wave admittance term in (5.2), which is related to the scaling of $\underline{\underline{\mathbf{S}}}^{(0)}$ and is close to unity except near mode cut-off, in order to show the trend as the number of modes increases. The actual situation as described by (5.1) is that modes couple at all apertures. This results in a series of maxima above the underlying efficiency curve given approximately by the expressions listed in Table 5.1. The maxima occur in the vicinity of the mode cut-off frequencies and can have levels exceeding 100% over a range of frequencies. This leads to the possibility of horn designs where efficiencies can exceed or approach 100% for part of their operating range as demonstrated [22].

Table 5.1 Maximum Aperture Efficiency for Various Geometries

Geometry Type	*Maximum Efficiency*
Circular	$\eta_{a\max} \sim \varepsilon_{0m}\sum_{n=1}^{N}\frac{1}{\left(\alpha_{mn}^2 - m^2\right)} => \left(\frac{1}{8\left(2-\varepsilon_{0m}\right)+m}\right) \quad as \quad N\to\infty$ $\alpha_{\mathrm{mn}} = k_{\mathrm{mn}}a$ where k_{mn} is the cut-off wave number of the TE mode mn
Rectangular	$\eta_{a\max} \approx \frac{8}{\pi^2}\sum_{n=1,3,..}^{N}\frac{1}{n^2} => 1 \quad as \quad N\to\infty$
Circular Coaxial	$\eta_{a\max} \sim \frac{\varepsilon_{0m}}{\left(1-c^2\right)}\sum_{p=1}^{N}\frac{(1-W(\alpha_{mn},\beta_{mn},c))^2}{((\alpha_{mn}^2-m^2)-W^2(\alpha_{mn},\beta_{mn},c)(\alpha_{mn}^2-(m/c)^2)}$ $W(\alpha_{mn},\beta_{mn},c) = c\frac{Z_m(\beta_{mn},\beta_{mn})}{Z_m(\alpha_{mn},\beta_{mn})},\ Z_p(x,y) = J_p(x) - \frac{J_p'(y)}{Y_p'(y)}Y_p(x),\ \ c = b\ /\ a,$ $\alpha_{\mathrm{mn}} = k_{\mathrm{mn}}a$ and $\beta_{\mathrm{mn}} = k_{\mathrm{mn}}b$ where k_{mn} is the cut-off wave number of TE mode mn and $Z_m'(\alpha_{mn},\beta_{mn}) = 0,\ \varepsilon_{0m} = 1$ when $m = 0$ and is 2 otherwise.

The aperture efficiency expressions given in Table 5.1 confirm that a rectangular aperture supporting only the TE_{10} mode has a maximum value of 81%, and for a circular or coaxial aperture with the TE_{11} mode only ($m = 1$) excited has a maximum of 100%. Higher efficiencies are physically possible over narrow bandwidths by exciting more than the fundamental mode and, in the present context, through design of the horn profile. With higher cut-off modes only in the aperture, such as only the axisymmetric TE modes ($m = 0$) or the double periodic TE modes ($m = 2$), the efficiency limits to a lower value. For the axisymmetric modes the limit is 12.5%, while for double periodic modes it is 50%. Another way to achieve high efficiency is with dielectric loading. Horns with dielectric loading have been used to give aperture efficiencies approaching 100% [10], although in some applications weight and materials properties, particularly outgassing and ohmic losses, become additional considerations especially in space-borne applications.

Small aperture horns, with sidelength or diameter less than one wavelength, are known to give high aperture efficiencies. This is due to combined effects of aperture reflection and significant currents on the surrounding flange [3]. In these and other applications, the length of either conventional or dual-mode horns is relatively long due to the use of linear tapers from the waveguide input to the waveguide step to excite the TE_{30} mode. Stepping or profiling can be used to reduce the length of these tapers (see Section 5.5.5).

5.2.4 Phase Center Stability

The phase center of the horn at any given frequency is determined mainly by the size of the aperture, the profile slope immediately inside the horn—the flatter the slope the better, and the mode content. For a reflector antenna with a fixed focal point, the horn phase center should be as constant as possible over the required frequency band while achieving the desired illumination. For operation over moderate or wide bandwidths, it is important to ensure that the horn pattern is stable and does not vary significantly with frequency. If it does, the apparent phase center also moves forward or back, causing loss of efficiency and aberrations. The best way to ensure there is stability is to have a stable co-polar pattern, which often means that the main modes contributing to the radiation pattern are well above cut-off. This means a slightly larger aperture may need to be adopted that is consistent with other requirements. The phase center can be obtained from measurement or from numerically obtained data.

One approach is to estimate the phase center from the two-dimensional discrete patterns using the method of least squares [34]. In the p^{th} azimuth plane, ϕ_p the phase center for a symmetric structure is approximated by [5, 35]

$$k d_p = (b_1 - a_1 b_0)/(a_2 - a_1^2) \tag{5.6}$$

where $k = 2\pi/\lambda$, $a_q = \left(\sum_{i=1}^{M} \cos^q \theta_i \right)/M$ and $b_q = \left(\sum_{i=1}^{M} \Phi(\theta_i, \phi_p) \cos^q \theta_i \right)/M$ with $q =$ 0,1,2, θ_i is angle i (= 1,…M) in the n^{th} pattern cut through ϕ_p, which is symmetric about boresight, M is the number of angular directions in the pattern, and $\Phi(\theta_i,\phi_p)$ is a continuous (unwrapped) phase function expressed in radians. The calculation is illustrated in Figure 5.3. An improved estimate of phase center is obtained by averaging several pattern cuts (p = 1,…, NP):

$$d_{pc} = \sum_{p=1}^{NP} d_p / NP \tag{5.7}$$

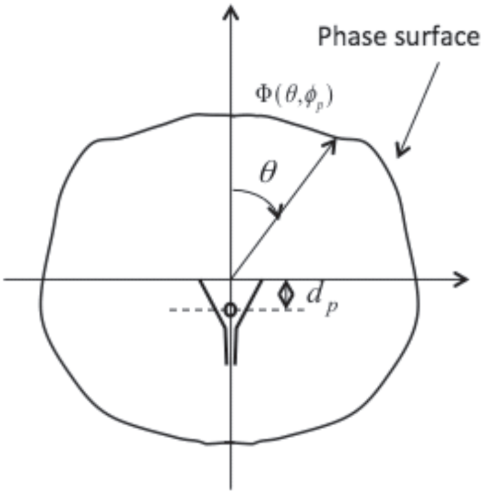

Figure 5.3 Phase center calculation in plane *p*.

The simplest estimate corresponds to a single cut ($NP = 1$). A better estimate is to average the phase centers of the two principal plane patterns ($NP = 2$). With circularly symmetrical feeds, an average of the two principal planes plus the intercardinal plane (45° and 135°) phase centers ($NP = 4$) is usually sufficiently accurate for most purposes. When the phase is uniform, (5.6) gives $kd_p = 0$ as expected. Also, (5.6) is invariant to integer multiples of 2π in Φ. Finally, (5.6) can be easily adapted to continuous functions by converting the summations to integrals and M over the subtended angle.

When (5.6) and (5.7) are used to determine the apparent phase center of a horn feeding a reflector, the angular range (and hence M) should encompass the opening angle of the reflector from the focus. For example, if a horn feeds a subreflector with a subtended angle of 20°, and the data for the feed pattern and phase is over a wider range, only the data for the angles subtended by the reflector should be used. For example, consider the main reflector subtending an angle of 72°, and the feed horn has a symmetric quadratic phase error of $+/-\theta^2$, which is typical of a flared horn. The phase center calculated from (5.6) over only a 20° range is $-/+ 0.344\lambda$, while for the subtended main reflector range the phase center is estimated to be $-/+ 0.356\lambda$. This difference is small, but it would lead to overall lower gain and filling of sidelobe nulls. Both calculations demonstrate that with an increasing phase from boresight, the phase center is inside the horn, while with decreasing phase from boresight the phase center is outside the aperture.

The phase center could also be included in the optimization process. This could be undertaken directly such as bounding it with a maximum radius or indirectly through another parameter such as beamwidth, whose range is limited over the frequency band, realizing that indirectly this will tend to make the phase center spread smaller.

The phase center is frequency dependent, and it is necessary to define an overall phase-center position for a given frequency band sampled over N discrete frequencies ($f_1, f_2, \ldots, f_N$). Let $f_{\min}$ be the minimum frequency in this frequency band. The frequency dependent phase-center position is defined at each frequency as given by (5.7), namely ($d_{pc}(f_1), d_{pc}(f_2), \ldots, d_{pc}(f_N)$). These estimates are used to define the overall phase center as:

$$D_{pc} = \sum_{i=1}^{N} d_{pc}(f_i)\left[1 + \sqrt{f_i - f_{\min}}\right] / \sum_{i=1}^{N}\left[1 + \sqrt{f_i - f_{\min}}\right] \tag{5.8}$$

From practice, this overall phase center position calculation has been shown to be a good compromise. Equation (5.8) shows that if the phase function does not vary greatly from one frequency to the next, then the overall phase center is stable.

5.2.5 Compactness and/or Physical Constraint Due to Existing Environment

In some reflector installations, there is limited space in the vicinity of the focus for installation of the feed horn and the associated feed system. For example, it is conventional, in radio astronomy installations, to have a focal cabin where several feed systems are mounted close to the focus before being moved into position. In other applications, such as for space flight, it is important that the horn weight is minimized. In these and other situations it is useful to have a horn design available that is compact and has a moderate to short length, without compromising performance. In some designs, the length can be one of the criteria in the optimization. There are several ways of doing this. Lengths, diameters, or number of horn sections can be optimized through a combination of manual and automatic means. For instance, the horn length could be set initially and the other parameters established automatically. The horn length could be altered and the design re-performed. The results from one computer run to the next are then compared. Usually there is a compromise between compactness and other parameters such as return loss. If the performance is acceptable at some specified length, a new, shorter length can be tried and the process repeated. This is continued until all parameters are acceptable for the application.

Regarding the horn weight, even with a compact horn, for further weight reduction it may be necessary to employ lightweight materials [36, 37]. Horns made in this way can usually be designed by the same methods as for fully metallic ones. For example, the corrugated bowl-shaped horn shown in Figure 5.4 was designed by conventional mode matching software [16]. It was manufactured from carbon fiber with a composite supporting shell that, fortunately, did not require much change to the original design [36]. However, in some cases, this may not be possible, such as when a full metallic seal cannot be achieved at the bottom of corrugations but only at spot welds. In such instances, it is important to have an analysis software package that is capable of taking into account the actual horn geometry. When this software package is linked to the automatic optimization method (to be described in Section 5.4), a profiled horn can still be designed to meet performance objectives as well as being physically realizable. Acceptable upper and lower bounds should be placed on the length of the horn in an automatic process to help control the optimization procedure.

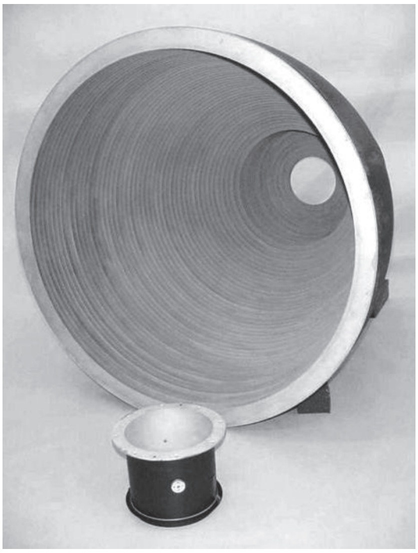

Figure 5.4 Bowl-shaped horn with low sidelobes. The exciter unit for two crossed dipole probes is shown in foreground (photo courtesy of COI).

5.3 Choice of Horn Profiles

This section describes how, by profiling, many of the conflicting demands of horn design can be satisfied. The theory provided in the previous section allowed us to make observations about the design of high-performance feeds and sets the scene for profiled horns. Such a horn is represented diagrammatically in Figure 5.5. The modes incident on the aperture can be excited individually, as originally described by Cohn [38], for example, or through design of the mode converter section, which is essentially the approach used here. In the next section, we describe a numerical optimization of the profile(s) of a horn to design the mode converter to achieve the highest efficiency possible over a specified frequency band. In addition, the aim is to reduce the length of the taper from the waveguide input; that is, achieve compactness. Results are given in Section 5.5 for a variety of profiled horns that meet additional constraints than imposed in Section 5.2.

The objectives described in Section 5.2 can be implemented in several different ways. The traditional approach is through a series of steps in the horn. The approach to be outlined here uses a smooth profile. In the traditional approach, the steps are chosen to achieve the appropriate phase transition of the modes from an earlier section to the next and also to arrive at the terminating aperture with the desired amplitude and phase. In this approach conventional mode matching can be used [3, 21]. In summary, this method is based on a number of usually uniform waveguide sections. If $\underline{\mathbf{a}}^{(i)}$ and $\underline{\mathbf{b}}^{(i)}$ are the incident and reflected waves from a uniform section i of the horn where $\underline{\mathbf{a}}^{(i)}$, $\underline{\mathbf{b}}^{(i)}$ are column vectors and $\underline{\mathbf{b}}^{(i)} = \underline{\underline{\mathbf{S}}}^{(i)}\,\underline{\mathbf{a}}^{(i)}$, then if the horn has N stepped sections, the amplitude of the modes in the aperture are

$$\begin{aligned} \underline{\mathbf{A}}^{e} &= \underline{\mathbf{a}}^{(N)} + \underline{\mathbf{a}}^{(N)} \\ \underline{\mathbf{A}}^{b} &= \underline{\mathbf{a}}^{(N)} - \underline{\mathbf{b}}^{(N)} \end{aligned} \tag{5.9}$$

The final horn section feeds into the aperture model, which couples modes of related properties, for example, with odd order azimuthal indices. Overall, the reflected

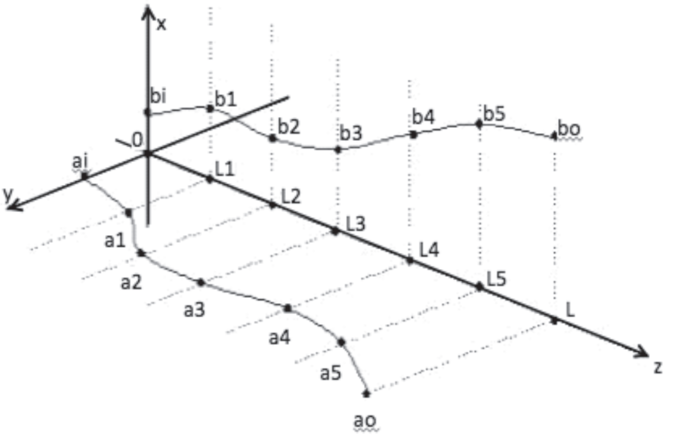

Figure 5.5 Horn profiles represented in two symmetry planes.

modes are related to the incident modes via the scattering matrix for the aperture $\underline{\underline{\mathbf{S}}}^{(0)}$ as follows: $\underline{\mathbf{b}}_O = \underline{\underline{\mathbf{S}}}^{(0)}\ \underline{\mathbf{a}}_O$ where $\underline{\mathbf{a}}_O = \underline{\mathbf{b}}^{(N)}$ and $\underline{\mathbf{b}}_O = \underline{\mathbf{a}}^{(N)}$.

A similar analysis applies for a profiled horn, except that there are usually many more sections and the resulting profile is almost continuous. The advantage of adopting a smooth profile for analysis is that the steps are small, usually $< \lambda/10$, and the modes are only partially reflected at each discontinuity. To simplify and speed up the optimization, a perturbation approach could be used to calculate the scattering matrices as described in Section 5.5.4.

5.4 Optimization of Horn Profile

5.4.1 Possible Approaches

There are basically two ways to approach profiling of a horn. One is to use known empirical curves, and the other one is to somehow generate a profile that is controlled by a set of parameters that can be manipulated automatically.

5.4.1.1 Empirical Profiles

There is a small set of empirical profiles that have been used in the past. The empirical curves were used mainly when the available computer power was not sufficiently fast to analyze the performance of the horn. A summary of these profiles was provided [39] but is repeated here for convenience.

We consider circularly symmetric horns with an input radius a_i, an output radius a_o, and a length L, as shown in Figure 5.6. In some of the profile options, we use the parameter p, the power of the function used for the profile, that is, "sin," "tan," and so on, which can take any value from 0 to ∞. In the literature, it is common to use $p = 2$ only. Experimenting with different values of p for a profile is very effective in radiation pattern shaping, especially with respect to the sidelobe and cross-polarization levels. The choice of the profile will depend on the particular application.

We now summarize the most common empirical profiles available to the horn designer [3, 13, 15, 19]:

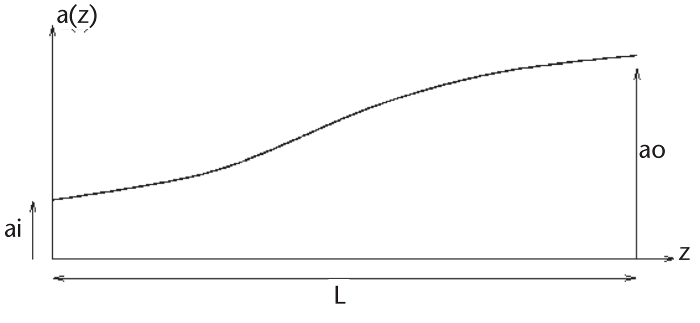

Figure 5.6 Typical horn profile.

$$\text{Linear Profile: } a(z) = a_i + (a_o - a_i)\frac{z}{L} \tag{5.10}$$

$$\text{Sinusoid Profile: } a(z) = a_i + (a_o - a_i)\left[(1 - A)\frac{z}{L} + A\sin^p\left(\frac{\pi z}{2L}\right)\right] \tag{5. 11}$$

$$\text{Tangential profile: } a(z) = a_i + (a_o - a_i)\left[(1 - A)\frac{z}{L} + A\tan^p\left(\frac{\pi z}{4L}\right)\right] \tag{5. 12}$$

$$x^p\text{-profile: } a(z) = a_i + (a_o - a_i)\left[(1 - A)\frac{z}{L} + A\left(\frac{z}{L}\right)^p\right] \tag{5. 13}$$

$$\text{Exponential profile: } a(z) = a_i \exp\left(\ln\left(\frac{a_o}{a_i}\right)\frac{z}{L}\right) \tag{5.14}$$

$$\text{Gaussian or Hyperbolic profile: } a(z) = \sqrt{a_i^2 + \frac{z^2\left(a_o^2 - a_i^2\right)}{L^2}} \tag{5.15}$$

$$\text{Polynomial profile: } a(z) = a_i + (p + 1)\left(a_o - a_i\right)\left(1 - \frac{pz}{(p + 1)L}\right)\left(\frac{z}{L}\right)^p \tag{5.16}$$

Asymmetric sine-squared profile:

$$a(z) = a_i + \frac{2\left(a_o - a_i\right)}{1 + \gamma}\sin^2\left(\frac{\pi z}{4L_1}\right) \text{ for } 0 \le z \le L_1 \tag{5.17a}$$

$$a(z) = a_i + \frac{2\left(a_o - a_i\right)}{1 + \gamma}\left[\gamma\sin^2\left(\frac{\pi\left(z + L_2 - L_1\right)}{4L_2}\right) + \frac{1 - \gamma}{2}\right] \text{ for } L_1 \le z \le L \tag{5.17b}$$

where $L = L_1 + L_2$ and $\gamma = \frac{L_2}{L_1}$ and $A \in [0;1]$ in (5.11–5.13).

Various antenna groups around the globe have also worked on combinations of such profiles; notably at the CSIRO (Australia), where Thomas and Greene [19] have used a linear profile followed by a spherical profile; and also Granet, Bird, and James [16], where a linear-profiled step is followed by a sine-power function; at the Queen Mary University of London (UK), multiple linear sections [40] have been adopted; at the University of Navarra (Spain) [15, 41], Gaussian profiles have been cascaded; and at the University of Florence (Italy) [42, 43], sine-squared and exponential profiles have been combined together.

5.4.1.2 Parametric Profiles

A parametric profile is fully represented by a mathematical curve with a small number of parameters. Some of the empirical profiles presented in the previous section fit this definition, by, for example, optimizing the power of the profile [44], but they are limited in the number of parameters that can be optimized. The authors, however, use these empirical profiles as a good starting point for further profile optimization as explained.

The majority of circular horns and also rectangular horns, smooth-walled, corrugated or dielectrically loaded, are analyzed using the mode-matching technique [3, 21] as outlined in Section 5.3. Considering the fact that the horn is approximated by a series of circular steps, some corrugated horns have been optimized based on varying the radius and length of each and every one of the circular steps under the control of an optimizer for a given penalty function [45, 46]. Although effective, this method requires either significant computing power or a long design phase. A variant of this method was used in [47], where a smooth-walled horn was optimized to provide the desired radiation pattern by allowing each section to have its radius and length optimized. A cubic spline was then fitted to the points defining the sections to provide a so-called serpentine-profile.

When the authors were investigating ways to optimize the profile of a horn by minimizing the number of optimization parameters to speed up the design process, a method of spline-profile optimization was devised that is loosely based on Deguchi, Tsuji, and Shigesuwa [47], and this method has proven very successful. It is summarized in Figure 5.7. The optimization of corrugated or smooth-walled spline-profile horns [6, 7], for example, allows the horn designer to limit the number of parameters to be optimized. Only a few points, or nodes, are used along the length of the horn to generate the profile. A cubic spline is then generated through these nodes to define the profile of the horn. The nodes are the parameters that are optimized by the design procedure. This minimizes a penalty function, taking into account user-defined performance indicators for the given application, for example, combinations of return loss, cross-polarization level, directivity, sidelobes, beamwidth, and so on.

The basic representation of the spline-profile optimization technique is shown in Figure 5.7, where the profile is described by an input radius (a_i), an output radius (a_o), and six intermediate nodes (a_1 to a_6) located at various distances from the input of the horn (L_1 to L_6, usually fixed values). The optimization procedure takes as input the radii (a_1 to a_6) as well as a_o and applies the geometry constraints, (d_1 to d_6 and d_o, which are usually fixed values, to minimize the searchable parameter-space and take into account the mechanical constraints of the application. Note that

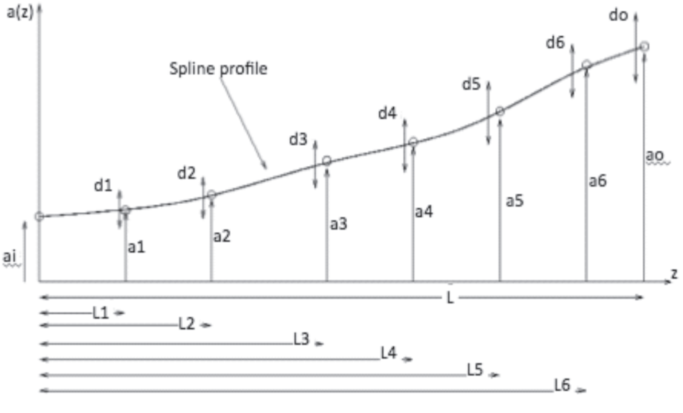

Figure 5.7 Spline-profile horn geometry and parameters.

the example shown in Figure 5.7 has seven parameters, but the authors and other researchers have optimized horns with fewer nodes, and also up to 17 nodes to define the spline-profile. A full explanation of the algorithm is provided in [7]. Note that this technique is now used by a number of horn designers [48–52], but note that in Lucci et al. [48], a NURB is used instead of a spline, but the technique is equivalent. This technique has also been included in commercial software packages, CHAMP from TICRA [91] and the Microwave Wizard from Mician [92].

Another method, pioneered in the 1970s [38], but now improved and used by a number of horn designers, is to have a multisectional profile of linear segments for which lengths and angular slopes can be optimized. This method has been used to design either smooth-walled or corrugated horns [38, 40, 53–56].

5.4.2 Optimization Methods

There are a wide variety of multivariable optimization methods that could be used in the present application to satisfy the various requirements. These methods may be constrained or unconstrained and global, for example, Genetic Algorithm, Simulated Annealing, Particle Swarm Optimization, and Differential Evolution, or local, such as Gradient Search, Steepest Descent, and others [57–60].

Know-how is needed in the use of these methods, however, to ensure a quick convergence of the design, by allowing sufficient parameters to be optimized, and, more importantly, to be able to tailor the penalty function to be minimized to the specifications of the application. An approach to optimization of the horn profile is illustrated in Figure 5.8.

A penalty function to be used in optimization can be constructed to take into account the N discrete frequencies of interest for the application (f_1, f_2, …, f_N) and apply associated weights (w_1, w_2, …, w_N) that can be used by the designer to favor selected frequencies in the performance. Another important parameter will also be a return-loss target at each frequency (RLT_1, RLT_2, …, RLT_N) (note that return loss is a positive quantity), a cross-polarization pattern target at each frequency ($XPT(1, \theta)$, $XPT(2,\theta)$, …, $XPT(N,\theta)$), and a radiation pattern target in either relative power, normalized to 0 dB or in dBi. The radiation pattern target is usually defined, for each frequency, as a set of lower and upper bounds at given θ angles with $0 \leq \theta \leq \theta_{Max}$, ($LB(1,\theta)$, $LB(2,\theta)$, …, $LB(N,\theta)$), and ($UB(1,\theta)$, $UB(2,\theta)$, …, $UB(N,\theta)$) [6, 7]. A typical radiation pattern envelope is shown in Figure 5.2.

A possible penalty function to be minimized sums up the different non-compliant contributions, that is, when the calculated value for the current geometry at a given frequency exceeds the target value specified for the design at this frequency. For example, a penalty function constructed in Fortran 2008 language is as follows:

```
$SumRL = 0$: The contribution due to the return loss non-compliance
$SumXpol = 0$: The contribution due to the cross-polarization non-compliance
$SumSL = 0$: The contribution due to the radiation pattern non-compliance
For $i = 1:N$
  Freq = frequency (i)
  Analyze the horn at Freq
```

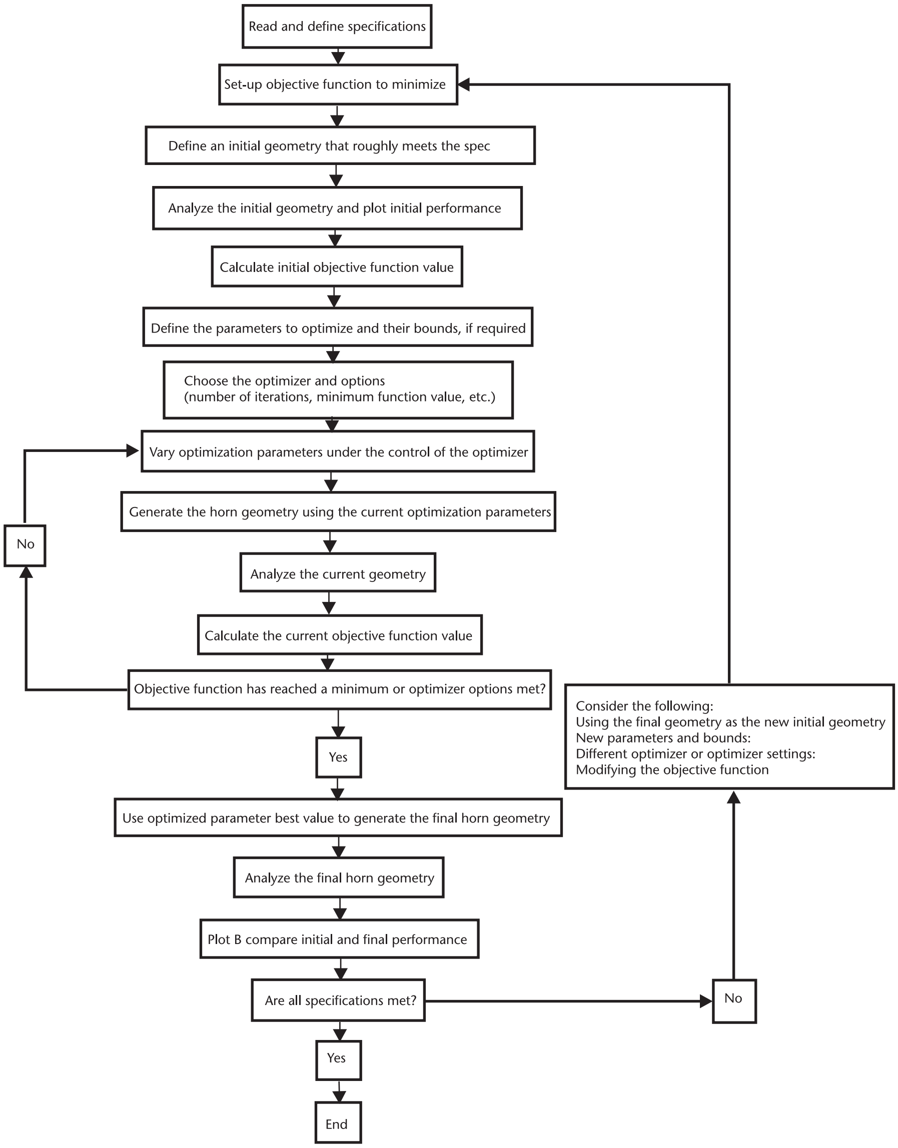
Read and define specifications
Set-up objective function to minimize
Define an initial geometry that roughly meets the spec
Analyze the initial geometry and plot initial performance
Calculate initial objective function value
Define the parameters to optimize and their bounds, if required
Choose the optimizer and options
(number of iterations, minimum function value, etc.)
Vary optimization parameters under the control of the optimizer
Generate the horn geometry using the current optimization parameters
No
Analyze the current geometry
Calculate the current objective function value
Objective function has reached a minimum or optimizer options met?
Yes
Consider the following:
Using the final geometry as the new initial geometry
New parameters and bounds:
Different optimizer or optimizer settings:
Modifying the objective function
Use optimized parameter best value to generate the final horn geometry
Analyze the final horn geometry
Plot B compare initial and final performance
Are all specifications met?
No
Yes
End

Figure 5.8 Basic flow graph of horn profile optimization.

```
If $(RL(i) < RLT(i))$
    $SumRL = SumRL + w_i \left(RLT(i) - RL(i)\right)^{N_{RL}}$
EndIf
For $\theta = 1{:}\ \theta_{\mathrm{Max}}$
 If $(PatternCoPolar(i,\theta) < LB(i,\theta))$
    $SumSL = SumSL + w_i \left(LB(i,\theta) - PatternCoPolar(i,\theta)\right)^{N_{SL}}$
EndIf
 If $(PatternCoPolar(i,\theta) > UB(i,\theta))$
```

```
      $SumSL = SumSL + w_i\left(PatternCoPolar(i,\theta) - UB(i,\theta)\right)^{N_{SL}}$
    EndIf
    If $(PatternCrossPolar(i,\theta) > XPT(i,\theta))$
      $SumXpol = SumXpol + w_i\left(PatternCrossPolar(i,\theta) - XPT(i,\theta)\right)^{N_{XP}}$
    EndIf
    EndTheta
  EndFor
  $ObjectiveFunction = SumRL + SumSL + SumXpol$
```

The optimizer is then set to minimize the *ObjectiveFunction* value.

Note that the indices N_{SL}, N_{RL}, and N_{xp} can be specified by the user to weight the different contributions of sidelobe, return loss, or cross–polar level, respectively.

Other contributions can be added to this simple objective function, for example, the phase center. It is good practice to record the different contributions to keep track of what the optimizer improves the most or the least, given the parameters currently optimized. By these means, the horn designer determines the various impacts on the performance and therefore can influence the selection of different optimization weights. Some other examples of objective functions are found in Jamnejad and Hoorfar [45] and Lucci et al. [61].

It is very important to have a good starting point for the optimization, as this will reduce the search-time of the optimizer and therefore will result in a shorter design phase. Keeping a database of older designs, such as design approaches [37, 62, 63] and configurations available from the open literature that can be scaled or modified to suit a new requirement is very important to ensure the optimization process starts with a geometry that has a good chance of success in meeting the performance requirements.

The authors favor constrained local optimization methods over the global methods in the present application because, in our experience, they provide a good compromise between design-time and realized performance. The reason for constraining the parameters, that is, providing the optimizer with a minimum and maximum value for each parameter, is to ensure the final design meets the mechanical constraints of the application, as well as minimizing the search-space of the optimizer. However, a number of designs have been successfully optimized using global optimizers (for examples, refer to [45, 49, 54, 61]). Combinations of different optimizers at various steps of the design phase can also prove valuable. If, for example, you do not have a good starting point, it is good practice to use a global optimizer to generate a reasonable starting solution and then use a local optimizer to further improve that solution.

5.5 Examples of Horn Designs

Some examples of profiled horn design are provided in this section. This selection is by no means complete for new designs are produced all the time. However, those described here give a sample of the power of profile optimization for feed applications.

5.5.1 Corrugated Horn

In one particular design [6], manual profile optimization was used by the authors originally to shorten the length of low-frequency horns at L-band in order to minimize the horn's weight and, therefore, the cost of the system. Initial work on a more automatic method of profiling was directed at designing compact, low sidelobe corrugated horns [6] to operate over the 10.70–12.75 GHz band. For this application, an initial corrugated horn design was produced with length of 680 mm. Through optimization, the length was gradually shortened after several cycles to arrive at an acceptable length that was 25% shorter. This new horn had 125 corrugations compared to 165 in the original design, and importantly it had a similar performance.

Since then, profiling has also been used to improve the cross-polarization performance as well as sidelobe levels of corrugated horns [15, 16, 41], and particularly horn designs employing the empirical profiles described in Section 5.4.1.1.

Profiling is also used widely to optimize the radiation pattern of a horn over two or multiple separated receive and transmit bands for satellite applications, both on-board and terrestrial [64–66].

Although a Gaussian-type radiation pattern is desirable in many reflector feed instances, some applications may be better addressed by a horn exhibiting sectoral-pattern behavior, [67–70].

5.5.2 Smooth-Walled Circular and Coaxial Horns

One of the advantages of smooth-walled horns is that they are easier to manufacture and are lighter weight than corrugated horns, they can work over a reasonably wide bandwidth, but they cannot achieve low cross-polarization performance over as wide a band as a corrugated horn.

The ease of manufacture is a big advantage for high-frequency applications greater than 60 GHz and into the THz region, where the manufacture of corrugated horn is extremely difficult and costly.

Another advantage of smooth-walled horn is in array applications, where they can be packed more closely than corrugated horns because the overall diameter, for a given aperture size, is smaller by about half a wavelength.

A large number of designs for high-frequency operations have now been reported, for example ≈100 GHz [7], ≈300 GHz [71], ≈700 GHz [56] and ≈840 GHz [72].

As in the case of corrugated horns, smooth-walled horns can be optimized for multiband applications, for instance C-band [73], Ku-band [49], and Ka-band [74, 75]. The overall length for a given diameter horn can also be controlled, which is important for applications where weight or compactness are required. Smooth-walled horns have also been optimized to provide high efficiency [29, 33, 53].

Additionally, adoption of a central conductor in a coaxial horn can provide an extra parameter with which to design and to provide wide beamwidths for deep dishes ($f/D < 0.35$) [5, 76] or for mechanical support as in self-supporting feeds [5]. Coaxial horns generally have higher reflection coefficient, wider beamwidth, and higher cross-polarization over a narrower bandwidth than an equivalent unfilled circular horn. Profiling can help to improve the performance of all properties.

The maximum gain that can be obtained with circular and coaxial horns was described in Section 5.2. This indicates efficiencies of the order of 100% are possible under conditions of modest requirements on sidelobes and cross-polarization. An example of what can be achieved is now provided for an application in Ku-band that required a short, lightweight horn with a −16 dB edge illumination at 35° from boresight. The minimum first sidelobe required was ≤ −20 dB, and the maximum cross-polar level was ≤ −30 dB below the peak. A high efficiency was also desired.

The method outlined in Section 5.4 was used to meet the specified sidelobe and cross-polar levels and also a high efficiency.

A circular horn with a 2λ aperture diameter was designed with these properties to operate over the frequency range 11.7–12.2 GHz [33]. The simplified theory described in Section 5.2 predicts a maximum efficiency of 100%. With an optimized profile, even though there were constraints on the patterns and input reflection coefficient, the predicted aperture efficiency at the center frequency was still able to achieve a value of 97%. The fabricated horn is shown in Figure 5.9. The measured return loss is >25 dB across the band, while the measured efficiency is greater than 95% (see Table 5.2). The length of the horn is 80 mm (3.2λ) and is significantly shorter than similar horns with linear profiles, which are typically twice as long for a similar bandwidth, higher sidelobe levels, and lower aperture efficiency. The profile, shown in Figure 5.10, contains several damped oscillations along its length, with peak-to-peak amplitude varying by about 8 mm.

The principal plane radiation patterns and gain were measured. The measured and computed gain is compared in Table 5.2 at several frequencies in the band, while the measured and computed radiation patterns at 11.95 GHz are shown in Figure 5.11. There is excellent agreement between the computed results from mode-matching

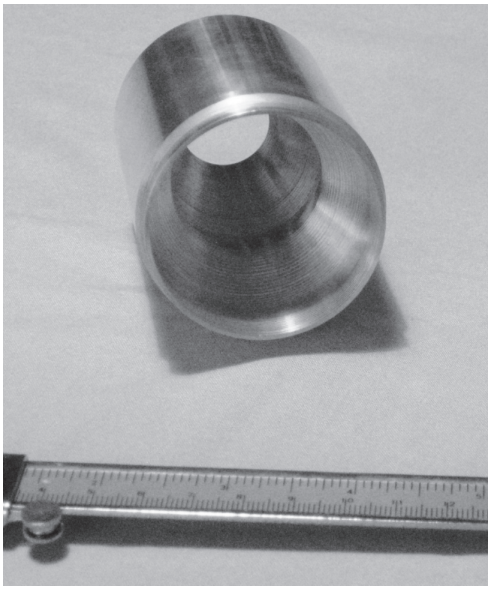

Figure 5.9 Fabricated Ku-band profiled circular horn.

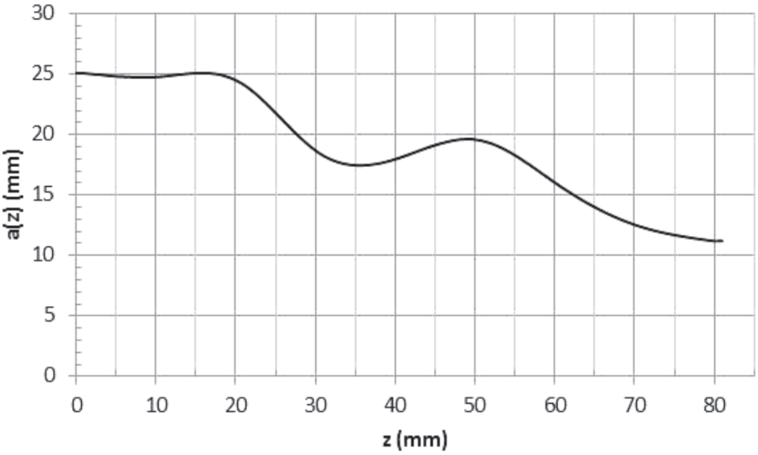

Figure 5.10 Profile of circular horn.

Table 5.2 Measured and Computed Gain of Profiled Circular Horn

Frequency (GHz)	*Computed Gain (MWS) dBi*	*Expt. Gain dBi*	*Expt. Efficiency %*
11.7	15.51	15.46 ± 0.3	96.4
11.95	15.72	15.56 ± 0.3	95.5
12.2	15.95	15.78 ± 0.3	95.9

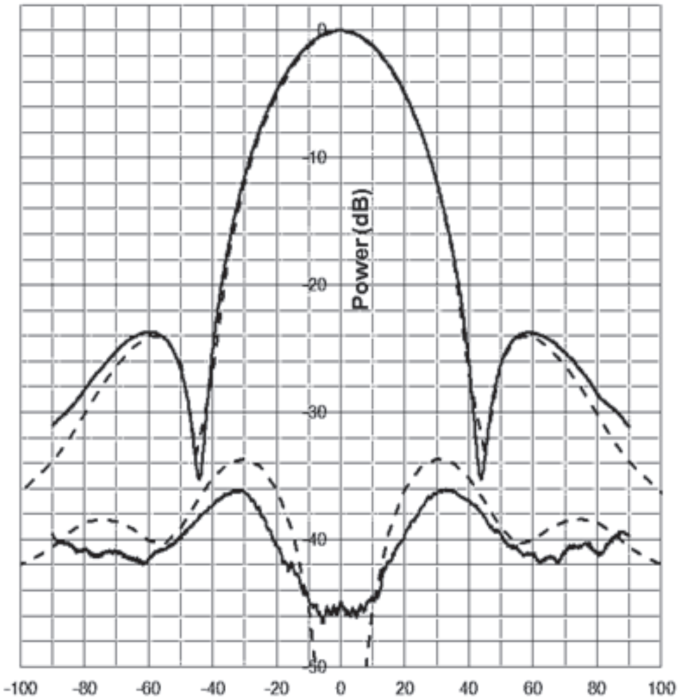

Figure 5.11 Radiation patterns in 45° plane of profiled circular horn at 11.95 GHz; dashed curve: theory; solid curve: measured.

software [77] and CST Microwave Studio (MWS) [93], as well as both measured radiation patterns and gain.

Coaxial horns can be designed using the same approach as employed for the circular horn, except that there are now two profiles to be optimized corresponding to the inner and outer conductors. A set of nodes and cubic splines are required for each profile.

5.5.3 Rectangular Horn

In common with the coaxial horn, two profiles have to be optimized for a rectangular horn; in this case the profiles are in orthogonal planes, as depicted in Figure 5.5. The profiled rectangular horn considered here has been optimized by the method described in Section 5.4 [22]. In this approach, profiled horns were designed with aperture sizes ranging from 1.25 to 3 wavelengths for use as array feeds in the 11.7–12.2 GHz band. The $2\lambda \times 2\lambda$ aperture horn design is shown in Figure 5.12, and the profiles are illustrated in Figure 5.13. The actual aperture distribution in the E-plane of this horn is compared in Figure 5.14 with that of a horn with a conventional $2\lambda \times 2\lambda$ aperture horn with a linear flare. We see that both amplitude and phase for the profiled horn vary across the aperture, and it is these variations that lead to high efficiencies. All horns achieve aperture efficiencies close to 100%, and at the same time have a return loss >20 dB and a cross-polar isolation >22 dB. The radiation pattern in the 45° plane of the horn at 11.95 GHz is shown in Figure 5.15. The measured aperture efficiency at this frequency was 101.1% [22]. The total length of the $2\lambda \times 2\lambda$ aperture horn is 3.2λ at 11.95 GHz, and as with the profiled circular horn, its profile undulates in amplitude along its length that reduces toward the aperture, as may be seen in Figure 5.13.

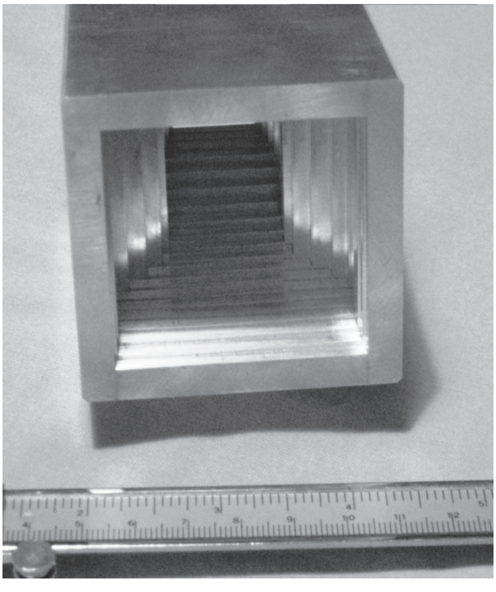

Figure 5.12 A profiled rectangular horn with high efficiency and low sidelobes.

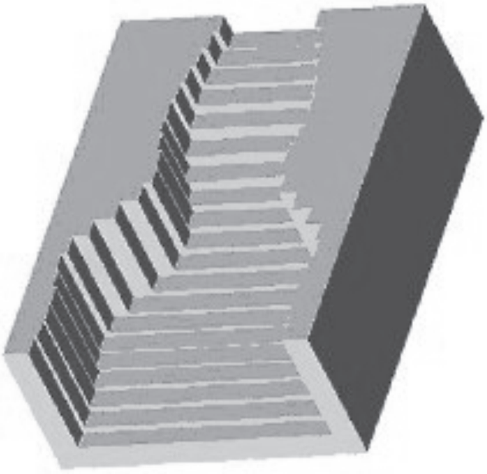

Figure 5.13 Rectangular horn profiles.

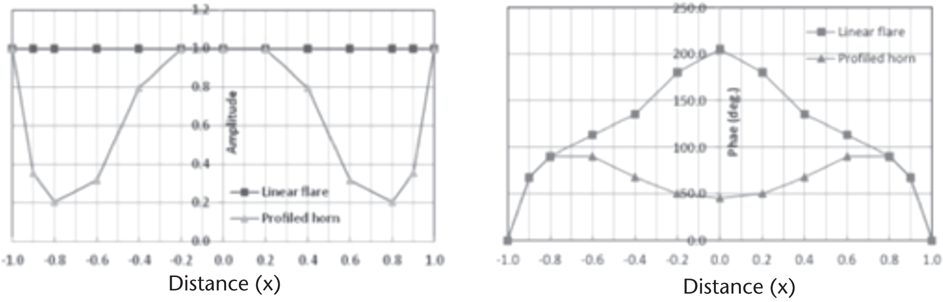

(a) (b)

Figure 5.14 Aperture distribution in the E-plane of $2\lambda \times 2\lambda$ aperture rectangular horn (a) amplitude and (b) phase.

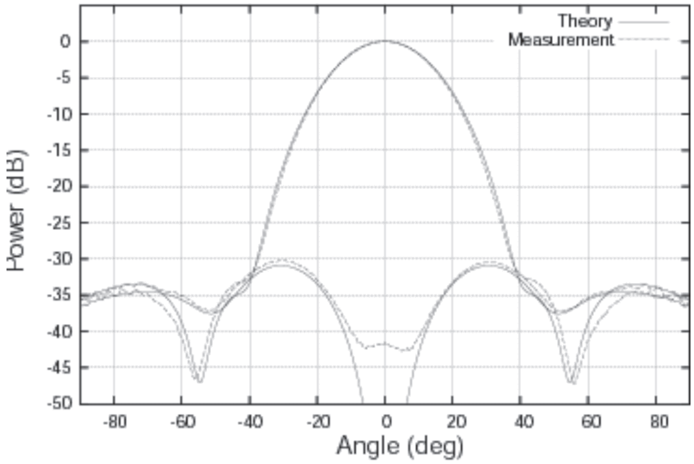

Figure 5.15 Measured and computed radiation pattern of spline-profile smooth-walled rectangular horn in the 45° plane at 11.95 GHz.

5.5.4 Dielectric Rod and Horn

The dielectric rod antenna may be preferred as a feed for some millimeter-wave and THz frequencies due to the potential of low insertion loss. In the design of such antennas, the relationship between the radiation pattern and the profile has been discussed by several authors, including, Zucker [78] and Ando et al. [79]. There are design guidelines for achieving specific radiation pattern objectives, such as maximum gain and minimum sidelobes [78]. However, in general, the optimum rod profile for a given radiation pattern is difficult to determine by analytic means.

Dielectric rod antennas have in the past been designed using the discontinuity radiation concept [78], in which the antenna is treated as a linear array of effective sources arising from the radiation at discontinuities experienced by the surface wave traveling along the antenna as well as a contribution from the feed radiation not converted into the surface wave by the exciting feed. The total radiated field is the sum of all these sources.

To produce maximum gain on boresight, the usual approach is to gently taper the dielectric rod profile toward its end. This tapering results in a larger starting diameter, which supports a slower surface wave that is more tightly bound to the rod than on smaller rods. This results in a higher excitation efficiency of the surface wave. Additionally, a smaller terminating diameter causes the surface wave to become weakly bound to the rod, and consequently the mode field, typically that of the fundamental HE_{11} mode, expands into the surrounding free–space region and radiates. This increases the size of the effective aperture at the rod termination, leading to an increase of overall gain. Tapering also reduces the difference between the surface wave propagation constant and the free-space propagation constant at the rod termination, minimizing the reflection of the surface wave at the end of the rod. The length of a tapered profile must be sufficient to ensure the appropriate phasing can be maintained between the feed radiation and radiation occurring along the rod profile, and particularly at the rod termination, in order to maximize gain.

Commonly employed rod profile tapers are linear, exponential, and curvilinear [78–80]. Ando et al. [81] demonstrated that high-order curvilinear tapers could be used to minimize the conversion of the surface wave into radiation modes along the length of the rod and hence maximize the amount of the power remaining in the surface wave at the rod termination. The taper also increased the radial extent of the equiphase region at the rod termination due to the surface wave, hence improving the gain.

The profiled horn approach can be applied to dielectric rod antennas as shown by Hanham et al. [82]. Rods with various profiles were created, depending on the constraints applied. Some of these dielectric rod antennas are seen in Figure 5.16. Pictured in Figure 5.16 is a linear profile design (LIN), a dielectric rod designed for a minimum sidelobe level (SL), and another designed for maximum gain (MG2). As an example, Figure 5.17 (solid curve) shows the SL profile design. Significantly, the rod has a slight flare near its termination, and this helps to control the input reflection coefficient. All profiles were designed using an approach similar to that described in Section 5.4, and the radiation patterns were calculated with MWS [93]. For the optimization procedure, a method of moments (MoM) analysis [83, 84] was used. The MoM approach uses an ideal ring slot feed [85] to excite the rod

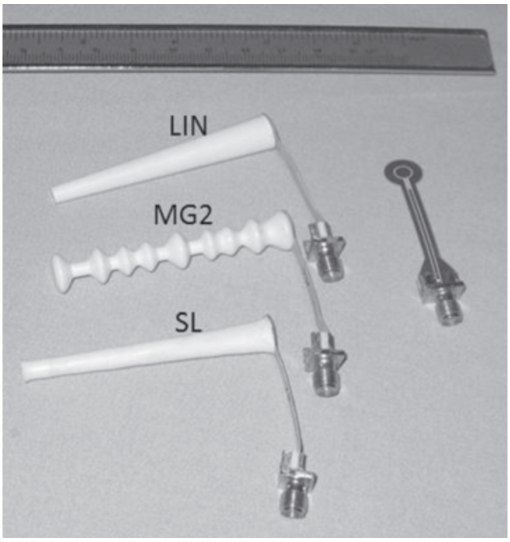

Figure 5.16 Profiled dielectric rod antennas and a ring slot feed input.

while MWS permits both this approximate model and also accurate feed models to be used. The introduction of a ring-slot feed disrupts the rotational symmetry of the structure and modifies the radiation pattern slightly from that predicted by the body of revolution-MoM approach.

The three rod antennas shown in Figure 5.16 were machined from Emerson & Cummings Eccostock HiK rods, with a measured permittivity $\varepsilon_r = 9.74$, using a CNC lathe with a carbide tip tool. The source ring-slot and feed was etched on a 0.010-inch thick, Rogers RT/Duroid 6010 high-frequency laminate with $\varepsilon_r = 10.2$. The feed consists of a coplanar waveguide (CPW) network with a quarter wavelength matching section for the ring slot.

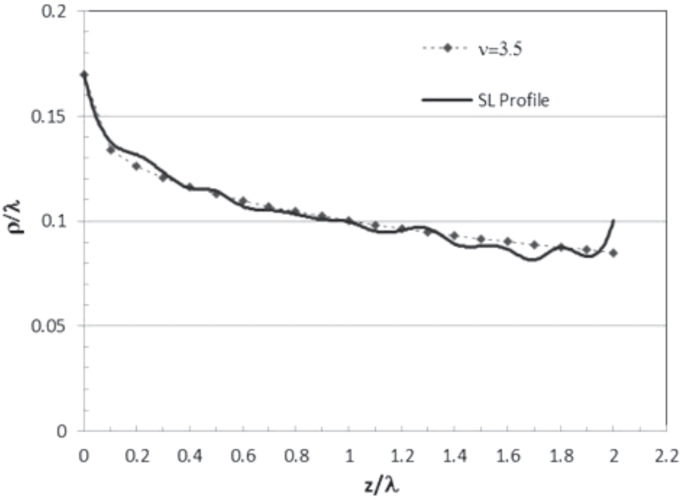

Figure 5.17 Profile of low sidelobe (SL) dielectric rod antenna. ρ is the rod radius and z is the distance along the rod. ν is the index in (5.18).

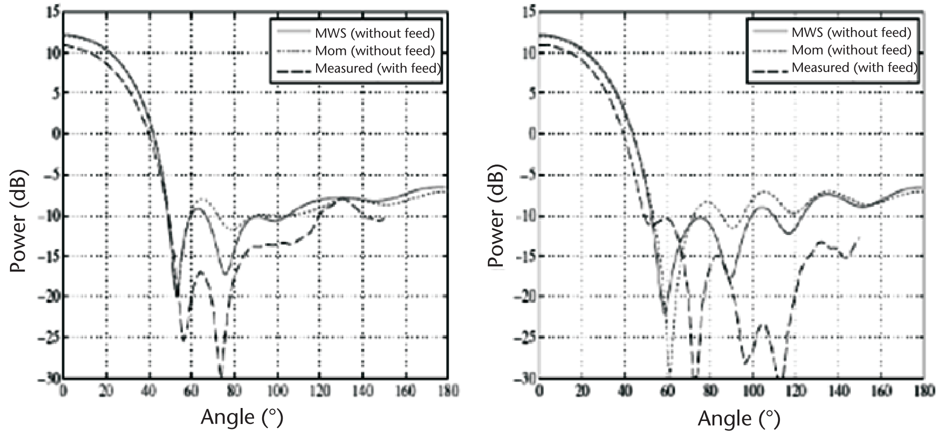

E-plane
(a)

H-plane
(b)

Figure 5.18 Measured and simulated radiation patterns in the principal planes of a dielectric rod antenna (SL) that was designed for low sidelobes. (a) E-plane and (b) H-plane.

The radius of the ring slot was tuned in each case based on simulation to achieve a 10 GHz resonant frequency. The radiation patterns of the three rod antennas were measured, and the results obtained were compared with the computed results in [82] at 10 GHz. A summary of the computed and measured gain results and also the first sidelobe level of the rods is given in Table 5.3; further results may be found in [82]. As an example of the results obtained, Figure 5.18 shows the principal plane patterns for the low sidelobe profile design (SL).

A number of different rod profiles were optimized to achieve low sidelobes. Several designs had oscillatory profiles where the oscillation amplitudes were too small to radiate significant power along the length of the rod. However, the rod profile, which gave the best sidelobe performance over a 10% bandwidth, had an optimized profile that is close to 1/νth-order power curvilinear. That is,

$$\rho(z) = \rho_{start} - (\rho_{start} - \rho_{end})(z/L)^{1/\nu} \tag{5.18}$$

where ρ_{start} and ρ_{end} are the radii of the rod at the feed and termination ends and $\nu > 1$. For the present SL case we see from Figure 5.17 that (5.18) gives a close match to the optimized profile when $\nu = 3.5$ with $\rho_{\text{start}} = 0.17\lambda$ and $\rho_{\text{end}} = 0.085\lambda$ except near the flare at the termination. The ρ_{start} and ρ_{end} values were found from the optimized design and are larger than those suggested by Zucker [78] for a longer $6\lambda_0$ rod antenna with low sidelobes. The expression (5.18) was proposed by Ando et al. [81], who showed that a 1/3 order profile ($\nu = 3$) minimizes radiation along the rod's length, ensuring that the amount of energy reaching the end is maximized. This leads to an inherently broadband design because the pattern is almost entirely determined by the radiation from the rod termination rather than the summation of multiple radiation points along the rod length. It is shown [82] that the rod profile causes a gentle expansion of the surface-wave along the entire length of the rod

Table 5.3 Summary of Performance for the Profiled Rods in Figure 5.16

	Boresight Gain (dBi)			*Relative 1st Sidelobe Level (dB)*			
	Calc. (MWS)	*Calc. (MoM)*	*Meas.*	*Meas. E-plane*	*Calc. E-plane*	*Meas. H-plane*	*Calc. H-plane*
Linear (LIN)	10.3	9.9	8.1	9.6	10.4	10.3	12.2
Low sidelobe (SL)	12.4	12.0	10.9	27.8	23.1	21.3	25.5
Max. gain (MG2)	13.2	13.1	12.3	13.7	13.0	12.6	13.3

with no observable radiation from the rod except at its end. The ring slot produces a small amount of feed radiation, which radiates to the rear of the rod and diffracts around the rod base, interfering with the field in the forward direction; however, this is a minor effect. The radiation pattern, shown in Figure 5.18, has a maximum first sidelobe level of –18.5 dB below boresight in the E- and H-plane. This is better than the –17 dB cited by Zucker [78] for a minimum sidelobe design. This improvement is primarily due to the low feed radiation resulting from the high launching efficiency of the ring slot. For the design shown in Figure 5.17, a first sidelobe level of <–17 dB is maintained across 7% of the frequency band. In addition to the low sidelobes, the gain of the SL rod is >2 dB above that of a rod with a linear profile; see Table 5.3. This increase is due to the better utilization of the rod length for expanding the surface-wave field. The measured radiation pattern varies slightly from the simulated results due to the interaction of the ring slot radiation with the ring slot feed. This effect is most evident in the sidelobe at angles greater than 60°. At most other angles the sidelobe level of the measured results are less than the simulated levels.

Table 5.3 summarizes the calculated and measured boresight gain for the three rod designs, and it can be seen for the SL design that the measured result is 1.1 dB less than the calculated value. This is partially due to losses not being included in the simulation such as dielectric loss and loss in the feed. Further analysis indicated the dielectric ohmic loss is approximately 0.2 dB and loss in the feed circuit board is 0.4 dB. The estimated total loss is 0.8 dB for the SL rod, including connector loss and impedance mismatch with the ring slot. The remaining loss is thought to be due to the ring slot operating slightly off resonant frequency. Although the gain is underestimated, there is still reasonable agreement between the shape of the measured and simulated SL radiation patterns (Fig. 5.18).

5.5.5 Arrays of Profiled Horns

Individual profiled horns can be designed and combined in the manner used for conventional horns for array feed applications [5]. For accurate design, mutual coupling should be included in the formulation as outlined in Section 5.3 [21, 77, 86, 87]. It is also possible to carry out a full design by restricting all the horns to be the same or allowing some or all to vary in the optimization process. A network representation of the array is shown in Figure 5.19. To outline an approach [21, 87] for an array of profiled horns, let the complex input mode amplitudes to an array of N horns be $\underline{\mathbf{a}}_I = [\mathbf{a}_1^{(1)}, \mathbf{a}_1^{(2)}, \dots \mathbf{a}_1^{(N)}]$ where $\mathbf{a}_1^{(i)}$ is the input to horn i and similarly

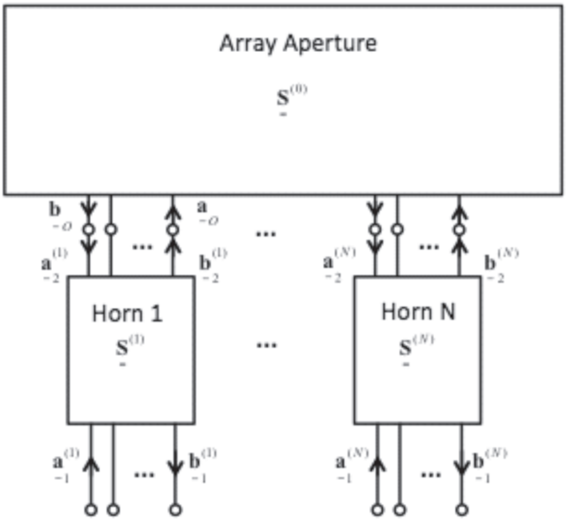

Figure 5.19 Scattering matrix representation of an array of profiled horns.

$\underline{\mathbf{b}}_I = [\mathbf{b}_1^{(1)}, \mathbf{b}_1^{(2)}, \dots \mathbf{b}_1^{(N)}]$ are the output mode amplitudes of the corresponding horns, as shown in Figure 5.19.

Assume that the scattering matrix for horn i is $\underline{\underline{\mathbf{S}}}^{(i)}$, which includes all effects up to the aperture plane. These individual horn scattering matrices are combined in a single scattering matrix $\underline{\underline{\mathbf{S}}}$ that is partitioned into four block $N \times N$ matrices $\underline{\underline{\mathbf{S}}}_{ij}\, i,\ j = 1, 2$ corresponding to the two input and output aperture ports of the horns. In addition, let $\underline{\underline{\mathbf{S}}}^{(0)}$ be the $N \times N$ scattering matrix of the aperture plane that includes the coupling between apertures. Therefore, the reflected mode amplitudes at the input for calculating the reflection coefficient and the mode amplitudes in the apertures for calculating the radiation pattern are expressed in terms of $\underline{\mathbf{a}}_I$ by:

$$\begin{aligned} \underline{\mathbf{b}}_I &= \left[\underline{\underline{\mathbf{S}}}_{11} + \underline{\underline{\mathbf{S}}}_{12}\,\underline{\underline{\mathbf{S}}}^{(0)}(\mathbf{I} - \underline{\underline{\mathbf{S}}}_{22}\,\underline{\underline{\mathbf{S}}}^{(0)})^{-1}\underline{\underline{\mathbf{S}}}_{21}\right]\underline{\mathbf{a}}_I \\ \underline{\mathbf{a}}_O &= (\mathbf{I} - \underline{\underline{\mathbf{S}}}_{22}\,\underline{\underline{\mathbf{S}}}^{(0)})^{-1}\underline{\underline{\mathbf{S}}}_{21}\,\underline{\mathbf{a}}_I \\ \underline{\mathbf{b}}_O &= \underline{\underline{\mathbf{S}}}^{(0)}(\mathbf{I} - \underline{\underline{\mathbf{S}}}_{22}\,\underline{\underline{\mathbf{S}}}^{(0)})^{-1}\underline{\underline{\mathbf{S}}}_{21}\,\underline{\mathbf{a}}_I \end{aligned} \tag{5.19}$$

where $\underline{\mathbf{a}}_O$ and $\underline{\mathbf{b}}_O$ are column vectors of the incident and reflected mode amplitudes in the apertures.

One need not alter the geometry of all horns during optimization. Some horn geometries could remain fixed. Also, for some applications it is simpler if the horns can be assumed to be identical and the performance improved by optimizing the profiles with full mutual coupling. If the mode content of the apertures and their diameters remain fixed, the mode coupling matrix is unchanged and need only be calculated once. The flow graph shown in Figure 5.8 can be used as a basis for the design software even for an array. The most time-consuming aspects are the initial assembly of the scattering matrices of the array coupling and the horns and particularly the inversion of the full $N \times N$ matrix $\mathbf{A} = (\mathbf{I} - \underline{\underline{\mathbf{S}}}_{22}\underline{\underline{\mathbf{S}}}^{(0)})$, which is required at each iteration step since the submatrix $\underline{\underline{\mathbf{S}}}_{22}$ is updated for each new profile. To save computation time, a perturbation approach could be employed to reduce the number of matrix inversions. For example, let $\mathbf{A}(new) = (\mathbf{I} - (\underline{\underline{\mathbf{S}}}_{22} + \Delta)\underline{\underline{\mathbf{S}}}^{(0)})$ where Δ is a small perturbation in the horn geometry due to the optimizer, if $\mathbf{A}(old)^{-1} = (\mathbf{I} - \underline{\underline{\mathbf{S}}}_{22}\underline{\underline{\mathbf{S}}}^{(0)})^{-1}$ is the fully inverted matrix from the previous iteration then

$$\mathbf{A}(new)^{-1} \approx (\mathbf{I} + \Delta(\underline{\underline{\mathbf{S}}}^{(0)^{-1}} + \mathbf{S}_{22})^{-1})\mathbf{A}(old)^{-1} \tag{5.20}$$

This new calculation requires only the storage of matrices $\underline{\underline{\mathbf{S}}}^{(0)^{-1}}$, $(\underline{\underline{\mathbf{S}}}^{(0)^{-1}} + \mathbf{S}_{22})^{-1}$ and $\mathbf{A}(old)^{-1}$ and entails only two $N \times N$ matrix multiplications.

An example of a design of a compact circular profiled horn for an array feed application is described by Hellicar et al. [88]. A multibeam array feed was required for a radiotelescope with a half-angle of 56.4° that operates from 0.95–1.45 GHz. A key aspect of the design was the transition from an input waveguide of specified diameter, which was set by the output of the orthomode transducer, to a suitable, larger aperture while achieving the desired edge illumination and frequency range. The design of a single horn was originally undertaken in isolation and then later tuned in the array environment using software that incorporates mutual coupling [77], assuming 19 identical elements and an array in a hexagonal cluster. The resulting horn design is only about 100 mm in length (~0.4λ), and is shown in Figure 5.20. The profiled horn is about half the length of a traditional stepped horn design that achieves a similar performance, and, as a consequence, the new design has less weight. An input return loss of >17 dB was achieved with this design over the desired frequency range, that is, about 42% bandwidth. The radiation pattern of the profiled horn design is typical for a TE_{11} mode horn in that the edge illumination varies from −8 dB to −14 dB across the band. The maximum cross-polar level

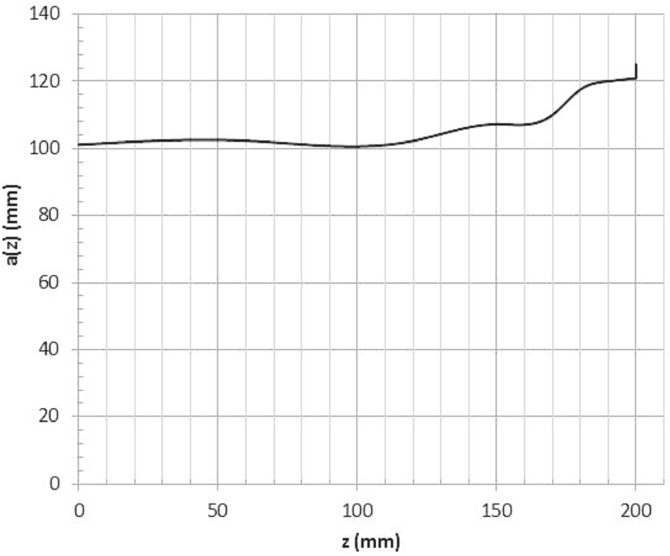

Figure 5.20 L-band profiled horn element for an array feed application.

in the 45° plane is < –20 dB. Other profiled horn designs for array applications are described in the literature for frequencies 30–38 GHz [89], 210–250 GHz [90], and 660–740 GHz [56].

5.6 Conclusion

This chapter has outlined the history of employing the horn profile in design to achieve a suitable operating performance. In particular, we have shown that by means of modern computational methods for both representing the horn structure and for automatic design through optimization, nonintuitive horn structures can be created that meet performance specifications. Representative examples were described that demonstrate the power of this design approach for general horn types that are metallic smooth-walled, corrugated, or open structures such as dielectric rods. It is anticipated that profiled horns will be employed more frequently in the future to develop designs that are fit for the purpose of meeting ever demanding requirements, whether for communications, science applications, radar, or security.

References

[1] Silver, S. (ed.), *Microwave Antenna Theory and Design*, New York: McGraw-Hill, 1949.

[2] Jakes, W. C., “Horn Antennas,” *Antenna Engineering Handbook*, Chap. 10, H. Jasik (ed.), 1st ed., New York: McGraw-Hill, 1961.

[3] Olver, A. D., et al., *Microwave Horns and Feeds*, IEE Electromagnetic Waves Series, Vol. 39, IEEE Press, 1994.

[4] Balanis, C. A., *Antenna theory*, New York: Harper & Row, 1982.

[5] Bird, T. S., and A. W. Love, “Horn Antennas.” In *Antenna Engineering Handbook*, Chap. 14, J. Volakis (ed.), 4th Ed., New York: McGraw-Hill, 2007.

[6] Granet, C., and T. S. Bird, “Optimization of Corrugated Horn Radiation Patterns Via a Spline-Profile,” *Proc. 9th Int. Symposium on Antenna Technology and Applied Electromagnetics (ANTEM 2002)*, Montréal, Canada, Jul. 27–29, 2002, pp. 307–310.

[7] Granet, C., et al., “A Smooth-walled Spline-Profile Horn as an Alternative to the Corrugated Horn for Wide Band Millimetre-wave Applications,” *IEEE Trans. on Antennas and Propagation*, Vol. 52, No. 3, Mar. 2004, pp. 848–854.

[8] Granet, C., and G. L. James, “Spline-Profile Smooth-walled C-band Horn,” *IEEE Antennas and Wireless Propagation Letters*, Vol. 6, 2007, pp. 415–418.

[9] Bhattacharyya, A. K., and G. Goyette, “A Novel Horn Radiator with High Aperture Efficiency and Low Cross-polarization and Applications in Arrays and Multibeam Reflector Antennas,” *IEEE Trans. on Antennas and Propagation*, Vol. AP–52, 2004, pp. 2850–2859.

[10] Tsandoulas, G. N., and W. D. Fitzgerald, “Aperture Efficiency Enhancement in Dielectrically Loaded Horns,” *IEEE Trans. on Antennas and Propagation*, Vol. AP–20, 1972, pp. 69–74.

[11] Lier, E., Y. Rahmat-Samii, and S. R. Rengarajan, “Application of Rectangular and Elliptical Dielcore Feed Horns to Elliptical Reflector Antennas,” *IEEE Trans. on Antennas and Propagation*, Vol. AP–39, 1991, pp. 1592–1597.

[12] Wolf, H., “The Scrimphorn, a New Compact Multimode Horn for Array Application,” *Journées Internationales de Nice sur les Antennes (JINA1988)*, Nice, France, 1988, pp. 446–449.

[13] James, G. L., “Design of Wide-band Compact Corrugated Horns,” *IEEE Trans. on Antennas and Propagation*, Vol. AP–32, No. 10, Oct. 1984, pp. 1134–1138.

[14] Thomas, B. MacA., G. L. James, and K. J. Greene, “Design of Wide-band Corrugated Conical Horns for Cassegrain Antennas,” *IEEE Trans. on Antennas and Propagation*, Vol. 34, No. 6, Jun. 1986, pp. 750–757.

[15] Gonzalo, R., J. Teniente, and C. del Rio, “Very Short and Efficient Feeder Design for Monomode Waveguide,” *Proc. IEEE Int. Symposium on Antennas and Propagation*, 1997, pp. 468–471.

[16] Granet, C., T. S. Bird, and G. L. James, “Compact Multimode Horn with Low Sidelobes for Global Earth Coverage,” *IEEE Trans. on Antennas and Propagation*, Vol. 48, No. 7, July 2000, pp. 1125–1133.

[17] Barrow, W. L., and L. J. Chu, “Theory of the Electromagnetic Horn,” *Proc. of the Institute of Radio Engineers, IRE*, Vol. 27, Jan. 1939, pp. 51–64.

[18] Bunger, R., R. Beyer, and F. Arndt, “Rigorous Combined Mode-matching Integral Equation Analysis of Horn Antennas with Arbitrary Cross-sections,” *IEEE Trans. on Antennas and Propagation*, Vol. AP–47, No. 11, 1999, pp. 1641–1648.

[19] Thomas, B. MacA., and K. J. Greene, “A Curved-aperture Corrugated Horn Having Very Low Cross-Polar Performance,” *IEEE Trans. on Antennas and Propagation*, Vol. 30, No. 6, Nov. 1981, pp. 1068–1072.

[20] Bird, T. S., “Contoured Beam Synthesis for Array-fed Reflector Antennas by Field-correlation,” *IEE Proc. (Part H), Microwaves, Optics and Antennas*, Vol. 129, 1982, pp. 293–298.

[21] Bird, T. S., “Mode Matching Analysis of Arrays of Stepped Rectangular Horns and Application to Satellite Design,” *Proc. IEE Conference on Antennas and Propagation, (ICAP)*, University of York, U.K, Apr. 15–18 1991, pp. 849–852.

[22] Bird, T. S., and C. Granet, “Optimization of Profile of Rectangular Horns for High Efficiency,” *IEEE Trans. on Antennas and Propagation*, Vol. 55, No. 9, 2007, pp. 2480–2488.

[23] Granet, C., and T. S. Bird, “Dual-polarized High-efficiency Spline-profile Square Horns for Satellite Array Applications,” *Workshop on Applications of Radio Science (WARS’08)*, Gold Coast, Feb. 10–12.

[24] Adam, J.-P., et al., “Design and Manufacture of Non-circular Spline-profile Horns,” *33rd ESA Antenna Workshop*, Noordwijk, Netherlands, Oct. 2011.

[25] Agastra, E., et al., “Genetic Algorithm Optimization of High-efficiency Wide-band Multimodal Square Horns for Discrete Lenses,” *Progress in Electromagnetics Research*, PIER 83, 2008, pp. 335–352.

[26] Love, A. W., *Electromagnetic Horn Antennas*, New York: IEEE Press, 1976.

[27] Potter, P. D., “A New Horn Antenna with Suppressed Sidelobes and Equal Beamwidths,” *Microwave Journal*, Vol. 6, Jun. 1963, pp. 71–18.

[28] Koch, G. F., “Coaxial Feeds for High Aperture Efficiency and Low Spill-over of Paraboloidal Reflector Antennas,” *IEEE Trans. on Antennas and Propagation*, Vol. 21, No. 3, 1973, pp. 164–169.

[29] Ruggerini, G., “A Compact Circular Horn with High Efficiency,” *Proc. European Conference on Antennas and Propagation (EuCAP2010)*, Barcelona, Spain, 2010.

[30] Bouwkamp, C. J., and N. G. de Bruijn, “The Problem of Optimum Antenna Current Distribution,” *Philips Research Reports*, Vol. 1, 1946, pp. 135–158.

[31] Riblet, H. J., “Note on the Maximum Directivity of an Antenna,” *Proc. of the Institute of Radio Engineer, IRE*, Vol. 36, 1948, pp. 620–623.

[32] Rhodes, D. R., *Synthesis of Planar Antenna Sources*, UK: Oxford University Press, 1974.

[33] Bird, T. S., and C. Granet, “Design of Profiled Circular Horn Feed with High Efficiency,” *Proc. IEEE Int. Symposium on Antennas and Propagation*, Chicago, Jul. 8–13, 2012.

[34] Rusch, W. V. T., and P. D. Potter, *Analysis of Reflector Antennas*, London, UK: Academic Press, 1970.

[35] Kildal, P.-S., “Combined E- and H-plane Phase Centers of Antenna Feeds,” *IEEE Trans. on Antennas and Propagation*, Vol. AP–31, No. 1, Jan. 1983, pp. 199–202.

[36] Bird, T. S., and C. Granet, “Fabrication and Space-qualifying a Lightweight Corrugated Horn with Low Sidelobes for Global-earth Coverage,” *IEEE Antennas and Propagation Magazine*, Vol. 50, No. 1, Feb. 2008, pp. 80–86.

[37] Granet, C., G. L. James, and A. R. Forsyth, “Aperture Antennas: Waveguides and Horns.” In *Modern Antenna Handbook*, Chap. 3, pp. 97–156, C.A. Balanis (ed.), Hoboken, NJ: John Wiley & Sons Inc., 2008.

[38] Cohn, S. B., “Flare-angle Changes in a Horn as a Means of Pattern Control,” *Microwave Journal*, Vol. 13, Oct. 1970, pp. 41–46.

[39] Granet, C., “Profile Options for Feed Horn Design,” *Proc. Asia Pacific Microwave Conference (APMC2000)*, Sydney, Dec. 3–6, 2000, pp. 1448–1451.

[40] Clarricoats, P. J. B., R. F. Dubrovka, and A. D. Olver, “A Novel Multi-section Compact Corrugated Horn,” *Proc. IEEE Int. Symposium on Antennas and Propagation*, Vol. 4, Jun. 22–27, 2003, pp. 498–501.

[41] Teniente, J., R. Gonzalo, and C. del Rio, “Modern Corrugated Horn Antenna Design for Extremely Low Sidelobe Level,” *26th ESA Antenna Technology Workshop*, Noordwijk, Netherlands, 2003, pp. 387–394.

[42] Gentili, G. G., et al., “Compact Dual-profile Corrugated Circular Waveguide Horn,” *Electronic Letters*, Vol. 36, No. 6, 16th March 2000, pp. 486–487.

[43] Gentili, G. G., et al., “Performance Analysis of Dual-profile Corrugated Circular Waveguide Horns for Radioastronomy Applications,” *IEE Proc. Microwaves, Antennas and Propagation*, Vol. 148, No. 2, April 2001, pp. 119–122.

[44] Granet, C., and T. S. Bird, “X-, Ku- and Ka-band Compact Feed Horns for Global-earth Coverage from a Geostationary Orbit,” *Proc. Asia Pacific Microwave Conference (APMC2000)*, Sydney, Australia, 2000, pp. 1436–1439.

[45] Jamnejad, V., and A. Hoorfar, “Design of Corrugated Horn Antennas by Evolutionary Optimization Techniques,” *IEEE Antennas and Wireless Propagation Letters*, Vol. 3, 2004, pp. 276–279.

[46] Teniente, J., R. Gonzalo, and C. del Rio, “Superb Gaussian Beam Efficiency Corrugated Horn Antenna,” *Proc. European Conference on Antennas and Propagation (EuCAP’2010)*, Barcelona, Spain, 2010.

[47] Deguchi, H., M. Tsuji, and H. Shigesawa, “A Compact Low-cross-polarization Horn Antenna with Serpentine-shaped Taper,” *Proc. IEEE Int. Symposium on Antennas and Propagation*, Vol. 2, 2001, pp. 320–323.

[48] Lucci, L., et al., “NURBS Profile Corrugated Circular Horns,” *Proc. IEEE Int. Symposium on Antennas and Propagation*, Vol. 1, 2003, pp. 161–164.

[49] Jensen, I., “A Smooth-walled Profiled Horn Antenna with Low Cross-polarization Generated by the Particle Swarm optimization Method,” *Proc. 28th ESA Antenna Technology Workshop*, Noordwijk, Netherlands, 2005, pp. 435–441.

[50] Zheng, L., et al., “A Low Cross-polarization Smooth-walled Horn with Improved Bandwidth,” *IEEE Trans. on Antennas and Propagation*, Vol. 58, No. 4, Apr. 2010, pp. 1383–1387.

[51] Gupta, R. C., et al., “Design of Dual-band Multimode Profiled Smooth-walled Horn Antenna for Satellite Communication,” *IEEE Antennas and Wireless Propagation Letters*, Vol. 9, 2010, pp. 338–341.

[52] Simon, P. S., P. Kung, and B. W. Hollenstein, “Electrically Large Spline Profile Smooth-wall Horns for Spot Beam Applications,” *Proc. IEEE Int. Symposium on Antennas and Propagation*, Spokane, WA, July 3–8, 2011, pp. 915–918.

[53] Chan, K. K., and S. K. Rao, “Design of High-efficiency Circular Horn Feeds for Multibeam Reflector Applications,” *IEEE Trans. on Antennas and Propagation*, Vol. 56, No. 1, Jan. 2008, pp. 253–258.

[54] Yang, D., Y. C. Chung, and R. Haupt, "Genetic Algorithm Optimization of a Multisectional Corrugated Horn Antenna," *Microwave and Optical Technology Letters*, Vol. 38, No. 5, Sep. 5, 2003, pp. 352–356.

[55] Ujihara, H., "Multimode Horns for VSOP–2 Satellite," *Proc. Int. Symposium on Antennas and Propagation (ISAP2007)*, Niigata, Japan, 2007, pp. 904–907.

[56] Yassin, G., et al., "A High Performance Horn for Large Format Focal Plane Arrays," *Proc. 18th Int. Symposium on Space Terahertz Technology*, California Institute of Technology, Mar. 21–23, 2007, pp. 199–210.

[57] Fletcher, R., "Fortran Subroutines for Minimization by Quasi Newton Methods," *AERE*, Harwell, UK, Report, No. 7125, 1972.

[58] Goldberg, D., *Genetic Algorithms in Search, Optimization and Machine Learning*, Boston: Addison–Wesley Longman Publishing Co., Inc., 1989.

[59] Kennedy, J., and R. Eberhart, "Particle Swarm Optimization," *Proc. IEEE Conference on Neural Networks*, Nov/Dec. 1995, pp. 1942–1948.

[60] Černý, V., "Thermodynamical Approach to the Traveling Salesman Problem: An Efficient Simulation Algorithm," *Journal of Optimization Theory and Applications*, Vol. 45, 1985, pp. 41–51.

[61] Lucci, L., et al., "Phase Centre Optimization in Profiled Corrugated Circular Horns with Parallel Genetic Algorithms," *Progress in Electromagnetics Research*, PIER 46, 2004, 127–142.

[62] Granet, C., and G. L. James, "Design of Corrugated Horns: A Primer," *IEEE Antennas and Propagation Magazine*, Vol. 47, No. 2, Apr. 2005, pp. 76–84. (Correction in *IEEE Antennas and Propagation Magazine*, Vol. 47, No. 4, Aug. 2005, p. 98).

[63] Abbas-Azimi, M., F. Mazlumi, and F. Behnia, "Design of Broadband Constant-beamwidth Conical corrugated–horn Antennas," *IEEE Antennas & Propagation Magazine*, Vol. 51, No. 5, Oct. 2009, pp. 109–114.

[64] Addamo, G., et al., "Dual use Ku/K–band Corrugated Horn for Telecommunication Satellite," *Proc. European Conference on Antennas and Propagation (EuCAP'2010)*, Barcelona, Spain, 2010.

[65] Granet, C., and T. S. Bird. "Optimized X-band Spline-profile Earth Illumination Horn," *Proc. Int. Symposium on Antennas (JINA'2004)*, Nice, France, Nov. 8–10, 2004, pp. 192–193.

[66] Pressense, J., et al., "Optimizing a Corrugated Horn for Telecommunication and Tracking Missions Using a New Flexible Horn Design Software," *Proc. European Conference on Antennas and Propagation (EuCAP'2010)*, Barcelona, Spain, 2010.

[67] Love, A. W., "Two Hybrid Mode, Earth Coverage Horn for GPS," *Proc. IEEE Int. Symposium on Antennas and Propagation*, 1985, pp. 575–578.

[68] Barker, S. J., et al., "The Development of an Inexpensive High-precision mm-wave Compact Antenna Test Range," *Proc. Antenna Measurements Techniques Association (AMTA)*, Newport, RI, Oct. 30–Nov. 4 2005, pp. 337–340.

[69] Granet, C., and R. Gough, "Design of Three Prime-focus 12mm-wavelength Horns for the Parkes Radio Telescope," *Microwave and Optical Technology Letters*, Vol. 50, No. 10, Oct. 2008, pp. 2537–2543.

[70] Thomas, B. MacA., "Prime-focus One- and Two-hybrid-mode Feeds," *Electronic Letters*, Vol. 6, No. 15, Jul. 23, 1970, pp. 460–461.

[71] Luthi, T., et al., "Expandable Fully Reflective Focal-plane Optics for Millimetre- and Submillimeter-wave Array Receivers," *Review of Scientific Instruments*, Vol. 77, 014702, Jan. 2006.

[72] Rabanus, D., et al., "Measurement of Properties of a Smooth-walled Spline-profile Feed Horn around 840 GHz," *Infrared Physics & Technology*, Vol. 48, Issue 3, 2005, pp. 181–186.

[73] Granet, C., and G. L. James, "Spline-profile Smooth-walled C-band Horn," *IEEE Antennas and Wireless Propagation Letters*, Vol. 6, 2007, pp. 415–418.

[74] Granet, C., and G. L. James, "Smooth-walled Spline-profile Ka–band Horn Covering Both the Full Commercial and Military Bands," *Microwave and Optical Technology Letters*, Vol. 50, No. 8, Aug. 2008, pp. 2119–2121.

[75] Granet, C., and G. L. James, "Optimized Spline-profile Smooth-walledtTri-band 20/30/44-GHz horns," *IEEE Antennas and Wireless Propagation Letters*, Vol. 6, 2007, pp. 492–494.

[76] Bird, T. S., "Coaxial Feed Array for a Short Focal-length Reflector," *Proc. IEEE Int. Symposium on Antennas and Propagation*, Jul. 13–18, 1997, pp. 1618–1621.

[77] Bird, T. S., "User Guide to CIRCAR4: A Computer Program for the Analysis of Arrays of Circular Horns," CSIRO Report, Mar. 14, 1997.

[78] Zucker, F. J., "Surface-Wave Antennas." In *Antenna Engineering Handbook*, Chap. 10, 4th Ed., J. L. Volakis (ed.), New York: McGraw-Hill, 2007.

[79] Ando, T., J. Yamauchi, and H. Nakano, "Numerical Analysis of a Dielectric Rod Antenna-demonstration of the Discontinuity-radiation Concept," *IEEE Trans. on Antennas & Propagation*, Vol. 51, 2003, pp. 2007–2013.

[80] Richter, J., and L.-P. Schmidt, "Dielectric Rod Antennas as Optimized Feed Elements for Focal Plane Arrays," *Proc. IEEE Int. Symposium on Antennas and Propagation*, Vol. 3A, Jul. 3–8, 2005, pp. 667–670.

[81] Ando, T., et al., "Linearly and Curvilinearly Tapered Cylindrical-dielectric-rod Antennas," *IEEE Trans. on Antennas and Propagation*, Vol. 53, No. 9, Sep. 2005, pp. 2827–2833.

[82] Hanham, S. M., et al., "Evolved-profile Dielectric Rod Antennas," *IEEE Trans. on Antennas & Propagation*, Vol. 59, No. 4, Apr. 2011, pp. 1113–1122.

[83] Mautz, J. R., and R. F. Harrington, "Electromagnetic Scattering from a Homogeneous Body of Revolution," *Dept. of Electrical and Computer Engineering*, Syracuse University, Syracuse, NY, Tech. Report, No. TR–77–10, Nov. 1977.

[84] Mautz, J. R., and R. F. Harrington, "H-field, E-field and Combined Field Solutions for Bodies of Revolution," *Dept. of Electrical and Computer Engineering*, Syracuse University, Syracuse, NY, Tech. Report, No. TR–77–2, Feb. 1977.

[85] Hanham, S. M., and T. S. Bird, "High Efficiency Excitation of Dielectric Rods Using a Magnetic Ring Current," *IEEE Trans. on Antennas and Propagation*, Vol. 56, No. 6, Jun. 2008, pp.1805–1808.

[86] Bird, T. S., "Mutual Coupling in Arrays of Coaxial Waveguides and Horns," *IEEE Trans. on Antennas and Propagation*, Vol. 52, 2004, pp. 821–829.

[87] Newell, P., and T. S. Bird, "Effects of Mutual Coupling in the Design of High Performance Multifeed Satellite Antennas," *Radio Science*, Vol. 29, Jan.–Feb. 1994, pp. 145–152.

[88] Hellicar, A. D., T. S. Bird, and S. M. Hanham, "Wideband Short Horn Design for a Multibeam Radiotelescope," *Proc. Electromagnetics in Advanced Applications (ICEAA)*, Sydney, Australia, Sep. 20–24, 2010, pp. 863–866.

[89] Chernobrovkin, R., et al., "Compact Efficient Feed-horn at 30–38GHz for a Multi-beam Radio Telescope," *Journal of Infrared, Millimeter and Terahertz Waves*, Vol. 31, Issue 7, pp. 840–851.

[90] Leech, J., et al., "Measured Performance of a 230GHz Prototype Focal-plane Feedhorn Array Made by Direct Drilling of Smooth–wall Horns," *Proc. 21st Int. Symposium on Space Terahertz Technology*, Oxford, Mar. 23–25, 2010, pp. 114–119.

[91] www.ticra.com

[92] www.mician.com

[93] www.cst.com

CHAPTER 6

Soft and Hard Horn Antennas

Erik Lier, Lockheed Martin

6.1 Introduction to Hybrid Mode Horn Antennas

Hybrid-mode horns were first described by Minnett and Thomas [1], who showed that linearly polarized (LP) modes with perfectly straight field lines can be supported if an anisotropic boundary on the waveguide or horn wall can be designed that meets the balanced hybrid condition

$$Z^{\mathrm{TE}} Z^{\mathrm{TM}} = \eta_0^2 \tag{6.1}$$

where Z^{TE} and Z^{TM} are the TE and TM boundary impedances, respectively, and η_0 is the free-space wave impedance. The hybrid mode produces radiation patterns with very low (ideally zero) cross-polarization at the design frequency. Due to the propagation of a single mode, these horns exhibit an inherently large bandwidth. In a circular waveguide, (6.1) applies to any LP mode, assuming the boundary (e.g., transverse corrugations) is implemented with rotational symmetry. Therefore, any two orthogonal modes will have identical field distributions in E-plane and H-plane, respectively, across the waveguide or horn aperture. This results in perfect circularly polarized (CP) radiation patterns with very low cross-polarization at the design frequency, assuming that a perfect 90° polarizer is connected to the horn.

Many horn antennas published in the literature show some of the characteristics of hybrid-mode horns but do not meet the criterion in (6.1). They have in general either lower bandwidth, higher loss, or higher cross-polarization when compared with hybrid-mode horns. These horns are often preferred if they meet the requirements needed for the specific application because they may offer lower weight or cost (e.g., dual mode or multimode horns; see Chapter 4). However, for applications where performance is the driving requirement, hybrid mode horns may be preferred.

Although (6.1) was developed for horns with a circular cross section, it applies in the most general sense to horns with any cross section. However, hybrid mode horns with circular symmetry have larger bandwidth than hybrid mode horns with other cross sections. One reason is that the balanced hybrid condition for the two orthogonal modes will have in practice different frequency variation over the band. Two hybrid mode horns with noncircular aperture known from the literature are elliptical and rectangular horns. These horns are particularly interesting because they generate elliptical beams and are used as feeds in elliptical reflector antennas for radar and satellite applications.

6.2 Definition of Soft and Hard Surfaces

The concept of soft and hard horn antennas was first published by Lier and Kildal [2]. This paper presented an analysis based on a circular cylindrical model of a hard horn with longitudinal strips on a dielectric wall liner, demonstrating that a TEM wave can actually be supported in the air-filled interior of a strip-loaded circular cylindrical waveguide. The paper also presented the first mathematical formulation of the concept of soft and hard electromagnetic surfaces based on anisotropic boundary impedances, as well as the first experimental proof-of-concept. Detailed derivation and discussion of these surfaces were later published [3, 4]. This work was inspired by the development of a horn with circumferential strips on a dielectric wall liner [5, 6], representing an alternative to the widely used corrugated horn. Both of these horns are soft horns according to the EM boundary definition described in this chapter.

The study of the hard strip-loaded horn was also inspired by a horn published by Aly and Mahmoud [7], which had longitudinal corrugations filled with dielectric. This corrugated horn represents the first published hybrid-mode high-efficiency horn or hard horn concept. Although the authors of that paper demonstrated analytically that the horn provided high directivity, they did not mention explicitly the generation and support of a TEM wave in the central horn region.

Soft and hard horns can be defined by the electric E and magnetic H field components tangential to the boundary xz-plane, expressed as

$$\textit{Soft:}\quad Z^{\mathrm{TE}} = Z_x = \frac{E_x}{H_z} = 0,\ Z^{\mathrm{TM}} = Z_z = -\frac{E_z}{H_x} = \infty \tag{6.2}$$

$$\textit{Hard:}\quad Z^{\mathrm{TE}} = Z_x = \frac{E_x}{H_z} = \infty,\ Z^{\mathrm{TM}} = Z_z = -\frac{E_z}{H_x} = 0 \tag{6.3}$$

where x is the transverse component of the wave relative to the direction of propagation and z is the direction of propagation. To meet these conditions the surface has to be anisotropic with respect to EM propagation.

The soft horn is characterized by tapered field distribution over the aperture, generating Gaussian-like radiation pattern with low sidelobes, as illustrated in Figure 6.1. This characteristic makes the horn ideal as a single feed for reflector antennas, resulting in high gain due to low spillover loss outside the reflector, and as a satellite antenna providing global or regional beams. The hard horn supports uniform field distribution over the aperture, which results in high directivity due to high aperture efficiency, and with corresponding high sidelobes (see Figure 6.1). Therefore, this horn is ideal as an antenna element in arrays, resulting in high gain and low grating lobes for boresight as well as scanned beams. It is also suited for other applications where high gain is needed but where the aperture size is restricted, for example, as a

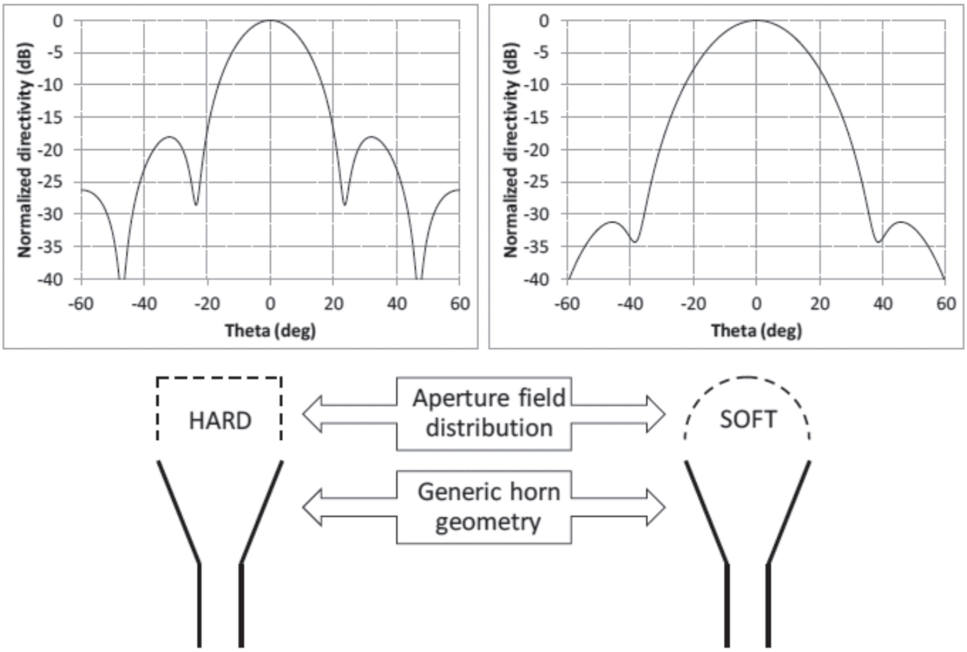

Figure 6.1 Illustration of soft and hard horns (axial cuts) and typical radiation patterns.

cluster feed element for reduction of spill-over loss in multibeam reflector antennas [8]. Finally, hard horns may find applications as spatial combiners for quasi-optical amplifier arrays [9, 10].

Lier and Kildal [11] published a qualitative analysis of aperture distributions and radiation patterns of soft and hard horn antennas, showing that any aperture distribution between the two extreme cases, soft and hard, could be envisioned. The relationship between peak directivity, sidelobe level, boundary impedance, and edge taper (relative signal strength at the boundary relative to the center of the waveguide) was presented. They also proposed how such an intermediate soft-hard horn or “selectable gain horn” could be designed by the use of a graded index dielectric core. An alternative concept for such a soft-hard horn was proposed [2] by loading the wall by metal patches on a dielectric liner.

Soft and hard surfaces can also find applications beyond horn antennas. Since soft surfaces suppress propagation along a boundary, they can be used to increase isolation between antennas or to reduce diffraction around corners and other discontinuities. Hard surfaces can be used to make objects invisible (cloak) with reduced radar cross sections for any polarization. This was first proposed and demonstrated experimentally [12, 13] on struts in reflectors where hard strip-loaded and corrugated liners were applied to the surface of the strut with elongated or rhombic-shaped cross section to further minimize reflections. This is possible when the direction of the incoming wave is known, which always occurs in fixed antenna systems but is less effective in applications where the incoming waves arrive simultaneously from different directions.

In summary, soft and hard horns are hybrid-mode horns, supporting a single mode under balanced hybrid condition with resulting low (ideally zero) radiated cross-polarization at the design frequency. This enables frequency reuse with high isolation between the dual polarized signals.

6.3 Soft and Hard Horn Designs and Implementations

6.3.1 Soft Corrugated Horns

The first known hybrid-mode horn, the corrugated horn, was invented in the 1960s [14, 15]. It was the only known type of hybrid-mode horn for almost 20 years. The corrugated horn has since been analyzed in depth, and numerous designs have been built and put to use [16]. It has been demonstrated to work with circular, elliptical, and rectangular aperture; with axial and radial corrugations; with ring-loaded and dual-depth corrugations; for single and dual hybrid modes; with flare angle from small to large, that is, from aperture controlled to flare angle controlled horn; with linear and profiled shape along the horn; and in applications for satellites and radars from microwaves to millimeter-waves.

This hybrid-mode horn does not need dielectric loading, which makes it particularly attractive for high-power or satellite applications. It is being used as a feed in reflector antennas for satellite communications, both in on-board satellites and in ground terminal antennas, because of its low sidelobes and low cross-polarization over a large bandwidth. Low sidelobes are important to achieve high antenna efficiency thanks to low spill-over loss outside the reflector. Low cross-polarization is critical to enable frequency reuse for dual polarization, resulting in doubling of the overall satellite communication bandwidth or capacity. Also, circular corrugated horns can be designed and analyzed quickly and very accurately with mode matching software [17] due to the absence of dielectric material. Finally, it has no outer boundary region with electromagnetic fields that could increase radiated cross-polarization, in contrast to all other known hybrid mode horns, which have some unwanted radiation from the boundary region. This effect will be described later in this chapter, during the discussion of the various soft and hard horn designs.

To support a balanced hybrid mode, the corrugation depth along the horn can approximately be expressed by

$$t_{corr-hm} = \frac{\lambda_0}{4} \tag{6.4}$$

where λ_0 is the free-space wavelength. This corrugation depth should be slightly modified for propagation in a cylindrical or conical waveguide [16]. To avoid higher order nonwanted modes, the corrugation depth has to be kept between a quarter and half a wavelength,

$$\frac{\lambda_0}{4} < t_{corr} < \frac{\lambda_0}{2} \tag{6.5}$$

In other words, the maximum achievable continuous bandwidth of a corrugated horn is under 100%. However, dual band design with band separation beyond an octave has been achieved with dual depth corrugations, although the achieved bandwidth is relatively narrow [16]. For best match from the smooth-walled input waveguide to the corrugated waveguide or horn section, the depth of the first corrugations should be approximately half a wavelength, which electrically is equivalent to a smooth wall.

As discussed in the introduction, (6.1) could be extended to horns with any cross sections. However, for a noncircular cross section the challenge is to implement the boundary such that it meets the balanced hybrid condition for both modes at the center frequency and has similar frequency variation over the required frequency band. As an example, in a noncircular corrugated horn, this could be achieved in an approximate sense by making corrugations with varying depth around the waveguide. Elliptical and rectangular corrugated horns have been thoroughly studied in the past [16, Chapter 7]. The elliptical corrugated horn can be analyzed by expressing the hybrid modes as Mathieu functions. It is assumed that the boundary impedance is constant everywhere around the waveguide, which is most correct for small ellipticities. The square and rectangular corrugated horns are not amenable to exact analysis due to the corner regions. However, an approximate solution can be obtained by treating the waveguide as a rotated pair of two-wall E-plane corrugated waveguides, where each can be analyzed exactly.

Figure 6.2 shows a Ku-band elliptical corrugated feed horn developed for a dual reflector Gregorian satellite antenna. Measured radiation patterns of the horn were shown [18], which also presented an approximate model predicting co-polarized and cross-polarized radiation patterns of elliptical hybrid-mode horns. The cross section of the horn changes gradually from circular in the throat to elliptical with a 1.2:1 aspect ratio in the aperture. This results in a very short and light feed horn without the need for an input transition section. The corrugation depth was held constant around the horn. Relative peak cross-polarization was well below –35 dB over almost the entire 11.7–14.5 GHz band, and below –33 dB at the lowest frequency.

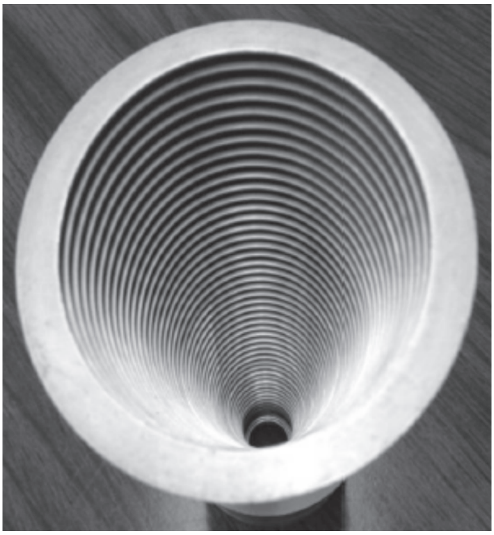

Figure 6.2 Photo of Ku-band elliptical corrugated feed horn for a Gregorian reflector antenna. Aperture aspect ratio is 1.2:1 [18].

This bandwidth is twice as wide as reported in the literature for other experiments with a 2:1 aperture aspect ratio. The most likely reason is the smaller aperture aspect ratio, although the gradual change from circular to elliptical cross section could in part contribute to the bandwidth improvement. In the more common design with a constant cross-sectional ellipticity along the horn, a circular to elliptical waveguide transition is needed at the horn throat for matching purpose and to reduce the excitation of higher order unwanted modes.

6.3.2 Horns with a Dielectric Core (Dielcore Horns)

6.3.2.1 Soft Dielcore Horns

The dielcore horn was independently discovered in the early 1980s by two European teams [19–21] and was the first hybrid-mode horn after the corrugated horn to be invented. If a dielectric core with relative permittivity ε_{r1} is inserted into the horn, leaving a gap between the core and the horn wall having a dielectric material with permittivity ε_{r2} (which for most practical cases is close to unity), the balanced hybrid condition can be met if (see Figure 6.3)

$$\varepsilon_{r1} > \varepsilon_{r2} \tag{6.6}$$

Clarricoats, Olver, and Rizk [19] proposed a low dielectric (foam) core with relative dielectric constant $\varepsilon_{r1} \approx 1.1$–$1.3$, Lier and Aas [20] and Lier [21] used a solid dielectric core with $\varepsilon_{r1} \geq 2$ which could be implemented with a low-loss dielectric material, such as PTFE (Teflon), polystyrene, or polyethylene for the soft dielcore horn in Figure 6.3. A balanced hybrid mode can be supported inside the core if the gap between the core and metal wall meets the following requirement [21]:

$$\begin{aligned} Z^{\mathrm{TE}} &= j\eta_1\sqrt{\frac{\varepsilon_r}{\varepsilon_r - 1}}\tanh(k_2' t_{gap}) \\ Z^{\mathrm{TM}} &= -j\eta_1\sqrt{\varepsilon_r}\sqrt{\varepsilon_r - 1}\tanh(k_2' t_{gap}) \end{aligned} \tag{6.7}$$

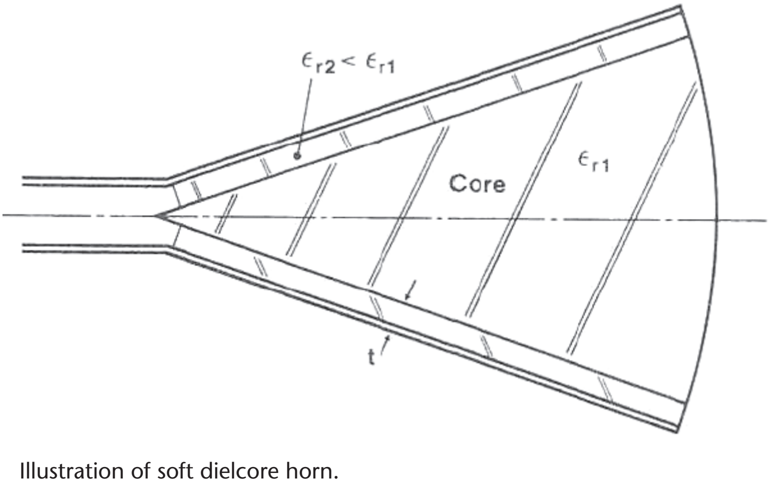

Figure 6.3 Illustration of soft dielcore horn.

meeting the balanced hybrid condition in (6.1), and where the propagation constant normal to and inside the boundary is given by

$$k_2' = \frac{2\pi}{\lambda_0}\sqrt{\varepsilon_{r1} - \varepsilon_{r2}} \tag{6.8}$$

Equations (6.7) and (6.8) show that the field propagation normal to the boundary is evanescent. By combining (6.1), (6.7), and (6.8), the formula for the outer gap thickness required to support balanced hybrid propagation inside the core for grazing incident waves can be derived, resulting in

$$t_{gap} = \frac{\lambda_0}{4\pi\sqrt{\varepsilon_{r1} - \varepsilon_{r2}}}\ln\left(\frac{\sqrt{\varepsilon_{r1}/\varepsilon_{r2}} + 1}{\sqrt{\varepsilon_{r1}/\varepsilon_{r2}} - 1}\right) \tag{6.9}$$

Since this formula was derived for plane wave incidence on a flat boundary, it is asymptotically exact for increasing waveguide diameter and approximately accurate in the radiating aperture.

Graphs of the thickness versus permittivity and versus aperture radius are derived based on a circular cylindrical model and are shown in Figure 6.4(a) and (b), respectively. They show that the thickness decreases with increasing core permittivity and increasing aperture size. The horn exhibits an ideal soft condition (6.2) in the limit when the core permittivity goes to infinity, which can be derived from (6.7–6.9). However, for all practical purposes, the condition is close to soft for a solid dielectric core with $\varepsilon_{r1} \geq 2$. For core permittivity close to unity the condition is far from soft, and the thickness of the outer gap increases exponentially, leaving less energy in the hybrid mode inside the core.

A crucial feature associated with this design is that the electromagnetic wave propagation normal to the boundary is evanescent in the outer region. This results in an intrinsic large bandwidth for propagation along the waveguide, in contrast to the propagation inside a corrugated horn where the resonant nature of the corrugated wall boundary limits the bandwidth. Unfortunately, the dielectric-air aperture discontinuity imposes a bandwidth limitation for dielcore horns with high dielectric constant. However, with a matching layer ("quasi-blooming" layer) on the dielectric-air aperture boundary, an octave bandwidth was achieved with peak cross-polarization 30 dB below co-polarization peak for a horn with a solid dielectric core material made of polystyrene [21]. This is shown in Figure 6.4(c), and the corresponding measured return loss is shown in Figure 6.4(d). Circular holes were machined into the dielectric aperture surface, where the hole diameter, hole depth, and hole spacing were designed properly to generate a quarter-wavelength matching layer with center frequency at 12.5 GHz. For horns with a low permittivity core a matching layer in the aperture may not be needed. The return loss in the horn throat is inherently low for these horns since the dielectric core can be easily shaped for optimum performance. The measurements show that although the cross-polarization bandwidth is an octave, the return loss bandwidth is smaller due to worse performance in the lower band. The return loss bandwidth can be extended by optimization of the throat region.

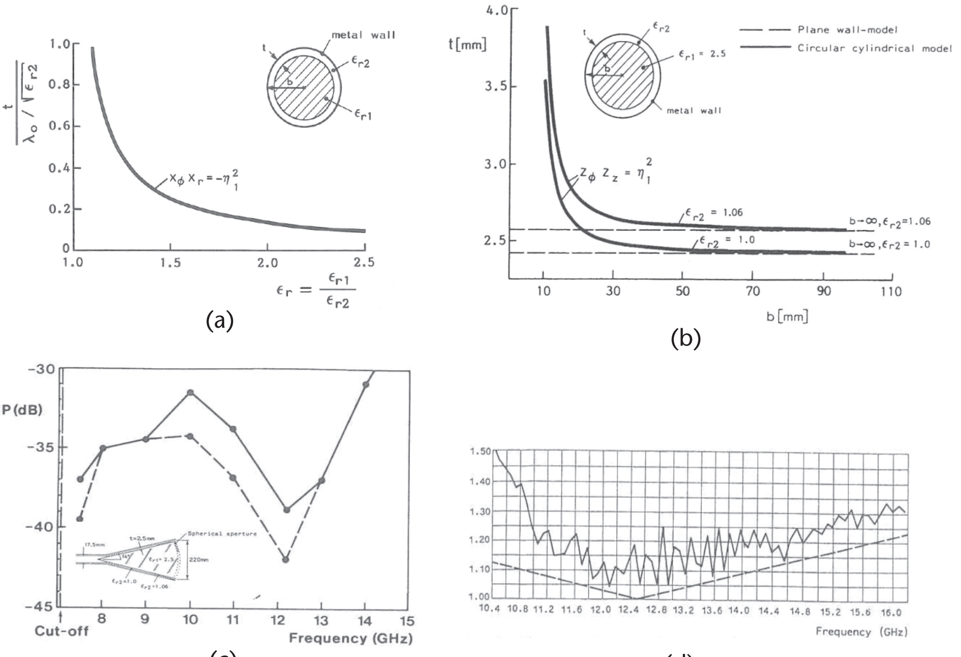

(a) (b)

(c) (d)

Figure 6.4 Predicted characteristics and measured performance of the soft dielcore horn illustrated in Figure 6.3 and referenced in Lier [21]. (a) Normalized thickness of the outer gap of the horn versus normalized permittivity of the core material, satisfying the balanced hybrid condition in a cylindrical waveguide, (b) thickness of the outer gap of the horn versus waveguide radius, satisfying the balanced hybrid condition in a cylindrical waveguide, and (c) measured relative peak cross-polarization versus frequency of the horn shown inserted. The two curves represent two orthogonal pattern cuts (d) measured return loss versus frequency of the horn shown inserted in Figure 4(c).

It should be noted that the electromagnetic field in the outer region will add to the radiation from the hybrid mode in the dielectric core region and modify the radiation pattern, which slightly deteriorates the rotational symmetry and increases cross-polarization of the radiation pattern. This effect is more pronounced for dielcore horns with low relative core permittivity [19] since their outer region is larger in area with higher relative field strength (field less confined to the core) compared to dielcore horns with high core permittivity [21]. Unwanted radiation from the boundary region could be reduced by placing an absorber ring around the outer aperture area.

The propagation characteristics in an elliptical dielcore waveguide were accurately analyzed by Lier and Rengarajan [22]. The study demonstrated that only an approximate balanced hybrid mode can be supported, assuming the dielectric core boundary and metal wall boundary has the same ellipticity. Lier, Rahmat-Samii, and Rengarajan [23] discussed the applications of dielcore horns with elliptical beams. An experimental verification of dielcore horns with a solid dielectric core and with elliptical and rectangular cross-sections were presented [24]. The horns were built for use as a reflector antenna feed in a microwave radar system (see Figure 6.5). The required feed beamwidth was 60° × 120° for –14 dB relative pattern level, corresponding to slightly under 2:1 aperture aspect ratio for both horns. Peak relative cross-polarization under –30 dB over more than 30% frequency band was achieved, which is a considerably wider band than what has been reported for elliptical and rectangular corrugated horns. Approximate analysis of propagation and radiation behavior in a rectangular dielcore waveguide with about 2:1 aperture aspect ratio was reported [25]. It was shown that for horns with a relative core permittivity of 2.5, relative peak cross-polarization under –30 dB is achievable for circularly polarized fields over more than 80% bandwidth, and probably over an even wider bandwidth for linear polarization. The corresponding bandwidth for a horn with relative core permittivity of 1.5 is 50%. Dielcore horns with a solid dielectric core have also been demonstrated for millimeter wave frequencies at 94 GHz and 175.5–191.5 GHz [26, 27]. For these implementations, the spacing between the core and the horn wall was provided by leaving radial spacers or rings as an integral part of the core wall. For lower frequencies the spacing can also be provided by rings or flexible sheets of low dielectric materials (e.g., foam or honeycomb).

A dielcore horn with a solid dielectric also has a natural built-in aperture lens that can be shaped for different applications. If designed as a focusing lens, the horn length can be reduced compared to a horn without a lens for the same gain [21]. The lens surface can also be synthesized to replace the secondary reflector in a dual reflector Gregorian antenna, generating similar co-polarized and cross-polarized radiation performance as the dual reflector antenna [28] (see Figure 6.6). Such a single feed reflector antenna can have packaging and cost advantages over the dual reflector system for some applications.

The soft dielcore horn in Figure 6.3 has so far seen few microwave applications due to either dielectric losses in the core, high-power limitations for use in ground station antennas, or potential ESD (electro-static discharge) issues and additional weight for satellite antenna use. Weight and dielectric losses can be reduced to a minimum if the core is built up as an artificial dielectric by sandwiching high permittivity dielectric plates together with foam or honeycomb spacers [29] (see Figure 6.7). Also, higher power could be enabled if the core is built from ceramic material. However, a better use for the soft dielcore horn in Figure 6.3 could be for millimeter-wave applications [26, 27] and potentially THz applications because of its simple design and potentially low cost constructions.

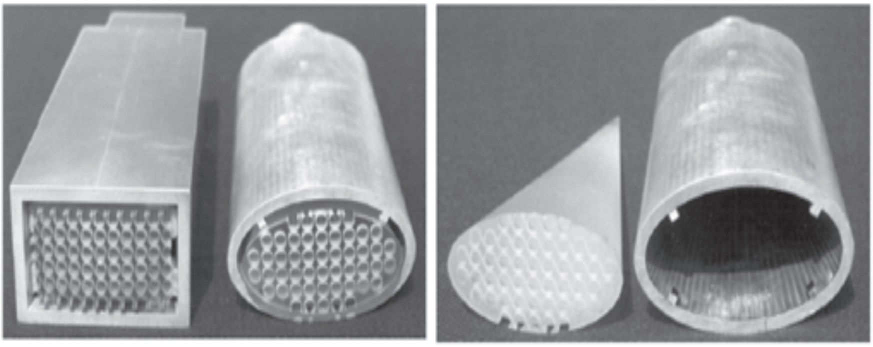

Figure 6.5 Photos of rectangular and elliptical soft dielcore horns designed to feed an elliptical reflector antenna.

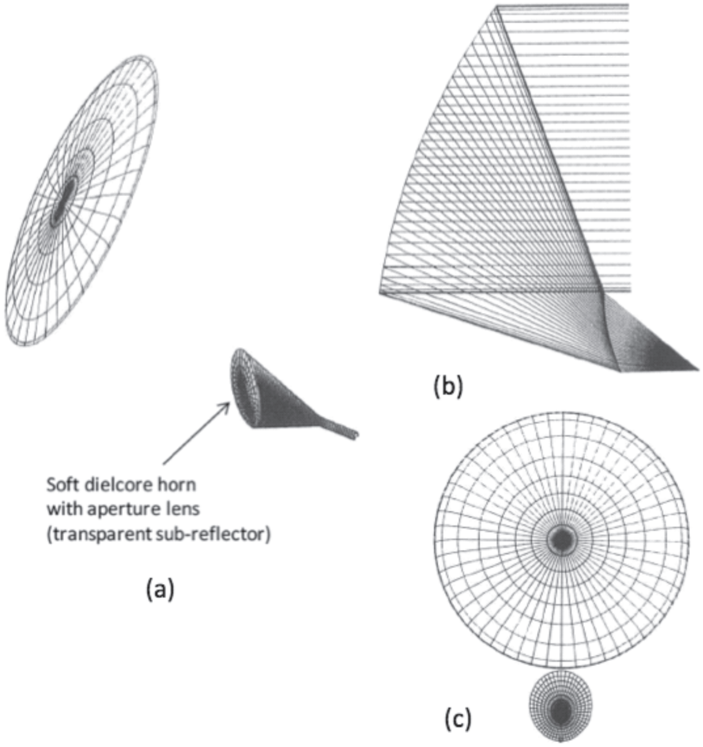

Figure 6.6 Illustration of a single reflector antenna fed by a soft dielcore lens horn, representing a compact alternative to a dual reflector antenna [28]. (a) Illustration of the feed-reflector system, (b) ray-tracing of the feed-reflector system, and (c) reflector aperture mapping of the feed-reflector system.

6.3.2.2 Hard or Selective Gain Dielcore Horns

A different dielcore horn concept was published [30, 31]. It applies an additional intermediate dielectric layer between the outer gap and the core, resembling the concept proposed in Lier [21]. This horn can be designed for any intermediate boundary condition between soft and hard, that is, a "*selective gain horn.*" Ideal soft or hard condition can be achieved by the right combination between the layer thicknesses and dielectric constants (see Figure 6.8). A design requirement is that the relative permittivity of the intermediate layer ε_{r2} is higher than that of the core material ε_{r1}, and that the relative core permittivity is higher than that of the outer gap material ε_{r3}. In other words, the horn can be designed to satisfy the balanced hybrid condition in the central core if

$$\varepsilon_{r2} > \varepsilon_{r1} > \varepsilon_{r3} \tag{6.10}$$

Similar to the propagation in the soft dielcore horn in Figure 6.3, the wave propagation normal to the boundary in the outer gap region is evanescent for this horn as well. Although the horn can be designed as a soft horn, its bandwidth is not as wide as for the simpler soft dielcore horn design in Figure 6.3 due to the additional dielectric layer. However, it may have lower weight and lower loss than the solid dielcore horn since the core may be made of a low density dielectric material,

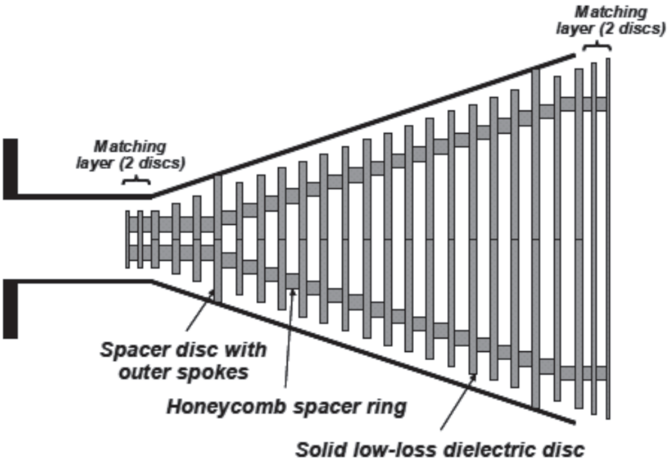
Matching layer (2 discs)
Matching layer (2 discs)
Spacer disc with outer spokes
Honeycomb spacer ring
Solid low-loss dielectric disc

Figure 6.7 Illustration of a soft dielcore horn implemented with an artificial dielectric core consisting of a multi-sandwich configuration of dielectric discs and honeycomb or foam spacer rings [29].

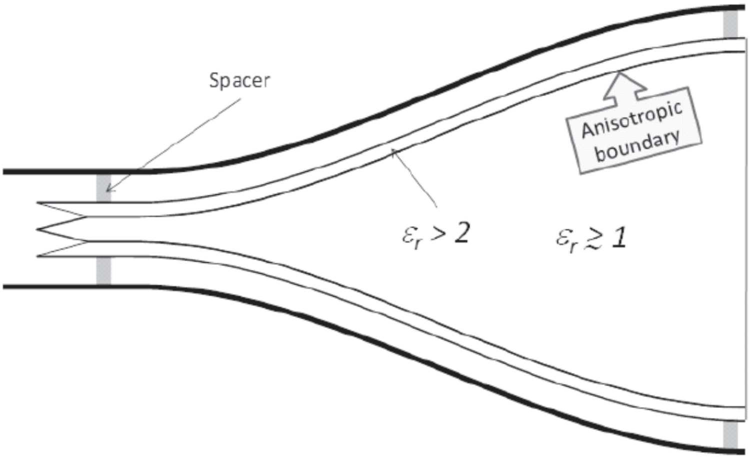
Spacer
Anisotropic boundary
$\varepsilon_r > 2$
$\varepsilon_r \gtrsim 1$

Figure 6.8 Illustration of hard or selective gain profiled dielcore horn [31].

such as foam, honeycomb, or artificial dielectric. This may in addition eliminate the need for a transformer layer in the dielectric-air aperture. It also represents the only known hard dielcore horn, as well as the first hybrid-mode horn to provide selective gain, depending on the design. For some antenna systems this enables the overall performance to be optimized beyond what is possible with only soft or hard horns.

Computing the co-polarized and cross-polarized radiation patterns of dielcore horns can be performed by using the model of a single hybrid-mode propagation in a cylindrical waveguide. This is demonstrated in Lier [21] for the soft horn and in Lier and Kishk [31] for the selective gain horn. The electrical and magnetic tangential field components on the boundaries between different layers are matched, resulting in a matrix equation for the determination of the propagation constants and field coefficients in the waveguide. By applying the solution to a waveguide with the same cross-section as the aperture of the horn under study, and by imposing a spherical phase front over the aperture corresponding to the horn flare angle, the far-field radiation patterns can be computed by standard aperture integration techniques. This approach is most accurate for relatively small flare angles since it models a single mode only. For large or nonlinear flare angles where higher order modes are no longer negligible, a mode matching approach would result in more accurate radiation patterns [32]. Although these analysis techniques are fast and efficient, they cannot easily be used on rectangular or nonsymmetric structures, and they require the generation of complex computer codes. For these applications, the method of moment (MoM) code is an alternative. Such codes are today commercially available and run relatively fast for most dielectric loaded horn designs (e.g., WIPL-D, FEKO).

To demonstrate the ability to design the horn with selective gain, the horn was designed with a number of aperture field distributions between soft and hard (see Figure 6.9(a)). Each distribution is designed to meet the balanced hybrid condition,

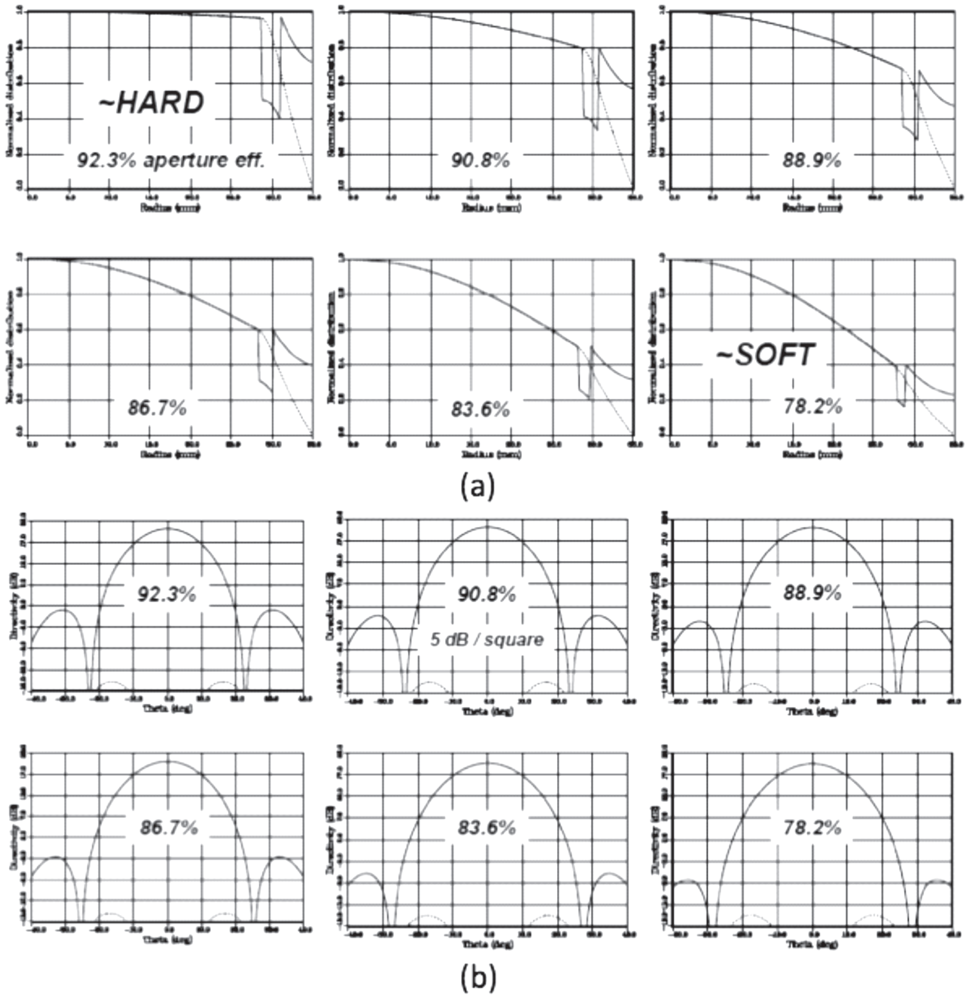

Figure 6.9 Computed performance of an open-ended waveguide, corresponding to a profiled dielcore horn shown in Figure 6.8, with approximately 3λ aperture diameter and uniform phase distribution. The analysis is based on a cylindrical model (single mode), and the horn is designed to satisfy the balanced hybrid condition for each case [31]. (a) Aperture field distribution (solid line is E-plane, dashed line is H-plane), and (b) co-polarized and cross-polarized radiation patterns, including aperture efficiency.

resulting in rotational symmetry and straight field lines inside the core with low cross-polarization. The aperture distributions are plotted in the 45° plane, and the transverse field components are identical over the aperture under balanced hybrid condition. In the boundary region between the core and the horn wall, the field distribution is not rotationally symmetric. The plotted aperture distribution shows that the transverse tangential φ-component of the field is continuous across the discontinuities, while the radial component is not, as expected. The corresponding antenna patterns are plotted in Figure 6.9(b). The first pattern models a hard horn with highest gain and relative sidelobes around –19 dB, exhibiting 92.3% aperture efficiency. This assumes a uniform phase front in the aperture that could be achieved by profiling the horn as shown inserted. The last pattern represents a soft horn, showing reduced directivity and lower relative sidelobes. The plots also demonstrate relative cross-polarization below –35 dB for all cases, proving that a hybrid mode under approximate balanced hybrid condition can be designed for any distribution between soft and hard for this horn.

To demonstrate the bandwidth potential for a hard dielcore horn, it was optimized for maximum aperture efficiency over the Ku-band based on a cylindrical model (see Figure 6.10). Two different designs were tried, one with more weight on efficiency (solid curve) and the other with more weight on bandwidth. The results indicate that high efficiency and low cross-polarization can be achieved over the band, allowing the horn efficiency and bandwidth to be traded for optimal antenna system performance.

A method-of-moments (MoM) analysis was performed on a profiled dielcore horn to study how much higher order modes will affect performance [31]. Figure 6.11 shows aperture efficiency (a) and relative peak cross-polarization (b) over the band. The computed aperture efficiency (dashed curves) is considerably higher than what was analyzed for a single mode based on a cylindrical model. This difference

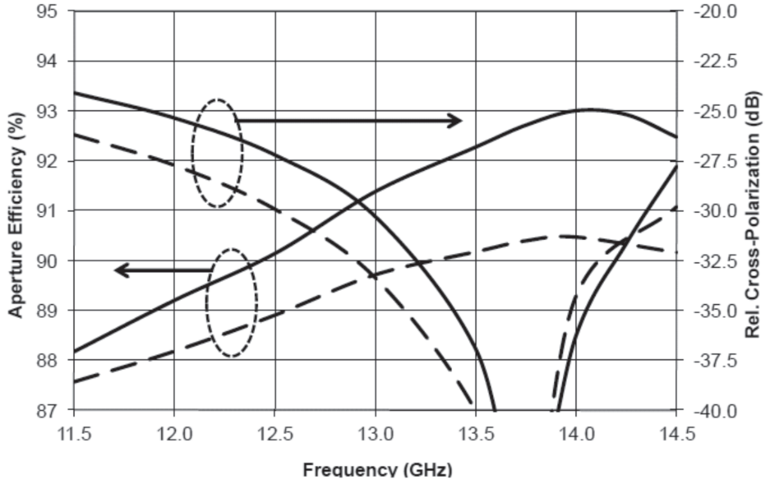

Figure 6.10 Computed aperture efficiency and relative peak cross-polarization versus frequency of an open-ended hard waveguide, corresponding to a profiled dielcore horn shown in Figure 6.8, with 70 mm aperture diameter and uniform phase distribution. The analysis is based on a cylindrical model (single mode). The two set of curves correspond to two slightly different designs, exemplifying the trade between aperture efficiency and bandwidth [31].

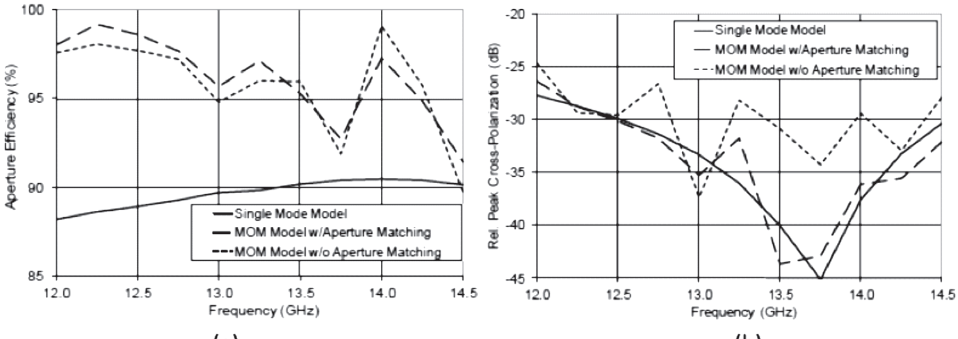

(a) (b)

Figure 6.11 Computed performance versus frequency of a profiled dielcore horn in Figure 6.8 with 70 mm aperture diameter and uniform phase distribution. The analysis is based on MoM (WIPL-D). (a) Aperture efficiency, and (b) relative peak cross-polarization. The solid curve is generated based on a cylindrical model, assuming a single mode. The two dashed curves correspond to analysis without aperture matching and with aperture matching by modeling a quarter-wave transformer layer in the circular dielectric ring in the aperture [31].

is due to a combination of higher order modes and aperture edge currents modeled by the MoM code. The oscillating nature of the plots is mostly due to reflections in the horn aperture and can be reduced by applying a matching layer in front of the two dielectric-air aperture boundaries, as shown in Figure 6.11. The analysis illustrates that aperture efficiency is only moderately affected while cross-polarization is considerably improved with aperture matching.

The horn in Figure 6.8 can also provide a flat-top pattern, as demonstrated in Figure 6.12. By exploiting the fields in the boundary region, as shown in Figure 6.12(a), a sinc-like aperture distribution can be obtained with a resulting flat-top pattern shown in Figure 6.12(b). This type of patterns can be used as global horns onboard satellites.

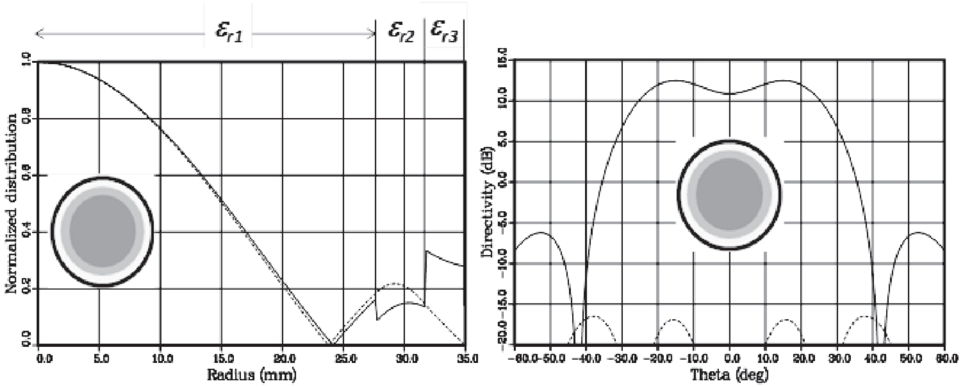

(a) (b)

Figure 6.12 Computed performance of an open-ended waveguide, corresponding to a profiled dielcore horn shown in Figure 6.8, with 70 mm aperture diameter and uniform phase distribution. The analysis is based on a cylindrical model (single mode). (a) Aperture distribution (solid line is E-plane, dashed line is H-plane), and (b) co-polarized (solid line) and cross-polarized (dashed curve) radiation patterns [31].

6.3.3 Soft Strip-Loaded Horns

A soft horn with circumferential strips on a dielectric wall liner was published [6] based on a plane wave model. A photo of the horn is shown in Figure 6.13(a). It was shown that the balanced hybrid condition could be met at two frequencies, in contrast to the corrugated horn, where balanced hybrid modes can be supported at a single frequency only. The work on the strip-loaded horn was extended [33], where a more accurate analysis was performed in a cylindrical waveguide (see Figure 6.13(b)). The paper also quantified the effects of radiation from the dielectric region in the aperture on the levels of cross-polarization.

For the soft strip-loaded horn, the thickness of the dielectric wall liner for balanced hybrid mode propagation is approximately given by

$$t_{diel} = \frac{\lambda_0}{4\sqrt{\varepsilon_r - 1}} \tag{6.11}$$

where ε_r is the relative permittivity of the liner. This formula is asymptotically exact for increasing waveguide diameter and corresponds to the lowest of the two balanced

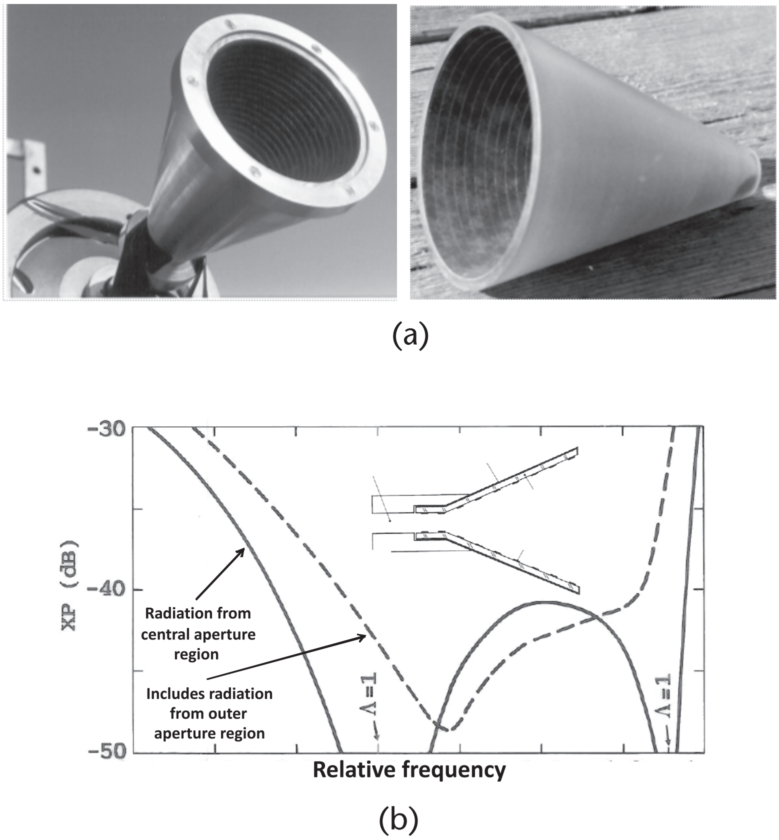

(a)

(b)

Figure 6.13 (a) Photo of soft strip-loaded horn, and (b) computed relative peak cross-polarization from a typical strip-loaded horn.

hybrid mode frequencies [33]. Compared to the thickness of a corrugated wall given in (6.4), we see that the two wall thicknesses are the same if $\varepsilon_r = 2$.

An experimental demonstration of the soft strip-loaded horn was presented [6], and a photo of this horn is shown in Figure 6.13(a). Relative cross-polarization under –27 dB from 11–14 GHz was achieved. Only limited effort was applied to optimize its performance due to the lack of design and analysis tools. Similar to corrugated horns, strip-loaded horns exhibit a resonant behavior caused by the strip-loaded wall, which limits its bandwidth to approximately an octave. However, since a balanced hybrid mode can be supported at two separate frequencies, the horn antenna is ideal for dual band transmit and receive satellite applications, such as Ku-band or Ka-band.

The circumferential strips can be etched out on a thin dielectric layer and wrapped and bonded inside of a hollow dielectric cone. This subassembly can then be mounted inside a conical metal horn (see Figure 6.13(a)). For rectangular or square horns, the boundary can be made from flat surfaces. This is a relatively low-cost process. When compared to a corrugated horn, the overall aperture diameter of the soft strip-loaded horn is smaller. This is because the thickness of the dielectric liner is smaller than the corrugation depth for $\varepsilon_r > 2$. The overall weight may also be less.

6.3.4 Hard Strip-Loaded and Corrugated Horns

The hard strip-loaded horn with longitudinal strips on a dielectric wall liner mentioned earlier in this chapter was analyzed [33] based on a cylindrical waveguide model. It was shown that a quasi-TEM balanced hybrid mode can be supported when the thickness of the dielectric liner approximately satisfies (6.11), which is the condition for balanced hybrid mode propagation in the soft strip-loaded horn. As in the soft horn case, this equation is asymptotically correct for increasing waveguide cross-sections and is therefore most accurate in the radiating aperture of the horn. The same formula also applies to the corrugation depth of the hard corrugated horn with longitudinal corrugations filled with dielectric material [7, 34]. A comparison between the two implementation approaches of hard horns was published in Lier [35] based on a cylindrical model analysis.

In Lier and Kildal [2, 34], an experimental investigation of hard strip-loaded and corrugated horns was presented. A photo of these horns is shown in Figure 6.14, and measured and predicted patterns are shown in Figure 6.15. Although the bandwidth was low due in part to the absence of accurate modeling and design software, the results represented the first experimental proof-of-concept of these horns.

It was further shown [33] that in addition to the hybrid mode, a microstrip line mode can be supported in the horn, which could significantly deteriorate antenna performance for many practical applications. A more accurate analysis of the hard strip-loaded horn was given [36], based on the mode matching approach, demonstrating that surface modes are indeed excited and supported in the horn, reducing the applicability of this horn. However, a way of suppressing this surface mode is to apply vias between the longitudinal strips and the horn wall as proposed and modeled by mode matching [37]. This offers similar performance to that of hard corrugated horns but may result in a lower cost implementation and lower weight.

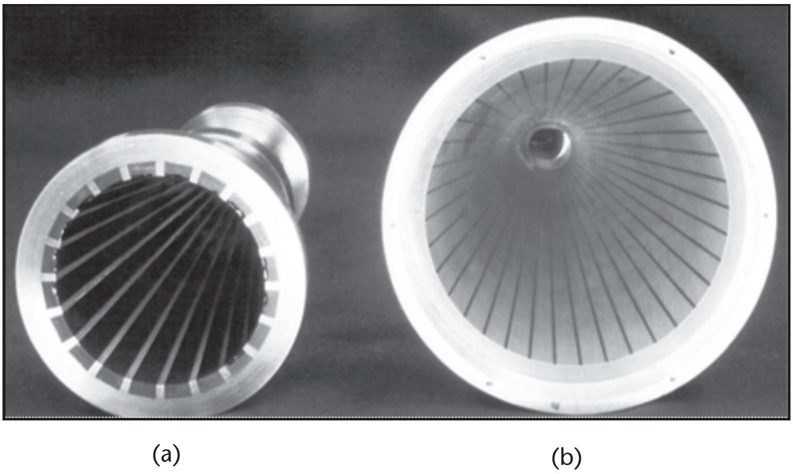

Figure 6.14 Photos of (a) hard corrugated, and (b) hard strip-loaded horns.

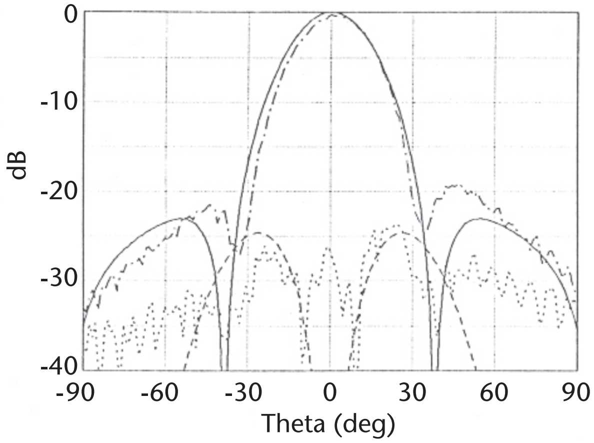

Figure 6.15 Measured (dashed) and predicted (solid) co-polarized and cross-polarized antenna patterns from the hard strip-loaded horn in Figure 6.14.

The hard corrugated horn was modeled and analyzed by mode matching [38]. A dual depth hard corrugated horn was proposed and studied [39]. An experimental demonstration of a dual band and multimode Ka-band hard corrugated horn was reported [40].

Finally, the bandwidth of a strip-loaded and corrugated hard horns based on a rectangular waveguide model was addressed [41]. The approximate analysis indicated that about 12% bandwidth for a 2λ aperture diameter is achievable for these horns.

6.3.5 Metamaterial Horns (Meta-horns)

6.3.5.1 Introduction

Metamaterials is an artificial material or structure with subwavelength unit cells, typically below $\lambda/5$, that can guide electromagnetic waves in unprecedented ways.

For example, it can be designed to provide an effective index of refraction for the wave between zero and unity or even negative, or a graded index of refraction. At RF frequencies it can be constructed from metal, dielectric, and/or air (vacuum).

The idea of the metamaterial horns or meta-horns came from studying the two dielcore horns presented in Section 6.3.2 [42, 43]. The requirement for supporting the balanced hybrid mode in these horns is that the dielectric core material has a higher permittivity than the material in the outer region next to the wall. In order to remove the central core, obtaining $\varepsilon_{r1} = 1$ (air, vacuum), the medium in the wall gap region has to be implemented effectively as a low permittivity metamaterial, that is, $\varepsilon_{r2} < 1$ in Figure 6.3 and $\varepsilon_{r3} < 1$ in Figure 6.8. This concept is illustrated in Figure 6.16. It is assumed that the relative permeability μ_r is close to unity for the dielcore horns. However, for the meta-horns the permittivity and permeability are dispersive in the metamaterial for all practical implementations, so the requirement for meeting the balanced hybrid condition is that the refractive index $n = (\varepsilon_r \mu_r)^{1/2} < 1$. In other words, supporting a balanced hybrid mode requires a low index metamaterial in the outer region for both the soft and the hard (or selective gain) meta-horns.

Meta-horns and dielcore horns yield theoretically similar performance since the internal hybrid mode propagation is governed by the same set of equations presented in Lier [21] and Lier and Kishk [31]. They have evanescent wave propagation orthogonal to the boundary in the outer region, facilitating large bandwidth. Also, the hard meta-horn can be designed for selective gain and with flat-top patterns as shown in Section 6.3.2. One advantage of meta-horns over dielcore horns is the absence of a central core, which reduces weight and insertion loss and eliminates reflections from the dielectric-air aperture boundary [43]. These benefits make these horns considerably more attractive as feeds in satellite antennas and enable them to be used in high-power applications, such as ground terminal antennas for satellites and radars. A second advantage of meta-horns over dielcore horns is that they provide a new electromagnetic boundary that can be applied to open EBG (electromagnetic band gap) surfaces, high impedance surfaces, artificial magnetic conductors (AMC)

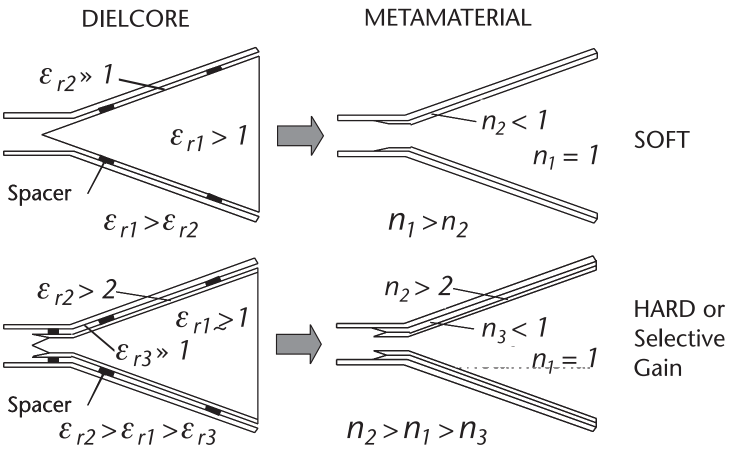

(a) (b)

Figure 6.16 Illustration of (a) dielcore horns, and corresponding (b) metamaterial horns.

or ground planes, radar cross-section (RCS) reduction, or RF cloaking, and soft and hard surfaces in general. The main challenge in building meta-horns lies in the implementation of the meta-liners, which will be discussed in this section.

Figure 6.17 [43] illustrates these soft and hard metamaterial boundaries and compares them to conventional surfaces for grazing incident fields. The soft surface is simply a low-index metaliner or metasurface on a metal ground plane or waveguide wall. The hard surface similarly contains a low index meta-liner on the metal ground, with an additional dielectric liner on top. As stated previously, corrugated and strip-loaded surfaces exhibit resonant nature, limiting the continuous bandwidth to typically under an octave. Meta-surfaces on the other hand have evanescent wave propagation inside the metamaterial layer and normal to the surface. This facilitates large potential bandwidth, in particular for the soft meta-horn.

Since the EM propagation in a general region is uniquely determined by its boundary conditions, the design of soft or hard waveguides and horns can be achieved by proper design of the wall impedances Z^{TE} and Z^{TM} satisfying (6.1). In the horn aperture, these anisotropic wall impedances can be approximately derived from a near grazing incident plane wave to the surface, resulting in approximate formulas for desired geometry and refractive index. These values can in turn be used as initial starting points in a cylindrical or spherical waveguide model with effective homogeneous liners, synthesizing the desired geometry (liner thicknesses) as well as the refractive index versus frequency. Low cross-polarization is automatically achieved if (6.1) is met. In the next step, the resulting geometry and refractive index dispersion are used as targets during the analysis and synthesis of the actual metasurface. This can be done most effectively by a full wave modeling software. A basic requirement for the metasurface geometry is that the unit cells or repetition period be much smaller than a wavelength such that the effective surface impedances and an equivalent refractive index can be found, ensuring good correlation between the uniform liner model and the actual implementation. In the final step, a parameter extraction technique can be performed to correlate the predicted complex reflection

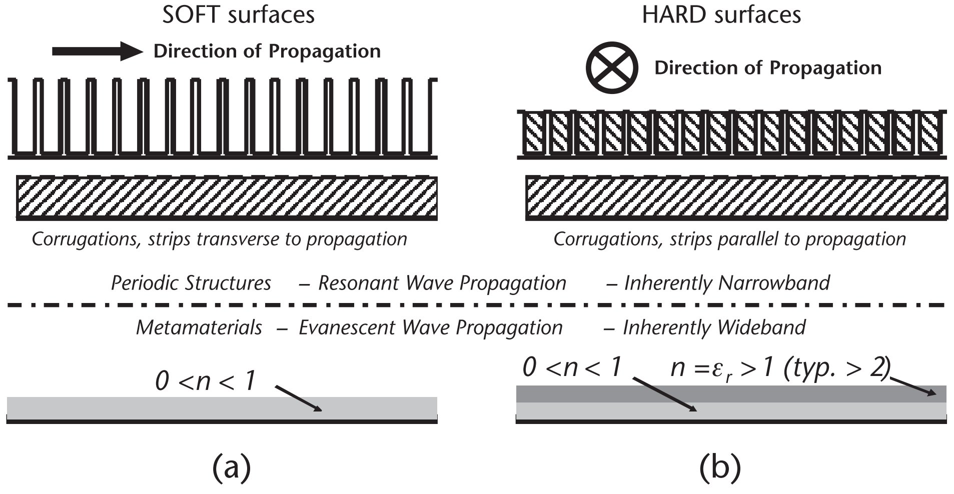
SOFT surfaces
Direction of Propagation
HARD surfaces
Direction of Propagation
Corrugations, strips transverse to propagation
Corrugations, strips parallel to propagation
Periodic Structures – Resonant Wave Propagation – Inherently Narrowband
Metamaterials – Evanescent Wave Propagation – Inherently Wideband
0 <n < 1
0 <n < 1
n =ε_r > 1 (typ. > 2)
(a)
(b)

Figure 6.17 Comparison of different implementations of soft and hard boundaries, including meta-boundaries [43].

coefficients from the surface to the effective index of refraction. This process will be demonstrated in the following section.

6.3.5.2 Soft Meta-Horns

For the meta-horn proposed in Lier and Shaw [42], it was not at all obvious that metaliners were realizable over a reasonable bandwidth due to dispersion in the actual composite or complex material. Therefore, in this paper feasibility studies of both soft and hard meta-horns based on a cylindrical model were presented to ensure that the horn was implementable. The effective permittivity of the metaliner has to follow a Drude-type behavior [44, 45] to ensure it works over a reasonably large bandwidth. The Drude curve approximately models the EM propagation in a dense material with subwavelength unit cells or electric and magnetic molecules. The feasibility studies [42] indeed showed that the desired dispersion increased monotonically like the Drude curve both for the soft and hard meta-horns, which opened the possibility that an actual metaliner can indeed be realized over more than a narrow bandwidth.

Here a similar feasibility study for the soft metahorn over a multi-octave frequency band is presented based on a cylindrical model. The relative permittivity providing minimum cross-polarization is analyzed and plotted against the frequency. The resulting curve is shown in Figure 6.18 [43]. The ideal permittivity increases monotonically between zero and unity, which constitutes a low index metamaterial, assuming the relative permeability μ_r is unity. The first order Drude term with an appropriate resonance frequency is plotted in the same chart, showing that the ideal permittivity curve approximately follows the monotonically increasing Drude curve over multiple octaves. This indicates that the low-index soft metaliner indeed can be implemented over a large or even multi-octave bandwidth. The bandwidth

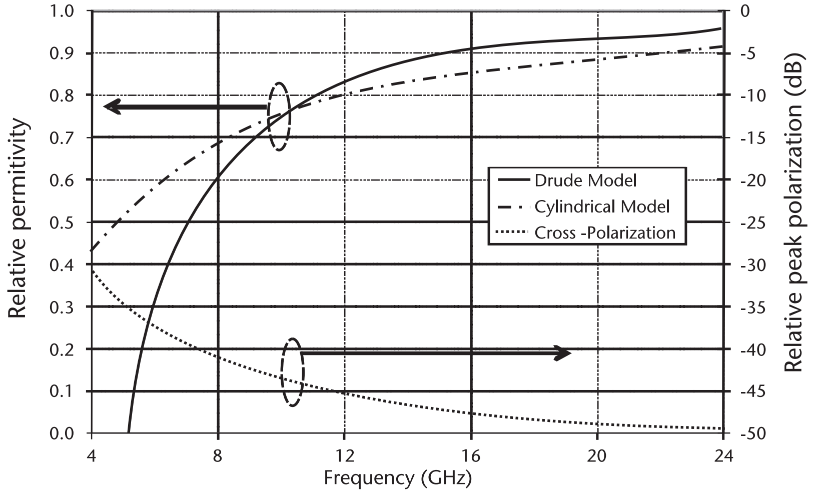

Figure 6.18 Optimal dispersion curve and cross-polarization for a soft meta-horn shown in Figure 6.16 supporting a balanced hybrid mode with minimum cross-polarization over the frequency band. The solid curve is the Drude dispersion curve with resonance around 4 GHz. The analysis is based on a cylindrical model with 70 mm aperture diameter and 7° semi-flare angle [43].

will be limited by the excitation of higher order modes in the input waveguide to the horn unless they are fed by a multi-octave input section, such as a ridged waveguide.

Even though the feasibility of realizing the metaliner has been established, the design of the actual liner poses a substantial challenge. First the desired or optimal liner geometry and effective dispersion characteristics of the refractive index have to be generated to meet the particular requirements. The second step is to design the actual liner meeting the desired characteristics. The unit cell or periodicity of the metamaterial has to be much smaller than a wavelength (e.g. $< \lambda/10$) for the structure to be modeled as an effective medium. The first meta-horn experiment was performed for a single polarization C-band pyramidal horn [46–48]. Single polarization was selected to simplify the first attempt and thereby increase the chance for success. A pyramidal horn with an E-plane metaliner was chosen to compare the performance to that of an E-plane trifurcated horn [49, 50], proving that meta-horns can be used in real-world applications and not only as an interesting science experiment. The extended C-band (3.4–4.2 GHz downlink, 5.85–6.725 GHz uplink) was targeted since it represents one of the greatest challenges with respect to antenna bandwidth, weight, and cost for microwave horn antennas.

A photo of the C-band horn is shown in Figure 6.19. The effective refractive index of a homogeneous metaliner with respect to the internal field was first optimized for best co-polarized and cross-polarized pattern performance and is shown in Figure 6.20(a). The real value of the relative permittivity increases monotonically with frequency from close to zero to close to 2, while the real value of the relative permeability is close to 0.2 over the entire band. The resulting refractive index increases monotonically from approximately 0.1–0.7 over the band (see Figure 6.20(b)). The imaginary parts of permittivity and permeability (and the refractive index) are close to zero over the entire frequency band, indicating negligibly low loss. The metaliner is built up of a wire grid with a radial wire connected to the wall, a transverse continuous wire, and a piecewise broken wire along the horn [46–48]. Predicted and measured radiation patterns are shown in Figure 6.21. This first experimental demonstration of meta-horns provides over an octave pattern bandwidth with negligible loss.

It should be noted that this horn is not a true hybrid mode horn or soft horn since it was designed for single polarization only. However, since the top part of the wire grid is continuous in the transverse direction, the tangential E-field will be forced to

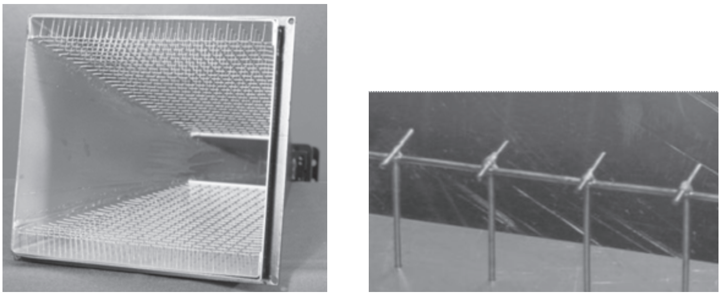
(a) (b)

Figure 6.19 Photo of (a) single polarization meta-horn, with (b) E-plane wire-grid metaliner [46–48].

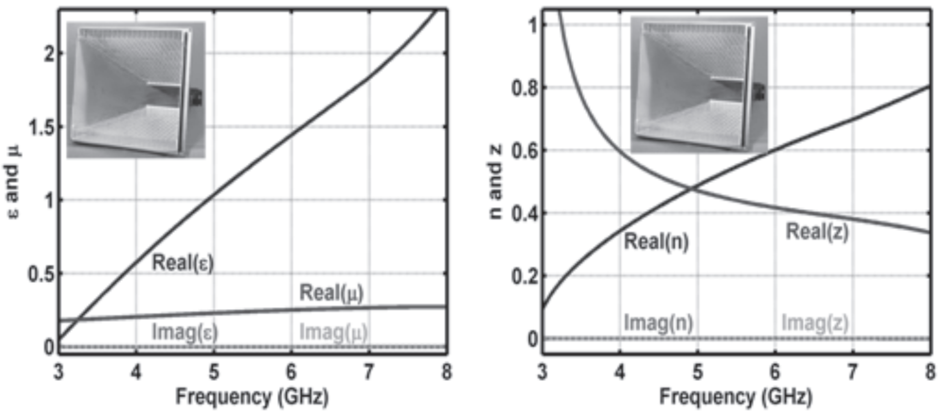

(a) (b)

Figure 6.20 (a) Optimized effective relative permittivity and permeability, and (b) effective refractive index and boundary impedance of a homogeneous metaliner in the horn in Figure 6.19.

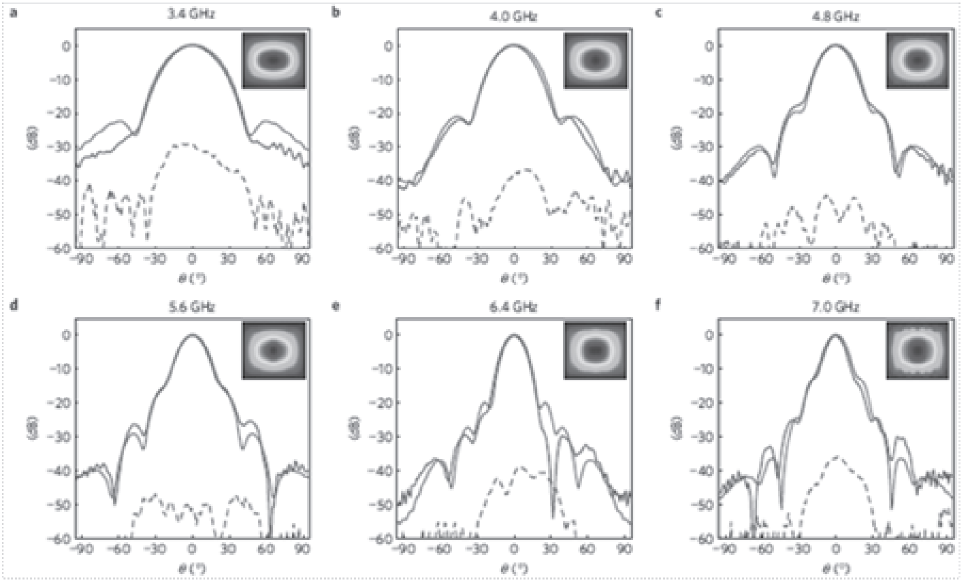

Figure 6.21 Measured co-polarized and cross-polarized radiation patterns of the horn in Figure 6.19 at several frequencies over the band. The graphics in the upper-right corner of each pattern show the predicted aperture distribution of the hybrid mode in the horn with highest value in the center [46–48].

zero on the boundary in the H-plane, and approximate soft hybrid mode propagation is expected for both circular and rectangular horns. This is demonstrated in Figure 6.22, where a similar soft boundary condition wire grid liner inside a conical horn was modeled and analyzed (graph provided by Q. Wu, C. P. Scarborough, and D. H. Werner at the Pennsylvania State University under contract with Lockheed Martin). Computed relative cross-polarization is below –33 dB from 11–17 GHz, and below –27 dB from 11–18 GHz. The wire grid liner has no dielectric material, which makes

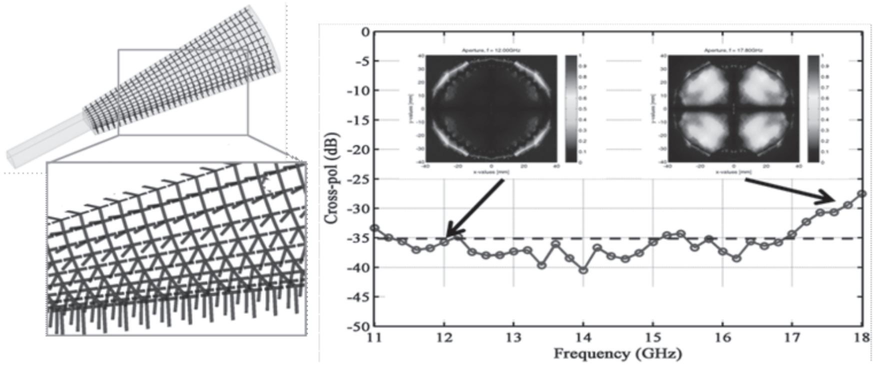

(a) (b)

Figure 6.22 Illustration of (a) conical soft wire grid horn, and (b) predicted relative peak cross-polarization.

this horn an excellent candidate for satellite applications and a real alternative to corrugated horns with the potential for lower weight and larger bandwidth.

A design approach for inhomogeneous metaliners with varying cell structure along the horn was demonstrated [51]. By engineering the metaliners with regard to their surface impedance as well as tailoring their spatial distributions along the wall of the horn, it was demonstrated that an inhomogeneous soft meta-horn with broader bandwidth compared to those with uniform liners was achieved. Relative peak cross-polarization below –30 dB was computed over an octave bandwidth, and return loss was above 20 dB over the upper 80% of the band. One particular challenge in the design of meta-horns is matching the band with low cross-polarization to the band with low return loss. This is due to the fact that the low index metaliner lowers the cut-off frequency in the horn throat, which drives the input diameter of the horn higher. The result is that cross-polarization in the upper band degrades due to excitation of higher order modes near the horn throat.

A nature-inspired optimization method was applied [52] in designing metasurfaces with customized electromagnetic properties for soft and hard horn antennas. The designs of several metasurfaces and their use as liners for coating the interior walls of horn antennas were explored. The design process combines the genetic algorithm optimization technique with a full-wave electromagnetic solver to create dispersion-engineered metamaterials that possess customized surface impedance properties. A metamaterial parameter extraction technique was developed and employed in the optimization process, which is based on the surface impedance expressions for a homogeneous slab backed by a perfectly conducting ground plane illuminated at near grazing incidence.

A square soft Ku-band meta-horn is shown in Figure 6.23 [53]. The metaliner in this horn was built with printed circuit board (PCB) technology, which ensures low cost manufacturing. The PCB consists of uniform metal patches on one side and a ground plane on the other, and with vias connecting the two sides. Figure 6.24 shows predicted boundary impedances (a) and effective refractive index (b) versus frequency for the meta-liner. From the impedance chart we notice that in the lower frequency band, the boundary condition is closest to soft as defined in (6.2), and the

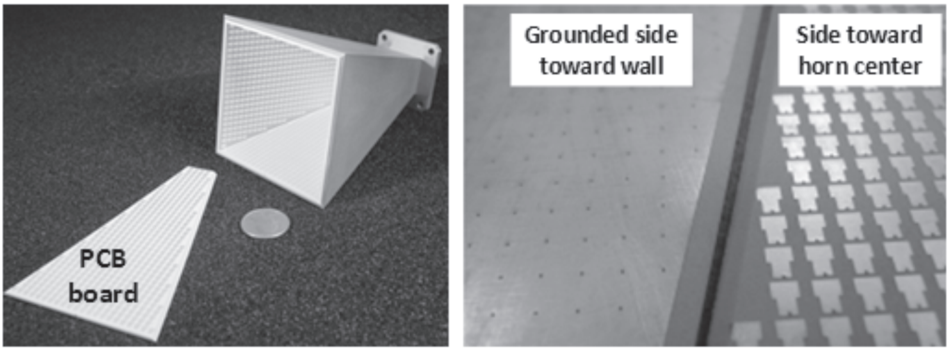
PCB
board
Grounded side
toward wall
Side toward
horn center

(a) (b)

Figure 6.23 Photo of (a) square soft meta-horn, with (b) PCB liners consisting of grounded unit-cell patches. The aperture diameter is 70 mm and the horn length is 100 mm [53].

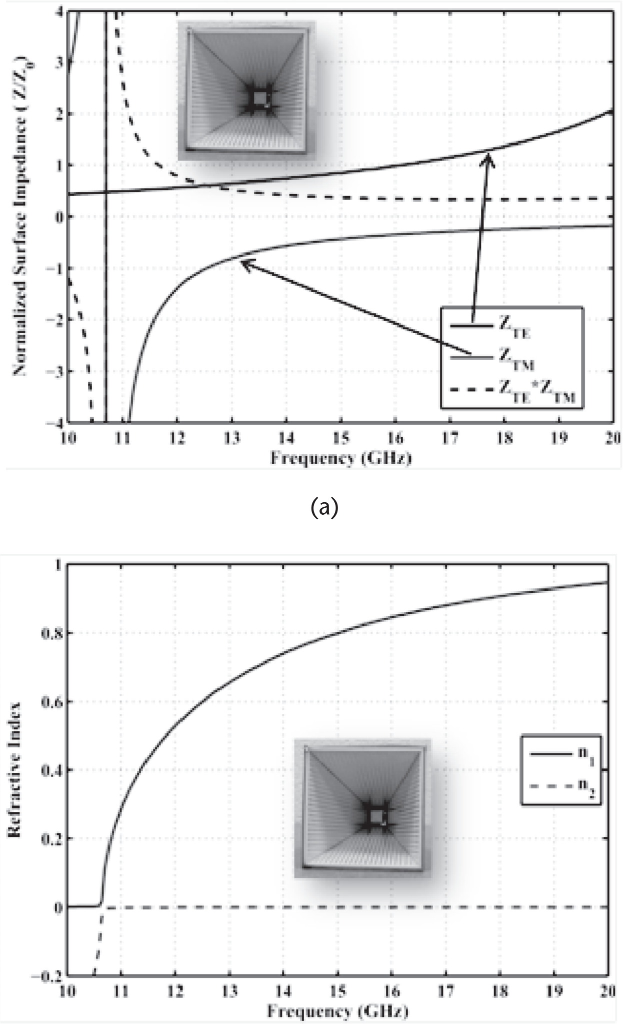

(a)

(b)

Figure 6.24 (a) Boundary impedances, and (b) refractive index of the metaliner with respect to the internal hybrid mode for the horn in Figure 6.23 [53]. The subscript "1" denotes real value and "2" imaginary value.

product of the impedances is closest to meeting the balanced hybrid condition as defined in (6.1). The refractive index stays below unity over the extended Ku-band. Similar to the E-plane meta-horn discussed previously, the curve is monotonically increasing similar to the Drude curve, and the imaginary part is small, indicating negligible propagation loss for the hybrid mode. Figure 6.25 shows predicted and measured radiation patterns. Relative peak cross-polarization close to –30 dB has been achieved in the lower band (12/14 GHz) and increases above –25 dB in the 17 GHz band, which would need some improvement for satellite applications. If PCB liners can be implemented on a conical wall, substantial wider bandwidth can be achieved compared to pyramidal horns. Although the PCB technology cannot easily be implemented on curved surfaces, a conical soft meta-horn offers substantially

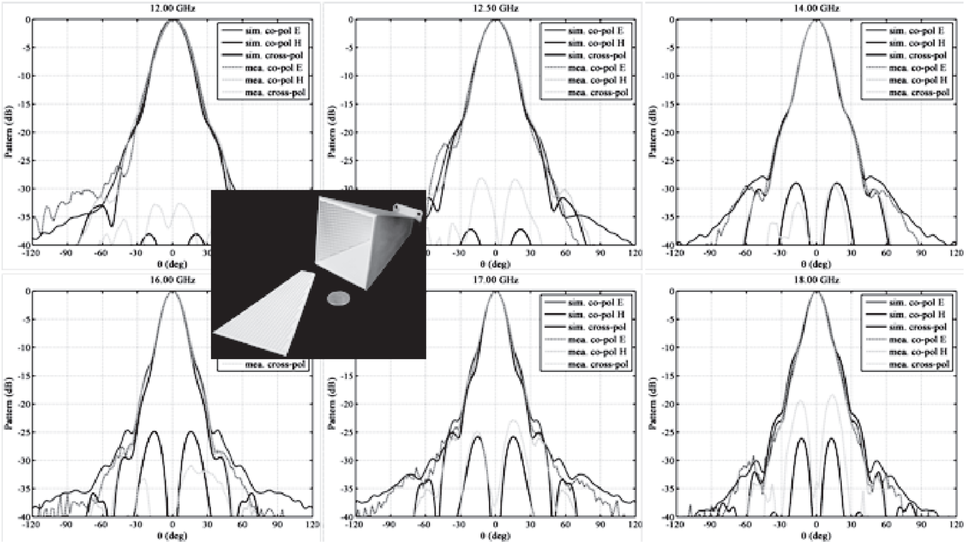

Figure 6.25 Measured and predicted co-polarized and cross-polarized radiation patterns at several frequencies from the square meta-horn in Figure 6.23.

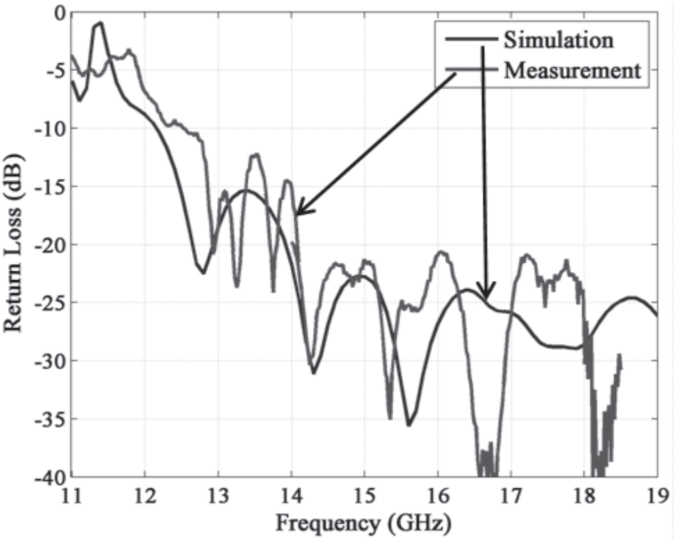

Figure 6.26 Measured and predicted return loss from the soft meta-horn in Figure 6.23.

larger bandwidth compared to pyramidal horns. Figure 6.26 shows measured return loss at the square waveguide input, which is below –15 dB over almost the entire band but with deteriorating return loss in the lower band. This exemplifies the previous discussion on the return loss challenge.

This horn represents the first experimental demonstration of a true soft meta-horn, proving that practical soft meta-horns with large bandwidth, very low loss and weight, and low manufacturing cost are achievable. Soft meta-horns may in the future replace corrugated and trifurcated horns with the potential for better overall antenna performance in a wide range of radar and satellite applications, such as tri-band [54] and extended C-band.

6.3.5.3 Hard Meta-Horns

As mentioned in the previous section, feasibility studies of both a soft and a hard meta-horn were performed based on a cylindrical waveguide model [42]. In Figure 6.27 the optimum relative permittivity curve for the hard metaliner generating maximum aperture efficiency and relative cross-polarization under –30 dB was plotted over the selected frequency band. A monotonically increasing dispersion curve from 10.5–14.5 GHz was obtained. Since the desired dispersion curve is similar to the Drude curve, feasibility has been established for the hard horn as well. This bandwidth is substantially larger than the 12% bandwidth estimated for the corrugated and strip-loaded hard horns presented [35, 41]. Corresponding co-polarized and

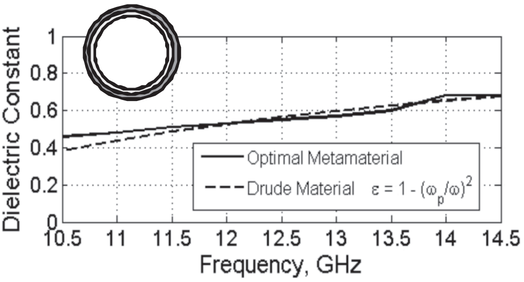

Figure 6.27 Optimal dispersion curve for a hard meta-horn shown in Figure 6.16 supporting a hybrid mode with maximal directivity and approximately –30 dB relative peak cross-polarization over the entire frequency band. The aperture of the horn is shown inserted. The dashed curve is the Drude dispersion curve. The analysis is based on a cylindrical model ($\varepsilon_{r2} = 3.0$, $\varepsilon_{r3} = 0.7$, dielectric thickness $t_2 = 1.8$ mm, metamaterial thickness $t_3 = 2.7$ mm, input waveguide diameter = 18 mm, aperture diameter = 80 mm, horn semi-flare angle = 7.5°) [42,43].

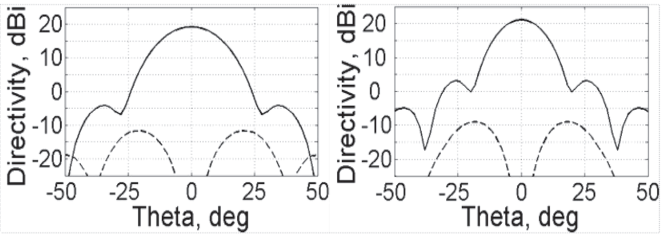

Figure 6.28 Computed co-polarized and cross-polarized directivity patterns based on a cylindrical model for the hard metamaterial horn defined in Figure 6.16 in the 45° phi-cut. The aperture of the horn is shown inserted. The semi-flare angle of the horn is 7.5° [43]. (a) 12.0 GHz, and (b) 14.5 GHz.

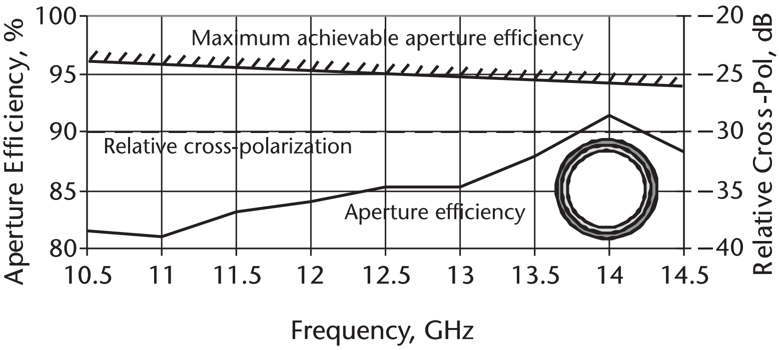

Figure 6.29 Computed aperture efficiency and relative peak cross-polarization versus frequency based on a cylindrical model for the hard horn defined in Figure 6.16. The aperture of the horn is shown inserted. Maximum achievable aperture efficiency is between 94 and 96% caused by the aperture phase error from the 7.5° semi-flare angle [43].

cross-polarized radiation patterns at low and high frequency over the band are plotted in Figure 6.28. The predicted low cross-polarization demonstrates that a hybrid mode approximately satisfying the balanced hybrid condition is supported in the horn. The corresponding aperture efficiency curve is shown in Figure 6.29, ranging from above 80% in the lower band to above 90% in the upper band.

6.4 Hard Horns as Feeds for Array Antennas

The hard horn is ideal as a feed element in arrays with typically 2.5λ or larger diameter, which is needed for limited scan phased arrays and as feeds in multibeam reflector antennas. Maximum gain can be achieved by profiling the flare of the hard horn to obtain uniform aperture phase. Also, by making the aperture hexagonal approximately 10% (0.42 dB) higher array packaging efficiency can be achieved over a circular aperture (see Figure 6.30). Profiled hard meta-horns with circular and hexagonal aperture cross-sections were compared based on a method-of-moments analysis [55, 56] (WIPL-D). Figure 6.31 shows the ideal dispersion curve over the Ku transmit frequency band 12.2–12.7 GHz, while Figure 6.32 shows the corresponding aperture efficiency and cross-polarization. For both horns aperture efficiency over 90% and relative peak cross-polarization below −30 dB was obtained over the band.

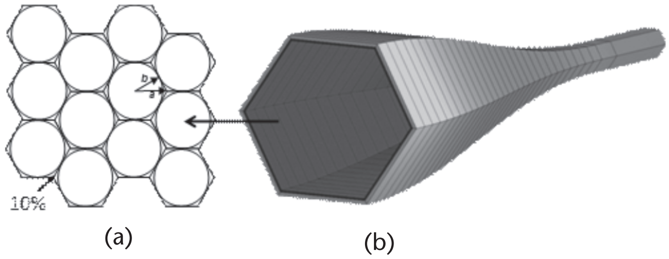

Figure 6.30 (a) Illustration of array with (b) hard profiled hexagonal metamaterial horn elements [56]. As indicated, the hexagonal horn aperture offers 100% packaging efficiency while a circular horn aperture has 10% less aperture efficiency (ideally).

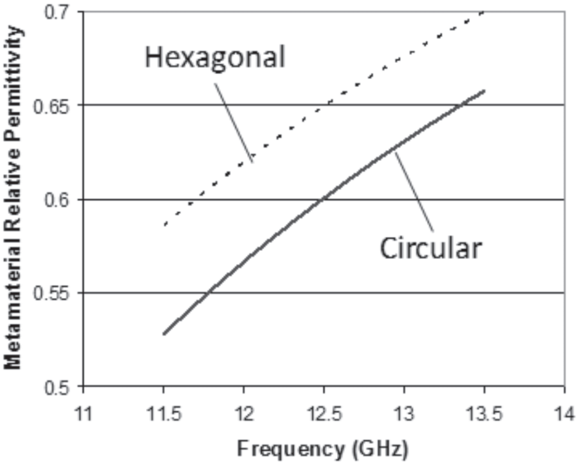

Figure 6.31 Optimized ideal permittivity versus frequency based on MoM (WIPL-D) analysis for maximum aperture efficiency and peak relative cross-polarization below −30 dB for profiled circular and hexagonal horns with 83 mm aperture diameter and 208 mm length [56].

The overall aperture efficiency of the array is unchanged for the hexagonal horn element due to 100% packaging density. However, for the circular horn element, the same efficiency is reduced by about 10%, resulting in 80–85% array aperture efficiency. As a result, the profiled hexagonal hard hybrid-mode horn has the largest potential array efficiency or gain of all known high-efficiency aperture horns. It should be mentioned that mutual coupling increases with increased horn and packaging efficiency, which should be accounted for when analyzing and designing the array.

For multibeam reflector antennas for fixed satellite services, this efficiency advantage can be used to increase the overall antenna gain by reducing feed spillover loss outside the reflector. Alternatively, the increased efficiency can be used to achieve higher resolution for the beams on the ground by placing the feeds closer together [57]. In effect, additional satellite beams become available to cover the same region on the ground, resulting in increased traffic capacity.

A typical requirement for multibeam reflector systems is congruency between transmit and receive beams. A study was done to achieve the optimum feed efficiency

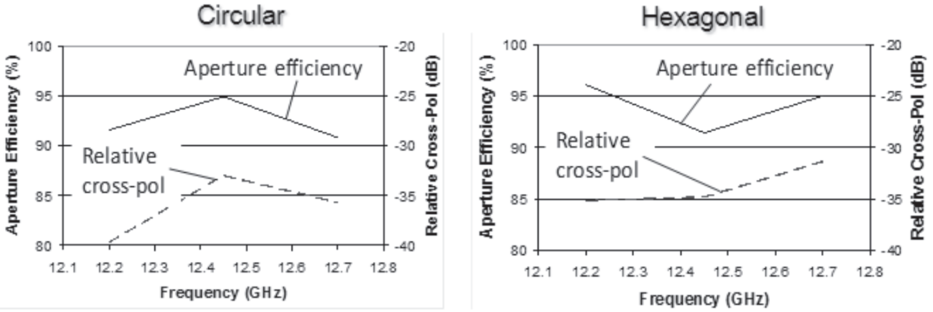

(a) (b)

Figure 6.32 Computed aperture efficiency and relative peak cross-polarization based on MoM (WIPL-D) analysis for (a) circular, and (b) hexagonal profiled horns with 83 mm aperture diameter and 208 mm length [56].

curve for an ideal hybrid-mode horn (i.e., symmetric aperture distributions) to achieve congruent beams from a multibeam parabolic reflector antenna [57]. Figure 6.33(a) shows the optimized feed efficiency curve versus frequency from 12–30 GHz, while Figure 6.33(b) shows the corresponding beam patterns, which demonstrate that the feed efficiency curve results in approximate beam congruency over the entire Ku-Ka band. The feed model used is described in Figure 6.33(c), which models an adjustable amplitude taper for optimization (parameter *p*). Feed-reflector spillover loss is naturally the highest at the lowest frequency, which is downlink or transmit; therefore high feed efficiency is more crucial in this band. The results show that for a 20/30 GHz Ka-band satellite antenna, the approximate ideal uplink feed horn efficiency is 9% less than the downlink horn efficiency. The corresponding numbers for a 12/14 and 12/17 GHz Ku-band antenna are approximately 3 and 6%, respectively. Lower required feed horn efficiency in the uplink or receive band is beneficial because it enables higher weight in the optimization of the downlink or transmit horn, resulting in higher efficiency. Following this approach in the design of the feed horn will result in a more optimum overall multibeam antenna system when compared to the more common requirement for constant or maximum feed efficiency over the transmit and receive bands.

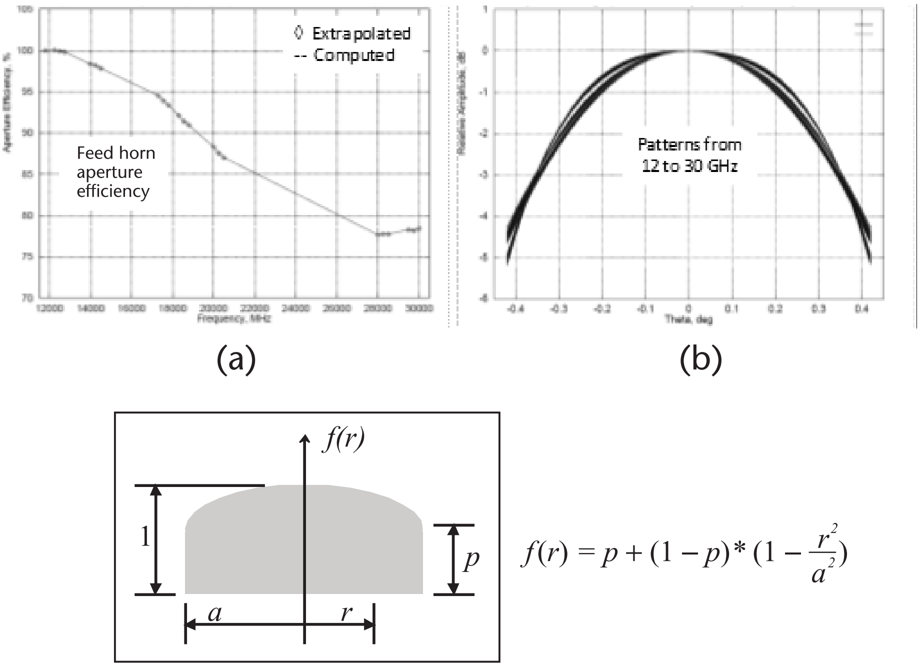

$$f(r) = p + (1 - p) * (1 - \frac{r^2}{a^2})$$

(a)

(b)

(c)

Figure 6.33 Optimized (a) feed horn aperture efficiency, (b) resulting beam patterns at multiple frequencies over the band corresponding to the predicted frequencies in (a), and (c) feed aperture model. The reflector antenna analysis is performed by GRASP. The feed horn model is a circular open-ended waveguide aperture with diameter $2a = 81$ mm with adjustable amplitude taper. The aperture distribution has perfect circular symmetry following the distribution in the radial direction according to the formula. The parameter *p* is optimized to provide an aperture efficiency that generates the desired secondary beam diameter. The reflector system has a focal length over diameter (*F*/*D*) of 1.4 [57].

6.5 Conclusions

Soft and hard horn antennas are hybrid-mode horns, which produce polarization-independent co-polarized patterns and low cross-polarization for dual linear or circular polarization. Soft horns are low gain horns with low sidelobes, which makes them useful as single feeds for reflector antennas in radar and satellite applications. Hard horns with their high aperture efficiency and high gain are ideal as antenna elements in limited-scan phased arrays, feed elements for multibeam reflector antennas [8], and potentially as spatial combiners for quasi-optical amplifier arrays [9, 10, 58]. Some dielcore and meta-horns can be designed with selective aperture distribution and thereby selective gain. This feature could be exploited to optimize gain and sidelobes in various antenna systems where soft or hard horns do not provide optimal performance. These horns can also be designed with flat-top patterns, which can be used as global horns for satellite applications.

Table 6.1 shows a list of soft and hard horns known from the open literature and presented in this chapter [59]. They are listed in chronological order based on the date they were first published. The table presents a brief list of advantages and disadvantages for each horn, which should be considered typical rather than absolute.

Although the corrugated horn has been the only practical soft horn for almost fifty years, there are today alternative designs which could improve RF performance in some applications and reduce weight and cost in others. This is particularly the case for the soft meta-horn, which can be designed to provide an octave bandwidth or more. Hard meta-horns offer higher efficiency and larger bandwidth than other high-efficiency horns, such as multimode horns. The technology behind meta-horns is rapidly advancing and made possible by the development over the last decade of efficient EM design, analysis, and synthesis tools.

Table 6.1 Classification of Hybrid-Mode Horn Antennas [59]

Illustration Photo	*Class Name*	*First Ref.*	*Pros (+) and Cons (–)*
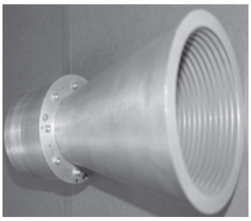	• Soft • Corrugated	1962–66 [14, 15]	+ Heritage at microwaves, widely used + Large bandwidth (<100%) + No dielectric + Accurate design and analysis – High weight and cost, particularly at low frequencies (C-band) – Large overall aperture due to corrugations
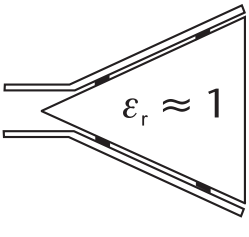	• Soft • Low index Dielcore	1983 [19]	+ Proven experimentally + Large bandwidth, performance degrades gracefully + Low weight and cost – Degraded cross-pol due to radiation from outer region and lack of homogeneity of core – Needs ESD treatment for space applications – Not applicable to open surface applications

Table 6.1 Classification of Hybrid-Mode Horn Antennas [59] *(Cont.)*

Illustration Photo	*Class Name*	*First Ref.*	*Pros (+) and Cons (–)*
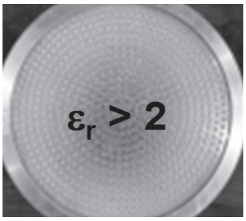	• Soft • Solid dielcore	1985 [20]	+ Proven experimentally at microwaves and mm-waves + Very large bandwidth (>100%) + Built-in aperture lens for focusing, beam-shaping – High weight and RF loss – Needs ESD treatment for space applications – Not applicable to open surface applications
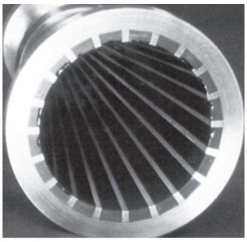	• Hard • Corrugated	1985 [7]	+ Proven experimentally + High aperture efficiency – High weight and cost
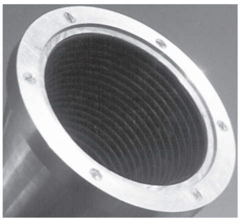	• Soft • Strip-loaded	1986 [5]	+ Proven experimentally + Large bandwidth (<100%), dual band + Low weight and cost – Needs ESD treatment for space applications
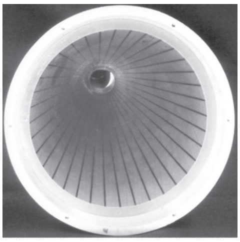	• Hard • Strip-loaded	1987 [2]	+ Proven experimentally + Low weight and cost – Supports surface waves – Needs ESD treatment for space applications
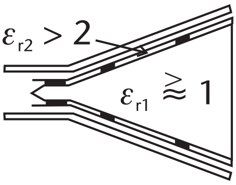	• Hard or selective gain • Dielcore	2003 [30]	+ Designed for high or selective gain + Moderately low weight – Degraded cross-pol due to lack of homogeneity of core – Needs ESD treatment for space applications – Not applicable to open surface applications.
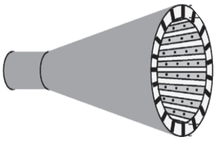	• Hard • Strip-loaded w/vias w/vias	2005 [37]	+ High aperture efficiency + Low weight – Moderate to high cost – Needs ESD treatment for space applications

(continues)

Table 6.1 Classification of Hybrid-Mode Horn Antennas [59] *(Cont.)*

Illustration Photo	*Class Name*	*First Ref.*	*Pros (+) and Cons (–)*
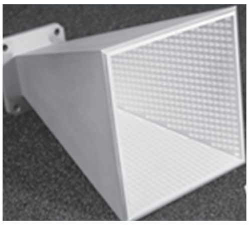	• Soft • Metamaterial	2008 [42]	+ Proven experimentally + Very large bandwidth potential (multi-octave) + Low weight, low to moderate cost + Can be implemented without dielectric (wire-grid) – Challenging to achieve low return loss – Needs ESD treatment for space applications
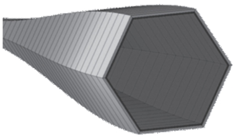	• Hard • Metamaterial	2008 [42]	+ Large bandwidth potential + Very high array efficiency (hexagonal horn) + Low to moderate weight – Moderate to high cost – Needs ESD treatment for space applications

References

[1] Minnett, H. C., and B. MacA. Thomas, "A Method of Synthesizing Radiation Patterns with Axial Symmetry," *IEEE Transactions on Antennas and Propagation*, Vol. AP-14, Sept. 1966, pp. 654–656.

[2] Lier, E., and P.-S. Kildal, "A Novel Type of High-gain Horn Antenna," *Proc. 5th Int. Conference on Antennas and Propagation, ICAP 87*, York, England, March 30–April 2, 1987, pp. 431–433.

[3] Kildal, P.-S., "Definition of Artificially Soft and Hard Surfaces in Electromagnetic Waves," *Electronics Letters*, Vol. 24, No. 3, Feb. 4, 1988, pp. 168–170.

[4] Kildal, P.-S., "Artificially Soft and Hard Surfaces in Electromagnetics," *IEEE Transactions on Antennas and Propagation*, Vol. AP-38, Oct. 1990, pp. 1537–1544.

[5] Lier, E., and T. Schaug-Pettersen, "The Strip-loaded Hybrid Mode Feed Horn," *Proc. 1986 IEEE AP-S/URSI Int. Symposium*, Philadelphia, June 1986, AP–03, pp. 107–108.

[6] Lier, E., and T. Schaug-Pettersen, "The Strip-loaded Hybrid-mode Feed Horn," *IEEE Transactions on Antennas and Propagation*, Vol. AP-35, Sept. 1987, pp. 1086–1089.

[7] Aly, M. S., and S. F. Mahmoud, "Propagation and Radiation Behaviour of a Longitudinally Slotted Horn with Dielectric-Filled Slots," *IEE Proc. H. Microwaves, Antennas and Propagation*, 1985, pp. 477–479.

[8] Kildal, P.-S., and E. Lier, "Hard Horns Improve Cluster Feeds of Satellite Antennas," *Electronics Letters*, Vol. 24, April 14, 1988, pp. 491–492.

[9] Ali, A., S. Ortiz, T. Ivanov, and A. Mortazawi, "Analysis and Measurement of Hard Horn Feeds for the Excitation of Quasioptical Amplifiers," *Proc. IEEE MTT-S Int. Microwave Symposium*, June 1998, pp. 1469–1472.

[10] Ortiz, S. C., J. Hubert, L. Mirth, E. Schlecht, and A. Mortazawi, "A High-power Ka-band Quasi-optical Amplifier Array," *IEEE Transactions on Microwave Theory and Techniques*, Vol. 50, No. 2, Feb. 2002, pp. 487–494.

[11] Lier, E., and P.-S. Kildal, "Soft and Hard Horn Antennas," *IEEE Transactions on Antennas and Propagation*, Vol. AP-36, Aug. 1988, pp. 1152–1157.

[12] Aas, J. A., and P.-S. Kildal, "Reduction of Forward Scattering from Blocking Struts in Reflector Antennas," *Proc. 18th European Microwave Conference*, 1988, pp. 494–499.

[13] Kildal, P.-S., A. Kishk, and A. Tengs, "Reduction of Forward Scattering from Cylindrical Objects Using Hard Surfaces," *IEEE Transactions on Antennas and Propagation*, Vol. AP-44, Nov. 1996, pp. 1509–1520.

[14] Kay, A. F., "A Wide Flare Angle Horn. A Novel Feed for Low Noise Broadband and High Aperture Efficiency Antennas," *U.S. Air Force Cambridge Research Laboratories*, Report 62-757, October 1962.

[15] Simons, A. J., and A. F. Kay, "The Scalar Feed—A High Performance Feed for Large Paraboloidal Reflectors," *IEE Conf. Pub. 21*, 1966, pp. 213–217.

[16] Clarricoats, P. J. B., and A. D. Olver, *Corrugated Horns for Microwave Antennas*, London: Peter Peregrinus Ltd., 1984.

[17] James, G. L., "Analysis and Design of TE_{11}-to-HE_{11} Corrugated Cylindrical Waveguide Mode Converters," *IEEE Transactions on Microwave Theory and Techniques*, Vol. 29, Oct. 1981, pp. 1059–1066.

[18] Lier, E., "An Elliptical Corrugated Horn Model for Radiation Pattern Predictions," *Proc. 1995 Int. AP-S/URSI Symposium*, Newport Beach, CA, June 1995, pp. 156–159.

[19] Clarricoats, P. J. B., A. D. Olver, and M. S. A. S. Rizk, "A Dielectric Loaded Conical Feed with Low Crosspolar Radiation," *Proc. URSI Symposium on Electromagnetics Theory*, Santiago, Spain, 1983, pp. 351–354.

[20] Lier, E., and J. A. Aas, "Simple Hybrid Mode Horn Feed Loaded with a Dielectric Cone," *Electronics Letters*, Vol. 21, June 20, 1985, pp. 563–564.

[21] Lier, E., "A Dielectric Hybrid-mode Antenna Feed: A Simple Alternative to the Corrugated Horn," *IEEE Transactions on Antennas and Propagation*, Vol. AP-34, Jan. 1986, pp. 21–29.

[22] Lier, E., and S. Rengarajan, "Radiation from Elliptical Hybrid-mode Waveguides," *IEE Proceedings Part H*, Vol. 137, Dec. 1990, pp. 417–419.

[23] Lier, E., Y. Rahmat-Samii, and S. Rengarajan, "Application of Rectangular and Elliptical Dielcore Feed Horns to Primary-fed Elliptical Reflector Antennas," *IEEE Transactions on Antennas and Propagation*, Vol. AP-39, Nov. 1991, pp. 1592–1597.

[24] Lier, E., "Broad-band Elliptical-beam Shape Horns with Low Cross-polarization," *IEEE Transactions on Antennas and Propagation*, Vol. AP-38, June 1990, pp. 800–805.

[25] Lier, E., and C. Stoffels, "Propagation and Radiation Characteristics of Rectangular Dielectric-loaded Hybrid-mode Horn," *IEE Proceedings Part H*, Vol. 138, Oct. 1991, pp. 407–411.

[26] Cahill, R., and C. J. Prior, "G-band Dielectric Core Horn," *Electronics Letters*, Vol. 29, Jan. 7, 1993, pp. 130–131.

[27] Cahill, R., "Design of Core Support Mechanism for mm-wave Dielectrically Loaded Horn," *Electronics Letters*, Aug. 31, 1989, pp.1248–1249.

[28] Lier, E., and S. Skyttemyr, "A Compact Shaped Single-reflector Offset Antenna with Low Cross Polarization Fed by a Dielectric Lens Horn," *IEEE Transactions on Antennas and Propagation*, Vol. AP-42, Apr. 1994, pp. 478–483.

[29] Lier, E., U.S. Patent Nos. 7,379,030 and 7,623,085.

[30] Lier, E., "Hybrid-mode Horn Antenna with Design-specific Aperture Distribution and Gain," *Proc. 2003 IEEE Antennas and Propagation Symposium*, Columbus, OH, June 22–27, 2003, pp. 502–505.

[31] Lier, E., and A. A. Kishk, "A New Class of Hybrid-mode Horn Antennas with Selective Gain: Design and Analysis by Single Mode Model and Method of Moments," *IEEE Transactions on Antennas and Propagation*, Vol. AP-53, Jan. 2005 (Special Issue on Soft and Hard Surfaces), pp. 125–138.

[32] Olver, A. D., P. J. B Clarricoats, and K. Raghavan, "Dielectric Cone Loaded Horn Antennas," *IEE Proceedings Part H*, Vol. 135, June 1988, pp. 158–162.

[33] Lier, E., "Analysis of Soft and Hard Strip-loaded Horns Using a Circular Cylindrical Model," *IEEE Transactions on Antennas and Propagation*, Vol. AP-38, June 1990, pp. 783–793.

[34] Lier, E., and P.-S. Kildal, "Theoretical and Experimental Investigation of Hard Horns," *Proc. JINA 88*, Nice, France, Nov. 1988, pp. 450–454.

[35] Lier, E., "Hard Waveguide Feeds with Circular Symmetry for Aperture Efficiency Enhancement," *Electronics Letters*, Vol. 24, Feb. 4, 1988, pp. 166–167.

[36] Skobelev, S. P., and P.-S. Kildal, "Analysis of Hard Strip-loaded Conical Horn by the Method of Generalized Scattering Matrices," *IEEE Transactions on Antennas and Propagation*, Vol. 51, No. 10, October 2003, pp. 2918–2925.

[37] Skobelev, S. P., and P.-S. Kildal, "Mode-matching Modeling of a Hard Conical Quasi-TEM Horn Realized by an EBG Structure with Strips and Vias," *IEEE Transactions on Antennas and Propagation*, Vol. AP-53, Jan. 2005, pp. 139–143.

[38] Skobelev, S. P., and P.-S. Kildal, "Analysis of Conical Quasi-TEM Horn with a Hard Corrugated Section," *IEEE Transactions on Antennas and Propagation—Special Issue on Metamaterials*, Vol. 51, No. 10, October 2003, pp. 2723–2731.

[39] Skobelev, S. P., and P.-S. Kildal, "Modal Solutions in Dual-depth Longitudinally Corrugated Hard Waveguide," *IET Microwaves, Antennas and Propagation*, Vol. 1, No. 4, Aug. 2007, pp. 827–831.

[40] Sotoudeh, O., P.-S. Kildal, P. Ingvarson, and S. P. Skobelev, "Single- and Dual-band Multimode Hard Horn Antennas with Partly Corrugated Walls," *IEEE Transactions on Antennas and Propagation*, Vol. 54, No. 2, Pt. 1, Feb. 2006, pp. 330–339.

[41] Kildal, P.-S., "Bandwidth of a Square Hard Horn," *IEE Proc. Microwaves, Antennas and Propagation, Part H*, 1988, pp. 275–278.

[42] Lier, E., and R. K. Shaw, "Design and Simulation of Metamaterial-Based Hybrid-Mode Horn Antennas," *Electronics Letters*, Vol. 44, No. 25, Dec. 4, 2008, pp. 1444–1445.

[43] Lier, E., and R. K. Shaw, "Metamaterial Hybrid Mode Horn Antennas," *Proc. 2009 Int. AP-S/URSI Symposium*, Charleston, SC, June 1–5 2009, Session 302.4.

[44] Rotman, W., "Plasma Simulation by Artificial Dielectrics and Parallel-plate Media," *IEEE Transactions on Antennas and Propagation*, Vol. 10, No. 1, Jan. 1962, pp. 82–95.

[45] Pendry, J. B., Holden, A.J, Robbins, D.J. and Stewart, W.J, "Low Frequency Plasmons in Thin Wire Structures," *Journal of Physics: Condensed Matter*, Vol. 10, 1998, pp. 4785–4809.

[46] Lier, E., R. K. Shaw, B. G. Martin, D. H. Werner, Q. Wu, C.P. Scarborough, and M. D. Gregory, "Status on Meta-Horn Development–Theory and Experiments," *Proc. 2010 Int. AP-S/URSI Symposium*, Toronto, ON, Canada, July 13–17 2010, Session 203.

[47] Lier, E., D. H. Werner, C. P. Scarborough, Q. Wu, and J. A. Bossard, "An Octave-Bandwidth Negligible-Loss Radiofrequency Metamaterial," *Nature Materials*, Vol. 10, No. 3, March 2011, pp. 216–222.

[48] Scarborough, C. P., Q. Wu, D. H. Werner, E. Lier, R. K. Shaw, and B. G. Martin, "Demonstration of an Octave Bandwidth Negligible Loss Metamaterial Horn Antenna for Satellite Applications," accepted for publication in *IEEE Transactions on Antennas and Propagation*.

[49] Peace, G. M., and E. E. Swartz, "Amplitude Compensated Horn Antenna," *Microwave Journal*, Vol. 7, 1964, pp. 66–68.

[50] Chan, K. K., C. C. Huang, and A. R. Raab, "Dielectric-loaded Trifurcated Horn for H-plane Stacked Reflector Feed Array," *IEE Proceedings, Pt. H*, Vol. 127, No. 1, Feb. 1980, pp. 61–64.

[51] Wu, Q., C. P. Scarborough, D. H. Werner, E. Lier, and R. K. Shaw, "Inhomogeneous Metasurfaces with Engineered Dispersion for Broadband Hybrid-mode Horn Antennas," submitted for publication in *IEEE Transactions on Microwave Theory and Techniques*.

[52] Wu, Q., C. P. Scarborough, D. H. Werner, E. Lier, and X. Wang, "Design Synthesis of Metasurfaces for Broadband Hybrid-mode Horn Antennas with Enhanced Radiation Pattern and Polarization Characteristics," *IEEE Transactions on Antennas and Propagation*, Vol. 60, No. 8, Aug. 2012, pp. 3594–3604.

[53] Wu, Q., C. P. Scarborough, B. G. Martin, R. K. Shaw, D. H. Werner, E. Lier, and X. Wang, "A Ku-band Dual Polarization Hybrid-mode Horn Antenna Enabled by Printed Circuit Board Metasurfaces," accepted for publication in *IEEE Transactions on Antennas and Propagation*.

[54] Granet, C., and G. L. James, "Optimized Spline-profile Smooth-walled Tri-band 20/30/44 GHz Horns," *IEEE Antennas and Wireless Propagation Letters*, Vol. 6, 2007, pp. 492–494.

[55] Shaw, R. K., and E. Lier, "Hexagonal Hard Metamaterial Hybrid-Mode Horn Antenna," *Proc. 2009 Int. AP-S/URSI Symposium*, Charleston, SC, June 1–5, 2009, Session 302.5.

[56] Shaw, R. K., E. Lier, and C. C. Hsu, "Profiled Hard Metamaterial Horns for Multi-Beam Reflectors," *Proc. 2010 Int. AP-S/URSI Symposium*, Toronto, July 13–17, 2010, Session 526.

[57] Lier, E., R. K. Shaw, M. Cuchanski, and S. Yang, "Meta-Horns Improve the Performance of Multi-Beam Reflector Antennas," *Proc. 2011 Int. AP-S/URSI Symposium*, Spokane, WA, July 4–7, 2011, Session 405.

[58] Lier, E., and A. Katz, U.S. Patent Nos. 7,629,937 and 8,072,386.

[59] Lier, E., "Review of Soft and Hard Horn Antennas, Including Metamaterial-Based Hybrid-Mode Horns," *IEEE Antennas and Propagation Magazine*, Vol. 52, No. 2, April 2010, pp. 31–39.

CHAPTER 7

Circularly Polarized Feed Antennas

Hisamatsu Nakano, Hosei University, Japan

7.1 Introduction

Consider a communication system where an x-directed linearly polarized (LP) receiving antenna is located facing a y-directed LP transmitting antenna. In this case, the receiving antenna cannot receive the transmitted signals because the polarization of the receiving antenna (x-direction) is perpendicular to that of the transmitting antenna (y-direction) [1, 2]. To receive the transmitted signals, the polarization of the receiving antenna must be oriented such that it is parallel to the transmitting antenna's polarization, and hence a 90° rotation is required in this case. On the other hand, in a communication system that uses circularly polarized (CP) receiving and transmitting antennas, the CP receiving antenna will receive signals as long as it faces the CP transmitting antenna; there is no need to adjust the orientation of the antenna polarization.

When high antenna gain is required for a CP communication system, a CP array antenna [3, 4] or a CP reflector antenna [5–7] is used. In the CP array antenna case, the complexity of the feed circuit design for each array element increases with the number of array elements; the loss in the feed circuits also increases, due to the increased path length from the source point to each array element. In the reflector antenna case, the issues with the CP array antenna case are not present, as long as the feed antenna for the reflector is composed of a single element or a small number of elements. For example, in a parabolic reflector antenna for direct broadcast satellite reception, a single CP feed antenna illuminates the reflector surface, and the reflector achieves a high gain (of more than 30 dBi) without significant feed line loss [7]. As a result, the parabolic reflector has higher aperture efficiency than its counterparts (microstrip array antennas) and has been widely applied.

There are numerous CP feed antennas for reflectors. Figure 7.1 shows techniques for generating a CP wave. One is based on synthesizing two LP waves, E_x and E_y, where the two waves have the same amplitude but have a ±90° phase difference. When the phase of E_y is regressive by 90° with respect to the phase of E_x, as shown in Figure 7.1(a), a right-handed CP (RH CP) wave is obtained in the z-direction; when the phase of E_y is progressive by 90°, a left-handed CP (LH CP) is realized in the z-direction, as shown in Figure 7.1(b). For brevity, synthesized circularly-polarized is often abbreviated as SYN CP in the following discussions.

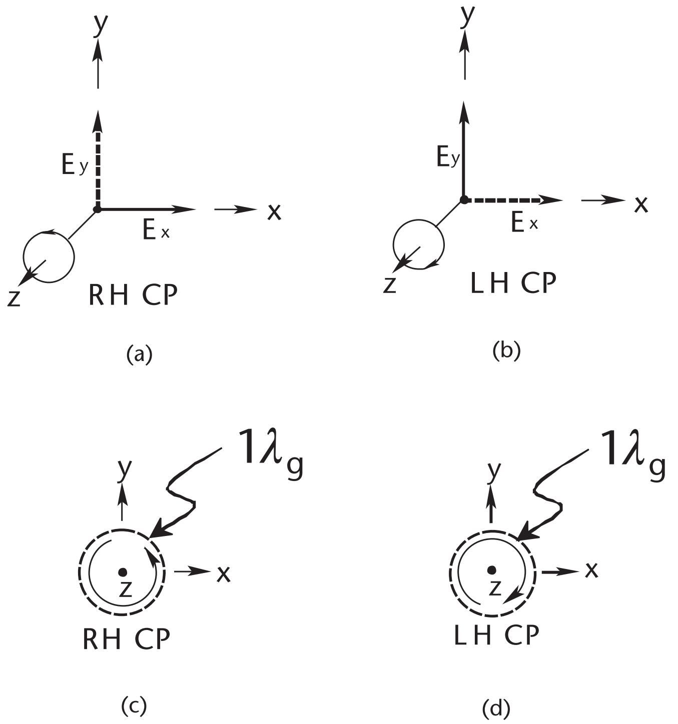

Figure 7.1 Techniques for generating a CP wave. (a) Synthesized RH CP wave, (b) synthesized LH CP wave, (c) loop-based RH CP wave, and (d) loop-based LH CP wave.

The other technique for obtaining a CP wave is based on distributing a traveling wave along a loop region on the antenna arm or arms; a CP wave is produced when the circumference of the loop region is one-guided wavelength ($1\lambda_g$). An RH CP wave is obtained in the z-direction, as shown in Figure 7.1(c), if the traveling wave flows in the counterclockwise direction; an LH CP wave is obtained in the z-direction, as shown in Figure 7.1(d), if the traveling wave flows in the clockwise direction. Note that this loop-based circularly polarized radiation, often expressed as LPB CP radiation, is distinguished from the SYN CP radiation.

This chapter presents feed antennas for CP reflectors and discusses their characteristics, including the radiation pattern and beamwidth, as a function of frequency. The axial ratio, gain, and input performance are also discussed.

Ten sections constitute this chapter. Section 7.2 summarizes analysis methods for CP feed antenna design, where the method of moments (MoM) [8–10] and the finite-difference time-domain method (FDTDM) [11, 12] are briefly described. Section 7.3 discusses CP radiation based on the SYN CP radiation technique; transformations into a CP wave using a parallel plate polarizer, a conducting fin in a circular waveguide, and the two-point excitation of a patch, are discussed. Sections 7.4–7.10 present CP feed antennas based on the LPB CP radiation technique, focusing on end-fire helical, back-fire helical, conical helical, spiral, and curl feed antennas. Note that feed antennas based on the LPB CP radiation technique have wideband characteristics.

7.2 Analysis Methods for CP Feed Antenna Design

The method of moments (MoM) [8–10] and the finite-difference time-domain method (FDTDM) [11, 12] are major analysis methods for CP feed antennas. This section briefly describes these two methods. Calculations for the antenna characteristics, including the radiation pattern, gain, and input impedance, are explained.

7.2.1 Method of Moments (MoM)

In the MoM, the current on a conducting wire is first formulated as a field integral equation and then expressed as a matrix equation. A closed form for the kernel of the field integral equation is derived to reduce the time for calculating the matrix elements. Equations for calculating the antenna characteristics based on the current are presented next.

7.2.1.1 Matrix Expression for an Unknown Current

Figure 7.2 shows an arbitrarily shaped wire located in free space, where the wire radius is assumed to be very small relative to the operating wavelength λ. The current on the conducting wire, $I(s')$, is formulated by applying the boundary condition at the wire surface [10]:

$$\frac{1}{j4\pi\omega\varepsilon_0}\int_{S_S}^{S_E} I(s')\left[-\frac{\partial^2}{\partial s\,\partial s'}+\beta^2\hat{s}\cdot\hat{s}'\right]\frac{e^{-j\beta r_{0,s}(s,\,s')}}{r_{o,s}(s,s')}ds' = -E_s^i(s) \tag{7.1}$$

where the left side is the tangential component of the electric field due to the current from s_S to s_E (called the tangential scattering field); the right side $E_s^i(s)$ is the tangential component of an incident electric field at point Q (observation point).

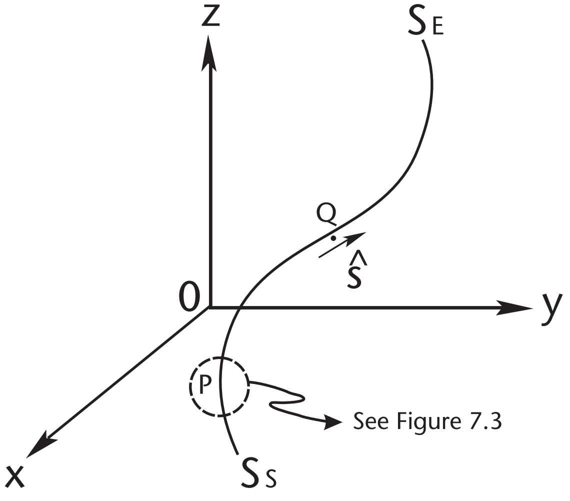

Figure 7.2 Arbitrarily shaped wire located in free space.

The notations in (7.1) are as follows: $\omega = (2\pi f)$ is the angular frequency; ε_0 is the permittivity in free space; s and s' are the distances measured along the wire from its origin to point Q and point P (source point) on the wire, respectively; $\hat{s}$ and $\hat{s}'$ are the unit vectors tangential to the wire axis at points Q and P, respectively; $r_{o,s}(s, s')$ is the distance between points P and Q; and β is the phase constant.

The current $I(s')$ in (7.1) is solved using the MoM. For this, first, the current is expanded as

$$I(s') = \sum_{n=1}^{N} I_n J_n(s') \tag{7.2}$$

where $J_n(s')$ and $I_n (n = 1, 2, \ldots, N)$ are the *expansion functions* and *unknown coefficients of the expansion functions*, respectively. Substitution of (7.2) into (7.1) leads to

$$\sum_{n=1}^{N} I_n e_n(s) = -E_s^i(s) \tag{7.3}$$

where

$$e_n(s) = \frac{1}{j4\pi\omega\varepsilon_0} \int_{S_S}^{S_E} J_n(s') \left[-\frac{\partial^2}{\partial s\,\partial s'} + \beta^2 \hat{s} \cdot \hat{s}' \right] \frac{e^{-j\beta r_{o,s}(s,s')}}{r_{o,s}(s,s')} ds' \tag{7.4}$$

Second, both sides of (7.3) are multiplied by weighting functions $W_m(s) (m = 1, 2, \ldots, N)$. Integrating the products over the wire length from S_S to S_E, we obtain the matrix equation

$$[Z_{mn}][I_n] = [V_m] \tag{7.5}$$

where $[Z_{mn}]$, $[I_n]$, and $[V_m]$ are called the *impedance*, *current*, and *voltage matrices*, respectively.

$$Z_{mn} = \int_{S_S}^{S_E} e_n(s)\ W_m(s)\, ds \tag{7.6}$$

$$V_m = -\int_{S_S}^{S_E} E_s^i(s) W_m(s)\ ds \tag{7.7}$$

From (7.5), we have $[I_n] = [Z_{mn}]^{-1}[V_m]$. This means that the unknown coefficients of the expansion functions (I_n: $n = 1, 2, \ldots, N$) can be calculated and hence the current $I(s')$ in (7.1) can be obtained.

It is recommended that a closed-form expression for $e_n(s)$ be used to reduce the computation time. The use of piecewise sinusoidal functions for the expansion functions J_n, shown in Figure 7.2, lead to the following closed Nakano form [10]

$$e_n(s) = -\,I_n j30\left[\frac{P_{n-1}\hat{\rho}_{n-1}}{\rho_{n-1}\sin\beta s_{n-1}} + \frac{P_n\hat{\rho}_n}{\rho_n\sin\beta s_n} - \frac{Z_{n-1}\hat{z}_{n-1}}{\sin\beta s_{n-1}} - \frac{Z_n\hat{z}_n}{\sin\beta s_n}\right]\cdot\hat{s} \tag{7.8}$$

where

$$P_{n-1} = \cos\beta s_{n-1}\cdot\cos\theta_U^{n-1}\cdot e^{-j\beta R_U^{n-1}} - \cos\theta_L^{n-1}\cdot e^{-j\beta R_L^{n-1}} - j\sin\beta s_{n-1}\cdot e^{-j\beta R_U^{n-1}} \tag{7.9}$$

$$P_n = \cos\beta s_n\cdot\cos\theta_L^n\cdot e^{-j\beta R_L^n} - \cos\theta_U^n\cdot e^{-j\beta R_U^n} + j\sin\beta s_n\cdot e^{-j\beta R_L^n} \tag{7.10}$$

$$Z_{n-1} = \cos\beta s_{n-1}\cdot\frac{e^{-j\beta R_U^{n-1}}}{R_U^{n-1}} - \frac{e^{-j\beta R_L^{n-1}}}{R_L^{n-1}} \tag{7.11}$$

$$Z_n = \cos\beta s_n\cdot\frac{e^{-j\beta R_L^n}}{R_L^n} - \frac{e^{-j\beta R_U^n}}{R_U^n} \tag{7.12}$$

The distances R_h^g ($g = n - 1$ or n, $h = U$ or L) and angles θ_h^g ($g = n - 1$ or n, $h = U$ or L) in the preceding equations are illustrated in Figure 7.3. Note that (7.8) is derived after the wire is divided into numerous small filaments, each approximated by a straight wire. Also, note that local cylindrical coordinate systems (ϕ_{n-1}, ρ_{n-1}, z_{n-1}) and (ϕ_n, ρ_n, z_n) are used for filament $n - 1$ of length s_{n-1} and filament n of length s_n, respectively, where the coordinate unit vectors are expressed as $\left(\hat{\phi}_{n-1}, \hat{\rho}_{n-1}, \hat{z}_{n-1}\right)$ and $\left(\hat{\phi}_n, \hat{\rho}_n, \hat{z}_n\right)$.

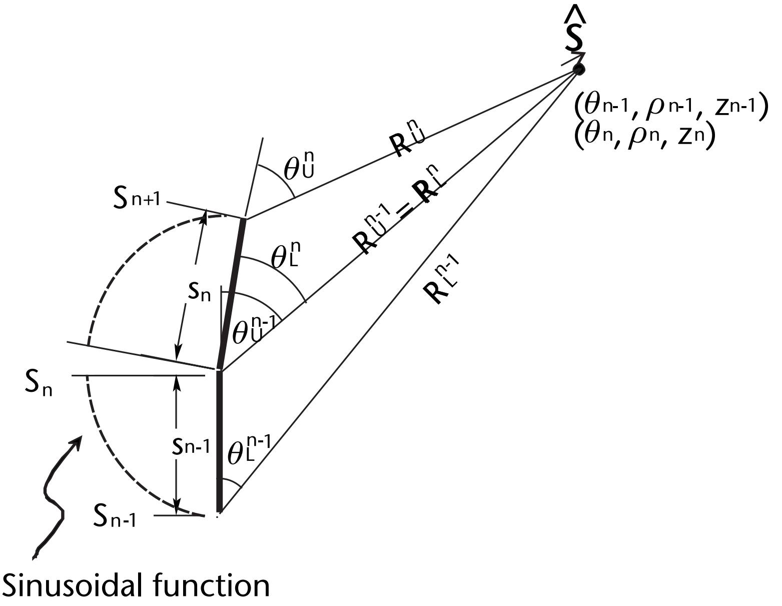

Figure 7.3 Piecewise function for a pair of wire elements $n - 1$ and n.

7.2.1.2 Post Processing for MoM

The current $I(s')$ is obtained by solving (7.5). The θ and ϕ components of the radiation field are calculated using the obtained current $I(s')$:

$$E_\theta(r,\theta,\phi) = -\frac{j\omega\mu_0}{4\pi}\frac{e^{-j\beta r}}{r}\hat{\theta}\cdot\int_{s_S}^{s_E}\hat{s}'\, I(s')\, e^{j\beta\hat{\mathbf{r}}\cdot\mathbf{r}'}ds' \tag{7.13}$$

$$E_\phi(r,\theta,\phi) = -\frac{j\omega\mu_0}{4\pi}\frac{e^{-j\beta r}}{r}\hat{\phi}\cdot\int_{s_S}^{s_E}\hat{s}'\, I(s')\, e^{j\beta\hat{\mathbf{r}}\cdot\mathbf{r}'}ds' \tag{7.14}$$

where $(\hat{r},\hat{\theta},\hat{\phi})$ are the unit vectors for the spherical coordinates (r, θ, ϕ); μ_0 is the permeability of free space; and vector $\mathbf{r}'$ is the position vector from the coordinate origin o to $I(s')$. Note that the other notations are already described in Section 7.2.1.1.

The gain relative to an isotropic antenna is defined as $G = \left\{\left(\left|E_\theta\right|^2 + \left|E_\phi\right|^2\right)/2\right\}r^2/30P_{in}$, where P_{in} is the power observed at the antenna input terminals (not at the starting point of the feed line, where the source is connected). This gain is often called the available gain. After transforming the radiation field $\mathbf{E}_{rad}(r, \theta, \phi) = \mathbf{E}_\theta(r, \theta, \phi)\hat{\theta} + \mathbf{E}_{\varnothing}(r, \theta, \phi)\hat{\phi}$ into

$$\mathbf{E}_{rad}(r,\theta,\phi) = E_R(r,\theta,\phi)(\hat{\theta} - j\hat{\phi}) + E_L(r,\theta,\phi)(\hat{\theta} + j\hat{\phi}), \tag{7.15}$$

the gains relative to right-handed and left-handed circularly polarized isotropic antennas are written, respectively, as

$$G_R = \left|E_R(r,\theta,\phi)\right|^2 r^2/30P_{in} \text{ and } G_L = \left|E_L(r,\theta,\phi)\right|^2 r^2/30P_{in}, \tag{7.16}$$

where the relationship $\left|E_\theta\right|^2 + \left|E_\phi\right|^2 = 2\left(\left|E_R\right|^2 + \left|E_L\right|^2\right)$ is used. Note that the first term in (7.15) represents a right-handed CP wave component and the second represents a left-handed CP wave component.

Using the two components E_R and E_L, the axial ratio (AR) is defined as

$$AR = \text{Absolute value of } \left(\left|E_R\right| + \left|E_L\right|\right)/\left(\left|E_R\right| - \left|E_L\right|\right) \tag{7.17}$$

For $\left|E_R\right| > \left|E_L\right|$, as the axial ratio decreases, G_R increases and G_L decreases, according to $G_R = G/\left[1+\left\{(AR-1)/(AR+1)\right\}^2\right]$ and $G_L = G/\left[1+\left\{(AR+1)/(AR-1)\right\}^2\right]$. Note that $G_R = G$ and $G_L = 0$ when $AR = 1$ (that is, the polarization is perfectly circular with a right-handed sense).

The input impedance is given as $Z_{in} = V_{in}/I_{in}$, where V_{in} is the voltage across the antenna input terminals and a known function. The current flowing at the antenna input terminals, I_m, has already been obtained using the MoM. Therefore, the input impedance is straightforwardly calculated.

7.2.2 Finite-Difference Time-Domain Method (FDTDM)

The antenna characteristics in Section 7.2.1 are derived based on the current distribution. Derivation of the antenna characteristics in this subsection is based on the electric and magnetic fields obtained using the finite-difference time-domain method (FDTDM) [11, 12].

7.2.2.1 Finite Difference

Figure 7.4 shows a situation where a feed antenna is located within a space whose volume is $X \times Y \times Z$. This space (called the analysis space) is subdivided into $N_x \times N_y \times N_z$ cells, each having a volume of $\Delta x \times \Delta y \times \Delta z$. The outer surface of the analysis space is terminated with absorbing boundary conditions (ABCs) [13–16]. To reveal the field distribution in the analysis space, Maxwell's curl equations are solved. For this, electric field components (E_x, E_y, E_z) and magnetic field components (H_x, H_y, H_z) are assigned to each cell, as shown in Figure 7.5, where the coordinates (x, y, z) are denoted by integers (i, j, k), based on the definition $(x, y, z) = (i\Delta x, j\Delta y, k\Delta z)$.

As with the spatial variables (x, y, z), a time variable t is denoted by an integer, n, based on the definition $t = n\Delta t$. Using these notations, the function $g(x, y, z, t)$ and its derivative with respect to x are expressed as

$$g(x, y, z, t) = g^n(i, j, k) \tag{7.18}$$

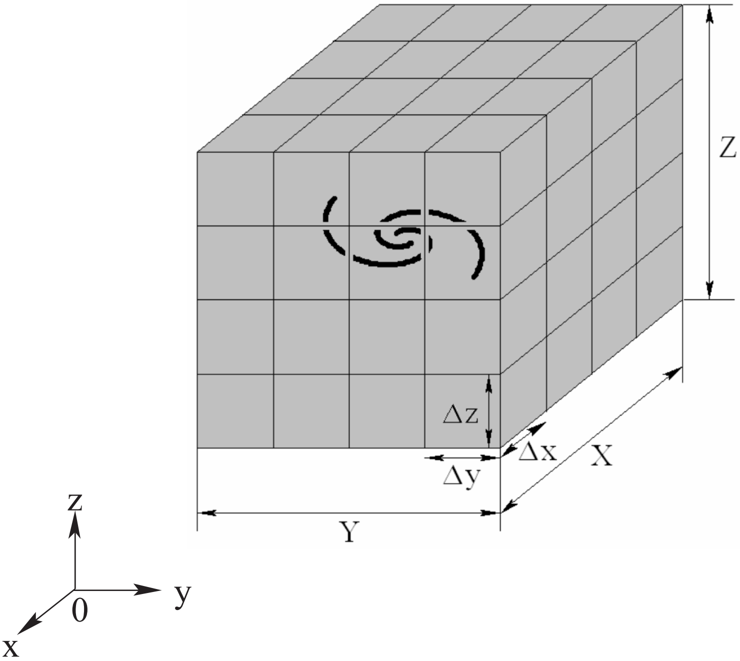

Figure 7.4 Feed antenna located within a space of volume of $X \times Y \times Z$.

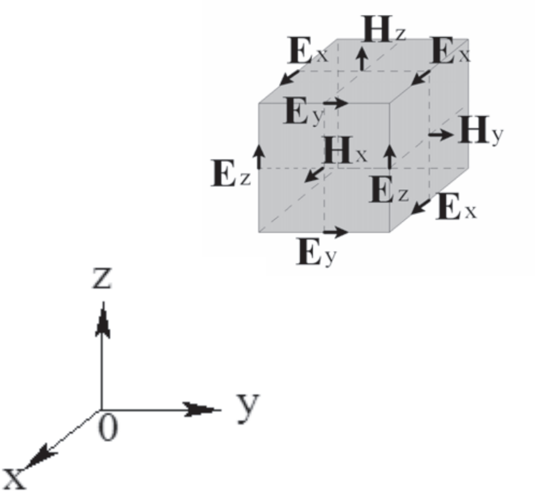

Figure 7.5 Field assignment.

$$\frac{\partial g^n(i,j,k)}{\partial x} \approx \frac{g^n\left(i+\frac{1}{2},j,k\right)-g^n\left(i-\frac{1}{2},j,k\right)}{\Delta x} \tag{7.19}$$

where a central finite-difference is used in (7.19). Similarly, the derivative of the electric field at time $t = (n - 1/2)\Delta t$ is expressed as

$$\left.\frac{\partial \mathbf{E}}{\partial t}\right|_{t = \left(n-\frac{1}{2}\right)\Delta t} \approx \frac{\mathbf{E}^n - \mathbf{E}^{n-1}}{\Delta t} \tag{7.20}$$

and the derivative of the magnetic field at time $t = n\Delta t$ is expressed as

$$\left.\frac{\partial \mathbf{H}}{\partial t}\right|_{t = n\Delta t} \approx \frac{\mathbf{H}^{n+\frac{1}{2}} - \mathbf{H}^{n-\frac{1}{2}}}{\Delta t} \tag{7.21}$$

7.2.2.2 Maxwell's Equations

Maxwell's curl E equation at time $t = n\Delta t$ and curl **H** equation at $t = (n - 1/2)\Delta t$ are

$$\nabla \times \mathbf{E}\Big|_{t=n\Delta t} = -\mu \frac{\partial \mathbf{H}}{\partial t}\Big|_{t=n\Delta t} \tag{7.22}$$

$$\nabla \times \mathbf{H}\Big|_{t=\left(n-\frac{1}{2}\right)\Delta t} = \sigma \mathbf{E}\Big|_{t=\left(n-\frac{1}{2}\right)\Delta t} + \varepsilon \frac{\partial \mathbf{E}}{\partial t}\Big|_{t=\left(n-\frac{1}{2}\right)\Delta t} \tag{7.23}$$

Using (7.20–7.21), the preceding equations are transformed to

$$\mathbf{H}^{n+\frac{1}{2}} = \mathbf{H}^{n-\frac{1}{2}} - \frac{\Delta t}{\mu}\nabla \times \mathbf{E}^{n} \tag{7.24}$$

$$\mathbf{E}^{n} = \frac{2\varepsilon - \sigma\Delta t}{2\varepsilon + \sigma\Delta t}\mathbf{E}^{n-1} + \frac{2\Delta t}{2\varepsilon + \sigma\Delta t}\nabla \times \mathbf{H}^{n-\frac{1}{2}} \tag{7.25}$$

where ε, μ, and σ are the permittivity, permeability, and conductivity, respectively. Note that $\sigma\mathbf{E}$ in (7.23) is evaluated at $t = (n - 1/2)\Delta t$. This term is approximated by the average of $\sigma\mathbf{E}^{n}$ and $\sigma\mathbf{E}^{n-1}$ to obtain (7.25).

The finite-difference form for the x-component of (7.25) is written as

$$\begin{aligned} \mathbf{E}_x^{n}(i+\tfrac{1}{2},\, j,\, k) &= e_{x/0}(i+\tfrac{1}{2},\, j,\, k)\,\mathbf{E}_x^{n-1}(i+\tfrac{1}{2},\, j,\, k) \\ &+ e_{x/y}(i+\tfrac{1}{2},\, j,\, k)\left[\mathbf{H}_z^{n-\frac{1}{2}}(i+\tfrac{1}{2},\, j+\tfrac{1}{2},\, k) - \mathbf{H}_z^{n-\frac{1}{2}}(i+\tfrac{1}{2},\, j-\tfrac{1}{2},\, k)\right] \\ &- e_{x/z}(i+\tfrac{1}{2},\, j,\, k)\left[\mathbf{H}_y^{n-\frac{1}{2}}(i+\tfrac{1}{2},\, j,\, k+\tfrac{1}{2}) - \mathbf{H}_y^{n-\frac{1}{2}}(i+\tfrac{1}{2},\, j,\, k-\tfrac{1}{2})\right] \end{aligned} \tag{7.26}$$

where

$$e_{x/0}(i+\tfrac{1}{2},\, j,\, k) = \frac{2\varepsilon(i+\frac{1}{2},\, j,\, k) - \sigma(i+\frac{1}{2},\, j,\, k)\Delta t}{2\varepsilon(i+\frac{1}{2},\, j,\, k) + \sigma(i+\frac{1}{2},\, j,\, k)\Delta t} \tag{7.27}$$

$$e_{x/y}(i+\tfrac{1}{2},\, j,\, k) = \frac{2\Delta t}{2\varepsilon(i+\frac{1}{2},\, j,\, k) + \sigma(i+\frac{1}{2},\, j,\, k)\Delta t}\,\frac{1}{\Delta y} \tag{7.28}$$

$$e_{x/z}(i+\tfrac{1}{2},\, j,\, k) = \frac{2\Delta t}{2\varepsilon(i+\frac{1}{2},\, j,\, k) + \sigma(i+\frac{1}{2},\, j,\, k)\Delta t}\,\frac{1}{\Delta z} \tag{7.29}$$

The two other components of electric field $\mathbf{E}^{n}$ and the three components of the magnetic field $\mathrm{H}^{n+\frac{1}{2}}$ are similarly formulated. The solutions to Maxwell's equations, **E** and **H**, are obtained by iterating (7.24) and (7.25) with $n = 1,2,\ldots,$ until these fields become constant (converge). This method is called the finite-difference time-domain method (FDTDM).

7.2.2.3 Post-Processing for FDTDM

The current along the antenna conductor, $I(t)$, can be calculated by integrating the magnetic field obtained with the FDTDM around the antenna conductor (Ampere's law). Also, note that the voltage between two points, $V(t)$, can be calculated by taking the product of the electric field obtained with the FDTDM and the distance between the two points. Based on these techniques, the input impedance $Z_{in} = R_{in} + jX_{in}$ is given as

$$F\left[V_{in}(t)\right] / F\left[I_{in}(t)\right] \tag{7.30}$$

where $F[V_{in}(t)]$ and $F[I_{in}(t)]$ are the Fourier-transformed antenna input voltage and current, respectively.

The radiation field is calculated using the equivalence theorem [17, 18]. For this, first, the electric- and magnetic-current densities on the closed surface of the analysis space are defined as $\mathbf{J}_s(t, \mathbf{r}') = \hat{n} \times \mathbf{H}(t, \mathbf{r}')$ and $\mathbf{M}_s(t, \mathbf{r}') = \mathbf{E}(t, \mathbf{r}') \times \hat{n}$, respectively, where $\mathbf{r}'$ is the position vector from the coordinate origin to the point located on the closed surface, and $\hat{n}$ is the outward unit vector normal to the closed surface. Second, these current densities are Fourier-transformed to $\mathbf{J}_s(\omega, \mathbf{r}')$ and $\mathbf{M}_s(\omega, \mathbf{r}')$ and, third, vectors $\mathbf{N}$ and $\mathbf{L}$ are defined as

$$N(\omega) = \int_{closed\ surface} \mathbf{J}_s(\omega, r')e^{jk_0\hat{r}\cdot r'}dS' \tag{7.31}$$

$$L(\omega) = \int_{closed\ surface} M_s(\omega, r')e^{jk_0\hat{r}\cdot r'}dS' \tag{7.32}$$

Then, the θ and ϕ components of the radiation field (in the frequency domain) are given as

$$E_\theta(\omega) = -\frac{jk_0}{4\pi}\frac{e^{-jk_0 r}}{r}\left[Z_0\mathbf{N}(\omega)\cdot\hat{\theta} + \mathbf{L}(\omega)\cdot\hat{\phi}\right] \tag{7.33}$$

$$E_\phi(\omega) = -\frac{jk_0}{4\pi}\frac{e^{-jk_0 r}}{r}\left[Z_0\mathbf{N}(\omega)\cdot\hat{\phi} - \mathbf{L}(\omega)\cdot\hat{\theta}\right] \tag{7.34}$$

where Z_0 is the intrinsic impedance (120πohms), and k_0 is the wave number in free space.

Note that the remaining characteristics (the axial ratio and gain) are calculated using the same techniques described in Section 7.2.1.2.

7.3 Polarizer and Two-Point Excitation Patch

This section presents circularly polarized (CP) feed antennas that are based on synthesized CP radiation. CP horn feed antennas, each having a polarizer, and a patch feed antenna having two excitation points are discussed.

Our discussion starts with a polarizer composed of conducting parallel plates [19]. As shown in Figure 7.6, the distance between neighboring parallel plates is denoted as b and the length of each parallel plate in the z-direction is denoted as l_z. The thickness of the parallel plates is assumed to be negligibly small with respect to the operating wavelength.

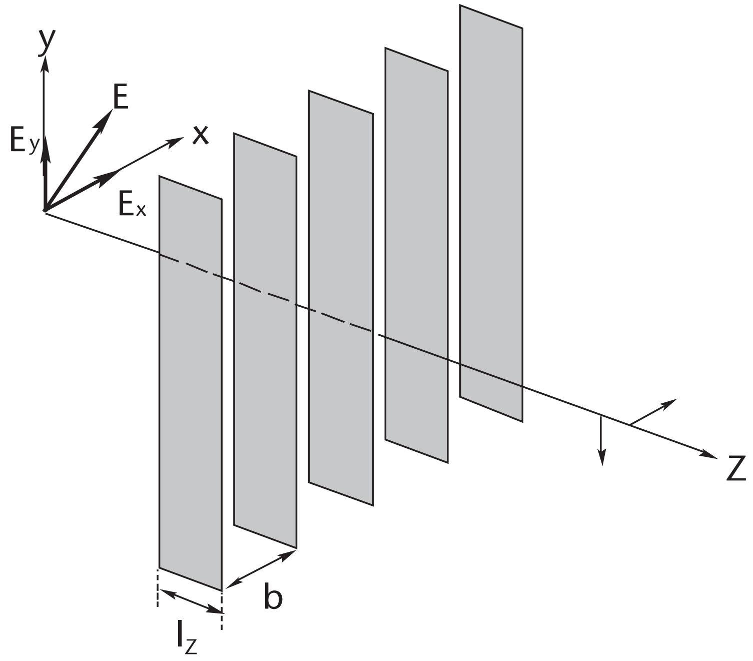

Figure 7.6 Parallel plate polarizer.

Consider a situation where a linearly polarized (LP) uniform plane wave (of wavelength λ) is incident on the polarizer, choosing distance b to be smaller than the wavelength λ. If the incident wave (electric field) is tilted by 45° with respect to the x-axis, then the x-directed electric component E_x is the same as the y-directed electric component E_y in both intensity and phase. Traveling through length l_z, these components experience different phase delays without affecting their amplitude. Therefore, it is possible to produce a 90°-phase difference between the two components E_x and E_y by choosing an appropriate length for l_z. This means that the polarizer can transform the incident LP wave into a CP wave, resulting in a synthesized CP wave.

When the space between the parallel plates is filled with air, the following condition is required for the polarizer to realize a CP wave:

$$2\pi l_z/\lambda - 2\pi l_z/\lambda_g = \pi/2 \tag{7.35}$$

where λ_g is the propagation wavelength for E_y within the polarizer, (7.35) is transformed to

$$l_z/\lambda = 1/[4(1 - \tau] \tag{7.36}$$

where

$$\tau = \sqrt{1 - (\lambda/2b)^2} \tag{7.37}$$

for E_y traveling in the TE_{10} mode.

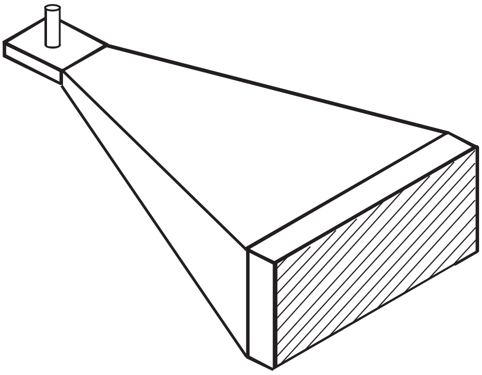

Figure 7.7 CP pyramidal horn feed antenna.

When length l_z is chosen to be $3\lambda/4$, the parameter τ is 2/3, and hence the distance b is given as 0.671λ [20]. Note that $l_z = 3\lambda/4$ corresponds to $\lambda_g/2$, contributing to the impedance matching between the air and the polarizer. Figure 7.7 shows an application of the polarizer to a pyramidal horn feed antenna.

Figure 7.8 also shows a horn feed antenna radiating a synthesized CP wave, where a conducting fin is inserted into a circular waveguide operating in the TE_{11} mode [20]. The fin is rotated by 90° with respect to the x-axis. The component E_x,

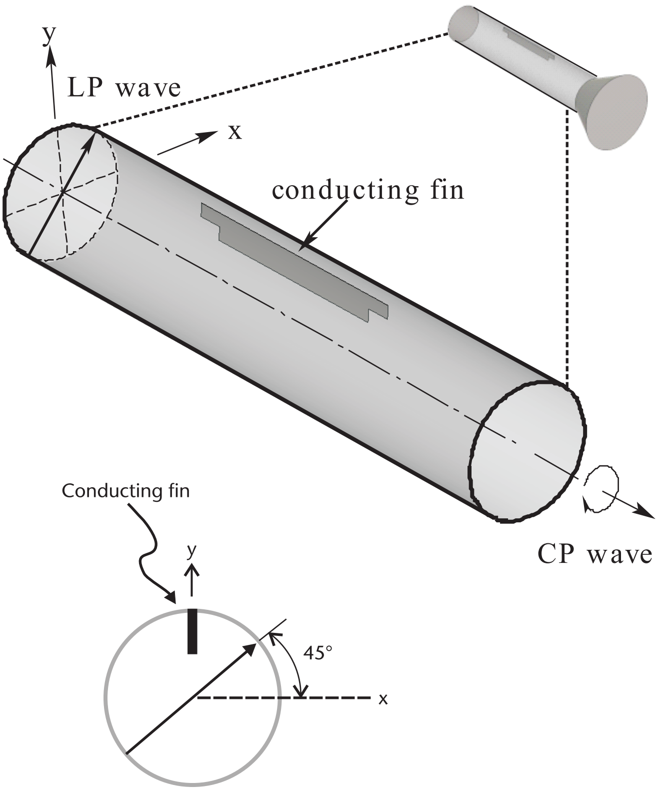

Figure 7.8 CP conical horn feed antenna with a conducting fin.

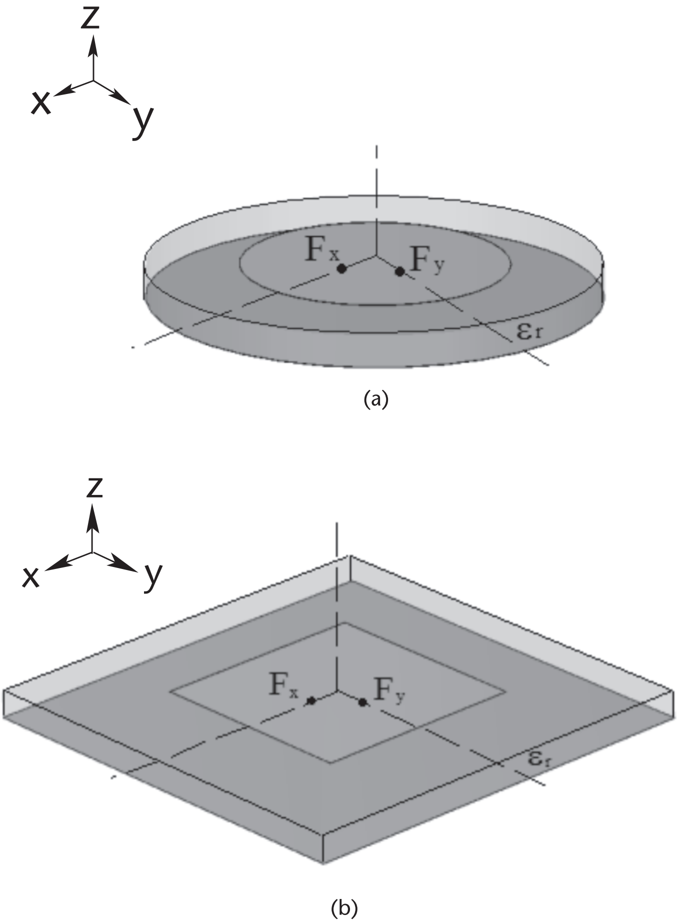

Figure 7.9 CP Patch feed antenna, (a) round patch, and (b) square patch.

which is perpendicular to the fin, is not affected when it moves past the fin. However, the fin acts as a capacitive element for the component E_y, which is parallel to the fin. As a result, the phase difference of the two components E_x and E_y can be adjusted to be 90°, that is, the incident LP wave is transformed into a CP wave by appropriately choosing the length of the fin. Note that the stairs in the fin are used to reduce the reflection of the incident LP wave.

Unlike CP horn feed antennas, a patch feed antenna has a planar structure. The patch shown in Figure 7.9 has two feed points, F_x and F_y. The excitation at F_x generates x-directed radiation and the excitation at F_y generates y-directed radiation. Therefore, by exciting these two feed points with the same amplitude and a 90° phase difference, a synthesized CP wave is radiated from the patch.

7.4 One-Point Excitation CP Patch Feed Antenna

The patch shown in Figure 7.10 is excited from one point (F), differing from the two-point excitation patches presented in Section 7.3. Clearly, the one-point excitation patch [21, 22] has a simpler structure than the two-point excitation patch.

Radiation of a CP wave from the one-point excitation patch is obtained using perturbation elements [23, 24]. Note that the area of the perturbation element is denoted as Δ*s* in Figure 7.10. Also note that the excitation point *F* is located at a distance of approximately *r*/3 from the coordinate origin, where r (= $D_{patch}/2$) is the radius of the patch, in order to achieve impedance matching to a 50-ohm feed line.

Figure 7.11 shows the radiation pattern for a one-point excitation CP patch designed as a feed antenna, where the ground plane has a finite size. The parameters used are presented in Table 7.1 [22]. The beamwidth for a 10 dB reduced field

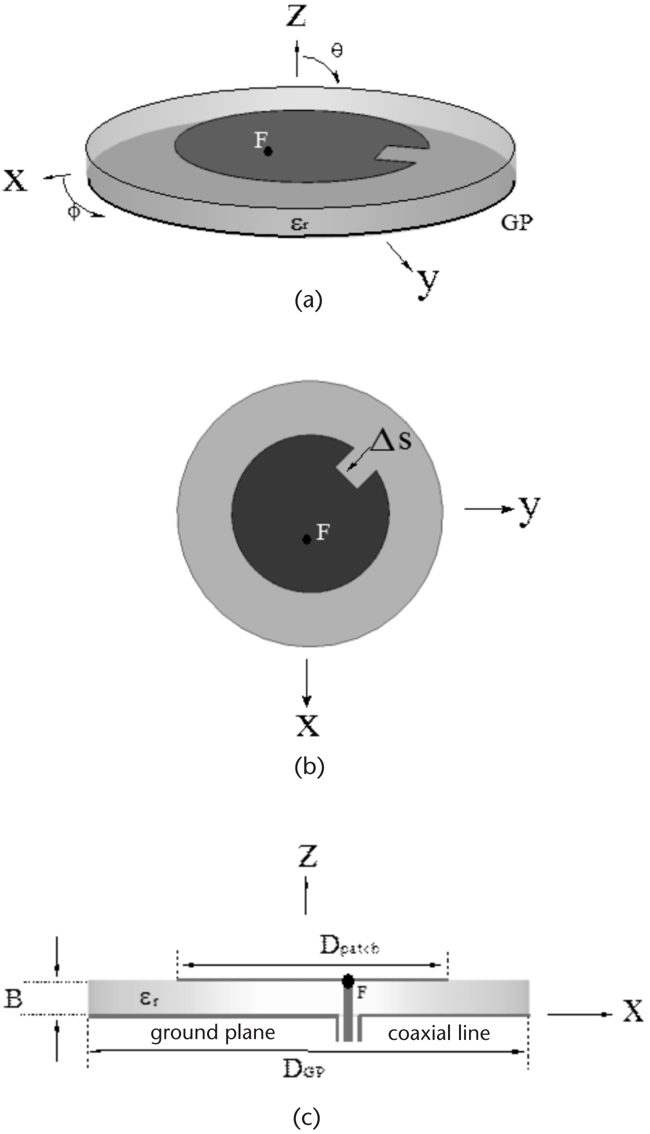

Figure 7.10 One-point excitation CP patch feed antenna. (a) Perspective view, (b) top view, and (c) side view.

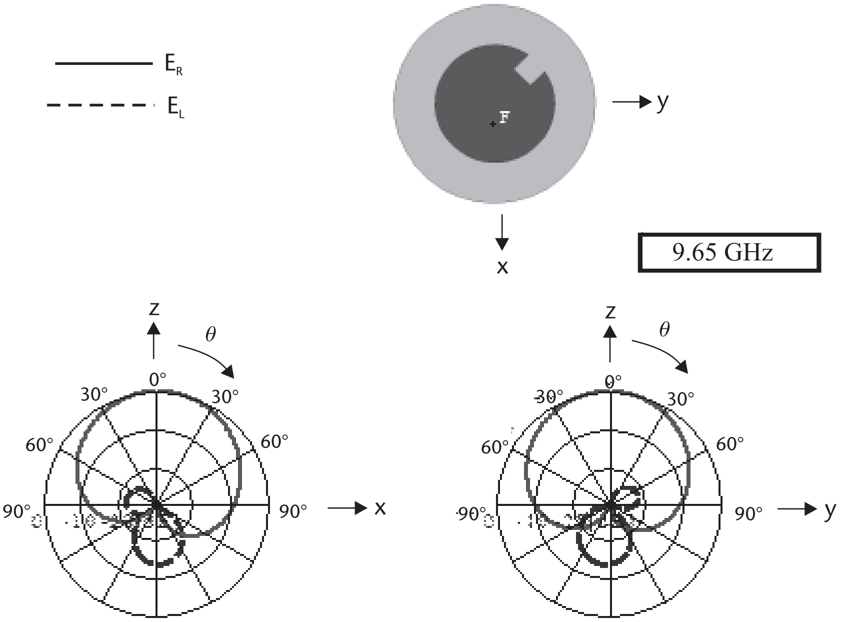

Figure 7.11 Radiation pattern for a one-point excitation CP patch feed antenna.

intensity criterion, 10BW, is approximately 173° [25]. The axial ratio bandwidth for a 3 dB criterion is approximately 2.3%. The gain is approximately 7 dBi at $f = 9.65$ GHz. The input impedance bandwidth for a VSWR = 2 criterion (corresponding to $|S_{11}| = 9.54$ dB) is between 2 and 7%, depending on the radius of the inner conductor of a coaxial feed line.

7.5 End-Fire Helical CP Feed Antenna

Figure 7.12 shows a helical element. The notation is defined as follows: wire radius ρ, axial length h, diameter D_{HLX}, pitch angle α, number of helical turns n, and ground plane diameter D_{GP}. For CP end-fire radiation, the helical element must have a circumference C_{HLX} ($= \pi D_{HLX}$) of approximately one wavelength (1λ) [26, 27] and be backed by a ground plane, whose circumference C_{GP} is larger than C_{HLX}, that is, $C_{GP}/C_{HLX} > 1$.

Table 7.1 Patch Parameters

Symbol	*Value*
B	1.2 mm ≈ $0.0388\lambda_{9.72}$
ε_r	2.55
D_{patch}	10 mm ≈ $0.324\lambda_{9.72}$
Δs	3.6 mm^2
D_{GP}	16.92 mm ≈ $0.548\lambda_{9.72}$

$^*\lambda_{9.72} \approx 30.86$ mm

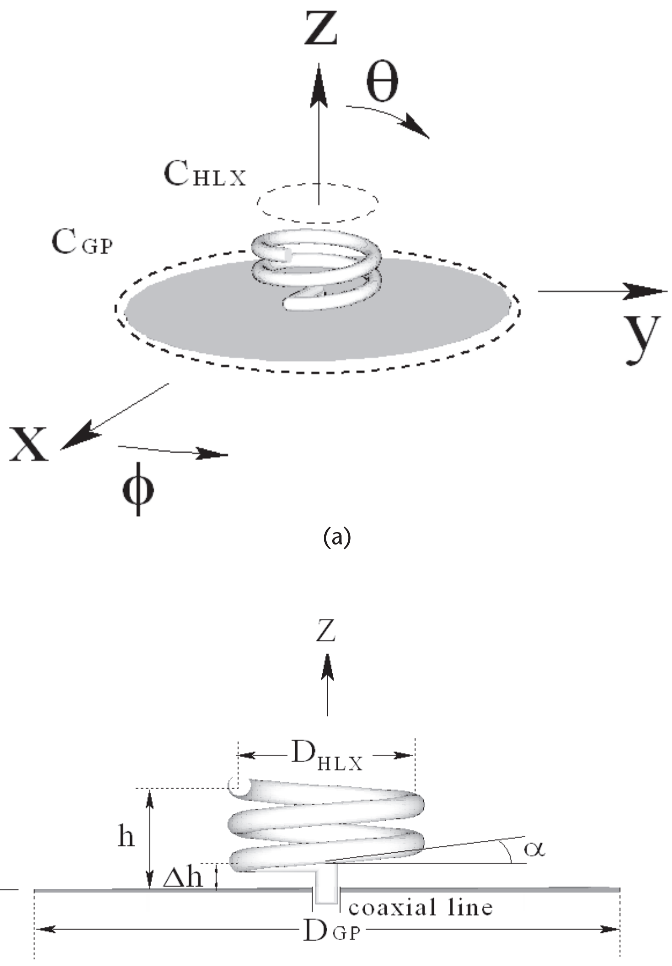

(b)

Figure 7.12 Helical element. (a) Perspective view, and (b) side view.

The helical element can be thought of as an array of loops whose circumference is approximately one wavelength. Each loop generates loop-based CP radiation, which is concentrated in the positive *z*-space, due to the effect of the ground plane. End-fire CP radiation occurs as a result. Note that as the number of helical turns is increased, the radiation (beam) becomes sharper due to the array effect.

7.5.1 Effects of a Cavity

For a CP feed antenna, a small number of helical turns is often recommended, because the antenna has a wide radiation beamwidth. Figure 7.13 shows a helical element with $n = 2$ helical turns [28], where a conducting cavity acts as the ground plane. Notations D_{cav} ($= D_{GP}$), H_{cav}, and Δt denote the diameter, height, and thickness of the conducting cavity, respectively.

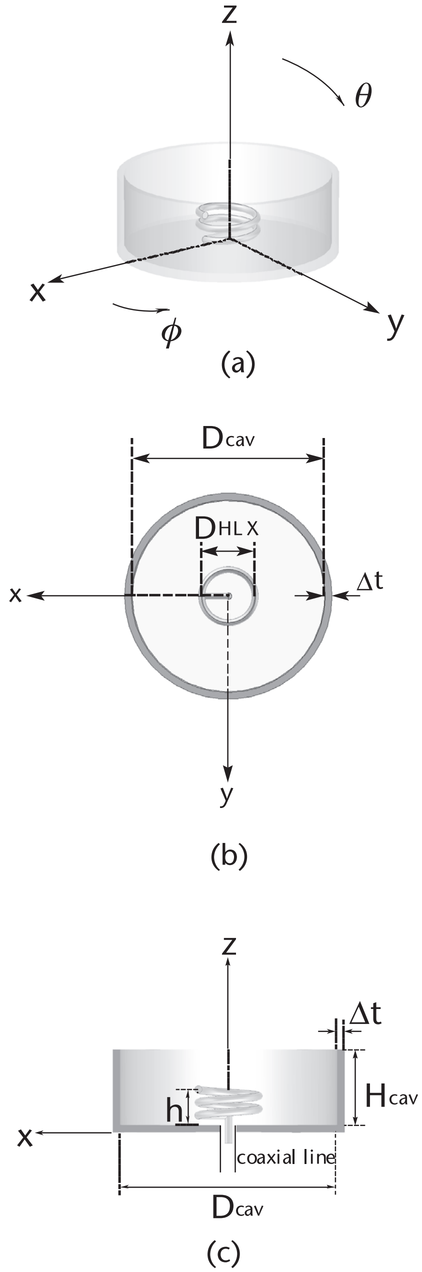

Figure 7.13 Helical element within a cavity. (a) Perspective view, (b) top view, and (c) side view.

Figure 7.14 depicts the beam width for an i-dB reduced field intensity criterion (iBW) as a function of the cavity diameter D_{cav}, where the cavity height and the operating frequency are held at $H_{cav} = 10$ mm and f =12.25 GHz (wavelength $\lambda = 24.49$ mm), respectively. The parameters used are summarized in Table 7.2. It is found that, as the cavity diameter D_{cav} is decreased, the beamwidth becomes wider. This is attributed to the fact that the region at the cavity aperture plane (at height

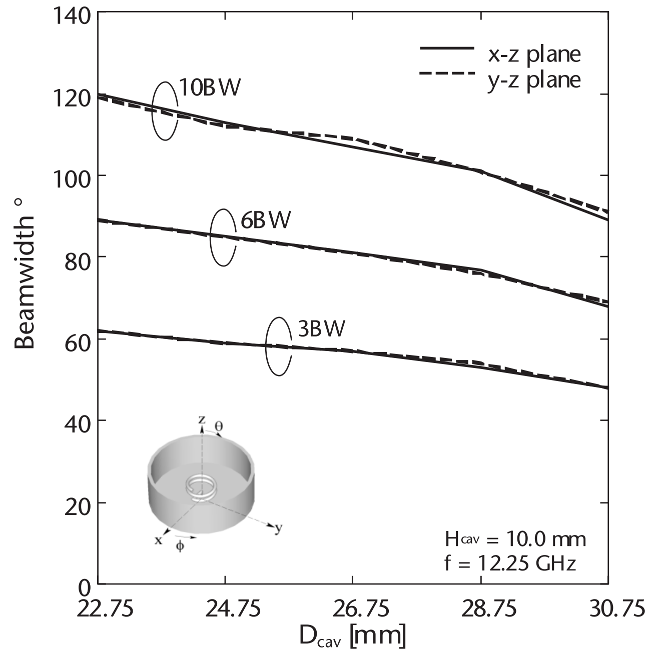

Figure 7.14 Effect of the cavity diameter D_{cav} on the beam width.

H_{cav}) where the electromagnetic field has equal or quasi-equal phase distribution becomes smaller.

The effect of the cavity height H_{cav} on the beamwidth is shown in Figure 7.15, where the cavity diameter and the operating frequency are held at $D_{cav} = 28.75$ mm and $f = 12.25$ GHz, respectively. Again, the parameters in Table 7.2 are used. It is found that, as the cavity height H_{cav} is decreased from 5 mm (0.2 wavelength), the beamwidth becomes wider.

7.5.2 Frequency Response

Let us investigate the frequency response of a CP helical feed antenna with a representative cavity that uses parameters (D_{cav}, H_{cav}) = (28.75 mm, 10 mm) [29, 30]. The parameters for the helical element are shown in Table 7.2.

Table 7.2 Helical Element Parameters

Symbol	*Value*
ρ	0.50 mm ≈ $0.02\lambda_{12.25}$
h	4.70 mm ≈ $0.19\lambda_{12.25}$
Δh	1.25 mm ≈ $0.05\lambda_{12.25}$
D_{HLX}	7.96 mm ≈ $0.33\lambda_{12.25v}$
C_{HLX}	25.0 mm ≈ $1.02\lambda_{12.25}$
α	4°
n	2 turns
Δt	1.00 mm ≈ $0.04\lambda_{12.25}$

$^*\lambda_{12.25} \approx 24.49$ mm

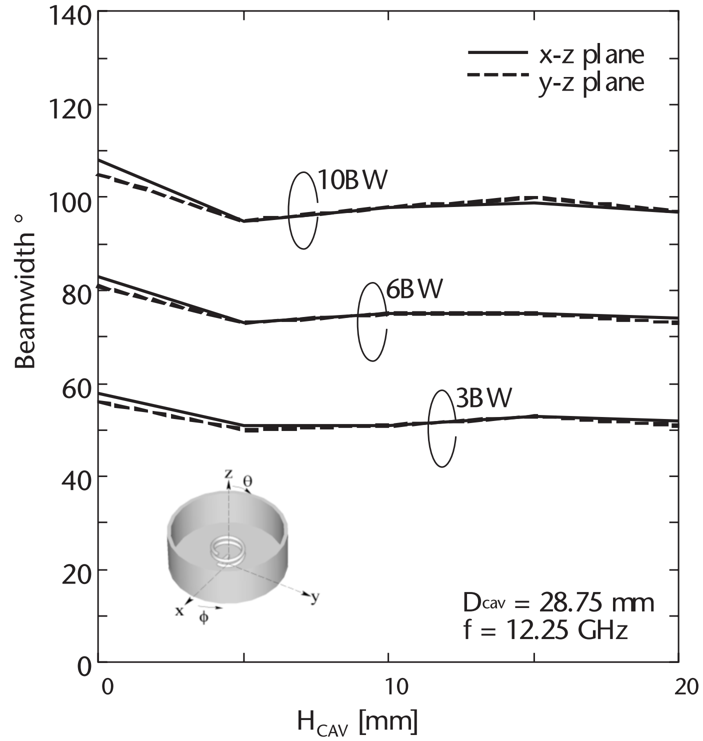

Figure 7.15 Effect of the cavity height H_{cav} on the beamwidth.

Figure 7.16 shows the radiation patterns in the x-z plane and y-z plane. It is found that CP radiation is obtained around the positive z-axis across a wide frequency range, and the right-handed CP electric field component E_R is dominant relative to the left-handed CP electric field component E_L. Note that the helical element is not symmetric with respect to the element axis (the z-axis), and hence, the radiation pattern is not perfectly symmetric with respect to the z-axis. However, this asymmetry is extremely small.

The frequency response of the axial ratio (AR) in the positive z-direction ($\theta = 0°$) is shown in Figure 7.17. The bandwidth for a 3 dB axial ratio criterion is moderately wide: approximately 14.8% (from 11.3–13.1 GHz). The front-to-back ratio (F/B ratio) for the radiation pattern is illustrated in Figure 7.18, where a maximum field intensity between angles $\theta = 180° - 60°$ and $\theta = 180° + 60°$ is used as a backward radiation field. It is found that the F/B ratio is large, as desired: greater than 20 dB from 11–13 GHz.

Figure 7.19 shows the frequency response of the beamwidth for an i-dB reduced field intensity criterion (iBW; i = 3, 6, and 10). It is found that the difference between iBWs in the x-z and y-z planes is small at each frequency. As the frequency is increased, iBW decreases; across a 3 dB axial ratio bandwidth (14.8% from 11.3–13.1 GHz), the reduction for 3BW is 6.6° in the x-z plane and 9.1° in the y-z plane.

The helical element is a nonresonant element and hence it is expected that the input impedance will have a wideband characteristic. Figure 7.20 shows the frequency response of the input impedance $Z_{in}(= R_{in} + jX_{in})$. As expected, the variation in the

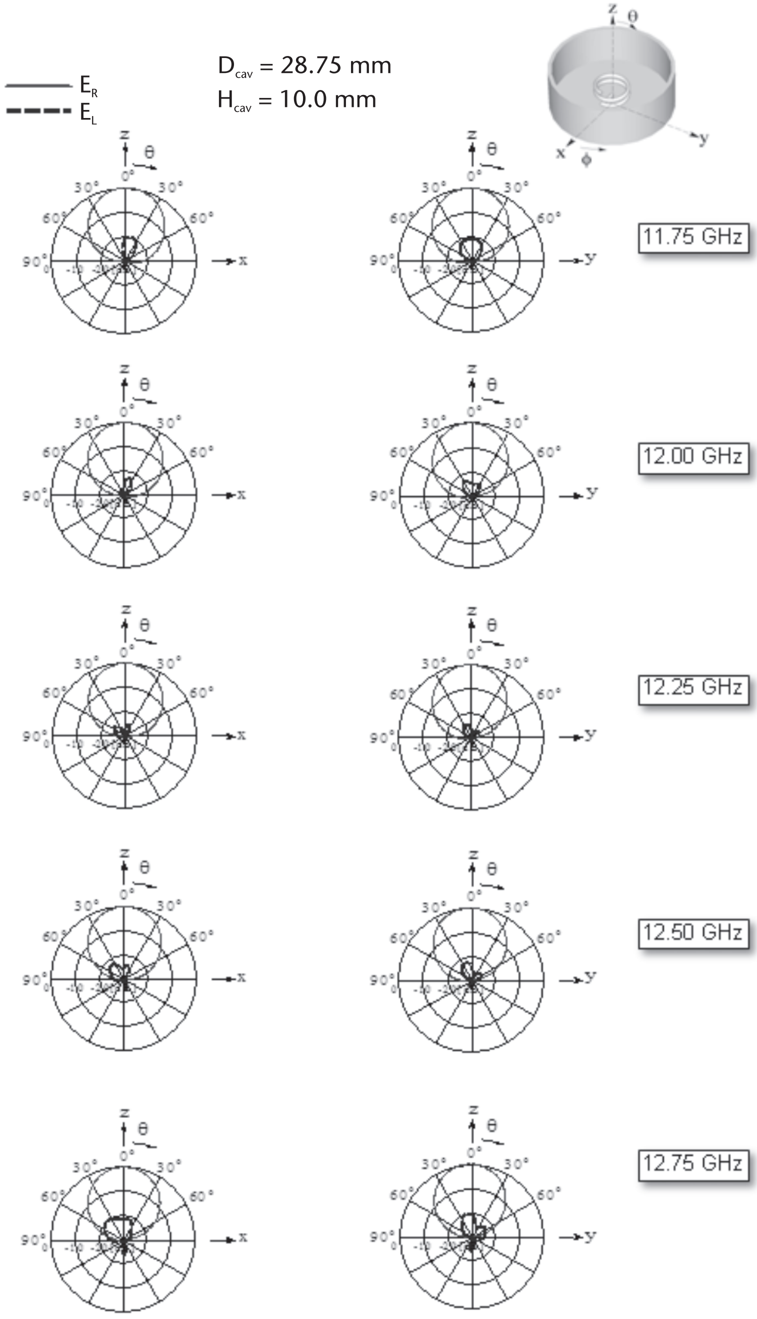

Figure 7.16 Radiation pattern as a function of frequency, where a cavity of diameter D_{cav} = 28.75 mm and height H_{cav} = 10 mm is used.

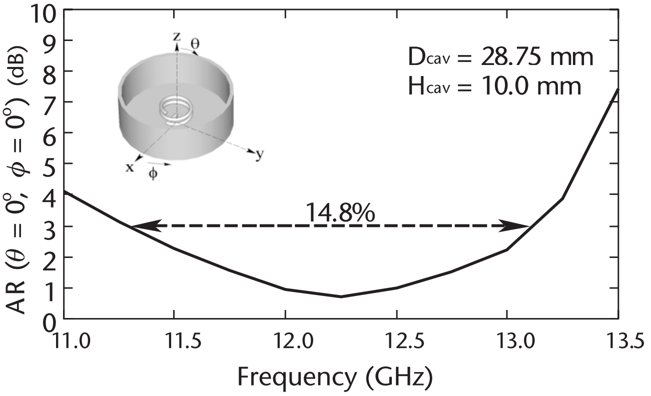

Figure 7.17 Frequency response of the axial ratio in the *z*-direction.

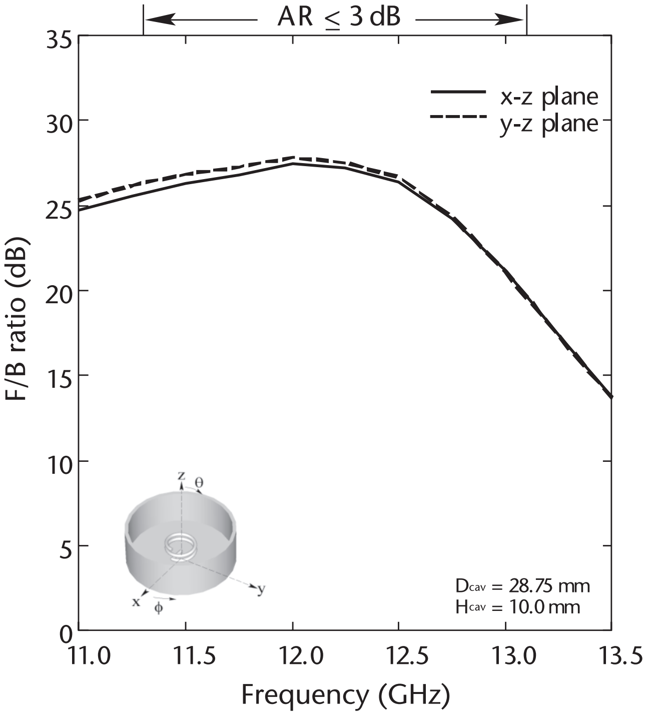

Figure 7.18 Front-to-back ratio (F/B ratio).

input impedance is small. Across the axial ratio bandwidth (14.8% from 11.3–13.1 GHz), variation in the resistive component is $\Delta R_{in} = 8.1\Omega$ and variation in the reactive component is $\Delta X_{in} = 8.3\Omega$. This small variation in the input impedance, together with the small variation in the beam width, contributes to the wideband characteristic of the gain. Figure 7.21, which shows the frequency response of the gain, confirms this. Note that G_R is the available gain for the co-polarized component E_R relative to an isotropic antenna.

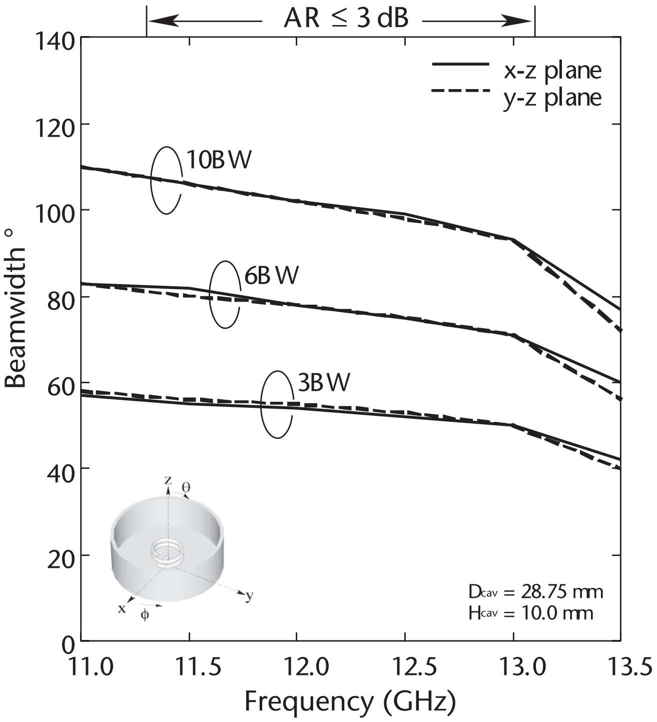

Figure 7.19 Frequency response of the beam width.

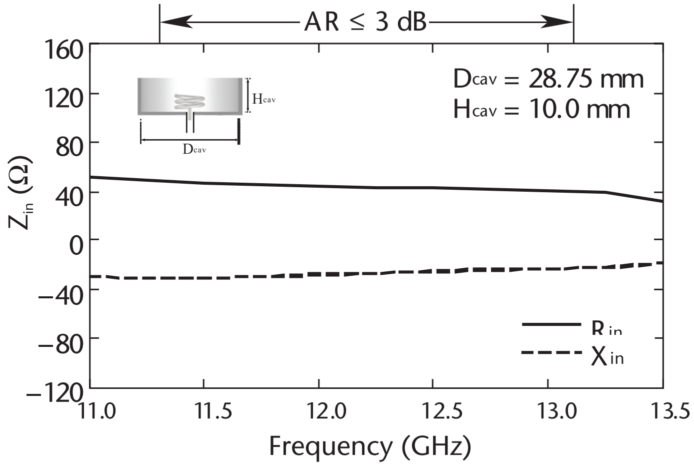

Figure 7.20 Frequency response of the input impedance $Z_{in}(= R_{in} + jX_{in})$.

We further investigate a situation where a dielectric layer of relative permittivity $\varepsilon_r = 2.1$ (Teflon) covers the top surface of the cavity to protect the helical element Figure 7.22. The investigation reveals that the effects of the dielectric layer thickness *B* on the antenna characteristics are small, as long as *B* is less than 0.04 wavelength. Note that when a thicker dielectric layer is used, the antenna configuration parameters must be reconsidered to obtain CP radiation.

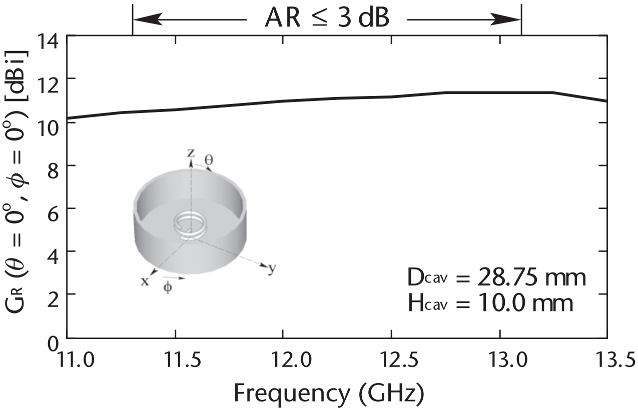

Figure 7.21 Frequency response of the gain.

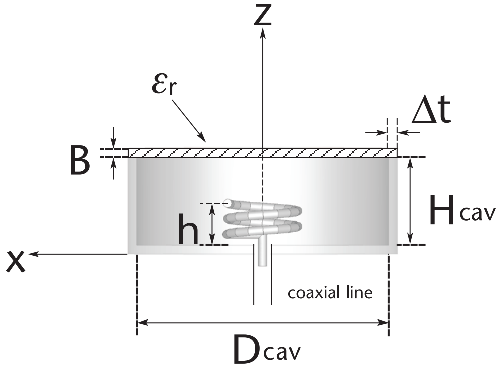

Figure 7.22 Dielectric layer on top of a cavity.

7.6 CP Feed Array Antenna Composed of End-Fire Helical Elements

An array of helical elements can also be used as a CP feed antenna for a reflector. Figure 7.23 shows a feed antenna composed of CP helical elements. The straight line (StL) connected to each helical element (of diameter D_{HLX}, pitch angle α, and number of helical turns n) is inserted into a circular cavity of diameter D_{cav} and height H_{cav} [31–33]. The spacing between the top and bottom conducting plates of the cavity is designated as H_{cav}. The array is excited by a probe located at the center of the bottom conducting plate [34]. The power input to the cavity through the probe electrically couples to the straight lines (StLs) connected to the helical elements and is radiated into free space by the elements. The StLs are coupled to the center probe through air (not rigid transmission lines), and hence the loss encountered in feed systems using wires, microstrips, or coaxial cables is avoided.

The radiation pattern is controlled by array techniques, where the excitation amplitude of each helical element is adjusted by the StL length and the excitation phase is adjusted by rotating the helical element around its axis (StL).

Figure 7.24 shows a helical array feed antenna with a two-layer structure, with each layer having a circular cavity. The upper layer feed antenna is used for

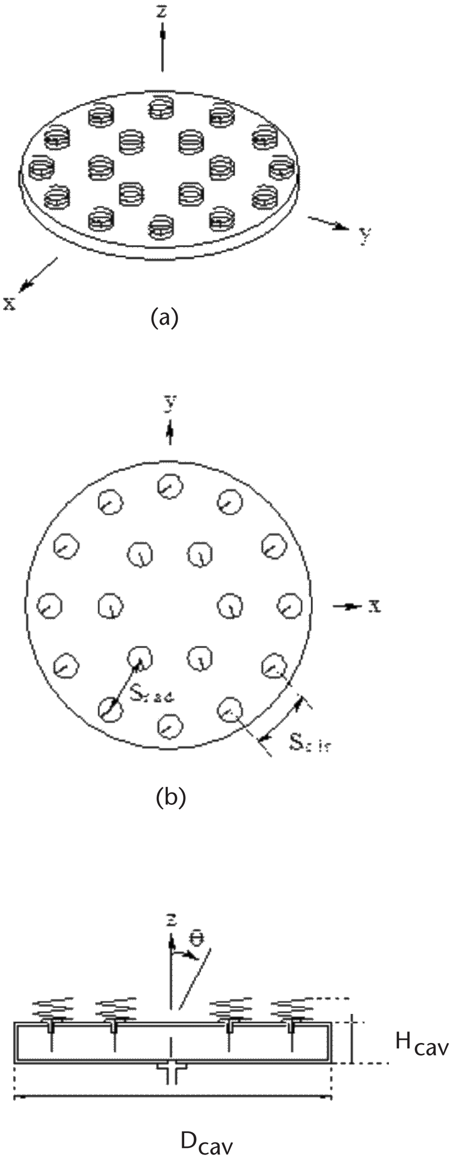

(a)

(b)

(c)

Figure 7.23 CP feed array antenna composed of helical elements. (a) Perspective view, (b) top view, and (c) side view.

a specific frequency band, and the lower layer feed antenna is used for a different frequency band. An application example of the two-layer feed antenna is found in Mimaki, Nakano, and Kasuga [35], and Kasuga, Mimaki, and Nakano [36], where an *S*-band feed antenna (2.1–2.6 GHz) and an *X*-band feed antenna (8.1–8.9 GHz) are designed for a Cassegrain reflector (Figure 7.25). Figure 7.26 shows the radiation from these feed antennas, where a beam width of 22° for a 7 dB reduced field intensity criterion is realized, meeting the requirement for both of the feed antennas. The parameters used for these feed antennas are summarized in Tables 7.3 and 7.4.

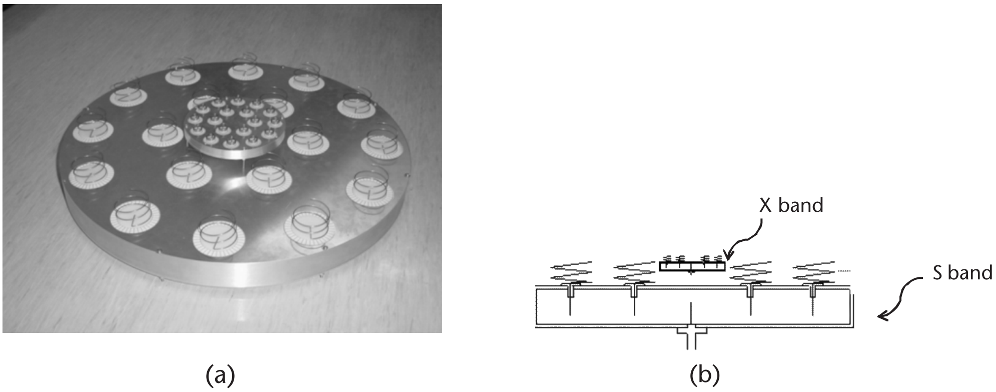

Figure 7.24 Helical feed array antenna with a two-layer structure. (a) Perspective view (photo), and (b) side view.

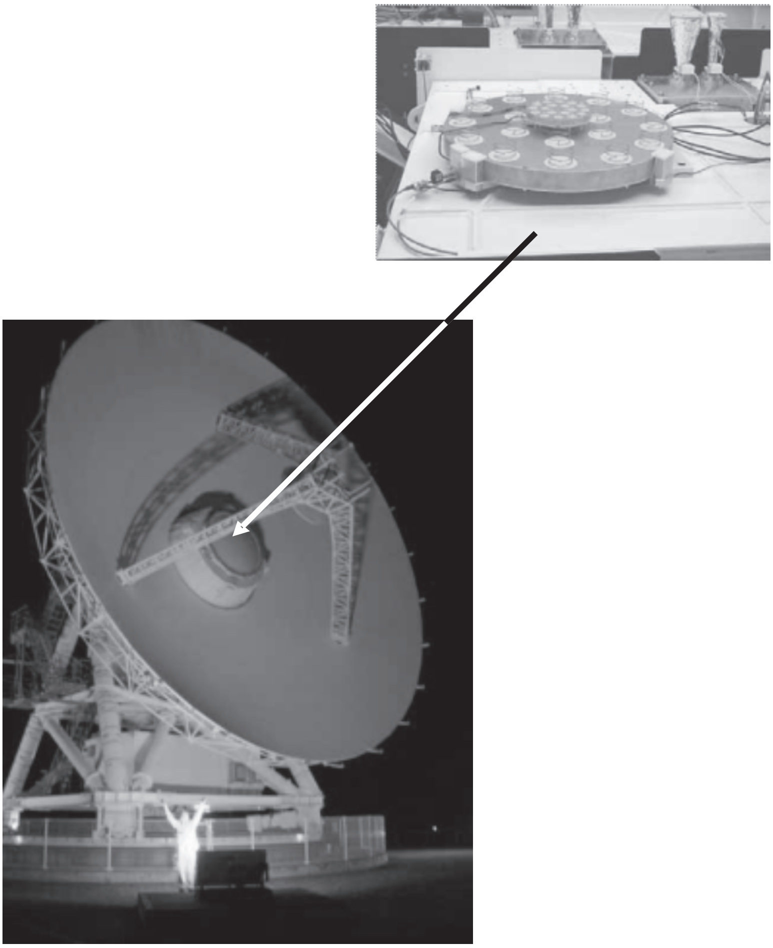

Figure 7.25 Application example of a two-layer feed antenna for a Cassegrain reflector. Diameter of circular main dish = 20 m, diameter of circular subdish = 2.6 m, and focal length of main dish = 6 m. and (Source: http://veraserver.mtk.nao.ac.jp/restricted/status05.pdf (Japanese).)

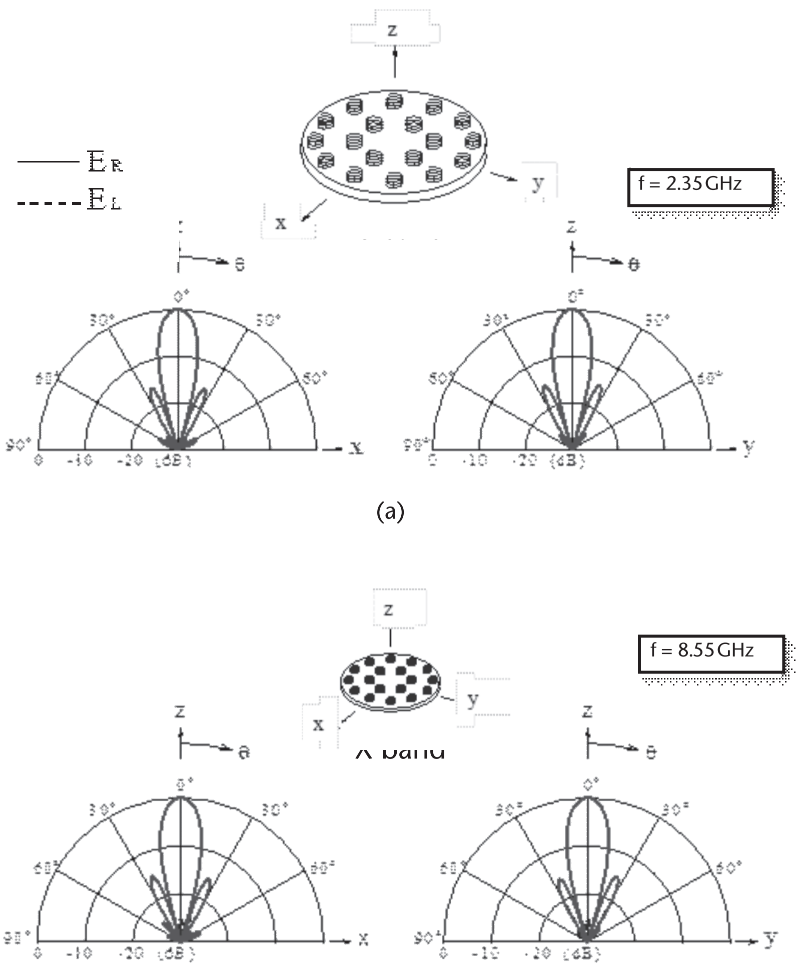

(a)

(b)

Figure 7.26 Radiation patterns (a) at 2.35 GHz (*S*-band), and (b) at 8.55 GHz (*X*-band).

Table 7.3 Parameters for *S*-Band

Symbol	*Value*
D_{HLX}	41.38 mm ≈ $0.3241\lambda_{2.35}$
n	3.1 turns
α	4°
ρ	0.5 mm ≈ $3.917 \times 10^{-3}\lambda_{2.35}$
H_{CAV}	495 mm ≈ $3.8775\lambda_{2.35}$
D_{CAV}	36 mm ≈ $0.282\lambda_{2.35}$
S_{cir}	109 mm ≈ $0.8538\lambda_{2.35}$
S_{rad}	104 mm ≈ $0.8147\lambda_{2.35}$

*$\lambda_{2.35}$ ≈ 127.66 mm

Table 7.4 Parameters for *X*-Band

Symbol	*Value*
D_{HLX}	11.169 mm ≈ $0.3183\lambda_{8.55}$
n	2.8 turns
α	4°
ρ	0.2 mm ≈ $5.7 \times 10^{-3}\lambda_{8.55}$
H_{CAV}	142 mm ≈ $4.047\lambda_{8.55}$
D_{CAV}	9.7 mm ≈ $0.27645\lambda_{8.55}$
S_{cir}	29.4 mm ≈ $0.8379\lambda_{8.55}$
S_{rad}	28.1 mm ≈ $0.8009\lambda_{8.55}$

*$\lambda_{8.55}$ ≈ 35.294 mm

7.7 Conical Helical CP Feed Antennas

The element shown in Figure 7.27 is a modified version of the end-fire helical element shown in Figure 7.12 and is called a conical helical (ConHLX) element [37–42]. The ConHLX element on a conducting ground plane of diameter D_{GP} is specified by flare angle θ_0, number of helical turns n, pitch angle α, wire radius ρ, and initial helical radius r_0. Due to the flared structure, the current from the feed point toward the arm end decays smoothly, helping to reduce the cross-polarized radiation.

The radiation from the ConHLX is categorized as loop-based CP radiation. This section summarizes the antenna characteristics for two representative ConHLXs [42]; one has a long structure specified by parameters in Table 7.5 and the other has a short structure specified by parameters in Table 7.6.

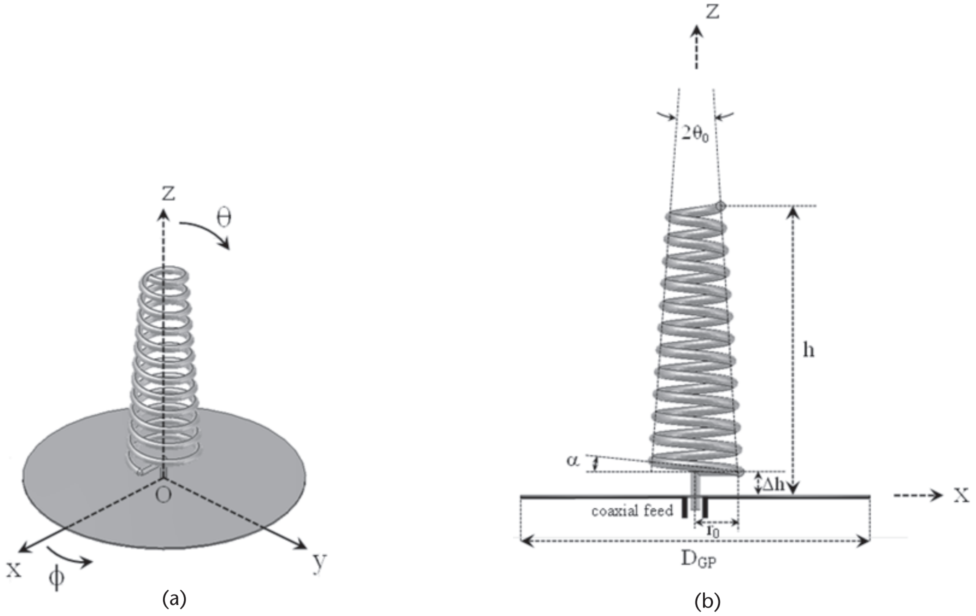

(a)

(b)

Figure 7.27 Conical helical element. (a) Perspective view, and (b) side view.

Table 7.5 Long Conical Helical Element Parameters

Symbol	*Value*
θ_0	4°
n	12 turns
α	6°
ρ	0.50 mm $\approx 0.0197\lambda_{11.85}$
r_0	4.575 mm $\approx 0.0181\lambda_{11.85}$
h	30.2 mm $\approx 1.192\lambda_{11.85}$
Δh	2.5 mm $\approx 0.09785\lambda_{11.85}$
D_{GP}	36.6 mm $\approx 1.446\lambda_{11.85}$

$^*\lambda_{11.85} \approx 25.32$ mm

Table 7.6 Short Conical Helical Element Parameters

Symbol	*Value*
θ_0	30°
n	4.25 turns
α	3°
ρ	0.3 mm $\approx 0.012\lambda_{11.85}$
r_0	5.5 mm $\approx 0.127\lambda_{11.85}$
h	6.04 mm $\approx 0.24\lambda_{11.85}$
Δh	1.25 mm $\approx 0.05\lambda_{11.85}$
D_{GP}	44 mm $\approx 1.74\lambda_{11.85}$

$^*\lambda_{11.85} \approx 25.32$ mm

Figures 7.28–7.33 show the frequency response for the antenna characteristics of the long ConHLX (Table 7.5), including the radiation pattern, axial ratio, beam width, *F/B* ratio, gain, and input impedance. It is found that the frequency bandwidth for a 3 dB axial ratio (AR) criterion is approximately 35%, and the available gain for the co-polarized component across this AR bandwidth is more than 11 dBi.

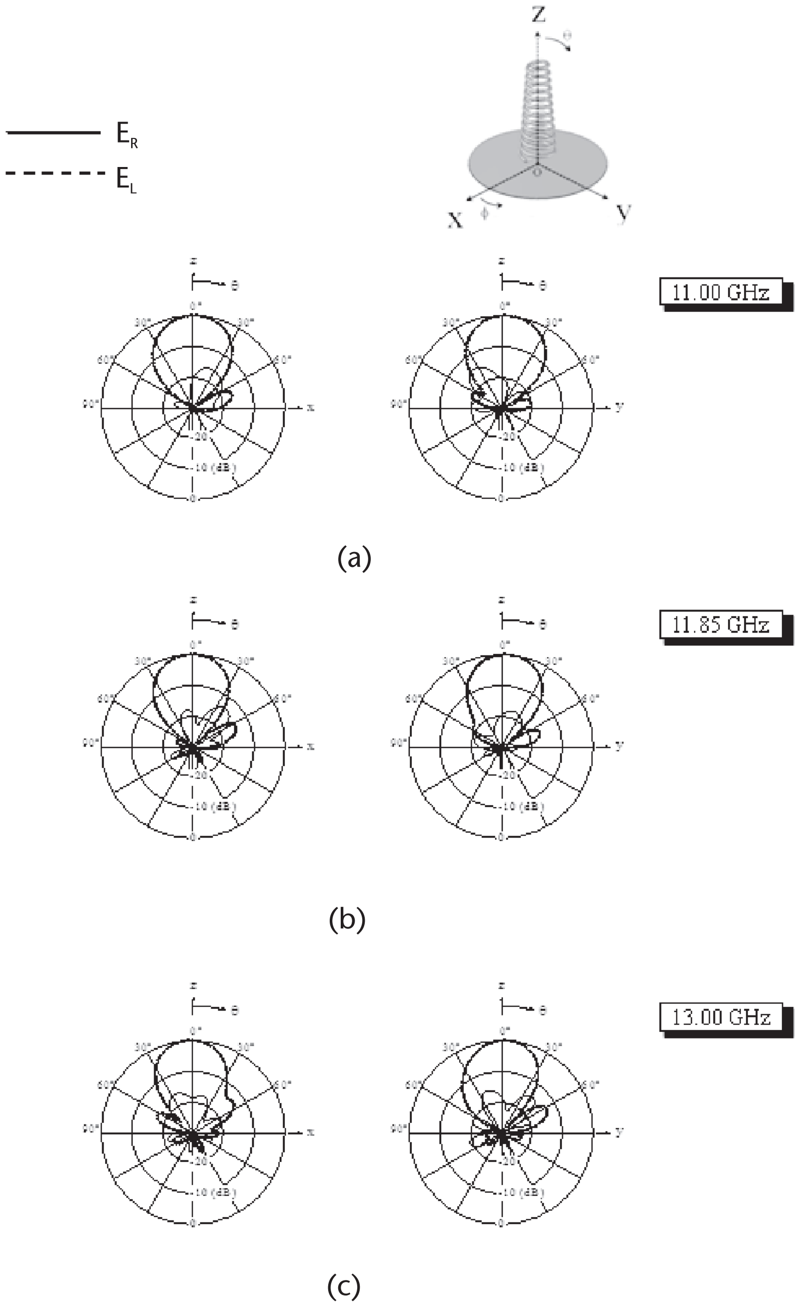

(a)

(b)

(c)

Figure 7.28 Radiation pattern of a long conical helical feed antenna.

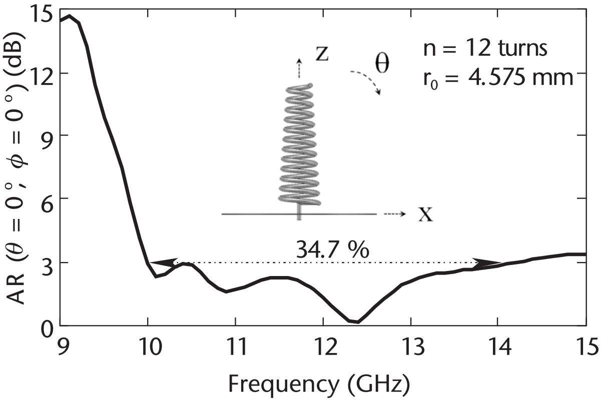

Figure 7.29 Axial ratio of a long conical helical feed antenna.

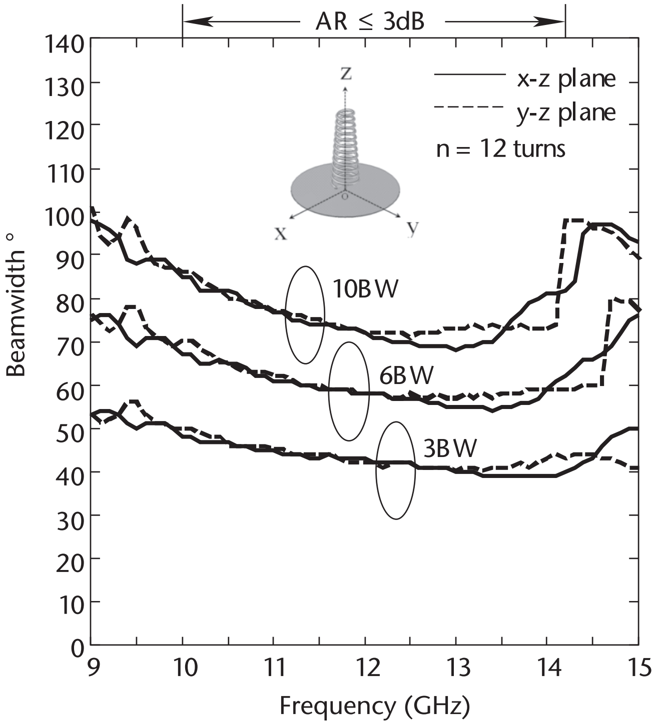

Figure 7.30 Beam width of a long conical helical feed antenna.

Figure 7.34 shows an application of this ConHLX as an offset CP feed antenna for a reflector.

The antenna characteristics of the short ConHLX (Table 7.6) are shown in Figures 7.35–7.40. This antenna has a wider beam width and a smaller gain than the long ConHLX. The available gain for the co-polarized component across an AR bandwidth of approximately 19% is less than 10 dBi. Note that, because of the wide beam width of the single short ConHLX elements, arraying these elements facilitates the formation of the beam required for the Cassegrain CP feed antenna.

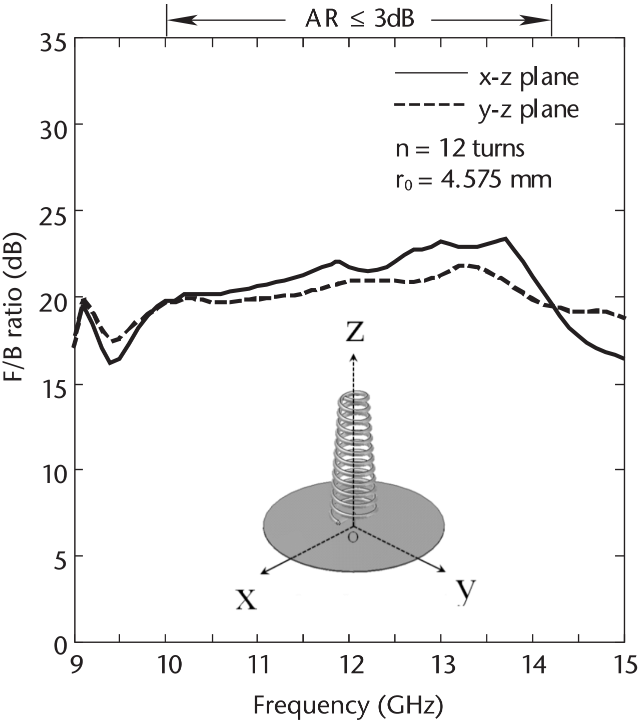

Figure 7.31 *F*/*B* ratio of a long conical helical feed antenna.

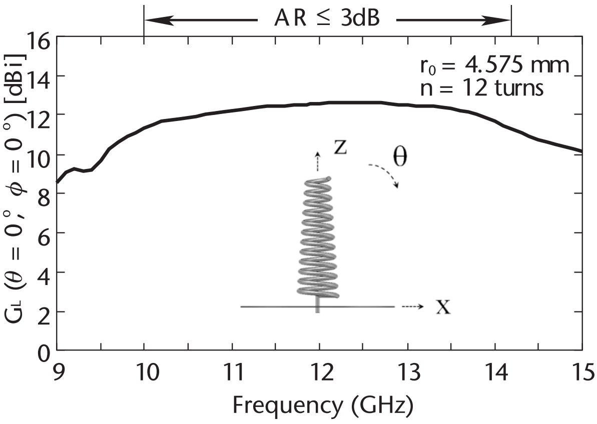

Figure 7.32 Gain of a long conical helical feed antenna.

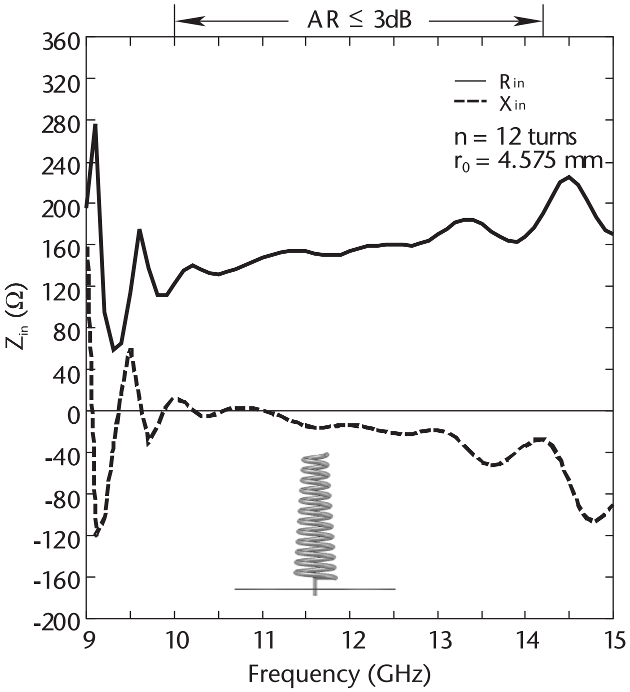

Figure 7.33 Input impedance of a long conical helical feed antenna.

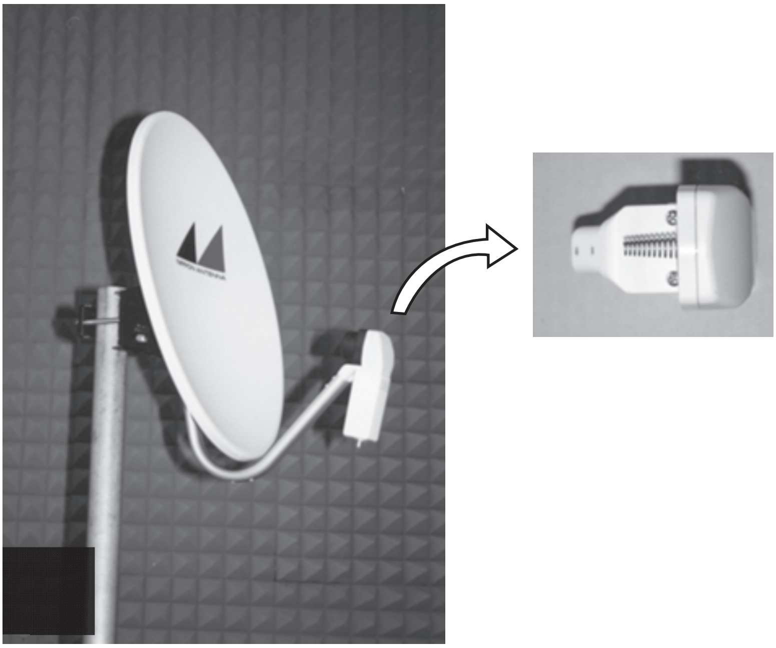
[redacted]

Figure 7.34 Offset feed using a long conical helical feed antenna. Major axis = 43.2 cm, minor axis = 38.0 cm, and focal length = 19 cm. (Courtesy of Nippon Antenna Co. Ltd.)

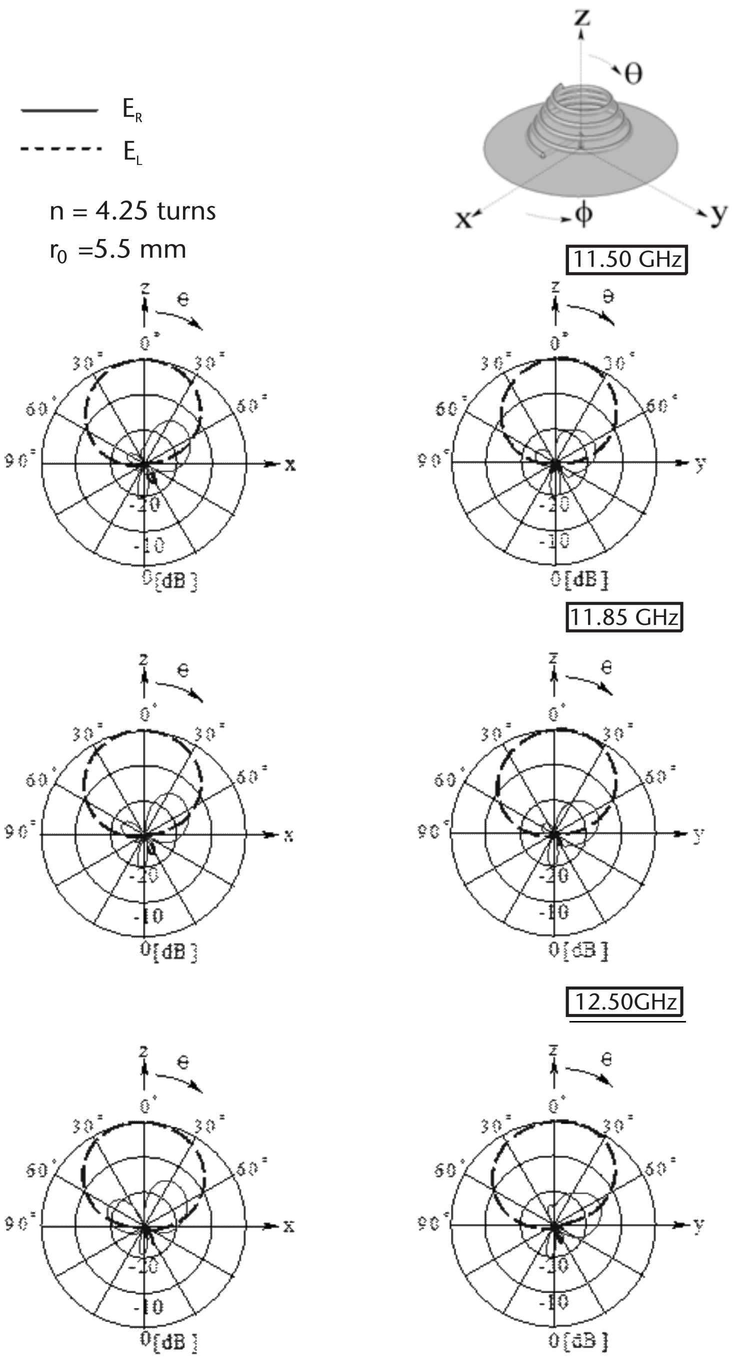

Figure 7.35 Radiation pattern of a short conical helical feed antenna.

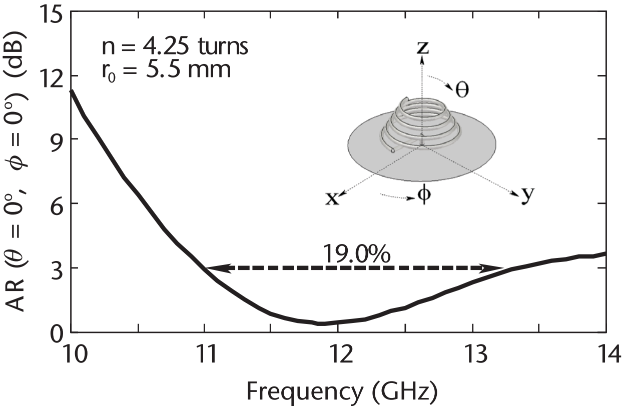

Figure 7.36 Axial ratio of a short conical helical feed antenna.

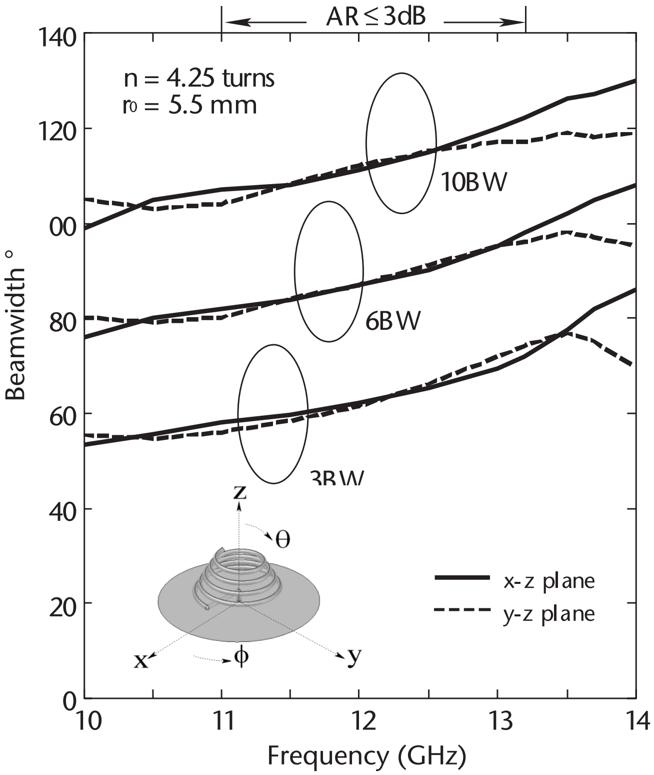

Figure 7.37 Beam width of a short conical helical feed antenna.

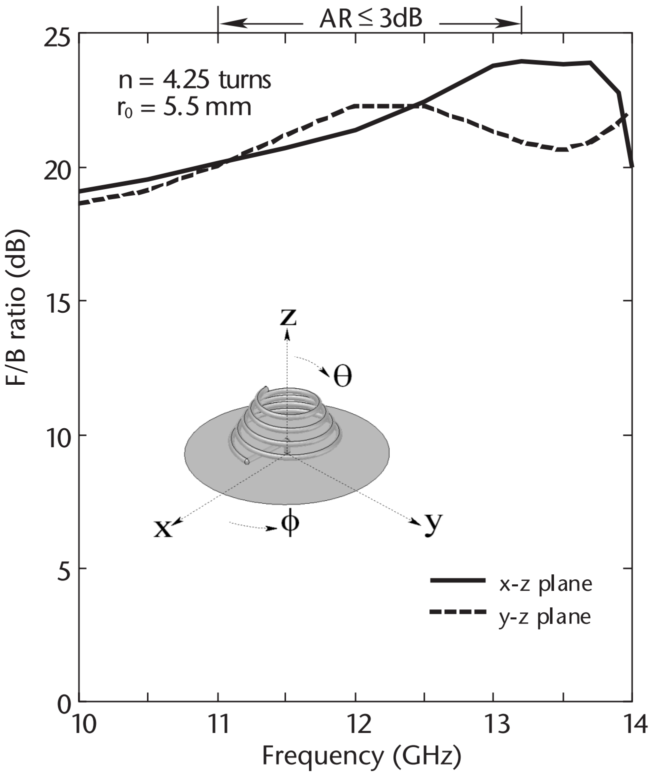

Figure 7.38 *F/B* ratio of a short conical helical feed antenna.

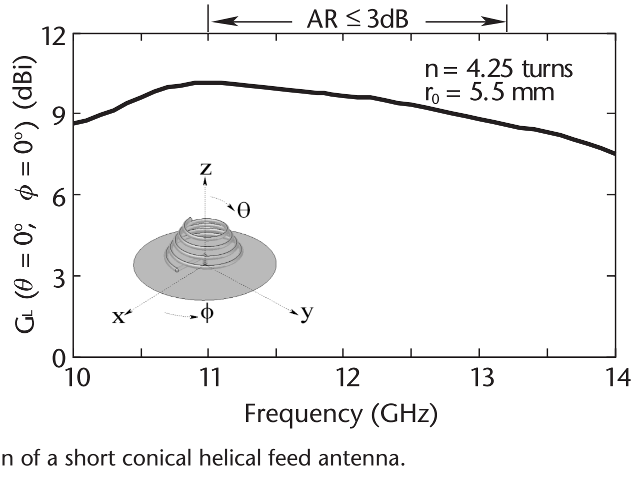

Figure 7.39 Gain of a short conical helical feed antenna.

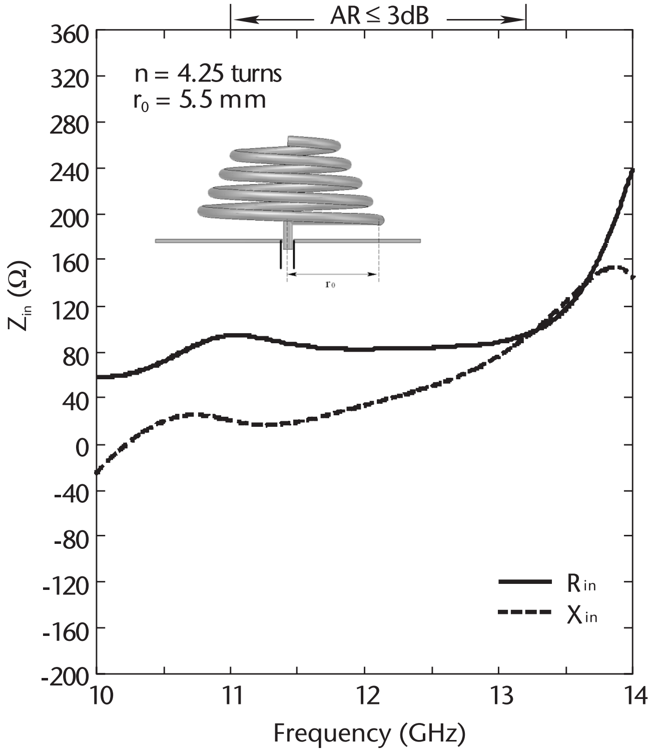

Figure 7.40 Input impedance of a short conical helical feed antenna.

7.8 Back-Fire-Mode CP Helical Feed Antenna

One aspect of reflector antenna design is minimization of the blockage of the transmitting/receiving signals by the feed antenna to increase the aperture efficiency. Figure 7.41(a) illustrates a reflector antenna fed by a CP helical element operating in end-fire mode. As the ground plane (GP) for this helical CP element becomes larger, the blockage of the transmitting/receiving signals increases, reducing the aperture efficiency. However, this issue is solved by replacing the end-fire helical CP element with a back-fire-mode helical CP element having a small ground plane [7, 43, and 44].

7.8.1 Back-Fire Radiation

We start by investigating how a helical element with a GP forms back-fire-mode radiation. Figure 7.42 shows the current ($I = I_r + jI_i$) flowing along the helical arm, with the GP diameter D_{GP} as a parameter, and where the helix has a circumference $C_{HLX} = \pi D_{HLX} = 1\lambda$ (λ is the free-space wavelength at frequency f), pitch angle $\alpha = 12.5°$, number of helical turns $n = 7$, initial height $\Delta h = 0.06\lambda$, and wire radius $\rho = 0.012\lambda$.

When the GP diameter D_{GP} is larger than the helical element diameter D_{HLX} ($D_{GP}/D_{HLX} = 1.89$), the current flowing out from feed point F decays rapidly and is minimum at point P, as seen from Figure 7.42(a). This current from point F to

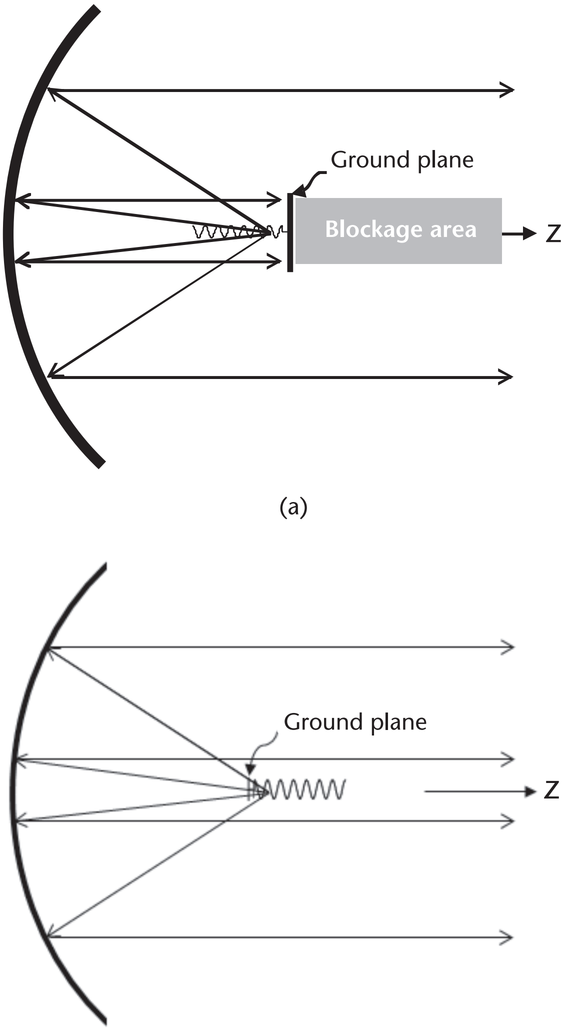

Figure 7.41 Parabolic reflector. (a) Feed blockage by a CP feed antenna with a large ground plane, and (b) reduced feed blockage using a back-fire-mode CP helical feed antenna with a small ground plane.

point *P* is called the *C*-current. The remaining current after point *P* travels with a relatively constant amplitude, except at the arm end region. This current is called the *S*-current, to distinguish it from the *C*-current. Calculation using all the currents flowing along the helical arm and GP reveals that the radiation field has a maximum intensity in the positive *z*-direction, that is, a helix forms end-fire radiation.

Figure 7.42(b) shows the current distribution when the GP diameter is slightly larger than the helical element diameter ($D_{GP}/D_{HLX} = 1.10$). *C*- and *S*-currents flow along the helical arm on their respective side of point *P* and the radiation has a bidirectional characteristic, with almost the same field intensity in both the positive and negative *z*-directions.

An interesting phenomenon occurs when the GP diameter is slightly smaller than the helical element diameter. As shown in Figure 7.42(c), where $D_{GP}/D_{HLX} = 0.91$, the current decays gradually from input point *F* and dies out at the arm end, that is, it forms a *C*-current but does not form an *S*-current. The radiation in this situation is directed in the negative *z*-direction, meaning, the helix forms back-fire-mode radiation. This reveals that the *C*-current is the source of the back-fire radiation. A detailed discussion on the *C*-current and *S*-current are found in Nakano [27].

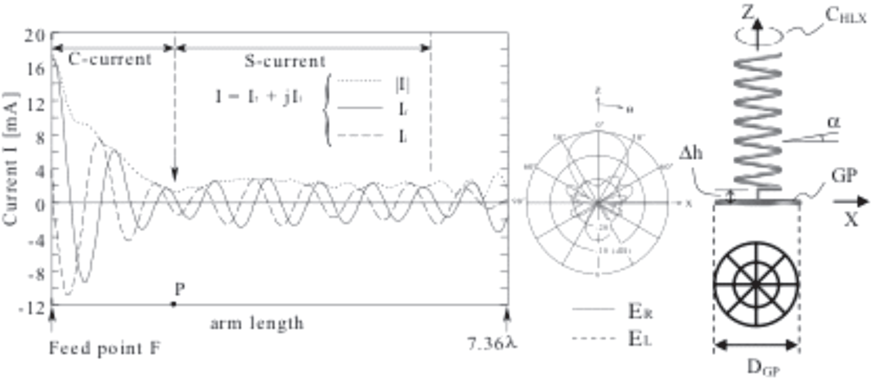

(a) $D_{GP} / D_{HLX} = 1.89$

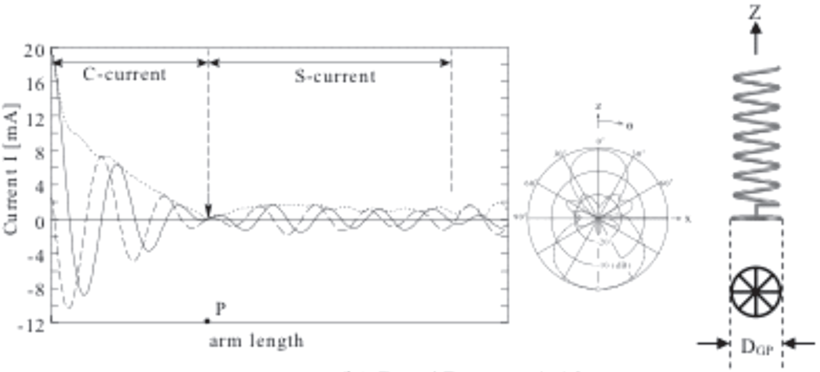

(b) $D_{GP} / D_{HLX} = 1.10$

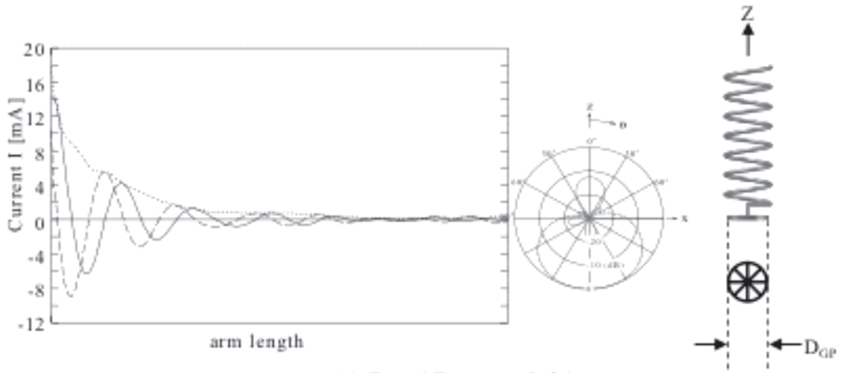

(c) $D_{GP} / D_{HLX} = 0.91$

Figure 7.42 Current distribution and radiation. (a) $D_{GP}/D_{HLX} = 1.89$, (b) $D_{GP}/D_{HLX} = 1.10$, and (c) $D_{GP}/D_{HLX} = 0.91$.

7.8.2 Frequency Response of the Current

The previous section focused on the GP size for a helical CP element, and it is revealed that, when the GP diameter is slightly smaller than the helical element diameter, the helical element operates in back-fire mode. The back-fire-mode helical CP feed antenna has the advantage that it reduces feed blockage of the transmitting/receiving signals due to its small GP.

This section focuses on the frequency response of the current along the helical arm, where the GP diameter D_{GP} is slightly smaller than the helical diameter D_{HLX}. The parameters used are as follows: $D_{GP} = 7.25$ mm, $D_{HLX} = 7.96$ mm [$C_{HLX} = \pi D_{HLX} = 25$ mm, which corresponds to one wavelength ($1\lambda_{12}$) at 12 GHz], helical turns $n = 7$, wire radius $\rho = 0.3$ mm, initial height $\Delta h = 1.5$ mm, and pitch angle $\alpha = 14°$.

As seen in Figure 7.43, a traveling wave current with gradual attenuation is dominant at 10 GHz and 11 GHz. As the frequency decreases from 10 GHz, variation in the amplitude of the current becomes considerable. This means that the incoming current from the arm end to the feed point has become larger, producing undesirable cross-polarized radiation (i.e., CP radiation whose rotational sense [RtS] is opposite to the RtS of the CP radiation due to the current flowing from the feed

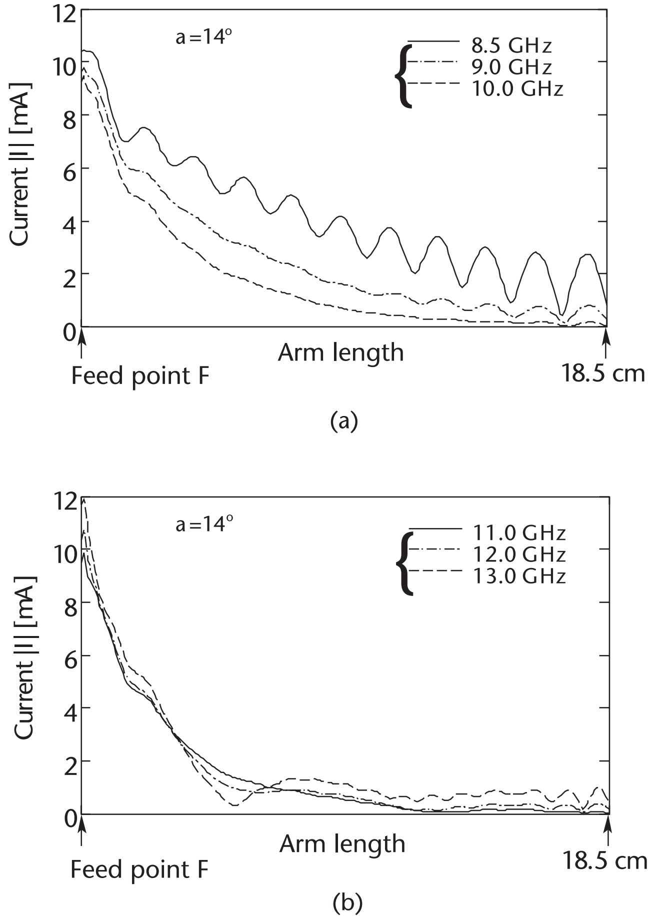

Figure 7.43 Frequency response of the current distribution along a helical arm.

point to the arm end). The cross-polarized radiation deteriorates the axial ratio, and hence the axial ratio becomes one factor in determining the lower frequency bound for the CP feed antenna.

Conversely, as the frequency is increased, an *S*-current becomes noticeable, increasing the forward-fire radiation. This results in an undesirable increase in the F/B ratio. Note that the inverse of the F/B ratio (i.e., the B/F ratio) should be large for back-fire radiation. In this context, the F/B ratio becomes one factor in determining the upper frequency bound of the CP feed antenna.

7.8.3 Effects of Pitch Angle on the Frequency Response of the Antenna Characteristics

Next, we investigate the effects of the pitch angle α on the antenna characteristics. For this, the pitch angle is varied from 6–18°. Other configuration parameters, including D_{HLX}, D_{GP}, n, and ρ, are chosen to be the same as those used in Section 7.8.2 (see Table 7.7).

The sense of the co-polarized CP radiation in the negative *z*-space is left-handed. Figure 7.44 shows the frequency response of the beamwidth for each i-dB reduced field intensity criterion, iBW, for the left-handed radiation field component E_L, with the pitch angle α as a parameter: 3BW in Figure 7.44(a), 6BW in Figure 7.44(b), and 10BW in Figure 7.44(c). It is found that, as the frequency decreases, the beamwidth for each iBW decreases. It is also found that a larger pitch angle α leads to a wider iBW.

A representative radiation pattern is shown in Figure 7.45, where a pitch angle of $\alpha = 14°$ is used. It is revealed that the co-polarized component in the negative *z*-space, E_L, is almost symmetrical with respect to the antenna axis (*z*-axis). It is also revealed that the E_L pattern forms a unidirectional beam without large side lobes in the negative *z*-space, as desired for a feed antenna.

As shown in Figure 7.45, the back-fire radiation for $\alpha = 14°$ is large relative to the front-fire radiation. This holds true for other pitch angles. More detail is shown in Figure 7.46, where the frequency response of the F/B ratio is illustrated, with the pitch angle α as a parameter. It is found that a minimum F/B ratio of less than –20 dB is obtained for each pitch angle. It is also found that the frequency region exhibiting a desirably small F/B ratio shifts toward the lower frequency band as the pitch angle α is increased.

Table 7.7 Back-Fire Helical Feed Antenna Parameters

Symbol	*Value*
C_{HLX}	25 mm ≈ $1\lambda_{12}$
D_{HLX}	7.96 mm ≈ $0.3\lambda_{12}$
D_{GP}	7.25 mm ≈ $0.29\lambda_{12}$
n	7 turns
Δh	1.5 mm
ρ	0.3 mm ≈ $0.012\lambda_{12}$

$^*\lambda_{12} \approx 25$ mm

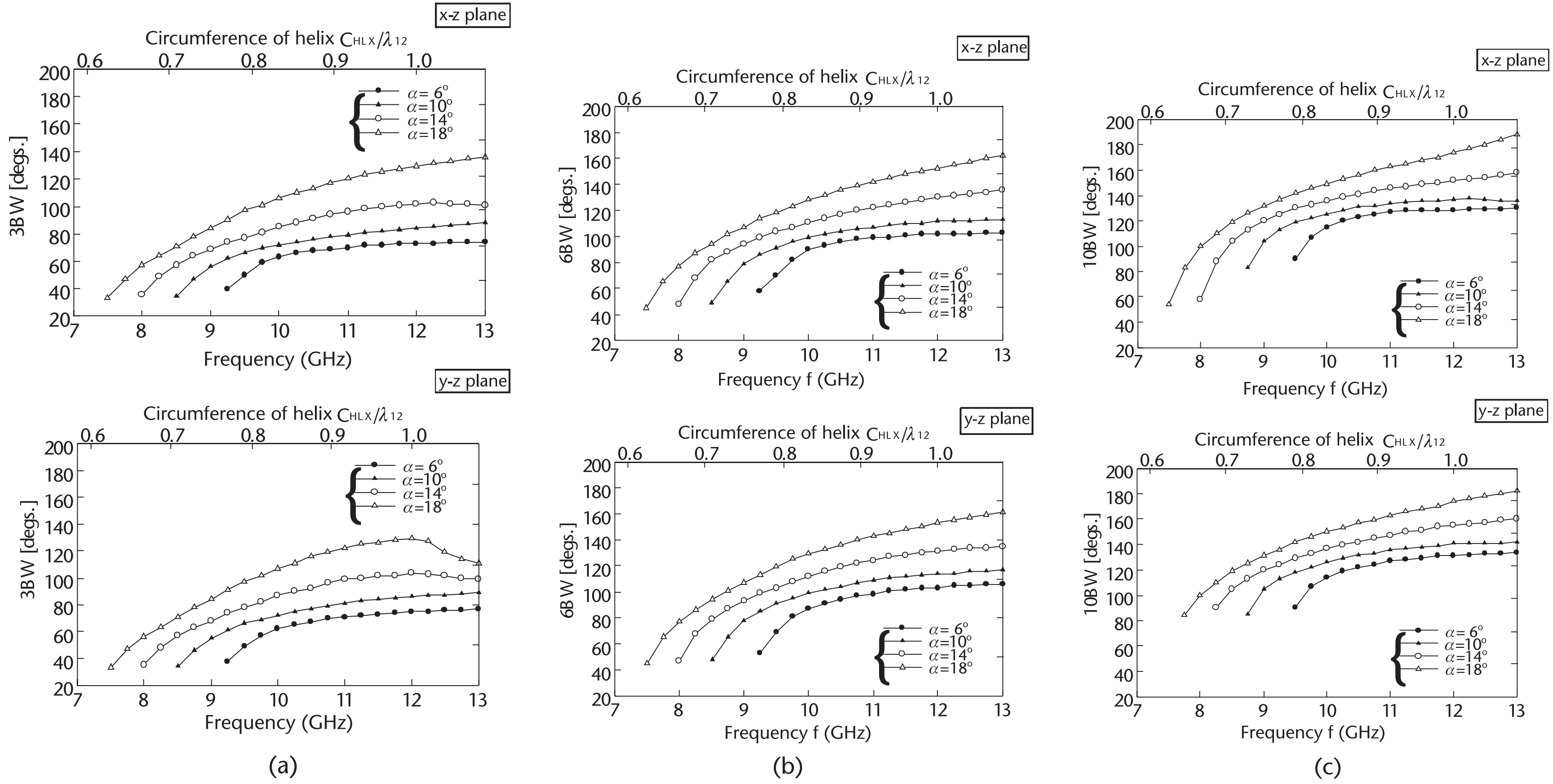

(a)

(b)

(c)

Figure 7.44 Frequency response of the beamwidth, with the pitch angle α as a parameter. (a) 3BW, (b) 6BW, and (c) 10BW.

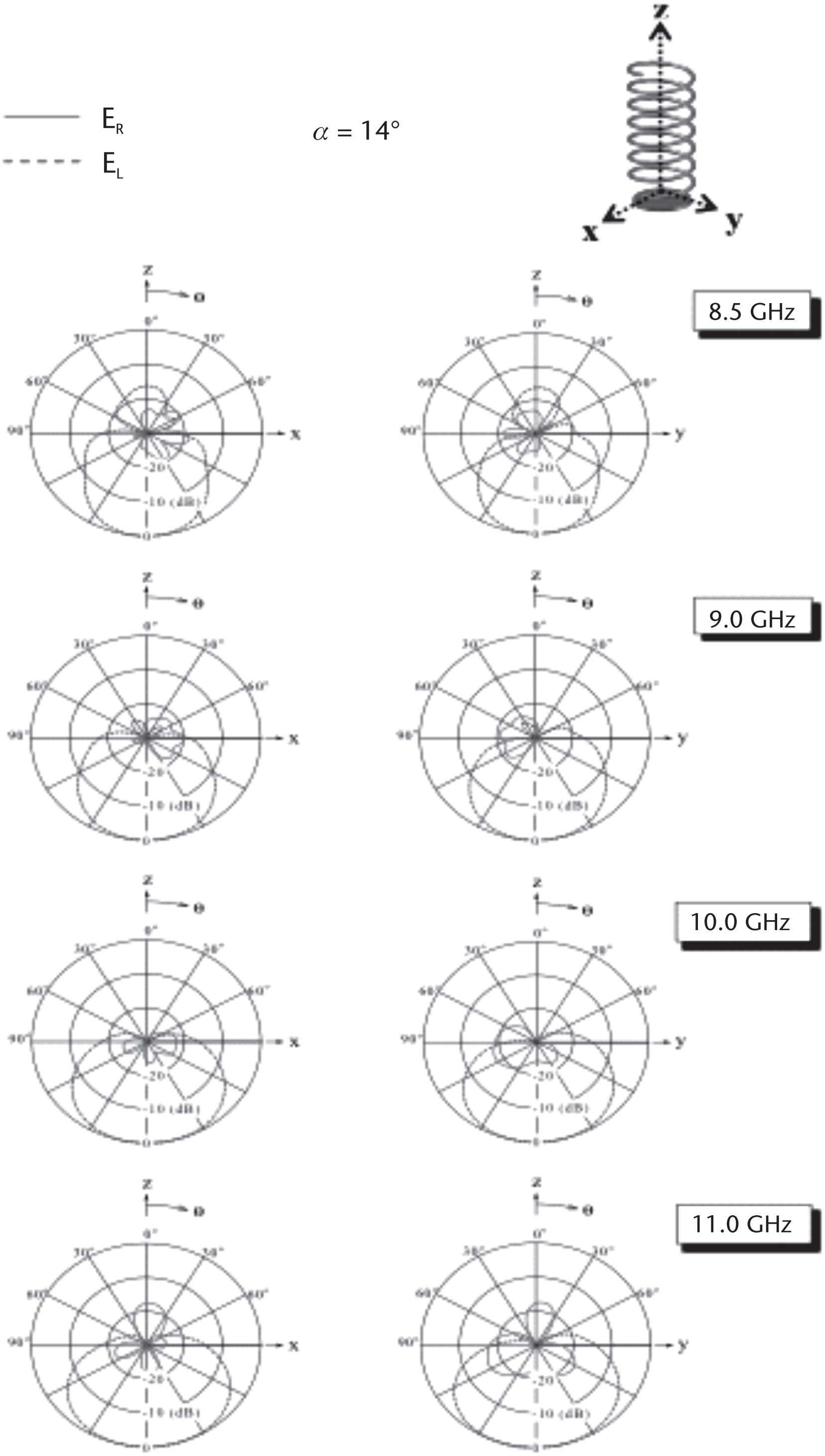

Figure 7.45 Frequency response of the radiation pattern when the pitch angle is 14°.

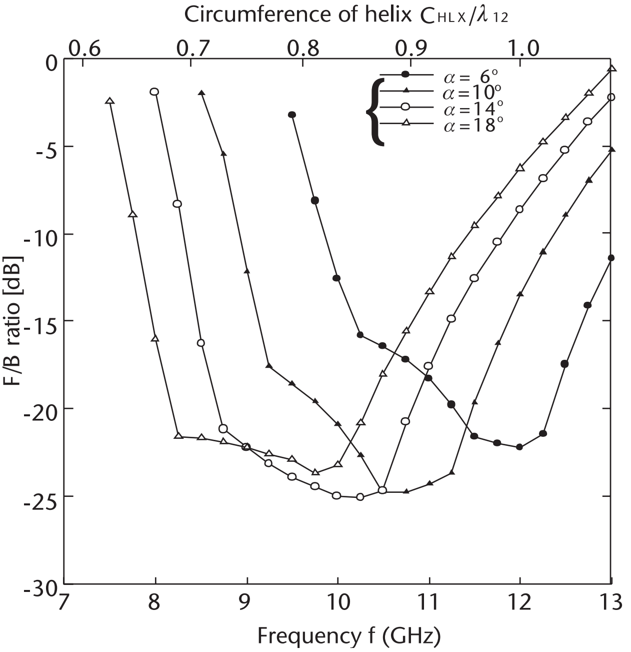

Figure 7.46 Frequency response of the F/B ratio, with the pitch angle α as a parameter.

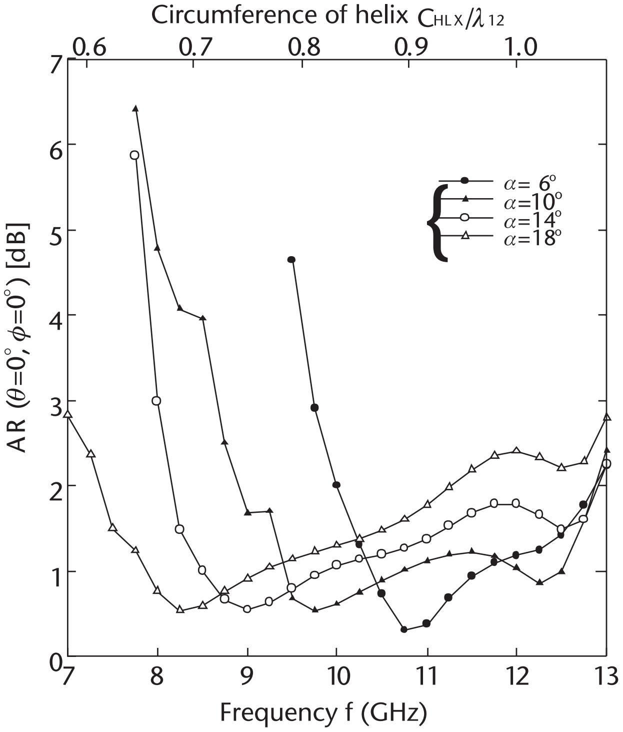

Figure 7.47 Frequency response of the axial ratio, with the pitch angle α as a parameter.

Figure 7.47 shows the frequency response of the axial ratio (AR) in the negative *z*-direction, with the pitch angle α as a parameter. As observed for the F/B ratio, the frequency region with a desirably small axial-ratio shifts toward the lower frequency band as the pitch angle α is increased. Note that as the pitch angle is increased, the bandwidth for a 3 dB axial ratio criterion becomes wider.

As long as the current does not return from the arm end toward the feed point *F*, the input impedance remains unchanged. It is expected that a current composed of only the *C*-current would create this condition for the input impedance, because it is a decaying traveling wave current, as seen in Figures 7.42 and 7.43. Figure 7.48 shows the frequency response of the input impedance $Z_{in} = R_{in} + jX_{in}$, with the pitch angle α as a parameter. It is found that there is a wide frequency region where the input impedance is nearly constant; the resistive part R_{in} is approximately 100 ohms and the reactive part X_{in} is approximately zero. These values produce an acceptable VSWR of approximately 2 for a 50-ohm feed line. Note that the VSWR can be further reduced by changing the initial height Δh.

Figure 7.49 shows the frequency response of the gain (available gain G_L for the co-polarized component E_L, not including mismatch with the feed line), with the pitch angle α as a parameter. It is found that, as the frequency increases, the gain reaches a maximum value and then gradually decreases, that is, the gain shows a wideband characteristic. The frequency region where the gain remains relatively constant shifts toward the lower frequency band as the pitch angle α is increased and coincides with the frequency regions for desirable F/B ratio and input impedance.

Figure 7.50 shows an application of the back-fire-mode helical CP feed antenna (pitch angle α = 18°) to a center-fed parabolic reflector that has been used as a direct

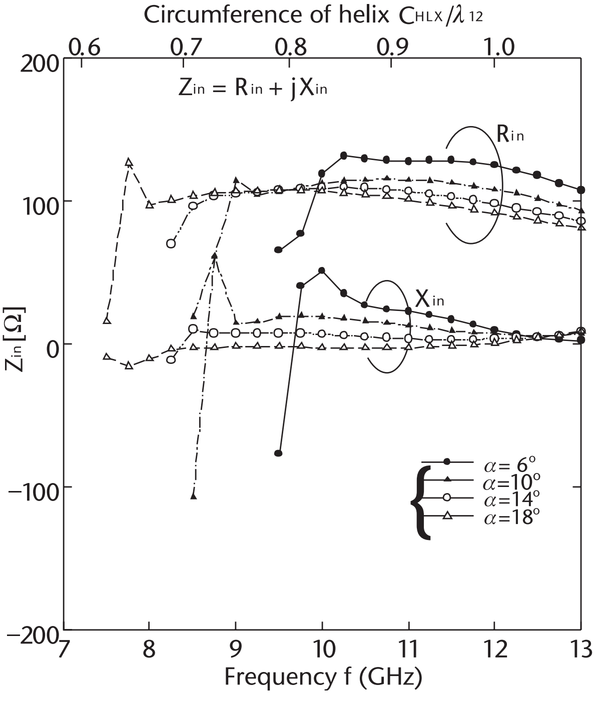

Figure 7.48 Frequency response of the input impedance $Z_{in} = R_{in} + jX_{in}$, with the pitch angle as a parameter.

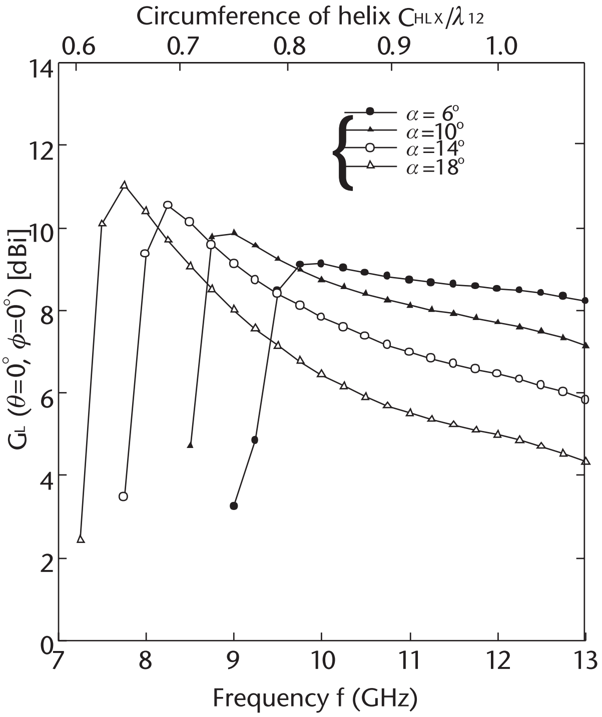

Figure 7.49 Frequency response of the gain, with the pitch angle α as a parameter.

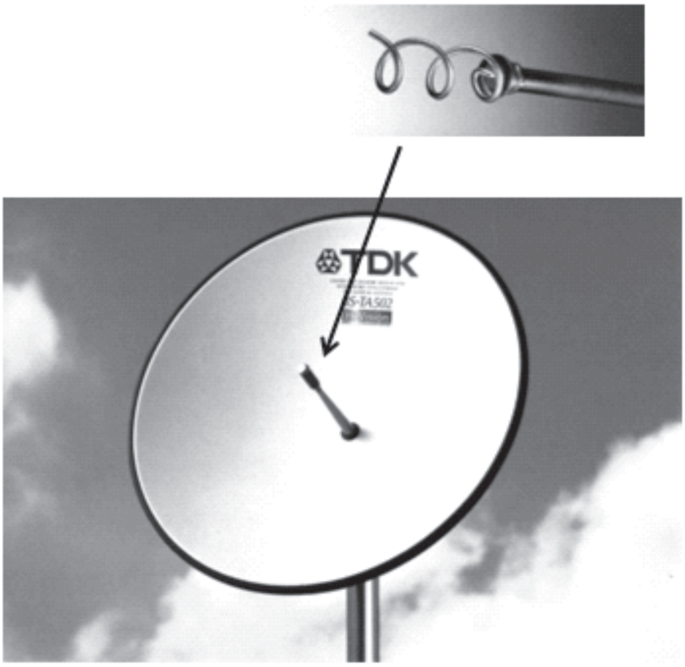

Figure 7.50 Parabolic reflector fed by a back-fire-mode helical CP feed antenna. (Courtesy of TDK Corporation.)

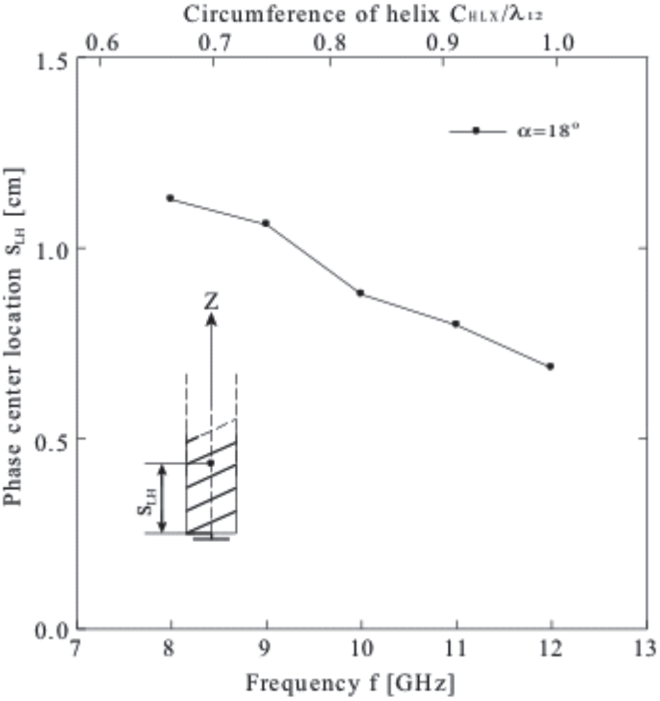

Figure 7.51 Phase center of the radiation field component E_L.

broadcasting satellite receiving antenna in Japan. The distance from the GP to the phase center [45] of the co-polarized radiation field component E_L, s_{LH}, is calculated for $\alpha = 18°$ and presented in Figure 7.51. Strictly speaking, the calculated distance s_{LH} in the x-z plane shows a different value from that in the y-z plane. Therefore, the distance s_{LH} in Figure 7.51 is expressed as the average of the x-z plane and y-z plane values. It is found that, as the frequency increases, the phase center moves toward the ground plane. This is attributed to the fact that the attenuation in the current becomes larger as the frequency increases, as shown in Figure 7.43. As a result, the current contributing to the radiation concentrates in a region close to the GP.

7.9 Spiral CP Feed Antenna

Figure 7.52 shows a two-arm spiral element in air, whose antenna circumference C_{SP} is approximated to be $2\pi r_{\max}$, where $r_{\max}$ is the maximum radius. The antenna is excited from its center point. CP radiation from the spiral is obtained when the circumference of the spiral C_{SP} is greater than one guided wavelength ($1\lambda_g$) and the currents along the spiral arms flow in a traveling wave fashion. This CP radiation is categorized as loop-based CP (LPB-CP) radiation [46].

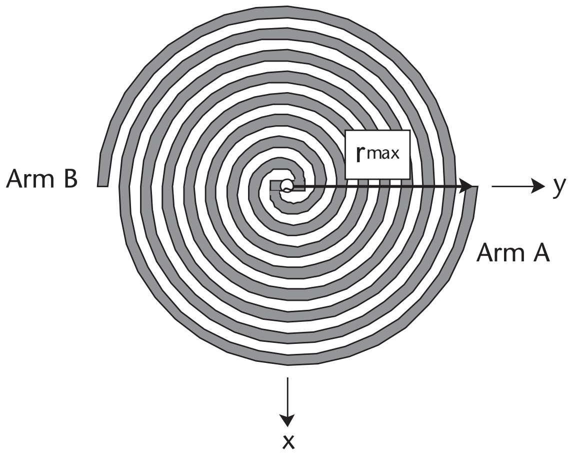
Arm B
r_{max}
y
Arm A
x

Figure 7.52 Spiral element in air.

The CP radiation is bidirectional; the maximum radiation occurs in the two directions normal to the antenna plane (positive and negative z-directions). When a CP feed antenna is used for a reflector, this bidirectional radiation is transformed into unidirectional radiation. One technique to obtain unidirectional radiation in the positive z-direction is to place a flat conducting plate behind the spiral, as shown in Figure 7.53 [47].

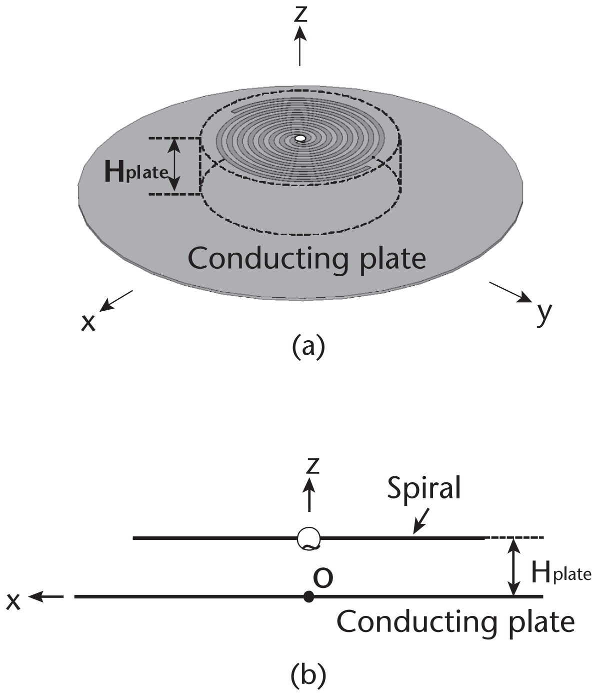
z
H_{plate}
Conducting plate
x
y
(a)
z
Spiral
H_{plate}
o
x
Conducting plate
(b)

Figure 7.53 Transformation from bidirectional radiation to unidirectional radiation using a flat conducting plate.

Waves radiated from the spiral in the negative *z*-direction are reflected at the conducting plate and travel in the positive *z*-direction (we call these waves cavity-reflected waves). When the distance between the conducting plate and the spiral, H_{plate}, is chosen to be one-quarter wavelength ($\lambda/4$) at the design center frequency, the waves that directly radiate from the spiral in the positive *z*-direction and the cavity-reflected waves add in phase in front of the spiral, forming a unidirectional beam.

A conducting cavity (of height H_{cav}), as shown in Figure 7.54, can also be used to form unidirectional radiation. It is found that, as the cavity height H_{cav} is decreased, the AR deteriorates; it is difficult to obtain an AR of less than 3 dB at a cavity height H_{cav} of less than $\lambda/10$. The AR deterioration is attributed to the strong influence of the cavity-reflected waves upon the current flowing on the spiral arms; the cavity-reflected waves interfere with the outgoing currents from the feed points to the arm ends, generating incoming currents toward the input terminals. These incoming currents radiate CP waves whose RtS is opposite to the RtS for the CP wave generated by the outgoing currents, resulting in a deterioration in the AR.

To mitigate the deterioration in the AR, an electromagnetic absorbing material (EM absorber [48–50] or resistor [51]) is used. Figure 7.55 shows a cavity-backed spiral feed having an EM absorber. In Figure 7.55(a), the absorber (ABS) entirely fills the space behind the spiral arms, while the absorber in Figure 7.55(b) fills only the space behind the outer region of the spiral arms (the absorber is called a ring-shaped

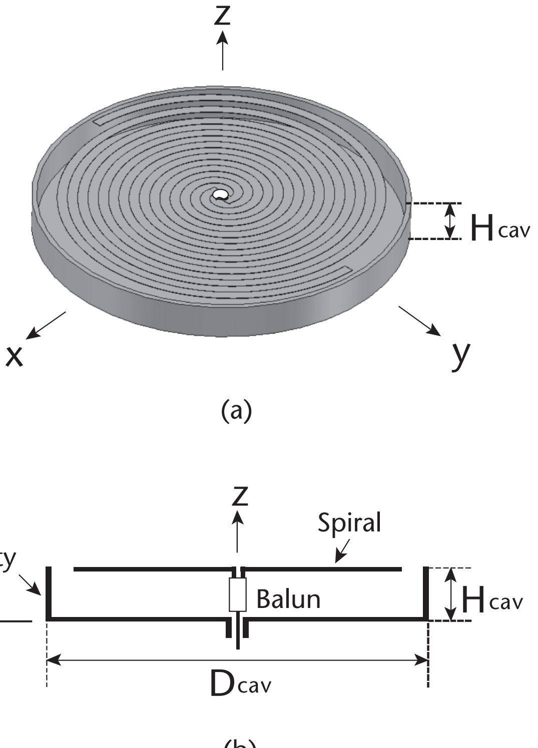

(b)

Figure 7.54 Cavity-backed spiral element feed.

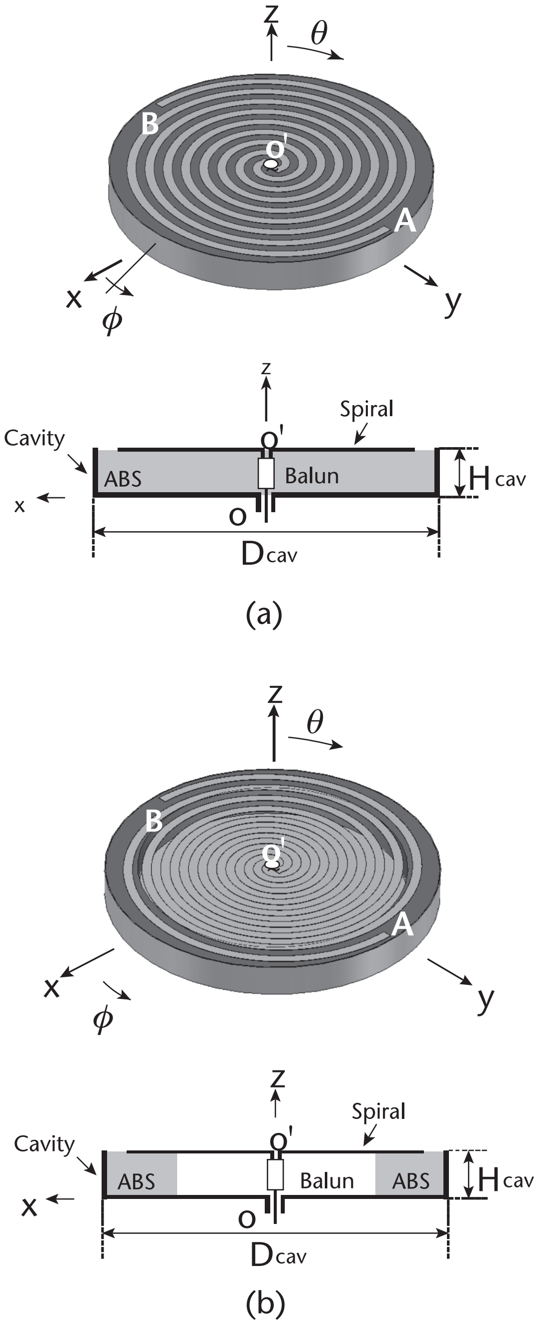
z
θ
B
o'
A
x
φ
y
z
Spiral
Cavity
o'
ABS
Balun
H cav
x
o
Dcav
(a)
z
θ
B
o'
A
x
φ
y
z
Spiral
Cavity
o'
ABS
Balun
ABS
H cav
x
o
Dcav
(b)

Figure 7.55 Cavity-backed spiral CP feed antenna. (a) Absorber fills the entire space behind the arms, and (b) ring-shaped absorbing strip fills only the space behind the outer region of the spiral arms.

Table 7.8 Spiral CP Feed Antenna Parameters

Symbol	*Value*
a	1.273 mm/rad
ϕ_{st}	0.5π rad
ϕ_{end}	6.5π rad
W	2 mm
D_{cav}	72 mm
H_{cav}	7 mm
Δt	0.1 mm

absorbing strip) [49, 50]. Note that the radiation efficiency for the spiral in Figure 7.55(a) does not exceed 50%; whereas the radiation efficiency for the spiral in Figure 7.55(b) can exceed 50%. However, the former is preferable to the latter in terms of the frequency response of the beamwidth; the former has a smaller variation in the beamwidth [52].

In the following paragraphs, our discussion focuses only on the spiral CP feed antenna shown in Figure 7.55(a). It is assumed that the thickness of the cavity conductor is negligibly small relative to the operating wavelength.

The radial distance from the translated origin o' (above the coordinate origin o) to a point on the center line of the spiral strip arm (the arm having width w) is defined using the Archimedean function $r = a\phi'$ for one arm and $r = a(\phi' + \pi)$ for the other arm, where a is the spiral growth rate (spiral constant) and ϕ' is the winding angle starting at ϕ_{st} and ending at ϕ_{end}. The absorber placed behind the arms is a nonconducting dielectric material: model ISFA with relative permeability $\mu_r = 1$, produced by TDK Corporation. Across the design frequency range of 3–9 GHz, the real part of relative permittivity of the ISFA varies from $\varepsilon' = 2.00(= 1.90 + 0.10)$ to $1.78(= 1.90 - 0.12)$ and the dielectric loss varies from $\tan\delta = 0.75(= 0.50 + 0.25)$ to $0.41(= 0.50 - 0.09)$. The configuration parameters used are summarized in Table 7.8.

Figure 7.56 shows the frequency response of the radiation pattern [52]. The radiation pattern is symmetric with respect to the antenna axis (z-axis) due to the structural symmetry with respect to the z-axis. As shown in Figure 7.57, the beam width varies smoothly with the change in frequency; the variation in the 3BW (beamwidth for a 3 dB reduced radiation field intensity criterion) is small across the octave from 4–8 GHz (approximately 15°).The radiation pattern has a desirably large F/B ratio across the same octave range, as shown in Figure 7.58, where the F/B ratio is larger than 16 dB.

Figure 7.59 shows more detail for the frequency response of the AR. The radiated wave is circularly polarized with an AR of less than 3 dB. For comparison, the AR when the absorber is removed is also presented. The absorber markedly mitigates the deterioration in the AR, particularly within the lower frequency band.

The absorber also contributes to mitigating the variation in the input impedance $Z_{in} = R_{in} + jX_{in}$. Figure 7.60 shows the input impedance with and without the absorber. The absorber leads to less variation in the input impedance, particularly within the lower frequency band, as is seen for the axial ratio. Note that the spiral

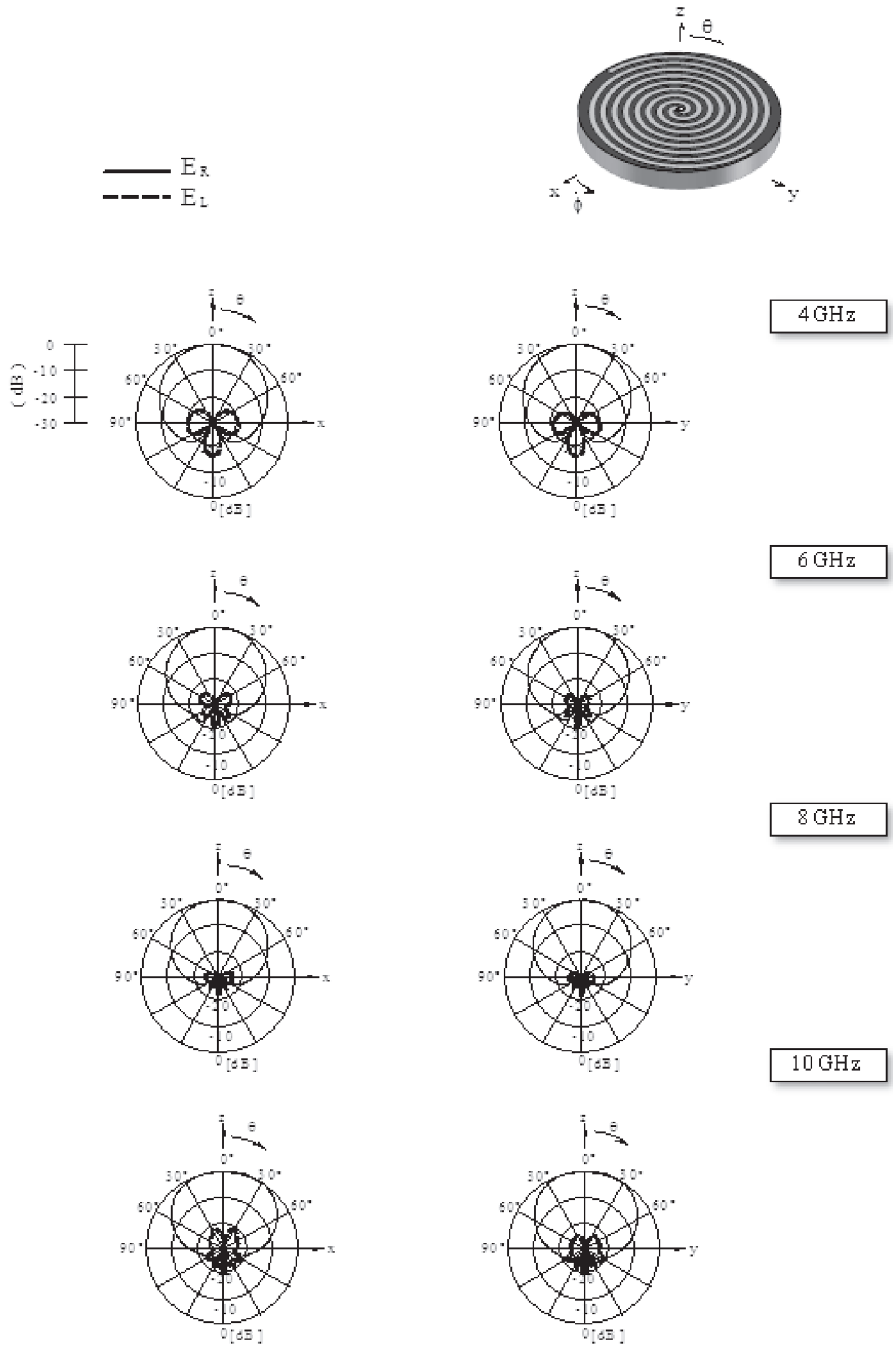

Figure 7.56 Frequency response of the radiation pattern, where an absorber fills the entire cavity.

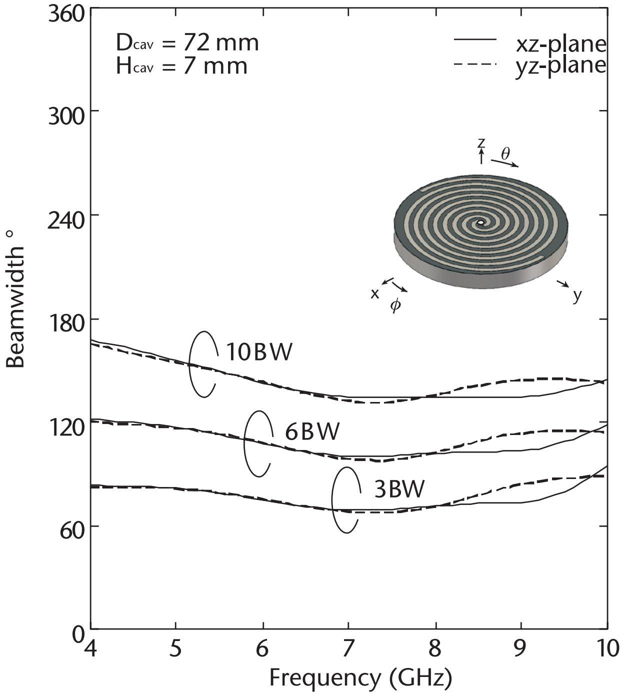

Figure 7.57 Frequency response of the beamwidth.

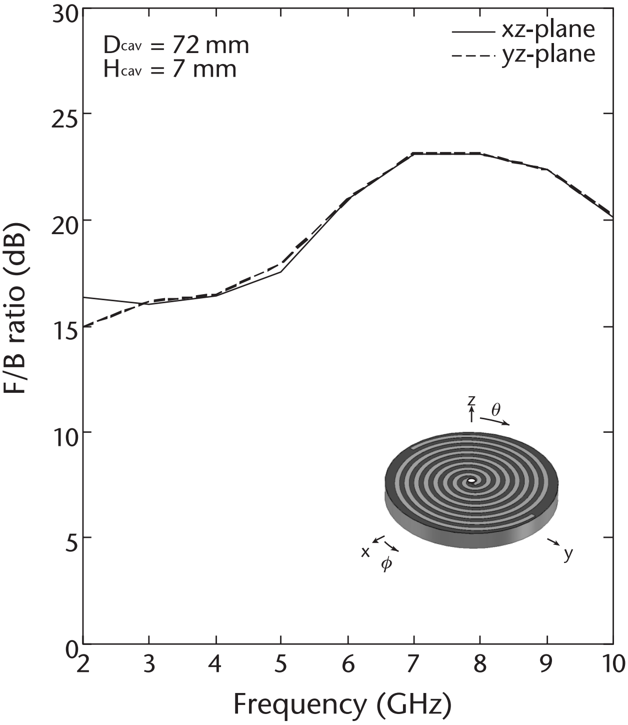

Figure 7.58 Frequency response of the F/B ratio.

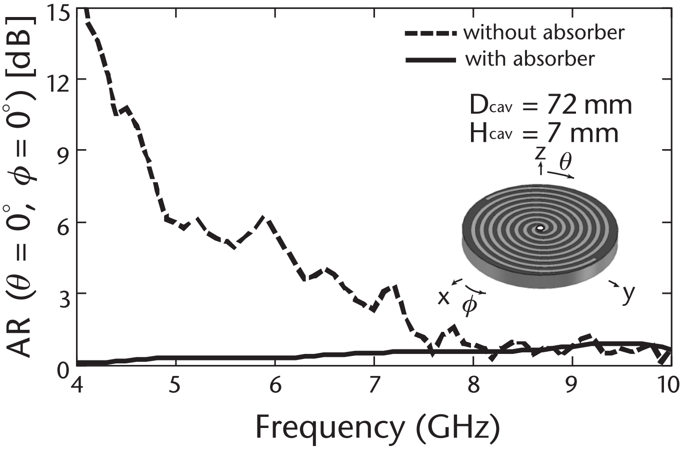

Figure 7.59 Frequency response of the axial ratio.

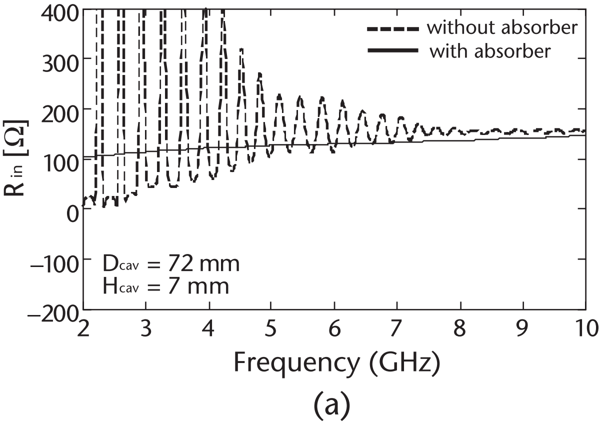

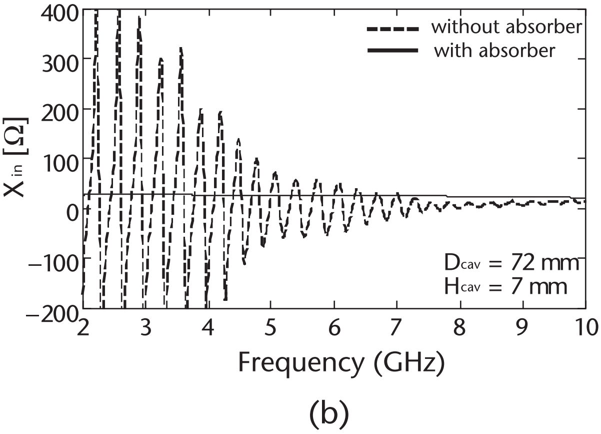

Figure 7.60 Frequency response of the input impedance.

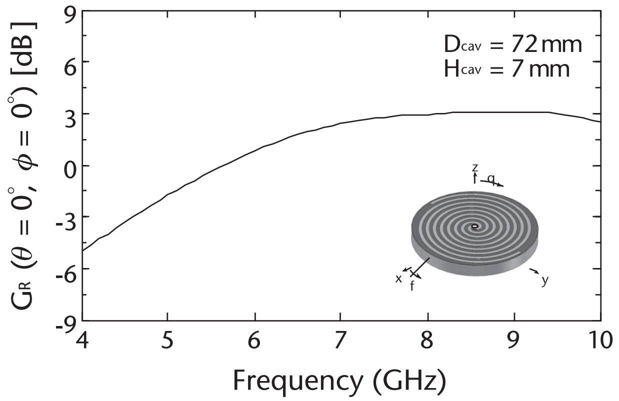

Figure 7.61 Frequency response of the gain.

feed antenna does not have a self-complementary input impedance (60π ohms) [53, 54] due to the presence of the cavity; it has a relatively constant value of less than 60π ohms. Also note that impedance matching to a 50-ohm coaxial feed line is achieved using a balun circuit [55–57].

Figure 7.61 shows the gain, where G_R denotes the available gain for the co-polarized component E_R relative to an isotropic CP antenna. Note that the G_R does not include the effect of input impedance mismatch but includes the effect of the absorber. The low gain at lower frequencies can be explained as follows. As the frequency decreases, absorption of undesirable incoming currents by the absorber increases; this means that the ratio of the undesirable power (not used for radiation) to the power input to the antenna increases, resulting in a low gain.

7.10 Curl CP Feed Antenna

The curl element shown in Figure 7.62 [58–62] is a simplified version of the spiral element described in Section 7.9. The arm is composed of only one arm (of wire radius ρ) and wound with a small number of turns. As with the spiral element, the radial distance from the translated origin o' (just above the coordinate origin o) to a point on the horizontal curl wire section is defined as $r = a\phi'$, where a and o' ($\phi_{st} \le \phi' \le \phi_{end}$) are called the curl constant and winding angle, respectively.

The circumference of the curl is defined by $C_{CURL} = 2\pi r_{\max} = \pi D_{CURL}$ and chosen to be more than one guided wavelength ($1\lambda_g$) but less than $2\lambda_g$ for CP radiation, where $r_{\max}$ is the maximum radial distance of the horizontal curl wire section. The antenna height (the height of the horizontal curl wire section above the GP) is denoted as h. The bottom end of the vertical straight wire section is excited from a coaxial feed line.

7.10.1 CP Radiation

Consider a situation where the current flows in one direction along the curl wire from the translated origin o' to the arm end (out-going current); there is no backward

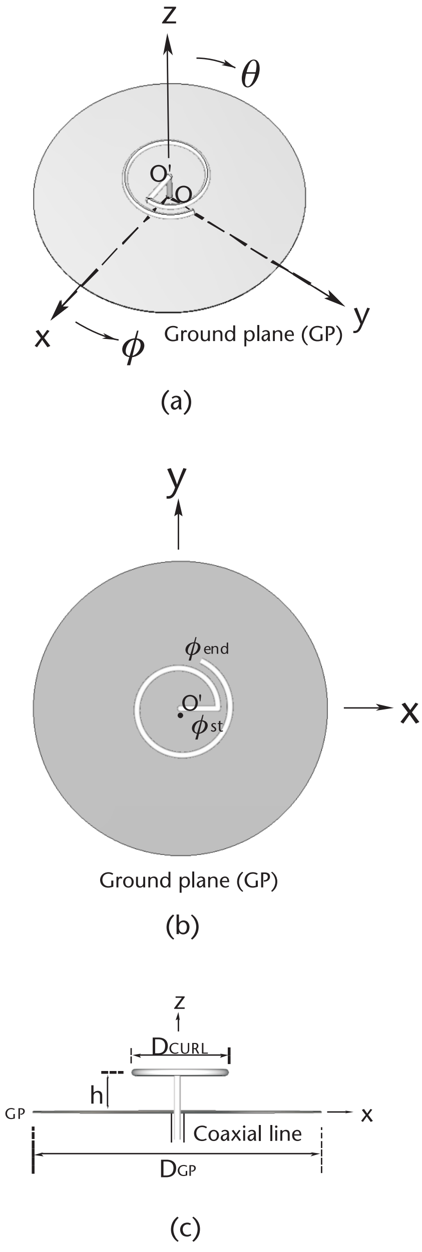
z
θ
O'
O
x
φ
Ground plane (GP)
y
(a)
y
φend
O'
φst
x
Ground plane (GP)
(b)
z
DCURL
h
GP
x
Coaxial line
DGP
(c)

Figure 7.62 Curl element. (a) Perspective view, (b) top view, and (c) side view.

(reflected) current flowing from the arm end to the translated origin o' (there is no incoming current). A point on the curl near a loop (illustrated by the dotted line in Figure 7.63(a)) is denoted as A, where the loop has a circumference of one guided wavelength ($1\lambda_g$), and the current at point A has an amplitude maximum and is expressed as a vector that is directed in the arm winding direction. This vector is called the vector current.

Another amplitude maximum is observed at a different point on the curl, near the loop of circumference $1\lambda_g$; the point is denoted as point B, as shown in Figure

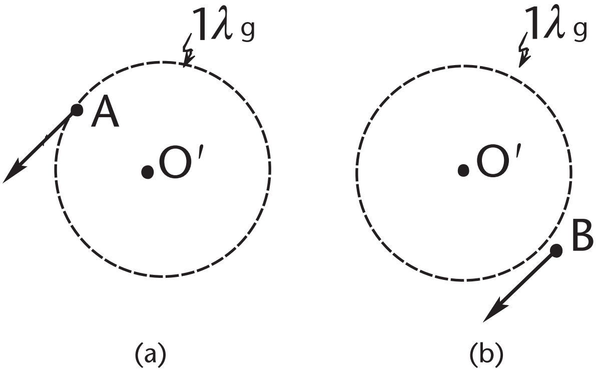

Figure 7.63 Loop region whose circumference is one guided wavelength. (a) Current at point *A*, and (b) current at point *B*.

7.63(b), where the distance between points *A* and *B* along the curl wire is one-half the guided wavelength (180° in terms of phase). When points *A* and *B* are very close to the loop, the points are nearly symmetric with respect to the translated origin *o*′. Then, the vector current at point *B* is directed in almost the same direction as the vector current at point *A*; these two vector currents are spatially in-phase. It follows that the resulting radiation field from the two vector currents becomes maximal in the *z*-direction, and the polarization coincides with the direction of the two vector currents. The in-phase vector currents rotate along the $1\lambda_g$-loop with time, and hence the radiation field rotates. Thus, a CP wave is generated in the *z*-direction. Based on this fact, the curl is categorized as an LPB-CP element.

7.10.2 Beamwidth

We investigate the antenna characteristics when a CP curl element is located in a conducting cavity of diameter D_{cav}, height H_{cav}, and thickness Δt (Figure 7.64). The

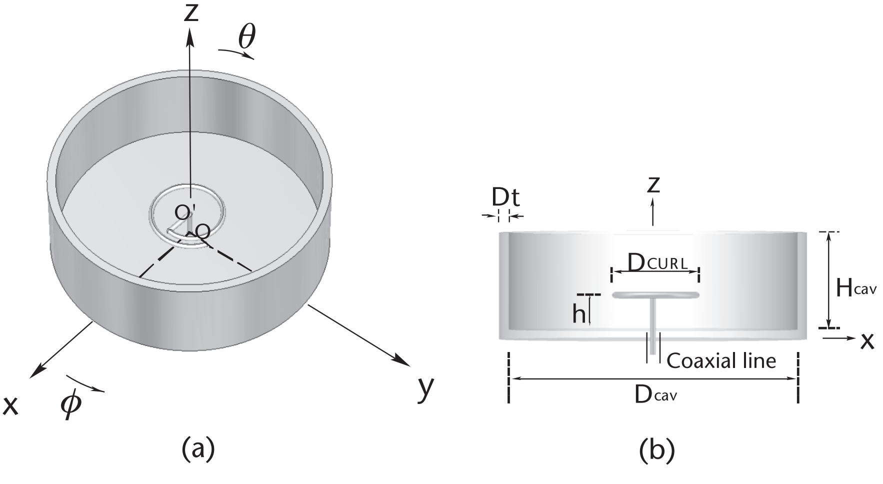

Figure 7.64 Curl element within a conducting cavity. (a) Perspective view, and (b) side view.

Table 7.9 Curl Element Parameters

Symbol	*Value*
h	3.55 mm ≈ $0.144\lambda_{12.2}$
a	0.18 mm/rad ≈ $0.0073\lambda_{12.2}$/rad
ϕ_{st}	6π rad
ϕ_{end}	26.3 rad
C_{CURL}	29.74 mm ≈ $1.210\lambda_{12.2}$
ρ	0.3 mm ≈ $0.012\lambda_{12.2}$
Δt	1 mm ≈ $0.04\lambda_{12.2}$

$^*\lambda_{12.2} \approx 24.59$ mm

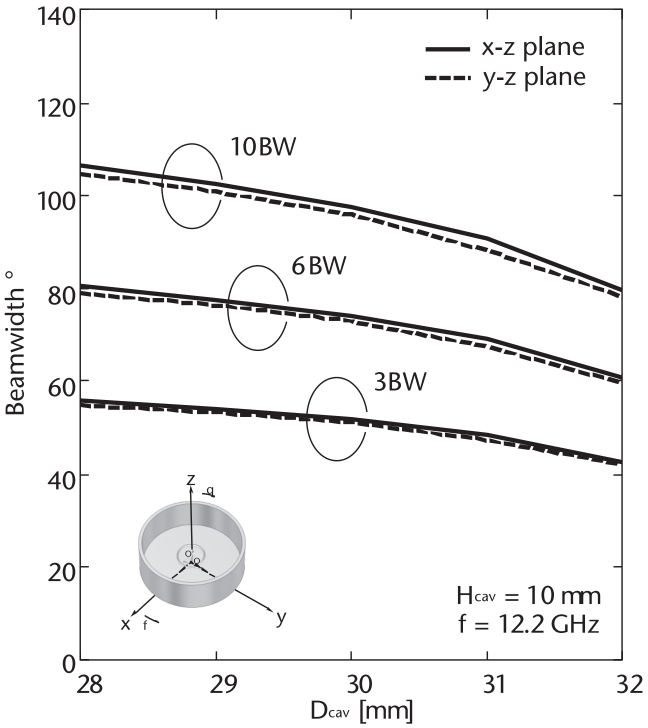

Figure 7.65 Beamwidth (BW) as a function of the cavity diameter D_{cav}, where the cavity height is held at H_{cav} = 10 mm and a frequency of 12.2 GHz is used.

parameters used for this investigation are shown in Table 7.9, where $\lambda_{12.2}$(= 24.59 mm) is the free-space wavelength at a frequency of 12.2 GHz. The cavity diameter D_{cav} and height H_{cav} are varied subject to the objectives of the analysis. Note that the guided wavelength λ_g is found to be always very close to the operating free-space wavelength $\lambda(\lambda_g \approx \lambda)$ and the curl circumference C_{CURL} satisfies the aforementioned CP condition at 12.2 GHz.

Figure 7.65 shows the beamwidth (BW) as a function of the cavity diameter D_{cav}, where the cavity height is held at H_{cav} = 10 mm and a frequency of 12.2 GHz is used

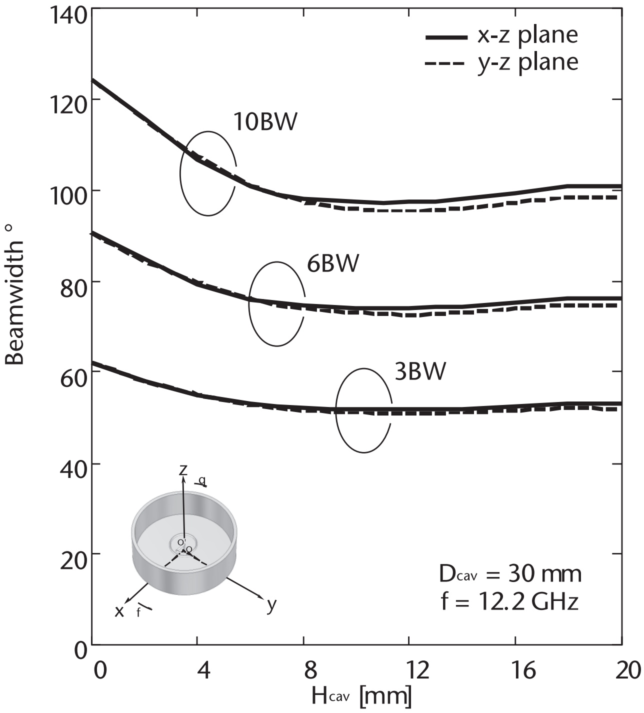

Figure 7.66 Beamwidth (BW) as a function of cavity height H_{cav}, where the cavity diameter is held at D_{cav} = 30 mm and a frequency of 12.2 GHz is used.

[62]. As in the end-fire helical feed antenna with a cavity, the beamwidth decreases with increasing cavity diameter D_{cav}. When D_{cav} is increased from D_{cav} = 28–32 mm, the decrease in the beam width for a 10 dB reduced field intensity criterion (10BW) is more than 20°.

A similar investigation is performed by changing the variable from the cavity diameter D_{cav} to the cavity height H_{cav}. Figure 7.66 shows the beamwidth as a function of the cavity height H_{cav}, where the cavity diameter D_{cav} is held at D_{cav} = 30 mm and a frequency of 12.2 GHz is used. Variation in the beamwidth is found to be relatively small at cavity heights of greater than 8 mm (0.33 wavelength).

7.10.3 Frequency Response

This section presents the frequency response of a representative curl feed antenna, where the configuration parameters shown in Table 7.9 are used. The cavity diameter and height are held at D_{cav} = 30 mm and H_{cav} = 10 mm, respectively.

Figure 7.67 shows the frequency response of the radiation pattern. The radiation around the z-axis is circularly polarized, with a small cross-polarized component. The radiation pattern of E_R is almost symmetric with respect to the z-axis, and the radiation in the negative z-direction is negligibly small. These findings are shown in greater detail in Figures 7.68 and 7.70.

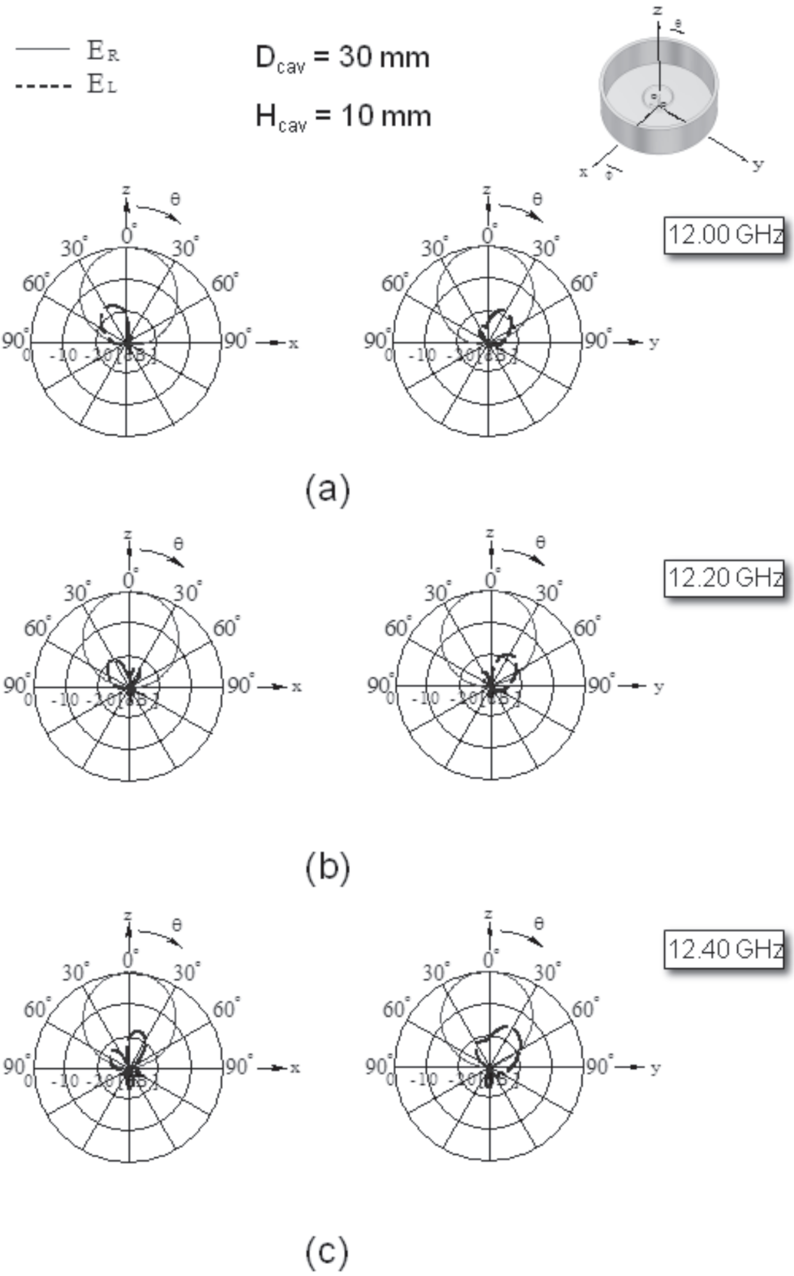

(a)

(b)

(c)

Figure 7.67 Radiation pattern as a function of frequency, with D_{cav} = 30 mm = $1.22\lambda_{12.2}$ and H_{cav} = 10 mm = $0.41\lambda_{12.2}$. Other parameters are shown in Table 7.9.

As seen from Figure 7.68, the frequency bandwidth for a 3 dB AR criterion is approximately 7%. Across this AR bandwidth, the difference in the beam width for a 10 dB reduced field intensity criterion (10BW) is small (less than 14°), as shown in Figure 7.69. Figure 7.70 reveals that the F/B ratio is more than 20 dB within the same axial ratio bandwidth.

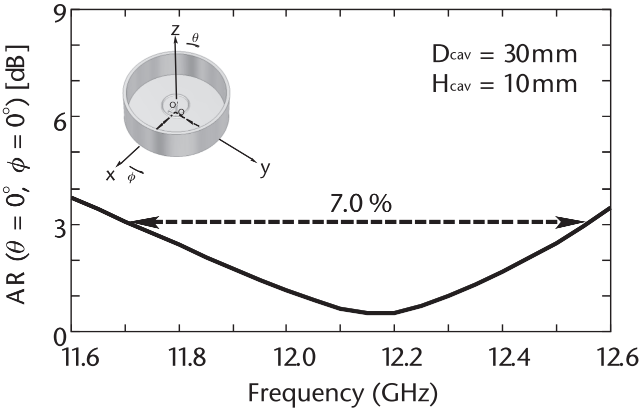

Figure 7.68 Axial ratio as a function of frequency, with D_{cav} = 30 mm = 1.22$\lambda_{12.2}$ and H_{cav} = 10 mm = 0.41$\lambda_{12.2}$. Other parameters are shown in Table 7.9.

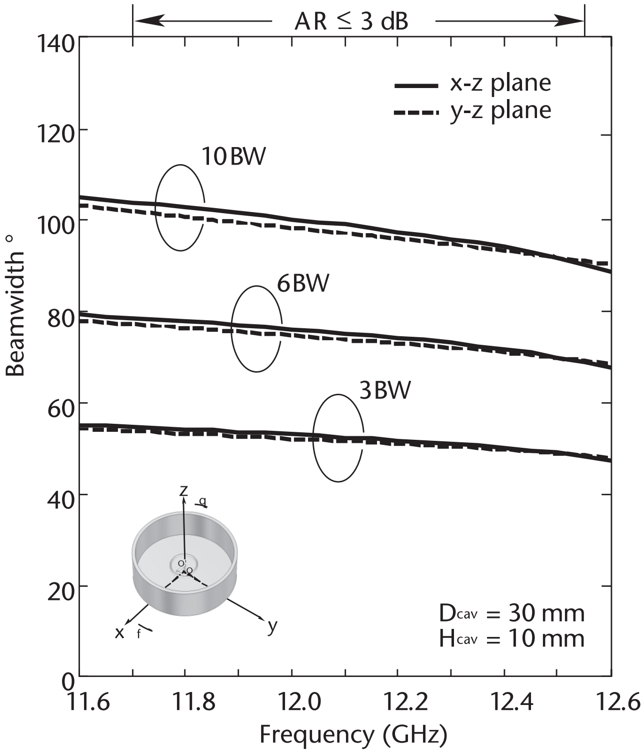

Figure 7.69 Beam width as a function of frequency, with D_{cav} = 30 mm = 1.22$\lambda_{12.2}$ and H_{cav} = 10 mm = 0.41$\lambda_{12.2}$. Other parameters are shown in Table 7.9.

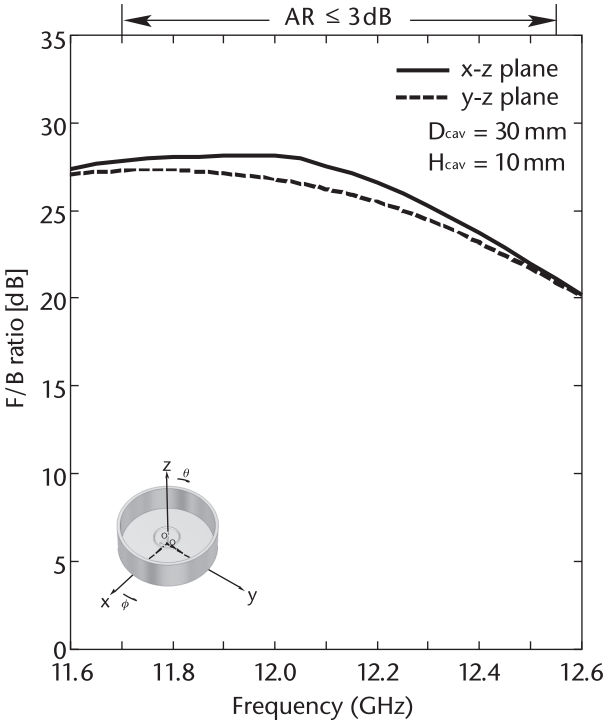

Figure 7.70 F/B ratio as a function of frequency, with D_{cav} = 30 mm = 1.22$\lambda_{12.2}$ and H_{cav} = 10 mm = 0.41$\lambda_{12.2}$. Other parameters are shown in Table 7.9.

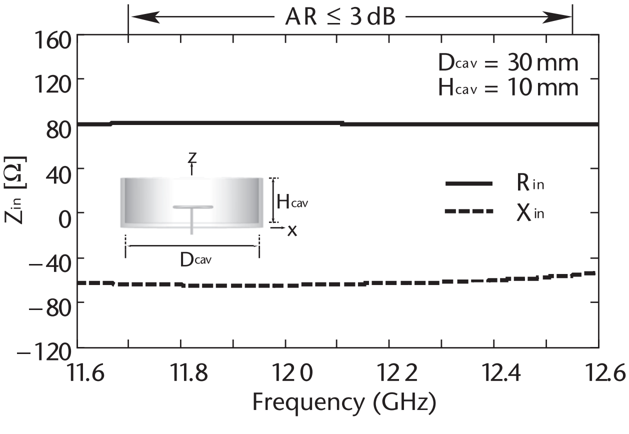

Figure 7.71 Input impedance as a function of frequency, with D_{cav} = 30 mm = 1.22$\lambda_{12.2}$ and H_{cav} = 10 mm = 0.41$\lambda_{12.2}$. Other parameters are shown in Table 7.9.

Analysis reveals that the current along the arm exhibits a nonresonant characteristic, that is, the out-going current is dominant compared to the incoming current, forming a traveling wave current distribution with decay. This leads to a wideband characteristic for the input impedance. Figure 7.71 confirms this conclusion. The gain also shows a wideband characteristic due to those of the input impedance and radiation pattern. Figure 7.72 shows the available gain G_R for the co-polarized radiation field E_R.

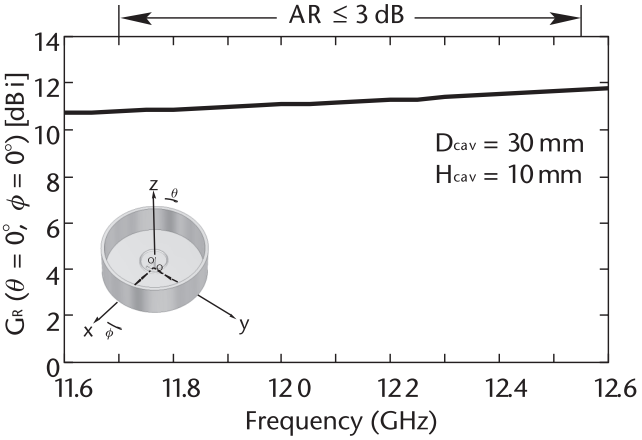

Figure 7.72 Gain G_R as a function of frequency, with D_{cav} = 30 mm = 1.22$\lambda_{12.2}$ and H_{cav} = 10 mm = 0.41$\lambda_{12.2}$. Other parameters are shown in Table 7.9.

Acknowledgments

I cordially thank V. Shkawrytko and H. Mimaki for their assistance in the preparation of this chapter. Also, I thank the following graduate students for their contributions to arranging the data for each section: K. Suzuki, Y. Murata, and T. Arao (Sections 7.1–7.4), K. Kuriyama and N. Mizobe (Section 7.5), K. Monma and R. Takebe (Section 7.7), K. Iyoku (Section 7.8), M. Oyama (Section 7.9), and K. Kawabe (Section 7.10).

References

[1] Collin, R. E., and F. J. Zucker, *Antenna theory, Part 1*, New York: McGraw Hill, 1969, chapter 4.

[2] Nakano, H., "Receiving antennas." In *Antennas and Propagation, Encyclopedia of Electrical and Electronics Engineering*, New York: John Wiley, 1999.

[3] Haneishi, M., S. Saito, and Y. Seshimo, et al., "Beamtilted Circularly Polarized Planar Antenna for DBS-reception," *Institute of Image Information and Television Engineers Technical Report*, Vol. 10, No. 44, RE87–1, Jan. 1987, pp. 1–6.

[4] Murata, T., T. Nomoto, and K. Ohmaru, et al., "A Flat Panel Antenna with Two Layer Structure for DBS Reception," *Spring National Convention Record, Institute of Electronics, Information and Communication Engineers (IEICE)*, B–78, Tokyo, March 1988.

[5] Urasaki, S., N. Miyahara, and T. Katagi, "An Offset Parabola Antenna with Dual Mode Horn Feed for Direct-broadcasting Satellite Receiver," *National Convention Record, Institute of Electronics and Communication Engineers (IECE) of Japan*, 765, Tokyo, March 1984.

[6] Nagaoka, S., Y. Nonaka, and M.Tateshita, et al., "High Efficiency Parabolic Reflector Antenna for DBS," *National Convention Record, Institute of Electronics and Communication Engineers (IECE) of Japan*, S6–1, Kanagawa, Japan, March 1985.

[7] Nakano, H., J. Yamauchi, and H. Mimaki, "Backfire Radiation from a Monofilar Helix with a Small Ground Plane," *IEEE Transactions on Antennas and Propagation*, Vol. 36, No. 10, October 1988, pp. 1359–1364.

[8] Harrington, R. F., *Field Computation by Moment Methods*, New York: Macmillan, 1968.

[9] Pizer, R., and J. Moore, "Scattering by Wire Structures." In *Moment Methods in Electromagnetics—Techniques and Applications*, J. Moore and R. Pizer (eds.), Hertfordshire, England: Research Studies Press, 1984, Chapter 6.

[10] Nakano, H., "Integral Equations for Antenna Analysis." In *Analysis Methods for Electromagnetic Wave Problems, Volume II*, E. Yamashita (ed.), Boston: Artech House, 1996, chapter 3.

[11] Yee, K. S., "Numerical Solution of Initial Boundary Value Problems Involving Maxwell's Equations in Isotropic Media," *IEEE Transactions on Antennas and Propagation*, Vol. 14, No. 3, May 1966, pp. 302–307.

[12] Taflove, A., *Computational Electrodynamics: The Finite-Difference Time-Domain Method*, Norwood, MA: Artech House, 1995.

[13] Mur, G., "Absorbing Boundary Conditions for the Finite-difference Approximation of the Time-domain Electromagnetic-field Equations," *IEEE Trans. Electromagnetic Compatibility*, Vol. EMC–23, No. 4, 1981, pp. 377–382.

[14] Higdon, R. L., "Absorbing Boundary Conditions for Difference Approximations to the Multi-dimensional Wave Equation," *Mathematics of Computation*, Vol. 47, No. 176, 1986, pp. 437–459.

[15] Liao, Z. P., H. L. Wong, and B. P. Yang, et al., "A Transmitting Boundary for Transient Wave Analysis," *Science Sinica (Series A)*, Vol. 27, No. 10, 1984, pp. 1063–1076.

[16] Berenger, J.-P., "A Perfectly Matched Layer for the Absorption of Electromagnetic Waves," *Journal of Computational Physics*, Vol. 114, No. 1, 1994, pp. 185–200.

[17] Harrington, R. F., *Time-Harmonic Electromagnetic Fields*, New York: McGraw-Hill, 1961, pp. 106–110.

[18] Balanis, C. A., *Antenna Theory: Analysis and Design* (2nd ed.), New York: Wiley, 1982, chapter 12.

[19] Offutt, W. B., and L. K. DeSize, "Methods of Polarization Synthesis." In *Antenna Engineering Handbook,* (3rd ed.), R. C. Johnson (ed.), New York: McGraw-Hill, 1993, chapter 23.

[20] Ochiai, N., and T. Mozai, *Theory and Practice of Radar Technologies*, Kaibundo, Tokyo, Japan, 1959.

[21] Sharma, P., and K. Gupta, "Analysis and Optimized Design of Single Feed Circularly Polarized Microstrip Antennas," *IEEE Transactions on Antennas and Propagation*, Vol. 31, No. 6, June 1983, pp. 949–955.

[22] Haneishi, M., S. Yoshida, and N. Oka, "Back-feed Type Circularly-polarized Microstrip Disk Antenna by One-point Feed," *Journal of Institute of Electronics and Communication Engineers (IECE),* Vol. J63–B, No. 6, June 1980, pp. 559–565.

[23] Nakano, H., K. Fujimori, and J. Yamauchi, "A Low-profile Conical Beam Loop Antenna with an Electromagnetically Coupled Feed System," *IEEE Transactions on Antennas and Propagation*, Vol. 48, No. 12, December 2000, pp. 1864–1866.

[24] Hirose, K., S. Okazaki, and H. Nakano, "Double Loop Antenna for a Circularly Polarized Beam," *Journal of Institute of Electronics, Information and Communication Engineers (IEICE)*, Vol. J85–B, No.11, November 2002, pp. 1934–1943.

[25] Suzuki, K., Y. Murata, and T. Arao, et al., "One-point Excitation CP Patch," *Nakano Laboratory Report*, No. 2012–1, Hosei University, 2012.

[26] Kraus, J., *Antennas* (2nd ed.), New York: McGraw-Hill, 1988, Chapter 7.

[27] Nakano, H., *Helical and Spiral Antennas*, Hertfordshire, England: Research Studies Press, 1987.

[28] Nakano, H. H. Takeda, and T. Honma, et al., "Extremely Low-profile Helix Radiating a Circularly Polarized Wave," *IEEE Transactions on Antennas and Propagation*, Vol. 39, No. 6, June 1991, pp. 754–757.

[29] Kuriyam, K., N. Mizobe, and H. Nakano, "End-fire Helical CP Feed Antenna," *Nakano Laboratory Report*, No. 2012–2, Hosei University, 2012.

[30] Nakano, H., N. Mizobe, and K. Kuriyama, et al., "Low-profile Helical Antenna with a Cavity," *Proc. IEEE International Conference on Wireless Information Technology and Systems*, Maui, HI, November 2012.

[31] Carver, K. R., "A Cavity-fed Concentric Ring Phased Array of Helices for Use in Radio Astronomy," Ph.D. dissertation, Ohio State University, 1967.

[32] Nakano, H., H. Takeda, and Y. Kitamura, et al., "Low-profile Helical Array Antenna Fed from a Radial Waveguide," *IEEE Transactions on Antennas and Propagation*, Vol. 40, No. 3, March 1992, pp. 279–284.

[33] Nakano, H., N. Asaka, and J. Yamauchi, "Short Helical Antenna Array Fed from a Waveguide," *IEEE Transactions on Antennas and Propagation*, Vol. AP–32, No. 8, August 1984, pp. 836–840.

[34] Marcuvitz, M., *Waveguide Handbook*, New York: McGraw-Hill, 1951.

[35] Mimaki, H., H. Nakano, and T. Kasuga, "Very Compact S and X Bands Coaxial Helical Array Feeds for VLBI Antenna," *Proc. Asia-Pacific Radio Science Conference*, *AP–RASCO'01*, Tokyo, August 2001, p. 240.

[36] Kasuga, T., H. Mimaki, and H. Nakano, "Compact Helical Array Antenna for VLBI Co-axial S-X Band Feeds," *Proc. XXVIIth General Assembly of Int. URSI*, Maastricht, Germany, August 2002, pp. 2.1–2.4.

[37] Wong, J. L., and H. E. King, "Broadband Quasi-taper Helical Antenna," *IEEE Transactions on Antennas and Propagation*, Vol. AP–27, No.1, January 1979, pp. 72–78.

[38] Lipman, D., and Y. Harlev, "A Low Sidelobes Helix Radiator for a High Power Tracking Antenna System," *Proc. IEEE Antennas and Propagation Society International Symposium*, Vol. 3, 1989, pp. 1461–1464.

[39] Mimaki, H., and H. Nakano, "A Low-profile Conical Helix Antenna," *Proc. 12th International Symposium on Antenna Technology and Applied Electronics (ANTEM)*, Montréal, Canada, July 2006, pp. 429–432.

[40] Mimaki, H., and H. Nakano, "A Conical Helix Antenna Array," *Proc. Institute of Electronics, Information and Communication Engineers (IEICE) General Conference*, B–1–105, Kitakyushu, Japan, March 2008.

[41] Mimaki, H., and H. Nakano, "Experimental Study of Conical Helix Array Antenna," *Proc. Institute of Electronics, Information and Communication Engineers (IEICE) Society Conference*, B–1–114, Niigata, Japan, September 2009.

[42] Monma, K., R. Takebe, and H. Mimaki, et al., "Conical Helical CP Feed Antenna," *Nakano Laboratory Report*, No. 2012–3, Hosei University, 2012.

[43] Hashimoto, Y., N. Misawa, and K. Ishino, et al., "DBS Receiving Parabolic Antenna Using a Backfire Helical," *Institute of Electronics and Communication Engineers (IECE) of Japan, National Conference Record*, *Optical and Radio Wave Electronics*, S3–7, 1986.

[44] Iyoku, K., H. Mimaki, and H. Nakano, "Back-fire-mode Helical CP Feed Antenna," *Nakano Laboratory Report*, No. 2012–4, Hosei University, 2012.

[45] Sander, S., and D. Cheng, "Phase Center of Helical Beam Antennas," *IRE International Convention Record*, Vol. 6, Part 1, 1958, pp. 152–157.

[46] Kaiser, J. A., "The Archimedean Two-wire Spiral Antenna," *IRE Transactions on Antennas and Propagation*, Vol. AP–8, No. 3, May 1960, pp. 312–323.

[47] Nakano, H., K. Nogami, and S. Arai, et al., "A Spiral Antenna Backed by a Conducting Plane Reflector," *IEEE Transactions on Antennas and Propagation*, Vol. AP–34, No. 6, June 1986, pp. 791–796.

[48] Wang, J. J. H., and V. K. Tripp, "Design of Multioctave Spiral-mode Microstrip Antennas," *IEEE Transactions on Antennas and Propagation*, Vol. 39, No. 3, March 1991, pp. 332–335.

[49] Nakano, H., K. Kikkawa, and Y. Iitsuka, et al., "Equiangular Spiral Antenna Backed by a Shallow Cavity with Absorbing Strips," *IEEE Transactions on Antennas and Propagation*, Vol. 56, No. 8, August 2008, pp. 2742–2747.

[50] Nakano H., S. Sasaki, and H. Oyanagi, et al., "Cavity-backed Archimedean Spiral Antenna with Strip Absorber," *IET Proc. of Microwaves, Antennas and Propagation*, Vol. 2, No. 7, October 2008, pp. 725–730.

[51] Nakano, H., H. Mimaki, and J. Yamauchi, et al., "A Low Profile Archimedean Spiral Antenna," *Proc. IEEE Antennas and Propagation Society International Symposium*, Vol. 1, 1993, pp. 450–453.

[52] Oyama, M., H. Mimaki, and H. Nakano, "Spiral CP Feed Antenna," *Nakano Laboratory Report*, No. 2012–5, Hosei University, 2012.

[53] Mushiake, Y., *Self-Complementary Antennas*, UK: Springer, 1996.

[54] Mushiake, Y., "Self-complementary Antennas," *IEEE Antennas and Propagation Magazine*, Vol. 34, No. 6, pp. 23–29, December 1992.

[55] Dyson, J., "Equiangular Spiral Antenna," *IRE Transactions on Antennas and Propagation*, Vol. 7, No. 2, April 1959, pp. 181–187.

[56] Bawer, R., and J. J. Wolfe, "A Printed Circuit Balun for Use with Spiral Antennas," *IEEE Transactions on Microwave Theory and Techniques*, Vol. 8, No. 3, May 1960, pp. 319–325.

[57] Tu, W.-H., and K. Chang, "Wide-band Microstrip-to-coplanar Stripline/slotline Transitions," *IEEE Transactions on Microwave Theory and Techniques*, Vol. 54, No. 3, March 2006, pp. 1084–1089.

[58] Nakano, H., S. Okuzawa, and K. Ohishi, et al., "A Curl Antenna," *IEEE Transactions on Antennas and Propagation*, Vol. 41, No. 11, November 1993, pp. 1570–1575.

[59] Nakano, H., M. Yamazaki, and J. Yamauchi, "Electromagnetically Coupled Curl Antennas," *Electronics Letters*, Vol. 33, No. 12, June 1997, pp. 1003–1004.

[60] Nakano, H., and H. Mimaki, "Axial Ratio of a Curl Antenna," *IEE Proc. on Microwaves Antennas and Propagation*, Vol. 144, No. 6, December 1997, pp. 488–490.

[61] Shafai, L., "Some Array Applications of the Curl Antenna," *Electromagnetics*, Vol. 20, No. 4, July 2000, pp. 271–293.

[62] Kawabe, H., H. Mimaki, and H. Nakano, "Curl CP Feed Antenna," *Nakano Laboratory Report*, No. 2012–6, Hosei University, 2012.

CHAPTER 8

Generalized Asymmetric Reflector Antenna Feeds for Polarization Control and Adaptive Virtual Array Design

L. Shafai, University of Manitoba
Z. A. Pour, University of Manitoba
S. K. Sharma, San Diego State University

8.1 Introduction

Historically, reflector antennas have been used for generating high gains. In this respect, they are unique since they offer many advantages over other high-gain antennas in geometrical and design simplicity, durability, and cost. The latter two are especially important as they influence the total cost (i.e. the costs of installation, operation, and maintenance). In addition, with increasing size, the cost per dB gain of reflector antennas improves in comparison to other antennas. As a result, practically all high-gain antennas in radio astronomy and deep space communications, where very high gains are required, are of reflector types. However, generating high gain is only one of the functions that reflector antennas can perform. As a focusing device, they can perform other functions as well. To understand them, one must note that a reflector antenna does not function alone and in isolation; it functions in conjunction with its feed or another reflector. With a single reflector, such as in prime focus reflectors, the responsibility for the reflector function transfers to its feed, which illuminates the reflector in its transmission mode or receives the signal in its reception mode. Therefore, the reflector feed is the key design feature for controlling the reflector function. In this chapter, we discuss two such functions, the polarization control and the formation of adaptive virtual arrays using a parabolic reflector.

The problem of investigating reflector antennas is simplified significantly by using the aperture antenna concepts, which can relate its aperture fields to the radiated far field. Further simplification is also possible by relating the reflector aperture field to its focal plane field [1, 2]. While the former helps in determining the radiation field of the reflector, the latter helps in designing the feed and thus the reflector antenna system. Using the matched feed concept [3], the aperture field of the feed must match the desired focal plane field. In this section, we use this concept to describe the reflector functions and the type of feeds that can help in performing such functions.

Mathematically, the focal plane field of the reflector extends to infinity. However, the focusing property of the reflector confines most of the energy to the vicinity of its focal point, where the feed will be located. From the practical point of view, the feed must also be small to reduce the reflector aperture blockage. We therefore need to know the focal plane field in a limited extent about the focal point. This simplifies the problem significantly, since in this limited range we can express the focal plane field in terms of a simple orthogonal set of appropriate functions. For convenience, we select the Fourier series and write the focal plane fields as

$$A_i = \sum_{n=0}^{\infty} a_{ni}(\rho) \begin{pmatrix} \cos\ n\phi \\ \sin\ n\phi \end{pmatrix} \tag{8.1}$$

where **A** represents a field vector, **E** or **H**, and the subscript i refers to one of its rectangular components x or y, and $a_{ni}\,(\rho)$ is the radial dependent part of the focal plane field. To transfer this set of functions to practical feeds we note that the most common reflector feeds are based on waveguide feed horn antennas. Thus, the aperture field of feed can be expressed in terms of the TE and TM waveguide modes, leading to

$$a_n(\rho) \begin{pmatrix} \cos\ n\phi \\ \sin\ n\phi \end{pmatrix} = \mathrm{TE}_{mn} \text{ or } \mathrm{TM}_{mn} \text{ Circular waveguide modes} \tag{8.2}$$

where

$$\mathrm{TE}_{mn}(\rho,\theta) = f_{mn}(\rho)\cos n\phi \tag{8.3}$$

and

$$\mathrm{TM}_{mn}(\rho,\theta) = g_{mn}(\rho)\sin n\phi \tag{8.4}$$

For small focal region, the first term in the series dominates, $m = 1$, and thus the focal plane field can be written as

$$A \cong \sum_{n=1}^{N} (\mathrm{TE}_{1n}, \mathrm{TM}_{1n}) \tag{8.5}$$

which means the azimuthal modes dominate the field in small focal region and thus the feed design. As practical examples, we consider the first four possibilities, and find the focal region field as:

Example (a): We select the first waveguide mode, which is the TE$_{11}$ mode and get

$$A = \mathrm{TE}_{11} = f_{11}(\rho)\ \cos\phi \tag{8.6}$$

This example is the case of conventional high-gain reflector antennas, where small feeds for prime focus reflectors are designed using smooth wall waveguides, fed by the TE$_{11}$ mode [3].

Example (b): We select the first two TE modes and get

$$A = \mathrm{TE}_{11} + \alpha\,\mathrm{TE}_{21} = f_{11}(\rho)\ \cos\phi + \alpha\ f_{21}(\rho)\ \cos 2\phi \tag{8.7}$$

where α is a complex constant representing the mode coefficient. The feed aperture is therefore dominated by two waveguide modes, which can generate a variety of radiation patterns for the feed by controlling the mode coefficient α. Later in this chapter we will show that for small values of this mode coefficient α and a phase quadrature between the two modes, as 90°, the feed cross polarization can be matched to the cross polarization of offset reflectors, thereby causing its reduction and resulting in a matched feed for offset reflectors. For large values of α, the feed will transfer the reflector to an adaptive virtual array, whose excitation and inter-element spacing can be controlled by the amplitude and phase of the mode coefficient α.

Example (c): We select one TE and one TM mode, and get

$$A = \mathrm{TE}_{11} + \alpha\ \mathrm{TM}_{01} = f_{11}(\rho)\cos\phi + \alpha\ g_{01}(\rho) \tag{8.8}$$

This case too transforms the reflector into an adaptive virtual array, whose properties will be studied later in this chapter.

Example (d): We select the first three waveguide modes and get

$$A = \mathrm{TE}_{11} + \alpha\ \mathrm{TE}_{21} + \beta\ \mathrm{TM}_{01} = f_{11}(\rho)\cos\phi + \alpha\ f_{21}(\rho)\cos 2\phi + \beta\ g_{01}(\rho) \tag{8.9}$$

which is a combination of two TE and one TM modes, with a new mode coefficient β. This case is similar to cases (b) and (c), except that having one additional mode allows better control of the feed field and a better match with the focal plane field. Thus, in either case, of cross polarization reduction of offset reflectors or in formation of the virtual arrays, one will have a better reflector performance in gain, sidelobe levels, and cross polarization.

In designing such reflector base antennas, the feed configuration is not limited to horn types. Any multimode antenna having a Fourier type mode description as (8.1) can be used to design the feed. For instance, selecting a circular microstrip patch antenna as the candidate we will have

$$a_n(\rho)\begin{pmatrix}\cos & n\phi\\ \sin & n\phi\end{pmatrix} = \mathrm{TM}_{mn}\ \text{circular microstrip patch modes} \tag{8.10}$$

with

$$\mathrm{TM}_{mn}(\rho,\theta) = f_{mn}(\rho)\ \begin{pmatrix}\cos & n\phi\\ \sin & n\phi\end{pmatrix} \tag{8.11}$$

Again, for small feeds with $m = 1$ and small substrate heights, one can design the feed as appropriate summations of the TM modes as

$$A \cong \sum_{n=1}^{N} (\mathrm{TM}_{1n}) \tag{8.12}$$

Possible feed designs can be one of the following

Microstrip feed (a), with only the first TM mode

$$A = \mathrm{TM}_{11} \tag{8.13}$$

Microstrip feed (b), with the first two TM modes as

$$A = \mathrm{TM}_{11} + \alpha \mathrm{TM}_{21} \tag{8.14}$$

Microstrip feed (c), with two asymmetric and symmetric modes as

$$A = \mathrm{TM}_{11} + \alpha \mathrm{TM}_{02} \tag{8.15}$$

Microstrip feed (d), with the first three TM modes as

$$A = \mathrm{TM}_{11} + \alpha \mathrm{TM}_{21} + \beta\, \mathrm{TM}_{02} \tag{8.16}$$

Obviously, this is a more restrictive case, since only TM modes can be used, which will result in lesser control over the reflector performance. Some applications of these feeds are discussed in the following sections of this chapter. Additional discussion and their performance on reflector antennas are in Chapter 4 of Volume 1 of this series.

8.2 Applications of Asymmetric Feeds

Symmetric reflector antennas, such as a prime focus reflector, generally have a low cross polarization, the level of which decreases with the reflector size. The overall cross polarization of the reflector feed system is therefore controlled by the feed, especially in prime focus reflectors where the feed aperture is small and the cross polarization cancellation is difficult to achieve. Design of a feed with a low cross polarization becomes the main challenge. The situation is different in offset reflector antennas, where the aperture asymmetry causes an inherent cross polarization by the reflector itself, the level of which is dependent on the reflector offset angle [4, 5]. However, in all high-gain applications of reflector antennas, low cross polarizations are required to reduce or eliminate the interference. Examples are the reflector antennas in frequency-reuse applications, where the same frequency band may be used in two orthogonal channels. Or beam squints in circularly polarized antennas, which cause misalignment of the antenna, operating simultaneously at both right- and left-handed circular polarizations. The next section shows that by using the asymmetric feeds of the previous section, the cross polarization of offset reflectors can be reduced significantly to make them competitive with symmetric reflectors, from the point of view of the cross polarization.

Another area of application for asymmetric feeds of the previous section is in the formation of multiple phase centers and design of virtual arrays. Multiple phase centers can replace multiple antennas and significantly reduce the complexity and cost. Traditionally, multiple antennas have been used in a variety of applications, such as radars to suppress the clutter due to stationary sources such as ground. Two or more identical antennas were exploited to provide multiple phase center locations. In such an application, all antennas must generate the same radiation patterns at the far-zone region [6, 7]. The drawback of this approach is the need for multiple antennas, which will be in fixed locations, fixing their phase center locations. With the asymmetric feeds of the previous section, multiple phase centers can be generated on the same aperture by using only one antenna, which greatly simplifies the hardware. In addition, the location of the phase centers on the reflector aperture can be moved electronically, making a single reflector antenna equivalent to an array of adaptive multiple phase centers. The use of such adaptive asymmetric feeds in parabolic reflector antennas opens a new window to explore the potential of such an economical solution. A few example cases will be discussed later in this chapter.

8.2.1 Cross Polarization Reduction in Offset Reflector Antennas

The symmetrically cut parabolic reflectors have the major drawback that the feed must be located at the focal point, which partly blocks the reflector aperture. It also needs supporting struts that will contribute to additional aperture blockage. The shadowing effect will become especially important in multibeam antennas having a relatively large feed array. This, in turn, leads to a decrease in the gain, an increase in the sidelobe levels and cross polarizations, and an increase in the mutual coupling between the feeds via the reflector and struts. These defects can be eliminated by the use of offset reflector antennas, where only a portion of the main paraboloid constitutes the antenna. The feed is still located at the focal point, but its axis must be tilted toward the center of the offset reflector. Hence, the blockage will be decreased or cancelled due to the asymmetrical geometry of the reflector, which is a major advantage. Another advantage of the offset structure is that the reaction of the reflector to the feed is of a very low order. Because there is no direct reflection back into the feed, excellent isolation between the reflector and the feed is achieved. Furthermore, the offset geometry provides structural advantages that may be easily deployed after launching in spacecraft antenna applications. Mechanically, the choice of supporting struts and means of thermal control can also be relaxed in the offset geometry. Finally, an offset reflector can accommodate larger focal length to diameter ratios while maintaining a reasonable structural rigidity and a larger feed array in comparison to its symmetric counterpart [8–12].

As indicated earlier, an offset reflector antenna has two drawbacks. Because of its geometrical asymmetry, it generates a cross polarized radiation in the plane of asymmetry when illuminated by a conventional linearly polarized feed. As for the circular polarization case, the reflector main beam generates a beam squint that is in the opposite direction for the right- and left-hand circular polarizations [4]. In this section, cross polarization reduction in offset reflector antennas is addressed. First, the classical matched feeds are discussed. Then, a simplified analytical model is described, which helps in further investigation of the problem and relating the cross polarization performance to the feed parameters.

8.2.1.1 Backgrounds on Focal Plane Distributions and Classical Matched Feeds

The electric field distribution in the focal plane of symmetric reflector antennas was mathematically driven [13, 14] for large focal length parabolas. It was extended to offset reflector antennas by Bem [2], illuminated with a uniform incident plane wave parallel to the optical axis of the reflector. He showed that the focal region electric field distribution in an offset reflector is close to that of a symmetric parabola with an equivalent focal length of $F' = 2F/(1 + \cos\theta_0)$, where F is the focal length of the symmetric parabola and θ_0 is the offset angle of the offset parabola. For an incident wave polarized in the symmetry plane (the x-direction), the electric field components in the focal region of offset reflector antennas, with large focal lengths, are expressed as [2]:

$$\begin{aligned} E_x &= 2\frac{J_1(u)}{u} + j\frac{D}{2F}\sin\theta_0\frac{J_2(u)}{u}\cos\phi_2 \\ E_y &= -j\frac{D}{2F}\sin\theta_0\frac{J_2(u)}{u}\sin\phi_2 \\ E_z &= -j\frac{D}{2F}(1+\cos\theta_0)\frac{J_2(u)}{u}\cos\phi_2 \end{aligned} \tag{8.17}$$

wherein $u = (D/4F)(1 + \cos\theta_0)k\, r_2 \sin\theta_2$, D is the diameter of the projected reflector aperture, and r_2, θ_2, ϕ_2 are the coordinates of a point in the focal plane. The y-component of the electric field does not vanish for nonzero values of offset angles. To cancel or reduce this component, it must be conjugately matched by appropriate primary feeds. A contour plot of the focal plane electric field of a typical offset reflector is shown in Figure 8.1(a) [5]. A high cross polarization component exists at the asymmetry plane with the zero cross polarization at the other orthogonal

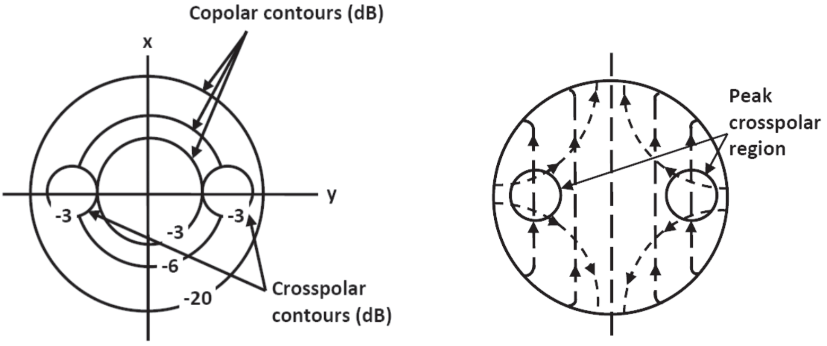

(a) (b)

Figure 8.1 (a) Typical focal plane electric field distribution of offset reflector, and (b) aperture distribution of over-mode circular waveguide horns.

plane. To conjugately match this focal region electric field distribution, the primary feed must possess similar polarization response at its aperture as shown in Figure 8.1(b), for an over-mode circular waveguide horn [5].

To prove the concept, Rudge and Adatia [5] experimentally validated the reduced cross polarization in offset reflector antennas through the use of a tri-mode primary feed. The geometry of their matched feed is shown in Figure 8.2. It was a small-flare angle horn with two small stepped waveguides. It generated the dominant TE_{11} and the higher order TE_{21} and TM_{11} modes. As discussed in [5], the mode content factors depend on the offset angle θ_0 and semi-angle θ^*, subtended by the reflector rim. The measured secondary radiation patterns of the offset reflector, illuminated by the conventional Potter horn [15] and the tri-mode matched feed [5], are shown in Figure 8.3, at the plane of asymmetry, $\phi = 90°$ plane. The aperture sizes of both feeds were equal to 2.8λ. The offset reflector had a focal length of 22.7λ, $\theta_0 = 44°$, and $\theta^* = 30°$. The cross polarization improved by about 10 dB, shown by curve b_1 for the first experimental trial. By adjusting the mode ratios, further improvement was measured, as illustrated by curve b_2 in Figure 8.3(b) [5].

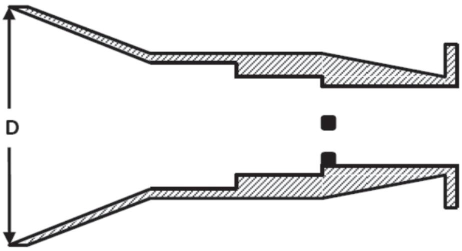

Figure 8.2 Geometry of the tri-mode matched feed by Rudge and Adatia.

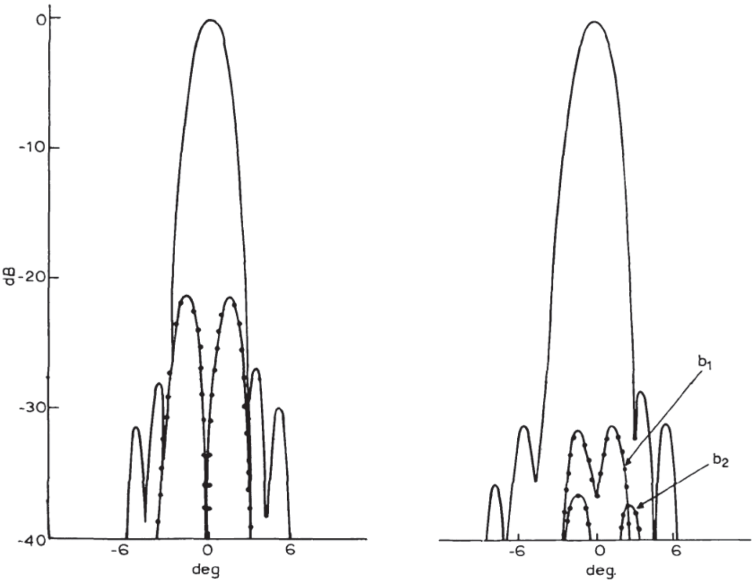

(a)

(b)

Figure 8.3 Measured secondary radiation patterns of offset reflector antenna with a focal length of 22.7λ, $\theta_0 = 44°$, and $\theta^* = 30°$, fed by (a) Potter horn and (b) the tri-mode horn. (©1975 IEE [5].)

The use of rectangular and corrugated horns was also proposed [5] as matched feeds. In these cases, only one extra mode is sufficient to provide the required polarization distribution, to reduce the unwanted cross polarization in offset reflectors. A dual-mode rectangular horn, as a matched feed, was addressed by Jacobson [9]. The use of corrugated matched feeds for cross polarization reduction was studied in [16]. Also, the idea of tri-mode matched feed has been recently revisited [17, 18] for balanced back-to-back reflectors with a reduced moment of inertia. As for the circular polarization, the main beam is squinted due to the depolarizing effects of the offset reflector. The same concept of matched feed is well suited for correcting this as well.

In summary, the main idea behind the matched feed is to combine with the dominant mode, appropriate higher order modes with proper amplitudes and phase shifts, to conjugately match the electric field distribution in the focal region. To understand the problem well, an analytic model is described in the next section to further study the depolarizing properties of offset reflector antennas.

8.2.1.2 A Simplified Analytical Model for Matched Primary Feed [19]

In this section, the polarization properties of offset reflector antennas are further investigated by expressing the feed radiation patterns in terms of analytic functions, which facilitate a more general investigation of the cross polarization reduction in both asymmetric and inter-cardinal planes. The model includes both first and second order azimuthal modes, primarily the TE_{11} and TE_{21} type modes, and allows selection of symmetric and asymmetrical patterns, with different field tapers in the principal planes. It also decouples the reflector performance from that of the feed, thus allowing a more general investigation of the reflector antenna cross polarization and its dependence on the second mode. It will be shown that the asymmetrical aperture distribution of the fundamental mode in the presence of the higher TE_{21} mode is sufficient to reduce the cross polarization of offset reflector antennas even for small *F*/*D* ratios. First, several examples for circular rim offset reflector antennas of different *F*/*D* ratios are presented. The results are obtained by the commercial software TICRA's GRASP V.7 [20], which is based on the physical optics, geometrical optics, and geometrical theory of diffraction. Elliptical-rim offset reflectors cases are also selected and studied to further investigate the concept. The effect of cross polarization reduction is studied on the sidelobe levels and aperture efficiencies of offset reflector antennas. With the proposed feed model, the aperture efficiency of the reflector antenna is improved compared with a standard Gaussian feed with the same edge taper.

In general, inside a circular waveguide, an infinite number of TE and TM modes can exist, and their radiated field can be expressed by double summations in the form:

$$\begin{aligned} E_\theta &= \sum_n \sum_m \left[A_{nm}^{\mathrm{TE}} f_{nm}^{\mathrm{TE}}(\theta,\phi) + A_{nm}^{\mathrm{TM}} f_{nm}^{\mathrm{TM}}(\theta,\phi) \right] \\ E_\phi &= \sum_n \sum_m \left[B_{nm}^{\mathrm{TE}} g_{nm}^{\mathrm{TE}}(\theta,\phi) + B_{nm}^{\mathrm{TM}} g_{nm}^{\mathrm{TM}}(\theta,\phi) \right] \end{aligned} \tag{8.18}$$

where A_{nm} and B_{nm} are the complex numbers in general to express both amplitude and phase differences of the nm^{th} mode. The $f_{nm}(\theta,\phi)$ and $g_{nm}(\theta,\phi)$ represent radiation properties of the nm^{th} mode and can be functions of spherical angles θ and ϕ.

The remarkable property of the round open-ended waveguides and horns is that both $f_{nm}(\theta,\phi)$ and $g_{nm}(\theta,\phi)$ functions are the products of two independent functions of θ and ϕ, in the forms of $f_{nm}(\theta,\phi) = F_{nm}(\theta)\sin(n\phi)$ and $g_{nm}(\theta,\phi) = G_{nm}(\theta)\cos(n\phi)$, assuming the field is y-polarized. This allows one to control the pattern of each mode independently in two orthogonal angular spaces by shaping the waveguide geometry while maintaining its circular cross-section. The required number of modes, and their excitation coefficients, normally depends on the application. In addition, the coefficient of each mode can be controlled by the geometry and type of the excitation ports, probes, or slots, and the waveguide aperture size, which can also cut off the unwanted higher order modes within the operating frequency band.

The modes of special interest in this study are those represented by $n = 1$ and $n = 2$ indices, which are led by TE_{11} and TE_{21} modes in circular waveguides. The first group of modes is led by the TE_{11} mode, the field of which for a y-polarized case can be written in the form

$$
\begin{aligned}
E_\theta &= \left(\sum_{m=1}^{\infty}\left(A_{1m}^{\mathrm{TE}}F_{1m}^{\mathrm{TE}}(\theta) + A_{1m}^{\mathrm{TM}}F_{1m}^{\mathrm{TM}}(\theta)\right)\right)\sin\phi \\
E_\phi &= \left(\sum_{m=1}^{\infty}A_{1m}^{\mathrm{TE}}G_{1m}^{\mathrm{TE}}(\theta)\right)\cos\phi
\end{aligned}
\tag{8.19}
$$

With an asymmetric excitation, the $n = 0$ mode is not excited and the second group of modes is led by the TE_{21} modes. Their radiated fields form a null along the waveguide axis and can be written as

$$
\begin{aligned}
E_\theta &= \left(\sum_{m=1}^{\infty}\left(A_{2m}^{\mathrm{TE}}F_{2m}^{\mathrm{TE}}(\theta) + A_{2m}^{\mathrm{TM}}F_{2m}^{\mathrm{TM}}(\theta)\right)\right)\sin 2\phi \\
E_\phi &= \left(\sum_{m=1}^{\infty}A_{2m}^{\mathrm{TE}}G_{2m}^{\mathrm{TE}}(\theta)\right)\cos 2\phi
\end{aligned}
\tag{8.20}
$$

where F and G are mainly governed by the Bessel functions with the exception of $G_{nm}{}^{\mathrm{TM}} = 0$, as the TM modes have no E_ϕ components [8]. These equations provide exact expressions for the radiated field of an open-ended circular waveguide. However, they are not suitable for our study yet. Instead, the preceding complex summations can be expressed in terms of simpler sine and cosine functions over the radiation main beams. For instance, since the TE_{11} mode radiates along the waveguide axis, its radiated field along the main beam can be represented by $\cos^{n'}\theta$ [8], where n' is an arbitrary constant and has different values in the two principal planes. The value of this constant can be controlled by several different ways. In a conventional waveguide it can be controlled by the mode excitation coefficients. However, if only the TE_{11} mode must be excited, the beam shaping, the value of the constant n', can be controlled by shaping the waveguide flare profile, and/or loading it with a suitable dielectric material [3]. Using the same analogy, an analytical model for the TE_{21} lead modes having a null at the boresight may be expressed by $[\sin(2\theta)\cos(\theta - \theta_m)]^p$, where p plays the same role as n', in the previous case for the $n = 1$ modes. Here too, the power p can be controlled by the waveguide mode excitations, or for selected TE_{21} mode, by shaping the feed geometry. For the sake of generality, we will refer to these two cases as the TE_{11} type and TE_{21} type modes. They could refer to the radiated fields of profiled single-mode, or dual- (multi-) mode feeds. The simple $\sin(2\theta)$ function provides a null at the boresight with the peak located at the $\theta = 45°$. The extra factor of $\cos(\theta - \theta_m)$ is multiplied by $\sin(2\theta)$ to move the beam peak to around the $\theta = 45°$. In other words, the angle θ_m also depends on the aperture radius supporting the TE_{21} type mode. Therefore, assuming both mode types are polarized along the y-axis, the analytical model describing the combined TE_{11} type and TE_{21} type modes can be expressed as follows

$$\begin{aligned} E_\theta &= C_1 \cos^{n1}\theta \sin\phi + jC_2\left(\sin(2\theta)\cos(\theta - \theta_m)\right)^{p1}\sin(2\phi) \\ E_\phi &= C_1 \cos^{n2}\theta \cos\phi + jC_2\left(\sin(2\theta)\cos(\theta - \theta_m)\right)^{p2}\cos(2\phi) \end{aligned} \tag{8.21}$$

wherein C_1 and C_2 are the content factors of TE_{11} type and TE_{21} type modes, respectively, and can be complex numbers in general to represent both amplitude ratio and phase difference of these modes. In the present study, two separate coefficients have been selected to simplify understanding the excitation level of each mode type. However, mathematically one only needs the mode ratio C_2/C_1 to describe the feed function completely. Herein, the feed parameter is shown by the mode ratio C_2/C_1. The exponential terms n_1, n_2, and p_1, p_2 define the tapering function in the E- and H-planes. Since the second term is led by the TE_{21} type mode, the factor j in the second term of (8.21) represents a 90° phase shift and is considered in order to be consistent with the radiation pattern of the TE_{21} mode according to Silver [8]. As an example, the normalized amplitude patterns of both TE_{11} type and TE_{21} type modes are illustrated in Figure 8.4, when it is assumed that each mode type has symmetric patterns at the principal planes. That is, $n_1 = n_2 = p_1 = p_2 = 1$ and $\theta_m = 0°$. The first term has a broadside radiation pattern, whereas the second term has a null at the boresight angle of $\theta = 0°$. They correspond closely to the radiation patterns of the TE_{11} and TE_{21} modes.

The geometry of an offset reflector antenna with a circular-rim is shown in Figure 8.5. The reflector is defined by the focal length F, the offset angle θ_0, the half-angle subtended by the reflector rim θ^*, the diameter of the projected aperture of the offset reflector D, and the offset clearance distance d_c, which is the distance between the axis of the parent parabola and the lower edge of the reflector rim [10] as shown in Figure 8.5. The analytic feed described by (8.21) is located at the focal point f of the reflector shown in Figure 8.5(a). It is shown that with appropriate amplitude and phase excitation of these two type modes, the cross polarization can be reduced at the far-field region. As reported in [5], the TE_{21} mode should have –90° phase shift with the TE_{11} mode to reduce the cross polarization of the secondary pattern, provided an appropriate amplitude ratio, and more importantly tapering factors for each mode at each principal plane are determined. To conduct an investigation on the cross polarization, offset reflector antennas with different F/D ratios are studied with $D = 20\lambda$, $d_c = \lambda$, where λ is the wavelength at the selected frequency of 10 GHz. After an extensive study, the angle θ_m in (8.21) was found equal to zero, the TE_{21}

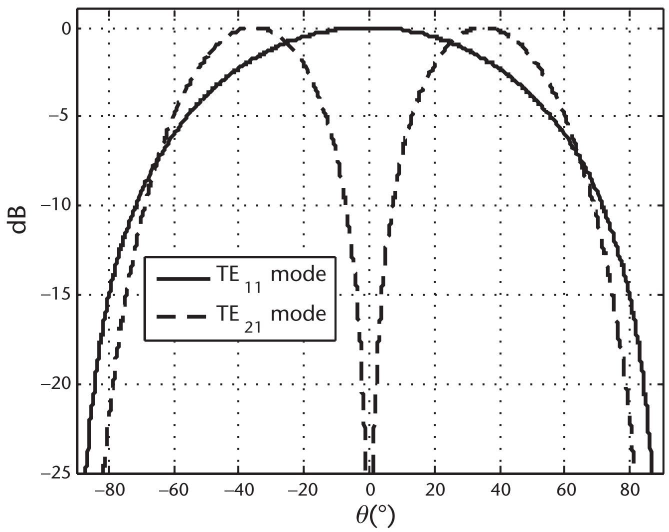

Figure 8.4 Normalized amplitude patterns of the feed model expressed by (8.21) for both TE_{11} and TE_{21} modes, when $n_1 = n_2 = p_1 = p_2 = 1$ and $\theta_m = 0°$.

type mode should have symmetric patterns at the principal planes, and both p_1 and p_2 are equal to unity. Therefore, the remaining parameters are the exponential terms n_1 and n_2 of the TE_{11} type modes, and the amplitude ratio C_2/C_1.

Tables 8.1 and 8.2 summarize the cross polarization levels of the secondary patterns of the offset reflector fed by the model given by (8.21) at the $\phi = 90°$ asymmetry plane and the diagonal $\phi = 45°$ plane, respectively, and compared with the single TE_{11} mode feed, $C_2 = 0$. With the dual-mode feed model given by (8.21), the cross polarization component is reduced to about –47 dB even for the large offset angles, at both the asymmetry and $\phi = 45°$ planes. Moreover, the value of C_2/C_1 increases as *F*/*D* decreases, to obtain the minimum cross polarization level, at both above-mentioned planes. This implies that a larger fraction of the TE_{21} type mode is needed to cancel the unwanted cross polarization at the far-field zone for large offset angles. Also, the tapering factor n_2 remains constant for all values of *F*/*D* ratios, whereas

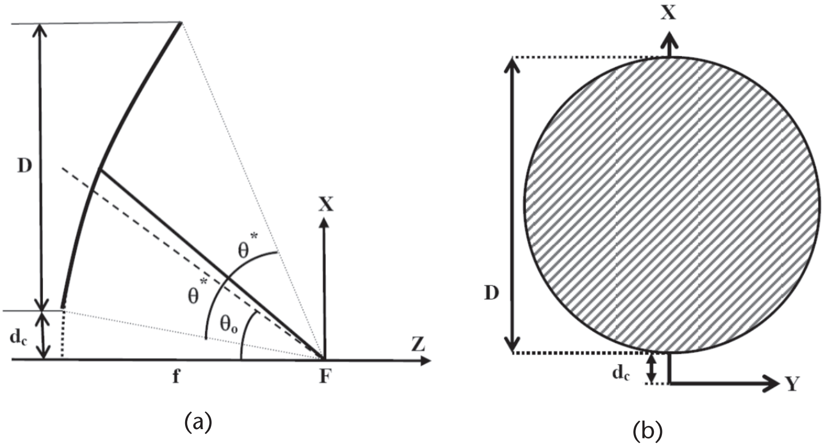

(a) (b)

Figure 8.5 The geometry of a circular-rim offset reflector antenna. (a) Cross-section view, and (b) front view.

Table 8.1 Reduced Cross Polarization of Offset Reflector Antennas in the Asymmetry $\phi = 90°$ Plane, for Different *F*/*D* Ratios with $D = 20\lambda$, $d_c = \lambda$ Fed by the Model given by (8.21) at $f = 10$ GHz (©2012 IEEE [19].)

F/D	θ_0	*XPOL*($C_2 = 0$)	*XPOL by (8.21)*	C_2/C_1	n_1	n_2
1.1	26.80°	–28.76	<–60	0.126	2.4	2.6
1.0	29.12°	–26.89	<–60	0.139	2.3	2.6
0.8	35.06°	–23.55	<–60	0.175	2.2	2.6
0.6	43.57°	–19.46	–50.03	0.243	2.1	2.6

Table 8.2 Reduced Cross Polarization of Offset Reflector Antennas in the $\phi = 45°$ Plane for Different *F*/*D* Ratios with $D = 20\lambda$, $d_c = \lambda$ Fed by the Model given by (8.21) at $f = 10$ GHz (©2012 IEEE [19].)

F/D	θ_0	*XPOL*($C_2 = 0$)	*XPOL by (8.21)*	C_2/C_1	n_1	n_2
1.1	26.80°	–31.24	–55.00	0.126	2.4	2.6
1.0	29.12°	–29.62	–53.55	0.139	2.3	2.6
0.8	35.06°	–26.22	–50.88	0.175	2.2	2.6
0.6	43.57°	–22.15	–47.25	0.243	2.1	2.6

n_1 varies from 2.4–2.1 as *F*/*D* changes from 1.1–0.6. As a result, more asymmetric patterns of the TE_{11} type mode are required to minimize the cross polarization for larger offset angles. It should be mentioned that the required phase difference between the TE_{21} and the TE_{11} type modes is always –90°, as explained earlier.

To conduct an investigation on the effect of tapering factors n_1 and n_2 on the cross polarization, an offset reflector antenna is selected with $F/D = 0.595$, $D = 66.5$ cm, $d_c = -6.25$ cm, $\theta^* = 41.80°$, and $\theta_0 = 32.77°$. The operating frequency is 10 GHz as before. Figure 8.6 shows the cross polarization and sidelobe levels of the secondary patterns in terms of C_2/C_1 in both the asymmetry plane of $\phi = 90°$ and the $\phi = 45°$ plane. Different values of n_1 and n_2 are considered as $n_1 = n_2 = 1$, $n_1 = n_2 = 2$, $n_1 = 2.2$, $n_2 = 2.6$, and $n_1 = 2.0$, $n_2 = 3.0$. The first two cases correspond to the symmetric E- and H-plane patterns for the TE_{11} type mode, and the second and third cases generate asymmetric ones. As can be seen, the sidelobe levels are almost unchanged for different amplitude ratios of C_2/C_1, and it is minimum when there is stronger tapered distribution for the TE_{11} type mode, $n_1 = 2.0$, $n_2 = 3.0$, as expected based on the aperture theory. However, the cross polarization levels mainly depend on C_2/C_1 and are well below –50 dB at both planes when $n_1 = 2.2$, $n_2 = 2.6$, and $C_2/C_1 = 0.177$.

The normalized secondary co-polar and cross-polar radiation patterns are shown in Figure 8.7 for the optimum case, when $n_1 = 2.2$, $n_2 = 2.6$ and $C_2/C_1 = 0.177$, with a –90° phase shift. They are also compared with a standard Gaussian feed with a –12 dB edge illumination. The cross polarization level of the secondary patterns is reduced from –25 dB, when fed by the Gaussian feed, to less than –50 dB when fed by the proposed tapered feed in (8.21) at both $\phi = 90°$ and 45° planes. The radiation patterns of the primary feed are shown in Figure 8.8 for the optimized case of $n_1 = 2.2$, $n_2 = 2.6$, and $C_2/C_1 = 0.177$ with a –90° phase shift. The feed mostly

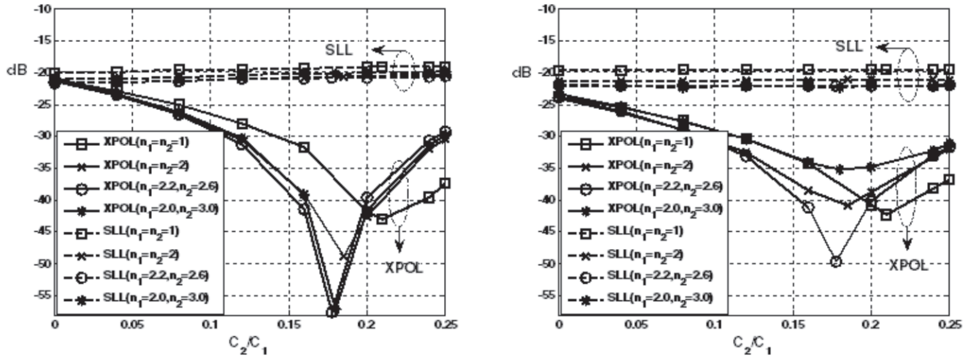

(a) (b)

Figure 8.6 Cross polarization and sidelobe levels of the circular-rim offset reflector antenna (F/D = 0.595, D = 66.5 cm, d_c = –6.25 cm, θ^* = 41.80°, and θ_0 = 32.77°), fed by the tapered dual-mode feed given by (8.21) at the frequency of 10 GHz. (a) ϕ = 90°, and (b) ϕ = 45° plane.

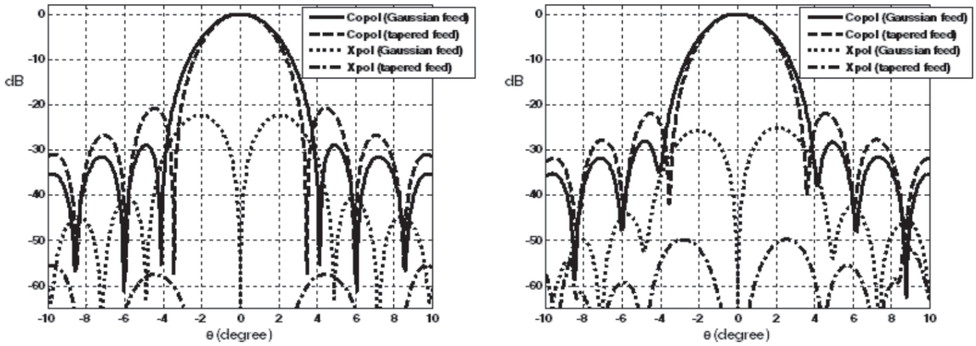

(a) (b)

Figure 8.7 Normalized co-polar and cross-polar radiation patterns of the circular-rim offset reflector antenna (F/D = 0.595, D = 66.5 cm, d_c = –6.25 cm, θ^* = 41.80°, and θ_0 = 32.77°), fed by a Gaussian feed (–12 dB edge illumination) and the optimized tapered dual-mode feed operating at TE_{11} and TE_{21} with C_2/C_1 = 0.177∠–90°, n_1 = 2.2 and n_2 = 2.6. (a) ϕ = 90°, and (b) ϕ = 45°.

illuminates the upper section of the offset reflector antenna aperture, with its phase center located at the focal point of the reflector.

The effect of the proposed feed is also studied on the elliptic-rim offset reflector antenna shown in Figure 8.9. The focal length and d_c remain similar to the example of circular-rim offset reflector. The minor axis, D_H, is selected to be equal to the diameter of the circular-rim offset reflector, which is 66.5 cm. First, the major axis of the ellipse, D as shown in Figure 8.9, changes from D_H to 90 cm, to gradually form an elliptical projected aperture. The resulting sidelobe levels and cross polarizations are shown in Figure 8.10, for the same values of n_1 and n_2 stated above at both asymmetry and inter-cardinal planes, when C_2/C_1 = 0.18 with a –90° phase shift. The sidelobe level decreases as the major axis of the ellipse increases and it is minimum when n_1 = 2.2 and n_2 = 2.6. As for the cross polarization, the same tapering numbers yield the minimum value of cross polarization at both ϕ-planes. They are less than –50 dB and –48 dB at ϕ = 90° and ϕ = 45° planes, respectively. Therefore,

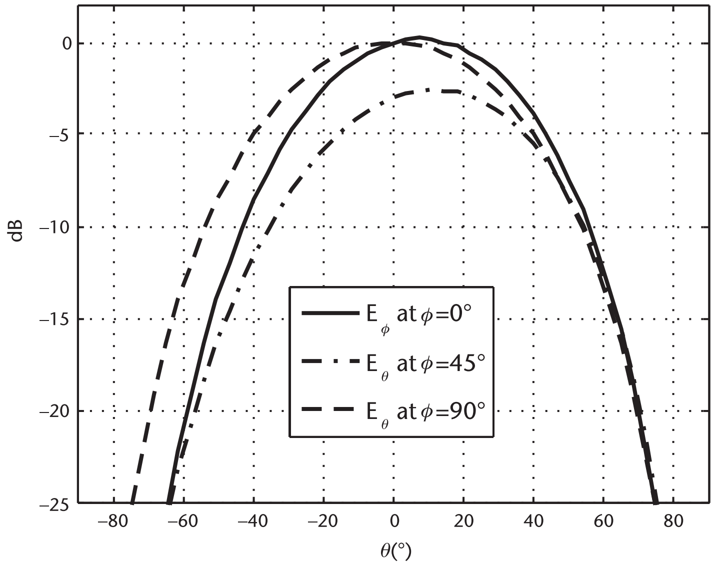

Figure 8.8 Normalized radiation patterns of the feed model defined by (8.21) with $n_1 = 2.2$, $n_2 = 2.6$, and $C_2/C_1 = 0.177\angle{-90°}$.

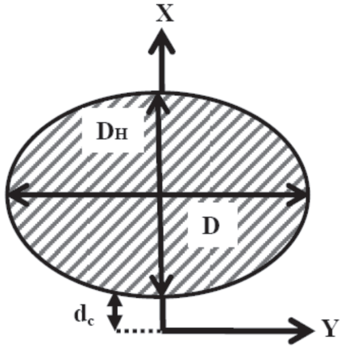

Figure 8.9 Cross-section view of the projected aperture of an elliptic-rim offset reflector antenna.

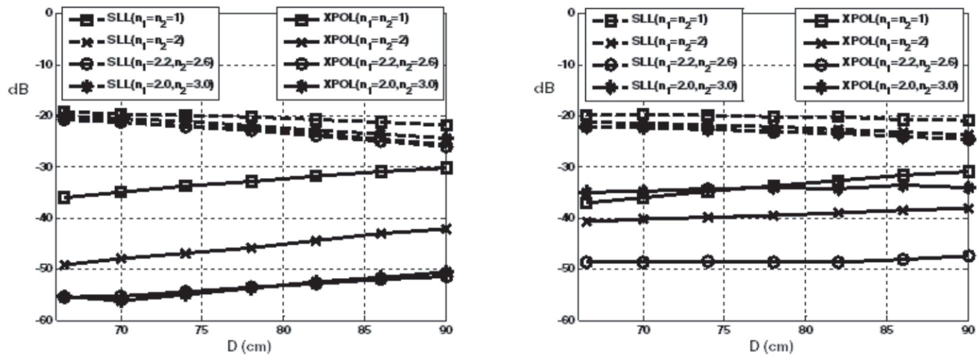

(a)

(b)

Figure 8.10 Cross polarization and sidelobe levels of the elliptical-rim offset reflector antenna fed by the tapered dual-mode feed operating at TE_{11} and TE_{21} when $C_2/C_1 = 0.18\angle{-90°}$ at (a) $\phi = 90°$, and (b) $\phi = 45°$ planes.

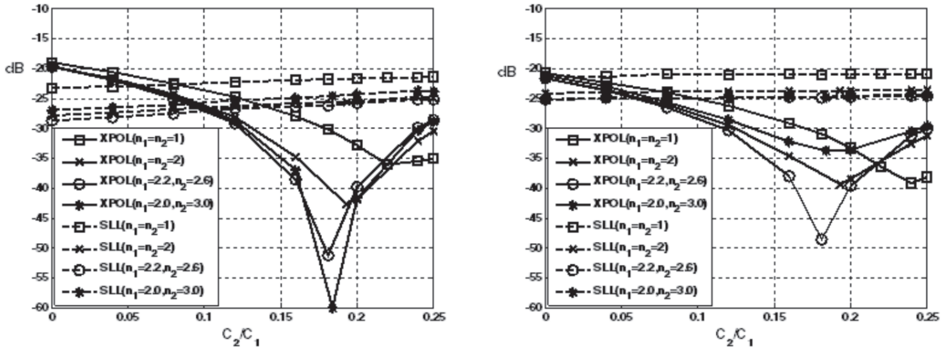

(a) (b)

Figure 8.11 Cross polarization and sidelobe levels of the elliptical-rim offset reflector antenna ($F = 39.6$ cm, $D = 90$ cm, $D_H = 66.5$ cm, and $d_c = -6.25$ cm) fed by the tapered feed given by (8.21). (a) $\phi = 90°$, and (b) $\phi = 45°$ planes.

it has been shown that the same tapering numbers can minimize the cross polarization of the elliptic-rim offset reflector antenna under study.

The major axis of $D = 90$ cm is selected to conduct a study on the sidelobe and cross polarization levels, in terms of the amplitude ratio C_2/C_1, for the same tapering numbers of $n_1 = n_2 = 1$, $n_1 = n_2 = 2$, $n_1 = 2.2$, $n_2 = 2.6$, and $n_1 = 2.0$, $n_2 = 3.0$ as before. The results are shown in Figure 8.11 at both ϕ-planes of 90° and 45°. The cross polarization reaches to less than –48 dB at both planes when $C_2/C_1 = 0.18\angle{-90°}$, $n_1 = 2.2$, and $n_2 = 2.6$. The corresponding secondary patterns of this optimized case are depicted in Figure 8.12 and are compared with a standard Gaussian feed with a –12 dB edge illumination as a primary feed. The cross polarization decreases from almost –23 dB to about –48 dB at both planes. The feed radiation patterns are almost the same as the ones shown in Figure 8.8.

The performance of the offset reflector antennas with the matched primary feed proposed in this section was also compared with three different primary feeds: the tapered feed with –12 dB, the Gaussian feed with –5 dB, and the Gaussian feed with –12 dB edge illuminations. The results are summarized in Tables 8.3 and 8.4

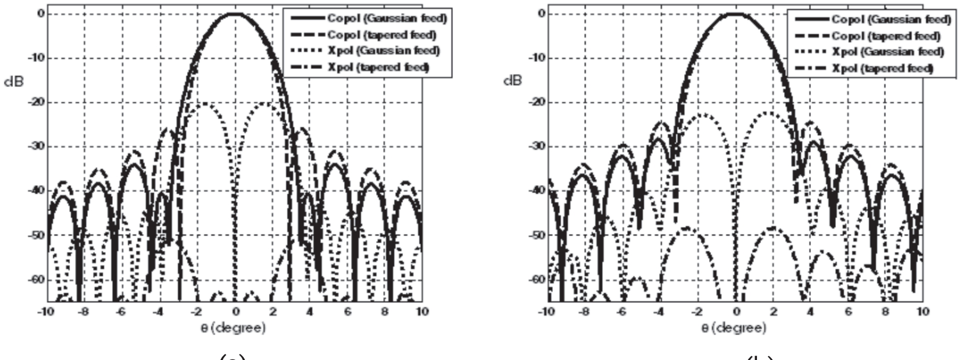

(a) (b)

Figure 8.12 Normalized co-polar and cross-polar radiation patterns of the elliptical-rim offset reflector antenna ($F = 39.6$ cm, $D = 90$ cm, $D_H = 66.5$ cm, and $d_c = -6.25$ cm), fed by a Gaussian feed with –12 dB edge illumination and the optimized tapered dual-mode feed, with $C_2/C_1 = 0.181\angle{-90°}$, $n_1 = 2.2$ and $n_2 = 2.6$. (a) $\phi = 90°$, and (b) $\phi = 45°$.

for the circular- and elliptical-rim reflectors, the two examples discussed earlier as illustrated in Figures 8.7 and 8.12, respectively. The proposed feed provides better aperture efficiencies, illumination, and spill-over factors, compared with a standard Gaussian feed of –5 dB edge illumination for both circular- and elliptical-rim reflectors with much reduced cross polarized components and comparable sidelobe levels. The –5 dB edge illumination has been considered in order to make a valid comparison. According to Figure 8.8, the value of the primary radiation pattern at the half-angle subtended by the rim (θ^*), which is around 40°, is approximately 5 dB below its value at the $\theta = 0°$. If the standard –12 dB Gaussian feed were to be used, the proposed tapered feed given by (8.21) needs to provide the same edge illumination of –12 dB according to the new mode content factor and exponential terms as denoted in the footnote of Tables 8.3 and 8.4. The corresponding results are listed under columns 3 and 5 of the mentioned tables. For the circular-rim case, with the –12 dB tapered feed the cross polarization levels are still below –35 dB compared with the Gaussian feed of –12 dB edge illumination, whereas their sidelobe levels and efficiencies are pretty much the same. However, for the elliptic-rim case, the –12 dB tapered feed results in low cross polarization at only the asymmetry plane and lower efficiency. It should be noted that the Gaussian Feed 1 provides –5 dB at the $\theta = 41.80°$ and –7.35 dB edge illuminations at the $\theta = 51.11°$, the two half-angles

Table 8.3 Gain, Aperture Efficiencies, Cross Polarization, and SLL of the Circular-Rim Offset Reflector Discussed in Figure 8.7 with the Proposed Tapered Feed and Standard Gaussian Feeds (©2012 IEEE [19].)

		Proposed Tapered Feed	*Tapered Feed with~ –12 dB**	*Gaussian Feed –5 dB*	*Gaussian Feed –12 dB*
Gain		35.54 dBi	35.69 dBi	34.90 dBi	35.80 dBi
η_{ap}		76.44%	63.72%	78.40%	73.84%
Xpol	$\phi = 45°$	–49.80 dB	–36.63 dB	–24.07 dB	–25.22 dB
Xpol	$\phi = 90°$	–56.54 dB	–39.96 dB	–21.38 dB	–22.41 dB
SLL	$\phi = 45°$	–22.02 dB	–27.93 dB	–21.38 dB	–28.17 dB
SLL	$\phi = 90°$	–20.87 dB	–28.31 dB	–21.76 dB	–29.06 dB

* –12 dB edge taper at $\theta = 41.80°$ with $n_1 = n_2 = 5.2$ and $C_2/C_1 = 0.1\ \angle{-90°}$.

Table 8.4 Gain, Aperture Efficiencies, Cross Polarization, and SLL of the Elliptical-Rim Offset Reflector Discussed in Figure 8.12 with the Proposed Tapered Feed and Standard Gaussian Feeds (©2012 IEEE [19].)

		Proposed Tapered Feed	*Tapered Feed with~ –12 dB**	*Gaussian Feed #1 (–5 dB)*	*Gaussian Feed #2 (–12 dB)***
Gain		37.05 dBi	36.62 dBi	36.62 dBi	36.94 dBi
η_{ap}		77.25%	69.96%	69.96%	75.31%
Xpol	$\phi = 45°$	–48.38 dB	–23.48 dB	–21.51 dB	–22.38 dB
Xpol	$\phi = 90°$	–51.12 dB	–41.04 dB	–19.64 dB	–20.51 dB
SLL	$\phi = 45°$	–24.68 dB	–31.49 dB	–24.25 dB	–29.18 dB
SLL	$\phi = 90°$	–26.11 dB	–40.12 dB	–28.09 dB	–40.70 dB

* –12 dB edge taper at $\theta = 51.11°$ with $n_1 = 5.2$, $n_2 = 3.2$ and $C_2/C_1 = 0.1\ \angle{-90°}$.

** First sidelobe levels are given.

subtended by the elliptical-rim case. Similarly, the edge illumination of the Gaussian Feed 2 is −8.25 dB at the $\theta = 41.80°$ and −12 dB at the $\theta = 51.11°$.

In summary, the idea of matched feeds was further studied to reduce the cross polarization of offset reflector antennas in both asymmetry and inter-cardinal planes. The feed was modeled by analytical functions representing asymmetric primary patterns. Such asymmetry patterns were obtained by combining the TE_{11} and TE_{21} type modes with a small mode ratio inside a circular waveguide feed. Consequently, the secondary cross polarization was minimized by adjusting the amplitude ratio and phase difference of the two modes and more importantly by selecting different tapering levels of the TE_{11} type mode in the principal E- and H-planes.

8.3 Asymmetric Feed Designs for Cross Polarization Reduction

In Section 8.2.1.2, simple mathematical expressions for the radiation field of the feed were selected to allow a complete investigation of the offset reflector performance. In general, the required radiation patterns of the optimum feed can be generated by a suitable combination of the TE and TM modes or by selecting the first two TE_{11} and TE_{21} modes and shaping the cross-section profile of the feed, as well as loading it preferentially by dielectrics [3]. However, such a feed can also be designed simply by a proper selection of circular waveguides of different diameters and lengths, and exciting efficiently the TE_{11} and TE_{21} modes. They are referred as adaptive feeds based on their capability to generate these modes with adjustable mode content factors.

In this section, two novel dual-mode circular waveguide feeds are presented. They generate both TE_{11} and TE_{21} modes with a quadrature −90° phase difference in different amplitude ratios for cross polarization reduction in offset reflector antennas. Traditionally, the input impedance matching of a multimode waveguide is adversely affected by exciting a higher order mode. The higher order TE_{21} mode has a negligible impact on the return losses of the proposed dual-mode feeds. The numerical computations for these are conducted by the finite element method, HFSS [21].

8.3.1 Feed 1: Ring Choke Excited Circular Waveguide with Slot [22, 23]

The geometry of the feed under study is shown in Figure 8.13. It consists of a central round waveguide with a single longitudinal slot opening on its wall into a single round choke. The physical dimensions of the slot are defined by its half-angular opening and height, as denoted by α and h, respectively, in Figure 8.13. The desired modes of operation are a combination of the TE_{11} and TE_{21} modes. The radius of the central waveguide is designed to excite the dominant TE_{11} mode. The slot is to couple some of its energy into the higher order TE_{21} mode inside the choke. In other words, the required cross-sectional change is made through the slot, right at the junction of the central cylinder and the choke. The outer radius of the choke is selected judiciously to support only the TE_{21} mode and suppress all other higher order modes. The inner and outer radii were finalized to 13 mm and 17.7 mm, respectively, to meet the above-mentioned criteria at the center frequency of 8.5 GHz. With a y-polarized wave port excitation, the antenna finds an asymmetrical structure, which is needed for the excitation of the TE_{21} mode. This structure can

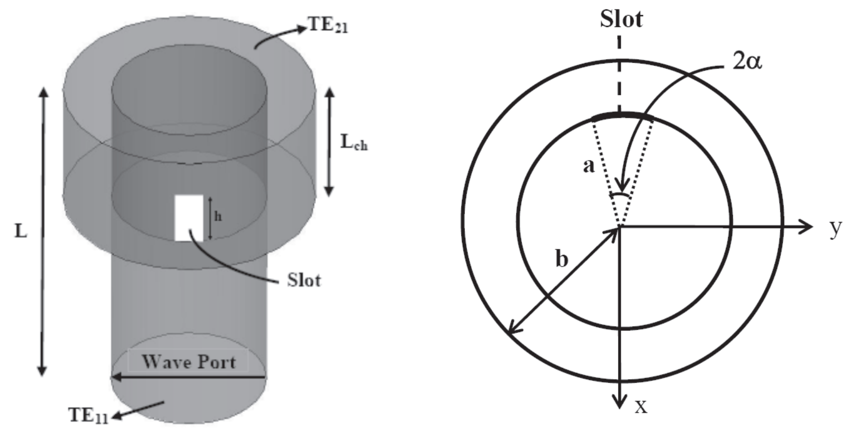

(a) (b)

Figure 8.13 Geometry of Feed 1 operating at the TE_{11} mode inside the waveguide and TE_{21} mode inside the choke, with $a = 13$ mm, $b = 17.7$ mm, $L_{ch} = 19$ mm, and $L = 7.75$ cm. (a) 3-D view, and (b) top-view. (©2012 IEEE [23].)

now operate as a dual-mode antenna. For this antenna to work as a primary feed for offset reflector antennas, the phase difference between the two modes must be −90° [5]. Therefore, the lengths of the choke and the waveguide are selected to provide such a phase shift, and they are equal to 19 mm and 77.5 mm, respectively. That is, $L_{ch} = 19$ mm and $L = 77.5$ mm.

To simplify understanding the contribution of each mode in the far-field region, especially the mode content factor, (8.21) is used to model the radiation patterns of the proposed dual-mode feed based on the curve-fitting method. Several studies were performed to investigate the effect of the slot height and its angular width on the mode content factor and exponential terms in the analytical model expressed by (8.21). It is found that the angle θ_m in (8.21) is equal to zero, the TE_{21} type mode should have symmetric patterns at the principal planes, and both p_1 and p_2 are equal to unity. Therefore, the remaining parameters are the exponential terms n_1 and n_2 of the TE_{11} type modes, and the amplitude ratio C_2/C_1 and (8.21) can be rewritten as

$$\begin{aligned} E_\theta &= C_1 \cos^{n1}\theta \sin\phi + jC_2 \sin(2\theta)\cos\theta\ \sin(2\phi) \\ E_\phi &= C_1 \cos^{n2}\theta \cos\phi + jC_2 \sin(2\theta)\cos\theta\ \cos(2\phi) \end{aligned} \tag{8.22}$$

Figure 8.14(a) shows the effect of the slot height on the amplitude ratio of C_2/C_1 over the frequency range of 7.0–9.0 GHz, for a fixed value of $\alpha = 6.8°$. The amplitude ratio increases with frequency. Also, the larger the height of the slot, the stronger the TE_{21} mode is, as expected. Similarly, the effect of angular width of the slot, α, is shown in Figure 8.14(b). It follows almost the same trend as explained for the height, except for $\alpha = 4°$, where the mode content factor decreases up to 8.0 GHz and starts increasing thereafter.

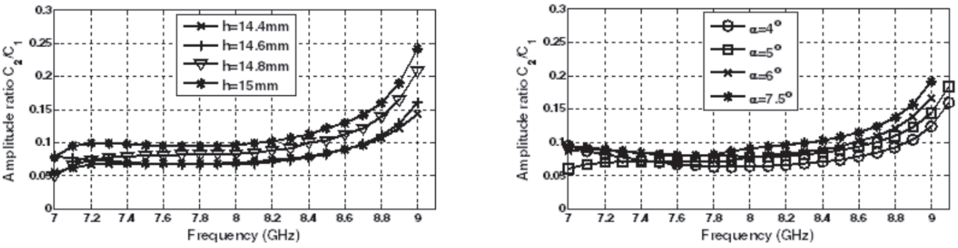

(a) (b)

Figure 8.14 Amplitude ratio of C_2/C_1 of Feed 1 shown in Figure 8.13 versus frequency. (a) Effect of h when $\alpha = 6.8°$, and (b) effect of α when $h = 14.6$ mm.

The normalized co-polar and cross-polar radiation patterns of the feed under study, with and without slot, are illustrated in Figure 8.15 at the operating frequency of 9.0 GHz. The slot size is selected as $h = 14.4$ mm and $\alpha = 6.8°$. The co-polar patterns with no slot are completely symmetric, as shown in Figure 8.15(a), with their main beam located at the boresight direction, whereas the main beam of the co-polar pattern with the slot at the $\phi = 0°$ is scanned due to the presence of the TE_{21} mode, as shown in Figure 8.15(b). In addition, the generated TE_{21} mode increases the cross polarization, the amount of which depends on the slot size, in terms of the percentage energy conversion to the TE_{21} mode through the slot. In fact, such an asymmetry and high cross polarization level, in the primary feed, are required to reduce the inherent cross polarization of the offset reflector antenna, as will be explained shortly.

The boresight gains of the antenna are plotted in Figure 8.16 for different slot sizes from 14.4–15 mm for a fixed value of $\alpha = 6.8°$. The boresight gain changes smoothly from 8.5–10 dBi. The feed performance is therefore stable over the frequency range of 7.0–9.0 GHz, and the gain change is only 1.5 dB. The effect of angular opening of the slot, α, on the gain is the same as the one shown in Figure 8.16.

The asymmetric feed, proposed in Figure 8.13, can be used as a primary feed for offset reflector antennas to reduce their inherent high cross polarization components. To verify this, the dual-mode feed with a slot height of 14.4 mm has been used as a primary feed to illuminate a commercial elliptic-rim offset reflector of 36" × 27" and $F/D = 0.6$ at the frequency of 9.0 GHz. The co-polar and cross-polar radiation patterns at the asymmetry plane, $\phi = 90°$ plane, are plotted in Figure 8.17 and

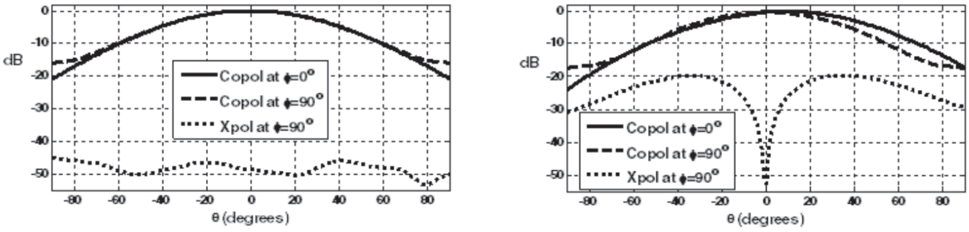

(a) (b)

Figure 8.15 Normalized co-polar and cross-polar patterns of Feed 1 at $f = 9.0$ GHz. (a) No slot ($\alpha = h = 0$), and (b) with slot $h = 14.4$ mm and $\alpha = 6.8°$.

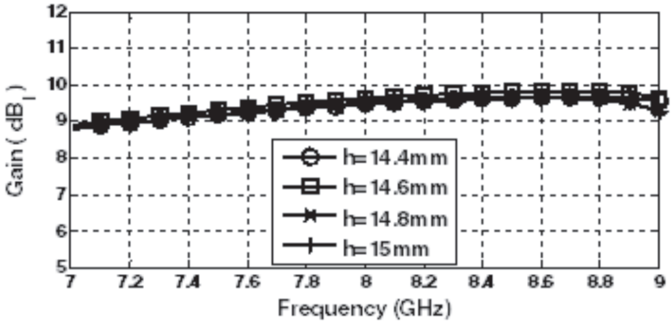

Figure 8.16 Boresight gain of Feed 1 versus frequency for different slot heights *h*, when $\alpha = 6.8°$.

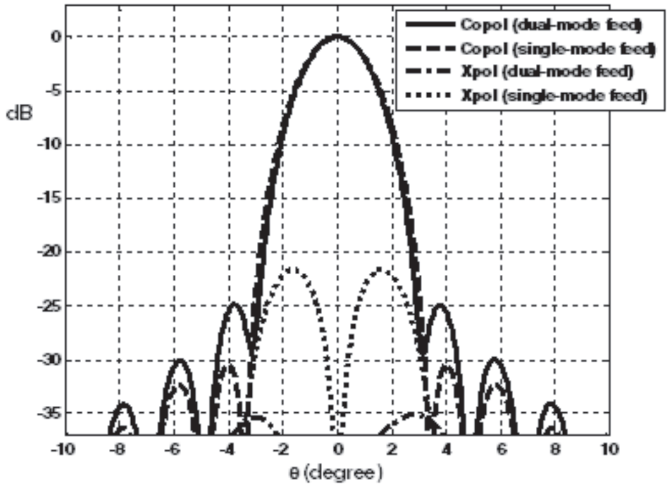

Figure 8.17 Co-polar and cross-polar radiation patterns of an elliptic offset reflector antenna with $F/D = 0.6$ at the $\phi = 90°$ plane and $f = 9$ GHz fed by a conventional single-mode circular waveguide and Feed 1 with the slot height of 14.4 mm.

compared with the case when the primary feed is a conventional single-mode circular waveguide with a radius of 18 mm. The cross polarization of the compound reflector and the feed improves by about 13 dB when the proposed dual-mode feed is used to illuminate the offset reflector antenna. The reflector gains, when illuminated by the dual-mode and single-mode feeds, are in the same order and equal to 35.45 dBi and 35.43 dBi, corresponding to aperture efficiencies of 62.97% and 62.68%, respectively.

To verify the simulation results, a prototype of Feed 1 was built and tested. The antenna parameters were the same as those in Figure 8.13, with the slot length of 14.5 mm and half-angular opening of 6.8°. A photograph of the feed is shown in Figure 8.18. The resulting mode content factor, which is the ratio of TE_{21}/TE_{11}, is around $0.15 \angle{-90°}$ at the frequency of 9.0 GHz. The measured co-polar and cross-polar radiation patterns of the fabricated antenna are compared with the corresponding simulated results at the principal planes and the operating frequency of 9.0 GHz. They are illustrated in Figure 8.19. They are in excellent agreement. The asymmetry of the co-polar pattern in $\phi = 0$ plane is due to the TE_{21} mode and is necessary for reduction of the cross polarization of the offset reflectors. The boresight gain of this

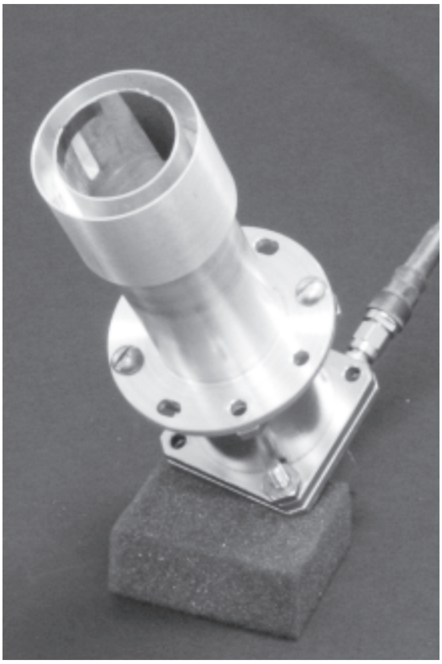

Figure 8.18 Photograph of the prototype Feed 1 (choke excited circular waveguide with slot).

antenna is near 10 dBi similar to the simulation result. The minor undulations on the measured data are due to small reflections from the support structure, holding it on the tower. Because there is no discontinuity inside the central waveguide, the antenna remains well matched to a standard 50Ω input. The measured and simulated scattering parameters of the antenna are compared in Figure 8.20, over the frequency range of 8.0–9.2 GHz, which agree well. The waveguide transition, from a rectangular cross section to a circular one, available in the laboratory, was designed to work over the *X*-band frequency range from 8–12 GHz. Thus, the measured S_{11} is shown only for frequencies above 8 GHz. The antenna bandwidth is much wider, as shown by the simulated S_{11}, exhibiting a broad 10 dB bandwidth from 7.1–9.2 GHz.

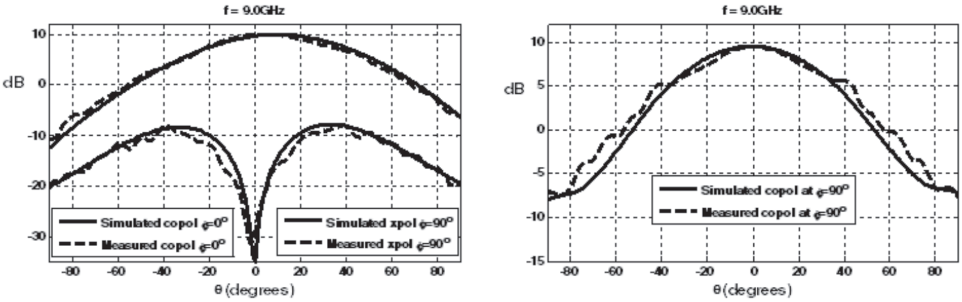

(a) (b)

Figure 8.19 Measured and predicted co-polar and cross-polar radiation patterns of Feed 1 at the frequency of 9.0 GHz. (a) Co-polarization at the $\phi = 0°$ and cross polarization at the $\phi = 90°$, and (b) co-pol at the $\phi = 90°$ plane.

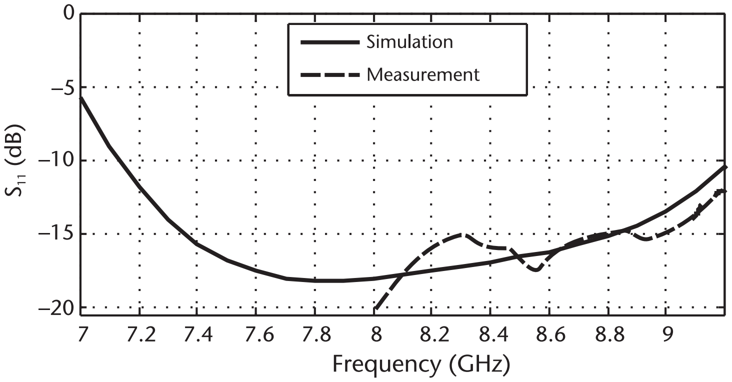

Figure 8.20 Measured and simulated S_{11} of Feed 1 versus frequency.

8.3.2 Feed 2: Stepped Circular Waveguide with Tuning Blocks [24]

The geometry of proposed feed is shown in Figure 8.21. It consists of only two waveguide sections. The diameter of the larger waveguide is selected as small as possible so that only the TE_{11} and TE_{21} modes can propagate and the latter higher mode can be excited efficiently. Its excitation sources are two radial blocks/screws, which can be placed at any arbitrary axial position. In the present design, they are placed on the feed aperture, to be far from the waveguide discontinuity, to cause maximum attenuation of the higher order modes at the junction. In this manner, the input waveguide port is not influenced by their presence, and the feed can be designed easily to be broadband. The radial excitation screws do not excite the TM modes efficiently [25] and the main operating modes are the TE_{11} and TE_{21} modes. However, a step discontinuity used in the proposed feed may excite the next higher order TM_{11} mode. This has been taken care of by selecting the appropriate aperture size to cut off the TM_{11} mode over the frequency band of interest. As a result, the TM_{11} mode ratio will be very small and its contribution on the cross polarization of the offset reflector is negligible. In addition, if a tri-mode feed is to illuminate an offset reflector to reduce its cross polarization, the TM_{11} mode ratio should be almost the same level as the TE_{21} mode ratio [5, 18]. The length of the larger waveguide is selected such that the phase difference between the two modes is –90° over the frequency range of interest, which is from 8.0–9.1 GHz. This frequency band was selected to enable experimental verification, because a waveguide transition at this band was available in the laboratory. The antenna dimensions can be scaled readily for operation at any other band. The inner and outer radii were found to be 13 and 17.3 mm, respectively. The length of the larger waveguide was 24 mm to provide the required –90° phase shift between the modes, and the total antenna length and waveguide wall thickness were 77.5 and 2 mm, respectively. This structure can now operate as a dual-mode feed with different mode content ratios using tuning screws.

It should be mentioned that the two blocks shown in Figure 8.21 are identical and their heights and widths are fixed and equal to 2 and 3 mm, respectively. Figure 8.22 illustrates how the amplitude ratio of C_2/C_1 varies as the length of the blocks changes from 3–5 mm, over the frequency range of 8.0–9.1 GHz. As can be seen, the longer the blocks, the stronger the TE_{21} mode is, as expected.

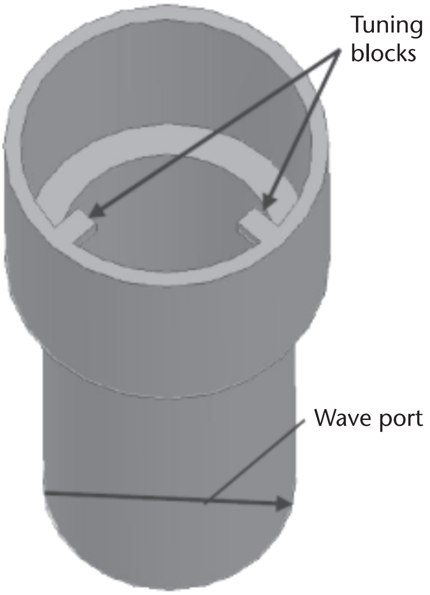

Figure 8.21 The geometry of the proposed dual-mode circular waveguide horn (Feed 2) with tuning blocks/screws to use as a primary feed in offset reflector antennas. (©2011 IEEE [24].)

The results of the input impedance matching with different block lengths are shown in Figure 8.23, and compared with those of two other antennas, namely, the same antenna with no blocks present and the same geometry when the 5 mm blocks are placed right at the discontinuity, as in traditional designs. When blocks are at the aperture, their reflections have negligible effects on the S_{11} of the proposed dual-mode antenna, as compared to the case when the blocks are inside the waveguide structure at the discontinuity, which significantly deteriorates S_{11} to above −10 dB, over the entire frequency range of interest. For the proposed antenna S_{11} remains well below −15 dB, for all block lengths, including the zero value, which implies no block is present.

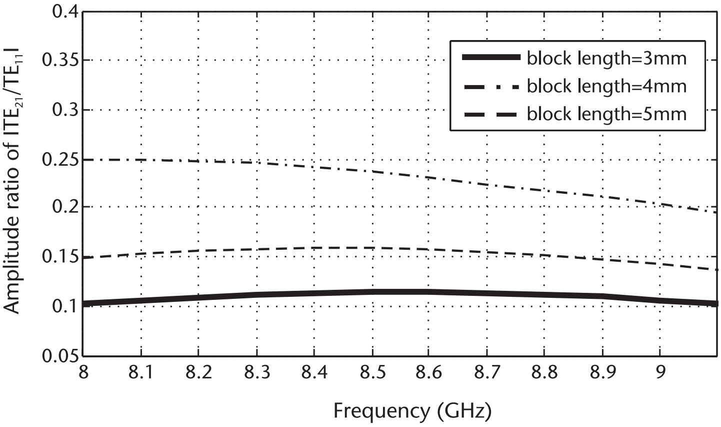

Figure 8.22 Effect of the block lengths on the amplitude ratio of TE_{21}/TE_{11} of Feed 2 versus frequency.

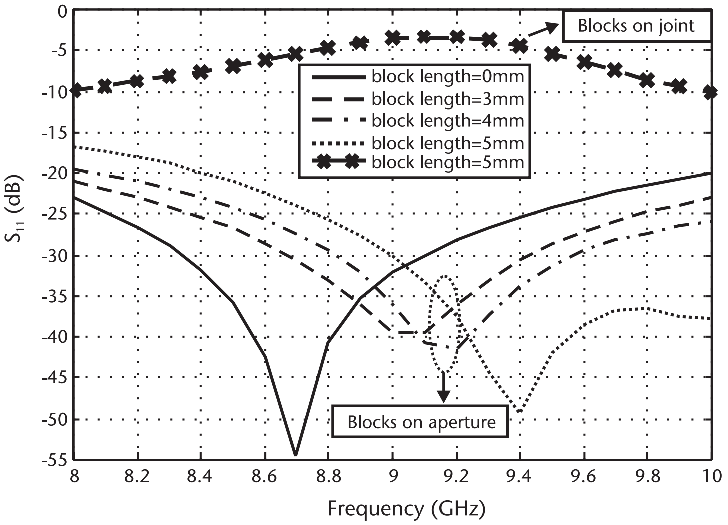

Figure 8.23 S_{11} of Feed 2 with different block lengths compared with the same antennas with no blocks and with 5 mm blocks placed right at the discontinuity joint.

The proposed dual-mode feed shown in Figure 8.21 is also used to illuminate the commercial elliptic-rim offset reflector of 36"× 27" and $F/D = 0.6$. The resulting reduced cross polarization levels versus frequency are shown in Figure 8.24 [19] at both the $\phi = 90°$ and 45° planes. They are well below –30 dB over the frequency range of 8.0–8.6 GHz. As an example, the secondary radiation patterns of the composite reflector and the proposed Feed 2 are plotted in Figure 8.25 [19] at the frequency of 8.3 GHz at both previously mentioned ϕ-planes. The cross polarization components are less than –35 dB and –42 dB at the inter-cardinal and asymmetry planes, respectively. This can be compared with the single TE_{11} mode feed case when the cross polarization components are in the order of –22 dB.

To verify the numerical results discussed, a prototype antenna was fabricated and tested. A photograph of the prototype antenna is shown in Figure 8.26. The measured co-polar and cross polarization far-field radiation patterns are plotted in

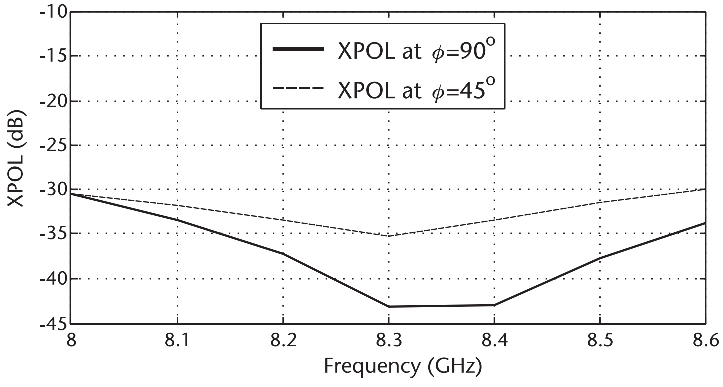

Figure 8.24 Reduced cross polarization levels at both $\phi = 90°$ and $\phi = 45°$ planes with the simulated primary Feed 2 illuminating the elliptical-rim offset reflector antenna.

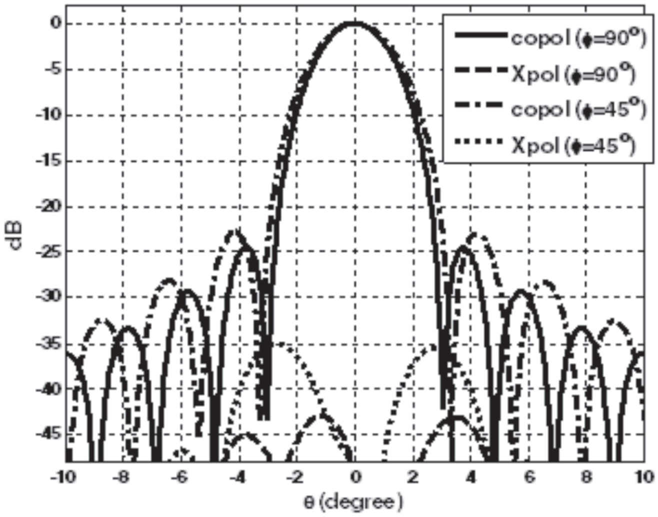

Figure 8.25 Normalized co-polar and cross polarization radiation patterns of the elliptical-rim offset reflector antenna fed by simulated Feed 2 at both $\phi = 90°$ and $\phi = 45°$ planes at $f = 8.3$ GHz.

Figure 8.27 at the start and end frequencies of interest, 8.0 and 9.0 GHz, when the length of the blocks is 4 mm. The measurement and simulated results agree quite satisfactorily with each other at both end frequencies. The measured S_{11} are shown in Figure 8.28(a) and compared with corresponding simulated ones, when the block length is 4 mm. They both follow almost the same trend and are well below −18 dB over the frequency range of 8.0–10.0 GHz. The measured co-polar and cross polarization radiation patterns of the compound reflector and the feed are shown in Figure 8.28(b) at the frequency of 8.43 GHz. The measured cross polarization is −30 dB, which is close to the cross polarization of the compact range in the anechoic chamber at this frequency.

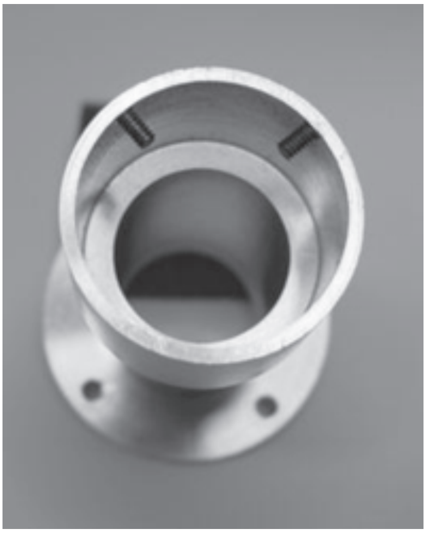

Figure 8.26 Photograph of the prototype Feed 2 (stepped waveguide with two tuning screws).

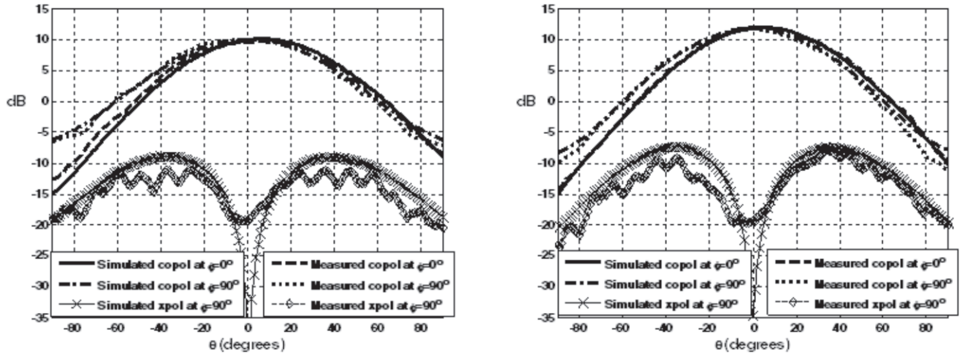

(a) (b)

Figure 8.27 Measured and simulated co-polar and cross-polar radiation patterns at the principal planes for Feed 2 with the block length of 4 mm. (a) $f = 8.0$ GHz, and (b) $f = 9.0$ GHz.

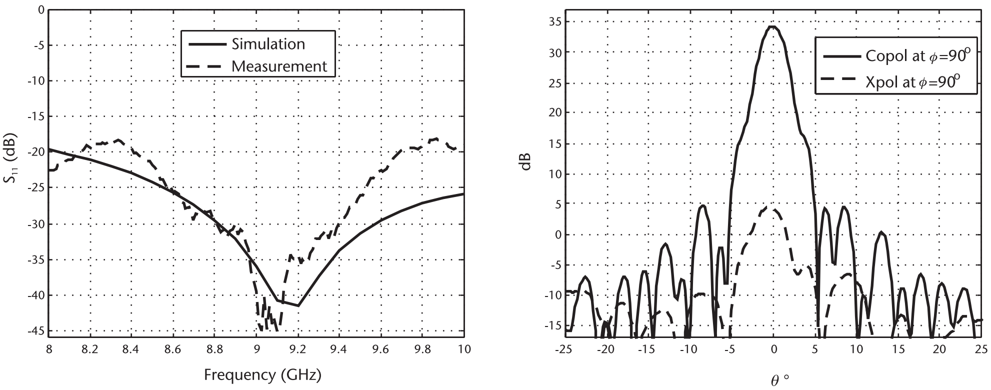

(a) (b)

Figure 8.28 (a) Measured and simulated S_{11} of Feed 2 with the block length of 4 mm, and (b) measured radiation patterns of the elliptic reflector and the Feed 2 at the $\phi = 90°$ plane and $f = 8.43$ GHz.

In this section, two separate asymmetric feeds were designed and used to investigate the cross polarization reduction in offset reflectors. These designs were aimed at using the case of *Example (b)*, in Section 8.1, the combination of the TE_{11} and TE_{21} modes. However, the higher order TE_{21} mode was not excited independently, and the feed performance was aimed at reducing the cross polarization. This meant the excitation of the TE_{21} mode was weak, just sufficient for cross polarization reduction. The case of strong higher order mode excitations, which leads to multiple phase centers at the reflector aperture, and formation of virtual arrays, is investigated in the next few sections.

8.4 Multiphase Center Reflector Antennas and Virtual Array Formation

Parabolic reflector antennas can be viewed as powerful devices capable of transforming a spherical wave, emanated from a point source located at their first focal point near the surface, into a plane wave at their second focal point at infinity. Interestingly, they can also be viewed as mathematical transform operators, based on the multiple Fourier transform and convolution operations, affecting the spatial distributions of their focal plane field [26], which may be carried out with signal processing functions. In this capacity, as shown in Section 8.1, their focal plane fields can be used to synthesize feeds with many desired radiation patterns, which then illuminate the reflector to generate aperture fields with multiple phase centers, with or without identical secondary reflector radiation patterns. The ability to control the mode excitations in the focal plane allows the control of the reflector aperture field and the location of the phase centers on the aperture. Thus, the reflector can be converted into an equivalent of a virtual array with multiple elements, with controllable parameters. A case of particular interest is when the resulting aperture distributions are made identical, to generate identical reflector radiation patterns, and thus form a uniform array [26, 27]. One application of such an array is in ground moving target indicator (GMTI) radars to adaptively suppress the stationary clutter from the signal [28]. In a traditional approach, multiple identical antennas were used to generate identical main beams at the far-field region with physically separated phase center locations due to each antenna. This, of course, increases the size and cost of the antenna system. Instead, a smart alternative is a single reflector with multiple phase center locations, which is normally preferred. In the following sections, we briefly describe the concept and investigate two possible feed designs for such a system implementation. Numerical results are provided to aid in understanding the process. More results are provided in Chapter 4 of Volume I.

8.4.1 The Concept Theory

In conventional applications, reflector antennas are used to generate high gains with low cross polarizations and low sidelobes. In this mode of operation, the reflector is illuminated by a feed with symmetric radiation patterns and a unique phase center that coincides with the reflector focal point [3, 10]. However, this need not be the case. A reflector antenna can also be viewed as an aperture antenna [8, 10], which re-radiates the feed power incident on its surface. For a symmetric reflector, the aperture is defined by its rim. However, in general, by neglecting the diffracted rays, the reflector aperture may be defined by a surface perpendicular to the reflected rays and bound by their cross section, regardless of the reflector geometry and direction of radiation. In such a case, if the aperture field distribution is symmetric, then the reflector phase center will be at the geometric center of its aperture. For asymmetric aperture field distributions, the phase center will not be at its geometric center, but it will be located near the peak field intensity. Its exact location will depend on the angular location and extent of the far-field wave front, over which the phase center is to be determined [3]. Herein, the reflector phase center will be determined by the wave fronts over an angular region around the main beam. In the following sections, the concept is applied to a symmetric paraboloid reflector antenna, since its geometry is symmetric and the location of its phase center, with a symmetric feed, is predictable (that is, it is on the reflector axis). Then, the feed radiation is made asymmetric by adding higher order modes, and shown that the reflector phase center moves away from its geometric center. The simulations are carried out using the finite-element method software HFSS [21] for the feed horn and the physical optics, geometrical optics, and geometrical theory of diffraction software GRASP [20] for reflector antennas.

8.4.2 Symmetrical-Cut Paraboloids [26]

In a symmetric reflector configuration, if the focal region field is due to a point source symmetric in the azimuthal direction, the reflector performs a conical transform generating a symmetric aperture field in azimuth and tapered radially, in accordance with the reflector curvature. The far field is the Fourier transform of the aperture field, which due to its symmetry results in a symmetric pencil beam. The main beam has an equivalent phase center at the physical center of the reflector aperture. A similar situation also holds for a vectorial field, such as that of a TE_{11} mode, where the aperture field maintains the focal field polarization, in addition to the field symmetry, thus retaining the far-field main beam phase center at the reflector aperture center. The situation is somewhat different for asymmetric fields, which can be represented by Fourier series of the azimuthal TE and TM modes, as shown in Section 8.1. Thus, by a judicial selection of the mode coefficients of the focal region field, one can cause desirable aperture field asymmetries and thus co-phasal asymmetric reflector aperture fields. However, since the reflector transforms its co-phasal aperture fields to axial far-field beams, these asymmetric aperture fields generate axial reflector beams, with physically different equivalent phase centers on the reflector aperture. The reflector aperture therefore becomes equivalent to multiple virtual planar arrays, centered individually at each equivalent phase center location. In practice, as shown in Section 8.1, one can synthesize the asymmetric focal region fields using azimuthal modes, employing waveguides, horns, or microstrips. Their analog or digital combination can simulate the virtual array that can be used as independent beams in signal processing algorithms. An example using TE_{11} and TE_{21} modes is given to generate a two-element virtual array case of *Example (b)* in Section 8.1. The array has two independent and widely separated phase centers, but identical far-field beams, similar to two planar arrays located centrally at the respective phase centers [26].

The geometry of a symmetric parabolic reflector is shown in Figure 8.29. It has an aperture diameter of $D = 50\lambda$ and $F/D = 0.375$ at 10 GHz. It is assumed that the focal region field is due to the combination of the TE_{11} and TE_{21} modes of circular waveguides. The corresponding aperture field distributions are illustrated in Figure 8.30 for different mode coefficients. When the excitation is due to the TE_{11} mode alone, Figure 8.30(a), the aperture field is symmetric as expected. For the combined dual-mode case, infinite possibilities can exist, but for simplicity, equal amplitudes for the modes are selected. As for their relative phase shifts, four different cases are considered: the in–phase case of $TE_{11} + TE_{21}$, out of phase case of $TE_{11} - TE_{21}$, and the two quadrature phase cases of $TE_{11} + jTE_{21}$ and $TE_{11} - jTE_{21}$. For the first two cases, the aperture field amplitudes are symmetric and identical, as shown in Figure 8.30(b). Their aperture phases are, however, asymmetric and cause main beam scanning at the far-field region, as depicted in Figure 8.31(a) and (b). The reflector aperture is therefore equivalent to two coincidental array elements with equal amplitudes and anti-symmetric phase distributions. The most interesting cases are

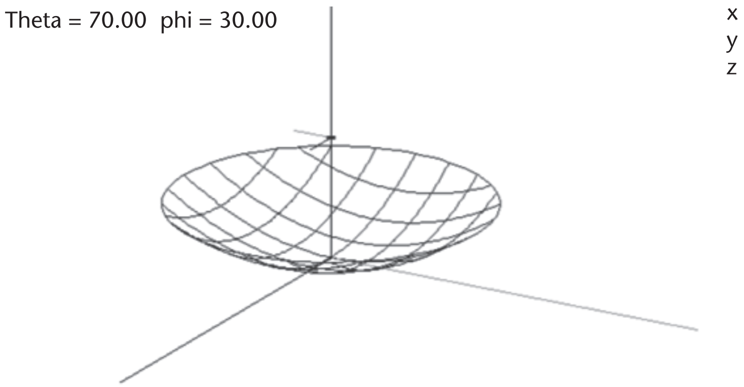

Figure 8.29 Symmetric parabolic reflector antenna geometry, $D = 50\lambda$ and $F/D = 0.375$. (©2004 IEICE [26].)

the last two, with quadrature relative phases according to the third and fourth cases. Their resulting aperture amplitude distributions are shown in Figure 8.30(c) and (d), having significant field values over only one half of the aperture, to the left or right. These distributions are similar to the TE_{11} mode, but shifted to the left or right of the aperture center. Their far-field patterns are also similar to that of the TE_{11} mode, as shown in Figure 8.31(c), with slightly lower gains, due to the reduced aperture sizes. These two excitations are thus equivalent to a two-element array, having elements

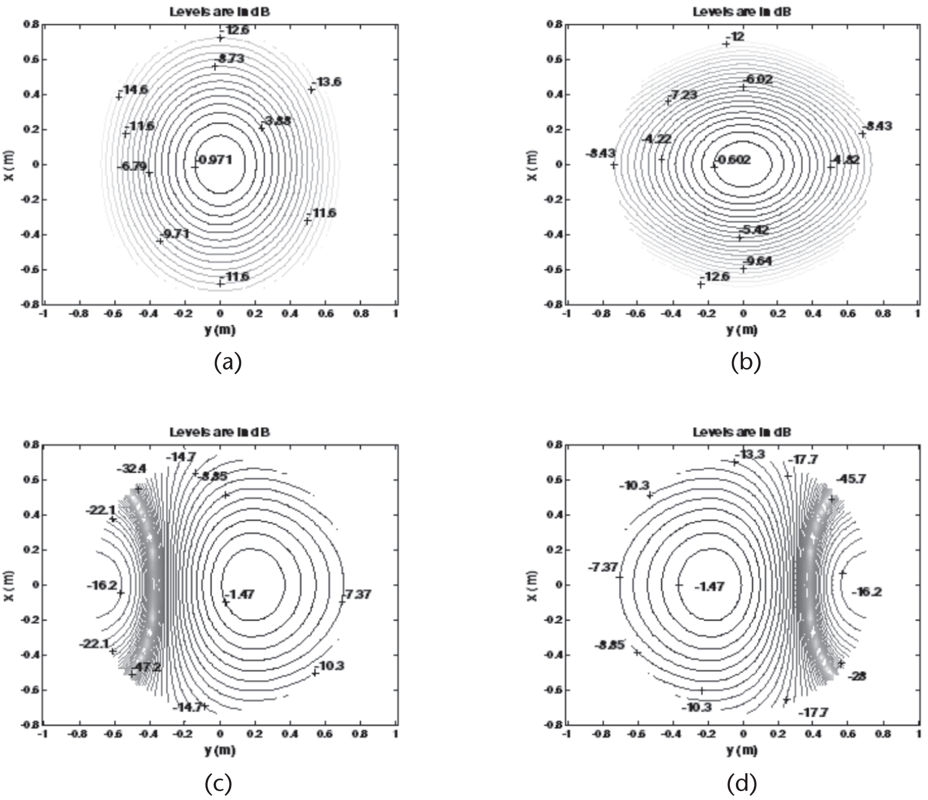

(a) (b)

(c) (d)

Figure 8.30 Reflector aperture field distributions due to. (a) TE_{11} mode alone, (b) $TE_{11} \pm TE_{21}$, (c) $TE_{11} + jTE_{21}$, and (d) $TE_{11} - jTE_{21}$.

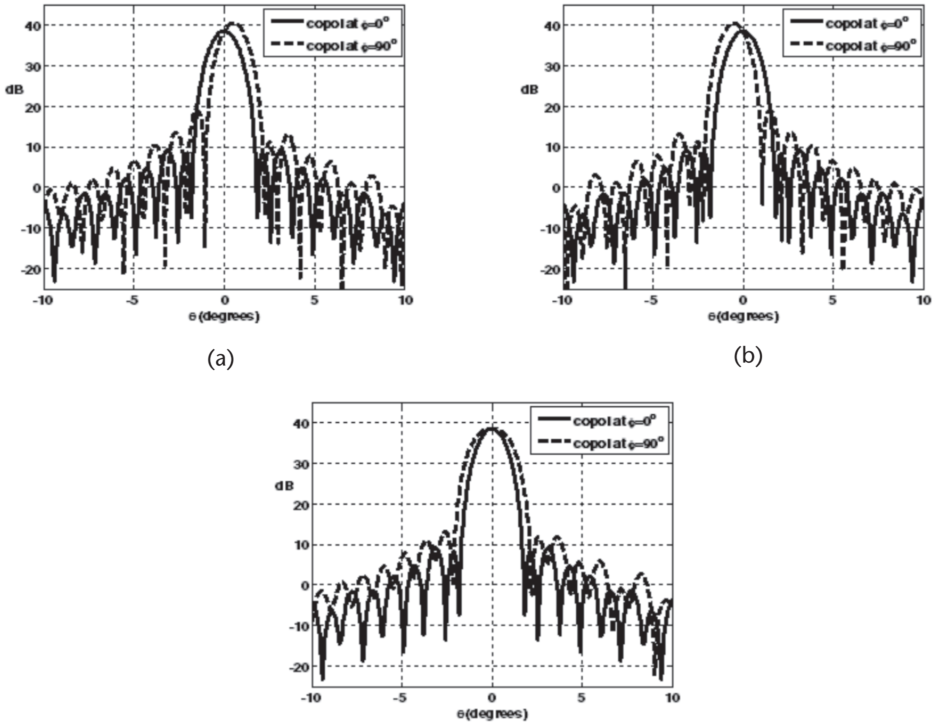

(a)

(b)

(c)

Figure 8.31 The principal plane secondary radiation patterns due to (a) $TE_{11} + TE_{21}$, (b) $TE_{11} - TE_{21}$, and (c) $TE_{11} \pm jTE_{21}$ ($\phi = 0°$).

occupying the left- or right-hand side of the reflector aperture. Their relative phase centers are therefore shifted to the left or right, near the centers of their field distributions. Because they generate far-field patterns, almost identical to the TE_{11} mode, but have distinctly different phase centers, they can be used together as elements of a virtual array. This possibility provides an opportunity for implementation of algorithmic signal processing in diverse applications, such as remote sensing or radar image processing. In the last two cases, the mode amplitude ratio influences the aperture distributions and phase center displacements. The resulting gains and phase center displacements are shown in Figure 8.32. With equal amplitude ratios, a maximum phase center displacement of ±21.50 cm was achieved by changing the phase difference between the modes. Thus, the maximum phase center separation of the last two distributions is equal to 43 cm, a significant distance, without causing any grating lobe formations [26]. The results can be readily extended to offset reflector antenna with the combined azimuthal modes of the TE_{11} and TM_{01} modes [27], discussed in the following section.

8.4.3 Adaptive Asymmetric Feed Designs for Multiphase Center Applications

In Section 8.4.2, the idea of multiphase center virtual array antennas was explained. It was shown that a single aperture antenna, illuminated by a multimode adaptive

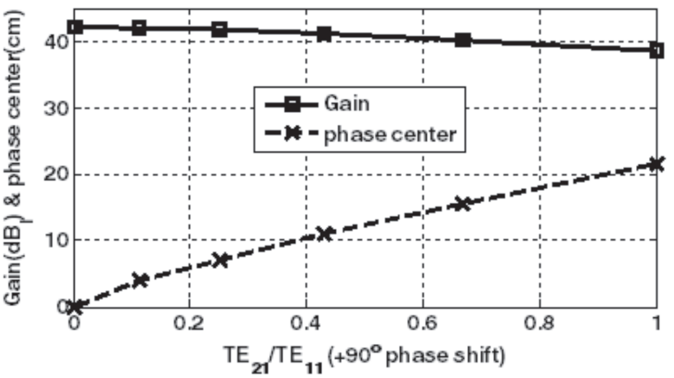

Figure 8.32 Effect of TE_{11} and TE_{21} mode amplitude ratios with +90° phase shift between the modes on the phase center displacement and gain.

feed, can provide multiphase center locations over the aperture. The idea is based on shifting the effective aperture illumination intensities away from the physical center of the aperture geometry. To this end, the primary feed must asymmetrically illuminate the aperture while its effective phase center location coincides with the focal point of the reflecting surface. Multimode feeds are the best candidates for such adaptive feeds. It is the aim of this section to introduce one such feed and address its adaptive functionality.

8.4.4 Feed 3: Adaptive Dual-mode TE_{11} and TE_{21} Feed [29]

This feed is a dual-mode feed operating at the TE_{11} and TE_{21} modes, which is the case of *Example (b)* in Section 8.1. It consists of a circular waveguide, which is tapered near the aperture to meet the edge illumination requirement of the reflector. The feed horn with the combined TE_{11} and TE_{21} modes is expected to generate multiphase center locations on the reflector aperture. The geometry for the tapered dual-mode horn antenna is shown in Figure 8.33. The desired frequency band is 9.25–10.25 GHz. The design consists of a main circular waveguide of diameter, $D_{cw} = 0.864\lambda = 26.60$ mm, where λ is the free-space wavelength at the center frequency of 9.75 GHz. The circular horn of diameter D_{ch} is separated from the main waveguide by a tapered section of waveguide. This tapering from the main circular waveguide to the circular horn permits the propagation of the additional secondary modes. The selection of the circular horn diameter D_{ch} depends on the requirement that both TE_{11} and TE_{21} mode can propagate but the next higher order mode cannot. To meet the first requirement, the diameter should be larger than the cut-off diameter supporting the propagation of the TE_{21} mode, $D_{ch} > 0.972\lambda = 31.53$ mm at the lowest end of the frequency band, 9.25 GHz. Similarly, the second requirement is that the horn diameter should not support the propagation of the zero-order mode $D_{ch} < 1.22\lambda = 40$ mm at the lowest end of frequency band, 9.25 GHz. Extensive simulations were carried out and $D_{ch} = 34.00$ mm was selected for the design. The total horn length was 121.50 mm. For exciting the TE_{21} mode inside the circular horn, two standard X-band waveguides are connected on the opposite direction of the circular waveguide in order to couple the TE_{21} mode only, and to reject the TE_{11} mode. To ensure this, the main waveguide is excited with an X-polarized TE_{11} field.

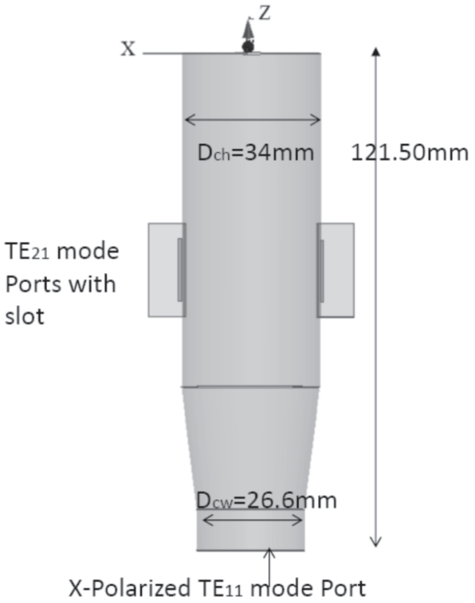

Figure 8.33 Geometry of Feed 3 exciting the TE_{11} and TE_{21} modes. (©2004 IEEE [29].)

The simulated scattering parameters of the three ports, shown in Figure 8.33, are illustrated in Figure 8.34. Figure 8.34(a) shows that Port 1, which corresponds to the TE_{11} mode, is very well impedance matched at better than –30 dB. Its coupling to Ports 2 and 3 are significantly low. Figure 8.34(b) shows that Ports 2 and 3, responsible for generating TE_{21} mode, are very well matched near the center frequency of the band but not at the band edges.

The feed shown in Figure 8.33 should be able to generate relatively pure mode when operating in a single-mode fashion. The corresponding primary radiation patterns of the feed at each mode are depicted in Figure 8.35 at the center frequency of 9.75 GHz. As shown in Figure 8.35(a), the feed generates symmetric patterns at its dominant TE_{11} mode, with a peak directivity of 10.40 dBi and cross polarization levels well below –40 dB. As for the higher order TE_{21} mode, Figure 8.35(b), the primary main beam has a null at the boresight direction, as expected. Its radiation patterns retain a good symmetry with cross polarization components well below –30 dB.

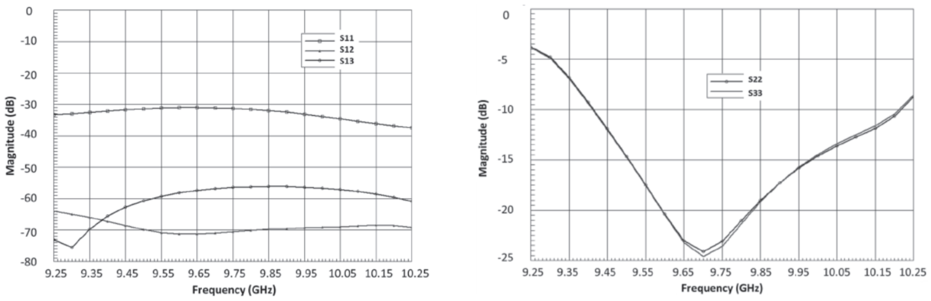

(a) (b)

Figure 8.34 (a) S_{11} of Port 1 and its coupling to other ports, and (b) S_{22} and S_{33} of Ports 2 and 3 of Feed 3. (©2004 IEEE [29].)

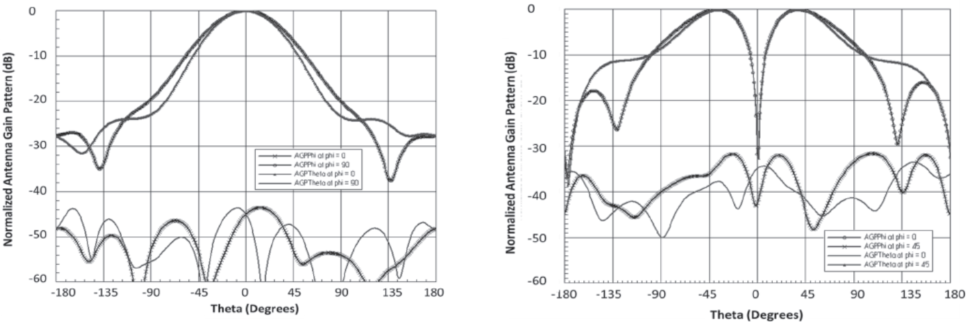

(a) (b)

Figure 8.35 (a) The TE$_{11}$ mode, (b) TE$_{21}$ mode principal radiation patterns of Feed 3 at 9.75 GHz. (©2004 IEEE [29].)

Now, in a dual-mode operation, the feed should be able to provide scanned main beam radiation patterns, at least in one of the ϕ-cut planes, in order to displace the phase center location of the reflector. This can be done by controlling the amplitude ratios of the mode with a quadrature phase difference between them. To show this, the mode power ratio of TE$_{11}$ (0.60/0°) + TE$_{21}$ (0.40/±90°) is selected. The corresponding dual-mode radiation patterns of the feed are shown in Figure 8.36 at the center frequency of 9.75 GHz. It is evident that the main beam of the H-plane patterns scans to $\theta = \pm 15°$, when there is a quadrature ±90° phase difference between the fundamental TE$_{11}$ and the higher order TE$_{21}$ modes. This will, in turn, shift the peak intensity of the reflector aperture distribution in one plane, and the resulting phase center location will thus move away from the center of the aperture accordingly.

Figure 8.37(a) illustrates the secondary phase patterns of the compound reflector and the feed for the above-mentioned mode power ratio after moving the coordinate origin to the new phase center locations. The selected reflector is an offset one, which has an F/D of 0.377, with a width of 101 cm, a height of 66 cm, and a focal length of 38.10 cm. Its offset distance is −13.53 cm. The phase center location displaces to $Y = +11.5$ cm and $Y = -11.5$ cm, when the phase shift between the modes is −90° and +90°, respectively. The constant phase beamwidth is around ±4°, which covers the secondary main beam angular range, as shown in Figure 8.37(b). As the phase center of the reflector moves away from its physical center, the far-field radiation

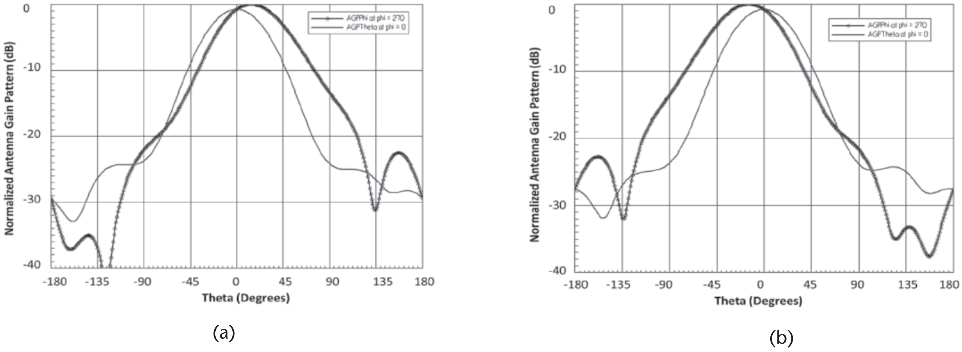

(a) (b)

Figure 8.36 The principal primary radiation patterns of Feed 3 as a dual-mode feed. (a) TE$_{11}$ (0.60/0°) + TE$_{21}$ (0.40/−90°), and (b) TE$_{11}$ (0.60/0°) + TE$_{21}$ (0.40/+90°) at 9.75 GHz. (©2004 IEEE [29].)

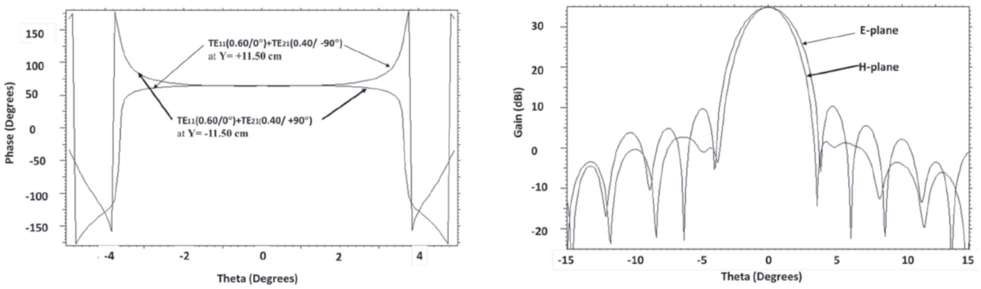

(a) (b)

Figure 8.37 (a) The constant secondary phase patterns, and (b) secondary radiation patterns of the offset reflector illuminated by Feed 3 with TE_{11} (0.60/0°) + TE_{21} (0.40/±90°) at 9.75 GHz. (©2004 IEEE [29].)

patterns have a broadside shape and are identical, which is required for uniform virtual array antenna applications.

In this section, the case of *Example (b)* in Section 8.1 was investigated. A feed for operation in both TE_{11} and TE_{21} modes was designed and used in a reflector antenna to investigate its performance. It was shown that for equal phasing of the modes, the reflector aperture had a single-phase center and generated a single beam. For quadrature phasing of the two modes, however, two separate phase centers could be obtained, which translated the reflector antenna into a two-element array. Since this array is made by a single hardware, it is therefore a virtual array. The advantage of such a virtual array is in the fact that its inter-element spacing, the separation of the reflector phase centers, could be controlled by the mode excitation ratio, or simply by changing the phase shift between the modes, which is a more convenient approach. Note that additional phase centers can also be generated, but the details are omitted here for brevity. Similarly, the results can be extended to other polarizations.

8.4.5 Feed 4: Adaptive Dual-mode TE_{11} and TM_{01} Feed [30]

In this section, another dual-mode feed is presented that generates the TE_{11} and TM_{01} modes inside a circular waveguide feed, which is the case of *Example (c)* in Section 8.1. The geometry of the proposed feed horn is shown in Figure 8.38(a). The frequency band of investigation is from 9.25 to 10.25 GHz. It consists of a main circular waveguide and horn. The waveguide has a diameter of 0.85λ, where λ is the free-space wavelength at the center frequency of 9.75 GHz. The circular horn diameter is 1.10λ and is separated from the waveguide by a tapered section. The total horn length is $L = 4.03\lambda$. The TM_{01} mode is excited from the bottom by using a symmetrically placed 50Ω *N*-type coaxial connector, which generates an axially symmetric electric field distribution. The coaxial probe's center conductor is connected to a symmetric bi-cone type solid metallic configuration, as shown in Figure 8.38(a), and is symmetrically placed inside the circular horn. The TE_{11} mode is excited with an *X*-band rectangular waveguide, attached to the circular waveguide from the side. The return loss of the feed horn, for both TE_{11} and TM_{01} modes, is shown in Figure 8.38(b).

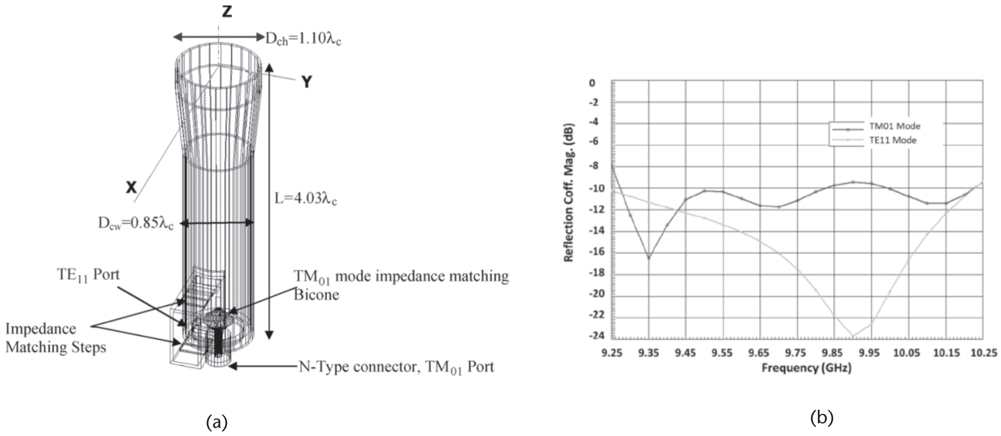
Z
D_{ch}=1.10λ_c
Y
X
L=4.03λ_c
D_{cw}=0.85λ_c
TE_{11} Port
TM_{01} mode impedance matching Bicone
Impedance Matching Steps
N-Type connector, TM_{01} Port
Reflection Coff. Mag. (dB)
0
-2
-4
-6
-8
-10
-12
-14
-16
-18
-20
-22
-24
9.25
9.35
9.45
9.55
9.65
9.75
9.85
9.95
10.05
10.15
10.25
Frequency (GHz)
TM01 Mode
TE11 Mode

(a) (b)

Figure 8.38 (a) Geometry of Feed 4 generating the TE_{11} and TM_{01} modes, and (b) corresponding return loss of its ports. (©2005 IEEE [30].)

In a single-mode operation, the radiation characteristics of each mode are shown in Figure 8.39 at the center frequency of 9.75 GHz. Figure 8.39(a) shows symmetric E- and H-plane radiation patterns for the TE_{11} mode with a cross polarization level less than –45 dB. However, the –10 dB beamwidth of the H-plane radiation pattern is narrower than that of E-plane. Figure 8.39(b) shows symmetric E- and H-plane radiation patterns for the TM_{01} mode with a split main beam as expected. Its cross polarization level is well below –35 dB. The radiation patterns for these modes within the band are almost invariant and hence are not shown.

Similar to Feed 3 in the preceding section, the quadrature phase shifts between the TE_{11} and TM_{01} modes are required in order to scan the primary main beam. The combined dual-mode radiation patterns of Feed 4 are shown in Figure 8.40, at the center frequency of 9.75 GHz, with an equal amplitude ratio for the modes and ±90° phase shifts between them. Figure 8.40(a) shows symmetric E-plane co-polarization radiation pattern for the $TE_{11}(0.50/0°) + TM_{01}(0.50/–90°)$ excitation. The H-plane co-polarization radiation pattern undergoes a beam shift of $\theta = +19°$. By changing the phase shift from –90° to +90°, the H-plane main beam scans to $\theta = –19°$. However, the E-plane beam always stays at the broadside angle, whereas H-plane retains the beam shift. For clarity, in Figure 8.41, a plot of the beam shifts for different TE_{11} and TM_{01} mode amplitudes, in the excitation $TE_{11}(0°) + TM_{01}(–90°)$, at 9.75 GHz are shown. Increasing the TM_{01} mode amplitude and, consequently, decreasing that of the TE_{11} mode results in an increased beam shift angle. Thus, different beam shifts can be achieved by controlling the relative mode amplitudes and phase values.

The preceding case will move the reflector phase center in the $\phi = 90°$ plane. The same offset reflector antenna, explained in the preceding section, is selected to conduct the study for virtual array applications. The reflector performance in terms of the phase center displacement and gain is shown in Figure 8.42, for different power contents of the TE_{11} and TM_{01} modes. As the TM_{01} mode power content increases, the phase center location moves away from the origin, while the gain drops. The TE_{11} and TM_{01} mode combination with 50% power content in each shows a gain

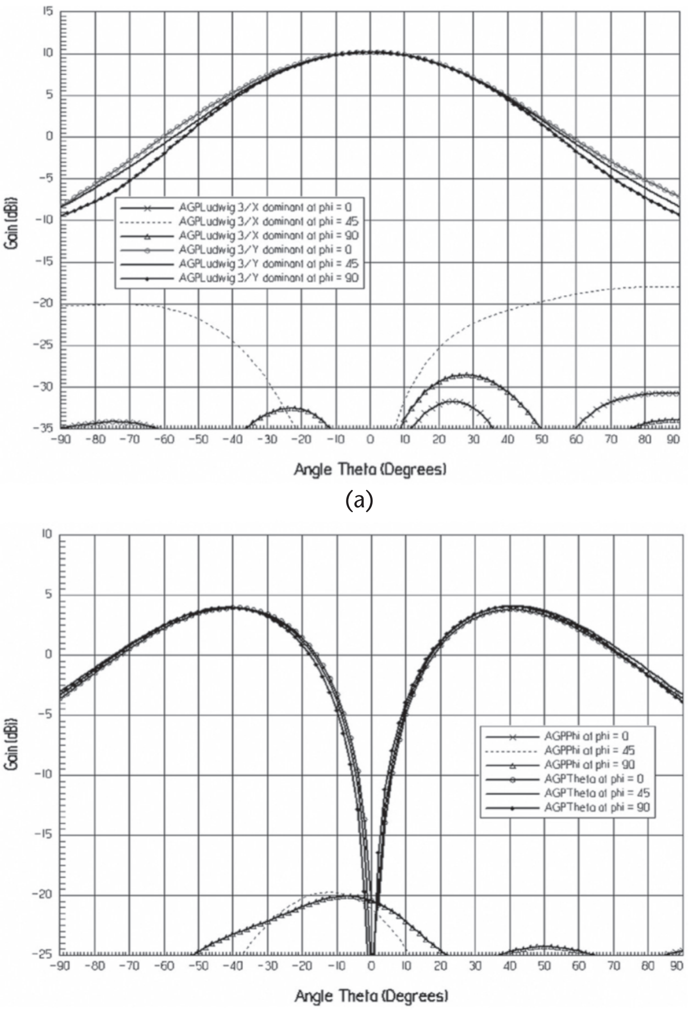

(a)

(b)

Figure 8.39 The principal plane radiation patterns of Feed 4 operating at a single mode of the (a) TE_{11}, and (b) TM_{01} modes at 9.75 GHz. (©2006 IEEE [27].)

of 34.10 dBi and phase center movement of $Y = 11.75$ cm. Also, by reversing the phase difference between the modes, a phase center movement in the opposite side will be observed.

Following the feed horn design, a prototype was fabricated and experimentally verified. The far-field radiation patterns of both TE_{11} and TM_{01} modes were measured in the Compact Range of the Antennas and Microwave Laboratory (AML) at the University of Manitoba and are shown in Figure 8.43(a) and (b), at 9.75 GHz. Figure 8.43(a), for the TE_{11} mode patterns in $\phi = 0°$, 45°, and 90° planes, shows a symmetric broadside radiation pattern, with a gain of around 10 dBi, and −10 dB beamwidth of 108°. Similarly, Figure 8.43(b), for the TM_{01} mode, shows symmetric radiation patterns, with a gain of around 5 dBi and null at the broadside. Since the horn length is small, the side feeding waveguide for the TE_{11} mode could not be fully covered and caused scattering that resulted in small undulation in the radiation

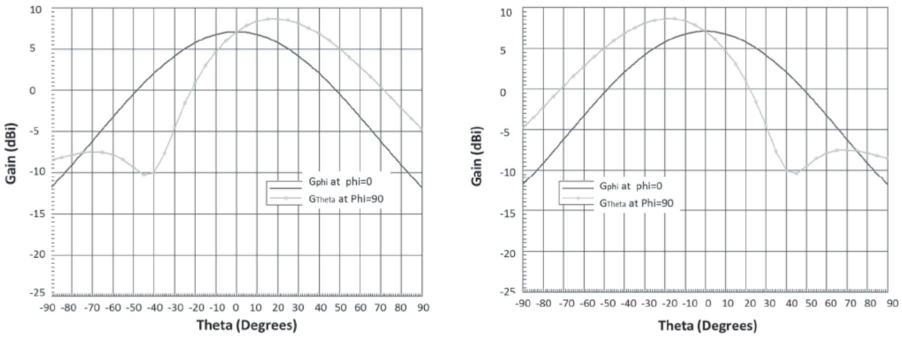

(a) (b)

Figure 8.40 The principal plane radiation patterns of Feed 4 operating at the combined TE_{11} and TM_{01} modes at 9.75 GHz. (a) TE_{11}(0.50/0°) + TM_{01}(0.50/–90°), and (b) TE_{11}(0.50/0°) + TM_{01}(0.50/+90°). (©2005 IEEE [30].)

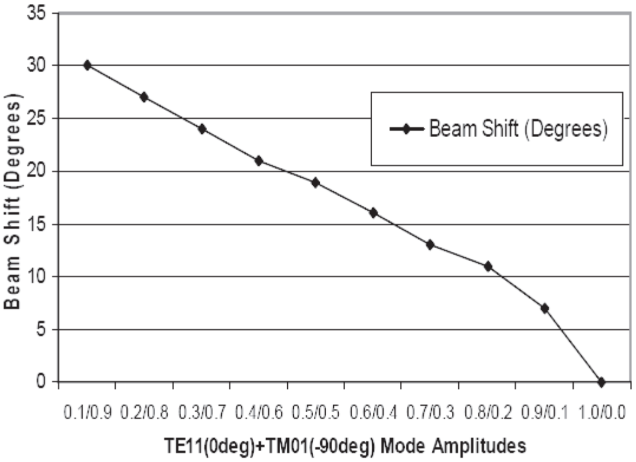

Figure 8.41 The beam shift in the $\phi = 90°$ plane for different TE_{11} and TM_{01} mode amplitudes. (©2006 IEEE [27].)

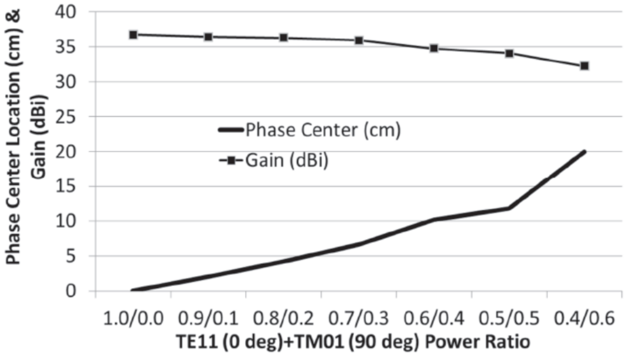

Figure 8.42 Variation of peak gain and phase center movement at $\phi = 90°$ plane versus the mode power contents in the TE_{11}(0°) + TM_{01}(+90°) phase combination at 9.75 GHz. (©2005 IEEE [30].)

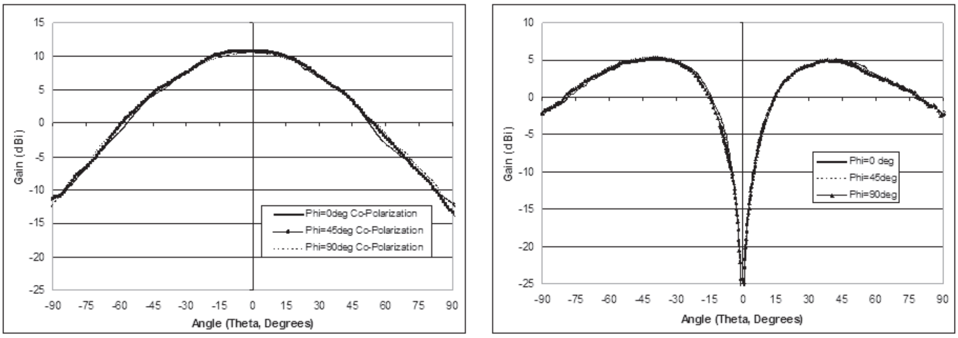

(a) (b)

Figure 8.43 Radiation patterns of the fabricated feed horn. (a) TE_{11} mode while the TM_{01} port is terminated in 50Ω, and (b) TM_{01} mode while the TE_{11} port is terminated in 50Ω. (©2006 IEEE [27].)

patterns. The near-field distribution of the feed horn was also measured in the Near-Field Chamber of the University of Manitoba for both excitations TE_{11}(0.50/0°) + TM_{01}(0.50/90°) and TE_{11}(0.50/0°) + TM_{01}(0.50/–90°). From the near-field data, the far-field amplitude contours were generated, which are shown in Figures 8.44(a) and (b). Figure 8.44(a), for the excitation TE_{11}(0.50/0°) + TM_{01}(0.50/–90°), shows that the far-field pattern is shifted to the left to about –20°, as expected from Figure 8.40(a). Figure 8.44(b) for the excitation TE_{11}(0.50/0°) + TM_{01}(0.50/90°) provides a similar beam shift but toward +20°. Thus, the feed radiation patterns for excitations TE_{11}(0.50/0°) + TM_{01}(0.50/90°) and TE_{11}(0.50/0°) + TM_{01}(0.50/–90°) are in agreement with the simulations. Again, the undulations, on the contour plots, are caused by scattering from the feed waveguide of the TE_{11} mode.

For the configuration presented, the performance of this feed, designed using the TE_{11} and TM_{01} modes, was very similar to that in the previous one, using the TE_{11} and TE_{21} modes. Of course, there are differences in their design parameters and performance in terms of the polarization and sidelobes. Their combination will result in the case of *Example (d)*, introduced in Section 8.1, where all three modes will be used. Such a feed will have more parameters and offer more flexibility in

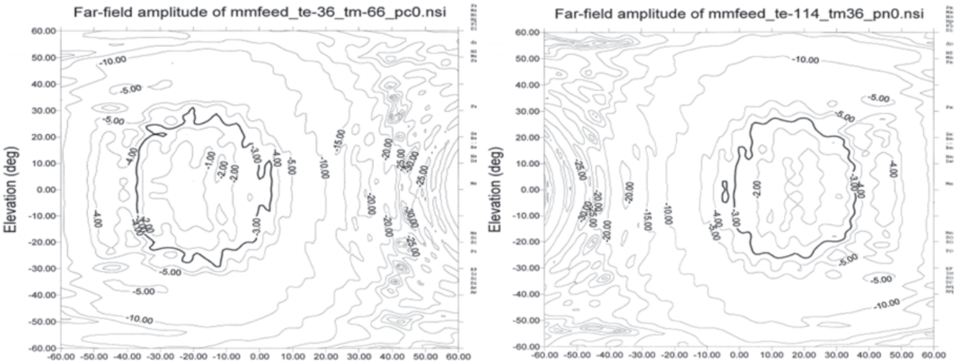

(a) (b)

Figure 8.44 Far-field amplitude contours of the feed horn with (a) mode excitations TE_{11}(0.50/0°) + TM_{01}(0.50/–90°), and (b) mode excitation TE_{11}(0.50/0°) + TM_{01}(0.50/+90°). (©2006 IEEE [27].)

controlling the reflector and the virtual array performance. It is presented in the following section.

8.4.6 Feed 5: Adaptive Triple-Mode $TE_{11} + TM_{01} + TE_{21}$ Feed [31]

This case corresponds to *Example (d)* of Section 8.1. The simulation model of the circular waveguide horn antenna is shown in Figure 8.45. The horn consists of two corrugations or chokes at the aperture of the triple mode horn such that it can illuminate a symmetrical parabolic reflector antenna of $F/D = 0.6$ with −10 dB edge illumination, when considering TE_{11} mode alone. Three circular waveguide sections were used to generate TE_{11}, TM_{01}, and TE_{21} modes. Their diameters are 1.34 cm for the TE_{11} mode, 1.53 cm for the TM_{01} mode, and 2.10 cm for the TE_{21} mode. The total length of the horn is 24 cm with an aperture diameter of 3.8 cm. The dominant TE_{11} mode is excited in the lowest section, which is fed using a single rectangular waveguide port, in the y-z plane. This section is coupled to another cylinder of relatively larger diameter supporting the TM_{01} mode and fed by using two horizontally orientated rectangular waveguide ports, placed spatially opposite to each other. In this case, the electric field in each of the rectangular waveguides will be along the axis of the horn. Since this mode is rotationally symmetric, the azimuthal location of its feeding waveguide is not important but may be selected orthogonal to the TE_{11} mode to minimize their coupling, that is, x-z plane. Another transition in the structure is made, from the middle section to the top most section, by another circular waveguide of even larger diameter, such that it supports the TE_{21} mode. This waveguide section too is fed by a pair of rectangular waveguide ports placed opposite to each other, but now the electric field in each of the rectangular waveguides are perpendicular to the axis of the horn. The feeding waveguides are in the same plane

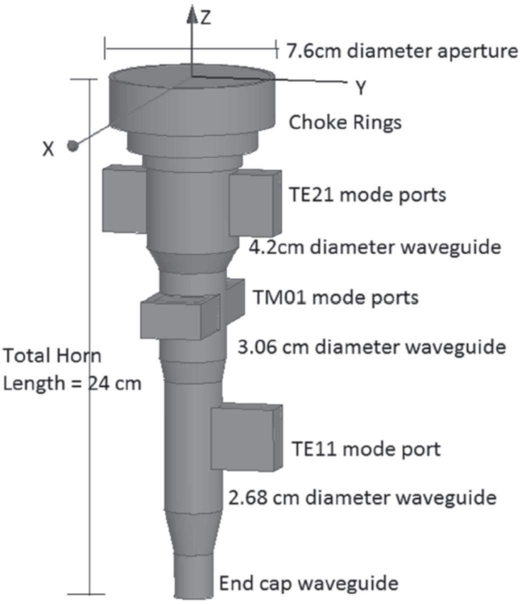

Figure 8.45 The triple mode circular waveguide horn showing TE_{11}, TM_{01}, and TE_{21} ports and respective diameters, all dimensions in cm. (©2010 IEEE [31].)

as that of the TE_{11} mode, that is, y-z plane. By combining the TE_{11} mode with the other two, in proper amplitudes and phase, arbitrary feed beam scan can be obtained. Their excitation can be selected to provide the required reflector aperture distributions to form the desired virtual arrays, with most desirable far-field patterns. This study can be done similar to the cases of Feed 3 and Feed 4. However, since in this case three Fourier modes are contributing to the radiation, the resulting far fields can be shaped with more accuracy.

The simulated return loss of the horn for all three modes (TE_{11}, TM_{01}, and TE_{21} modes) is shown in Figure 8.46. The TE_{11}, TM_{01}, and TE_{21} modes show impedance bandwidths ($S_{11} = -10$ dB) of 550 MHz, 720 MHz, and more than 1 GHz, respectively. However, they show a common frequency match bandwidth from 7.48–8.00 GHz. Their respective single-mode radiation patterns are shown in Figure 8.46(b), (c), and (d). Considering the symmetric characteristics of each mode, their radiation patterns show good isolation between the modes.

As indicated earlier, having an additional mode allows a better control of the phase center displacement and the reflector radiation patterns. Thus, the inter-element spacing of the virtual array elements and their radiation patterns can be controlled more accurately. The details have not been provided here.

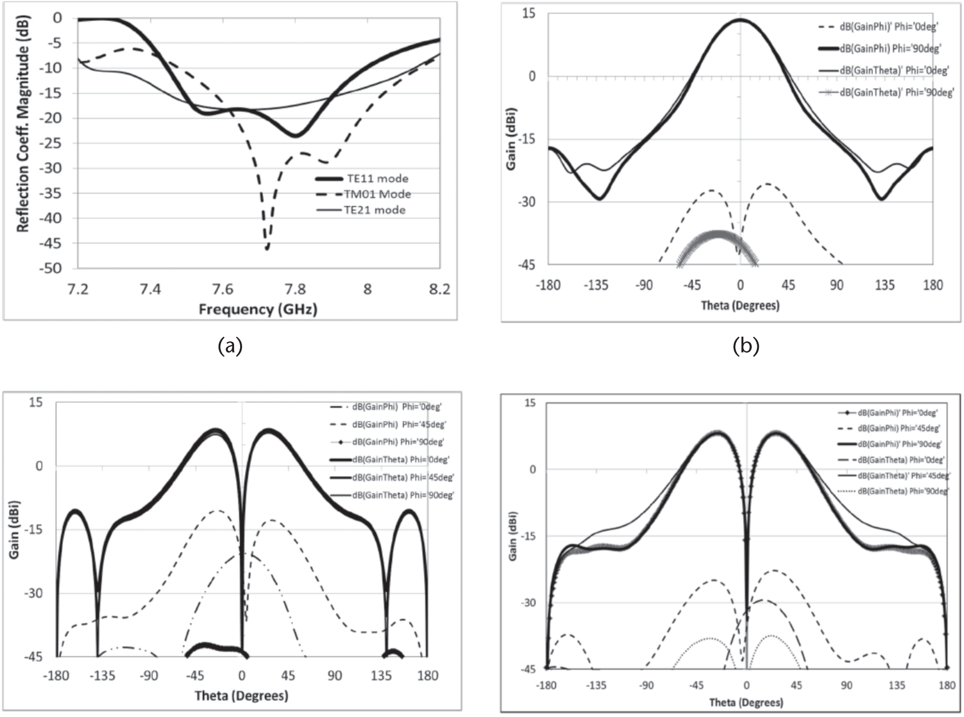

(a) (b)

(c) (d)

Figure 8.46 (a) Magnitude of reflection coefficient (S_{ii}, dB) vs. frequency (GHz) for the three modes, and radiation patterns at the center frequency of 7.73 GHz for (b) TE_{11} mode, (c) TM_{01} mode, and (d) TE_{21} mode. (©2010 IEEE [31].)

8.5 Concluding Remarks

This chapter discussed the use of a reflector antenna with more complex feed structures. It was shown that by expanding the focal plane field of the reflector in terms of orthogonal modes, the reflector antenna can be converted into more interesting devices. The simplest case was the high-gain antenna operation, traditionally used in practice. The more general case resulted in single or multiple phase centers on the reflector aperture, which could be used for clutter suppression, cross polarization reduction, and virtual array formations. Example feeds for polarization control and phase center displacements were presented and discussed.

References

[1] Minnett, H. C., and B. MacA. Thomas, "Fields in Image Space of Symmetric Focusing Reflectors," *Proc. of IEE*, Vol. 115, No. 10, October 1968, pp. 1419–1430.

[2] Bem, D. J., "Electric-field Distribution in the Focal Region of an Offset Paraboloid," *Proc. of IEE*, Vol. 116, No. 5, May 1969, pp. 679–684.

[3] Olver, A. D., P. J. B. Clarricoats, A. A. Kishk, and L. Shafai, *Microwave Horns and Feeds*, IEE Electromagnetic Waves Series, Vol. 39, London: Peter Peregrinus Ltd.,1994.

[4] Chu, T., and R. H. Turrin, "Depolarization Properties of Offset Reflector Antennas," *IEEE Trans. on Antennas and Propagation*, Vol. 21, No. 3, May 1973, pp. 339–345.

[5] Rudge, A. W., and N. A. Adatia, "New Class of Primary-feed Antennas for Use with Offset Parabolic-reflector Antennas," *Electron. Lett.*, Vol. 11, November 1975, pp. 597–599.

[6] Skolnik, M. L., *Radar Handbook*, 2nd ed., New York: McGraw-Hill, 1990.

[7] Muehe, C. E., and M. Labitt, "Displaced-Phase-Center Antenna Technique," *Lincoln Laboratory Journal*, Vol. 12, No. 2, 2000, pp. 281–296.

[8] Silver, S., *Microwave Antenna Theory and Design*, New York: McGraw-Hill, 1949.

[9] Jacobson, J., "On the Cross Polarization of Asymmetric Reflector Antennas for Satellite Applications," *IEEE Trans. on Antennas and Propagation*, Vol. 25, March 1977, pp. 276–283.

[10] Rudge, A. W., Milne, K., Olver, A. D., and Knight, P., *The Handbook of Antenna Design*, IEE Electromagnetic Waves Series 15, Vol. II, London: Peter Peregrinus Ltd., 1982.

[11] Wood, P. J., *Reflector Antenna Analysis and Design*, IEE Electromagnetic Waves Series 7, London: Peter Peregrinus Ltd.,1986.

[12] Balanis, C.A., *Antenna Theory and Design*, 3rd ed., New York: John Wiley, 2005.

[13] Kennaugh, E. M., and R. H. Ott, "'Fields in the Focal Region of a Parabolic Receiving Antenna," *IEEE Trans. on Antennas and Propagation*, Vol. 12, No. 3, 1964, pp. 376–377.

[14] Watson, W. H., "The Field Distribution in the Focal Plane of a Paraboloidal Reflector," *IEEE Trans. on Antennas and Propagation*, Vol. 12, No. 5, 1964, pp. 561–569.

[15] Potter, P. D., "A New Horn Antenna with Suppressed Sidelobes and Equal Beamwidths," *Microwave Journal*, 1963, pp. 71–78.

[16] Sharma, S. B., D. Pujara, S. B. Charabarty, and R. Dey, "Cross-Polarization Cancellation in an Offset Parabolic Reflector Antenna Using a Corrugated Matched Feed," *IEEE Antennas and Wireless Propagation Letters*, Vol. 8, 2009, pp. 861–864.

[17] Bahadori, K., and Y. Rahmat-Samii, "Back-to-back Reflector Antennas with Reducement of Inertia for Spacecraft Spinning Platforms," *IEEE Trans. on Antennas and Propagation*, Vol. 55, No. 10, October 2007, pp. 2654–2661.

[18] Bahadori, K., and Y. Rahmat-Samii, “Tri-mode Horn Feeds Revisited: Cross-Pol Reduction in Compact Offset Reflector Antennas,” *IEEE Trans. on Antennas and Propagation*, Vol. 57, No. 9, September 2009, pp. 2771–2775.

[19] Allahgholi Pour, Z., and L. Shafai, “A Simplified Feed Model for Investigating the Cross Polarization Reduction in Circular- and Elliptical-Rim Offset Reflector Antennas,” *IEEE Trans. on Antennas and Propagation*, Vol. 60, No. 3, March 2012, pp. 1261–1268.

[20] *TICRA’s GRASP 7.0 Software*, TICRA Engineering Consultants Læderstræde 34, DK-1201 Copenhagen, Denmark.

[21] *High Frequency Structure Simulator (HFSS)*, Boston: Ansoft Corporation.

[22] Allahgholi Pour, Z., and L. Shafai, “A Novel Dual Mode Circular Waveguide Horn Antenna,” *Proc. 2010 Int. Symposium on Antennas and Electromagnetics, ANTEM*, Ottawa, Canada, July 5–9, 2010.

[23] Allahgholi Pour, Z., and L. Shafai, “A Ring Choke Excited Compact Dual-mode Circular Waveguide for Offset Reflector Antennas,” *IEEE Trans. on Antennas and Propagation*, Vol. 60, No. 6, June 2012, pp. 3011–3015.

[24] Allahgholi Pour, Z., and L. Shafai, “A Novel Impedance Matched Mode Generator for Excitation of the TE_{21} Mode in Compact Dual-mode Circular Waveguide Feeds,” *IEEE Antenna and Wireless Propagation Letters*, Vol. 10, May 2011, pp. 427–430.

[25] Nagelberg, E. R., and J. Shefer, “Mode Conversion in Circular Waveguides,” *The Bell System Technical Journal*, September 1965, pp. 1321–1338.

[26] Shafai, L., and S. K. Sharma, “A Virtual Array Concept for Reflector Antenna Aperture,” *Proc. 2004 Int. Symposium on Antennas and Propagation*, Japan, August 17–21, 2004.

[27] Shafai, L., S. K. Sharma, B. Balaji, A. Damini, and G. Haslam, “Multiple Phase Center Performance of Reflector Antennas Using a Dual Mode Horn,” *IEEE Trans. on Antennas and Propagation*, Vol. 54, No. 11, November 2006, pp. 3407–3417.

[28] Damini, A., B. Balaji, L. Shafai, and G. Haslam, “Novel Multiple Phase Centre Reflector Antenna for GMTI Radar,” *IEE Proc. Microwaves, Antennas and Propagation*, Vol. 151, No. 3, June 2004, pp. 199–204.

[29] Sharma, S. K., L. Shafai, B. Balaji, A. Damini, and G. Haslam, “Performance of Multimode ($TE_{11} + TE_{21}$) Feed Horn for Offset Reflector Antenna Providing Multiphase Centres,” *Proc. 10th Int. Symposium on Antenna Technology and Applied Electromagnetics and URSI Conference*, Ottawa, Canada, July 2004, pp. 155–158.

[30] Sharma, S. K., L. Shafai, B. Balaji, A. Damini, and G. Haslam, “Multimode Feed Horn Providing Multiphase Centres with Offset Reflector Antenna,” *Proc. Antennas and Propagation Society International Symposium*, Vol. 3A, July 2005, pp. 355–358.

[31] Sharma, S. K., and A. Tuteja, “Investigations on a Triple Mode Waveguide Horn Capable of Providing Scanned Radiation Patterns,” *Proc. IEEE Int. Symposium on Antennas and Propagation*, Toronto, July 2010.

CHAPTER 9

Array Antennas and Low-Gain TT&C Antennas

Sudhakar Rao, Northrop Grumman
Francisco Mayol, RYMSA
Marta Padilla, RYMSA
Raj Sudarsanam, Consultant
Sebong Chun, Northrop Grumman

9.1 Introduction

This chapter covers array antennas and telemetry, tracking, and control (TT&C) antennas that are widely used in satellite communications. While the array antennas are used by themselves or as feed arrays for reflector antennas, the low-gain TT&C antennas are critical components of the antenna payloads and are part of any communication satellite together with reflector antennas. Practical design aspects of array antennas and design equations are presented. TT&C antennas are not covered in detail in any textbook and are included here in this volume for the first time. Design, RF performance, and hardware pictures are provided for the low-gain antennas.

This chapter is divided into two separate sections, array antennas and TT&C antennas. Array antennas have been extensively used for remote sensing, radar, aircraft, satellite communications, wireless, vehicular, and ground applications. The array antennas are very compact compared to reflector antennas but require complex beam-forming networks, large number of amplifiers, phase shifters, digital control units, and power electronics. They are attractive in applications requiring high gain, beam scan, beam shape reconfigurability, anti-jamming applications, and multiple beam capability. The advantage with arrays relative to reflectors is that they can provide multiple beams with a single aperture instead of multiple apertures. A number of satellite and aircraft payloads have flown array antennas at several frequency bands such as L-band, X-band, Ku-band, Ka-band, and EHF band on programs like GPS-2, WGS, Connexion, AEHF, and so on [1, 2].

The low gain TT&C antenna provides telemetry and telecommand functions for satellites when they are in the transfer orbit and also when the satellite is on orbit. During the transfer orbit, TT&C is the only communication link between the satellite and the ground and is very critical to proper functionality of the satellite. Once the satellite is on orbit, TT&C antennas provide data related to the heath of the satellite such as thermal and power monitoring to ground on a regular basis. The TT&C antenna system typically comprises a bi-conical antenna providing a toroidal pattern shape and a wide coverage horn that has cardioidal radiation pattern. Combination of these two antennas provides the required coverage during transfer orbit and during on-station. Global coverage horns are also used for other satellite functions such as on-orbit tests of satellite payloads and serving as beacons for a ground terminal.

9.2 Array Antennas

The array antennas can be classified into two categories: passive array antennas with fixed beam shape and phased array antennas with electronic beam scanning. Passive arrays employ high-level beam-forming network (BFN) to form the beam. The BFN is designed to provide desired amplitude and phase excitations to the array elements in order to shape the beam over the coverage region with required gain and side lobe levels. An advantage of the active phased array is that it provides beam scanning over the desired coverage with electronic phase shifters. Phased array also has low front-end losses since the beam forming is implemented at low level with printed circuit technology (stripline or microstrip media). However, it requires a large number of amplifiers (LNAs or SSPAs), phase shifters, attenuators, couplers for low-level BFN, digital controls, heat pipes, DC power units, connectors, and harness. The two types of arrays are illustrated in Figures 9.1 and 9.2 for receive function. The transmit arrays are similar to the receive arrays except that they have SSPAs/TWTAs instead of LNAs. Both types can be implemented for single or multiple beams. Phased arrays provide beam flexibility through the use of active components.

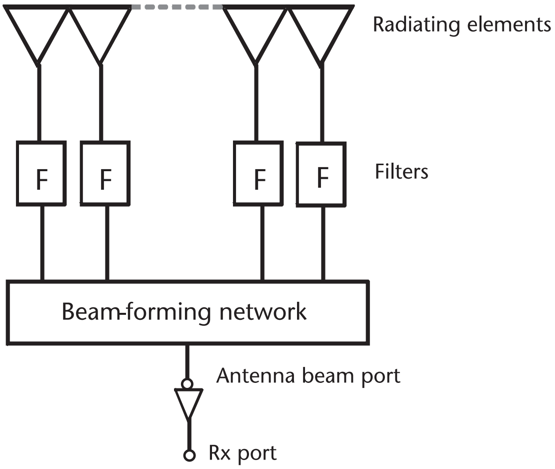

Figure 9.1 Passive array schematic of a receive antenna for single beam.

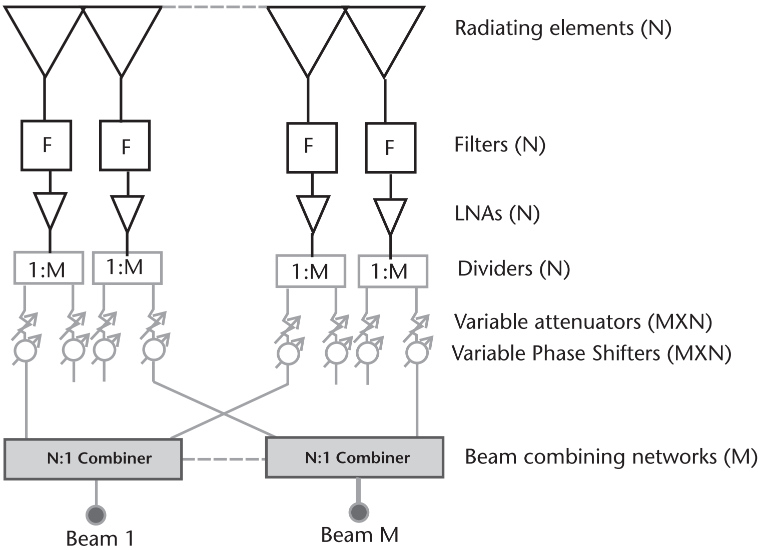
Radiating elements (N)
F
Filters (N)
LNAs (N)
1:M
Dividers (N)
Variable attenuators (MXN)
Variable Phase Shifters (MXN)
N:1 Combiner
Beam combining networks (M)
Beam 1
Beam M

Figure 9.2 Phased array schematic of a receive antenna for multiple beams.

9.2.1 Array Design

The array design depends on the antenna gain, beam width, and coverage requirements. Key design parameters are the radiating elements, lattice of the array, interelement spacing, and the number of elements. The array design is common to both types discussed in the previous section. Element spacing depends on the maximum scan angle or the maximum coverage angle, lattice type, and the highest frequency of operation.

Two types of array lattice that are widely used are square lattice and hexagonal lattice [3, 4]. Square lattice for a given maximum scan angle requires more elements than the hexagonal lattice. Figure 9.3 shows array layouts with square and hexagonal lattices. The advantage with hexagonal lattice is that the element spacing can be increased by about 15% compared to the square lattice for identical coverage/scan requirements with identical worst-case grating lobe locations. The increased element spacing of hexagonal lattice allows decreased number of elements and simplifies the back-end hardware (BFNs, LNAs, filters, and so on) for identical gain as the square lattice. The element spacings for the two lattice types are selected in order to satisfy the grating lobe free condition and are given as

$$\frac{d_s}{\lambda_h} \le \frac{1}{sin\theta_{sm} + sin\theta_G} \tag{9.1}$$

$$\frac{d_h}{\lambda_h} \le \frac{1.1547}{sin\theta_{sm} + sin\theta_G} \tag{9.2}$$

d_s and d_h in the above equations are the interelement spacing for the square and hexagonal lattice arrays, θ_{sm} is the maximum coverage/scan angle from the antenna boresight, θ_G is the location of the closest grating lobe, and λ_h is the wavelength at

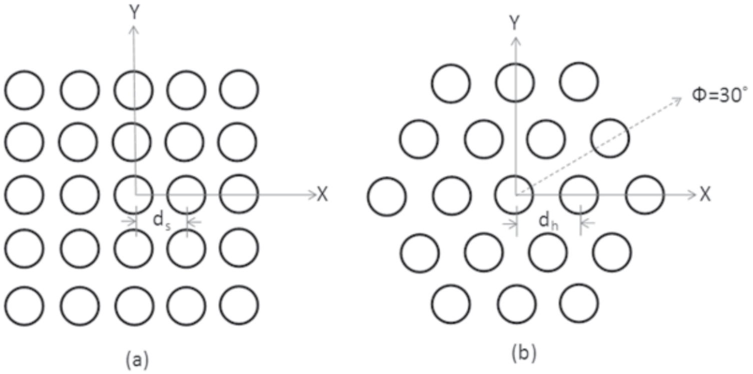

Figure 9.3 Array layout of elements using (a) square grid and (b) hexagonal grid.

the highest frequency of operation. The closest grating lobes occur in the Φ = 0° and 90° planes for the square lattice array and in the Φ = 30° and 90° planes for the hexagonal lattice array. The grating lobes occur in the opposite direction of the beam scan. The worst-case grating lobe location θ_G is typically selected such that it is larger than θ_{sm} in order to keep the side lobe levels of the grating lobes at angular location $-\theta_{sm}$ at least 15 dB lower than the peak gain. Table 9.1 shows the element spacing required for arrays with both lattices as a function of maximum scan angle. The grating lobe location is assumed slightly larger than the maximum scan angle and could be changed based on the requirements. It shows that for satellite applications, large element spacing of about 3.6λ could be used whereas for aircraft and radar applications requiring about 60° scan, small element spacing of about 0.66λ have to be used.

9.2.1.1 Array Design Example Using Square Lattice

A 42λ diameter array with 3λ interelement spacing is used in this example. The elements are arranged in a square grid layout, and the elements are arranged to fit close to a circular aperture shape. Circular aperture shape is preferred in most applications due to lower side lobe levels compared to a square aperture. There are 169 elements in the array as shown in Figure 9.4. Computed array patterns for square lattice array are shown in Figures 9.5–9.8 for boresight and scanned beams. Figure 9.5 shows the beam plot in the orthogonal θ, ϕ-planes showing the grating lobes for

Table 9.1 Element Spacing for Square and Hexagonal Lattices as a Function of Scan Angle

Θ_{sm}	Θ_G	d_s/λ	d_h/λ
5.0	6.0	5.22	6.02
8.7	9.7	3.13	3.61
15.0	16.0	1.87	2.16
30.0	32.0	0.97	1.12
45.0	47.0	0.70	0.80
60.0	65.0	0.56	0.66
70.0	75.0	0.52	0.61
80.0	85.0	0.50	0.58

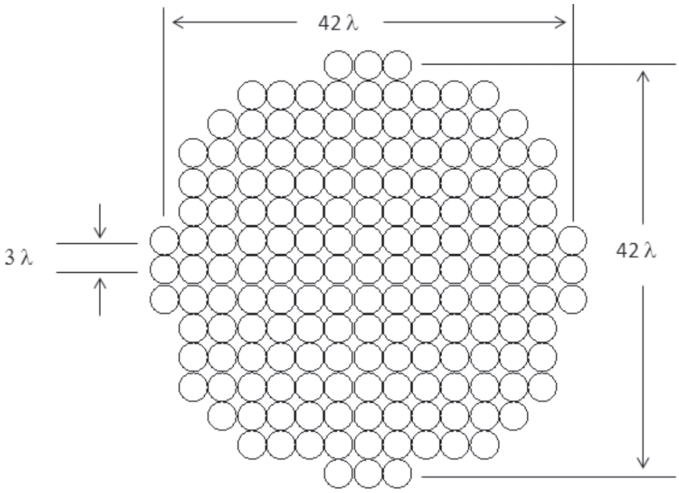

Figure 9.4 Planar array geometry with 169 elements arranged in square lattice.

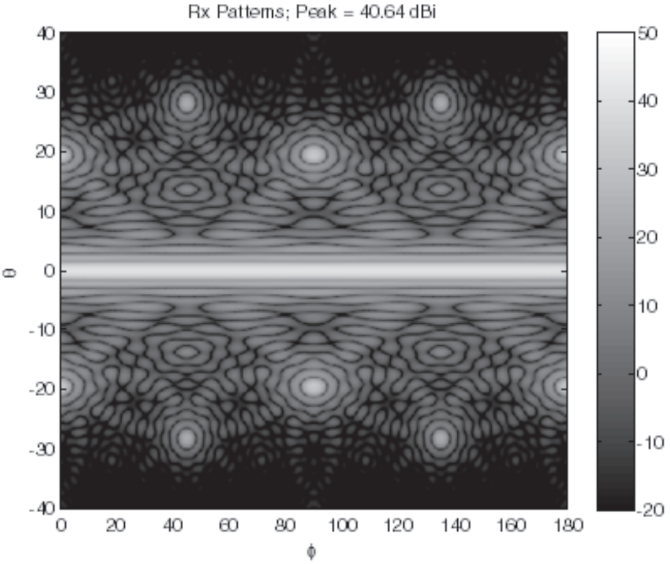

Figure 9.5 Computed patterns of boresight beam in the θ, ϕ-plane showing grating lobes for the array geometry in Figure 9.4.

various ϕ-cuts for the boresight beam with the worst-case grating lobes located in the $\phi = 0°$ and $\phi = 90°$ and at $\theta = 19.4°$. The directivity plot of the boresight beam as function of θ is shown in Figure 9.6, and the nearest grating lobe is at 19.4°. The grating lobe plot for the beam scanned to 9° and the corresponding directivity plot are shown in Figures 9.7 and 9.8, respectively. The scanned beam gain is 1.64 dB lower than the unscanned beam. This is the scan loss of the array, which is due to the element roll-off at 9° relative to peak element gain.

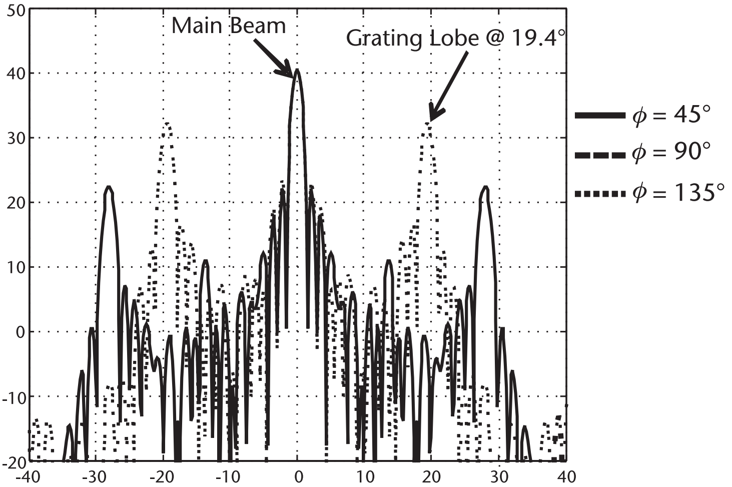

Figure 9.6 Computed directivity patterns of the boresight beam in $\phi = 0°$, 45°, and 90° planes showing for the array geometry in Figure 9.4. Closest grating lobe is at 19.4°.

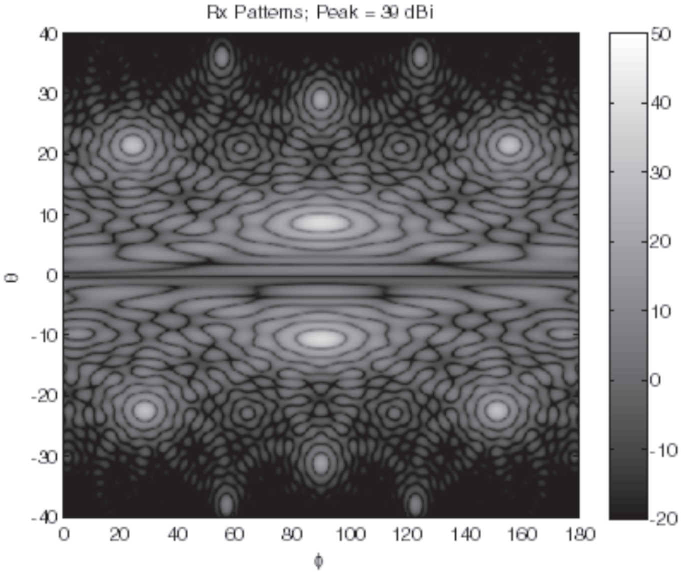

Figure 9.7 Computed patterns of scanned beam in the θ, ϕ-plane showing grating lobes for the array geometry in Figure 9.4.

9.2.1.2 Array Design Example Using Hexagonal Lattice

A $42\lambda \times 44.57\lambda$ array with 3λ interelement spacing is used in this example. The elements are arranged in a hexagonal grid layout, and the elements are arranged to fit close to a circular aperture shape. There are 169 elements in the array as shown in Figure 9.9. Computed array patterns for hexagonal lattice array are shown in Figures 9.10–9.13 for boresight and scanned beams. Figure 9.10 shows the beam plot in the orthogonal θ, ϕ-planes showing the grating lobes for various ϕ-cuts for

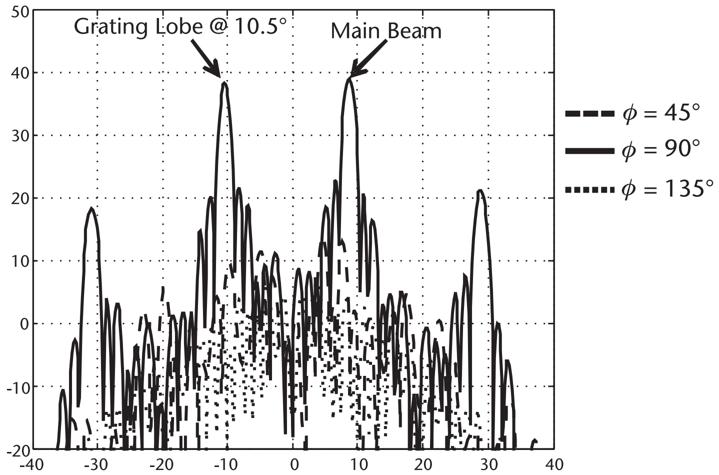

Figure 9.8 Computed directivity patterns of the scanned beam in the $\phi = 45°$, 90°, and 135° for the array geometry in Figure 9.4. Closest grating lobe is at 10.5°.

the boresight beam and demonstrating that the worst-case grating lobes are located in the $\phi = 0°$ and $\phi = 90°$ and occurs at 22.5° (19.4° with square lattice). The directivity plot of the boresight beam as function of θ is shown in Figure 9.11. Nearest grating lobe is at 22.5°. The grating lobe plot for the beam scanned to 9° and the corresponding directivity plot are shown in Figures 9.12 and 9.13, respectively. Scanned beam grating lobes are at 13.5°. The gain values are similar to the square array, but the advantage with the hexagonal lattice is that it allows increasing the element spacing by about 15% relative to the square array, which results in about 30% saving in the number of elements.

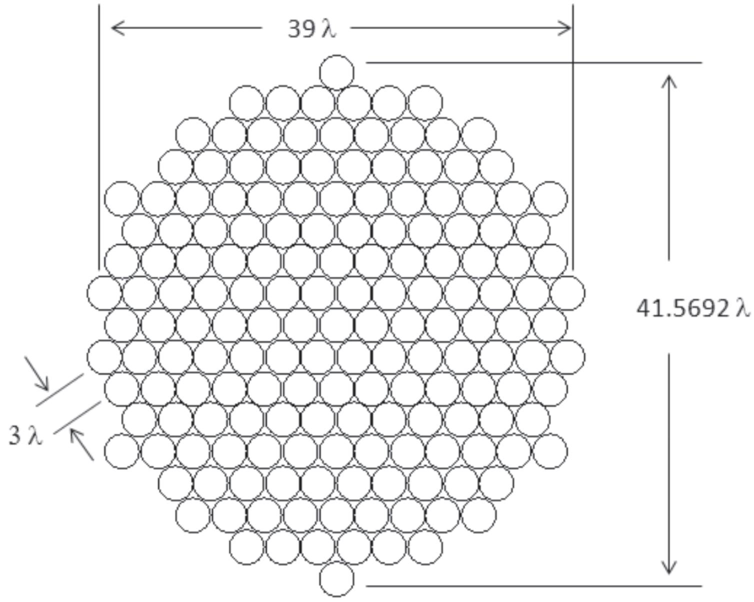

Figure 9.9 Planar array geometry with 169 elements arranged in a hexagonal lattice.

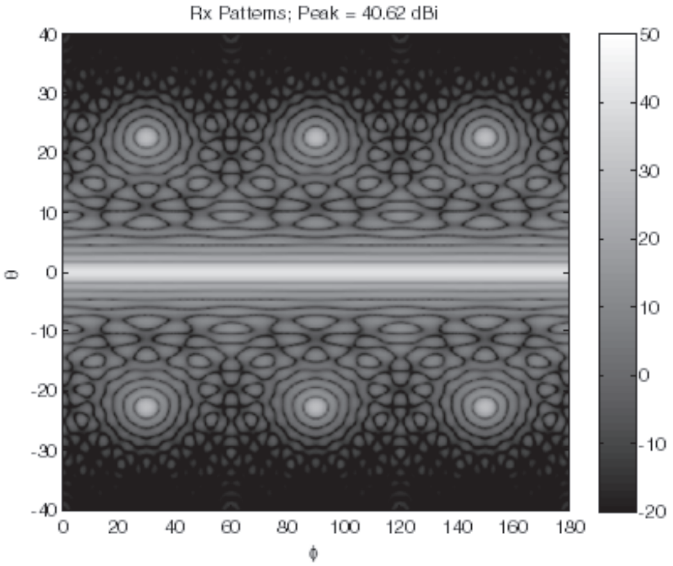

Figure 9.10 Computed patterns of boresight beam in the θ, ϕ-plane showing grating lobes for the array geometry in Figure 9.9.

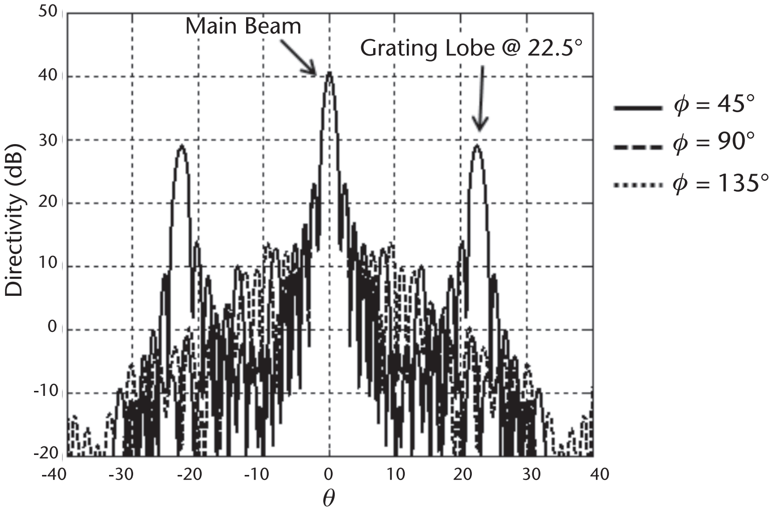

Figure 9.11 Computed directivity patterns of the boresight beam in $\phi = 0°$, 45°, and 90° planes showing for the array geometry in Figure 9.9. Closest grating lobe is at 22.5°.

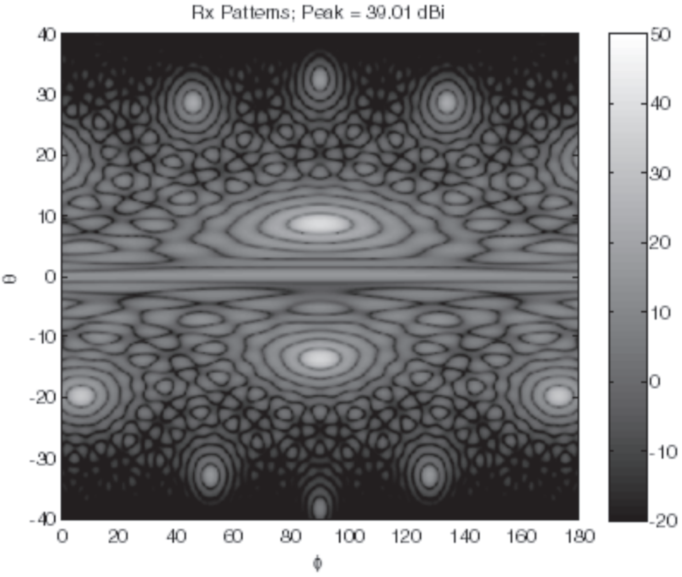

Figure 9.12 Computed patterns of scanned beam in the θ, ϕ-plane showing grating lobes for the array geometry in Figure 9.9.

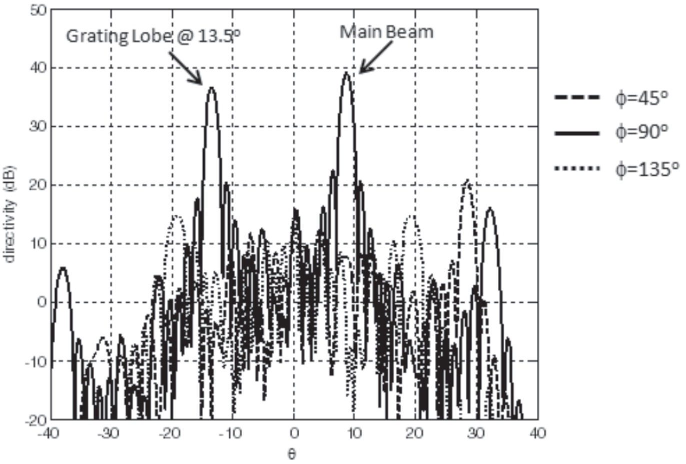

Figure 9.13 Computed directivity patterns of the scanned beam in the $\phi = 0°$, 45°, and 90° for the array geometry in Figure 9.9. Closest grating lobe is at 13.5°.

9.2.1.3 Number of Elements

The next design parameter is the number of elements. It depends on the minimum gain that the array needs to meet over the scan region. The array peak directivity at boresight is given by [5]:

$$D_p = 10\log_{10}(N) + 10\log_{10}\left[\eta_e \frac{4\pi A_e}{\lambda_l^2}\right] \tag{9.3}$$

The peak directivity D_p is in dBi and is the product of the element gain and the number of elements in the array. The parameters in (9.3) are the following: A_e is the unit cell area of the element, λ_l is the wavelength at the lowest frequency of operation, η_e is the element efficiency, and N is the number of elements in the array. The first tem on the right-hand side of (9.3) is the array factor, and the second term is the element directivity D_e. The number of elements can be calculated as

$$N = 10^{\left(0.1D_p - 0.1D_e\right)} \tag{9.4}$$

The peak directivity can be derived from the minimum gain requirement over the coverage region and is given as

$$D_p = G_{\min} + L_s + SL + GL_{pe} + T_L + X + I_m \tag{9.5}$$

where $G_{\min}$ is the minimum coverage gain of the array, L_s is the antenna loss that includes all front-end losses (from array aperture to amplifiers), mismatch losses, polarization losses, and so on, SL is the scan loss, GL_{pe} is the gain loss due to pointing error (satellite, aircraft, ground pointing error), T_L is the illumination taper loss of the array in dB, X is the beam overlap loss (3–4 dB for multiple overlapping beams and is 0 dB if only the beam peak is the requirement), and I_m is the implementation margin required for practical array antennas that include thermal effects, gain degradation due to amplifier failures, array excitation amplitude, and phase errors (typically about 0.5 dB). The scan loss depends only on the element and is given by the active element gain roll-off from beam peak to the maximum scan angle. The element roll-off for directive elements (>1.0λ typically used for satellites with small coverage regions or scans) is given as

$$SL = 3\left(\frac{\theta_{sm}}{0.5\theta_3}\right)^2 \tag{9.6}$$

where θ_{sm} is the maximum scan or coverage angle and θ_3 is the half power beamwidth of the radiating element, which is highly dependent on the type of radiating elements and is given by

$$\theta_3 = A\ (\lambda_h/d_e) \tag{9.7}$$

In (9.7), d_e is the element diameter and λ_h is the wavelength at highest frequency of operation, and A is the constant, which depends on the type of radiating element. A is 63 for high-efficiency multimode horn, 70 for Potter horn, 58 for cup-dipole radiating element, 55 for dominant mode square horn, and 52 for high-efficiency square or rectangular horn.

The scan loss for element sizes close to 0.5λ used for large scan applications is given as

$$SL = 10\ \log_{10}(\cos^n\theta) \tag{9.8}$$

The value of n varies and is typically in the range 1–1.5. For small elements a value of $n = 1.5$ in (9.8) better fits the element roll-off than the conventional $\cos(\theta)$ roll-off for practical antennas. For example, the scan loss is 2.26 dB for a 45° scan, 4.52 dB for a 60° scan, and 6.99 dB for a 70° scan.

9.2.1.4 Amplitude Taper

The array amplitude taper is one of the key critical parameters impacting the gain and the side lobe levels. The arrays are uniformly illuminated if low side lobes are not required. This is due the fact that BFN is simpler, and also all the distributed amplifiers for transmit arrays could have uniform size SSPAs. A tapered, illumination distribution lowers the side lobe levels but broadens the beam and lowers the antenna efficiency. A parabolic aperture distribution over a pedestal maximizes the antenna efficiency for a given side lobe level and is often used in practical arrays. The aperture field illumination function is defined as

$$E(r) = T + (1 - T)(1 - r^2)^n \tag{9.9}$$

where r is the normalized radius, T is the pedestal height at the edge of the array, and n is the shape factor. Edge illumination taper in dB is given as $20\ \log_{10}(T)$. The higher value the shape factor gives lower efficiency. Shape factor of $n = 1$ is generally used in practice. The efficiency value for $n = 1$ as a function of pedestal height T is given in closed form as

$$\eta = 75\frac{(1+T)^2}{(1+T+T^2)} \tag{9.10}$$

The efficiency value η in (9.10) is in percentage value. For example, a −5 dB edge taper ($T = 0.562$) gives an efficiency values of 97.4% and a −10 dB illumination taper ($T = 0.316$) provides an aperture efficiency of 91.7%. Gain loss due to −10 dB taper is only 0.38 dB. This has to be taken into account in array sizing. The amplitude taper across the array for different n values is shown in Figure 9.14. The efficiency value for shape factor $n = 1$ as a function of T is shown in Figure 9.15.

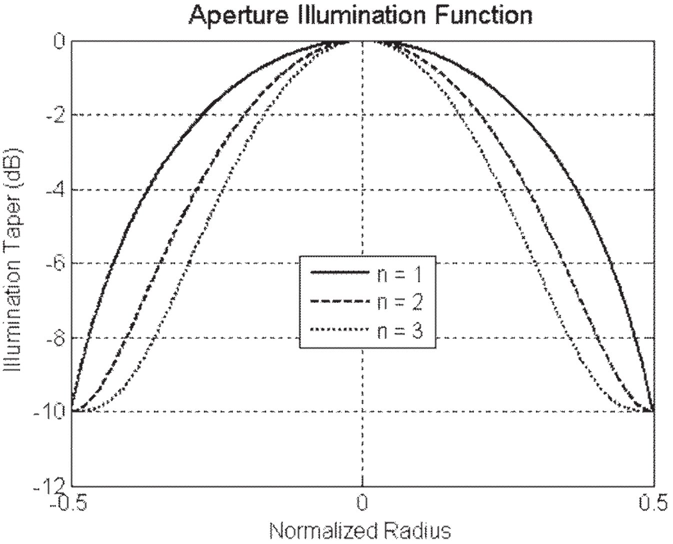

Figure 9.14 Plot of array illumination taper as a function of shape factor *n*.

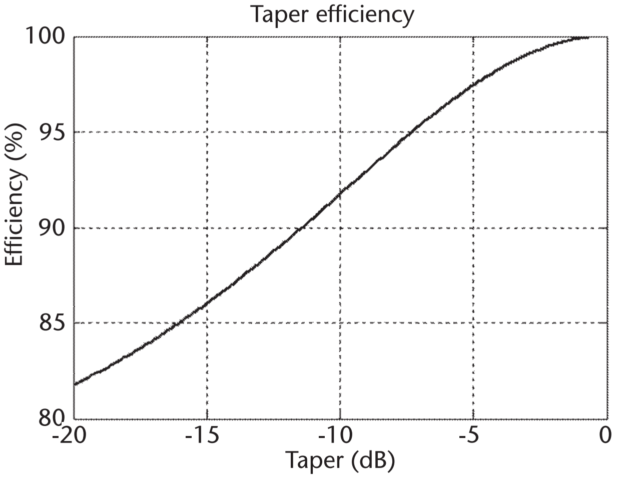

Figure 9.15 Plot of array efficiency as a function of illumination taper ($n = 1$).

9.2.2 Radiating Elements

The type of radiating element used for the array is the key design choice. It depends on several factors such as polarization, application, and percentage bandwidth, but the key factor is the scan/coverage requirements. For satellite applications where the maximum scan angle is 8.7° from boresight, the element size could be large and up to 3.6 wavelengths in diameter. For large scan applications, the element spacing is about 0.6 wavelengths or less. Antenna engineers tend to over-design arrays for large scan applications with spacing of 0.5 wavelengths or less, which increases the number of elements by 44% with significant impact on back-end electronics, which is not required. A brief description of the elements for array antennas is given here. Details of the radiating elements are discussed in other chapters of this book. The radiating elements for array antennas are classified into the following two categories:

- Low-scan array radiating elements;
- Large-scan radiating elements.

9.2.2.1 Low-Scan Array Radiating Elements

For low-scan array applications with scan angles of about 30°, the radiating elements suitable are waveguide type and are:

- Potter horns;
- Dominant mode circular horns;
- Multimode high-efficiency circular horns;
- Rectangular or square dominant mode horns;
- Cup-dipole radiating elements;
- Helical radiating elements.

Potter Horns

It employs TE_{11} and TM_{11} modes in order to create a tapered amplitude distribution in the E-plane of the horn. As a result, symmetric distribution is achieved in the two principal planes with low cross-polar levels. Minimum diameter of the horn required for Potter horn implementation is about 1.25λ. The half power beamwidth of a Potter horn is $70\lambda/d_e$ (d_e is the horn internal diameter) and has an efficiency of about 74%. Although Potter horns could be used for array antennas, they are not optimal due to the highly tapered aperture illumination. The tapered aperture illumination does not combine well in an array efficiently and hence is not used often for array applications.

Dominant Mode Circular Horns

Dominant mode TE_{11} circular horns have been used for limited satellite applications. They are simple to fabricate and are compact in size. Although the conical horns have about 30% bandwidth, low cross-polar radiation is obtainable over limited frequency range when the aperture diameter is in the range 1.10λ to 1.15λ. Another disadvantage is that it produces elliptical beam with principal plane E- and H-plane half-power beamwidths as

$$\theta_E = 60\left(\frac{\lambda}{d_m}\right) \tag{9.11}$$

$$\theta_H = 74\left(\frac{\lambda}{d_m}\right) \tag{9.12}$$

The antenna peak gain is a function of normalized phase error across the aperture S and is given as

$$G = 20\log_{10}\left(\frac{\pi d_m}{\lambda}\right) - 0.8 + 1.71S - 26.25S^2 + 17.79S^3 \qquad (9.13)$$

where $S = d_m^2/(8\lambda L)$ and L is the axial length of the horn from aperture to the apex of the horn.

Multimode High-Efficiency Circular Horns

These horns are widely used for satellite applications due to high efficiency combined with low cross-polar levels. They also have an advantage of supporting dual-band (transmit and receive) and multiband application [6, 7]. Typical efficiency values range from 84–92% depending on the bandwidth. The half-power beamwidth of the horns vary from 60–65λ/d_m depending on the efficiency. Details of the design and radiation characteristics of this horn are given in other chapters of this book.

Rectangular and Square Horns

Square horns are not suitable for hexagonal grid lattice, but could be used when the lattice angle among the three closest horns forming a triangle is changed to 63.43° instead of 60°, which is not optimal from the grating lobe aspect of the array design. Rectangular horns with an aperture aspect ratio of 0.866 can fit with the hexagonal lattice and are suitable for large element spacings since the cross-polar levels are very low. Multimode rectangular and square horns to increase the efficiency of these horns have been developed for array applications [8, 9].

Cup-Dipole Radiating Elements

Cup-dipole radiating elements are widely used for mobile satellites for LEO, MEO, and GEO applications as feeds for direct radiating array antenna or as feeds for large reflectors. The advantage of cup-dipoles is that they are very compact, have very high efficiency, and circular polarization can be generated without the need for polarizer. Disadvantages are narrow bandwidth limiting their use to UHF, L-band, and S-band arrays. The basic element comprises a crossed-dipole (CP) or a dipole (LP) exciting a circular cup. The cup-size is selected to support the dominant mode waveguide modes. The combined radiation is due to direct radiation from dipoles and the reflected radiation from the circular cup. The key parameters are the cup-diameter, the dipole-to-ground spacing, which is typically in the range 0.20–0.25λ depending on the cup-diameter, and the cup height, which is about 0.50λ. Circular apertures are preferred over square cups due to better off-axis cross-polar levels. Conventional cup-dipoles are used for cup-sizes of 1.2λ or less. For larger cup sizes, a splash-plate above the cup is required to illuminate the aperture more uniformly to realize high efficiency. This is also called short-backfire antenna. There are two types of coaxial feeding for cup-dipoles: (a) Single coaxial feed with unequal dipole lengths, feeding a slot in the 45° plane relative to dipoles. The slot excites the two dipoles with equal power and the desired phase quadrature required for CP generation is obtained by using unequal length dipoles. Bandwidth of this design is limited to about 4%. (b) Equal-length dipoles with hybrid coupler for CP generation. It requires two coaxial lines with balun and combined with a 3 dB hybrid coupler. Bandwidths of about 25% can be achieved with this design.

Helical Radiating Elements

Helical radiators are used for array applications requiring single sense of circular polarization (LHCP or RHCP). They are used for frequencies ranging from 100 MHz to Ku-band. The main advantages are wide bandwidths (about 50%), simple method for generating the circular polarization, and simpler structure allowing close packing of elements in the array. The helix radiator requires a ground plane for unidirectional patterns, which are often in the shape of a shallow cup. There are three modes for helix: normal mode, axial mode, and conical mode, but the axial mode helices are widely used. The circumference of the helix normalized with wavelength is about 1.1 for optimal gain with pitch angle of 12.8°. The length of the helix dictates the gain and is given as [10]

$$L = N.\, C \tan(\alpha) \tag{9.14}$$

where C, is the circumference of the helix (πD) and α is the pitch angle. The half-power beamwidth and the gain of the helix are given approximately as

$$\theta_3 = \frac{52}{\left(\frac{C}{\lambda}\right)\left(\frac{NS}{\lambda}\right)^{0.5}} \tag{9.15}$$

$$G(dBi) = 8.3\left(\frac{\pi D}{\lambda}\right)^{\sqrt{N+2}-1} \frac{(NS)^{0.8}}{\lambda}\left(\frac{\tan 12.5^0}{\tan\alpha}\right)^{\sqrt{N/2}} \tag{9.16}$$

The gain of the helical radiating element needs to be determined based on the interelement spacing satisfying the following equation:

$$G \le 10\log_{10}\left(\frac{\pi D_e}{\lambda}\right)^2 \tag{9.17}$$

Equation (9.17) ensures that the element gain does not exceed the 100% gain based on the interelement spacing of the array.

9.2.2.2 Large-Scan Array Elements

For large-scan applications of 45° or larger, the element spacing is electrically small and is in the range 0.5–0.8λ. For larger scans, waveguide type elements are not suitable since they do not support waveguide modes when the element spacing is close to 0.5λ.

Microstrip Patch Element

Microstrip patch radiating elements are often used for wide-scan applications. Square, rectangular, and circular patches are often used. Advantages are low profile, low cost, and ease of manufacturing. The disadvantages are narrow bandwidth and dielectric losses. The bandwidth of a single layered patch is given as

$$\mathrm{BW} \approx 128\, F^2 T \tag{9.18}$$

where BW is the bandwidth in MHz, F is the frequency in GHz, and T is the thickness of the substrate. T is typically less than 0.05λ in order to avoid the surface waves.

The feeding includes coaxial line, inset feeding, and slot feeding through the ground plane. The bandwidth of a single patch can be increased significantly to about 20% by using stacked patch configuration with a feed patch and an electromagnetically coupled patch on the top of the feed patch.

Slot Radiating Element

Slot radiators are also used for narrow-band applications. They are used in waveguides and also on dielectric boards. Both longitudinal and transverse slots have been used in waveguide media. Printed slots require another layer behind the ground plane for feeding the slots and combining them through stripline or microstrip networks. Details on slot radiators can be found in the literature [11].

Annular Ring-Slot Element

Annular ring etched on a microstrip substrate is a very compact radiating element applicable to wide-scan applications. The element is typically excited with a stripline or micro-stripline feed behind the ground plane [12]. This element can be used for single-linear, dual-linear, single-CP, or dual-CP applications. For wide-scan applications it is important to have several via holes shorts around the radiating ring and the feed lines. The shorted vias act like a metallic cavity preventing the higher order modes and surface wave propagation through the array.

Connected Element

A connected long-slot radiator, with periodic feeding by a connected dipole element with a ground plane in an array, has been reported by J. J. Lee et al. [13]. This element is the lowest weight radiator reported to date and is suitable for large arrays. In smaller array implementation (less than $8\lambda \times 8\lambda$), it suffers from large mismatch losses. This element also requires a balun to transform the 400 ohm array impedance to 50 ohm. The height of the radiator is compact and is about $0.29\lambda_c$ at center frequency. The long slot aperture is intrinsically wideband due to the fact that the slot elements support TEM modes with extremely low cut-off frequencies.

Flared Notch Element

The flared notch, which is also called as Vivaldi radiating element, has multi-octave bandwidth and wide scan capabilities [14]. It can support dual-orthogonal linear polarizations or dual-circular polarizations. The disadvantage with this element is that it is not compact and is typically $0.50–0.75\lambda_c$. Another disadvantage with this element is that it has high cross-polar levels in the nonprincipal planes of the element pattern.

Ridged Waveguide Element

Ridged waveguide elements are more compact than the flared notch elements. It is capable of operating over a wide frequency bandwidth ratio of greater than 4:1 and scan capability of about +/–45°. The H-plane dimension of the element restricts the scan capability due to appearance of grating lobes and limiting the low-frequency operation. By removing the sidewalls of the ridged waveguide, the cut-off frequency of the fundamental quasi-TEM mode, as well as the cut-off frequencies of the higher order modes, are significantly reduced, extending the bandwidth capability of this element. This element when used in an array results in a ridged parallel plate waveguide array [15, 16]. This element supports dual polarization when placed in an egg-crate structure with square lattice where top and bottom parallel plates are cut out to form the ridges of the element, as shown in Figure 9.16. Typical cross-polar levels of better than –15 dB (relative to peak co-polar gain) and VSWR of better than 2:1 are reported over +/–45° scan with this element in large arrays.

9.2.3 Array Radiation Patterns

The radiation properties of the arrays can be analyzed by several methods. The key parameter is the embedded or sometimes called an active element pattern. The finite-element method (FEM) can be used to characterize the element radiation in an array. FEM is a numerical procedure to obtain approximate solutions to boundary-value problems of mathematical physics. FEM is recognized as a generic method applicable to a wide variety of engineering and mathematical problems, including those in antenna and microwave engineering. A few examples of the successful commercial software packages based on FEM are HFSS, CST, and FEKO.

9.2.3.1 Infinite Array Modeling Using FEM in the Frequency Domain

An infinitely periodic structure with a uniform progressively phased excitation enables the numerical analysis to be confined to a single array element, or a unit cell. The standard FEM discretization is then applied to the defined unit cell. On the

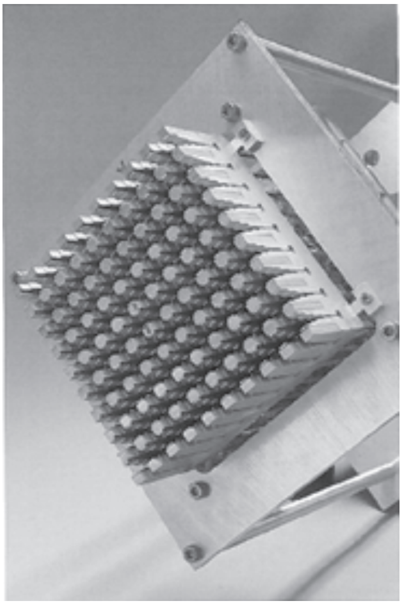

Figure 9.16 Ridged waveguide element array in an egg-crate structure for UWB applications [15].

boundaries of the unit cell, proper boundary conditions are imposed to correctly model the field behavior on both the periodic and radiation boundaries. When a phased array is analyzed in the frequency domain, each antenna element is excited by an individual source with a specific phase difference relative to the other sources, which results in a main beam being radiated in a desired direction. In order to steer the beam, the relative phase shift between the elements is changed such that the beam radiates in a new direction. An infinite antenna array can be analyzed using a single unit cell, where the field at one periodic surface of a unit cell is related to the field at the opposite parallel surface of the unit cell through a simple phase shift. This makes it straightforward to utilize a unit cell to numerically analyze infinitely periodic phased array antenna structures in the frequency domain. Since the array factor in the infinite array is the delta function, the peak gains of the array as a function of the scan angle are mainly due to the element pattern variation with the polar angles θ and ϕ.

9.2.3.2 Finite Array Modeling

Finite array modeling requires HFSS analysis of the complete array, which is time-consuming. Planar finite-sized arrays can be approximated by an infinite array (unit cell) model, in conjunction with array factor, even though such an analysis neglects the complicated edge truncation effects, which often are dealt with by expensive and time-consuming measurements. Typically, the element radiation pattern is calculated in an infinite array environment, and the array factor is calculated with two-dimensional FFT. All brute-force-type summing algorithm for array factor takes considerable amount of time so that it becomes impractical when the array becomes large or the analysis requires generating many events.

9.2.3.3 Element Pattern

The embedded element pattern for wide-scan applications is impacted by mutual coupling effects and is quite different from an isolated element. Typical measured embedded element pattern of a CP element with 0.54λ interelement spacing with hexagonal grid lattice is plotted in Figure 9.17 with and without sequential rotation. The sequential rotation of the elements in the array improves the cross-pol and also improves the element roll-off, resulting in lower scan loss for the array. Element roll-off is close to $\cos^{1.5}\theta$ function with sequential rotation of elements in the array and is $\cos^{1.8}\theta$ without sequential rotation. This is much steeper than $\cos\theta$ roll-off that is often used in the array designs.

In several aircraft and spacecraft applications, different aperture shapes and different grids are used for arrays because of the practical accommodation limitations or design constraints. The grating lobe impact of these geometries is illustrated in Figure 9.18. It is plotted in the wave number plane (K_x, K_y); the dotted outer circle represents visible space and the solid inner circle represents the field of view (+/–70°). Circular aperture shape is best in terms of grating lobes and lower side lobe levels. Rectangular or square apertures are the worst, and parallelogram shaped apertures are in between the two. Circular/hexagonal aperture with hexagonal grid layout is the best choice for planar arrays. The impact of the grating lobes and side lobes of the grating lobes on the scanned patterns is illustrated in Figure 9.19 for different element spacings. Increasing the element spacing helps in reducing the number of

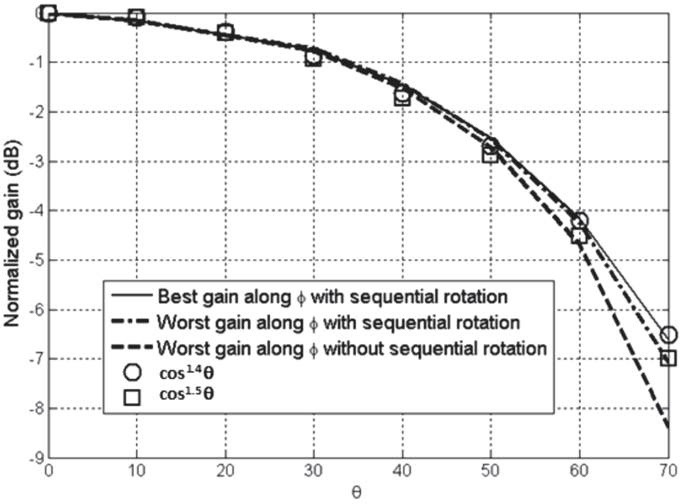

Figure 9.17 Typical element pattern useful for wide-scan arrays.

elements, but the grating lobes come in closer, and the grating lobe side lobes have impact in the desired coverage region. When the element spacing is increased by 5% more than the optimized spacing, the grating lobes appear in the visible space. The impact of the grid angle and element spacing is illustrated in Figure 9.20. Intention of the plot is to show the effect of the grid angle and element. For example, with grid angle as 70°, the element space has to decrease by 8% in order to keep the grating lobe away from the visible space by the same amount of the angular space compared to the 60° grid angle case.

For planar arrays with small scan region such as a geo-stationary satellite, the element spacing can be much larger since the worst-case scan is about +/–8.7° in

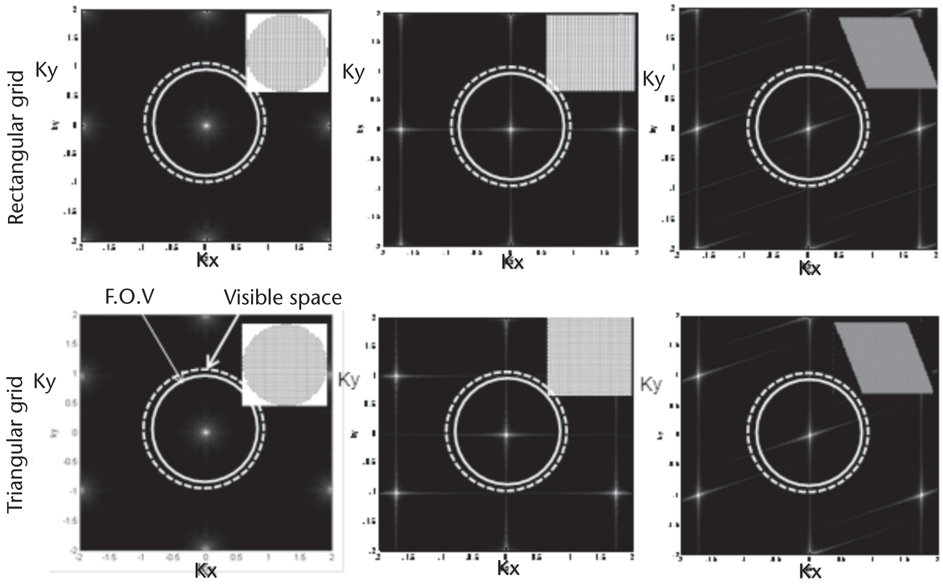

Figure 9.18 Grating lobe patterns are shown for various grid and boundary shape.

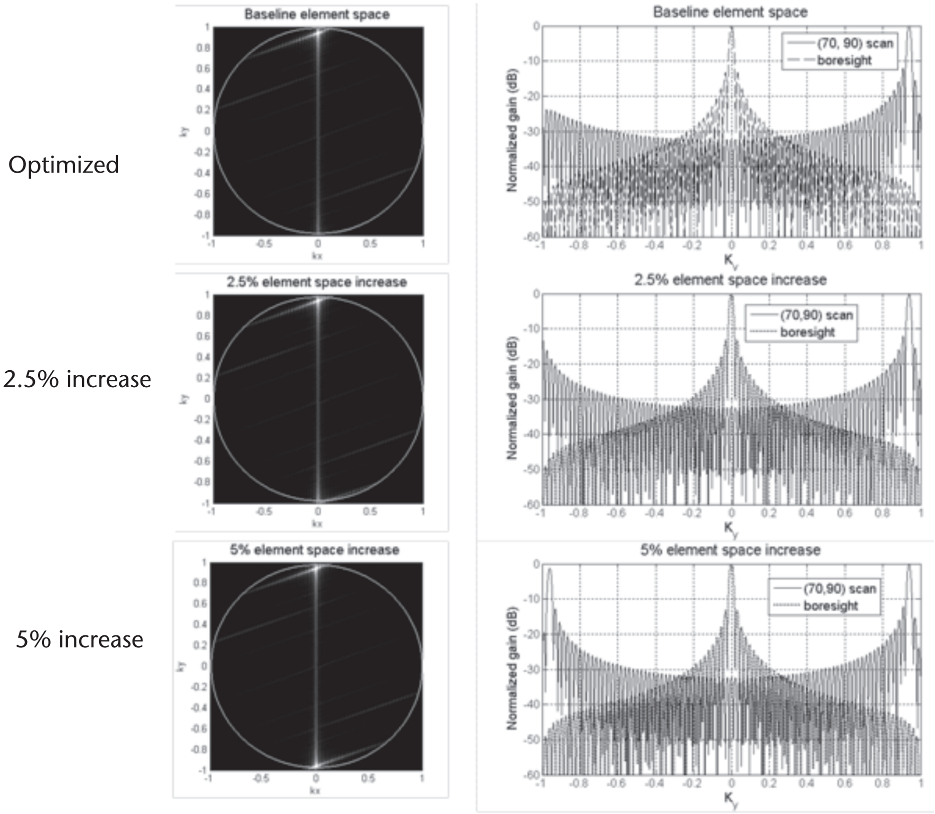

Figure 9.19 Grating lobe level in the visible space increases as the element spacing increases.

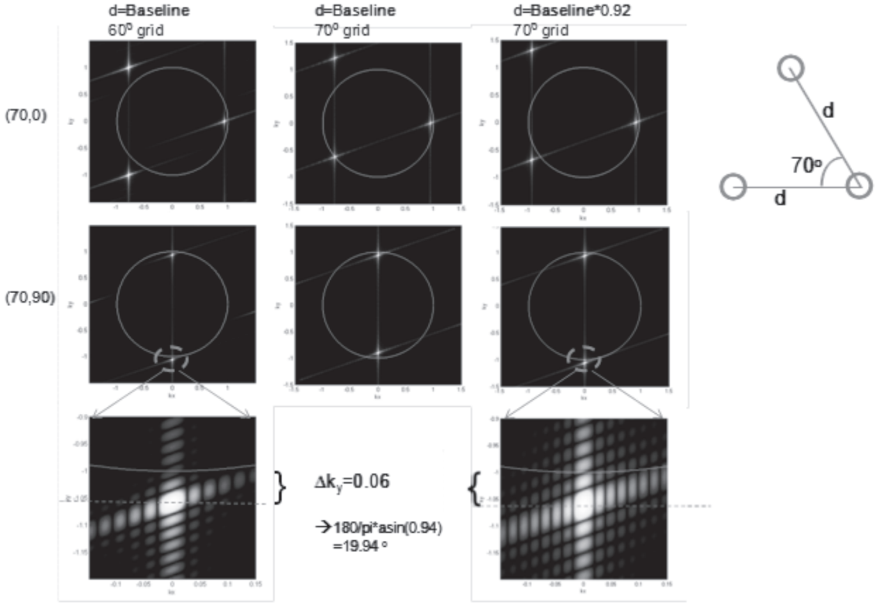

Figure 9.20 In order to separate the grating lobe from the visible space with the same angular distance, the element spacing has to decrease for 70° grid compared to 60° grid.

azimuth and elevation. The directivity and location of grating lobes as a function of element spacing (normalized to wavelength) are plotted in Figure 9.21. The number of elements is kept constant in the results shown in Figure 9.21 and are arranged in the hexagonal grid layout. Array directivity at the center of coverage and edge of the scan are shown. The difference between the two curves is the scan loss and also due to energy lost in the grating lobes. The element spacing has to be less than 3.7λ in order to keep the grating lobes away from the earth.

The antenna noise temperature varies a lot for geostationary applications, especially near the scan edges. Since the antenna sees a hot earth over the visible space and cold sky outside the earth's field-of-view, the computed antenna patterns need to be integrated with weighted temperature for each beam location in order to compute the antenna noise temperature. This is computed using the equation

$$T_A = \frac{1}{4\pi}\int_0^{2\pi}\int_0^{\pi} R(\theta,\Phi)T(\theta,\Phi)\sin\theta\, d\theta\, d\Phi \tag{9.19}$$

where $R(\theta,\Phi)$ is the array radiation patterns and the temperature $T(\theta,\Phi)$ is given as

$$T(\theta,\Phi) = 290°K, \text{ if } K_x^2 + K_y^2 < \sin^2(8.7°) \tag{9.20a}$$

$$= 3°K, \text{ if } K_x^2 + K_y^2 > \sin^2(8.7°) \tag{9.20b}$$

The antenna noise temperature is low when the beam is scanned to the edge, since half the power is radiated into cold sky and it depends on the element spacing. Larger element spacing creates the grating lobes on earth, increasing the noise temperature. The antenna directivity, noise temperature, and computed G/T are plotted in Figure 9.22 for boresight and scanned beam as a function of element size. Variation of directivity and grating lobe locations as function scan are shown over a 14% frequency bandwidth in Figure 9.23. High frequency determines the closest grating

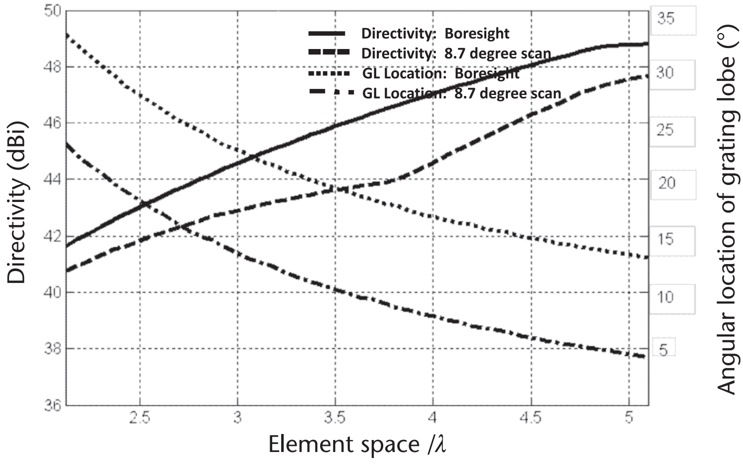

Figure 9.21 Directivity and grating lobe location for boresight and 8.7° scan.

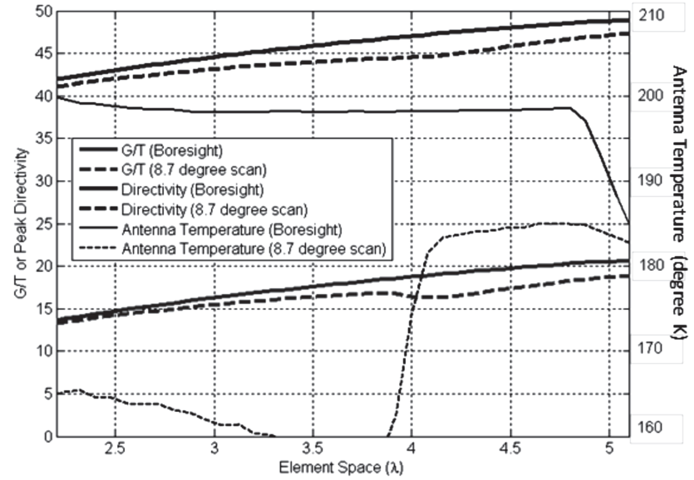

Figure 9.22 G/T, directivity, and antenna temperature for boresight and 8.7° scan.

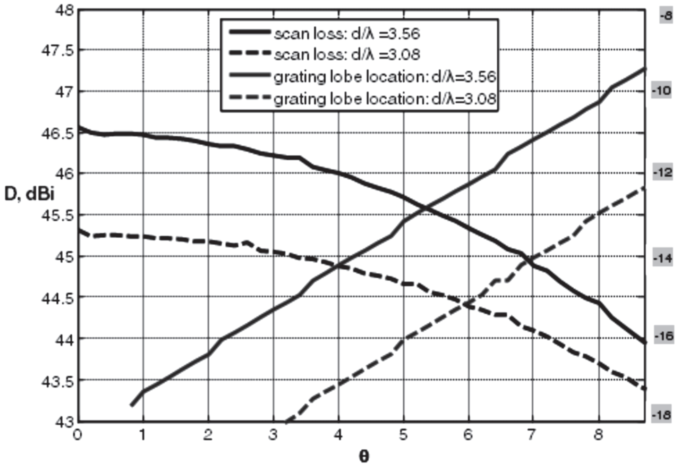

Figure 9.23 Scan loss and antenna noise temperature variation over a 14% frequency bandwidth. Θ is the polar angle from the array boresight direction.

lobe, and the low frequency determines the minimum directivity. These two factors are useful guidelines for a phased array design with limited scan. Beam plots in the wave number plane often give useful information in the array design. An example is shown in Figure 9.24 for boresight and scanned beams of an array illustrating the grating lobes over the earth and beyond.

9.3 Low Gain TT&C Antennas

The telemetry, tracking, and control (TT&C) subsystem using low-gain antennas provides vital communication to and from the spacecraft. TT&C is the only way to observe and to control the spacecraft's functions and conditions from the ground. The subsystem provides essential spacecraft management and control functions to keep

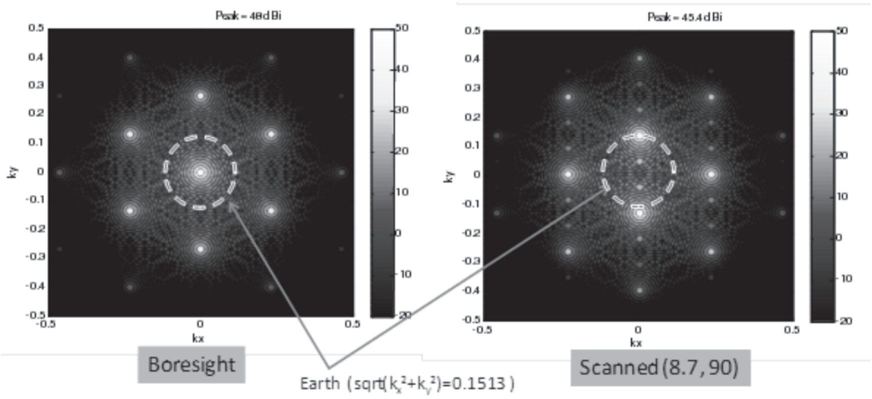

Figure 9.24 Plot in the wave number plane for boresight and scanned beams.

the satellite operating safely in orbit. Therefore, the TT&C subsystem provides the capability for simultaneous housekeeping telemetry, telecommand, and ranging for any satellite attitude, for all anticipated attitude rates, and during all mission phases. The TT&C links between the spacecraft and the ground are usually separate from the communications system links. TT&C links may operate in the same frequency bands or in other bands. TT&C is most often accomplished through a separate earth terminal facility specifically designed for the complex operations required to maintain a spacecraft in orbit. One TT&C facility may maintain several spacecrafts simultaneously in orbit through TT&C links to each vehicle.

TT&C Subsystem performs the following basic functions:

- Receive signals from the earth (uplink beam);
- Demodulate the command signals for further processing by the baseband equipment;
- Demodulate the ranging signal for remodulation on the telemetry carrier signals;
- Transmit the signals back to the earth (downlink beam).

The International Telecommunications Union (ITU) recommended frequency assignments for satellite communications developed at WARC-85, which are listed as follows:

Sub Band Designation	*Frequency Range*
L-Band	1.5–1.6 GHz
S-Band	2.5–2.6 GHz
C-Band	3.4–4.2, 5.9–6.7 GHz
Ku-Band	10.7–14.5, 17.3–17.8 GHz
Ka-Band	18.3–22.2, 27.0–31.0 GHz

Within each beam/coverage area, frequency reuse is accomplished by using orthogonally polarized beams

- Linear polarization schemes use vertical and horizontal electric field (e-field) beams;

- Circular polarization schemes use left- and right-hand circularly rotating e-field beams;
- The choice of polarization scheme affects the design and cost of the ground terminals, ease of ground installation, adjacent satellite interference, and cross-polarization interference.

Key TT&C requirements for satellite payloads are:

- Receive, decrypt, authenticate, and process commands;
- Collect, format, encrypt, and transmit satellite telemetry;
- Support satellite control functions;
  - Attitude determination and control;
  - Battery charge management, solar array pointing;
  - Autonomous configuration management;
- Support range determination from ground station(s);
- Provide antenna coverage for transfer and drift orbit operations and during on-orbit attitude anomalies.

During launch and early orbit phases (LEOP), the primary antennas for the spacecraft telemetry and ranging transmissions and the spacecraft command and ranging receptions are the TT&C antennas. A typical list of TT&C antennas includes the omni antennas, wide-coverage horn antennas, hemispherical antennas, and global horns. The omni antennas are either bi-conical antennas that generate toroidal radiation patterns or the horn antennas with cardioid type of pattern. While the bi-conical omni antennas can be configured with either linear or circular polarization, the cardioids predominantly are designed with circular polarization. Typical components of a TT&C RF subsystem are shown in Figure 9.25. Figure 9.26 also shows typical TT&C functional elements for a communications satellite application.

9.3.1 TT&C Subsystem and Antenna Applications

The satellite TT&C subsystems comprise the antenna, command receiver, tracking and telemetry transmitter, and possibly tracking sensors. Telemetry data are received from other subsystems of the spacecraft, such as the payload, power, attitude control, and thermal control. Command data are relayed from the command receiver

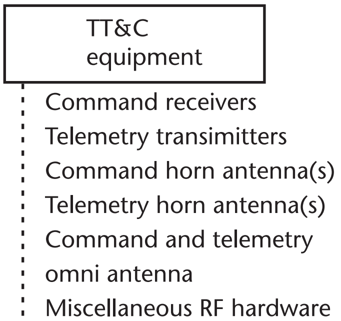
TT&C equipment
Command receivers
Telemetry transimitters
Command horn antenna(s)
Telemetry horn antenna(s)
Command and telemetry omni antenna
Miscellaneous RF hardware

Figure 9.25 Typical components of a TT&C RF subsystem.

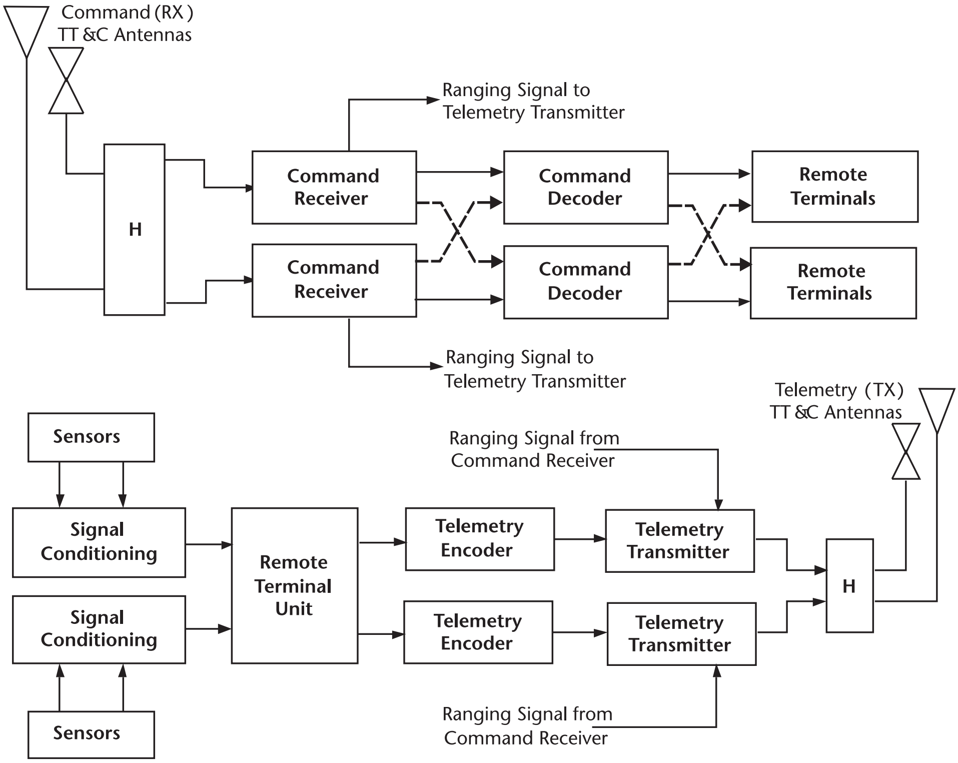
Command (RX)
TT&C Antennas
H
Command Receiver
Command Receiver
Ranging Signal to Telemetry Transmitter
Ranging Signal to Telemetry Transmitter
Command Decoder
Command Decoder
Remote Terminals
Remote Terminals
Telemetry (TX)
TT&C Antennas
Sensors
Signal Conditioning
Signal Conditioning
Sensors
Remote Terminal Unit
Telemetry Encoder
Telemetry Encoder
Ranging Signal from Command Receiver
Ranging Signal from Command Receiver
Telemetry Transmitter
Telemetry Transmitter
H

Figure 9.26 TT&C subsystem basic block diagram.

to other subsystems to control such parameters as antenna pointing, transponder modes of operation, battery and solar cell changes, and so on.

The elements on the ground include the TT&C antenna, telemetry receiver, command transmitter, tracking subsystem, and associated processing and analysis functions. Satellite control and monitoring is accomplished through monitors and keyboard interface.

Tracking refers to the determination of the current orbit, position, and movement of the spacecraft. The tracking function is accomplished by several techniques. A simple method usually involves transmitting beacon signals from the satellite, which are received at the TT&C earth station. The doppler shift of the beacon (or the telemetry carrier) is monitored to determine the rate at which the range is changing (the range rate). Angular measurements from one or more earth terminals can be used to determine spacecraft location. The range can be determined by observing the time delay of a pulse or sequence of pulses transmitted from the satellite.

The telemetry function involves the collection of data from sensors on board the spacecraft and relaying this information to the ground. Fundamental telemetry parameters include:

- Unit on/off status;
- Unit temperatures;
- Transponder channel gain setting status;

- Power amplifier health status parameters (i.e., helix or gate current, DC current and anode voltage);
- Antenna pointing position (if applicable).

The telemetered data also include such parameters as voltage and current conditions in the power subsystem, temperature of critical subsystems, status of switches and relays in the communications and antenna subsystems, fuel tank pressures, and attitude control sensor status. The telemetry signals are phase shift keyed on subcarriers, which in turn phase modulate the downlink telemetry carrier.

The command system relays specific control and operations information from the ground to the spacecraft, often in response to telemetry information received from the spacecraft. Parameters involved in typical command links include changes and corrections in attitude control and orbital control, antenna pointing and control, transponder mode of operation, and battery voltage control. The command system is used during launch to control the firing of the boost motor, deploy appendages such as solar panels and antenna reflectors, and “spin-up” a spin-stabilized spacecraft body.

Telemetry and command during the launch and transfer orbit phases usually requires a backup TT&C system, since the main TT&C system may be inoperable because the antenna is not deployed, or the spacecraft attitude is not proper for transmission to earth. The backup system usually operates with an omnidirectional antenna in conjunction with a wide-angle coverage antenna resonant at the TT&C operating frequencies, with sufficient margin to allow operation in the most adverse conditions. The backup system is also used if the main TT&C system fails on orbit.

9.3.2 TT&C Antennas Introduction

The TT&C antenna systems on the spacecraft are used for transmitting and receiving the RF signals and are a critical part of the satellite communications system. The most important parameters that define the performance of an antenna are antenna gain, antenna beamwidth, cross polarization isolation, and antenna side lobes. The gain defines the increase in signal strength achieved in concentrating the radio-wave energy, either in transmission or reception mode, by the antenna system.

The common types of antennas used in satellite systems are the omni directional transmit and receive antenna and the wide coverage receive and transmit horn antennas. These are low gain antennas and as such are susceptible to mutual interference and multipath effects, especially if the coverage from each antenna is combined to a single combined output. In addition, these low-gain antennas are susceptible to proximity effects from spacecraft structures and cause scattering. Omni antennas are used primarily for tracking, telemetry, and command links during launch and early orbit phase, where the spacecraft attitude has not yet been established. The omni antennas can be designed with either linear polarization or circular polarization.

Wide coverage horn antennas are used when relatively wide beams are required. These horns provide wide beam coverage with half-power beamwidth of ±30° and adequate gain to close the TT&C radio links. The wide-coverage antennas can be designed with linear polarization or integrated with septum polarizers that provide circular polarization. When combined with the omni antenna pattern, the combined pattern is as shown in Figure 9.27.

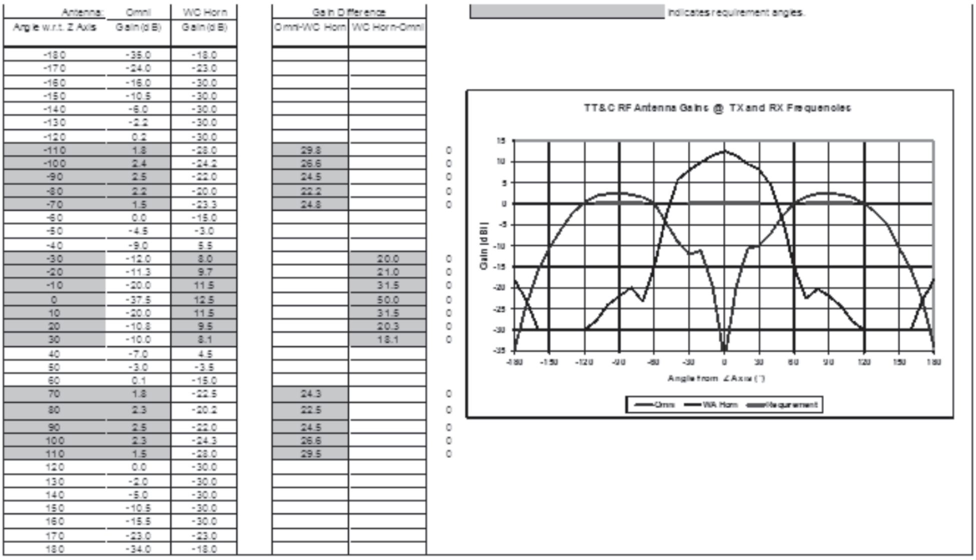

Antenna:	Omni	WC Horn	Gain Difference		
Angle w.r.t. Z Axis	Gain (dB)	Gain (dB)	Omni-WC Horn	WC Horn-Omni	
-180	-35.0	-18.0			
-170	-24.0	-23.0			
-160	-16.0	-30.0			
-150	-10.5	-30.0			
-140	-6.0	-30.0			
-130	-2.2	-30.0			
-120	0.2	-30.0			
-110	1.8	-28.0	29.8		0
-100	2.4	-24.2	26.6		0
-90	2.5	-22.0	24.5		0
-80	2.2	-20.0	22.2		0
-70	1.5	-23.3	24.8		0
-60	0.0	-15.0			
-50	-4.5	-3.0			
-40	-9.0	5.5			
-30	-12.0	8.0		20.0	0
-20	-11.3	9.7		21.0	0
-10	-20.0	11.5		31.5	0
0	-37.5	12.5		50.0	0
10	-20.0	11.5		31.5	0
20	-10.8	9.5		20.3	0
30	-10.0	8.1		18.1	0
40	-7.0	4.5			
50	-3.0	-3.5			
60	0.1	-15.0			
70	1.8	-22.5	24.3		0
80	2.3	-20.2	22.5		0
90	2.5	-22.0	24.5		0
100	2.3	-24.3	26.6		0
110	1.5	-28.0	29.5		0
120	0.0	-30.0			
130	-2.0	-30.0			
140	-5.0	-30.0			
150	-10.5	-30.0			
160	-15.5	-30.0			
170	-23.0	-23.0			
180	-34.0	-18.0			

indicates requirement angles.
TT&C RF Antenna Gains @ TX and RX Frequencies
Gain [dBi]
15
10
5
0
-5
-10
-15
-20
-25
-30
-35
-180
-150
-120
-90
-60
-30
0
30
60
90
120
150
180
Angle from Z Axis (°)
Omni
WA Horn
Requirement

Figure 9.27 Combined omni antenna and wide-coverage horn pattern.

A critical performance aspect of the wide-coverage horn and the omni antenna patterns, when each antenna coverage is combined to produce a composite coverage of the TT&C signals, is that the wide-coverage horn antenna (WCA) is designed such that its gain falls rapidly beyond ±60° in order to lower or minimize multipath interference on the TT&C antenna coverage caused by scattering of signals from the spacecraft nadir panel. The omni antenna gain variation is less pronounced, but its interference contribution to the wide-coverage horn has to be minimized. A typical layout of the omni and WCA on the spacecraft deck is shown in Figure 9.28 where the omni is placed much higher that the deck and WCA is at the deck level. Combined omni and WCA patterns without deck and including scattering effects from spacecraft deck are shown in Figure 9.29. The spacecraft scattering increases the co-polar ripples, increases the cross-polar levels, and reduces the coverage gain. It is important that the scattering analysis is performed to optimize locations of the Omni & WCA and assess the worst-case RF performance of these low-gain antennas [17].

Hemispherical antennas are used in satellites that have a different early orbit/transfer orbit profile. These antennas have hemispherical coverage pattern with peak

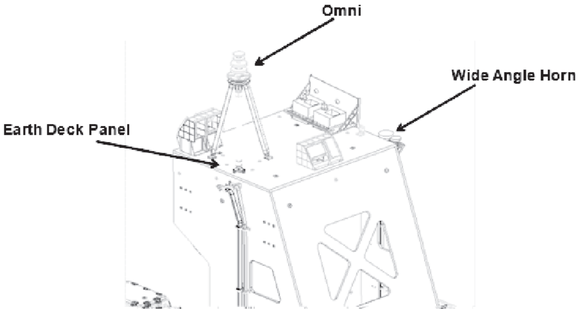

Omni
Wide Angle Horn
Earth Deck Panel

Figure 9.28 Typical locations of omni and WCA on spacecraft.

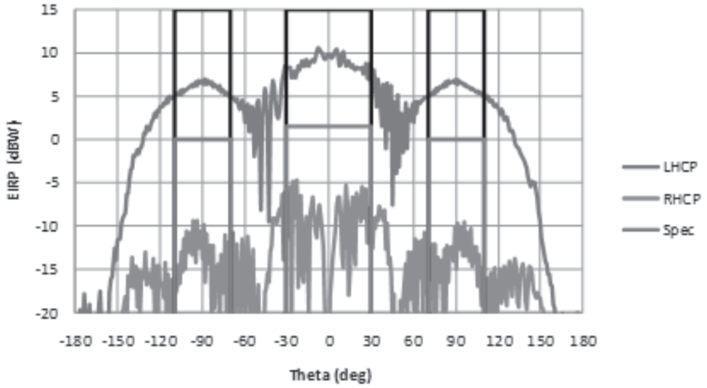

(a)

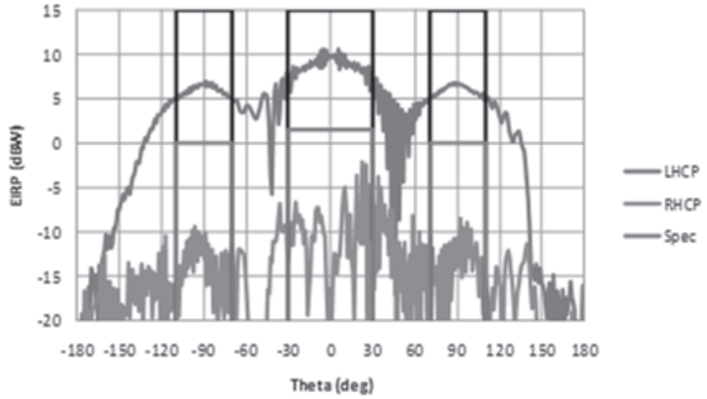

(b)

Figure 9.29 Spacecraft scattering impact on the combined omni and WCA antenna system (a) omni + WCA, and (b) omni + WCA + Spacecraft Deck.

gain in the boresight tapering off to 10 dB below the peak but providing sufficient gain to close the command and telemetry link. The orbit profile is compatible with the spacecraft having achieved three-axis stabilization after launch vehicle separation. The hemispherical antennas are typically circularly polarized, either single or dual orthogonal.

Global horns are used for command and telemetry transmission during on-station operation after the spacecraft has achieved geosynchronous operation when there is a need for the TT&C subsystem antenna coverage to be independent of the payload antenna and payload system. The global horn, as the name implies, has a half-power beamwidth of ±9° that covers the earth diameter equatorially and provides 17 dBi gain. The peak gain is typically 20 dBi. The global horn can be designed with linear polarization or circular polarization.

The global horns are also used for on-station beacon tracking for pointing the ground station antennas to the beacon signal from the satellite. It is important to remember that antenna misalignment can lead to offset earth coverage and degraded uplink and downlink performance. Poor polarization congruency can lead to cross-polarization interference from within the satellite.

9.3.3 TT&C RF Block Diagram and Link Budgets

A typical block diagram of an RF section of the subsystem is shown in Figure 9.30. Uplink command signals received by the wide coverage receive horn and the receive omni antenna are combined in the quadrature hybrid and fed to the redundant command receivers. Similarly, the telemetry transmitter output power from one or both telemetry transmitters are combined in the transmit quadrature hybrid and fed to the wide-coverage transmit horn and the transmit omni antenna. The telemetry transmitter has typically two mutually exclusive modes of operation, namely the high-power and the low-power mode, respectively. The transmitters operate in high-power mode during LEOP. During on-station operation, the high-power mode of each transmitter is switched off and the transmitters operate in low-power mode. Since the low-power output of the telemetry transmitters is low, the high gain of the communications antenna provides high on-station telemetry EIRP ensuring that the power flux density of the telemetry radiation does not exceed the ITU regulatory limits.

Figure 9.31 summarizes the mutual multipath interference losses for each antenna path utilizing the combined radiation patterns of the wide-coverage horn and the omni antenna and the coverage requirements for each antenna. Losses in each antenna path are those encountered from the antenna to the hybrid where the signals from each antenna are combined.

Figure 9.32 shows a typical command link budget based on the command flux density at each antenna and the command receiver threshold performance signal level of –142 dBW. Figure 9.33 shows a typical telemetry EIRP link performance based on the telemetry transmitter high-power output and the line losses including

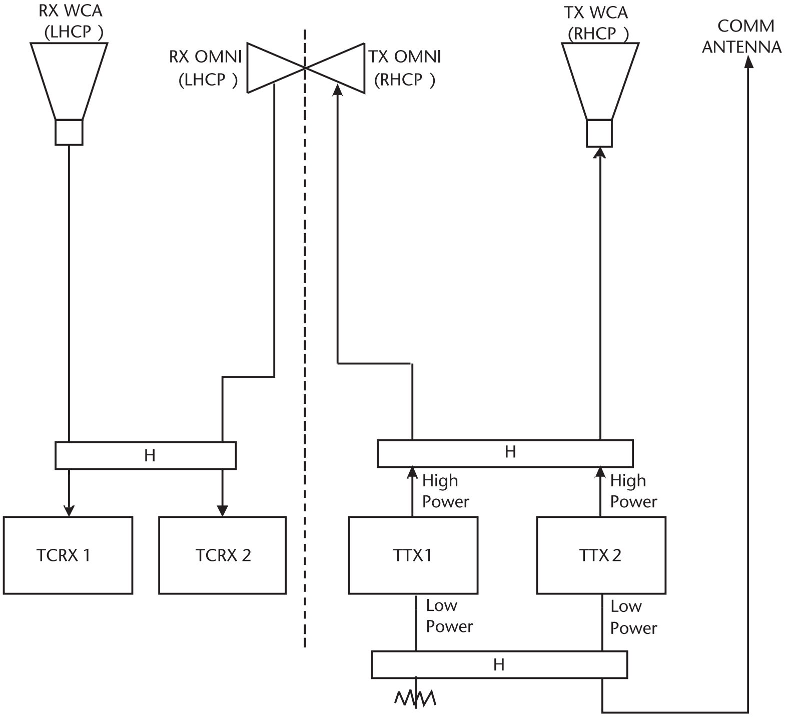

Figure 9.30 Simplified TT&C RF block diagram.

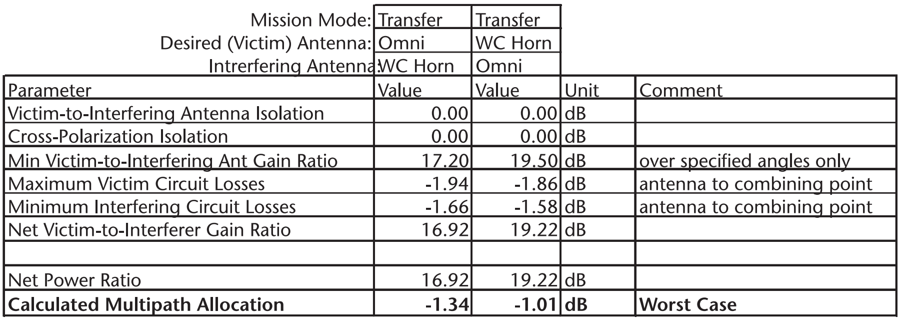

Mission Mode:	Transfer	Transfer		
Desired (Victim) Antenna:	Omni	WC Horn		
Intrerfering Antenna:	WC Horn	Omni		
Parameter	Value	Value	Unit	Comment
Victim-to-Interfering Antenna Isolation	0.00	0.00	dB	
Cross-Polarization Isolation	0.00	0.00	dB	
Min Victim-to-Interfering Ant Gain Ratio	17.20	19.50	dB	over specified angles only
Maximum Victim Circuit Losses	-1.94	-1.86	dB	antenna to combining point
Minimum Interfering Circuit Losses	-1.66	-1.58	dB	antenna to combining point
Net Victim-to-Interferer Gain Ratio	16.92	19.22	dB	
Net Power Ratio	16.92	19.22	dB	
Calculated Multipath Allocation	**-1.34**	**-1.01**	**dB**	**Worst Case**

Figure 9.31 Multipath prediction from the radiation patterns and losses.

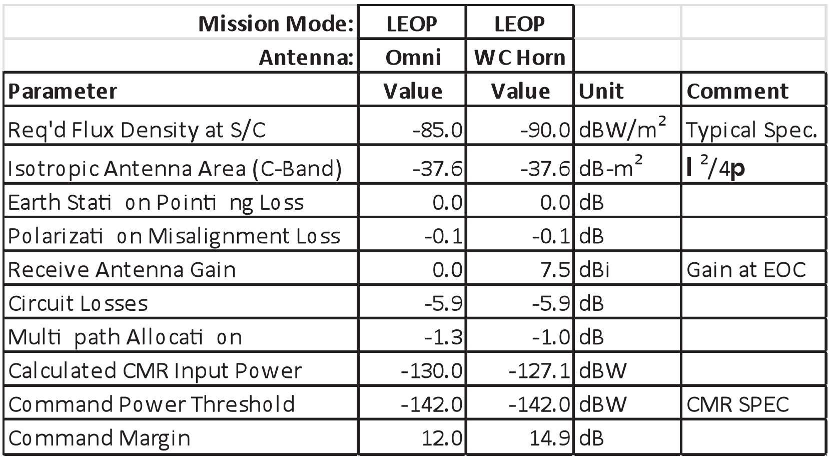

Mission Mode:	**LEOP**	**LEOP**		
Antenna:	**Omni**	**WC Horn**		
Parameter	**Value**	**Value**	**Unit**	**Comment**
Req'd Flux Density at S/C	-85.0	-90.0	dBW/m^2	Typical Spec.
Isotropic Antenna Area (C-Band)	-37.6	-37.6	$dB\text{-}m^2$	$\lambda^2/4\pi$
Earth Station Pointing Loss	0.0	0.0	dB	
Polarization Misalignment Loss	-0.1	-0.1	dB	
Receive Antenna Gain	0.0	7.5	dBi	Gain at EOC
Circuit Losses	-5.9	-5.9	dB	
Multipath Allocation	-1.3	-1.0	dB	
Calculated CMR Input Power	-130.0	-127.1	dBW	
Command Power Threshold	-142.0	-142.0	dBW	CMR SPEC
Command Margin	12.0	14.9	dB	

Figure 9.32 Command link budget with the Omni antenna and the wide-coverage horn.

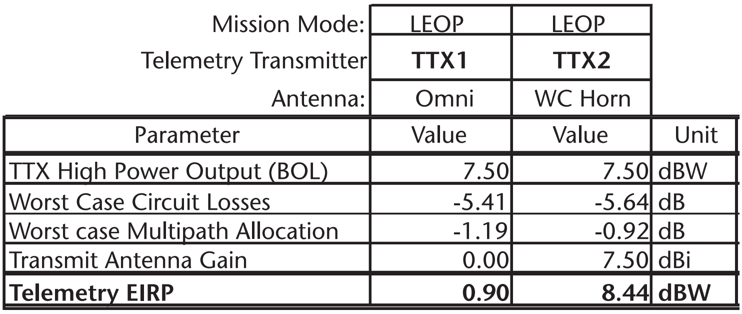

Mission Mode:	LEOP	LEOP	
Telemetry Transmitter	**TTX1**	**TTX2**	
Antenna:	Omni	WC Horn	
Parameter	Value	Value	Unit
TTX High Power Output (BOL)	7.50	7.50	dBW
Worst Case Circuit Losses	-5.41	-5.64	dB
Worst case Multipath Allocation	-1.19	-0.92	dB
Transmit Antenna Gain	0.00	7.50	dBi
Telemetry EIRP	**0.90**	**8.44**	**dBW**

Figure 9.33 Telemetry EIRP budget with the Omni antenna and the wide-coverage horn.

multipath interference losses to the antenna. The links are relevant to e-band uplink and downlink.

9.3.4 Low-Gain TT&C Antennas

A number of low-gain antennas are used in TT&C subsystem in a satellite to maintain continuous communication with the ground station during launch, early orbit phase, geostationary transfer orbit, and geosynchronous mission orbit. TT&C

communication is of paramount importance under all modes of spacecraft operation, including but not limited to spacecraft attitude anomalies, loss of earth-lock or others that may prevent the spacecraft from earth-pointing. For this reason, the TT&C subsystem primarily utilizes low-gain antennas that provide omnidirectional radiation pattern. Since no single antenna can achieve spherical radiation in the presence of large scattering objects, such as spacecraft earth panel, structures, and waveguide feeds, it is augmented with one or more additional antennas of different configuration and combining each pattern to form a composite radiation pattern that satisfies the spacecraft requirements in terms of antenna coverage angles and gain to provide positive radio link performance.

There are two commonly used configurations to provide the omnidirectional pattern:

a) A combination of a bi-conical antenna (that has a toroidal radiation pattern) with a wide-coverage antenna that has a cardioidal pattern shape is often used to provide more than hemispherical coverage. Since the antennas are resonant at either the command frequency or the telemetry frequencies, it is necessary to implement this antenna combination for the TT&C receive and transmit frequencies, respectively. The omni antenna itself is composed of a transmit bi-cone located at the bottom with the receive bi-cone at the top in a single antenna structure. This structure is typically located on the spacecraft and mounted on a boom or a tripod for obstruction-free field of view from the radiating bi-cones. The receive bi-cone operates at either edge of the communications receive band while the transmit bi-cone operates at either edge of the transmit communications band. This configuration is predominantly implemented on some North American spacecraft bus. A schematic view of this configuration on the satellite is shown in Figure 9.34, which shows the ideal contributions from each radiating element (continuous lines) and the combined omnidirectional radiation pattern (dashed line). The measured radiation pattern of the actual implementation will be different from the ideal spherical shape; however, it will be shown to be compliant to the TT&C subsystem specification requirement as described later in this section.
b) A combination of two hemispherical antennas, one located on the nadir facing side and the other on the zenith facing side of the spacecraft. This is typically the preferred configuration in spacecraft bus of European satellite suppliers. Figure 9.35 shows the schematic of this configuration and the resultant combined radiation patterns. It should be noted that this is an ideal theoretical pattern; in real practice, it is not usually possible to achieve perfectly symmetric omnidirectional patterns.

An overview of the main types of low-gain antennas (LGA) designed for TT&C RF applications with an explanation of the omni directional antenna design configuration is provided in this section. Antennas with specific TT&C applications are also included.

9.3.4.1 Bi-conical Antennas

Bi-conical omni antennas are used widely in satellites as a constituent part of the TT&C RF Subsystem. They provide a toroidal radiation pattern and are mainly used

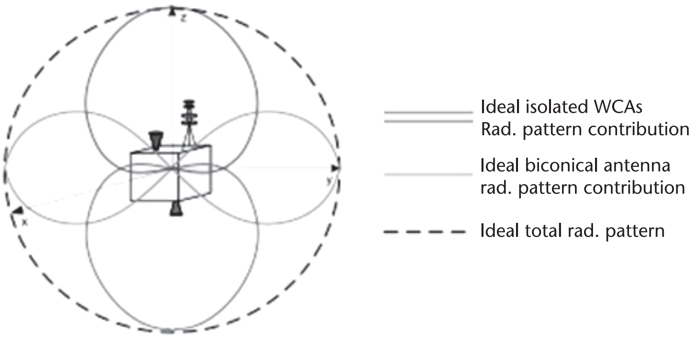

Figure 9.34 Satellite TT&C antenna configuration with bi-conical omni antenna and the WCA.

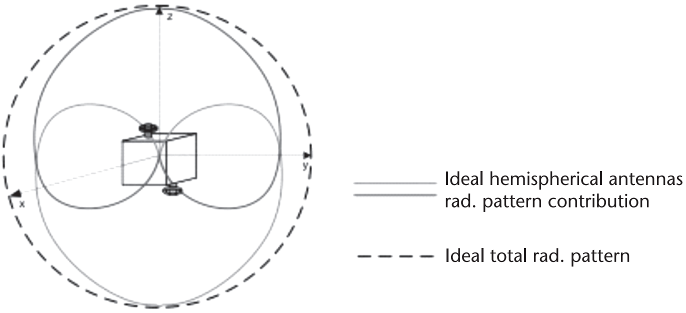

Figure 9.35 Satellite TT&C antenna configuration with two hemispherical antennas.

in combination with other LGA to provide omnidirectional coverage during transfer orbit, drift orbit, and on-station mission orbit for communications between satellite and the ground stations. A generic requirement of the omni antenna is shown in Figure 9.36. An example of the radiation pattern of the toroidal omni antenna with both copolar and cross-polar components is shown in Figure 9.37. It usually covers the range of ±20° from the horizontal plane, providing a gain above 0 dBi with good polarization purity (cross-polar values below –20 dBi). Figure 9.38 shows typical gain mask requirement for the omni antenna.

The omni antennas cover various frequency bands, from S-band to Ka-band. The most common configuration of this toroidal antenna design is to stack the transmit and receive antennas vertically one on top of the other. The transmit bi-cone is located at the bottom of the omni antenna structures while the receive bi-cone is located at the top. This is due to the fact that the receive bi-cone is smaller than the transmit bi-cone due to higher frequency. The mechanical design of the omni antenna is such that it endures those demanding mechanical stresses imposed by the launch vehicles and also the thermal environment that the antenna has to experience in all the satellite operating modes through the life of the satellite. The electrical design is such that the electrical performance is consistently maintained in all satellite operating modes and environments. Some examples can be seen in Figure 9.39. The antenna on the left operates in the Ku-band and is circularly polarized. The omni antenna shown on the right operates in the C-band and has linear polarization. Both receive and transmit bi-cones have linear vertical polarization. It can be seen that the polarization

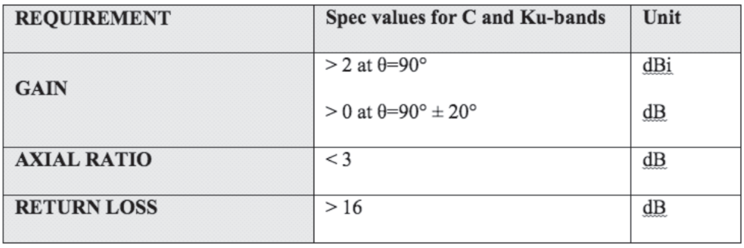

REQUIREMENT	Spec values for C and Ku-bands	Unit
GAIN	> 2 at θ=90° > 0 at θ=90° ± 20°	dBi dB
AXIAL RATIO	< 3	dB
RETURN LOSS	> 16	dB

Figure 9.36 Generic requirements for bi-conical antennas.

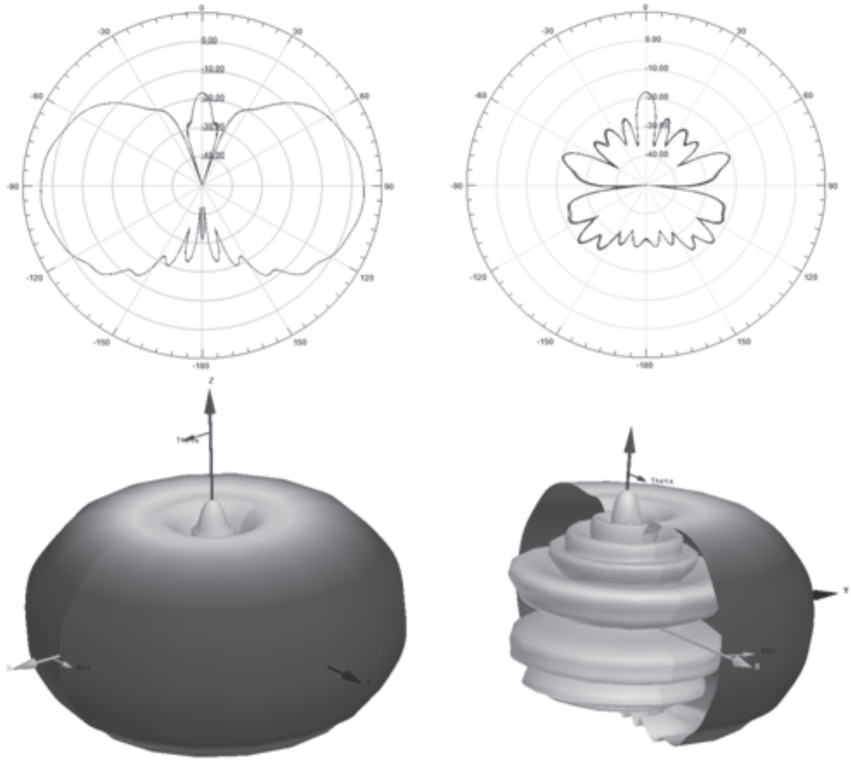

Figure 9.37 Toroidal radiation pattern of bi-conical omni antenna (co-polar and cross-polar).

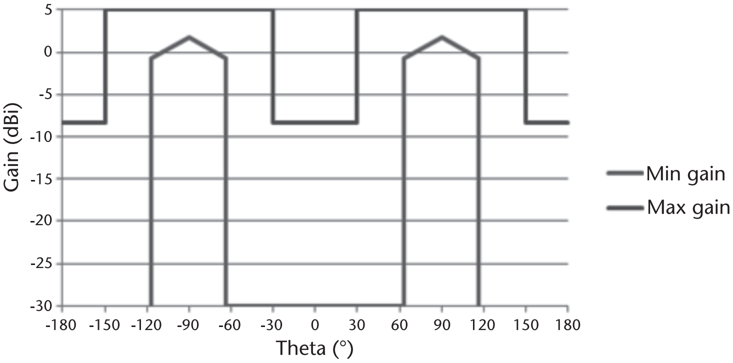

Figure 9.38 Omni antenna gain template for minimum and maximum gain.

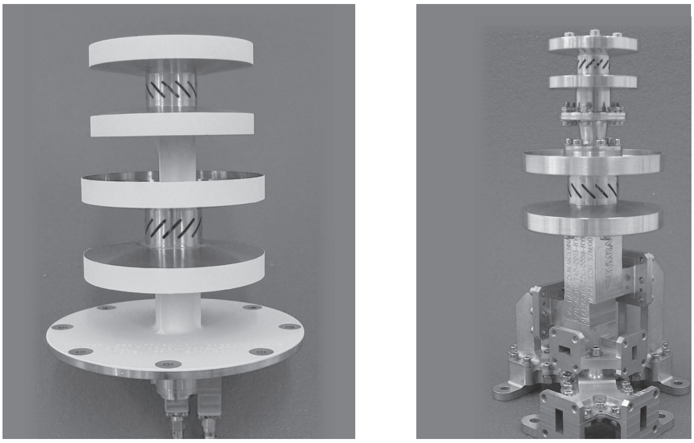

Figure 9.39 Examples of bi-conical antennas. (Courtesy of Rymsa Espacio.)

depends on the inclination of the cavity slots. The coaxial feeds for transmit and receive bi-cones are shown at the bottom of the mounting baseplate.

Principle of Operation

The bi-cones are fed by a resonant cavity with a number of rectangular apertures or slots within the bi-cone aperture. The electric field waves traveling up the waveguide feed will couple into these slots, create surface currents around the slot edges on the exterior wall of the cavity, and these currents in turn will radiate to the open space between the bi-cones. Although a simple process, certain design considerations have to be taken into account.

The slots are designed to be narrow and of a certain length at the operating frequency. The slot length is approximately $\lambda/2$. However, since the position of the slots, the number of slots, and thickness affect the resonant frequency, it has to be determined experimentally. In terms of fields, a resonant slot can only be excited by an electric field normal to its length, and this field will radiate outwards. Therefore, the orientation of the slot will determine the radiated polarization. It may be located vertically, horizontally, or in a 45° inclination angle to the left or the right. The design concept can be seen in Figure 9.40 for the isolated narrow rectangular slot, together with its characteristic radiation pattern. It presents a commonly used

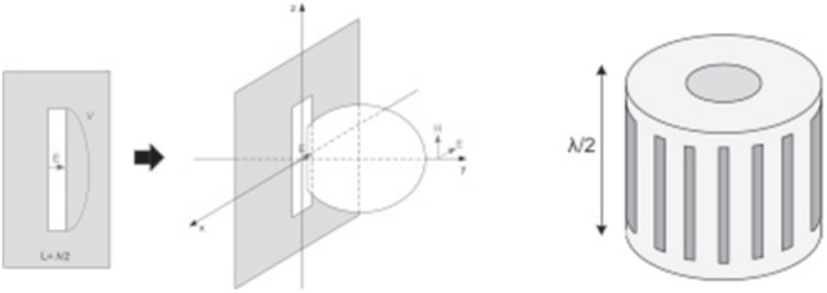

Figure 9.40 Radiation mechanism of resonant slots (left) and vertical slot distribution on the cavity (right).

vertical slot distribution to achieve horizontal linear polarization. Typically, the slots are uniformly distributed on the wall of a circular or coaxial resonant cavity.

Figure 9.41 shows a simplified representation of the fields and currents for the TE_{11} mode in the circular waveguide and the TEM mode in the coaxial waveguide. It can be seen how the waveguide may support two currents of opposite orientation, namely, the axial and transverse currents directed in the xy-plane. At a given point, these two currents alternate as the wave propagates along the waveguide. In order to support the excitation of the fields for radiation, the slots must generate these currents. Depending on the desired radiated polarization (i.e., orientation of the slots), the appropriate mode needs to be fed with the proper polarization (either linear or circular).

Depending on the choice of the feeding method, the resonant cavity has to be either $\lambda/2$ or λ height to ensure that the maximum of current will be located at the center position of the slots. The short must then be located at $\lambda/4$ or $\lambda/2$ from the center of the slot. The number of slots placed on the waveguide wall must be sufficient to ensure acceptable rotational symmetry around the longitudinal z-axis of the radiated pattern.

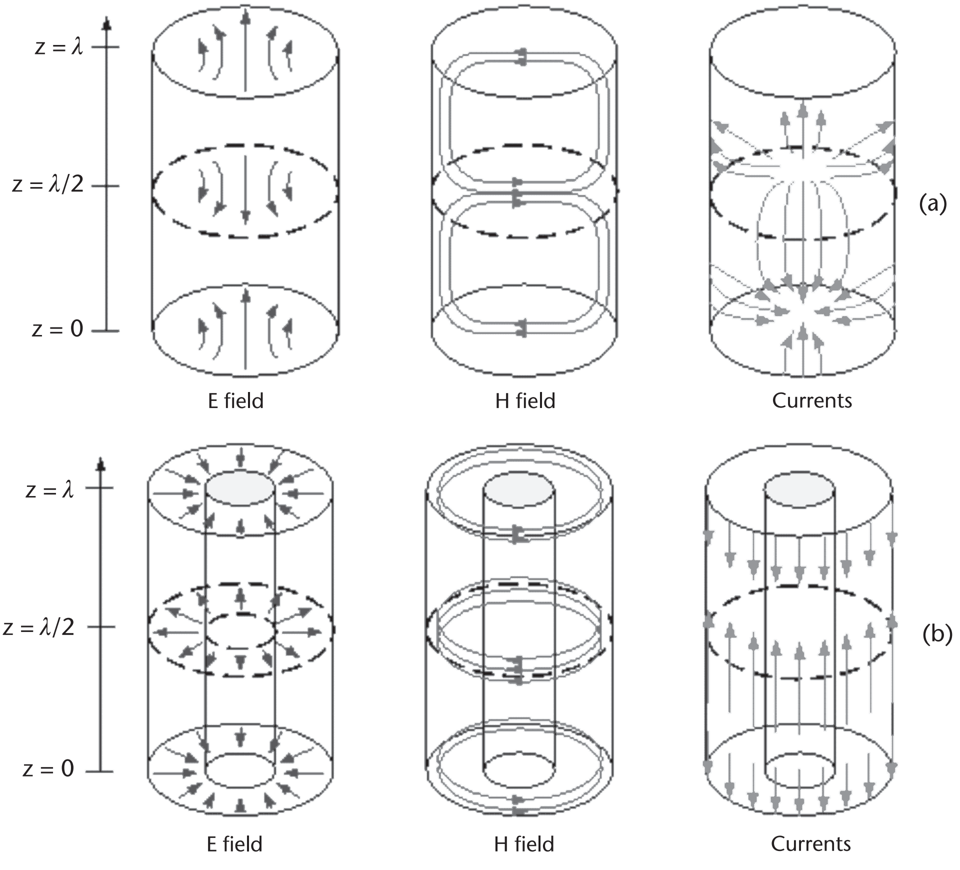

Figure 9.41 Simplified fields and currents distribution for (a) TE_{11} mode in a circular WG, and (b) TEM mode in a coaxial.

Once the fields are radiated from the slots, they travel along the space between the bi-cones of the antenna as spherical waves, producing a toroidal pattern that is non-directional in the horizontal plane. The main function of the bi-cones is to produce a uniform phase-front with a larger aperture than that of the slotted circular waveguide such that the desired polarization is achieved with increased directivity.

Bi-conical antennas are considered as conical horn aperture antennas by many classic authors. Under this assumption, the radiation pattern can be determined if the aperture geometry and fields distribution are known. Figure 9.42 shows a bi-cone geometry.

For all practical purposes, the bi-cone can be regarded as a cylindrical aperture with quadratic phase distribution, considering that the antenna has rotational symmetry around the z-axis, which results in the gain approximation [18]:

$$\text{Gain} = 10\log(2H/\lambda) - \text{ATL} - \text{PEL} \tag{9.21}$$

where H, is the distance between the end of the cones. Phase error loss (PEL) is extracted from well-known tables, depending on the quadratic phase distribution constant $S = H^2/(8\lambda R)$ and the field distribution. Note that for vertical linear polarization, the distribution of the fields will be uniform and will present no amplitude taper loss (ATL). Horizontal polarization, however, presents both PEL and ATL = 0.91, since it has a cosine distribution between the cones. R is the slant radius of the cone. The result will be accurate enough for an initial design stage. Refinement to the final co-polar and cross-polar components will need to be performed by simulations. Figure 9.43 shows an example of the measured radiation pattern of a bi-conical antenna. The pattern refers to the upper bi-cone of the antenna, which is the receive section of the omni antenna.

The bi-cone was designed to radiate at 14.5 GHz with horizontal polarization. Applying (9.21), the calculated gain is 4.56 dBi, which is very close to the measured gain of 4.3 dBi.

In the case of a bi-conical antenna radiating with circular polarization, gain may be approximated using either uniform or cosine distribution, since both will produce a very similar result. The slots will be inclined 45° to provide to orthogonal components with the same amplitude. The 90° phase offset between orthorgonal components required for the circular polarization will be introduced by the bi-cones, since the horizontal component will travel as if in free space while the vertical component

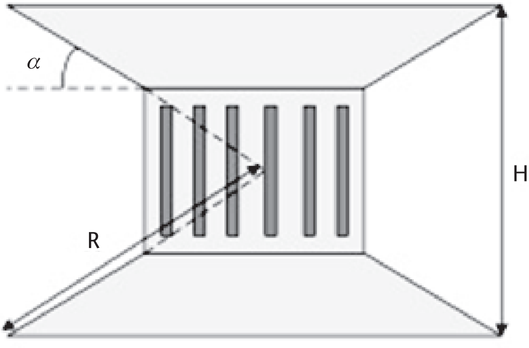

Figure 9.42 Bi-cone geometry.

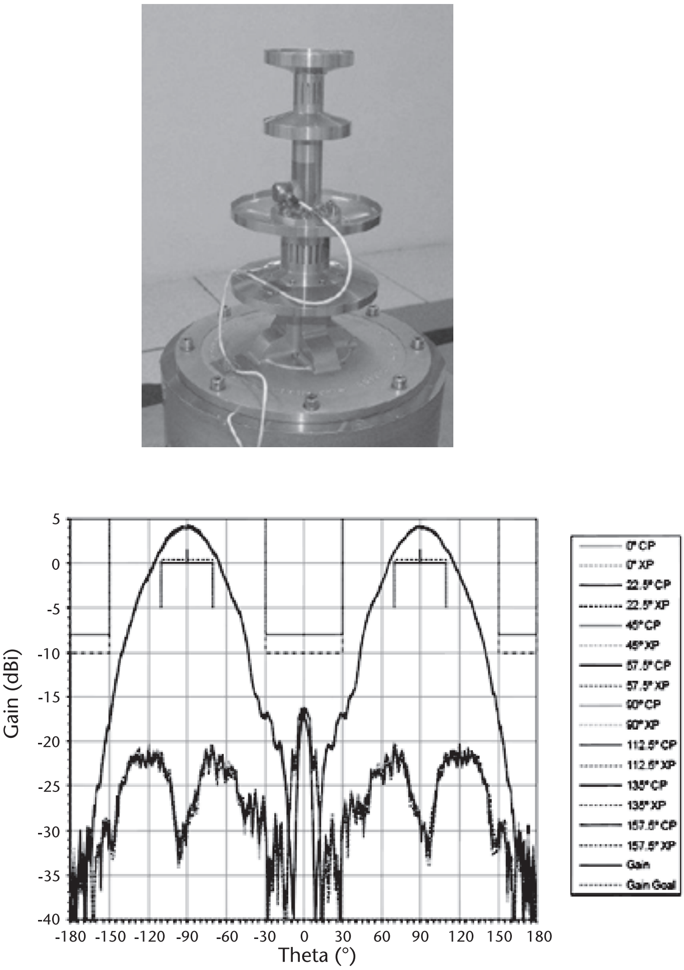

Figure 9.43 Radiation pattern of a bi-conical antenna. (Courtesy of Rymsa Espacio.)

is a spherical wave traveling in a parallel plate waveguide. This difference in paths will determine the axial ratio performance.

Thin metal corrugations, or chokes, of height $\lambda/4$ are added to the end of the cones to reduce edge diffraction and, therefore, cross-polarization. This $\lambda/4$ chokes behave like an open-ended transmission line, preventing the surface currents to flow past the edge and outwards and hence reducing the electric field radiating from outside the bi-cones. Both axial and radial chokes have been used in this type of antennas, presenting similar performances.

The design of the feeding network of this type of antennas is critical, since the receive antenna is located right on top of the transmit one. It is necessary to have the RX feed lines reaching the antenna across the TX antenna without interfering with it. For circularly polarized and linear vertically polarized omni antennas, the feeding of the radiating elements is implemented by a single feed point, including a simple transmission line for each of the antennas (TX and RX). The resulting electrical scheme is simple and the physical configuration is easy to implement, as shown in the left part of Figure 9.44. In the case of a horizontally polarized antenna, the

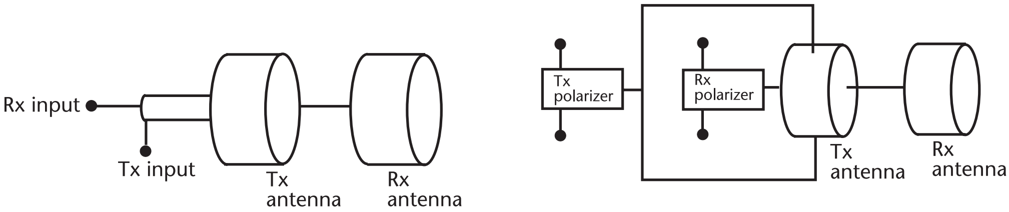

Figure 9.44 Electrical feeding configuration for vertically/circular polarized antennas (left) and horizontally polarized antennas (right).

radiating element has to be fed with a circularly polarized signal. This means that two polarizers are to be implemented in the assembly, one for each bi-cone antenna. This configuration can be seen in the right part of the same figure.

One known solution [19] is to route the signals to the antennas by means of coaxial cables. This has the drawbacks of introducing intermediate connectors and soldering between elements, while reducing the mass and envelope. Another known solution is to use a Turnstile junction as bypassing element [20]. This avoids the use of cables and intermediate junctions, resulting in a robust and reliable solution.

Interaction with Environment

As the bi-cone antenna configuration has the receive and transmit bi-cones stacked one on top of the other with the need of a baseplate to be attached to the mounting structure, it is necessary to avoid interference between both bi-cones and the baseplate. Typically, the antenna is mounted on a boom on the spacecraft antenna panel or on a tripod on the earth deck to elevate the omni antenna to a sufficient height to provide a clear, obstruction-free field of view to the RX and TX radiators. The baseplate is mounted on the tripod or the boom so that the coaxial cables feeding the two antennas can be easily accessible for mounting and integration. Therefore, appropriate selection of the distance between the omni antenna sections is required so that the radiation patterns are not affected and at the same time minimize the size and the mass of the unit.

The effect of the transmitting bi-cone (lower bi-cone) pattern on the receive bi-cone (upper bi-cone) radiation pattern can be controlled and minimized by increasing the separation distance between them. The baseplate under the TX bi-cone is critical, since the ground plane is much larger in comparison. The distance required to completely avoid the effect of the baseplate on the transmitting radiation pattern is in most cases unacceptable from the mechanical point of view, so a trade-off between mass and antenna performances is necessary. Figure 9.45 presents the effect of the size of the baseplate on the transmitting antenna radiation pattern. As the diameter of the baseplate becomes larger, the cross-polarization degrades and the gain ripple increases due to undesired reflections. The effect of the distance from the baseplate to the antenna is similar to the effect of its radius.

As an example of how sensitive the toroidal pattern of the bi-cone is to the elements surrounding it, Figure 9.46 shows the measurements for a configuration of the bi-conical antenna on top of a pole plus two global horns mounted on the same ground plane. In the conical theta cuts, the effect of the horns can be easily seen for ϕ greater than 90°, since the bi-cones are situated a short distance above the aperture levels of the horns. As ϕ increases, so do the reflections from the two side

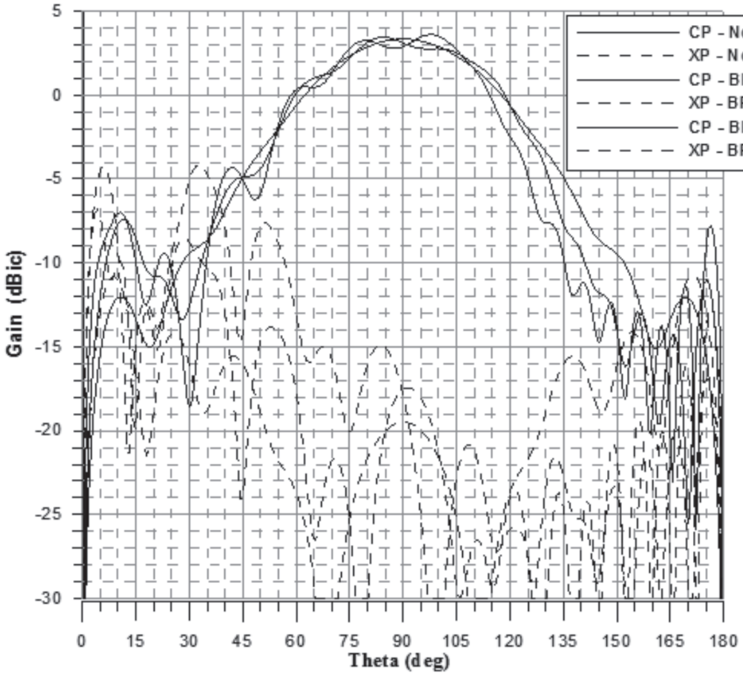

Figure 9.45 Effect of baseplate radius on bi-cone radiation pattern.

antennas. This shows that the location and positioning of the bi-conical antenna on the satellite is critical, and the reason why it is elevated well above other spacecraft structures to present a clear field of view minimizing the scattering from other elements, solar panels, and reflectors.

9.3.4.2 Wide Coverage Antennas (WCA)

Wide coverage antennas are used in conjunction with the omni antennas in the TT&C RF subsystem to provide ±30° coverage along the nadir axis to enable earth updates for the earth sensor and also provide on-station emergency coverage, should the spacecraft lose earth-lock and the spacecraft attitude is temporarily unstable. The WCA pattern fills the coverage where the toroidal omni antenna patterns have nulls [17]. In some cases, the wide-coverage horn is also used for telemetry transmission with limited telemetry EIRP for on-station operations, contingent on the requirement that the telemetry EIRP is sufficient to close the link with the ground station with adequate margin under worst-case propagation condition, including rain loss and maximum modulation loss. This combined antenna coverage approach yields omnidirectional coverage that extends from ±70° to ±110° in addition to the WCA coverage. Figure 9.47 summarizes key requirements of a WCA. Figure 9.48 shows the typical WCA requirement.

These antennas are typically required to provide ±30° from the satellite spin axis, with a gain of 7 dBi at the edge of coverage with a peak gain of 12 dBi. Secondary lobes are usually controlled by design synthesis to ensure that the WCA gain does not interfere with the omni antenna gain and that the WCA radiation pattern itself

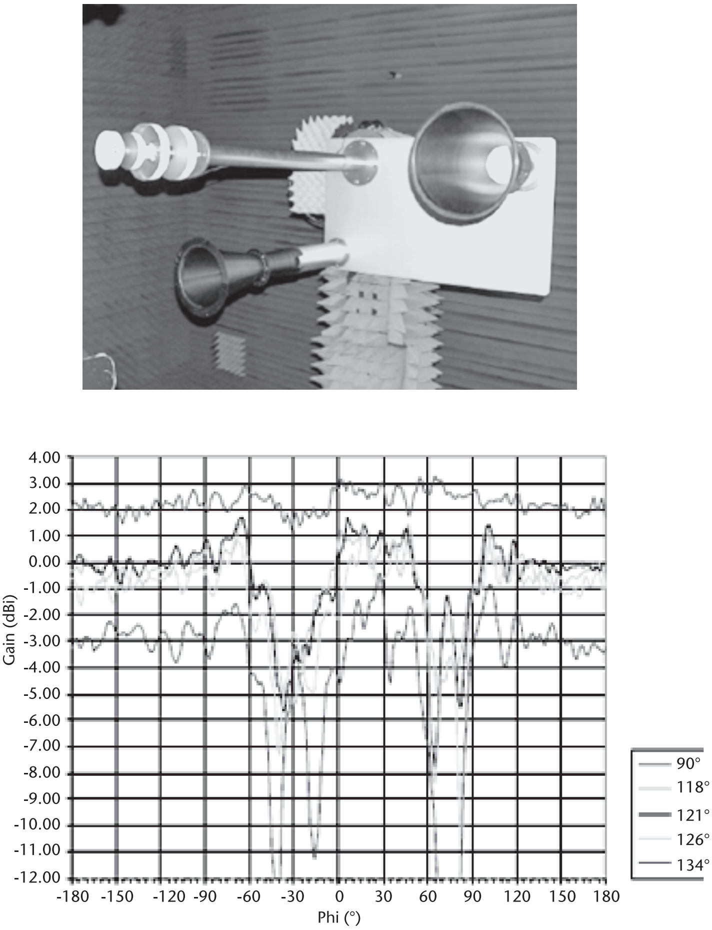

Figure 9.46 Bi-conical antenna with mockup and conical measurements of TX bi-cone. (Courtesy of Rymsa Espacio.)

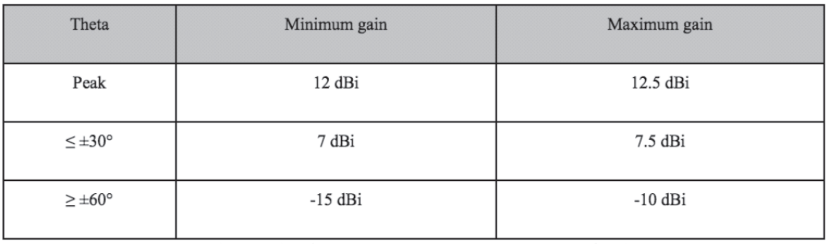

Theta	Minimum gain	Maximum gain
Peak	12 dBi	12.5 dBi
≤ ±30°	7 dBi	7.5 dBi
≥ ±60°	-15 dBi	-10 dBi

Figure 9.47 Wide coverage antenna key parameter specification.

falls off as rapidly as is practically possible. Therefore, the WCAs are required by design to confine secondary lobes to –10 dBi or less.

A radiation pattern with good pattern symmetry, low secondary lobes, and good cross-polarization can be achieved with a relatively simple multimode horn. There are many types of multimode horns as there are just as many ways to generate higher order modes. An overview of multimode horns is given earlier [21]. They basically consist in "introducing an axial symmetrical discontinuity in radial direction." Among them, the stepped discontinuity was studied by P. D. Potter [22], and

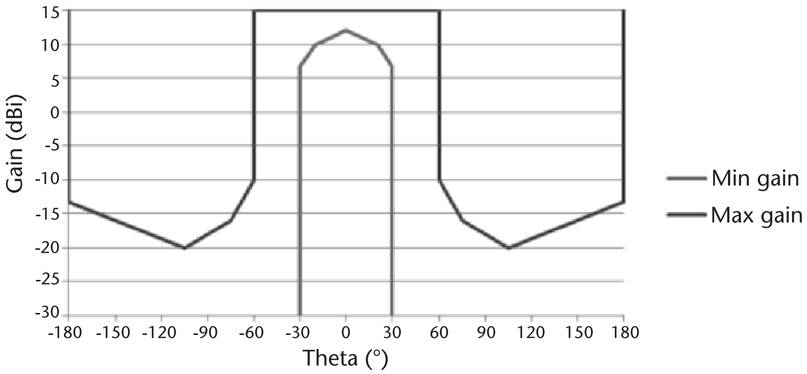

Figure 9.48 Wide coverage antenna typical gain requirements.

based on it, the sharp flare angle section by Turrin [23]. Two types are described, namely, the dual flare horn and the hybrid mode horn.

9.3.4.3 Dual-Flare Horn

A dual flare horn [23] is a type of conical multimode horn, which combines the TE_{11} and TM_{11} modes to provide the required performance characteristics. The starting point is a conical horn, which from the well-known curves of A. P. King [24] will be around 2λ in length and diameter. Figure 9.49 shows a receive and a transmit dual flare wide coverage antennas.

Principle of Operation

The TE_{11} mode is propagating in the waveguide that feeds the horn, and the TM_{11} mode is generated by a sharp flare angle discontinuity (θ) past the throat of the horn. Figure 9.50 shows a dual flare horn cross section.

The flare angle determines the amount of TM_{11} mode that is generated, and the section of length l ensures that the two modes combine at the aperture with

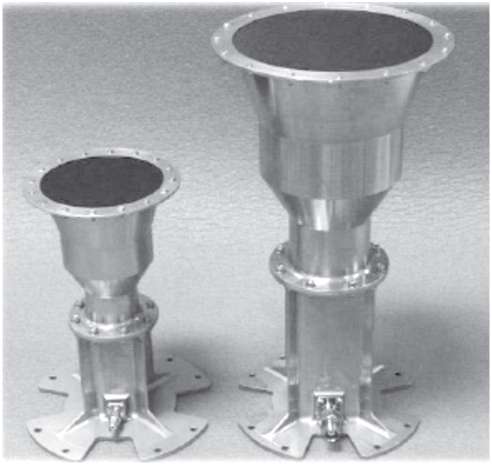

Figure 9.49 Ku-band Dual Flare Horns. (Courtesy of Rymsa Espacio.)

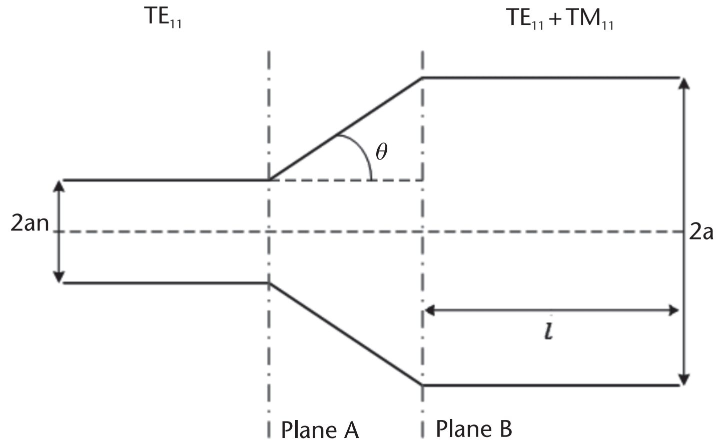

Figure 9.50 Dual flare horn cross section.

the correct phase. Based on the study from Turrin [23], the TM_{11} mode needs to be phase-shifted by 90° with respect to the TE_{11} at the end of the flared section (Plane B), and therefore a 270° phase difference between the two modes is obtained in the phase section. The values of the flare angle (θ in degrees) and phasing section length (l) are then extracted to give the optimum amount of TM_{11} mode that combines with the TE_{11} for optimum cross-polar and secondary lobes levels:

$$\theta = 22.3\lambda/a \tag{9.22}$$

$$l\left(\beta_{TE} - \beta_{TM}\right) = 3\pi/2 \tag{9.23}$$

where $\beta_{TE} = k\sqrt{1-(\lambda/4a)^2}$, and $\beta_{TM} = k\sqrt{1-(\lambda/4a)^2\left(4+(2a/2a_n)^2\right)}$.

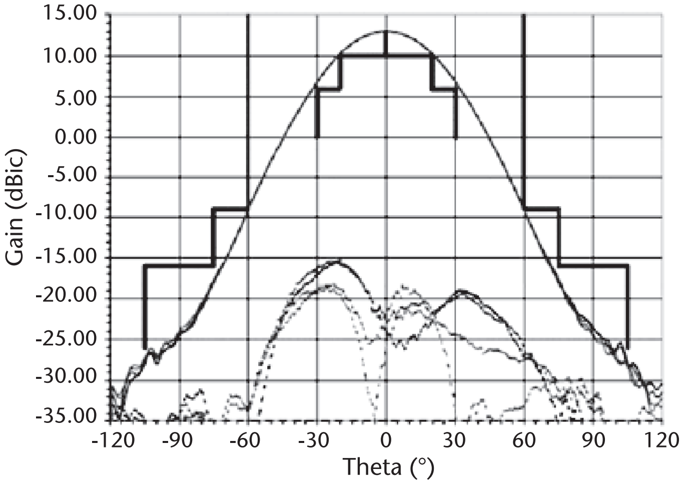

Figure 9.51 Typical performance of a dual flared conical WCA antenna.

Further optimization of the flare angle and the phasing section of the horn allow very low cross-polarization, and secondary lobe level over a wide bandwidth (up to 20%) can be achieved. An example of a real antenna's typical performance is shown in Figure 9.51.

The amount of TM_{11} mode that combines with the TE_{11} determines the level of cross-polar and secondary lobes. The optimum value between the two is 47% TM mode and 53% TE mode [23, 25].

9.3.4.4 Hybrid Mode Horn

The hybrid mode horn is another type of multimode antenna, which uses the HE_{11} and HE_{12} modes. They appeared as a response to the need for a uniform illumination in prime focus reflectors [25]. The performance of this type of horn can be very similar to the dual flare horn, but the resulting antenna is much shorter. A flight model of a transmit and receive WCA assembly of this type of antennas is shown in Figure 9.52. Figure 9.53 shows the measured radiation pattern of the hybrid mode WCA. The Hybrid mode WCA pattern exhibits a faster gain roll-off from the required coverage angles of ±30° compared to the dual flare horn.

Thomas and Bathker [26] evolved on Potter's concept [22] of the TE_{11} and TM_{11} modes combination. They applied the same principles over a corrugated surface, which would support hybrid modes: the lower order mode HE_{11} plus the higher order HE_{12}. As with Potter's, an abrupt step discontinuity is used to generate the higher order HE_{12} mode with the appropriate level, and $\lambda/4$ depth corrugations support the propagation of the hybrid modes along the horn. Figure 9.54 shows the hybrid mode WCA cross section.

The corrugated line from the abrupt transition to the aperture determines the phase difference between the two modes. The characteristic radiation pattern of this type of antenna presents a dip at the boresight. Clarricoats and Olver [27] present a parametric study on the resulting radiation pattern from different phase combinations between the two modes, or, in other words, from different lengths of the corrugated section.

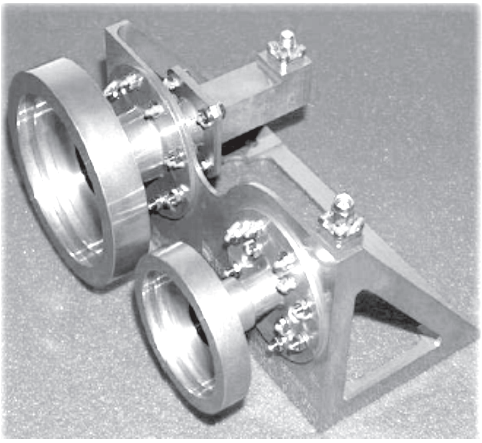

Figure 9.52 Hybrid mode horns assembly. (Courtesy of Rymsa Espacio.)

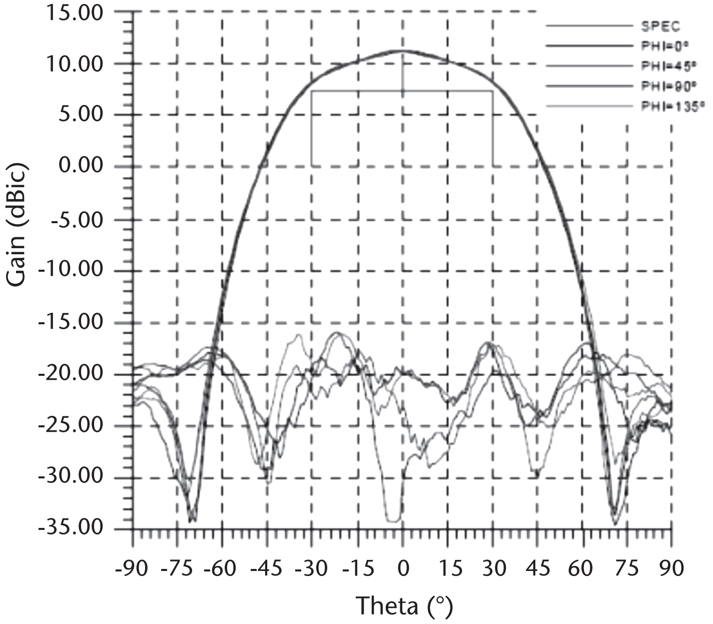

Figure 9.53 Radiation pattern of the hybrid mode WCA.

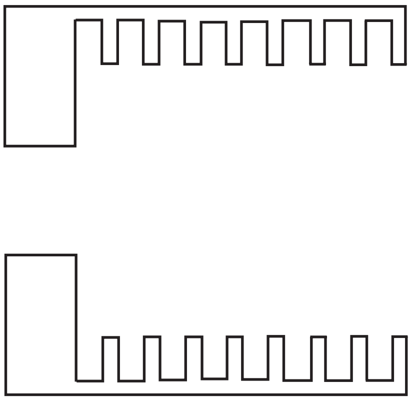

Figure 9.54 Hybrid mode horns cross section.

9.3.4.5 Hemispherical Antennas

Hemispherical antennas are commonly used by the European satellite bus to produce the omnidirectional radiation pattern required for TT&C coverage. They are known as choked waveguide feeds, since they are also used as feeds for reflectors, or choked aperture antennas. By using two of these antennas facing opposite directions, one on the nadir facing side and the other on the zenith facing side, a practically spherical radiation pattern is achieved. Therefore, a set of transmit and receive hemispherical antennas facing opposite directions would yield the required coverage. The hemispherical antenna generates a cardioidal pattern that has a θ coverage extending ±90.

REQUIREMENT	C AND Ku BANDS	Ka BAND
GAIN	> -3 dB at θ=70°	> 0 dB at θ=70°
	> -12 dB at θ=110°	> -10 dB at θ=110°
AXIAL RATIO	< 3 dB	< 3 dB
RETURN LOSS	> 20dB	> 20dB

Figure 9.55 Generic requirements for hemispherical choked antennas.

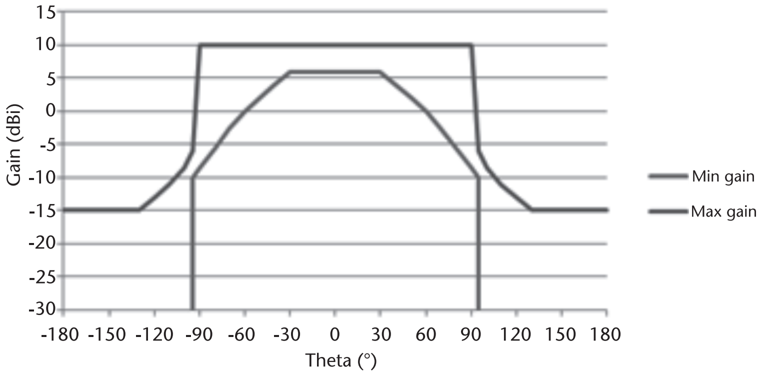

Figure 9.56 Typical gain template for hemispherical antennas.

The gain fall at the end of coverage varies depending on the specific requirements. An example of typical specification for a generic choked antenna is shown in Figure 9.55. Figure 9.56 shows the typical gain template for a hemispherical antenna.

Figure 9.57 shows the photographs of a C-band hemispherical antenna with radome and a Ku-band hemispherical antenna. Together with the minimum gain that must be achieved within the antenna coverage, it is also important to minimize to a minimum the back lobe radiation. The return loss must be maintained for the whole frequency range, which in this type of antennas may reach 20% (typically less).

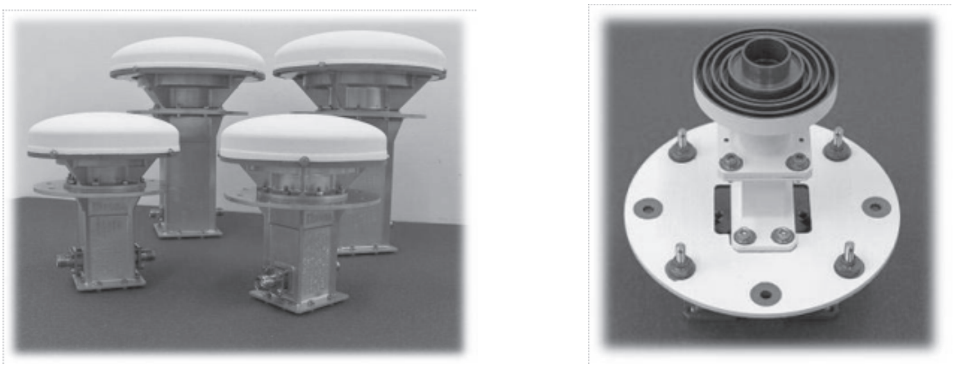

(a) (b)

Figure 9.57 Hemispherical antennas. (a) C-band with radome, and (b) Ku-band. (Courtesy of Rymsa Space.)

The hemispherical antennas consist of a circular waveguide aperture with a corrugated flange at the end, which contributes to a very simple and robust configuration. The concentric corrugations, or chokes, are excited by the aperture coupling through the open end of the waveguide. The radius of the waveguide will determine the gain, beamwidth, cross-polarization, and back lobes level of the radiating waveguide opening. Adding the axial chokes provides an overall improvement. By controlling the chokes geometry on the flange and its position with respect to the aperture, symmetry on the *E*- and *H*-planes radiation patterns over a wide coverage range (typically $\theta = 70°$) is achieved, together with increased bandwidth and cross-polarization reduction. A study on the effects of the distance of the corrugated flange to the circular aperture can be found in Agarwal and Nagelberg [28], together with the variation of the main planes phase centers.

This type of antenna is generally implemented with circular polarization, both RHCP and LHCP. The antenna feed is provided through polarizers situated below the mounting plate. Typical radiation patterns are shown in Figure 9.58.

9.3.4.6 Global Coverage Antennas

Global coverage antennas are used as part of the TT&C subsystem when the spacecraft has achieved geosynchronous operation mode. It is used for receiving command

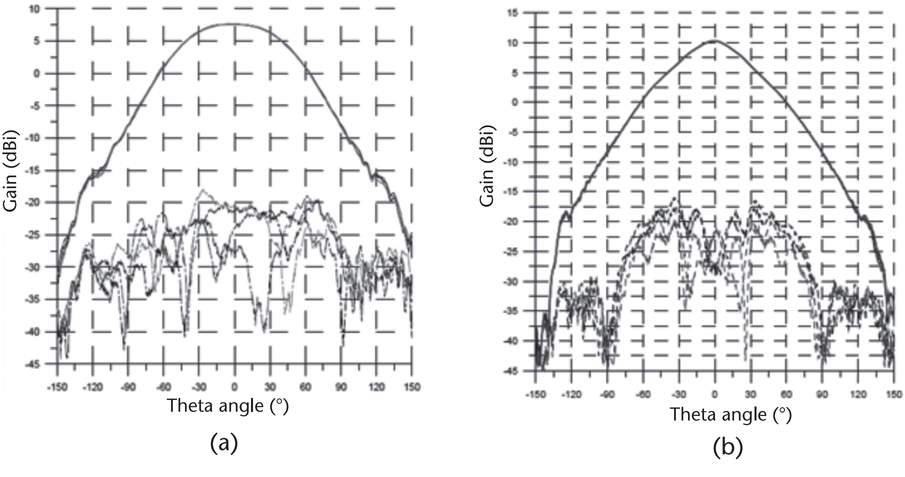

Figure 9.58 Hemispherical antennas radiation patterns. (a) C-band, and (b) Ku-band. (Courtesy of Rymsa Espacio).

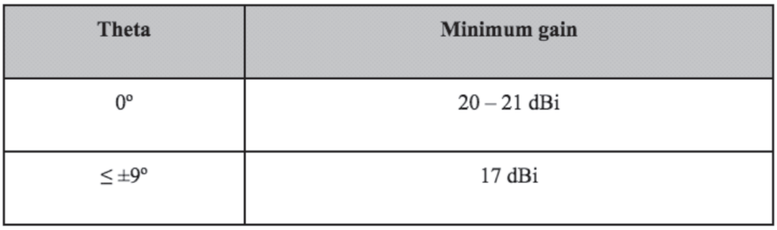

Theta	Minimum gain
0°	20 – 21 dBi
≤ ±9°	17 dBi

Figure 9.59 Generic requirements for global coverage antennas.

signals and transmitting telemetry signals from and to the ground stations. It is also used for transmitting unmodulated beacon signals to the ground for spacecraft pointing of the ground antenna terminals. Global horns are also used for transmitting telemetry signal with residual carrier for pointing. A global horn antenna can perform only one of these tasks or several, and they vary in complexity since the bandwidth of the horn can be very narrow, for a horn operating only as beacon transmitter, to wide band if both transmit and receive functions are assigned to the same antenna. Due to these varied possibilities, practical implementations of global horns range from simple smoothed wall horns like Potter horns of dual-flared conical horn to the more complex and expensive (but wideband) corrugated horns.

They provide global coverage of the earth from the geostationary orbit, so the coverage of these antennas is about ±9°. Figure 9.59 summarizes the salient gain features of a global coverage antenna.

The pattern requirement means that global horns are typically larger than 6λ, which, depending on the band of operation, can lead to a big and heavy device. They are normally implemented in aluminum, but other materials such as carbon fiber can be used for some of the larger examples of global horns. Figure 9.60 shows examples of C-band global horns.

Global horns can be divided into three groups:

- Narrowband, implemented with simple Potter horns;
- Medium band, implemented with dual-flared horns;
- Broadband, implemented with corrugated horns.

For the dual-flared conical global horns, the principles of operations are the same as for the WCAs described earlier.

A brief description of the Potter horn and the corrugated global horn follow. More details are given in other chapters of this book.

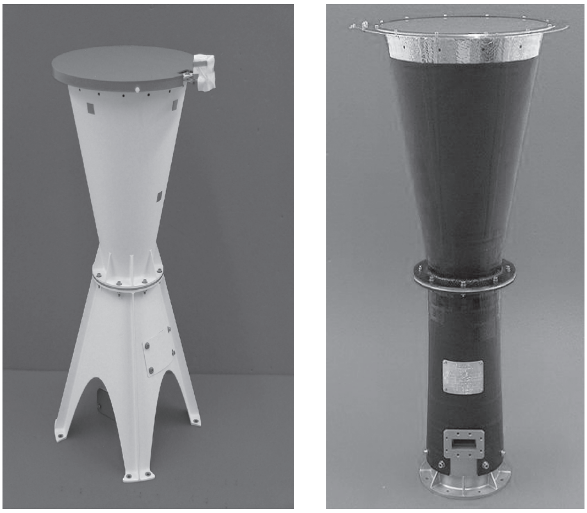

Figure 9.60 Examples of C-band global horns. (Courtesy of Rymsa Espacio.)

Potter Horn

Potter horns find application as global horns when very narrow bandwidth requirements are set, such as beacon horns. Potter [22] presented a solution for pattern symmetry and low side lobes, which consisted of utilizing a combination of the TE_{11} and TM_{11} modes. The intrinsic benefits on cross-polarization were not studied at that time. Later publications [21] addressed this aspect.

To generate the TM_{11} mode, an abrupt step is introduced in the path of the input waveguide, which carries the dominant TE_{11}. The amount of TM_{11} mode that is generated depends on the step dimension. The relation between the step and the percentage between the modes has been studied earlier [28, 29].

Corrugated Horn

The corrugated horns provide good axial symmetry and very low cross-polarization over very wide bandwidths of more than 50%. They support the HE_{11} hybrid mode, which is a combination of the TE_{11} and TM_{11} modes. The electric fields can be seen in Figure 9.61.

A cross section of a corrugated horn profile and its main parameters are shown in Figure 9.62.

The corrugated surface presents different reactances in the z and phi directions. By providing $X_\phi = 0$ and $X_z = \infty$, the conditions to lock the TE_{11} and TM_{11} mode into the hybrid mode are realized. By selecting $h = (2n - 1)\ \lambda/4$ deep slots along the horn walls, a short circuit appears at each corrugation, and the previously mentioned

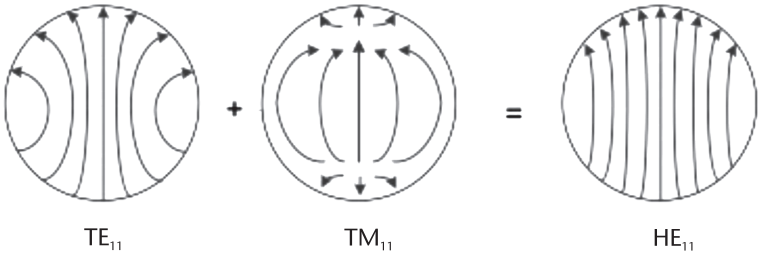

Figure 9.61 Creation of hybrid mode HE_{11}.

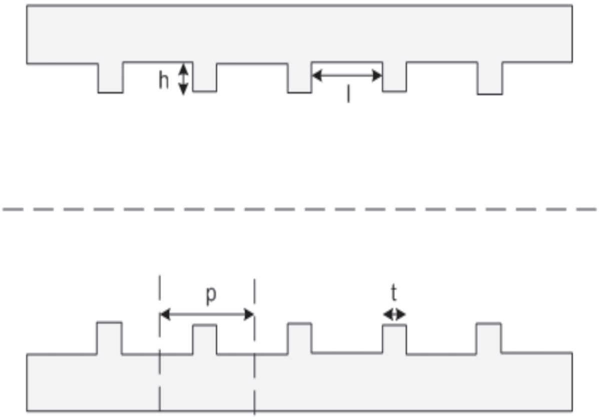

Figure 9.62 Corrugated cross section.

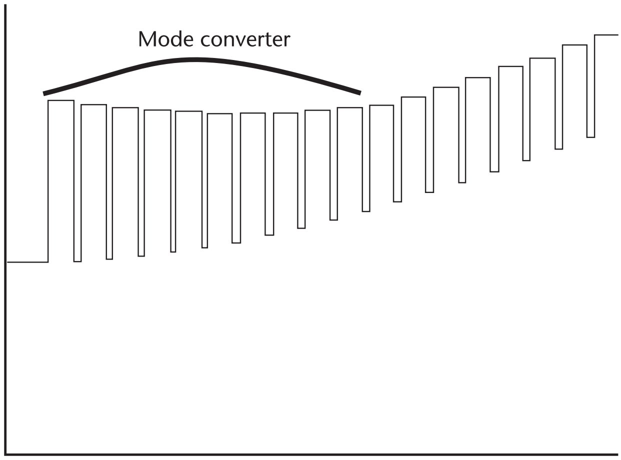

Figure 9.63 Mode converter cross-section detail.

reactance conditions are achieved; thus, the horn walls support the propagation of the hybrid mode along it. Normally, due to manufacturing issues, the shortest depth ($\lambda/4$) is chosen.

The corrugated horn is excited by a circular waveguide carrying the fundamental TE_{11} mode. A mode converter at the beginning of the corrugated section excites

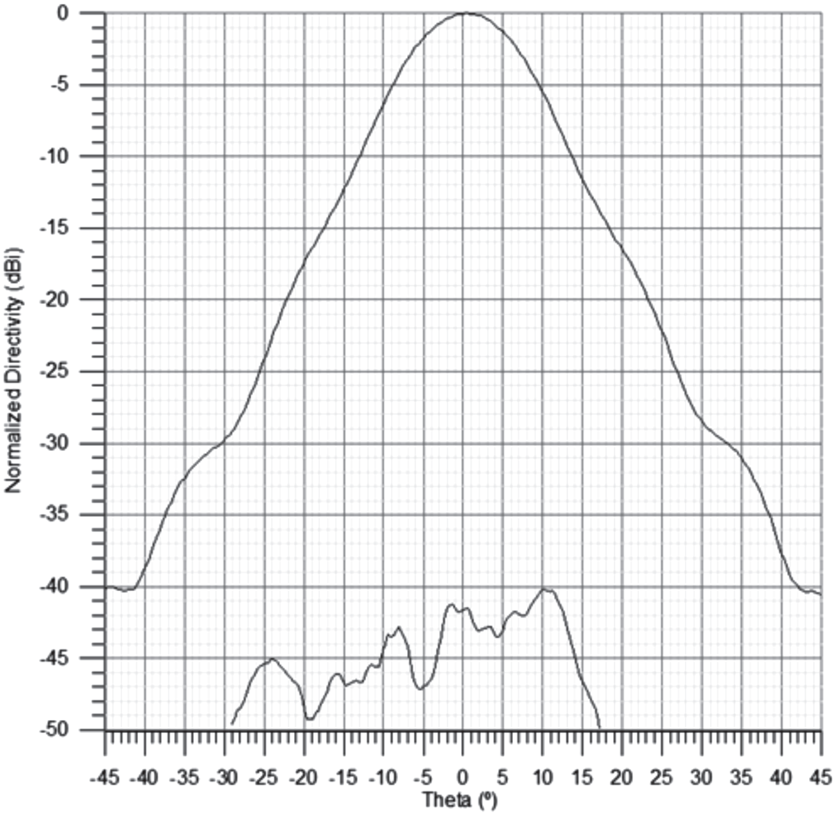

Figure 9.64 Corrugated horn radiation pattern.

the TM_{11} mode to generate the hybrid mode, which will propagate along the horn. A section of $\lambda/2$ slots, the mode converter, excite the higher order mode, and then the slots are tapered until the nominal $\lambda/4$ depth is reached. A cross section of the mode converter can be seen in Figure 9.63.

Extensive design criteria for the slot design can be found [27, 29]. A simple example of a typical radiation pattern from a corrugated horn is shown in Figure 9.64.

References

[1] Raby, S. A., et al., "Ku-Band Transmit Phased Array Antenna for Use in FSS Communication Systems," *Proc. IEEE Antennas and Propagation International Symposium*, 2000, pp. 227–229.

[2] Jones, W., and M. Chapelle, "Connexion by Boeing—Broadband Satellite Communication System for Mobile Platforms," *Proc. IEEE Antennas and Propagation International Symposium*, 2001, pp. 755–758.

[3] Mailloux, R., *Phased Array Antenna Handbook*, Norwood, MA: Artech House Inc., 1994.

[4] Kildal, P-S., "Foundations of Antennas—A Unified Approach," Studentlitteratur, Lund, Sweden, 2000.

[5] Rao, S., M. Tang, and C. Hsu, "Multiple Beam Antenna Technology for Satellite Communications Payloads," Invited Paper for Special Issue on Phased and Adaptive Array Antennas, *Applied Computational Electromagnetics Society Journal*, Vol. 21, No. 3, November 2006, pp. 353–364.

[6] Chan, K. K., and S. Rao, "Design of High Efficiency Circular Horn Feeds for Multi-beam Reflector Antennas," *IEEE Trans. on Antennas and Propagation*, Vol. 56, January 2008, pp. 253–258.

[7] Rao, S., et al., "Antenna System Supporting Multiple Frequency Bands," *IEEE Trans. on Antennas and Propagation*, Vol. 56, October 2008, pp. 3327–3329.

[8] Bhattacharyya, A., and S. Rao, "Dual-Linearly Polarized Multi-mode Rectangular Horn for Array Antennas," U.S. Patent # 6,137,450, October 2000.

[9] Rao, S., and A. Bhattacharyya, "Multi-mode Square Horn with Cavity-Suppressed Higher-Order Modes," U.S. Patent # 6,535,174, March 2003.

[10] Johnson, R. C., and H. Jasik, *Antenna Engineering Handbook*, 2nd ed., New York: McGraw-Hill, 1984.

[11] Elliott, R.S., *Antenna Theory and Design*, New Jersey: Prentice-Hall Inc., 1981.

[12] Sze, J.-Y., and W.-H. Chen, "Axial-ratio-bandwidth Enhancement of a Micro-stripline Fed Circularly Polarized Annular Ring-slot Antenna," *IEEE Trans. on Antennas and Propagation*, Vol. 56, July 2011, pp. 2450–2456.

[13] Lee, J. J., et al., "A UHF Wideband SAR Antenna," *Proc. IEEE International Conference on Phased Array Systems and Technologies*, Dana Point, CA, May 2000, pp. 437–440.

[14] Schubert, D., et al., "TSA Element Design for 500–1500 MHz Array," *Proc. IEEE Antennas and Propagation International Symposium*, 2000, pp. 178–181.

[15] Chan, K. K., and B. T. Toland, "Field Analysis of an Ultra Wideband Broad Scan Dual Polarized Array of Ridged Elements," *Proc. IEEE Antennas and Propagation International Symposium*, 2001, pp. 94–97.

[16] Chan, K. K., et al., "Measured Performance of an Ultra Broadband Widescan Dual-polarized VHF-UHF Array," *Proc. ICAP*, 2003.

[17] Rao, S., C. Hsu, and R. Sudarsanam, "Low Gain Antenna Performance Impact Due to Spacecraft Scattering," *Proc. IEEE Antennas and Propagation International Symposium*, July 2010.

[18] Milligan, T., *Modern Antenna Design*, Hoboken, NJ: John Wiley & Sons, 2005.

[19] Bäck, J., and J. Zackrisson "Circularly Polarized Slot Antenna with Toroidal Coverage," *Proc. EuCAP 2006*, Nice, France 6–10 November 2006 (*ESA SP*-626, October 2006).

[20] Mayol, F., and M. Padilla, "Turnstile Junction based Omni antennas for Space Applications," *IEEE Antennas and Propagation Magazine*, Vol. 53 No. 3., pp. 255–262.

[21] Lier, E., "Cross Polarization from Dual Mode Horn Antennas," *IEEE Trans. on Antennas and Propagation*, Vol. 34, January 1986.

[22] Potter, P. D., "A New Horn Antenna with Suppressed Sidelobes and Equal Beamwidths," *Microwave Journal*, June 1963, pp. 71–78.

[23] Turrin, R. H., "Dual Mode Small Aperture Antennas," *IEEE Trans. on Antennas and Propagation*, Vol. 15, March 1967, pp. 307–308.

[24] King, A. P., "The Radiation Characteristics of Conical Horn Antennas," *IRE Proceedings*, Vol. 38 March 1950, 249–251.

[25] Volakis, J. L., *Antenna Engineering Handbook*, 4th ed., New York: McGraw-Hill, 2007, chapter 14.

[26] Thomas and Bathker, "A Dual Hybrid Mode Feed Horn for DSN Antenna Performance Enhancement," *JPL Deep Space Network Progress Report*, 42–22, 1974, pp. 101–108.

[27] Clarricoats, P. J. B., and A. D. Olver, *Corrugated Horns for Microwave Antennas*, 1984.

[28] Agarwal, K. K., and E. R. Nagelberg, "Phase Characteristics of a Circularly Symmetric Dualmode Transducer," *IEEE Trans. on Microwave Theory and Techniques*, Vol. MTT-18, December 1970, pp. 69–71.

[29] Olver, A. D., *Microwave Horns and Feeds*, IEEE Electromagnetic Waves Series, 1994.

About the Editors

Lotfollah Shafai completed a B.Sc. degree from the University of Tehran in 1963 and M.Sc. and Ph.D. degrees from the Faculty of Applied Sciences and Engineering, University of Toronto, in 1966 and 1969.

In November 1969, he joined the Department of Electrical and Computer Engineering, University of Manitoba as a Sessional Lecturer, Assistant Professor 1970, Associate Professor 1973, and Professor 1979. To enhance the University of Manitoba contact with industry, in 1985 he established The Institute for Technology Development and was its director until 1987, when he became the head of the Electrical and Computer Engineering Department. His assistance to industry was instrumental in establishing an Industrial Research Chair in Applied Electromagnetics at the University of Manitoba in 1989, which he held until July 1994.

In 1986, he established the symposium on Antenna Technology and Applied Electromagnetics (ANTEM) at the University of Manitoba, which has grown to be the premier Canadian conference in antenna technology and related topics.

He has been the recipient of numerous awards. In 1978, his contribution to the design of a small ground station for the Hermes satellite was selected as the most Meritorious Industrial Design. In 1984, he received the Professional Engineers Merit Award and in 1985, "The Thinker" Award from Canadian Patents and Development Corporation. From the University of Manitoba, he has received Research Awards in 1983, 1987, 1989, 1999, and 2000, the Outreach Award in 1987, and the Sigma Xi Senior Scientist Award in 1989. In 1990 he received the Maxwell Premium Award from IEE (London) and in 1993 and 1994 the Distinguished Achievement Awards from the Corporate Higher Education Forum. In 1998 he received the Winnipeg RH Institute Foundation Medal for Excellence in Research. In 1999 he received the professional Engineers Outstanding Engineering Achievement Award and from the Winnipeg Chamber of Commerce the Innovation of the Year Award for design of dual-band satellite pico-terminal. He is a life Fellow of IEEE and a life Fellow of The Royal Society of Canada. He was a recipient of the IEEE Third Millenium Medal in 2000, and in 2002 was elected a Fellow of The Canadian Academy of Engineering and Distinguished Professor at the University of Manitoba. In 2003 he received an IEEE Canada Reginald A. Fessenden Medal for Outstanding Contributions to Telecommunications and Satellite Communications, and a Natural Sciences and Engineering Research Council (NSERC) Synergy Award for Development of Advanced Satellite and Wireless Antennas. He holds a Canada Research Chair in Applied Electromagnetics and was the International Chair of Commission B of the International Union of Radio Science (URSI) for 2005–2008. In 2009 he was elected a Fellow of the Engineering Institute of Canada, and was the recipient of

IEEE Chen-To-Tai Distinguished Educator Award from IEEE antennas and Propagation Society. In 2011 he received the Killam Prize in Engineering from The Canada Council for his “outstanding Canadian career achievements in engineering, and his research on antennas.”

Satish Kumar Sharma received a B. Tech. degree from Kamla Nehru Institute of Technology, Sultanpur in 1991 and a Ph.D. degree from the Indian Institute of Technology (IIT), Banaras Hindu University (BHU), Varanasi in 1997, both in electronics engineering. From March 1999 to April 2001, he was a Post Doctoral Fellow in the Department of Electrical and Computer Engineering, University of Manitoba. He was a senior antenna engineer with InfoMagnetics Technologies Corporation in Winnipeg, Manitoba, Canada, from May 2001 to August 2006. Simultaneously, he was a research associate at the University of Manitoba from June 2001 to August 2006.

In August 2006, he joined San Diego State University (SDSU) as an assistant professor in the Department of Electrical and Computer Engineering. Since August 2010, he is an associate professor. He is also director of the Antenna and Microwave Laboratory (AML). He teaches courses in applied electromagnetics and advises several BS, MS. and Ph.D students. He also served as visiting professor and principal electrical engineer at Space Systems Loral, Palo Alto, CA during the summer months of 2009 and 2010, respectively. He is author/coauthor of more than 125 research papers published in the refereed international journals and conference proceedings. He is coauthor of “Printed Antennas for Wireless Applications” a chapter from *Microstrip and Printed Antennas: New Trends, Techniques and Applications* (Wiley Inter-Science, UK). He also holds one U.S. patent.

Dr. Sharma received the National Science Foundation’s prestigious faculty early development (CAREER) award in 2009 and the Young Scientist Award of URSI Commission B, Field and Waves, during the URSI Triennial International Symposium on Electromagnetic Theory, Pisa, Italy, in 2004. He was area editor of *International Journal of Electronics and Communications* (Elsevier, UK). Currently, he serves as an associate editor of the *IEEE Transaction on Antennas and Propagation* journal. He was Chair of the Student Paper Contest of the IEEE Antennas and Propagation Society Symposium 2008, co-chair of the Student Paper Contests of the International Microwave Symposium 2010 and IEEE Applied Electromagnetic Conference (AEMC) 2011, and currently serving as a chair of the Student Paper Contest of the ACES 2013. He also served on the subcommittee of the Education Committee for the IEEE Antennas and Propagation Society for the organization of the Student Paper Contests. He is a Senior Member of IEEE, a full member of the USNC/URSI, Commission B, fields and waves, and a member of the Applied Computational Electromagnetic Society (ACES).

Sudhakar Rao received a B.Tech degree from Regional Engineering College, Warangal, India in 1974, an M.Tech degree from Indian Institute of Technology, Kharagpur, in 1976, and a Ph.D. degree from the Indian Institute of Technology, Madras in 1980, all in electrical engineering. He was a post-doctoral fellow at the University of Trondheim, Norway and later worked as a research associate at the University of Manitoba, Canada during 1981–1983.

Dr. Rao contributed to more than 60 satellite programs during his 38 years of professional experience that involved conceptual design, payload trades, detailed component design, and hardware test for both commercial and military satellites. Dr. Rao's original work on the development of analytical models/templates for complex radiation of satellite payloads was adopted by the CCIR/ITU as an international standard in 1992. He has published more than 150 technical papers, holds 40 U.S. patents, 2 trade secrets, and is listed in Marquis Who's Is Who in the World, Who's Who in America, and Who's Who in Science and Engineering. He is currently working as a Technical Fellow in the Electronics and Payload directorate of Northrop Grumman Aerospace Systems, Redondo Beach, CA. His previous work experience includes corporate senior fellow at Lockheed Martin (2003–2010), chief scientist and technical fellow at Boeing/Hughes (1996–2003), staff scientist at Spar Aerospace Limited, Canada (1983–1996), senior scientist at Electronics and Radar Devl. Establishment, India (1980–1981), and technical officer at ECIL, Hyderabad, India (1976–1977).

He is an IEEE Fellow, an IETE Fellow, Chair of the IEEE APS Industry Initiatives Committee, associate editor for the *IEEE AP-Magazine*'s Antenna Applications Corner, reviewer for IEEE APS since 1983, technical program committee member for the IEEE APS/URSI Symposium since 2003, and is a member of the IEEE APS AdCom 2010–2013. Dr. Rao received several awards during his career, including 2008 Asian American Engineer of the Year (AAEOY), 2008 IEEE Delaware Valley Engineer of the Year Award, 2006 IEEE Benjamin Franklin Key Award, Professional Excellence Award from Council of Indian Origin (CIO) in greater Philadelphia in 2009, Lockheed Martin's Inventor of New Technology awards in 2005 and 2007, Lockheed Martin's Invention & Publication awards in 2005 and 2006, and Boeing's Special Invention Award in 2002. Sudhakar received the IEEE Judith Resnik Technical Field Award in 2009 for his pioneering work in aerospace engineering.

List of Contributors

Dr. S. K. Sharma, San Diego State University
Dr. Z. A. Pour, University of Manitoba
Dr. K. Sertel, Ohio State University
Dr. S. I. Latif, University of Manitoba
Dr. G. Goyette, Boeing Company
Dr. C. Granet, BAE Systems Australia
Mr. F. Mayol, RYMSA
Ms. M. Padilla, RYMSA
Dr. R. Sudarsanam, Consultant
Dr. S. Chun, Northrop Grumman
Dr. L. Shafai, University of Manitoba
Dr. C. J. Reddy, EM Software & Systems (EMSS) USA, Inc.
Dr. A. K. Bhattacharyya, Northrop Grumman Corporation
Dr. T. S. Bird, Principal Antengenuity & CSIRO Fellow
Dr. E. Lier, Lockheed Martin
Dr. H. Nakano, Hosei University
Dr. S. Rao, Northrop Grumman

Index

A

Adaptive-cross approximation (ACA) method, 38
Adaptive dual-mode TE_{11} and TE_{21} feed, 287–90
  defined, 287
  geometry, 288
  ports, simulated scattering parameters, 288
  radiation patterns, 289
  secondary phase patterns, 290
Adaptive dual mode TE_{11} and TM_{01} feed, 290–95
  beam shift, 293
  defined, 290
  far field amplitude contours, 294
  geometry, 291
  peak gain, 293
  phase center movement, 293
  quadrature phase shifts, 291
  radiation patterns, 292–93
  reflector phase center, 291
Adaptive triple-mode TE_{11} + TM_{01} + TE_{21} feed
  defined, 295
  illustrated, 295
  radiation patterns, 295
  return loss, 296
Amplitude taper
  defined, 309
  efficiency value, 309
  plots, 310
  See also Array antennas
Annular ring-slot element, 314
Aperture efficiency
  circular-rim offset reflectors, 272
  elliptical-rim offset reflectors, 272
  hard dielcore horn, 169
  hard meta-horns, 183
  high, 99–102
  maximum, 127, 129
  MoM (WIPL-D) analysis, 184
  optimum horns, 126–29
  rectangular horns, 126
  square horn, 113
  step-and-flared horn, 113
Array antennas, 300–320
  amplitude of taper, 309–10
  categories, 300
  design, 301–10
  element diameter, 309
  element pattern, 316–20
  finite array modeling, 316
  hard horns as feeds for, 183–85
  hexagonal lattice, 304–7
  introduction to, 299–300
  lattice, 310
  layout of elements, 302
  modeling using FEM in frequency domain, 315
  number of elements, 308–9
  passive, 300
  peak directivity, 308
  phased, 300, 301
  radiating elements, 310–15
  radiation patterns, 315–20
  square lattice, 302–4
Arrays of profiled horns
  defined, 148–49
  multibeam, 150
  optimization, 149–50
  scattering matrix representation, 149
Artificial magnetic conductors (AMC), 174–75
Asymmetric feeds, 90–92, 257–97
  adaptive, 286–96
  adaptive dual-mode TE_{11} and TE_{21}, 287–90
  adaptive dual mode TE_{11} and TM_{01}, 290–95
  adaptive triple-mode TE_{11} + TM_{01} + TE_{21}, 295–96

Asymmetric feeds *(Cont.)*
  applications of, 260–73
  co-polarization, 91
  cross polarization, 91
  cross polarization reduction, 261–73
  defined, 90
  designs, 260
  geometry, 91
  introduction to, 257–60
  for multiphase center applications, 286–87
  radiation patterns, 92
  ring choke excited circular waveguide with slot, 273–78
  stepped circular waveguide with tuning blocks, 278–82
Asymmetric profile, 135
Axial choke corrugated horns, 28
Axial ratio (AR)
  back-fire-mode CP helical feed antenna, 234
  curl CP feed antennas, 251
  end-fire helical CP feed antenna, 211
  long conical helical CP feed antennas, 221
  short conical helical CP feed antennas, 225
  spiral CP feed antenna, 244

B

Backfire feeds
  cross polarization, 70–71
  defined, 70
  geometry, 71
  modified cup, 72–74
  radiation patterns, 71
Back-fire-mode CP helical feed antenna, 227–37
  axial ratio (AR), 234
  back-fire radiation, 227
  beamwidth, 232
  C-current, 228–29
  current distribution and radiation, 229
  F/B ratio, 234
  frequency response of current, 230–31
  gain, 236
  input impedance, 235
  parabolic reflector, 236
  parameters, 231
  phase center of radiation field component, 237
  pitch angle and, 231–37
  radiation patterns, 233
  See also CP feed antennas
Backfire printed dipole feeds, 83–90
  coordinate system, 84
  defined, 83
  design approach, 83–84
  geometry, 84
  impedance bandwidth, 85–86
  miniaturizing printed dipole feed, 86–87
  pattern equalization, 88–89
  pattern symmetry, 86
  performance results, 84–89
  performance with reflector, 89–90
  radiation patterns, 90
Basis functions
  fast multipole method (FMM), 38
  known, 18
  method of moments (MoM), 22, 31–33
  Rao-Wilton-Glisson (RWG), 22
  representation as surface vector fields, 19
Beamwidth
  back-fire-mode CP helical feed antenna, 232
  curl CP feed antennas, 247–49, 251
  curl element parameters, 248
  end-fire helical CP feed antenna, 214
  long conical helical CP feed antennas, 221
  short conical helical CP feed antennas, 225
  spiral CP feed antenna, 243
Bi-conical antennas, 329–37
  applications, 329–30
  baseplate radius, 337
  chokes, 335
  circular polarization, 334
  electrical feeding configuration, 336
  examples of, 332
  feeding network design, 335–36
  fields and currents distribution, 333
  frequency bands, 330
  generic requirements, 331
  geometry, 334
  illustrated, 330
  interaction with environment, 336–37
  principle of operation, 332–36
  radiation patterns, 335
  toroidal radiation pattern, 331
  TX bi-cone, 338
  See also Telemetry, tracking and control (TT&C) antennas
Bi-conjugate gradient (BiCG), 24

Boundary conditions, method of moments (MoM), 17
Bowl-shaped horns, 132
Bowtie antenna geometry, 20, 25

C

Calvin feed, 51, 70
Cavity-backed spiral CP feed antenna, 240
C-current, 228–29
CHAMP, 137
Circular aperture, 102–11
  horn design, 105–10
  realization of the modes, 103–5
  three-step horn, 110–11
Circular horns
  aperture diameter, 141
  cross polarization, 98
  dominant mode, 311–12
  multimode, 312
  profiled, 141, 142
  radiation patterns, 142
Circularly polarized feed antennas. *See* CP feed antennas
Circular patch antenna
  bandwidth control, 80–81
  co-polarization, 76–78, 82
  cross polarization, 76–78
  as feed, 74–81
  gain factors, 79
  geometry, 75
  ground plane size, 79
  patch size, 79
  pattern control, 80
  pattern optimization, 74–79
  with shaped ground plane, 80
  on substrate, 75
  two-layer stacked, 81
Circular-rim offset reflectors
  aperture efficiency, 272
  cross polarization, 269, 272
  gain, 272
  geometry, 267
  radiation patterns, 269
  SLL, 272
Circular waveguides
  back lobe levels, 60
  cavity-loaded, 68
  with corrugations, 65
  geometries with chokes, 63
  geometry, 57
  peak cross polarization, 58
  principal radiation patterns, 59
  radiation patterns, 58
  ring choke excited, with slot, 273–78
  stepped, with tuning blocks, 278–82
Coaxial feeds, 64–67
  gain factors, 66–67
  geometry, 66
  radiation patterns, 66
Coaxial horns, 140–43
Coaxial waveguides, 64
Compactness, 131–32
Computational electromagnetics (CEM) method, 14–17
Conical helical CP feed antennas, 219–27
  axial ratio (AR), 221
  beamwidth, 221, 225
  defined, 219
  F/B ratio, 222, 226
  gain, 222, 226
  horns, 204
  illustrated, 219
  input impedance, 223, 227
  long conical helical element, 219
  offset feed, 223
  radiation patterns, 220, 224
  short conical helical element, 219
Conjugate gradient (CG), 24
Conjugate gradient squared (CGS), 24
Connected element, 314
Coplanar waveguide (CPW) network, 146
Co-polarization
  asymmetric feeds, 91
  circular patch antenna, 76–78, 82
  components, 4
  dielcore horns, 167
  hard meta-horns, 182
  high-efficiency horns, 107
  multiple-beam reflectors, 118
  soft meta-horns, 178
Corrugated horns, 140
  cross section, 346
  as global coverage antenna, 346–48
  hard, 172–73
  hybrid modes using, 52
  radiation characteristics, 27
  radiation patterns, 347
  soft, 160–62

Corrugated microstrip dipole antennas
  geometry, 88
  radiation and impedance characteristics, 89
  simulated parameters, 88
  simulated performance, 89
CP feed antennas, 193–253
  back-fire-mode, 227
  conical helical, 219–27
  curl, 245–53
  design methods, 194, 195–202
  end-fire helical, 207–15
  finite-difference time-domain method (FDTDM) analysis, 199–202
  introduction to, 193–94
  method of moments (MoM) analysis, 195–99
  one-point excitation patch, 205–7
  parameters, 218
  post processing for MoM, 198–99
  spiral, 237–45
  two-point excitation patch, 202–5
  unknown current, matrix expression for, 195–97
CP feed array antenna
  application example, 217
  composed of helical elements, 215–18
  illustrated, 216
  radiation patterns, 218
  two-layer structure, 217
CP wave generation techniques, 193–94
Cross polarization
  asymmetric feeds, 91
  backfire feeds, 70–71
  circular horns, 98
  circular patch antenna, 76–78
  circular-rim offset reflectors, 269, 272
  circular waveguides, 58
  dielcore horns, 167
  dielectric loaded cavity back feed, 67
  elliptical-rim offset reflectors, 271, 272
  feeds, 7
  hard meta-horns, 182
  high-efficiency horns, 107
  meta-horns, 175, 176
  small feeds, 53–54
  soft meta-horns, 178
  soft strip-loaded horn, 172
Cross polarization reduction
  asymmetric feed designs for, 273–82
  classical matched feeds, 262–64
  focal plane distributions, 262–64
  matched primary feed, 264–73
  in offset reflector antennas, 261–73
  stepped circular waveguide with tuning blocks, 280
Cup-dipole radiating elements, 312
Curl CP feed antennas, 245–53
  axial ratio (AR), 251
  beamwidth, 247–49, 251
  CP radiation, 245–47
  curl element, 246
  defined, 245
  F/B ratio, 252
  frequency response, 249–53
  gain, 253
  input impedance, 252
  loop region, 247
  radiation patterns, 250
Cutler feed, 51

D

Dielcore horns, 162–70
  co-polarization, 167
  cross polarization, 167
  hard, 166–70
  meta-horns versus, 174
  radiation patterns, 167
  soft, 162–66
  with solid dielectric core, 165
Dielectric loaded cavity back feed
  cross polarization, 67
  defined, 67
  gain factors, 70
  geometry, 69
  radiation patterns, 70
Dielectric loaded helix antennas, 37
Dielectric rod and horn, 145–48
Dipoles
  electric, 4, 5, 6, 53
  field equivalence, 4
  magnetic, 4, 5, 6, 53
Direct radiating arrays, 115–17
Discretization
  finite-element method (FEM), 31–33, 315
  method of moments (MoM), 21
  volumetric, 31–32
Dual-flare horn
  cross section, 340

- defined, 339
- flare angle optimization, 341
- performance of, 340
- principle of operation, 339–41

Dyadic Green's function, 16–17, 23, 37

E

Electric field integral equation (EFIE), 19
Electromagnetic band gap (EBG) superstrate, 93
Element matrix, 32
Element pattern
- directivity, 319–20
- embedded, 316
- grating lobe, 317–18
- noise temperature, 320
- scan loss, 320
- for wide-scan arrays, 317
- *See also* Array antennas

Elliptical horns, soft dielcore, 165
Elliptical-rim offset reflectors
- aperture efficiency, 272
- cross polarization, 271, 272
- defined, 269
- gain, 272
- projected aperture, 270
- radiation patterns, 271
- SLL, 272

Empirical profiles, 134–35
End-fire helical CP feed antenna
- axial ratio (AR), 211
- beamwidth, 214
- cavity diameter and, 210
- cavity effects, 208–10
- cavity height and, 211
- defined, 207
- dielectric layer, 215
- F/B ratio, 213
- frequency response, 210–15
- gain, 215
- helical element, 208
- helical element parameters, 210
- helical element within cavity, 209
- input impedance, 214
- radiation patterns, 212
- *See also* CP feed antennas

Exponential profile, 135

F

Fast-frequency sweep, 41–43
Fast multipole method (FMM)
- basis functions, 38
- defined, 38
- multilevel, 40
- steps, 39

Feed efficiency
- defined, 7
- factors, 7
- overall, 8
- small waveguide feeds, 61
- subefficiencies, 8

Feeds
- adaptive, 5
- aperture size, 3
- asymmetric, 90–92, 257–97
- backfire, 70–74
- backfire printed dipole, 83–90
- coaxial, 64–67
- cross polarization, 7
- functions, 6
- hard horns as, 183–85
- microstrip, 74–83
- pattern shaping, 92–93
- phase center determination, 6–7
- radiating field, 5
- small, 4, 51–93
- waveguide, 56–74
- wide angle, 67–70

FEKO, 20, 24–25
Finite array modeling, 316
Finite-difference time-domain method (FDTDM)
- in CP feed antenna design, 199–202
- defined, 199
- finite difference, 199–200
- Maxwell's equations, 200–201
- post-processing for, 201–2

Finite-element method (FEM), 28–34
- boundary conditions, 31
- discretization, 31–33, 315
- examples, 34
- feed modeling, 31
- as full-wave method, 13
- functional formalism and discrete formulation, 30–31
- high-order absorbing boundary conditions, 33

Finite-element method (FEM) (Cont.)
  h-refinement, 33
  material modeling, 31
  mesh density, 33
  p-refinement, 33
  radiation boundary condition, 30
  in solving Maxwell's equations, 28–30
  system assembly, 32
  unknown, 30
  See also Numerical methods
Flared notch element, 314
Focal plane field
  distribution of offset reflector, 262
  as extending to infinity, 257
  in limited context, 258
Free-space Green's function, 37
Frequency derivatives, 42, 43
Frequency response
  back-fire-mode CP helical feed antenna, 230–31
  curl CP feed antennas, 249–53
  end-fire helical CP feed antenna, 210–15
  spiral CP feed antenna, 241–45
Front-to-back ratio (F/B ratio)
  back-fire-mode CP helical feed antenna, 234
  curl CP feed antennas, 252
  end-fire helical CP feed antenna, 213
  long conical helical CP feed antennas, 222
  short conical helical CP feed antennas, 226
  spiral CP feed antenna, 243

G

Gain
  back-fire-mode CP helical feed antenna, 236
  circular-rim offset reflectors, 272
  curl CP feed antennas, 253
  elliptical-rim offset reflectors, 272
  end-fire helical CP feed antenna, 215
  long conical helical CP feed antennas, 222
  short conical helical CP feed antennas, 226
  spiral CP feed antenna, 245
  wide-coverage horn antenna (WCA), 337, 339
Gain factors
  circular patch antenna, 79
  coaxial feeds, 66–67
  cross polarization, 70
  small feeds, 54–55
  small waveguide feeds, 61, 64
Galerkin's testing, 29
Gaussian or hyperbolic profile, 135
Gauss' law, 16
Generalized minimal residual (GMRES), 24
Geometrical optics (GO)
  approximation, 45
  electric field, 46
  incident field wavefronts, 46
  radiation characteristics using, 47
  utilization, 46
Geometrical theory of diffraction (GTD), 43, 48
Global coverage antennas
  corrugated horn, 346–48
  generic requirements, 344
  Potter horn, 346
  types of, 345
  See also Telemetry, tracking and control (TT&C) antennas
GRASP V.7, 264
Green's functions, 16–17
Green's theorem, 101
Ground moving target indicator (GMTI) radars, 283

H

Hard dielcore horn
  aperture efficiency, 169
  bandwidth potential, 169
  computed performance versus frequency, 170
  defined, 166
  illustrated, 167
  MoM analysis, 169
  propagation characteristics, 166–67
  See also Dielcore horns
Hard horns
  classifications of, 186–88
  concept of, 158
  corrugated, 172–73
  defined, 158
  as feeds for array antennas, 183–85
  as hybrid-mode horns, 159–60
  illustrated, 159
  strip-loaded, 172–73
  See also Soft horns
Hard meta-horns
  aperture efficiency, 183
  boundaries, 175

  co-polarization, 182
  cross polarization, 182
  defined, 182
  directivity patterns, 182
  implementations, 175
  optimal dispersion curve, 182
  See also Meta-horns
Helical elements
  with cavity, 210
  CP feed array antenna composed of, 215–18
  illustrated, 208
  radiating, 313
Helix-fed reflector antenna, 47
Hemispherical antennas
  applications, 342–43
  circular waveguide aperture, 344
  gain template, 343
  generic requirements, 343
  illustrated, 343
  radiation patterns, 344
  See also Telemetry, tracking and control (TT&C) antennas
Hexagonal lattice array
  boresight beam, 306
  directivity patterns, 306, 307
  element spacing, 304
  geometry, 305
  scanned beam, 307
High aperture efficiency
  circular aperture, 102–11
  smooth wall multimode horns for, 97–119
  theory of, 99–102
High-efficiency horns, 97–119
  alternative structures, 115
  aperture efficiency versus normalized frequency, 108
  applications, 115–19
  bandwidth performance, 108
  circular aperture, 102–11
  conclusions, 119
  co-polarization, 107
  cross polarization, 107
  design, 105–10
  design dimensions, 110
  in direct radiating arrays, 115–17
  electric field lines, 106
  gain enhancement, 98
  geometry, 104
  illustrated, 99, 110
  input return loss, 108, 109
  introduction to, 97–99
  inward and outward steps, 104
  multiflared, 113–14
  in multiple-beam reflectors, 117–19
  normalized modal voltages, 105
  performance comparison, 108, 109
  physical aperture size, 97
  square, 111–13
  three-step, 110–11
  two-step, 102–10
Horn aperture
  with cross-sectional geometry, 101
  transverse magnetic field, 100
Horn designs, 123, 139–51
Horn-fed Gregorian axis-symmetrical dual reflector, 40
Horn length, 132
Horn profiles, 123–51
  asymmetric, 135
  choice of, 133–34
  conclusion, 151
  empirical, 34–35
  examples of, 124
  exponential, 135
  flow graph, 138
  Gaussian or hyperbolic, 135
  illustrated, 124
  L-band, 150
  optimization approaches, 134–37
  optimization methods, 137–39
  parametric, 135–37
  polynomial, 135
  sinusoid, 135
  symmetry planes, 133
  tangential, 135
  typical, 134
Horns
  bowl-shaped, 132
  circular, 140–43
  coaxial, 140–43
  corrugated, 140, 346–48
  dual-flare, 339–41
  global, 326
  hybrid-mode, 157–58, 341–42
  optimum, 124–32
  Potter, 51, 311, 346
  rectangular, 143–44, 312
  round, 265
  smooth-walled, 140–43
  smooth wall multimode, 97–119
  square, 312
Horn weight, 132

H-refinement, 33
Hybrid finite-element boundary integral (FE-BI) formulation
  defined, 35
  example, 36
  surface magnetic field intensity, 35
Hybrid-mode horns
  with circular symmetry, 157
  classifications of, 186–88
  dielcore, 162–70
  hard strip-loaded, 172–73
  introduction to, 157–58
  meta-horns, 173–83
  soft corrugated, 160–62
  soft strip-loaded, 171–72
  TT&C, 341–42

I

Input impedance
  back-fire-mode CP helical feed antenna, 235
  curl CP feed antennas, 252
  end-fire helical CP feed antenna, 214
  long conical helical CP feed antennas, 223
  short conical helical CP feed antennas, 227
  spiral CP feed antenna, 244
Input mismatch, 126
Integral equations
  approximated, 18
  electric field (EFIE), 19
  fast methods for, 36–43
  magnetic field (MFIE), 21
  method of moments (MoM), 18–19

K

Krylov subspace methods, 24

L

Large-scan radiating elements, 313–15
Launch and early orbit phases (LEOP), 322
Linear profile design (LIN), 145
Loop-based CP (LPB-CP) radiation, 237
Low-gain antennas (LGA), 329
Low gain TT&C antennas. *See* Telemetry, tracking and control (TT&C) antennas
Low-scan radiating elements, 311–13

M

Magnetic field integral equation (MFIE), 21
Matched feeds
  classical, 262–64
  simplified analytical model for, 264–73
  tri-mode, 263
Maxwell's equations
  CEM methods for, 14
  in electromagnetic analysis, 14–17
  phasor form, 15
  solving with FEM, 28–30
Mesh conductivity, 21
Meshing, 18, 19–21
Meta-horns, 173–83
  cross-polarization, 175, 176
  defined, 174
  dielcore horns versus, 174
  hard, 182–83
  illustrated, 174
  introduction to, 173–76
  optimal dispersion curve, 176
  performance of, 174
  soft, 176–82
Metamaterials, 173–74
Method of moments (MoM), 17–28
  basis functions, 22, 31–33
  boundary conditions, 17
  in CP feed antenna design, 195–99
  CPU time requirements, 25–26
  defined, 17
  direct/iterative solution methods, 23–-24
  discretization, 21
  examples, 24–28
  as full-wave method, 13
  geometry representations, 19–21
  impedance matrix equation, 22–23
  integral equation formulation, 18–19
  meshing, 18, 19–21
  post processing for, 198–99
  surface mesh elements, 21
  testing process, 18
  See also Numerical methods
Microstrip feeds, 74–83
  bandwidth control of, 80–81
  defined, 74
  planar antenna array, 81–83
  single patch antenna, 74–81
Microstrip patch element, 313–14
Microwave Wizard, 137
Model order reduction, 41–43

Modified cup feed
  defined, 72
  far-field radiation patterns, 72
  phase center locations, 73
  photo, 72
  results summary, 74
  secondary radiation patterns, 72, 73
MoM (WIPL-D) analysis, 183, 184
Multibeam array feed, 150
Multiflared high-efficiency horns, 113–14
Multilevel FMM (MLFMM), 40
Multiphase center reflector antennas, 282–96
  adaptive asymmetric feed designs for, 286–87
  concept theory, 283–84
  phase center, 283
  radiation patterns, 286
  symmetrical-cut paraboloids, 284–86
Multiple-beam reflectors
  co-polarization, 118
  hexagonal beam layout, 117
  high-efficiency horns in, 117–19

N

Natural boundary conditions, 15–16
Natural electromagnetic boundary conditions, 15–16
Numerical methods, 13–49
  fast, 36–43
  finite-element method (FEM), 13, 28–34
  high-frequency, 13–14, 43
  hybrid FE-BI, 13, 35–36
  introduction to, 13–14
  Maxwell's equations and, 14–17
  method of moments (MoM), 13, 17–28
  system matrix equation, 41

O

Offset reflectors, 261–73
  circular-rim, 267–69
  classical matched feeds, 262–64
  cross polarization reduction in, 261–73
  elliptical-rim, 269–72
  focal plane electric field distribution, 262
  geometry, 266
  matched primary feed, 264–73
  normalized amplitude pattern, 267
  secondary radiation patterns, 263
Omni antennas
  EIRP budget, 328
  frequency bands, 330
  gain template, 331
  link budget, 328
  location on spacecraft, 325
One-point excitation CP patch feed antenna
  defined, 205
  illustrated, 206
  radiation patterns, 207
Optimum horns
  aperture efficiency, 126–29
  basis of, 124–32
  compactness, 131–32
  input mismatch, 126
  pattern constraints, 125–26
  phase center stability, 129–31
  See also Horns
Organization, this book, 9–11

P

Parabolic reflectors
  aperture field distributions, 285
  back-fire-mode CP helical feed antenna, 236
  focal plane field, 55
  illustrated, 228
  as powerful devices, 282–83
  symmetric, geometry of, 284–85
Parametric profiles, 135–37
Passive array antennas, 300
Perfectly electrically conducting (PEC) surfaces, 18–19
Phase center
  back-fire-mode CP helical feed antenna, 237
  calculation, 130
  determination, 6–7
  distance from coordinate origin, 7
  modified cup feed, 73
  multiphase center reflector antennas, 283
  in optimization process, 131
  small waveguide feeds, 60
  stability, optimum horns, 129–31
  uniqueness, 54
Phased array antennas
  defined, 300
  schematic, 301
Phase error, 7

Physical constraint, 131–32
Physical optics (PO)
  approximation, 43–46
  implementation simplicity, 45
  mesh-based, 45
  radiation characteristics using, 47
Planar antenna array feeds, 81–83
Point matching, 23
Polynomial profile, 135
Potter horns, 311, 346
Poynting vector, 127
P-refinement, 33
Prime focus reflectors, 2, 52
Printed circuit board (PCB) technology, 179, 181
Profiled horns, 123–51
  arrays of, 148–51
  circular, 141, 142
  dielectric rod and, 145–48
  introduction to, 123–24
  rectangular, 143–44
Profiled rods
  boresight gain, 148
  defined, 145
  illustrated, 146
  optimization, 147
  performance summary, 148
  radiation patterns, 147
  side lobes, 146
Pyramidal horns
  CP feed antenna, 204
  radiation characteristics, 26, 34

Q

Quasiminimal residual (QMR), 24

R

Radiating elements
  annular ring-slot, 314
  categories of, 311
  choice of, 31
  connected, 314
  cup-dipole, 312
  dominant mode circular horns, 311–12
  flared notch, 314
  helical, 313
  large-scan, 313–15
  low-scan, 311–13
  microstrip patch, 313–14
  multimode high-efficiency circular horns, 312
  Potter horns, 311
  rectangular and square horns, 312
  ridged waveguide, 314–15
  slot, 314
  See also Array antennas
Radiation characteristics
  axial choke corrugated horns, 28
  corrugated conical horns, 27
  pyramidal horns, 26
Radiation patterns
  adaptive dual-mode TE_{11} and TE_{21} feed, 289
  adaptive dual mode TE_{11} and TM_{01} feed, 292–93
  adaptive triple-mode TE_{11} + TM_{01} + TE_{21} feed, 295
  array antennas, 315–20
  asymmetric feeds, 92
  backfire feeds, 71
  back-fire-mode CP helical feed antenna, 233
  backfire printed dipole feeds, 90
  bi-conical antennas, 335
  circular-rim offset reflectors, 269
  circular waveguides, 58, 59
  coaxial feeds, 66
  corrugated horns, 347
  CP feed array antenna, 218
  curl CP feed antennas, 250
  dielcore horns, 167
  elliptical-rim offset reflectors, 271
  end-fire helical CP feed antenna, 212
  envelope constraints, 125–26
  hemispherical antennas, 344
  long conical helical CP feed antennas, 220
  modified cup feed, 72, 73
  multiphase center reflector antennas, 286
  offset reflectors, 263
  one-point excitation CP patch feed antenna, 207
  profiled circular horn, 142
  profiled rectangular horn, 144
  profiled rods, 147
  ring choke excited circular waveguide with slot, 275, 277
  short conical helical CP feed antennas, 224
  small waveguide feeds, 64
  soft meta-horns, 178
  spiral CP feed antenna, 242

- square high-efficiency horn, 112
- stepped circular waveguide with tuning blocks, 281, 282

Rao-Wilton-Glisson (RWG) basis function, 22
Ray-tracing based methods, 45
Rectangular horns
- aperture distribution, 144
- aperture efficiency, 126
- as low-scan radiating element, 312
- profiled, 143–44
- radiation patterns, 144
- soft dielcore, 165

Reflection-shadow boundary (RSB), 48, 49
Reflectors
- applications, 1
- compact range, 3
- configurations, 1
- dimensions, 1
- fed by soft dielcore lens horn, 166
- focal plane field, 257–58
- geometries, 2
- high-gain, 258
- multiphase center, 282–96
- offset, 261–73
- parabolic, 228, 236, 282–83, 285
- prime focus, 2, 52
- symmetric, 2, 260, 284

Ridged waveguide element, 314–15
Ring choke excited circular waveguide with slot, 273–78
- amplitude ratio, 275
- geometry, 273, 274
- modes in far-field region, 274
- prototype photo, 277
- radiation patterns, 275, 277

S

Scalar Green's function, 17, 37, 38
Selective gain profiled dielcore, 166–70
Simplex triangular mesh, 21
Singular value decomposition (SDV), 38
Sinusoid profile, 135
Slot radiating element, 314
Small feeds, 51–93
- asymmetric, 90–92
- backfire printed dipole, 83–90
- conceptual design, 52
- cross polarization, 53–54
- design requirements, 53–56
- early, 51–52
- high antenna gain factor, 54–56
- introduction to, 51–53
- microstrip, 74–83
- pattern shaping by superstrate loading, 92–93
- phase center uniqueness, 54
- waveguide, 57–64

Small waveguide feeds, 57–64
- chokes, 62–63
- gain factors, 61, 64
- phase center locations, 60
- principal radiation patterns, 64
- waveguide aperture distance from phase centers, 63

Smooth-walled horns, 140–43
- advantages of, 140
- high aperture efficiency, 97–119
- multimode, 97–119
- optimization, 140

Soft corrugated horns
- applications, 160
- bandwidth, 162
- defined, 160
- photo, 161

Soft dielcore horn
- applications, 165
- with artificial dielectric core, 167
- characteristics of, 164
- defined, 162
- electromagnetic wave propagation, 163
- elliptical, 165
- illustrated, 162
- performance of, 164
- propagation characteristics, 164
- rectangular, 165
- reflector antenna fed by, 166
- thickness, 163
- *See also* Dielcore horns

Soft horns
- characterization of, 158–59
- classifications of, 186–88
- concept of, 158
- defined, 158
- as hybrid-mode horns, 159–60
- illustrated, 159
- strip-loaded, 171–72
- *See also* Hard horns

Soft meta-horns
- boundaries, 175
- boundary impedances, 180

Soft meta-horns *(Cont.)*
  co-polarization, 178
  cross polarization, 178
  defined, 176
  effective relative permittivity and permeability, 177
  experimental demonstration, 182
  feasibility study, 176–77
  implementations, 175
  nature-inspired optimization method, 179
  photo, 177
  radiation patterns, 178
  refractive index, 180, 181
  return loss, 181
  square Ku-band, 179–80
  See also Meta-horns
Spiral CP feed antenna
  absorber, 241
  axial ratio (AR), 244
  beamwidth, 243
  cavity-backed, 239, 240
  conducting plate, 238
  CP radiation, 237–38
  defined, 237
  F/B ratio, 243
  frequency response, 241–45
  gain, 245
  input impedance, 244
  parameters, 241
  radial distance, 241
  radiation patterns, 242
  spiral element, 238
Spline-profile horn, 136
Square high-efficiency horn, 111–13
  aperture efficiency, 113
  defined, 111
  design dimensions, 112
  gain of spot beams, 116
  gain patterns, 115
  radiation patterns, 112
  return loss performance, 113
Square horns, 312
Square lattice array
  boresight beam, 303–4
  element spacing, 302
  planar geometry, 303
  scanned beam, 304
Stabilized bi-conjugate gradient (BiCCGStab), 24
Step-and-flared horns
  aperture efficiency, 114
  defined, 113
  performance, 114
Stepped circular waveguide with tuning blocks, 278–82
  cross polarization reduction, 280
  different block lengths, 280
  effect of block lengths on amplitude ratio, 279
  geometry, 278, 279
  input impedance matching, 279
  prototype photograph, 281
  radiation patterns, 281, 282
Strip-loaded horns, 171–73
  hard, 172–73
  soft, 171–72
Superstrate loading, 92–93
Symmetrical-cut paraboloids, 284–86

T

Tangential profile, 135
Telemetry, tracking and control (TT&C) antennas, 320–48
  applications, 322–24
  bi-conical, 329–37
  block diagram, 323, 327
  components, 322
  configurations, 329
  defined, 324
  dual-flare horn, 339–41
  EIRP budget, 328
  function of, 320–21
  global coverage, 344–48
  hemispherical, 342–44
  hybrid mode horn, 341–42
  introduction to, 299–300
  link budget, 328
  list of, 322
  locations on spacecraft, 325
  low-gain, 328–48
  Omni, 326, 328
  parameters, 323–24
  requirements for satellite payloads, 322
  subsystem, 321
  types in satellite systems, 324
  WCA, 325–26, 337–39
TE modes, 259
Tetrahedral finite elements, 31–33

Three-step horn, 110–11
TM modes, 259, 260
Two-point CP feed antennas
  conical horn, 204
  defined, 202
  parallel plate polarizer, 203
  pyramidal horn, 204
  round patch, 205
  square patch, 205
Two-step horns, 102–10

U

Uniform theory of diffraction (UTD), 43, 48
Unknown coefficients, 18, 22

W

Waveguide feeds, 56–74
  backfire, 70–74
  coaxial, 64–67
  small, 57–64
  wide angle, 67–70
Waveguides
  circular, 56, 57–60
  diameter, increasing, 5
  open-ended, 170
  round, 265
Wide angle feeds, 67–70
Wide-coverage horn antenna (WCA), 337–39
  defined, 325
  EIRP budget, 328, 337
  gain, 337, 339
  linear polarization, 324
  link budget, 328
  location on spacecraft, 325
  parameter specification, 338

Z

Z-buffer based methods, 45